

**CHEMICAL
RESEARCH,
DEVELOPMENT &—
ENGINEERING
CENTER**

AD-A256 171



12

**CRDEC-SP-000
048**

**PROCEEDINGS OF THE 1991 SCIENTIFIC CONFERENCE
ON OBSCURATION AND
AEROSOL RESEARCH**

**S DTIC
ELECTE
OCT 14 1992
A D**

**Deborah A. Clark
Janice E. Rhodes
Barbara A. Claunch**

**BATTELLE-EDGEWOOD OPERATIONS
Edgewood, MD 21040**

June 1992

Approved for public release; distribution is unlimited.

**U.S. ARMY
ARMAMENT
MUNITIONS
CHEMICAL COMMAND**



Aberdeen Proving Ground, Maryland 21010-5423

92 1-50 021

422796

92-26950



31128

Disclaimer

The findings in this report are not to be construed as an official Department of the Army position unless so designated by other authorizing documents.

REPORT DOCUMENTATION PAGE

Form Approved
OMB No. 0704-0188

Public reporting burden for this collection of information is estimated to average 1 hour per response, including the time for reviewing instructions, searching existing data sources, gathering and maintaining the data needed, and completing and reviewing the collection of information. Send comments regarding this burden estimate or any other aspect of this collection of information, including suggestions for reducing this burden, to Washington Headquarters Services, Directorate for Information Operations and Reports, 1215 Jefferson Davis Highway, Suite 1204, Arlington, VA 22202-4302, and to the Office of Management and Budget, Paperwork Reduction Project (0704-0188), Washington, DC 20503.

1. AGENCY USE ONLY (Leave blank)		2. REPORT DATE 1992 June		3. REPORT TYPE AND DATES COVERED Final, 91 Jun - 91 Jun	
4. TITLE AND SUBTITLE Proceedings of the 1991 Scientific Conference on Obscuration and Aerosol Research				5. FUNDING NUMBERS PR-10161102A71A	
6. AUTHOR(S) Clark, Deborah A.; Rhodes, Janice E.; and Claunch, Barbara A. (Compilers)					
7. PERFORMING ORGANIZATION NAME(S) AND ADDRESS(ES) Battelle - Edgewood Operations 2113 Emmorton Park Road, suite 200 Edgewood, MD 21040				8. PERFORMING ORGANIZATION REPORT NUMBER CRDEC-SP-048	
9. SPONSORING/MONITORING AGENCY NAME(S) AND ADDRESS(ES) CDR, CRDRC, ATTN: SMCCR-RSP-B, APG, MD 21010-5423				10. SPONSORING/MONITORING AGENCY REPORT NUMBER	
11. SUPPLEMENTARY NOTES POC: Edward Stuebing, SMCCR-RSP-B, (410) 671-3089					
12a. DISTRIBUTION/AVAILABILITY STATEMENT Approved for public release; distribution is unlimited.				12b. DISTRIBUTION CODE	
13. ABSTRACT (Maximum 200 words) In this report, 16 papers presented at the 1991 Scientific Conference on Obscuration and Aerosol Research are included under the headings of Physical and Chemical Properties of Aerosols, Aerosol Characterization Methods, and Optical Properties of Aerosols.					
14. SUBJECT TERMS Obscurants Aerosols Extinction Transmission Obscuration Aerosol Absorption Infrared Scattering Sizing Smoke (Continued on page 2)				15. NUMBER OF PAGES 399	
17. SECURITY CLASSIFICATION OF REPORT UNCLASSIFIED				18. SECURITY CLASSIFICATION OF ABSTRACT UNCLASSIFIED	
19. SECURITY CLASSIFICATION OF ABSTRACT UNCLASSIFIED				20. LIMITATION OF ABSTRACT UL	

14. SUBJECT TERMS (Continued)

Electromagnetic scattering	Optical constants
Millimeter wave radiation	Optical properties
Submillimeter wave radiation	Anomalous diffraction
Visible radiation	Attenuated total reflection
Electromagnetic waves	Reflection spectroscopy
Spherical particles	ATR
Mie scattering	Far-infrared
Rayleigh scattering	Refractive index
Raman scattering	Index of refraction
Concentration sampling	Inversion
Particle dynamics	Inversion techniques
Diffusive mixing	Gypsum
Aerosol growth	Natural minerals
Nucleation	Minerals
Smoke generation	Metal
Aerosol generation	Metallic particles
Photolionization	Powdered minerals
Conductivity	Complex refractive index
Chemical characterization	Effective media
Phosphorus smoke	High energy laser
Fluorescence	Particles
Aerosol clusters	Aerosol particles
Spheres	SERS
Cylinders	Surface Enhanced Raman Scattering
Rough particles	Dielectric particles
Irregular particles	Conducting particles
Nonspherical particles	Cylindrical particles
Particle aggregates	Fibers
Particle chains	Conducting fibers
Infrared emission	Gas-aerosol reactions
Cooperative scattering	Transport phenomena
Dependent scattering	Aerosol measurement
Multiple scattering	Spheroids
Radiative transfer	Laser pulses
Coagulation	Optical pulses
Condensation	Pulse propagation
Liquid drop	Clouds
Drop growth	Laser
Fog oil smoke	Radiation transport
Diesel oil smoke	Fourier analysis
Particle mechanics	Plume mechanics
Atmospheric optics	Light
Atmospheric dispersion	Plumes
Cloud dynamics	Properties
Scavenging	
Aerosol collectors	
Aerosol elimination	
Aerosol characterization	
Particle sizing	
Hygroscopic smokes	
Particle size distribution	
Particle orientation distribution	

PREFACE

The 1991 U.S. Army Chemical Research, Development and Engineering Center Scientific Conference on Obscuration and Aerosol Research was held 24 - 28 June 1991 at the Edgewood Area Conference Center of Aberdeen Proving Ground, MD. The Conference is held annually, the last full week in June, under the direction of Dr. Edward Steubing, Research Area Coordinator, Aerosol Science. This report was authorized under project number 1O161102A71A, Research in CW/CB Defense.

The Conference is an informal forum for scientific exchange and stimulation among investigators in the wide variety of disciplines required for aerosol research, including a description of an obscuring aerosol and its effects. The participants develop some familiarity with the U.S. Army aerosol and obscuration science research programs and also become personally acquainted with the other investigators and their research interests and capabilities. Each attendee is invited to present any aspect of a topic of interest and may make last minute changes or alterations in his presentation as the flow of ideas in the Conference develops.

While all participants in the Conference are invited to submit papers for the proceedings of the Conference, each investigator, who is funded by the U.S. Army Research Program, is requested to provide one or more written papers that document specifically the progress made in his funded effort in the previous year and indicating future directions. Also, the papers for the proceedings are collected in the Fall to allow time for the fresh ideas that arise at the Conference to be incorporated. Therefore, while the papers in these proceedings tend to closely correspond to what was presented at the Conference, there is not an exact correspondence.

The reader will find the items relating to the Conference itself, photographs, the list of attendees, and the agenda in the appendixes following the papers and in the indexes pertaining to them.

The use of trade names or manufacturers' names in this report does not constitute an official endorsement of any commercial products. This report may not be cited for purposes of advertisement.

Reproduction of this document in whole or in part is prohibited except with permission of the Commander, U.S. Army Chemical Research, Development and Engineering Center, ATTN: SMCCR-SPS-T, Aberdeen Proving Ground, MD 21010-5423. However, the Defense Technical Information Center and the National Technical Information Service are authorized to reproduce this document for U.S. Government purposes.

This report has been approved for release to the public.

BLANK

TABLE OF CONTENTS

I.	AEROSOL DYNAMICS	9
A.	VAPOR - PARTICLE INTERACTIONS	
	CONDENSATION OF ORGANIC VAPORS BY EVAPORATING WATER DROPS M. Seaver and J.R. Peele	9
	DETERMINATION OF ABSORPTION OF MINUTE AMOUNTS OF VAPOR IN MICRO-DROPLETS USING ELASTIC-SCATTERING DATA A.K. Ray and J.L. Huckaby	15
B.	TRANSPORT AND DISPERSION OF AEROSOLS	
	DYNAMICS OF INTEGRATED CONCENTRATION FLUCTUATIONS ACROSS PLUMES DIFFUSING IN GRID-GENERATED TURBULENCE M. Poreh, A. Hadad and J.E. Cermak	33
	FORMATION OF GRAPHITE FIBERS IN CORONA DISCHARGES J. Brock and P. Lim	41
	ACCELERATING GAS-SOLIDS DILUTE PHASE FLOW IN A VERTICAL TRANSPORT LINE H. Littman, M.H. Morgan, III, J. Paccione, X-D Fu and S. Jovanovic	47
II.	AEROSOL CHARACTERIZATION METHODS	51
A.	SPECTROSCOPY OF SINGLE PARTICLES AND AEROSOLS	
	AEROSOL ABSORPTION SPECTROSCOPY J.D. Eversole, A.J. Campillo, H.-B. Lin and C.D. Merritt	51
	LASER ABLATION MASS SPECTROMETRY OF LEVITATED MICROPARTICLES J.M. Dale, W.B. Whitten and J.M. Ramsey	57
	APPLICATION OF FACTOR ANALYSIS-RANK ANNIHILATION TECHNIQUE TO INTERPRETATION OF AEROSOL FLUORESCENCE D.L. Rosen and J.B. Gillespie	61
	A ROOM TEMPERATURE MICROPARTICLE BASED PERSISTENT SPECTRAL HOLE BURNING MEMORY S. Arnold, C.T. Liu, W.B. Whitten and J.M. Ramsey	73

B.	PHYSICAL CHARACTERIZATION - LIGHT SCATTERING & INVERSION	
	CONSTRAINED LINEAR INVERSION OF LIGHT SCATTERED FROM NON- ABSORBING, NEARLY IDENTICAL SPHERICAL PARTICLES FOR SIZE AND REAL REFRACTIVE INDEX	
	M.R. Jones, B.P. Curry and M.Q. Brewster	83
	MULTIPHASE ELECTRODYNAMIC TRAPPING AND MANIPULATION OF MICROPARTICLES	
	E.R.F. Kendall, D.S. Weyandt and M.F. Vollero	93
	SCATTERING AT AND NEAR 0° BY SPHERES AND GLASS FIBERS	
	E.S. Fry, G.G. Padmabandu and C. Oh	99
	QUASI-BINARY DECISION MAKING USING LIGHT SCATTERING	
	Po Hu and M. Lax	109
	A FINITE ELEMENT SOLUTION OF THE MAXWELL EQUATIONS FOR ABSORPTION AND SCATTERING OF ELECTROMAGNETIC RADIATION BY A SPHERICAL PARTICLE	
	L. Liebman and J. Brock	117
	SIZING SPHERES WITH THE SUBMICRON PARTICLE ANALYZER	
	J.R. Bottiger	125
	OPTICAL RECOGNITION CHARACTERISTICS OF BIOLOGICAL MICROPARTICLES - FLUORESCENCE AND LIGHT SCATTERING AS COMPLIMENTARY TECHNIQUES	
	B.V. Bronk, W.P. Van De Merwe and L. Reinisch	135
	POLARIZED IR SCATTERING USED TO IDENTIFY CONTAMINANT COATINGS OVER ROUGH SURFACES	
	S.M. Haugland, E. Bahar and A.H. Carrieri	143
	A SIDE LOOKING LIDAR FOR MEASURING CLOUD DROPLET SIZE DISTRIBUTION BY MULTIPLE SCATTERING	
	Y. Benayahu, S. Fastig, A. Cohen, R. Haracz and L.D. Cohen	157
III.	NONLINEAR EFFECTS	191
	THE EFFECTS OF PARTICLE NONSPHERICITY ON INTERNAL ELECTROMAGNETIC FIELD DISTRIBUTION	
	J.P. Barton and D.R. Alexander	191
IV.	OPTICAL PROPERTIES OF AEROSOLS	201
	BRIDGING THE GAP BETWEEN THE RAYLEIGH AND THOMSON LIMITS FOR VARIOUS CONVEX BODIES	
	G.R. Fournier and B.T.N. Evans	201

EXACT FORMULAS FOR REACTIVE INTEGRALS ARISING IN THE ELECTROMAGNETIC SCATTERING PROBLEM FOR NONHOMOGENEOUS ANISOTROPIC BODIES OF REVOLUTION D.K. Cohoon	213
SCATTERING BY SPHERES OF NARROW SIZE DISTRIBUTION R.T. Wang	227
VARIATIONAL SCATTERING CALCULATIONS WITH IMPEDANCE BOUNDARY CONDITIONS B.J. Stoyanov and R.A. Farrell	239
ON USING DIFFERENTIAL EQUATIONS TO INVERT INTEGRAL EQUATIONS DESCRIBING ELECTROMAGNETIC SCATTERING BY HETEROGENEOUS BODIES D.K. Cohoon	257
AN ALGORITHM FOR THE EIGENVALUES OF THE ANGULAR SPHEROIDAL HARMONICS AND AN EXACT SOLUTION TO THE PROBLEM OF DESCRIBING ELECTROMAGNETIC INTERACTION WITH ANISOTROPIC STRUCTURES DELIMITED BY N CONFOCAL SPHEROIDS D.K. Cohoon	269
OPTICAL AND ABSORPTION EFFICIENCIES OF, AND POWER DENSITY DISTRIBUTIONS WITHIN N LAYER BIANISOTROPIC SPHERES SUBJECTED TO ELECTROMAGNETIC WAVES R.H. Frickel and D.K. Cohoon	285
DISCRETIZATION OF INTEGRAL EQUATION FORMULATIONS OF ELECTROMAGNETIC SCATTERING PROBLEMS D.K. Cohoon	365

INDEXES FOR THESE PROCEEDINGS

A. Index of Authors	381
B. Index of Author's Organizations	383

APPENDIXES FOR THESE PROCEEDINGS

A. Photograph of 1991 Conference Attendees	385
B. List of 1991 Attendees	387
C. Conference Agenda	397

Approved For	
DTIC Class	✓
DTIC TAB	
Unannounced	
Justification	
By	
Dist. Location	
Availability Codes	
DTIC	Availability
A-1	

BLANK

PROCEEDINGS OF THE 1991 SCIENTIFIC CONFERENCE ON
OBSCURATION AND AEROSOL RESEARCH

I. AEROSOL DYNAMICS
A. VAPOR - PARTICLE INTERACTIONS

CONDENSATION OF ORGANIC VAPORS BY EVAPORATING WATER DROPS

Mark Seaver and J. R. Peele
Naval Research Lab
Code 6540
Washington, DC. 20375

RECENT PUBLICATIONS, SUBMITTALS FOR PUBLICATION, AND PRESENTATIONS:

A) M. Seaver, A. Galloway and T. J. Manuccia, "Water Condensation onto an Evaporating Drop of 1-butanol", *Aerosol Science and Technology* **12**, 741 (1990).

B) M. Seaver, J. R. Peele and G. O. Rubel, "Gas Scavenging of Insoluble Vapors: Condensation of Methyl Salicylate Vapor onto Evaporating Drops of Water", *Atmos. Environ.* (accepted for publication).

C) M. Seaver and J.R. Peele, "Condensation of Miscible and Immiscible Vapors by Evaporating Drops of Water", in *Precipitation Scavenging and Atmosphere Surface Exchange Processes*, S.E. Schwartz, ed. (American Meteorological Society, Boston, 1992).

D) M. Seaver and J. R. Peele, "Scavenging of Miscible and Immiscible Vapors by Evaporating Drops of Water", 5th International Conference on Precipitation Scavenging and Atmosphere-Surface Exchange Processes, July 15-19, 1991, Richland, WA.

Abstract:

Experiments in which a levitated a drop of water evaporates into a flowing airstream which is nearly saturated with methyl salicylate vapor show that the amount of methyl salicylate collected exceeds its solubility by a factor of 50. A simple model, which treats the methyl salicylate as an insoluble substance, accurately accounts for the amount of methyl salicylate collected. When the air stream contains the completely soluble substance, dimethyl methyl phosphonate, an extension of the model to nonideal solutions only accounts for 80% of the amount of vapor scavenged by the evaporating drop. Future work will focus on resolving this discrepancy between the experiment and the model prediction (which should be an upper limit).

Introduction:

The air/water distribution plays a central role in determining the fate and mobility of chemicals in our environment. Aqueous solution models predict that, at equilibrium, the air/water distribution can be found by applying

Henry's law. However, recent field measurements of pesticides in fog water have shown that the pesticide concentrations can exceed their solubility as predicted from Henry's law and the measured vapor concentrations by as much as three orders of magnitude (Glotsfelty et. al., 1987, 1990). The chemical similarity between pesticides and chemical agents suggests that these findings should also apply to chemical agents.

In an attempt to delineate mechanisms whereby Henry's law may be violated and therefore define the conditions under which models applying Henry's law are valid, we have begun a series of laboratory experiments where we evaporate single drops of water into a moving gas stream which contains one organic chemical vapor and varying amounts of water vapor. In this paper we report the results obtained when the organic vapors methyl salicylate (MS) or dimethyl methyl phosphonate (DMMP) are added to the gas stream. The MS simulates the pesticide paraoxon in terms of its water solubility, 0.07% by vol. The DMMP represents a low vapor pressure species which is completely soluble in water.

Experimental:

The apparatus has been described in detail (Seaver et. al., 1989). However, a brief description is in order. The experiments are carried out by levitating single drops of liquid with an acoustic standing wave in the center of the jet of a small horizontal wind tunnel. Vapors are added to the dry nitrogen carrier gas by flowing (in parallel) the nitrogen over a heated pool of each liquid. Subsequent passage through a condenser held at constant temperature then establishes the partial pressure of that vapor in the gas stream. When both water and an organic vapor are present, the separate nitrogen streams are mixed prior to entering a heat exchanger. The heat exchanger sets the ambient temperature of the gas mixture in the wind tunnel at a value somewhat higher than the saturation temperature of the organic vapor. Insulation of the wind tunnel and gas delivery apparatus allows us to run at gas temperatures above room temperature without condensation on the walls.

Model:

The model is a steady-state continuum model for condensation and evaporation that takes into account the relative motion between the drop and the gas stream and tracks the drop temperature. For a two component system the total mass of the drop is given by:

$$\left(\frac{dm_{tot}}{dt} \right) = \left(\frac{dm_w}{dt} \right)_0 \bar{f}_{v,w} + \left(\frac{dm_o}{dt} \right)_0 \bar{f}_{v,o}.$$

The drop temperature is given by:

$$T_{\infty} - T_d = \frac{D_{V,W} M_W L_W}{R k_a} \left(\frac{P_{W,\infty}}{T_{\infty}} - \frac{P_{W,d}}{T_d} \right) \left(\frac{f_{V,W}}{f_{h,W}} \right) + \frac{D_{V,O} M_O L_O}{R k_a} \left(\frac{P_{O,\infty}}{T_{\infty}} - \frac{P_{O,d}}{T_d} \right) \left(\frac{f_{V,O}}{f_{h,O}} \right).$$

A description of the parameters in these equations are given in Pruppacher and Klett (1978) ch. 13 or Seaver et. al. (1989).

For an insoluble species we assume that the substance deposits as a uniform layer on the surface of the water drop. We also assume that the presence of this layer does not effect the evaporation rate of the inner water drop (infinite diffusivity). (This assumption should be adequate for all but the thickest layers of organic liquid.) The mass of each species is calculated independently and converted to a volume. The surface area, for comparison with experiment, is then obtained by adding the volumes of the two liquids and assuming a spherical drop.

For a nonideal solution the partial pressure of a given component above the liquid is given by: $p_i = g_i x_i p_i^0$. This is substituted for $p_{w,d}$ and $p_{o,d}$ as needed. Again, for simplicity, we assume infinite diffusivity in the liquid phase. (Thus, our model establishes an upper limit on the gas-->liquid transport.) Drop volume is converted to surface area through the molar volume of the solution (V_m). V_m is obtained from the mole fractions (x_i) and the partial molar volumes ($V_{i,m}$) of the two components: $V_m = x_w V_{w,m} + x_o V_{o,m}$.

Results:

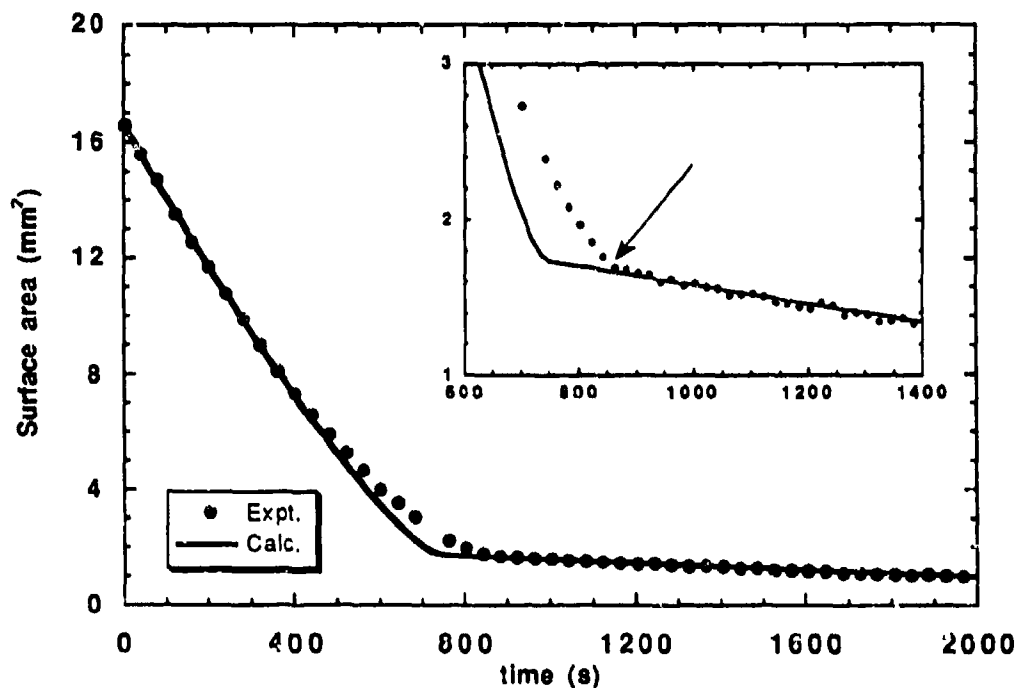


FIGURE 1. MS SCAVENGING AND MODEL COMPARISON

Fig. 1 displays the results when a drop of water evaporates in a gas stream which is nearly saturated with MS vapor ($p_{\text{MS}}=0.15\text{torr}$) but contains no water vapor. The solid circles represent every 8th experimental data point. What we see is an evaporation curve where the drop initially evaporates as a pure water drop and ultimately evaporates as a pure MS drop. Note the sudden change in the evaporation rate near 850s (marked by the arrow in the inset). Because the measured evaporation rate after this time corresponds to that of a pure MS drop, it is valid to assume that at 850s the drop is pure MS. The surface area of the drop at this point is 1.68mm^2 . The volume at this point is $2.05 \times 10^{-14}\text{m}^3$. Thus, the volume of condensed MS is 56 times greater than the volume of MS that would be dissolved in the initial waterdrop were it saturated with MS.

To investigate the mechanism by which MS condenses onto the waterdrop, we compare the experimental results with the evaporation/condensation model described in the preceding section. The model predicts that, under our experimental conditions, evaporative self-cooling reduces the waterdrop temperature to 11°C , sixteen degrees below the dew point temperature of the gas stream for the MS ($T_{\text{sat}} = -27^\circ\text{C}$). Thus, MS condensation is driven by evaporative self-cooling. The solid line in Figure 1 is the surface area predicted by our two-component model. What we see is that the model accurately predicts both the initial and final slopes of the evaporation curve. More importantly, the model predicts that at 750s the water has all evaporated leaving only a MS drop whose surface area is 1.73mm^2 . This surface area compares well with the experimentally determined value of 1.68mm^2 . The agreement between these two values demonstrates that evaporative self-cooling dominates the MS condensation.

Fig. 2 displays the results when we evaporate a pure waterdrop into a dry nitrogen stream containing DMMP vapor, $p_{\text{DMMP}}=0.71\text{torr}$. The solid circles represent the experimental data. The dashed line shows the results when the two phase liquid model that worked so well for MS is applied to the DMMP/water system. The solid line shows the results obtained from the nonideal solution model. In neither case do we get satisfactory agreement with the experimental data. What we see is that the two phase liquid model underpredicts the DMMP condensation volume by a factor of 42% while the nonideal solution model underpredicts the DMMP condensation volume by 25%. (Inclusion of finite liquid phase diffusivity in the model can only result in less DMMP condensation.) We have compared the nonideal solution model with the evaporation data for six different drops of water. The results are all similar to what we show in fig. 2. For every drop, the model underpredicts the DMMP collection volume by amounts that vary from 17% to 25%.

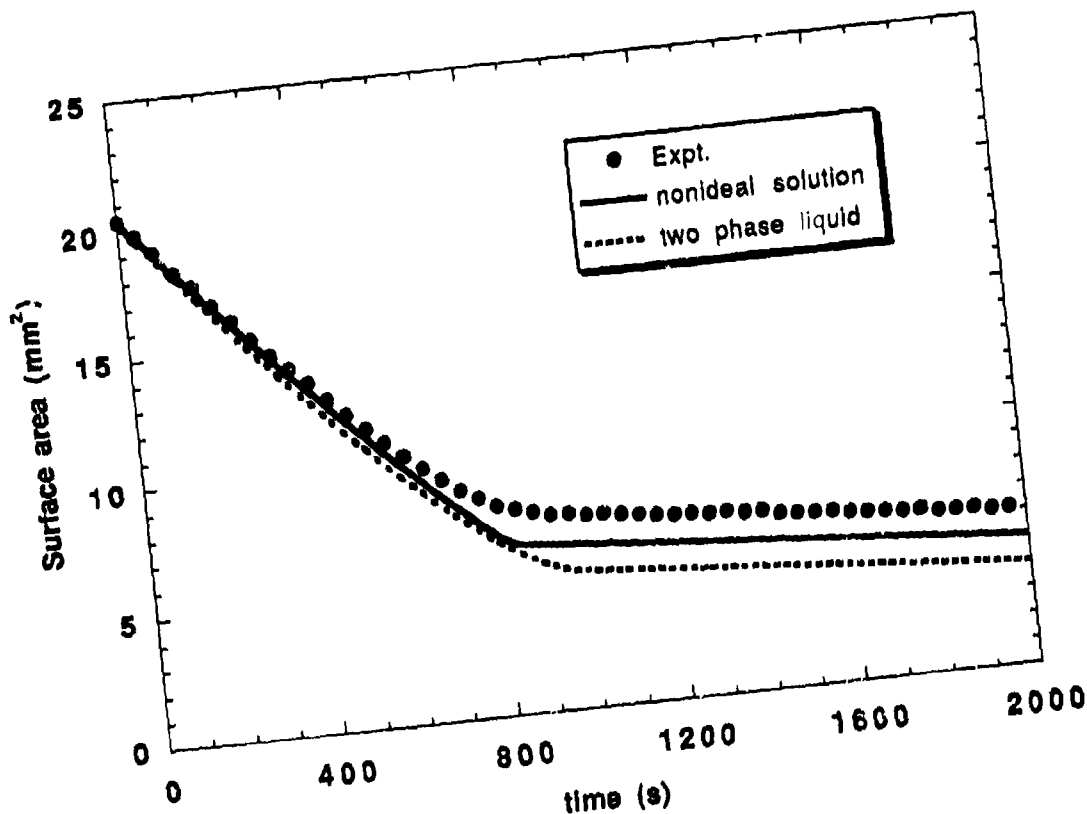


FIGURE 2. DMMP SCAVENGING AND MODEL COMPARISONS

Conclusions:

We have investigated the evaporation of individual water drops in the presence of either methyl salicylate or dimethyl methyl phosphonate vapor. A two-component continuum model, which accounts for evaporative self-cooling, accurately predicts the amount of methyl salicylate collected by the waterdrops. A nonideal solution version of this model, which should provide an upper limit, underpredicts the amount of dimethyl methyl phosphonate condensed by 20%.

The methyl salicylate results demonstrate that evaporative self-cooling can induce the condensation of large amounts of insoluble vapors onto a drop. The presence of a second liquid phase precludes the use of Henry's law as a predictor of the amount of insoluble vapor present in the liquid phase when evaporative self-cooling occurs. The amount of condensate can only be predicted provided one knows the drop history with respect to its local humidity and wind speed.

The dimethyl methyl phosphonate results are inconclusive with respect to the use of nonideal solution behavior as a predictor of liquid phase concentrations. Further experiments are required using organic molecules whose interactions with water are well characterized in order to determine what predictive methods will describe gaseous scavenging by waterdrops.

References:

Glotfelty, D. E., Seiber, J. N. and Liljedahl, L. A. (1987) Pesticides in Fog. Nature 235, 602-605.

Glotfelty, D. E., Majewski, M. S. and Seiber, J. N. (1990) Distribution of Several Organophosphorus Insecticides and their Oxygen Analogues in a Foggy Atmosphere. Environ. Sci. Technol. 24, 353-357.

Pruppacher, H. R. and Klett, J. D. (1978) Microphysics of Clouds and Precipitation, Reidel, Dordrecht.

Seaver, M., Galloway, A. and Manuccia, T. J. (1989) Acoustic Levitation in a Free-Jet Wind Tunnel. Rev. Sci. Instrum. 60, 3452-3459.

DETERMINATION OF ABSORPTION OF MINUTE AMOUNTS OF VAPOR IN MICRO-DROPLETS USING ELASTIC-SCATTERING DATA

A. K. Ray and J. L. Huckaby
Department of Chemical Engineering
University of Kentucky, Lexington, KY40506-0045.

ABSTRACT

A technique, based on transverse magnetic (TM) and transverse electric (TE) mode resonances observed in the scattered light, has been developed for the detection of trace amount of absorbed material in a microdroplet. The technique has been applied to determine absorption of immiscible water vapor in dioctyl phthalate droplets. Experiments were conducted in an electrodynamic balance where a charged droplet was suspended in the path a tunable ring dye laser. Intensities of scattered light in the planes parallel and perpendicular to the plane of polarization were detected using two photomultipliers to isolate the TE and TM resonances in the scattered light. Wavelengths of the TE and TM mode resonances were interpreted to determine the absolute size and refractive index as a function of wavelength of a pure DOP droplet. The droplet was subsequently exposed to environments with precisely controlled humidities. At each humidity level, the droplet size and refractive index changes were obtained from the observed shifts in the TE and TM resonating wavelengths. The size and refractive change data were then used to determine the absorbed amount of water in the droplet as a function of relative humidity.

INTRODUCTION

The interaction of small droplets with surrounding vapor is an important phenomenon in atmospheric, industrial and indoor air processes. Such an interaction results in absorption of molecules from the vapor phase to the droplet phase. When the vapor molecules are miscible in the liquid state with the droplet phase, droplets can remove vapor only by absorptions, and the concentration of absorbed species increases as the partial pressure of the vapor increases. Rubel¹ and Ray et al² have experimentally examined the problem of absorption of water vapor on single phosphoric acid and glycerol droplets. When the vapor molecules are partially miscible in the liquid state with the droplet phase, droplets only absorb vapor molecules as long as the partial pressure of the

vapor is below the equilibrium partial pressure corresponding to the miscibility limit. Currently no accurate technique exists for the determination of the concentration of absorbed molecules as a function of the partial pressure of the vapor if the miscibility limit of the vapor molecules in the droplet phase is small. In such a situation, data on the miscibility limit of the vapor component in the droplet phase component and vice versa are used in a thermodynamic activity model (e.g. van Laar equation) to predict the miscibility of vapor molecules as a function partial pressure.

The objective of the present study is to develop a technique for the detection of the absorbed amount of partially miscible component in a droplet as a function of its partial pressure in the gas phase. The technique is based on the precise determination of size and refractive index of a droplet from the transverse magnetic (TM) and transverse electric (TE) mode resonances observed in the scattered light as the wavelength of the incident beam is varied. This study is unique in the sense that it utilizes a technique for the determination of dispersion (i.e., variation of refractive index with wavelength) in the droplet. In previous studies involving size and/or refractive index determination from wavelength-dependent resonance spectra, either the size and refractive index were simultaneously determined neglecting the effect of dispersion³, or an absolute size was obtained using a known dispersion formula⁴. These techniques have limited applicability or accuracy. In this study these limitations are avoided by utilizing the shapes of the scattered intensity spectra as well the positions of resonating wavelengths.

THEORY

For a linearly polarized plane electromagnetic wave of intensity I_1 and wavelength λ , incident on a sphere, the far-field scattered intensities I_1 and I_2 in the planes parallel and perpendicular to the plane of polarization are, respectively, given by⁵⁻⁷

$$I_1 = \frac{I_1 \lambda^2}{4\pi^2 r^2} |S_1(\theta)|^2 \quad (1)$$

and

$$I_2 = \frac{I_1 \lambda^2}{4\pi^2 r^2} |S_2(\theta)|^2 \quad (2)$$

where

$$S_1(\theta) = \sum_{n=1}^{\infty} \frac{2n+1}{n(n+1)} (a_n \pi_n + b_n \tau_n), \quad (3)$$

$$S_2(\theta) = \sum_{n=1}^{\infty} \frac{2n+1}{n(n+1)} (b_n \pi_n + a_n \tau_n), \quad (4)$$

r ($\gg \lambda$) is the distance from the center of the sphere. The angular functions are defined by

$$\pi_n = \frac{P_n^1(\cos \theta)}{\sin \theta} \quad \text{and} \quad \tau_n = \frac{d}{d\theta} P_n^1(\cos \theta)$$

where $P_n^1(\cos \theta)$ is the associated Legendre function of degree n and order 1, and θ is the scattering angle. For a homogeneous sphere of radius a the scattering coefficients a_n and b_n , associated with the transverse magnetic (TM) and transverse electric (TE) modes can be written, respectively, in the forms^{8,9}:

$$a_n = \frac{A_n(x, m)}{A_n(x, m) + iC_n(x, m)} \quad (5)$$

$$b_n = \frac{B_n(x, m)}{B_n(x, m) + iD_n(x, m)} \quad (6)$$

where

$$A_n(x, m) = \psi_n(x) \psi_n'(mx) - m \psi_n(mx) \psi_n'(x) \quad (7)$$

$$B_n(x, m) = m \psi_n(x) \psi_n'(mx) - \psi_n(mx) \psi_n'(x) \quad (8)$$

$$C_n(x, m) = \chi_n(x) \psi_n'(mx) - m \psi_n(mx) \chi_n'(x) \quad (9)$$

$$D_n(x, m) = m \chi_n(x) \psi_n'(mx) - \psi_n(mx) \chi_n'(x) \quad (10)$$

where $\psi_n(x)$ and $\chi_n(x)$ are the Ricatti-Bessel functions of the first and second kinds of order n , respectively, $x = 2\pi Na/\lambda_0$ is the size parameter, $m = N_1/N$ is the relative refractive index, and N_1 and N are the refractive indices of the sphere and surrounding

medium corresponding to the the vacuum wavelength λ_0 , respectively.

For given relative refractive index m and a mode number n , the denominators of the scattering coefficients a_n and b_n , vanish for an infinite number of complex values of the size parameter x , and the complex frequencies corresponding to these values are called the natural frequencies or modes of vibration of a sphere. These vibration modes can not be excited by an imposed field whose frequency is real, and thus, no resonance in the strict sense can be observed. However, when the imposed frequency is the same as the real part of a natural frequency, the denominator reduces to a minimum, and the scattering amplitude achieves a maximum value. For practical purposes these maxima are considered as resonances. For a dielectric sphere (real m), the functions A_n , B_n , C_n and D_n are real, and the scattering coefficients are complex except at the resonances which occur for the values x for which $C_n(x, m) = 0$, or $D_n(x, m) = 0$. At a resonance, a_n or b_n is real and reaches a peak value of 1 as the imaginary part goes from a positive to a negative value. The locations of the peaks of the coefficients can be calculated from the roots of $C_n(x, m) = 0$, and $D_n(x, m) = 0$ or from the roots of the characteristic equations obtained by equating the denominators of Eq.(5) and (6) to zero. The real roots of the former equations are identical to the real parts of the complex roots of the latter equations¹⁰. Resonance peaks associated with the scattering coefficients a_n and b_n , are referred to as TM and TE mode resonances, respectively.

The width of a peak depends on the imaginary part of the root, and decreases with smaller imaginary part. In general, for a given mode number n , the width of a peak increases as the order ℓ of the root of $C_n(x, m) = 0$, or $D_n(x, m) = 0$ increases where the first positive root is labeled as $\ell = 1$, and for a given order the width decreases as the mode number n increases. The width of a peak of a given mode and order also decreases as the refractive index increases. Probert-Jones⁹ has provided relations that approximately provides the width of a peak of a given mode and size parameter. The approximate spacing between two successive order resonances of the same mode and polarization is given by^{20,22}

$$x_{n+1, \ell+1} - x_{n, \ell} \approx \frac{\pi}{\rho} \quad (11)$$

where $\rho = (m^2 - 1)^{\frac{1}{2}}$. The approximation is valid for large values of x (≥ 30), and the accuracy increases as the size parameter x increases. Similarly, the approximate distance

between two resonances of successive modes having the same order and polarization can be obtained from the following expression^{9,11}

$$\Delta x_0 = x_{n+1,\ell} - x_{n,\ell} \approx \frac{\tan^{-1}\rho}{\rho} \quad (12)$$

Recently, Chýlek¹² has shown that the above relation is accurate to within 1% if $(n - x) < 4$, and for $(n - x) \geq 4$, the following relation applies

$$\Delta x_m = x_{n+1,\ell} - x_{n,\ell} \approx \frac{x \tan^{-1}[(mx/n)^2 - 1]^{\frac{1}{2}}}{n[(mx/n)^2 - 1]^{\frac{1}{2}}} \quad (13)$$

Equations (11) to (13) can be used to determine an approximate droplet size from a wavelength-dependent intensity spectrum in which resonances of successive order and mode can be identified.

Due to the presence of slight asphericity and small imaginary component in the refractive index, extremely narrow resonances cannot be detected experimentally. For a given experimentally detectable peak width limit the observable lowest order resonance depends on the size parameter. For example, for a detectable limit of peaks with full width at half maximum $\Delta x_{\frac{1}{2}} \geq 10^{-3}$, the lowest order resonance detectable for $m = 1.4750$, is 3 when $x \approx 30$, and is 16 when $x \approx 200$. Higher order resonances due to their increasing widths overlap with resonances of other mode, and moreover, their contributions become comparable with higher mode terms. As a result, these resonances become indistinguishable in an elastic scattering spectrum. Only a two to four successive order resonances of a given mode, with the lowest order being dictated by the size parameter, can be observed in an elastic scattering spectrum. Moreover, a detectable resonance may not be observed in the scattered light at all angles. Whether a particular resonance will be observed in a measured spectra depends on the contribution of the resonating term to the overall sum as indicated by Eqs.(3) and (4). The number of observable resonances in scattered light depends on the scattering angle. The maximum number can be detected in the backscattering ($\theta = 180$), and this is followed by the forward scattering ($\theta = 0$) direction, since for a given mode the coefficients associated with TE and TM mode contribute oppositely in backscattering, whereas in forward scattering they contribute identically. Moreover, the resonances of both modes appear in these two directions. At any other angle, the relative contributions of TE and TM mode coefficients for a given

mode number n , are dictated by the functional values of π_n and τ_n at that angle. At $\theta \cong 90^\circ$, $\tau_n/\pi_n \gg 1$ when $x > 100$, and as a consequence, the terms due to transverse electric modes dominate over the terms due to transverse electric modes in Eq.(3) while a reverse situation occurs for Eq.(4). For $x > 100$, intensities of scattered light at around $\theta = 90^\circ$, in the planes parallel and perpendicular to the plane of polarization of the incident beam can be approximated by

$$I_1(\theta \cong 90^\circ) \cong \frac{I_0 \lambda^2}{4\pi^2 r^2} \left[\sum_{n=1}^{\infty} \frac{2n+1}{n(n+1)} b_n \tau_n(\theta \cong 90^\circ) \right]^2 \quad (14)$$

$$I_2(\theta \cong 90^\circ) \cong \frac{I_0 \lambda^2}{4\pi^2 r^2} \left[\sum_{n=1}^{\infty} \frac{2n+1}{n(n+1)} a_n \tau_n(\theta \cong 90^\circ) \right]^2 \quad (15)$$

Thus, only TE mode resonances are observed by a detector recording $I_1(\theta \cong 90^\circ)$, and only TM mode resonances by a detector recording $I_2(\theta \cong 90^\circ)$. Equations (14) and (15) form the basis for the design of the experimental system for the present study.

On the basis of the theory, an experimental scattered intensity data at a fixed angle as a function of the size parameter can be interpreted to obtain particle size and refractive index. Intensity versus size spectra can be measured two ways: (i) using a fixed wavelength laser beam for an evaporating or growing droplet, and (ii) by varying the wavelength of the incident beam for a droplet with an invariant or a slowly changing size. The former method is useful to situations where the droplet size changes significantly. The variable wavelength method used in the present study provides highly accurate size and refractive index information for a droplet with an invariant size, and can be used to detect minute size and refractive index changes that occur due to the absorption of a trace amount of vapor. Moreover, the technique can be used to detect the formation of an adsorbed layer on the surface of a spherical particle.

An intensity spectrum obtained by varying the incident wavelength shows a series of resonances. The positions of resonating wavelengths along with the shape of the intensity spectrum are used for the absolute size and refractive index determination. Since the positions of the resonating wavelengths depend on the size and refractive index of a droplet, the positions change when the size and refractive index of the droplet change due

to the absorption of a vapor. The data on the shifts of the resonating wavelengths can be utilized to determine minute size and refractive index changes. Since in the present study we examined the absorption of a vapor which is relatively immiscible in the liquid state with the component of the droplet, we had to assure that the droplet remained homogeneous when it was exposed to the vapor, that is, an absence of a second phase in the form of a layer on the surface of the droplet. The data of the present experimental scheme can precisely discern the presence of a layer on the surface of a droplet. The theoretical basis for such a discrimination can be understood on the basis of the theory of scattering by a coated sphere. Equations (1) through (4) apply for scattering by a coated sphere. However, the expressions for the scattering coefficients a_n and b_n , depend on the inner size parameter $x_c = 2\pi a_c/\lambda$, the outer size parameter $x = 2\pi a/\lambda$, and the relative refractive indices of m_c and m of the inner core and outer layer, respectively. The expressions for the scattering coefficients for a coated sphere were derived by Aden and Kerker¹³, and can be found in references 6 and 7. The scattering coefficients for a coated sphere also show resonance features similar to a homogeneous sphere. However, for two droplets, one homogeneous and one layered, having identical amounts of two components, the position of a resonance for the homogeneous droplet differs the position of the same order and mode resonance for the coated droplet. When a homogeneous droplet undergoes changes in the

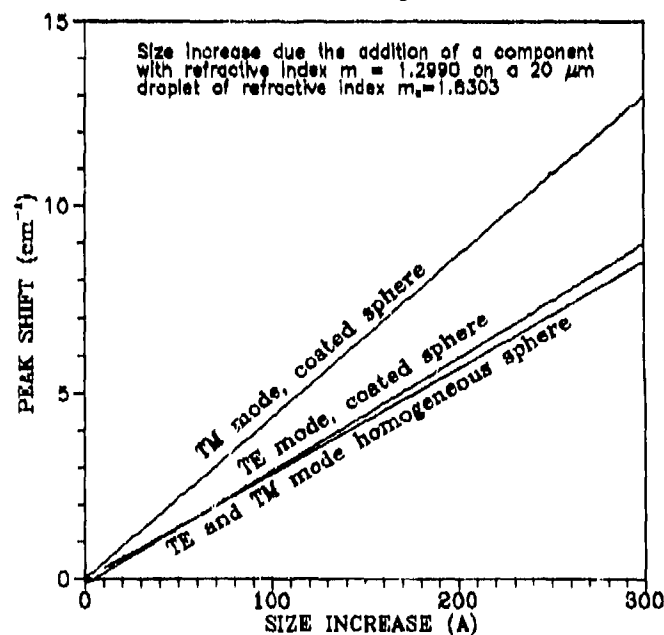


Figure 1. TE and TM resonance peak shifts for homogeneous and coated droplets

size and refractive index during an absorption process, its resonating wavelengths of TE and TM modes shift by almost equal amounts. However, for a size change due to the formation of a layer the shift of a resonating wavelength of TE mode differs from the shift of a resonating wavelength of TM mode. The difference between the shifts depends on the difference between the refractive indices of the core and layer. Figure 1 shows calculated shifts of a TM and a TE mode resonances of a 20 μm

size droplet with a refractive index $m = 1.6303$ due to the homogeneous and

inhomogeneous addition of a component with a refractive index $m_0 = 1.2990$. The results show that as long as the droplet remains homogeneous TE and TM resonances shift almost identically, and the shift increases as the size increases. When the component is added in the form of a layer, the shift of a resonating wavelength of TE mode is lower than the shift of a resonating wavelength of TM mode, and is also almost identical to the situation where the droplet remains homogeneous. Since in the present experimental scheme TE and TM resonances are detected individually by two separate detectors we can precisely determine the formation of a layer on a droplet by comparing the shifts of resonances of the two detectors.

EXPERIMENT

Experiments were performed on single charged dioctyl phthalate (DOP) droplets in an electrodynamic balance which consists of two central ring electrodes and two endcap electrodes above and below the central electrodes. An a.c. voltage drives the central ring electrodes while a bipolar d.c. potential is applied across the endcap electrodes. A schematic of the experimental system is shown in Figure 2. The balance is mounted inside a sealed chamber whose temperature is controlled to within $\pm 0.05^\circ \text{C}$ by using a constant temperature water circulator. A air stream, selected from a dry and a humid stream, enters through a port at the base of the chamber, and flows past a suspended droplet. The humid air is generated by passing a dry air stream through a flask of heated water and successively through West and Graham condensers. A second constant temperature water circulator is used to control the dew point of the air leaving the chamber.

A tunable ring dye laser beam entering vertically through a hole in the bottom electrode is used to illuminate the droplet. The wavelength of the laser beam can be varied continuously in the range of 560 nm to 610 nm. The laser is computer controlled, has its own wavemeter with a resolution of 1 part in 10^7 , and a linewidth less than 10^{-6} nm. Two fixed-position photo-multiplier tubes (PMT's) are arranged to measure the intensity of light scattered by the droplet in the planes parallel and perpendicular to the plane of polarization of the laser beam. Both PMT's are placed at about $\theta = 90^\circ$, and collect scattered light with an acceptance angle of $\Delta\theta = 0.05^\circ$. As discussed in the theory section, the PMT in the plane parallel to the plane of polarization of the incident beam detects only the TM mode resonances while the other PMT detects only TE mode resonances.

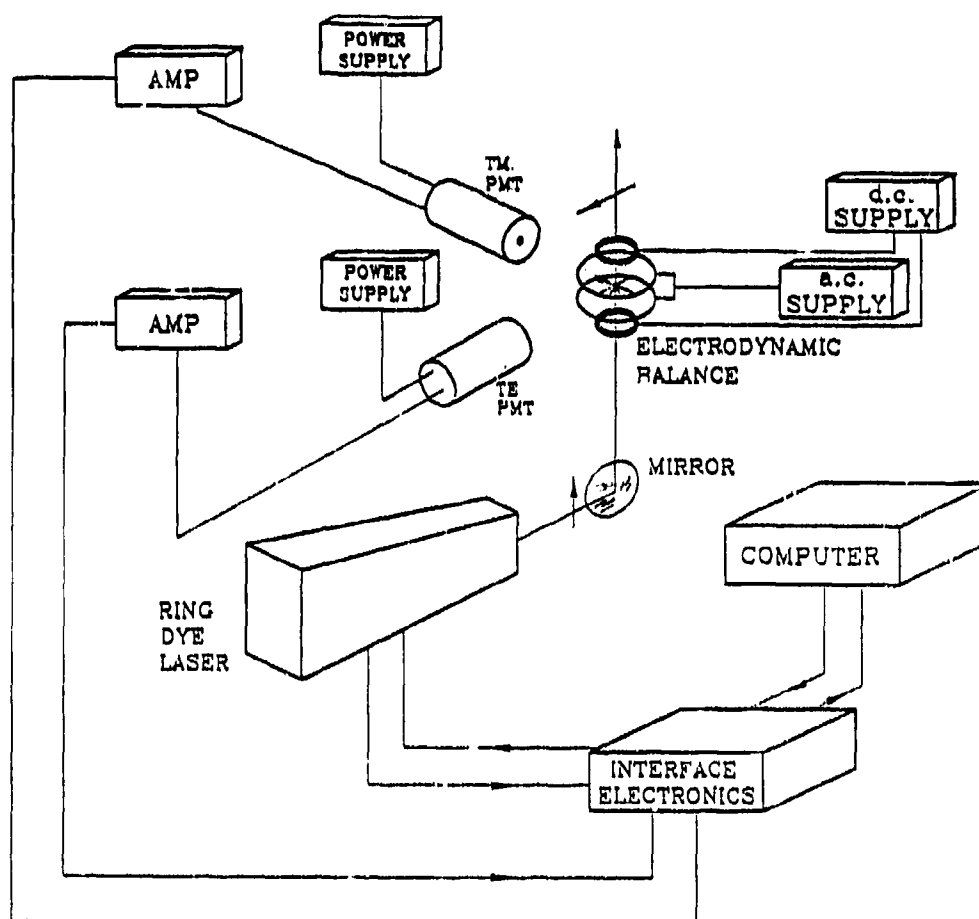


Figure 2. A schematic of the experimental system

In a typical experiment, a DOP droplet was suspended into a steady stream of dry air, and the laser was scanned from 17100 cm^{-1} to 17600 cm^{-1} with data being collected at intervals of 5000 MHz (0.1667 cm^{-1}) to establish the positions of sharp resonances, and an approximate droplet size. The regions around the observed sharp resonances from both the detectors were then rescanned with a data interval of 250 MHz (0.00833 cm^{-1}) to determine the positions of the resonances more accurately. After determining the resonance locations in the dry air stream, a steady humid stream was introduced by switching off the dry stream. The positions of the sharp resonances from each of the detectors were monitored until the droplet growth due to the change in humidity terminated. After establishing new positions for the resonances, the humid air stream was switched off and dry air was reintroduced. The entire process was repeated for various humidity levels.

RESULTS AND DISCUSSIONS

In the present study, to estimate the amount of absorbed water in a droplet as a function of the relative humidity, we needed to determine the absolute size and refractive index of the droplet when exposed to dry air, and then determine the change in the droplet size and refractive index when the humidity of the surrounding air was altered. To this purpose, the resonances of successive modes having the same order was first visually identified from the patterns observed in the experimental intensity versus wavelength spectra of the droplet. The approximate size corresponding to an assumed refractive index was estimated from Eq.(12). Plots of the theoretical scattered intensity as a function of the size parameter corresponding to the range of experimentally scanned wavenumbers were compared with the experimental spectra from the two detectors. The process was repeated for a number of refractive indices, and it was found that over a range of refractive index both TE and TM mode experimental intensity spectra showed good visual agreements with the theoretically calculated spectra. In this range, a change in the refractive index shifted the theoretically calculated spectra to higher or lower size range without affecting the visual appearances as well as the mode and order numbers of the individual resonances. This means that the accuracy with which size can be determined is inter-related with the accuracy with which refractive index is known. The visual matching provides an acceptable range for the refractive index and a corresponding range for

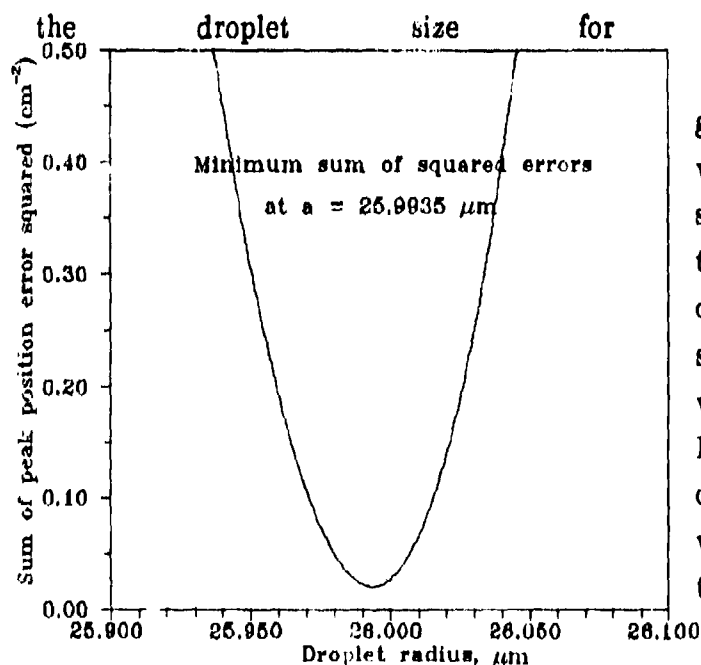


Figure 3. Sum of squared error in peak alignment as a function of size

Even though the theoretically generated spectra for over a range of wavelength independent refractive index showed excellent visual agreements with the experimental spectra, the positions of all the resonances in the observed spectra could not be aligned perfectly with those calculated from the theory. However, the positions of a number of observed resonances over a small wavenumber range could be aligned with the positions of the theoretically

calculated resonances for a given refractive index. This indicated the existence of dispersion, and we needed a model for dispersion for a comparison between the theory and experiments. In this study we chose Cauchy dispersion formula given by

$$m = A + B\omega^2 + C\omega^4 \quad (16)$$

where ω is the wavenumber in vacuum. This formula can describe the dispersion of a compound in the region where no absorption bands are present¹⁴.

The problem now involves determination of four parameters, the droplet size and the constants of the dispersion formula, from the experimental resonance positions. As mentioned before the position of a theoretically computed resonance peak depends on the refractive index, that is,

$$x_{n,\ell} = f(m) \quad (17)$$

where $x_{n,\ell}$ is a resonance of n th mode and ℓ th order. The form of $f(m)$ is dictated either by Eq.(9) for TM mode or Eq.(10) for TE mode. Equation (17) suggests that for an assumed droplet size a , in the acceptable size range obtained from the visual matching, we can align an observed resonance in the experimental spectrum of a given mode with the corresponding peak in the theoretical spectrum of the same mode by adjusting the refractive index. We followed this procedure to obtain a refractive index $m_{i,obs}$ corresponding to the each observed resonating wavenumber, $\omega_{i,obs}$. The set $m_{i,obs}$ versus $\omega_{i,obs}$ data points were fitted to Eq.(16) using a regression routine which provided the best estimates for the parameters A,B and C. The resulting dispersion formula was then used, with the assumed droplet size a , to calculate theoretical resonance peak positions $\omega_{i,cal}$. An estimate of error between the observed and calculated peak positions was obtained using the following equation

$$\phi(a) = \sum_{i=1}^N (\omega_{i,obs} - \omega_{i,cal})^2 \quad (18)$$

where N is the number of observed resonances. Using a computer program with a double precision accuracy, this procedure was repeated by changing the droplet size by $\pm \Delta$, and a minimum in the error estimate ϕ , was obtained. The minimum value of ϕ is assumed to be

associated with the best determination of the droplet radius and its dispersion. The function ϕ , is a smooth function of droplet radius and has only one minimum. Figure 3 shows the value of ϕ as a function of radius for the resonances observed in the light scattered by a DOP droplet. The minimum value of ϕ for this droplet occurs at a droplet radius $a = 25.9935 \mu\text{m}$, and the corresponding dispersion formula is given by

$$m_{\text{DOP}} = 1.4627815 + 9.5402029 \times 10^{-11} \omega^2 - 4.88811802 \times 10^{-20} \omega^4 \quad (19)$$

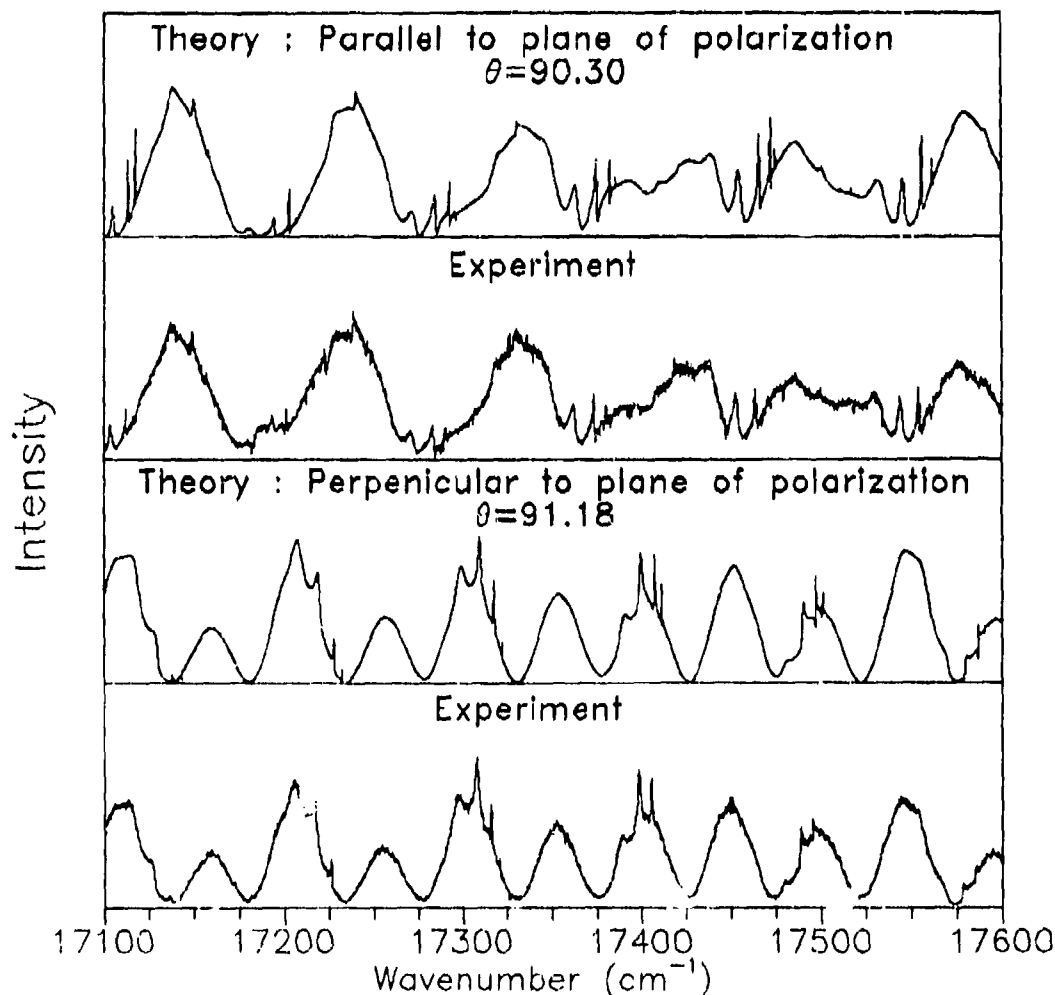


Figure 4. Comparison between experimental and theoretical spectra for a DOP droplet.

The theoretical intensity spectra calculated for the estimated size and dispersion formula are compared with the experimental spectra in Figure 4. Except for the absence of

very sharp resonances in the experimental spectra, the theoretical and experimental spectra show excellent agreements. The absence of sharp resonances in the experimental spectra is, as discussed before, due to the presence of slight imaginary component in the refractive index which has been neglected from consideration in the present study. A comparison between the theoretical and experimental resonance peak positions is given in Table I. The results show that a maximum difference of 0.075 cm^{-1} between the observed and calculated values of resonating wavenumbers. This difference corresponds to an error of about 1 \AA in the estimate for the droplet radius.

Table I. A comparison between the observed and calculated peak positions

Observed resonance peak position cm^{-1}	Calculated resonance peak position cm^{-1}	Mode number	Order number
16788.862	16788.833	281	21
16878.637	16878.712	287	21
16968.512	16968.506	289	21
17237.266	17237.298	295	21
17322.150	17322.120	293	22
17501.930	17501.767	297	22
16938.033	16937.971	288	21
17028.078	17028.095	290	21
17207.948	17207.971	294	21
17560.536	17560.577	298	22
17650.561	17650.576	300	22

After we introduced humid air into the chamber the droplet size increased due to the absorption of water vapor, and as a consequence, the resonances of TE and TM modes observed in the dry environment shifted to lower wavenumbers. We continuously monitored one resonance peak of each mode as a function of time after each step change in the humidity level. When the positions of these two peaks indicated a cessation of droplet

growth, we determined the positions of a number of resonances of both modes. Figure 5 shows the shifts of a TE and a TM mode resonances of a droplet from dry environment to when it reached equilibrium with the surrounding air having a relative humidity of 94%.

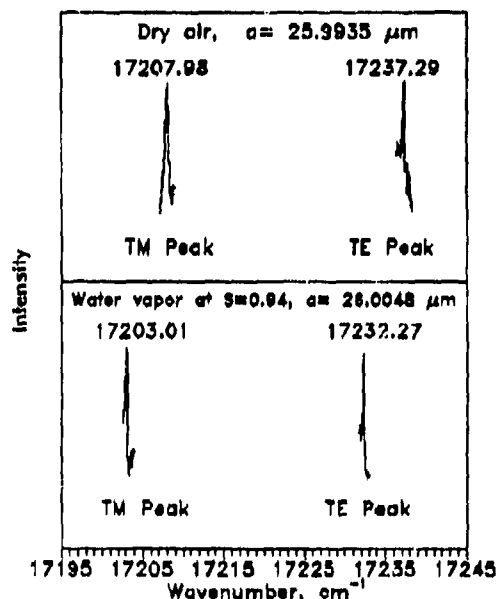


Figure 5. Shifts TE and TM resonance peaks due to absorption of water.

underwent ideal volumetric mixing, and that the droplet was a single phase, homogeneous solution of DOP and water. Furthermore, we assumed that the refractive index of a homogeneous solution of DOP and water can be described by

$$m(\omega) = m_{DOP}(\omega)v_{DOP} + m_{H_2O}(\omega)v_{H_2O} \quad (20)$$

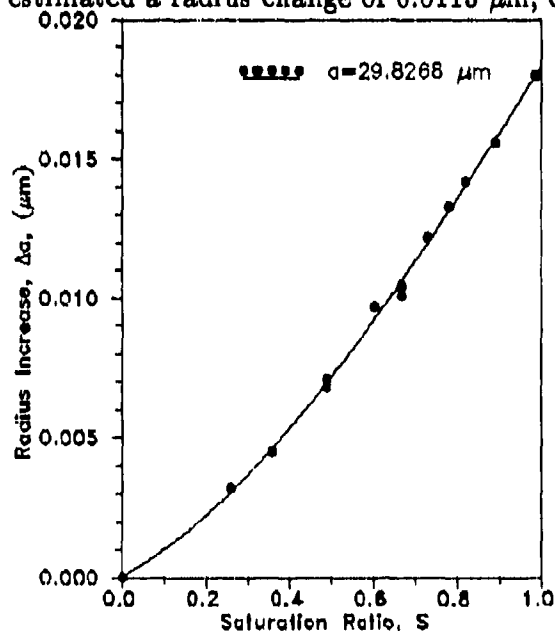
where v and m are the volume fraction and pure component refractive index, respectively, of the subscripted species. The following dispersion formula¹⁵ was used for water at 25°C

$$m_{H_2O}(\omega) = \left[1.7602512 - \frac{1.17487 \times 10^6}{\omega^2} + \frac{0.4345906 \omega^2}{6.742816 \times 10^8 - \omega^2} \right]^{\frac{1}{2}} \quad (21)$$

Assuming an initial value for the volume of water absorbed by the droplet, we estimated the droplet size and its refractive index using Eq.(20). Using the size and refractive index we calculated the theoretical shifts of the resonance peaks observed under a humid environment, and compared the calculated shifts with the observed values.

Successive approximations were then used to find the volume of water that when added to the DOP droplet in dry environment results in a droplet radius and refractive index which in turn cause the observed shifts of the resonance peaks. The resultant estimate of absorbed water by this successive approximation scheme was always found to be unique and unambiguous.

For the peak positions shown in Figure 5, the TM mode peak shifted by 4.97 cm^{-1} and the TE mode peak shifted by 5.01 cm^{-1} when a pure $25.9935 \text{ }\mu\text{m}$ radius DOP droplet was exposed to a relative humidity of 94%. Both the peaks shifted by almost the same wavenumbers, indicating that the droplet remained homogeneous after the exposure to the humid air. Using the successive approximation procedure described above, we estimated a radius change of $0.0113 \text{ }\mu\text{m}$, or the final droplet radius after equilibration with

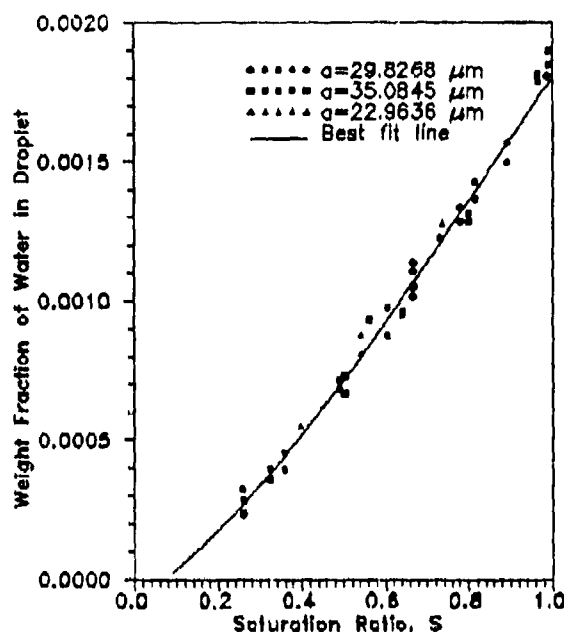


water vapor at 94% relative humidity was 26.0048 .

Figure 6 shows the calculated size change of a droplet as a function of the saturation ratio of water vapor. The results show the droplet size increases monotonically as the saturation ratio of water vapor increases. The size increase of a droplet due to the absorption at a given saturation ratio depends on its initial size. However, the equilibrium weight fraction of water in a droplet at a given saturation ratio is independent of its size. To

Figure 6. Droplet size change as a function water saturation ratio.

examine the reproducibility of our results we have plotted in Figure 7 the observed weight fraction of water as a function of the saturation ratio of water vapor for three different droplets having different initial radii. The results show that all three droplets have almost identical water content at a given saturation ratio, thus, demonstrating the reproducibility of the experimental data.



CONCLUSIONS

We have developed an experimental scheme by which TE and TM mode resonances can be recorded separately by two detectors located on the planes parallel and perpendicular to the plane of polarization of the incident beam. We have used the experimental system to obtain intensity spectra from single suspended droplets. By matching the shapes of the spectra with the theoretical spectra, and by aligning the observed resonance peaks with theoretical peak positions, we have simultaneously determined the size of and

Figure 7. Weight fraction of water in different droplets as a function of saturation ratio.

the dispersion in a droplet. The results show that the absolute size can be detected with a resolution of 1 nm, and the size change with a resolution of 1 Å. From the observed shifts of resonating wavelengths of TE and TM modes, we have detected minute amounts of absorbed material in a droplet. The technique used in this study can also be used to detect the formation of a layer on the surface of a droplet. Results on adsorbed layers on single particles will be presented in a future paper.

REFERENCES

1. G. O. Rubel, *J. Aerosol Sci.* **2**, 551 (1981).
2. A. K. Ray, R. D. Johnson, and A. Souyri, *Langmuir* **5**, 133 (1989).
3. P. Chylek, V. Ramaswamy, A. Ashkin, and J. M. Dziedzic, *Appl. Opt.* **22**, 2302-2307 (1983).
4. S. C. Hill, C. K. Rushforth, R. E. Benner, and P. R. Conwell, *Appl. Opt.* **24**, 2380-2390 (1985).
5. H. C. van de Hulst, *Light Scattering by Small Particles* (Dover, New York, 1981).
6. M. Kerker, *The Scattering of Light and Other Electromagnetic Radiation* (Academic Press, New York, 1983).

7. C. F. Bohren, and D. R. Huffman, *Absorption and Scattering of Light by Small Particles* (Interscience, New York, 1983).
8. P. Chýlek, *J. Opt. Soc. Am.* 63, 699–706 (1973).
9. J. R. Probert Jones, *J. Opt. Soc. Am.* 1, 822–830 (1984).
10. P. R. Conwell, P. W. Barber, and C. K. Rushforth, *J. Opt. Soc. Am.* 1, 62–67 (1984).
11. H. M. Nussenzveig, *J. Math. Phys.* 82–124 (1969).
12. P. Chýlek, *J. Opt. Soc. Am. A* 7, 1609–1613 (1990).
13. A. L. Aden and M. Kerker, *J. Appl. Phys.* 22, 1242 (1951).
14. M. Born, and E. Wolf, *Principles of Optics* (Macmillan, New York, 1964, p. 95–96)
15. L. W. Tilton and J. K. Taylor, *J. Res. Nat. Bur. Std.*, 20, 419–442 (1938).

BLANK

B. TRANSPORT AND DISPERSION OF AEROSOLS

DYNAMICS OF INTEGRATED CONCENTRATION FLUCTUATIONS ACROSS PLUMES DIFFUSING IN GRID-GENERATED TURBULENCE

Michael Poreh, Avichai Hadad
Technion-Israel Institute of Technology
Haifa 32000, Israel

and

Jack E. Cermak
Colorado State University
Fort Collins, Colorado 80523

RECENT PUBLICATIONS, SUBMITTALS FOR PUBLICATION, AND PRESENTATIONS:

- A) M. Poreh and J. E. Cermak, "Small Scale Modeling of Line Integrated Concentration Fluctuations," J. of Wind Engineering and Industrial Aerodynamics, 36 (1990) 665-673.
- B) M. Poreh and J. E. Cermak, Wind Tunnel Measurements of Line Integrated Concentrations," Atmospheric Environment, 25A, No. 7 (1991) 1181-1187.
- C) M. Poreh and J. E. Cermak, "Fluctuations of Integrated Concentrations Across a CO₂ Plume Diffusing in Grid Generated Turbulence," Eighth International Conference on Wind Engineering, London, Ontario, Canada, 8-12 July 1991.
- D) M. Poreh, A. Hadad, and J. E. Cermak, "Fluctuations of Line Integrated Concentrations Across a Plume Diffusing in Grid-Generated Turbulence," Final Report to CRDEC through the U.S. Forest Service (in preparation).
- E) A. Hadad, M. Stiassnie, M. Poreh, and J. E. Cermak, "Fractal Aspects of Integrated Concentration Fluctuations Across Plumets," Submitted to the Oholo Conference to be held in October 1991.

INTRODUCTION

The dynamics of concentration fluctuations is of considerable basic and practical interest. The visibility of an object viewed through aerosol plumes is determined, for example, by the instantaneous value of the integral of the concentration along the line of vision. As the instantaneous concentrations in turbulent flows fluctuate strongly in time and space, one is interested in estimates of the probability that instantaneous values exceed the mean or other critical values, and in the time variation and intermittency of the concentration fluctuations. The correlation of statistical properties of the concentration fluctuations with those of the turbulence in the flow is also of interest, as it provides a better understanding of the dynamics of diffusing plumes and enables prediction of diffusion characteristics when turbulence data are available. A fast-response IR/CO₂ system for measuring the fluctuations of IC, see Figure 1, has been developed and is described in Poreh and Cermak [1,4]. The system has been previously used to study the statistical properties of Vertically Integrated Concentrations (VIC) across plumes diffusing in simulated atmospheric surface

layers [3-5]. To advance understanding of turbulent diffusion of plumes, the fluctuations of Integrated Concentrations (IC) along lines normal to a plume diffusing in grid-generated turbulence, which is one of the simplest and most studied turbulent flows, have been measured and analyzed. Initially, a grid with relative porosity $p = 0.54$ was used to generate the turbulence. During the analysis of the data it was suspected that the flow might have been affected by possible coalescence of jets from neighboring openings in the grid. It was therefore decided to repeat the measurements with a more porous grid; $p = 0.64$. Differences between the two experimental series (I and II) were not large, although the scatter of the data in Series I was larger. Only data from Series II are presented in this paper.

THE EXPERIMENTAL SYSTEM AND PROCEDURES

The experiments were conducted in the Industrial Wind Tunnel at the Fluid Dynamics and Diffusion Laboratory at Colorado State University. The experimental system for measuring IC is schematically described in Figure 1. A plume of carbon dioxide (CO_2) mixed with helium (He), to produce a neutrally buoyant mixture, was generated in the wind tunnel. The horizontal exit velocity of the gas at the source was matched with the mean velocity in the wind tunnel, which was set to approximately $U = 2.5$ m/sec. A blackbody was used to emit infrared (IR) radiation toward a circular sapphire window (4 mm diameter) at the floor of the wind tunnel. The IR beam crossed a light chopper and a calibration chamber. It was then focused on liquid nitrogen cooled Indium-Antimonide Photovoltaic IR detector [InSb(PV)], with a narrow-band ($4.257 \pm 0.04 \mu\text{m}$) optical filter. The amplified AC signal from the detector and the reference frequency of the light chopper were fed via a preamplifier to a lock-in amplifier which produced a DC signal proportional to the intensity of the IR beam. The signal was then filtered ($f_c = 160$ Hz) and digitized at 600 samples/s. The response of the system was determined using calibrated mixtures of CO_2 in nitrogen, which filled the calibration chamber. The distance of the source from the grid area in all the experiments was constant, ($x_0/M = 20$). A detailed description of the system is presented in [7].

PRESENTATION AND ANALYSIS OF THE RESULTS

Mean and fluctuating dimensionless values of $IC^*(t) = ICM^* + ic^*(t)$, defined as $IC^* = IC U M/Q$, where U is the mean velocity, M is the mesh size of the grid, (7.62 cm), and Q is the strength of the source, were calculated from the data. The lateral distributions of $ICM^*(y)$ were found to be Gaussian, namely: $ICM^* = ICM^*(0) \exp[-(y)^2/(2\sigma^2)]$, where $\sigma(x)$ is the local lateral length parameter of the plume. Typical measurements of IC^* at different off-center locations at a distance of $x/M = 20$ downwind of the source plotted versus the dimensionless time $T^* = tU/M$ are shown in Figure 2. The measurements show that values of $IC > 0$ were continuously recorded at the centerline of the plume, whereas the appearance of an IC signal at off-center locations was intermittent. Figure 3 shows the lateral distribution of the dimensionless rms/mean values of IC^* . The data suggest that the IC^* fluctuations at different distances from the source are similar, in the sense that they are functions of y/σ and almost independent of x , at least in the range of the experiments: $20 < x/M < 120$.

Many statistical characteristics of the fluctuations are described by the Probability Distribution Function (PDF) $P(IC^*/ICM^*)$, defined so that $P(a)$ is

equal to the probability that the relative instantaneous value $IC^*/ICM^* \geq a$. Figure 4 shows the measured PDFs at different off-center locations at $x/M = 20$. Figure 5 shows the measured PDFs along the centerline of the plume. Figures 6 and 7 show the measured PDFs at other values of y/σ . Again, the data suggest an approximate similarity of the relative fluctuations at the different distances, although a small effect of the distance on the PDFs is noticed in Figure 5.

The value of $P(0)$ indicates the intermittency γ of the signal, namely the percentage of time for which $IC = 0$ was measured. The measured values of the intermittency are presented in Figure 8. These values of γ were corrected for the effect of noise, as outlined in [6]. One sees that there is no intermittency, $\gamma = 1$, near the centerline of the plume, up to approximately $y/\sigma = 0.8$.

Figure 9 shows the dimensionless spectral density distribution (SDD) of the integrated concentrations, $S^* = S(n) U / [\sigma (\overline{v_i'^2})^{1/2}]$, along the centerline of the plume plotted versus a dimensionless frequency $n\sigma/U$, where $S(n)$ is the SDD of the IC^* fluctuations. The similarity of these dimensionless distributions indicates that the time variation of the fluctuations at different distances is scaled as σ/U . A $-5/3$ inertial subrange behavior is observed at $0.5 < n\sigma/U < 1.5$, followed by a $-11/3$ law up to $n\sigma/U = 5$. A similar $-5/3$ law was observed in SDD of point concentration measurements [8-11], except that it extended to higher frequencies. It appears that the observed $-11/3$ law is the result of integrating in-plume point concentration fluctuations at this higher frequency range. Measured autocorrelations of the fluctuations are plotted in Figures 10 and 11. The data confirm the conclusion that the time variation of the fluctuations is scaled as σ/U and suggest that periods of elevated concentrations at a given distance will be of the order of σ/U or smaller.

It should be stressed that the observed similarity of the IC fluctuations, as well as that of the VIC fluctuations in plume diffusing in the ASL, is not expected to extend indefinitely. At large distances from the source, particularly where shear and surface roughness are present, the concentration fluctuations and the intermittent nature of the plume should decay and eventually disappear. It is planned to substantiate these expectations experimentally.

ACKNOWLEDGEMENTS

The work was supported by a grant from the U.S. Army Chemical Research and Development Center, Aberdeen Proving Ground, Maryland.

REFERENCES

1. Poreh, M. and J. E. Cermak, "Small Scale Modeling of Line Integrated Concentration Fluctuations," Proceeding of the Sixth U.S. National Conference on Wind Engineering, Houston, Texas, 1989.
2. Poreh, M., A. Hadad and J. E. Cermak (1989a), "Analysis of the Fluctuations of Obscuration Through a Ground Level Aerosol Source," Proceeding of the 1989 CRDC Conference on Obscuration and Aerosol Research, Aberdeen Proving Ground, MD.
3. Poreh, M., A. Hadad and J. E. Cermak, "Fluctuations of Visibility Through Ground Level Aerosol Plume," Preprint Volume, Ninth American Meteorological Society Symposium on Turbulence and Diffusion, Roskilde, Denmark, 1990.

4. M. Poreh and J. E. Cermak, "Small Scale Modeling of Line Integrated Concentration Fluctuations," J. of Wind Engineering and Industrial Aerodynamics, 36 (1990) 665-673.
5. M. Poreh and J. E. Cermak, "Wind Tunnel Measurements of Line Integrated Concentrations," Atmospheric Environment, 25A, No. 7 (1991) 1181-1187.
6. M. Poreh and J. E. Cermak, "Fluctuations of Integrated Concentrations Across a CO₂ Plume Diffusing in Grid Generated Turbulence," Eighth International Conference on Wind Engineering, July 1991.
7. M. Poreh, A. Hadad and J. E. Cermak, "Fluctuations of Line Integrated Concentrations Across a Plume Diffusing in Grid Generated Turbulence," Final Report to CRDEC through the U.S. Forest Service (in preparation).
8. Hanna, S. R., "Concentration Fluctuations in a Smoke Plume," Atmospheric Environment, 18 (1984) 1091-1106.
9. Hanna, S. R. and E. M. Insley, "Time Series Analyses of Concentration and Wind Fluctuations," Boundary-layer Meteorology, 47 (1989) 131-147.
10. Lewellen, W. S. and R. I. Sykes, "Analysis of Concentration Fluctuations from Lidar Observations of Atmospheric Plumes," J. of Climatic and Applied Meteorology, 25 (1986) 1145-1154.
11. Myline, K. R. and P. J. Mason, "Concentration Fluctuation Measurements in a Dispersing Plume at a Range of Up to 1000 m," Meteorological Office, London Rd. Bracknell, Berks, RG12 2SZ, UK, 1990.

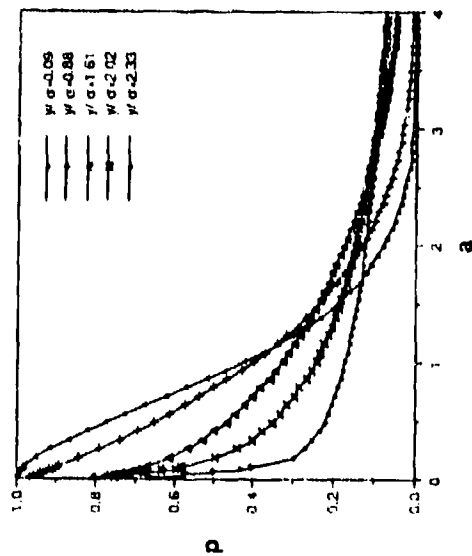


FIGURE 4. MEASURED DISTRIBUTIONS OF THE PROBABILITY THAT $IC^*/ICM^* > 0$ EXCEEDS THE VALUE a , AT $x/M = 20$.

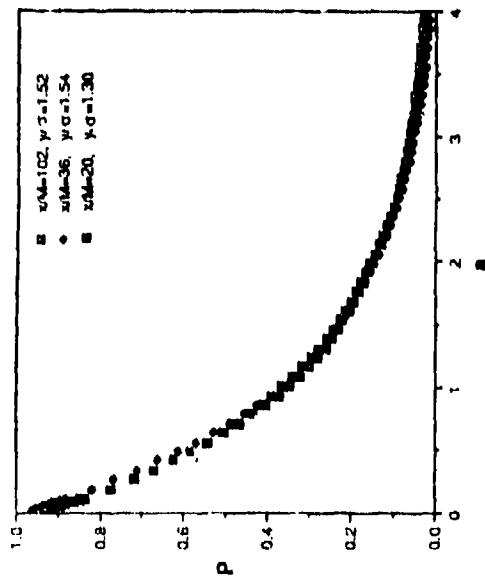


FIGURE 5. TYPICAL DISTRIBUTIONS OF THE PROBABILITY THAT $IC^*/ICM^* > 0$ EXCEEDS THE VALUE a AROUND $y/\sigma = 1.5$.

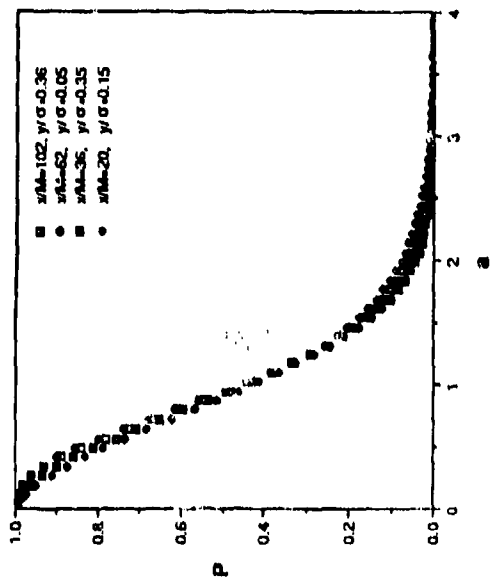


FIGURE 6. TYPICAL DISTRIBUTIONS OF THE PROBABILITY THAT $IC^*/ICM^* > 0$ EXCEEDS THE VALUE a NEAR THE CENTERLINE OF THE PLUME.

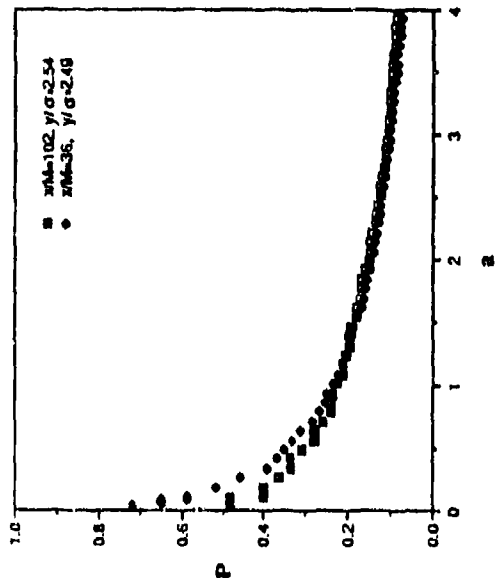


FIGURE 7. TYPICAL DISTRIBUTIONS OF THE PROBABILITY THAT $IC^*/ICM^* > 0$ EXCEEDS THE VALUE a AROUND $y/\sigma = 2.5$.

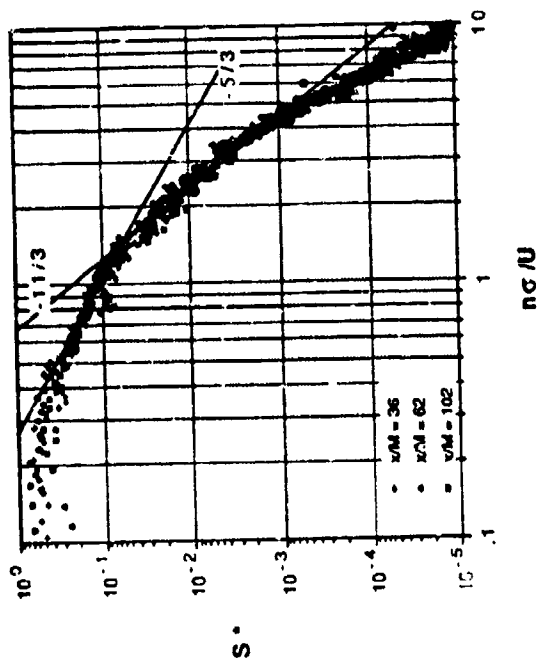


FIGURE 9. DIMENSIONLESS SPECTRAL DENSITY DISTRIBUTIONS.

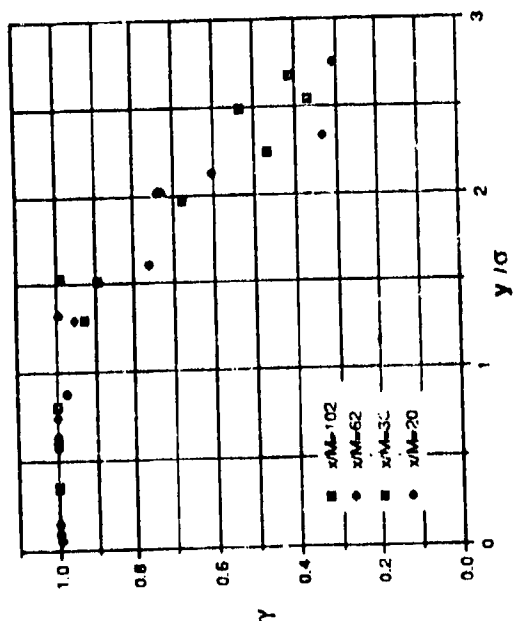


FIGURE 8. LATERAL DISTRIBUTION OF THE INTERMITTENCY ($p = 0.64$).

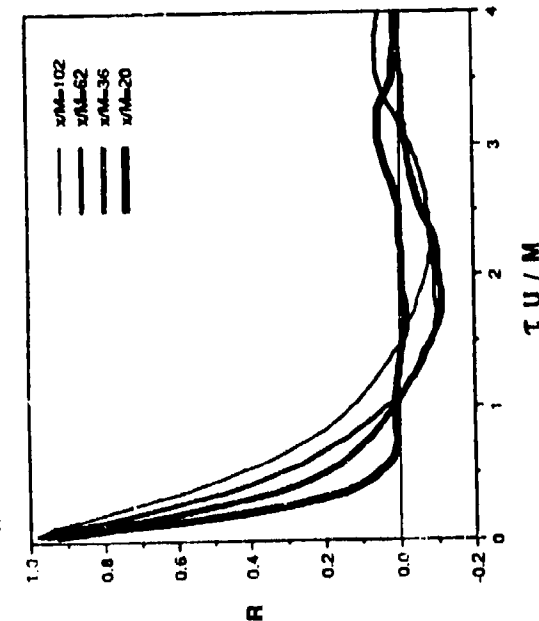


FIGURE 10. PLOT OF THE AUTOCORRELATION OF IC^* VERSUS $\tau U/M$ NEAR THE CENTERLINE OF THE PLUME.

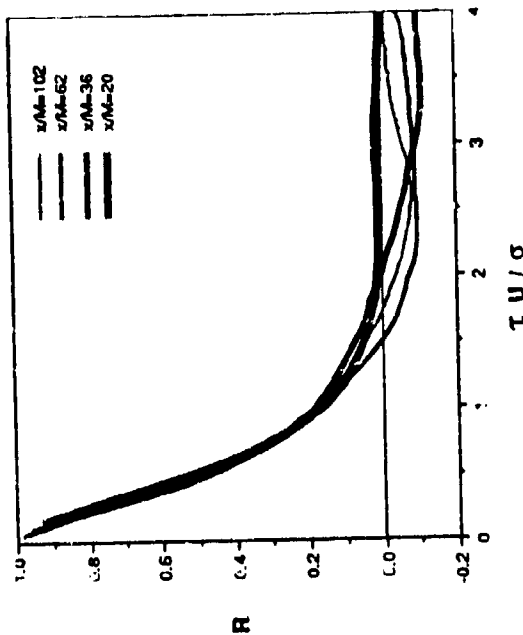


FIGURE 11. PLOT OF THE AUTOCORRELATION OF IC^* VERSUS $\tau U/\sigma$ NEAR THE CENTERLINE OF THE PLUME.

BLANK

Formation of graphite fibers in corona discharges

J. Brock and P. Lim

Chemical Engineering Department

University of Texas, Austin, Texas 78712

RECENT PUBLICATIONS, SUBMITTALS FOR PUBLICATION AND PRESENTATIONS

- "Time resolved Raman spectroscopy from reacting, optically levitated microdroplets", J. C. Carls, G. Moncivais, and J. R. Brock, *Applied Optics* 29, 2913-18, 1990.
- "Formation of carbon fibers in corona discharges", J. R. Brock and P. Lim *Applied Physics Letters*, 58,1259-1261 (1991)
- "Time-resolved Raman spectroscopy from reacting optically levitated microdroplets" J. R. Brock and J.C. Carls, *SPIE Proceedings, Nonlinear Optics and Materials* 1497,(1991).
- "Laser-induced breakout and detonation waves in droplets: II. Model", J. C. Carls, Y. Seo and J. R. Brock, *J. Optical Soc. America B*, 8,329-336(1991).
- "Anisotropic etching of SiO₂ with a 38.2 weight percent hydrofluoric acid aerosol" B. J. Jurcik, and J. R. Brock, *J. Electrochem. Soc.* 138,2141 (1991).
- "Laser-assisted wet etching of silicon", P. Lim and J. R. Brock, *Applied Physics Letters*, In Press, 1991
- "Aerosol jet etching of Hg_{1-x}Cd_xTe", *Applied Physics Letters* 56, 1682-1685(1990)(with B. J. Jurcik and I. Trachtenberg)
- "Explosive vaporization of single droplets" J.C. Carls and J. R. Brock, *J. Appl. Phys.*, In Press
- "Numerical simulation of particle formation and growth in rapidly expanding axisymmetric flows", B. J. Jurcik and J.R. Brock, *Physics of Fluids A* (In Press)(1991)
- "Laser induced etching of silicon in hydrofluoric acid", *J. Electrochem. Soc.*, 138, 2141-2145 (1991).(with P. Lim, H. Gerischer and I. Trachtenberg)
- "Finite element approach to solution of the Maxwell equations for scattering and absorption by dielectric spheres" L. Liebman and J. R. Brock, *Proceedings of the 1990 CRDEC Scientific Conference on Obscuration and Aerosol Research*, CRDEC, U. S. Army, 1991
- "A new measure for plume obscurant effectiveness", J. R. Brock, *Proceedings of the 1990 CRDEC Scientific Conference on Obscuration and Aerosol Research*, CRDEC, U. S. Army, 1991.
- "Particle formation by homogeneous nucleation in rapidly expanding flows" B. J. Jurcik and J. R. Brock, *Proceedings of the 1990 CRDEC Scientific Conference on Obscuration and Aerosol Research*, CRDEC, U. S. Army, 1991.
- "Research on aerosol plume mechanics and particle growth", J. R. Brock, Final Report, Contract DAAA15-86-K0015, Department of the Army, U. S. Army Armament Munitions Chemical Command, Chemical Research Development & Engineering Center, Aberdeen Proving Ground, MD 21010, July 1991.

ABSTRACT

During experiments on electrocatalyzed dimerization of hydrocarbons, it was observed that carbon fibers grow at the ends of corona wires during negative point-to-plane corona discharges in hydrocarbon atmospheres. Under certain growth conditions, these fibers are hollow tubes with smooth walls; under other growth conditions, the fibers are also hollow tubes, but have rough surfaces. Scanning electron micrographs of these fibers are discussed and possible applications for these fibers are noted.

INTRODUCTION

There is a large literature on the formation of carbon filaments by catalytic processes¹⁻¹⁰. Also some work has been done on fiber formation associated with electric discharges. For example, Bacon reported¹¹⁻¹³ formation of graphite whiskers in an arc struck between graphite electrodes under a pressure of 92 atm. of argon at 3900 °C. More recently, Kwong et al¹⁴ showed that hydrocarbon polymer whiskers, believed to be of polyethylene type, were formed by hydrocarbon polymerization on drift chamber wires.

We report here observations of carbon fibers grown at the ends of corona wires during negative point-to-plane corona discharges in hydrocarbon atmospheres. Under certain growth conditions, these fibers are hollow tubes with smooth walls; under other conditions, the fibers are also hollow tubes, but have rough and apparently self-similar surfaces. First, the experimental system is described. Then some scanning electron microscope (SEM) photographs of these fibers are presented and discussed.

EXPERIMENT

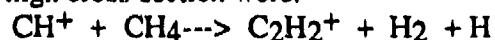
During studies of hydrocarbon reactions in negative discharges at atmospheric pressure we observed that, during negative corona discharge, fibers grew from the tips of the corona wires in a point-to plane discharge. Fig. 1 is a schematic diagram of the experimental arrangement. Fibers grew from tips of corona wires of tungsten, nickel, and platinum. Initially, the end of the negative corona wire was approximately 1.5 cm. from the plane anode and a visible corona developed at the wire tips at around -3000 volts, when fibers commenced to grow at the rate of a few mm/sec; the corona discharge was maintained thereafter from the growing fiber tip. In an alkane atmosphere, we noted that electrically conductive fibers always grew from the tip of any corona wire sustaining a corona discharge. During many of the experiments, various alkane (n-C7- n-C10) vapors in nitrogen carrier gas flowed with an average axial velocity of ~2.4 cm/sec through the reaction tube past the corona wires toward a plane aluminum anode. In other experiments, pure methane (99.9%) flowed through the reaction tube. In all cases, regardless of the alkane, either with or without flow, fibers always grew from the corona wire tips so long as a corona discharge existed. If flow ceased, the corona current and fiber growth rate tended to decrease after around a minute, apparently because of the development of space charge. In all cases the pressure in the reaction tube was one atmosphere.

At corona currents less than the order of 1. mA per wire (this obviously depends on the point to plane distance, which was here ~1 - 2 cm.), the growing fibers were found to have smooth, uniform surfaces and to be stiff with noticeable elasticity. Figs. 2-3 show a few examples of fibers grown under these conditions from n-heptane vapor. Fig. 2 shows a branched fiber with a rough surface, grown at 2 mA in n-heptane vapor, lying on a long smooth fiber which was grown at a current of around 1 mA. in n-heptane vapor. Close examination of the surface of the smooth fiber shows a seam toward the left of the figure. Fig. 3 examines a break in one of the smooth fibers; Fig. 3 shows that these fibers are hollow tubes, the one shown having a wall thickness somewhat greater than 5 μ m. Apparently, the interior surface is also smooth. Associated with the ends of these smooth tubes, we have seen many small tubes truncated at both ends at angles of from 12° to 30° with lengths of around 10 μ m and diameters of a few μ m. The mechanism of their formation remains to be determined.

At currents in excess of the order of 2 mA per fiber, the fiber morphology changes, and branching of the fiber can occur. The surface becomes rough with a pebble texture. At corona currents in excess of 1 mA in methane, the fibers have the characteristic pebble texture surface shown in Fig. 4. At the end of the fiber shown, branching has taken place, with three distinct tubes projecting from the end. Fig. 5 shows in detail the surface

of such fibers. It can be seen that the surface is not continuous, but that there are apparent voids present. Further magnification of these surfaces reveals that they may be self-similar and fractal. Fig. 6 shows a break in one of these rough surfaced fibers. Apparently, these fibers are also hollow tubes with interior surfaces matching the exterior surfaces.

Several previous studies suggest chemical mechanisms in the fiber growth process. Ion formation was investigated in a glow discharge in methane¹⁵. In this study, highest ion intensities were measured in the region close to the cathode. Some of the reactions with high cross-section were:



It seems likely that these species contribute to the formation of the graphite fibers, although close to the growing fiber tip, we suggest that hydrogen would be removed. This is consistent with conclusions from a recent study¹⁶ of carbon cluster growth kinetics indicating that a rapid mechanism exists for eliminating hydrogen from carbon clusters formed by polymer ablation.

THEORY

The surface morphology of the fibers suggests the growth mechanism. The morphologies displayed in Figs. 2,4-6 are similar to those found with ballistic growth models and in thin films formed by sputtering¹⁷. This is consistent with the occurrence of rough surfaces when corona currents are high, implying large electric fields and ballistic trajectories for charged species depositing on the growing fiber tip; at lower electric fields, diffusive motion is more important and permits deposition of hydrocarbon species to take place at preferred sites on the growing fiber tip, thereby leading to smooth, closed surfaces. It is significant that with either ballistic or diffusive deposition, hollow tubes are formed.

Models have been proposed to account for the phenomena displayed here in which growth takes place through diffusion as well as through ballistic trajectories for the monomer responsible for solids formation. A model giving surfaces very similar to those observed here has the general form:

$$\mathbf{v}_n(s) = \int_{\theta_1}^{\theta_2} \mathbf{J}(\alpha) \cdot \mathbf{n}(s) d\alpha + D \partial^2 \kappa(s) / \partial s^2 \quad (1)$$

where the two angles in limits of integration are the angles defining that part of a rough surface that can be "seen" a molecule with a linear trajectory. $\mathbf{v}_n(s)$ is the velocity of the growing surface and s is a surface position and $\mathbf{n}(s)$ defines the surface normal at s . $\mathbf{J}(\alpha)$ is the flux of monomers at s . The second term on the r.h.s. accounts for the diffusive flux of monomer.

Of course, a model of the growing fiber must allow for all the electrodynamic and ionization processes occurring in a corona discharge. Assuming pseudo stationary conditions the set of equations required for a model would be:

$$\text{div } \mathbf{J}_- = - \alpha(\mathbf{E}) \cdot \mathbf{J}_- \quad (2)$$

$$\text{div } \mathbf{J}_+ = \alpha(\mathbf{E}) \cdot \mathbf{J}_+ \quad (3)$$

where the current vectors, \mathbf{J} , are given in terms of the negative and positive charge carrier densities, their corresponding mobilities and the electric field:

$$\mathbf{J}_- = - n_- e \mu_- \mathbf{E} \quad (4)$$

$$J_{-} = n_{+} e \mu_{+} E \quad (5)$$

the electric field is given by the relation:

$$\text{div } \mathbf{E} = 4\pi e (n_{+} - n_{-}) \quad (6)$$

This set of equations would be coupled to the ion balance equations for electron impact ionization, recombination, etc. The identification of the charge carriers in a highly stressed hydrocarbon atmosphere will require spectroscopic studies. The relation for the mobilities is a complicated function of the field and must depend again on the properties of the charge carriers. Therefore, additional experimental work would be needed for testing of a complete model of the fiber growth process.

CONCLUSION

The fibers formed during the corona discharge have some interesting properties, which could be exploited for a number of purposes. It has been noted¹ that for present liquid double layer capacitors to be more effective, major improvements are necessary. For one, while the active carbon now used has high surface area, its electrical conductivity is very low. Fibers grown by corona discharge obviously have high electrical conductivity since the fibers sustain a corona discharge. The fibers grown at high currents have a complex surface, as Figs. 4-6 show. Also, these fibers might be easily produced in the presence of other chemical species, leading to fibers with interesting properties. Additional work is necessary to determine the feasibility of producing these conductive fibers using typical diesel fuels. By careful design, based on present observations, one fiber (~ 100 μm x 0.1 μm) per second could be produced at power levels of ~ 10⁻⁴- 10⁻⁶ watts. An additional subject for further investigation is the growth of diamond-like fibers in these discharges.

ACKNOWLEDGMENT

This work was supported under a contract from the Chemical Research and Development Engineering Center, U. S. Army.

REFERENCES

1. R. T. K. Baker, Carbon 27, 315-323 (1989)
2. R. T. K. Baker, M. A. Barber, P. S. Harris, F. S. Feates and R. J. Waite, J. Catal. 26, 51 (1972)
3. G. G. Tibbetts, Carbon 27, 745-747 (1989)
4. R. T. K. Baker, P. S. Harris, R. B. Thomas and R. J. Waite, J. Catal. 30, 86 (1973)
5. P. A. Tesner and I. S. Rafalkes, Dokl. Akad. Nauk. SSSR 87, 821 (1952)
6. P. A. Tesner, Y. Robinovich, I. S. Rafalkes, and E. F. Arefieva, Carbon 8, 435 (1970)
7. T. Baird, J. R. Fryer, and B. Grant, Nature 233, 329 (1971)
8. T. Baird, J. R. Fryer, and B. Grant, Carbon 12, 591 (1974)
9. M. Audier, A. Oberlin, and M. Coulon, J. Cryst. Growth 55, 549 (1974)
10. M. Audier, A. Oberlin, M. Oberlin, and M. Coulon, Carbon 19, 217 (1981)
11. R. Bacon, J. Appl. Phys. 11, 283-290 (1960)
12. R. Bacon, Bull. Am. Phys. Soc. Ser II 2, 131 (1958)
13. R. Bacon, in R. H. Doremus, B. W. Roberts, and D. Turnbull, Eds. *Growth and Perfection of Crystals*, Wiley, N. Y., 1958, p.197

14. K. Kwong, J. G. Layter, C. S. Lindsey, S. O. Melnikoff, B. C. Shen, G. J. Vandalen, and M. C. Williams, *Nuclear Instruments and Meth. Phys. Res. A* **238**, 265-272 (1985)
15. J. Rutkowsky, H. Drost, and H. J. Spangenberg in *Proceedings of the XIIIth International Conference on Phenomena in Ionized Gases*, Physical Society of the German Democratic Republic, Berlin, September 12-17, 1977, pp.385-386
16. W. R. Creasey, *J. Chem. Phys.* **92**, 7225-7232 (1990)
17. G. S. Bales, R. Bruinsma, E. A. Eklund, R. P. U. Karunasiri, J. Rudnick, and A. Zangwill, *Science* **249**, 264-268 (1990)

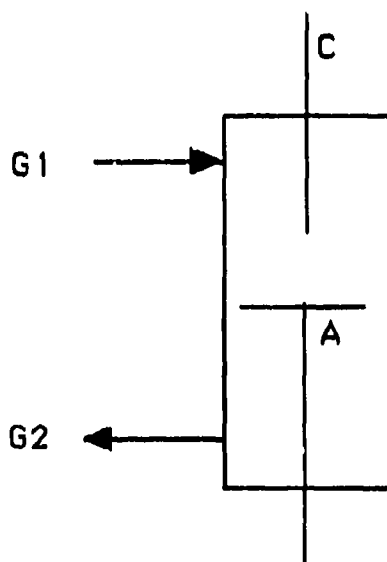


FIG. 1. Simplified schematic diagram of experimental arrangement production of carbon fibers. *C* is the cathode wire, *A* the plane anode, is a flow tube for admitting alkane vapor, *G2* the outlet for flowing alk vapor.

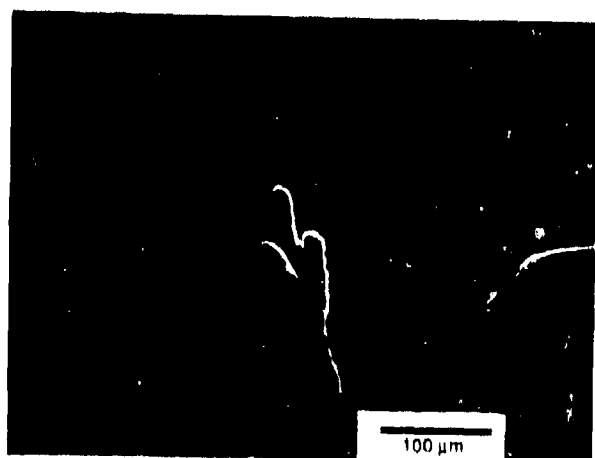


FIG. 2. Branched fiber with a rough surface grown at a corona current of ~ 2 mA lying on a long smooth fiber grown at ~ 1 mA, both in *n*-heptane vapor.



FIG. 3. Details of a break in a smooth-surfaced fiber showing that these fibers are hollow tubes.



FIG. 4. Rough-surfaced fiber grown at 2 mA in pure methane with characteristic pebble texture and branching.



FIG. 5. Detail of a rough-surfaced fiber grown in pure methane showing presence of voids. Additional magnification suggests that these surfaces may be self similar.



FIG. 6. Detail of a break in a rough-surfaced fiber showing that these fibers are also hollow tubes. Interior walls resemble the exterior surfaces.

ACCELERATING GAS-SOLIDS DILUTE PHASE FLOW IN A VERTICAL TRANSPORT LINE

H. Littman, M. H. Morgan, III, J. Paccione, X-D Fu and S. Jovanovic
Department of Chemical Engineering
Rensselaer Polytechnic Institute
Troy, N.Y. 12180-3590

RECENT PUBLICATIONS, SUBMITTALS FOR PUBLICATION, AND PRESENTATIONS:

H. Littman, M.H. Morgan, III, D.K. Prapas and G.O. Rubel, "Automated System for Measuring the Mass Flowrate of Powders in Transport Lines," NTIS No. AD-A225 560/2/HDM (1990).

Introduction

The practical difficulties in producing deagglomerated aerosol sprays of fine particles exposes the weakness in our understanding of the phenomena involved in their transport. Particles of the order of 1 micron in size tend to be cohesive, that is, they often stick together so strongly that they cannot be aerated to any extent. Unless they can be aerated they will not flow into a transport line from a hopper to produce the deagglomerated aerosol sprays needed to obscure tanks and armored vehicles from heat seeking missiles.

In this work, we report experiments with 1 mm glass particles where surface forces (van der Waal's, electrostatic, etc.) do not play a significant role in their transport through a pipe. In this way, we can focus on the purely hydrodynamic aspects of the problem which are formidable in their own right. The data will be analyzed in terms of the basic equations of dilute phase fluid and particle flow in a vertical transport line. The two unknown parameters are the interphase drag coefficient between the fluid and particles and the frictional

effects of the flow at the pipe wall. Since our application is concerned with dilute phase flow in small diameter lines, both drag forces and wall friction must be taken into account in modeling the flow.

When the particles enter the transport line from the hopper in Figure 1, they accelerate to a terminal steady flow condition. In the acceleration zone, the voidage (or solids fraction) varies significantly and it is important to describe this region properly for design purposes. For example there is a need to know the solids fraction in the spray and the pressure at the inlet to the line.

Experimental

The experiments were performed in a 28.45 mm ID stainless steel line 5.49 m in length using 1.004 mm glass particles of density 2500 kg/m³ in our computer controlled transport line. This apparatus has been described in detail (see aforementioned reference) and a schematic diagram is given in Fig. 1.

Air at a controlled temperature and pressure is fed into the feed hopper through flowmeter F_1 causing particles to be sucked into the line and to flow through it. The cyclone at the top of the line separates the air and particles leaving the line. The solids flowing through the line are collected and weighed to obtain the solids flowrate. The air flowrate is the sum of the flowrates $F_1 + F_2 - F_3$ measured by the meters.

Summary and Conclusions

The basic equations for dilute phase fluid and particle flow in a vertical transport line have been analyzed and experimental data obtained using large glass particles to test the equations. We have found that

1. The solids flowrate is sensitive to the feeder gap above V2 in Figure 1.

2. The acceleration zone is about 3 meters long for 1.004 mm glass particles. In short pipelines, the flow may be accelerating and the drag coefficient must be measured in each case at present. The non-acceleration drag coefficients are in reasonable agreement with predictions.
3. Using the experimental pressure profile and a wall friction correlation, gas velocity, particle velocity, pressure and drag coefficient have been calculated by solving continuity and momentum equations in vertical dilute phase flow.
4. The drag coefficient in the acceleration zone is not just a function of voidage as in non-acceleration flow.
5. Importance of various hydrodynamic forces in the acceleration zone.
 - a. In small diameter pipes at high voidage, the wall friction is important.
 - b. The inertia force of the particle phase diminishes with distance from inlet.
 - c. The inertia force of gas phase is negligible.
 - d. The gravitational force on the particle phase is the largest force.

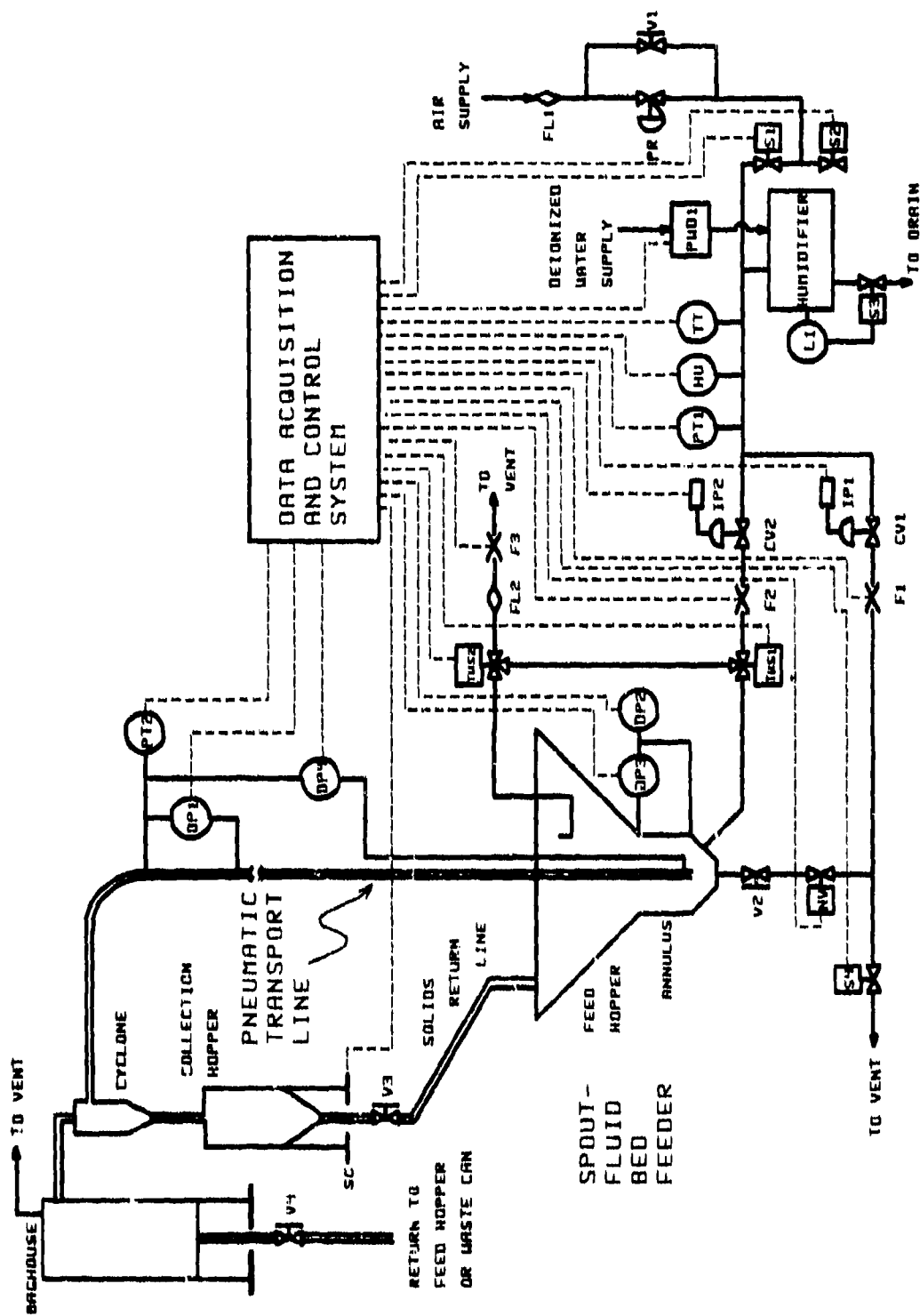


Figure 1 Schematic Diagram of Transport Line

AEROSOL ABSORPTION SPECTROSCOPY

J.D. Eversole

Potomac Photonics Inc., Lanham, MD 20706

A.J. Campillo, H.-B. Lin and C. D. Merritt
Optical Sciences Division, Naval Research Laboratory
Washington, D.C. 20375

RECENT PRESENTATIONS, AND PUBLICATIONS:

(A) J.D. Eversole, C. D. Merritt, H.-B. Lin and A.J. Campillo,
"Broadband Aerosol Absorption Measurements Using Photothermal
Interferometry with FTIR Spectrometry", Proceedings of the LEOS 1990
Annual Meeting, Boston, MA; November 1990.

(B) A.J. Campillo, J.D. Eversole and H.-B. Lin, "Cavity Quantum
Electrodynamic Enhancement of Stimulated Emission in Microdroplets",
Phys. Rev. Lett., **67** 437-40 (1991).

(C) P. Chylek, H.-B. Lin, J. D. Eversole and A. J. Campillo, "Effect of
Absorption on Microdroplet Resonant Emission Structure", Accepted by
Optics Lett., August 1991.

(D) H.-B. Lin, J. D. Eversole and A. J. Campillo, "Spectral Properties of Lasing
Microdroplets", Accepted by JOSA B, September 1991.

(E) J. D. Eversole, H.-B. Lin and A. J. Campillo, "Cavity Mode Identification of
Fluorescence and Lasing in Dye-doped Microdroplets", Accepted by
Applied Optics, September 1991.

ABSTRACT

Continuous 2 to 14 micrometer absorption spectra of aerosols may be obtained using photothermal interferometric detection in conjunction with step-scanned Fourier Transform Infrared spectrometry. Aerosol absorption of broadband black body radiation is deduced by detecting time-dependent thermally induced refractive index changes in the carrier gas interferometrically. It may be possible to extend this same approach to visible and ultra-violet wavelengths.

The technical goal of this program is to answer a "how" question regarding true optical absorption of suspended aerosols. Scattering makes traditional extinction measurements difficult to interpret. Therefore one must use some sort of indirect thermal mechanism to determine when absorption occurs. The main physical consequences of absorbed heat by a particle are changes in temperature, pressure and density of the surrounding gas.

Interferometers offer extreme sensitivity in detection of refractive index changes. For spherical particles the changes in surrounding gas refractive index and resulting phase shift in the interferometer can be estimated as shown in Fig. 1. A schematic detector arrangement is shown here with PZT driven mirror to maintain interferometer in quadrature for maximum sensitivity.

Such an interferometer detector arrangement has been utilized in prior work to detect trace amounts of ammonium sulfate aerosol in nitrogen carrier gas. The

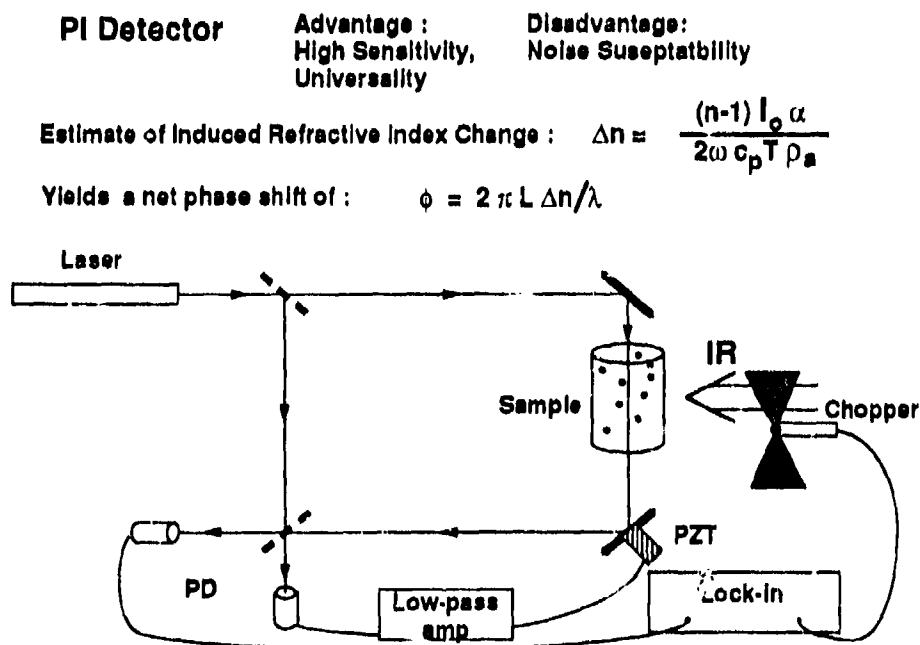


Figure 1 - Aerosol Absorption Detection Schematic

interferometer was formed with a He-Ne laser and the IR source used was a CO₂ laser. By measuring the interferometer phase shift signal for different available CO₂ laser wavelengths a minimum detectable concentration of about 9 mg/m sulfate aerosol was determined. The advantage of a laser IR source is high intensity, but its major disadvantage is lack of tuning or small tuning range. For the current project we proposed using a broadband IR source of moderate intensity similar to commercial FTIR instruments. Two design characteristics of such a source not commercially available are: (1) step-scan approach to be compatible with aerosol thermal time response, and (2) high intensity blackbody source. It should be noted that unlike traditional extinction measurements, the interferometer detector signal is directly proportional to IR intensity.

A prototype "high" intensity step-scan FTIR has been constructed and calibration tests are presently being conducted. Figure 2 shows a schematic

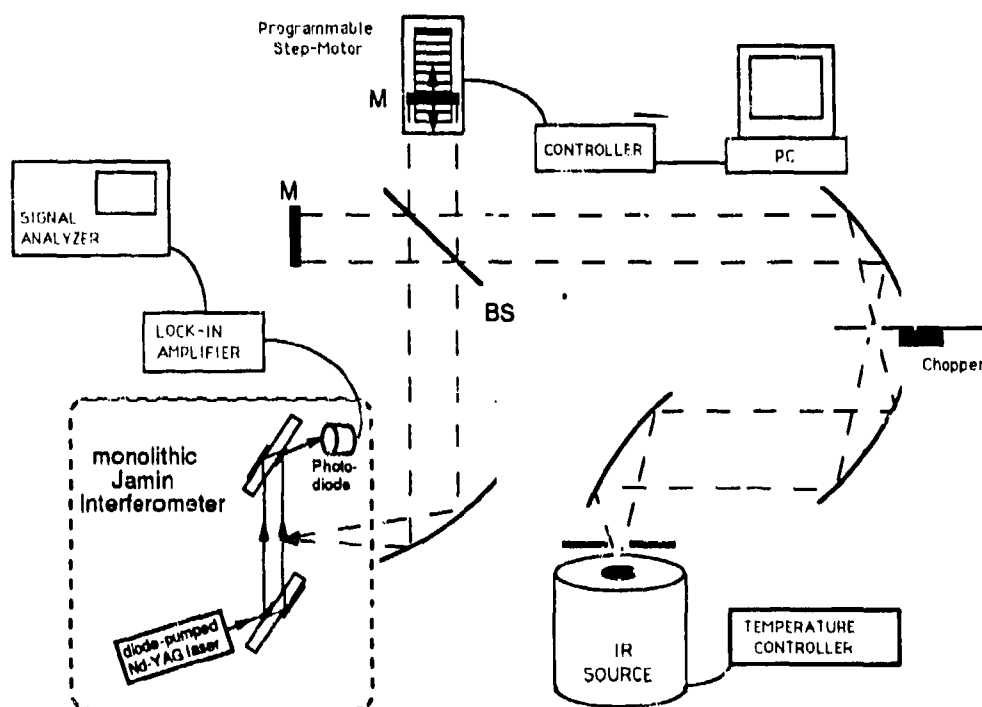


Figure 2 - Schematic of FTIR source and interferometric detector

diagram of the complete instrumentation for aerosol absorption measurement. The box indicated with the dashed line delineates the interferometric detector system, while the optical elements exterior to the box represent the "FTIR" source. Figure 3 shows two "single beam" spectra computed from interferograms obtained by attenuation measurement with an IR detector. The upper spectrum is just through normal atmosphere while the lower spectrum has a sample of tetranitromethane gas placed in the path....three additional absorption dips are seen superimposed on the normal water and carbon dioxide structure. By taking the ratio of these two spectra the normalized absorbance can be plotted as shown in Fig. 4. A similar absorbance spectrum taken on a commercial (rapid scan) FTIR is shown as an inset for comparison which shows that the constructed FTIR is functioning properly. These spectra were obtained at a blackbody temperature of only 250° C. When the temperature is increased to 950° the total IR intensity was measured to be 0.7 Watts which will provide more than 0.3 W in the average output beam of the FTIR

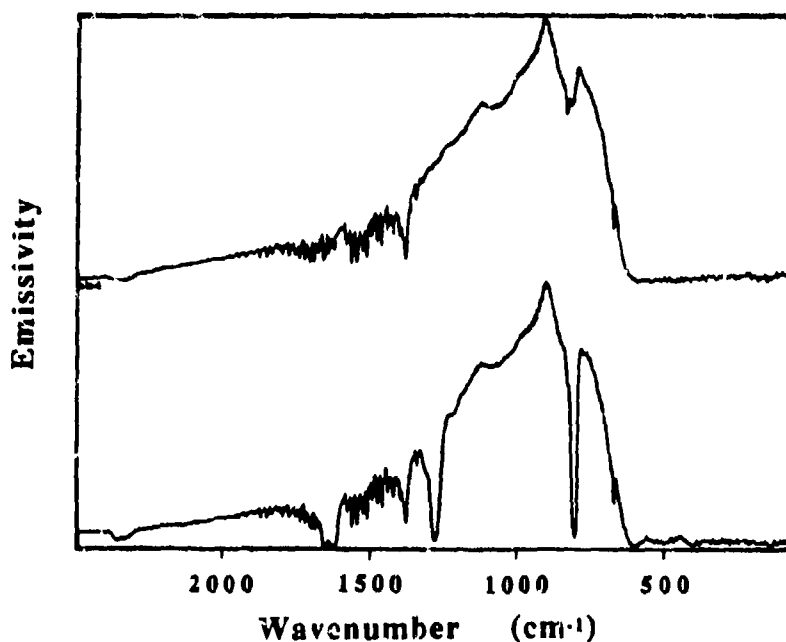


Figure 3 - Single beam absorption spectra of FTIR source

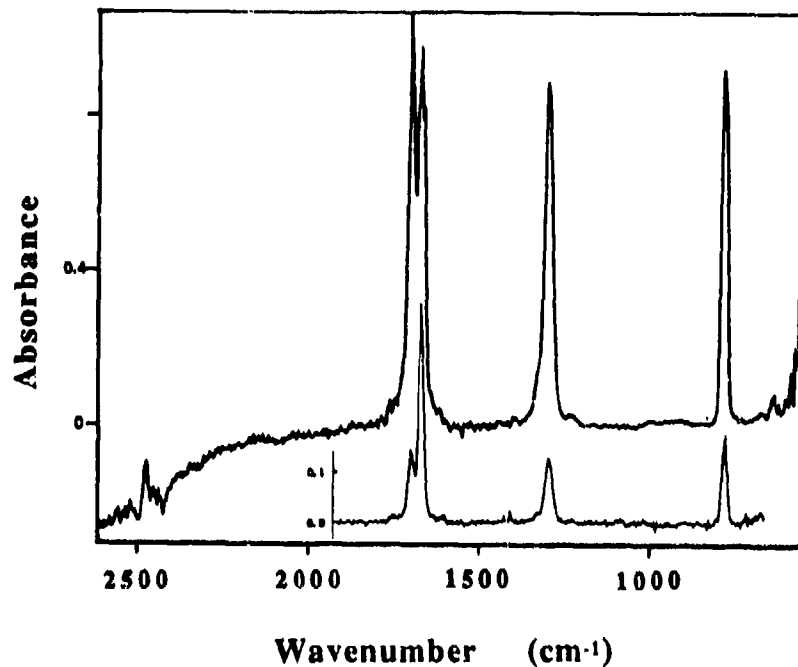


Figure 4 - Absorbance spectrum from ratio of spectra in Fig 3

Based on these measured IR intensities, calculations were performed to estimate the sensitivity of the overall system for a hypothetical aerosol absorption band having a peak absorbance of 5×10^{-3} cm⁻¹. Using the formulae similar to those shown in Fig. 1 for estimating the interferometer phase shift and integrating over the aerosol absorption band, an interferogram of the interferometer detector was computed for different assumed absorption band widths. The expected Fourier relations of higher peak and narrower width interferogram for broader absorption were readily apparent, however, the significant point of these calculations is that the magnitude of the phase shifts are on the order of milliradians which should be an achievable sensitivity.

A prototype interferometer detector using a Mach-Zehnder configuration has been constructed and was capable of easily resolving a calibration phase shift signal set at 30 mrad rms (tuned to 35 Hz). This calibration peak is 40 dB (two orders of magnitude) above the noise floor, so that even without an optimal experimental arrangement, it would appear that aerosol detection will be feasible.

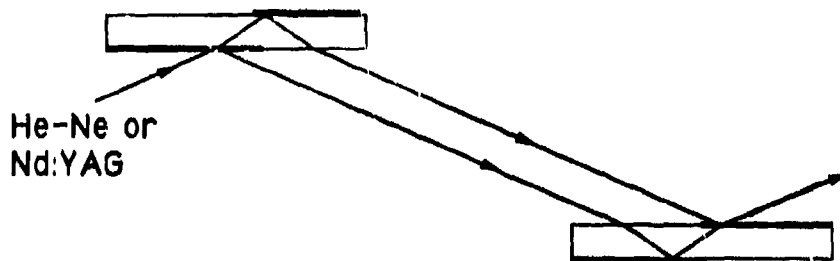


Figure 5 - JAMIN INTERFEROMETER

An interferometer aerosol detector is currently being constructed based on a Jamin configuration (having only two distinct optical elements Figure 5) to minimize mechanical noise. Actual application of the Jamin interferometer detector to measuring aerosol absorption requires good overlap of the Jamin probe beam with the IR excitation beam. The ideal case with the two beams to be colinear may not be realized due to the severe optical materials constraints. A practicable optical arrangement will most likely be a shallow angle crossed beam geometry as shown in Figure 6. The figure is shown in two perspectives to clarify that the IR beam and Jamin probe beam are in a plane orthogonal to the plane of the Jamin probe and reference beams.

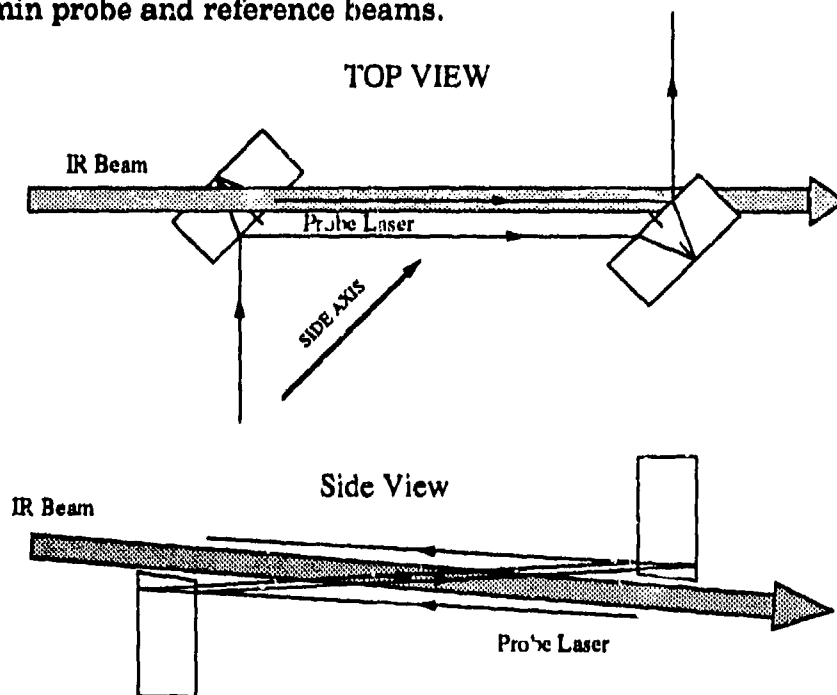


Figure 6 - Jamin interferometer and IR beam geometry

LASER ABLATION MASS SPECTROMETRY OF LEVITATED MICROPARTICLES

J. M. Dale, W. B. Whitten, and J. M. Ramsey
Oak Ridge National Laboratory
Oak Ridge, Tennessee 37831-6142

RECENT PUBLICATIONS, SUBMITTALS FOR PUBLICATION, AND PRESENTATIONS

- A) W. B. Whitten, J. M. Ramsey, S. Arnold, and B. V. Bronk, "Progress in the Detection of Single Molecules in Levitated Droplets", Proceedings of the 1990 CRDEC Scientific Conference on Obscuration and Aerosol Research, in preparation.
- B) S. Arnold, C. T. Liu, W. B. Whitten, and J. M. Ramsey, "Room Temperature Persistent Spectral Hole Burning", U.S. Dept. of Energy Contractors Workshop on Laser Spectroscopy, Oak Ridge, TN, Oct. 1990.
- C) J. M. Dale, W. B. Whitten, and J. M. Ramsey, "Laser Ablation of Microparticles in an Ion Trap Mass Spectrometer", Workshop on Laser Ablation, Oak Ridge, TN, April 8, 1991.
- D) S. Arnold, C. T. Liu, W. B. Whitten, and J. M. Ramsey, "Room-Temperature Microparticle-Based Persistent Spectral Hole Burning Memory", *Optics Lett.*, 16, 420 (1991).
- E) J. M. Dale, W. B. Whitten, and J. M. Ramsey, "Chemical Characterization of Microparticles by Laser Ablation in an Ion Trap Mass Spectrometer", Annual meeting of the ASMS, Nashville, TN, May, 1991.
- F) W. B. Whitten, J. M. Ramsey, S. Arnold, and B. V. Bronk, "Single Molecule Detection Limits in Levitated Microdroplets", *Anal. Chem.* 63, 1027 (1991).

ABSTRACT

We are developing a technique to sample levitated microparticles by laser ablation or laser desorption and analyze the resulting ions by ion trap mass spectrometry. Both the particle levitation and mass analysis will be carried out within the same quadrupole trap. Experiments with laser ablation and mass analysis of particles dropped through the trap will be described.

Charged microparticles can be levitated in a three-dimensional quadrupole by a combination of AC and DC electric fields (1) or by a DC field with optical feedback stabilization (2). With different voltage and frequency conditions, the same quadrupole can be used to confine ions and to measure their mass to charge ratio (3). We are developing techniques to produce atomic or molecular ions by laser ablation or desorption from levitated microparticles and mass analyze the ions in the quadrupole trap. These techniques will complement our work on fluorescence spectroscopy of levitated microparticles and will permit the characterization of a single microparticle by a combination of optical methods and mass spectrometry.

Our initial experiments have been made on particles falling through the trap to test these ideas with less complicated instrumentation. Light scattered by a falling particle from a weak HeNe laser beam triggers a Nd-YAG laser. A 10-ns pulse of 532-nm light is focused on the particle, ablating and ionizing a portion of its surface. The resulting ions are trapped and mass analyzed by conventional ion trap techniques (3). We have obtained representative mass spectra of quaternary alkylammonium halides (4) on the surface of silicon carbide particles in this way. A typical mass spectrum, in this case of tetraphenyl phosphonium bromide, is shown in Fig. 1. The spectrum shows the cation resulting from loss of bromine along with lines from the loss of 2 and 3 phenyl or benzene groups. Sodium and potassium appear to be present as well as smaller molecular fragments. Our present sensitivity is such that a useful mass spectrum can be obtained from a fraction of a monolayer of analyte on a 100 μm SiC particle.

Measurements have also been made on metallic particles. A spectrum obtained from a niobium particle is shown in Fig. 2. Niobium has only one stable isotope, 93 amu. The signal observed at other masses from 92 to 96 amu is presumably due to mass 93 ions that were poorly resolved. A trace of iron at mass 56 amu is also observed.

ACKNOWLEDGEMENTS

This research was sponsored by the U.S. Department of Energy under contract DE-AC05-84OR21400 with Martin Marietta Energy Systems, Inc.

REFERENCES

1. R. F. Wuerker, H. M. Goldenberg, and R. V. Langmuir, *J. Appl. Phys.*, **30**, 441 (1959).
2. L. M. Folan, S. Arnold, T. R. O'Keeffe, D. E. Spock, L. B. Schein, and A. F. Diaz, *J. Electrostat.*, **25**, 155 (1990).
3. G. C. Stafford, P. E. Kelley, J. E. P. Syka, W. E. Reynolds, and J. F. J. Todd, *Int. J. Mass Spectrom. Ion Proc.*, **60**, 85 (1984).
4. G. L. Glish, D. E. Goeringer, K. G. Asano, and S. A. McLuckey, *Int. J. Mass Spectrom. Ion Proc.*, **94**, 15 (1989).

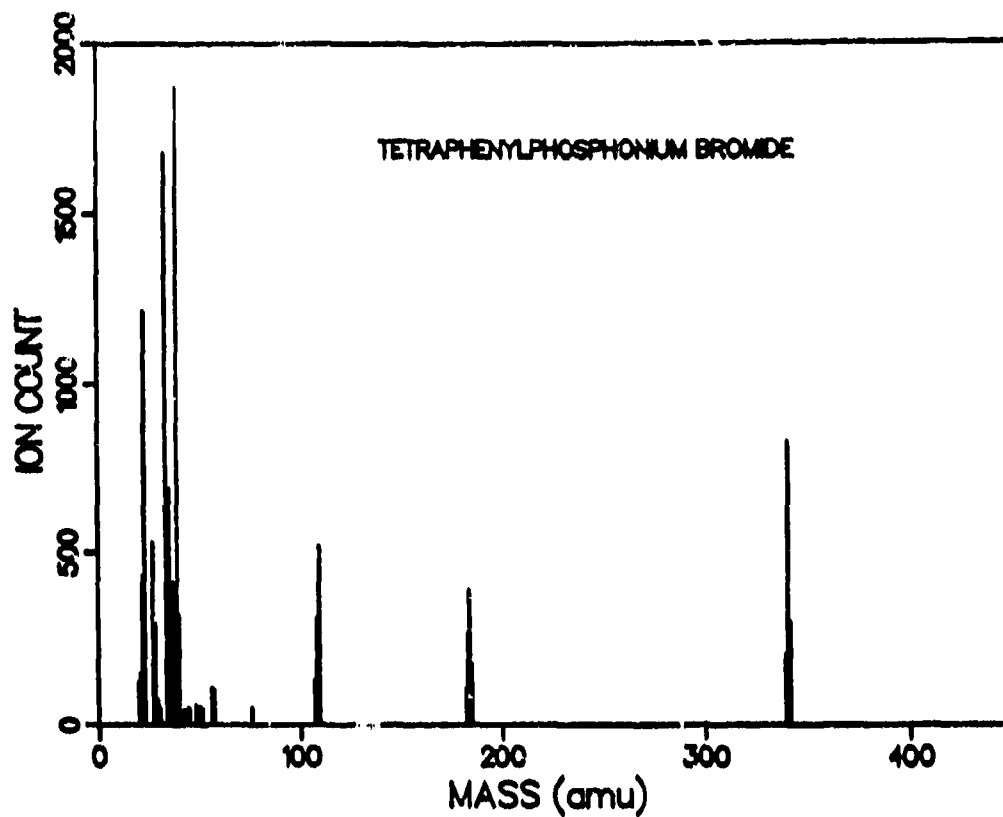


Fig. 1 Mass spectrum of laser-desorbed tetraphenyl phosphonium bromide on a silicon carbide particle.

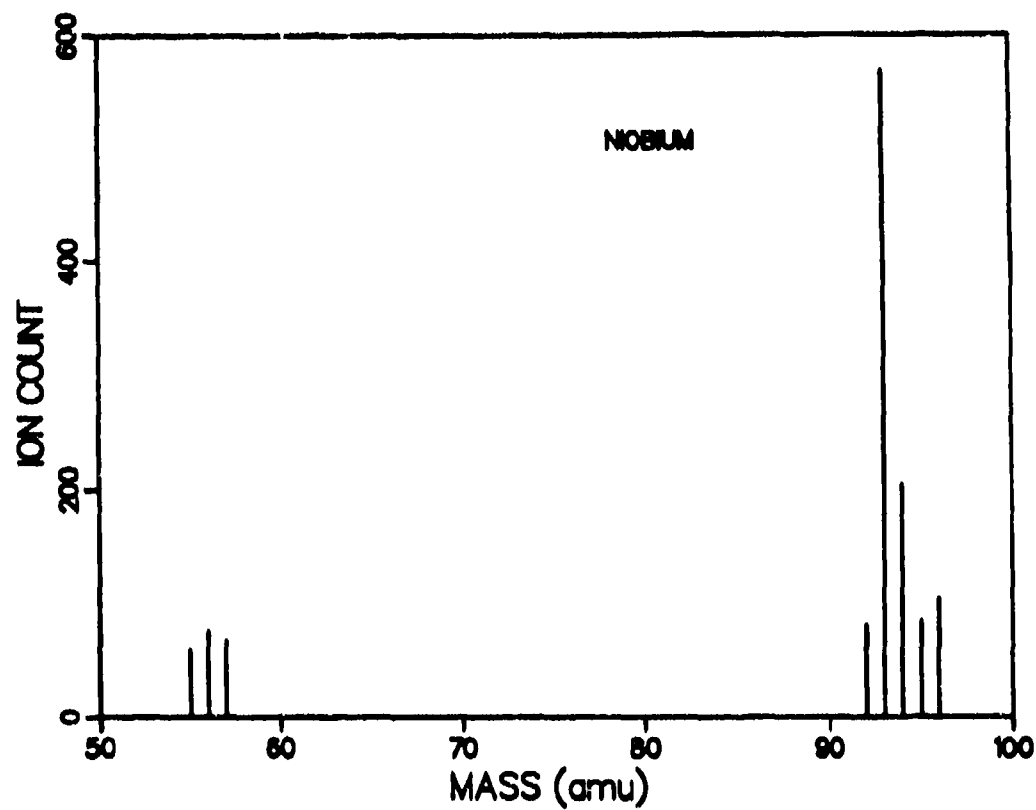


Fig. 2 Mass spectrum of laser-ablated niobium particle.

BLANK

Application of Factor Analysis-Rank Annihilation Technique to Interpretation of Aerosol Fluorescence

D.L. Rosen and J. B. Gillespie
U.S. Army Atmospheric Sciences Laboratory
U.S. Army Laboratory Command
White Sands Missile Range, NM 88002-5501, USA

I. Introduction

Laser induced fluorescence (LIF) is sometimes used for lidar because LIF spectra contain information about chemical composition. Fluorescence lidar has been limited because the LIF spectra of most constituents in the troposphere are very broad and devoid of line structure. The LIF spectra of aerosol particles do not have line structure because of inhomogeneous broadening by vibrational states. Sharp fluorescence lines from gases in the troposphere are quenched by collisional de-excitation. The broad LIF spectra from an atmospheric constituent overlaps LIF spectra from other constituents and the spectrum of sky radiance. An atmospheric constituent is not easily distinguished from the background spectra because of this overlap.

Rank annihilation-factor analysis (RAFA) is a set of algorithms for interpreting broad fluorescence spectra in complex mixtures. RAFA compares the excitation-emission matrix (EEM) of an unknown to the EEM of a calibrant. An EEM is a matrix containing the spectral intensity as a function of excitation wavelength and emission wavelength. RAFA can only detect the EEM of a calibrant within the EEM of a complex mixture under the following conditions. First, the fluorescence of the various components of the mixture should add up linearly. Second, the EEM can only be analyzed if both the number of excitation and emission wavelengths are greater than the number of fluorescing compounds in the mixture. Many more excitation wavelengths than fluorescing compounds may be necessary due to noise and uniqueness problems. This means that a wavelength tunable excitation source is necessary for RAFA.

This paper describes a computer simulation of a RAFA detection algorithm applied a hypothetical fluorescence lidar return with noise and sky radiance. Detection algorithms determine whether or not the concentration of the calibrant in an

unknown mixture is zero. Previous simulations done by us² have analyzed RAFA algorithms that can calculate only nonzero concentrations of the calibrant in the unknown mixture from a fluorescence lidar return. Noise and sky radiance were not included in our previous studies.

If the spectra of the components are both nonoverlapping and free of random noise, RAFA requires a calibrant EEM only from the compound of interest. This suggests that RAFA may be useful in remote sensing where an unknown background may also be fluorescing. However, real lidar measurements often contain large amounts of random noise and overlap. A priori information is necessary to eliminate random noise. We will show that detection by RAFA may require some knowledge of the fluorescence background in order to set a rejection level. A detailed knowledge of the fluorescence background may not be necessary if one has used the worst possible fluorescence background to set the rejection level. We consider an aerosol, fly ash, as the source of the fluorescence background in this paper. RAFA can also be applied to analyze a compound of interest in an aerosol.

II. Theory

The theory behind the simulation is described in two parts: the RAFA detection algorithm and the UVTRAN model for lidar.

A. Detection Algorithm

We used the overlap index method³ to determine the presence or absence of the calibrant compound in the mixture. The overlap index method assumes that the calibrant EEM is bilinear, i.e., the emission spectrum of the calibrant is independent of excitation wavelength. Pure compounds generally have bilinear EEM because of rapid nonradiative transitions within a molecule. The overlap index method will not work if the EEM of the calibrant is linearly dependent with a set of EEM from other components in the unknown.

We now define the overlap index, p . In the following discussion, the row vectors of an EEM correspond to emission spectra and the column vectors of an EEM correspond to excitation spectra. The overlap index method requires a bilinear calibrant EEM, N , and the EEM, D , from an unknown mixture. Then,

$$p = \frac{\sum_{i=1}^I |u_i \cdot x|^2}{\sum_{j=1}^J |v_j \cdot y|^2} \quad , \quad (1)$$

where x is a normalized excitation spectrum of the calibrant, y is a normalized emission spectrum from the calibrant, i and j are subscripts designating the significant nonzero eigenvalues of DD^T or $D^T D$, u_i is an eigenvector of DD^T associated with a significant eigenvalue, v_j is an eigenvector of $D^T D$ associated with a significant eigenvalue, and r is the number of significant nonzero eigenvalues of DD^T and $D^T D$.

The value of r is necessary for calculating a precise value of p . Underestimating r generates a numerical error in p while overestimating r causes p to be sensitive to noise and experimental error. Algorithms for finding r are available^{4,5} but were not included in this study. We simulated EEM whose values of r were known, modified these EEM using a lidar model that accounted for atmospheric effects, and then used the unmodified values of r in our calculations of p .

The overlap index, p , is used to compare spectra in a similar way to correlation functions. The overlap index algorithm will work under certain conditions even in the presence of unknown fluorescing spectra, where correlation functions can not work. If p is zero, the calibrant EEM and the unknown EEM are completely uncorrelated and the calibrant is not part of the unknown mixture. If p is one, the calibrant EEM and the unknown EEM are completely correlated and the calibrant may be part of the mixture. A detection criterion is necessary if p is between zero and one. We will propose a possible detection criterion in the Discussion section. However, this criterion requires partial knowledge of the background fluorescence.

B. Lidar Model

UVTRAN is an ultraviolet and visible wavelength atmospheric propagation model recently reported by Patterson and Gillespie.⁶ UVTRAN calculates the atmospheric extinction coefficient, optical atmospheric transmission, sky radiance, and the total lidar signal for backscatter and fluorescence. Only calculations for the atmospheric extinction coefficient have been previously described. The other parts of the model are currently being documented and verified.

A modified version of UVTRAN simulated the fluorescence lidar return signals. The new version includes RAFA analysis and photon counting (i.e., shot) noise. The calculation of photon noise required the detector integration time and fluorescence lifetime as input parameters. The new model enters the concentration and laboratory EEM of the unknown mixture, the excitation and emission spectrum of the calibrant, the

visibility, desired options, and other parameters. The program calculates fluorescence lidar returns. The overlap index is then calculated from the fluorescence lidar return as a function of distance or detection integration time.

The new model has several options concerning sky radiance and noise. The overlap index can be calculated with or without photon noise, and with or without sky radiance. Typical sky radiance can be calculated for night, overcast day, or clear day. The calculations shown are for night time sky radiance.

The fluorescence detector is assumed to be a shot noise limited photon counter. The photon detector has a shutter. The detector has a temporal window over which the detector counts photons. With photon noise, the mean collection rate of photons is calculated and multiplied by the detector integration time. The photon count is assumed Poisson distributed about the mean number of photons. Once the random number is generated, the mean sky radiance signal was subtracted from the noisy signal.

III. Computer Simulation

The following scenario was chosen for our simulation. The fluorescence lidar was being used in the troposphere to detect the presence or absence of nitrogen dioxide, NO_2 , in a plume which contained carbon particles. The overlap index for an NO_2 calibrant was calculated using simulated lidar returns from aerosol plumes with and without NO_2 as the unknown EEM. The overlap index for unknowns with and without NO_2 were compared. The computer simulation will be described in three parts: parameters for the NO_2 vapor, parameters for the carbon particles, and parameters for the fluorescence lidar apparatus.

We used emission spectra of NO_2 at 0.1 Torr pressure measured by Sakuria and Broida.⁷ The emission spectrum has two components: a broad band component and a narrow line component. The narrow band component is far more easily quenched at higher pressures than the broad band component. The simulation therefore did not include the sharp lines.

Our²⁴ simulation used a peak fluorescence cross section of $9 \times 10^{-24} \text{ cm}^2$ and a fluorescence decay time of 1.65 nsec. These values were estimated for atmospheric pressure by multiplying the low pressure values by the quenching factor. The fluorescence cross section without quenching (peak value of $3 \times 10^{-19} \text{ cm}^2$) and the quenching factor (3×10^5) at atmospheric pressure of NO_2 were taken from Measures book. The fluorescence lifetime for NO_2 of 55 μs was measured without quenching by Keyser et. al.

We chose Kansas City fly ash studied by Tucker et. al.⁹ as the background fluorescence source. Fly ash and NO₂ are often emitted together from smoke stacks. This is only² one of several possible fluorescence backgrounds because the fluorescence spectra of fly ash changes with the source.

The emission spectra of NO₂ and fly ash was measured from journal illustrations using a digitizer. The excitation spectrum in the literature was incomplete in the literature for both NO₂ and fly ash. It was necessary to interpolate the excitation spectrum from only a few points. The interpolation was done in such a way that the EEM of NO₂ and the EEM of fly ash were each bilinear (i.e., $r=1$ for each).² The fly ash EEM was definitely not bilinear out to 355 nm in the literature, but the simulation was done over a much narrower range of excitation wavelengths.

The fluorescence lidar EEM was a linear combination of the NO₂ and the fly ash EEM. Emission spectra of the NO₂, the fly ash, and the mixture at one excitation wavelength are shown in Fig. 1. A concentration for NO₂ of 100 ppb was chosen for the unknown because it was the maximum¹⁰ concentration measured by Gelbachs et. al.¹⁰ in the ambient atmosphere of a city. The concentration of the fly ash was chosen so the peak fluorescence of fly ash was twice the peak fluorescence of NO₂, which was also consistent with measurements by Gelbachs et. al.²² The EEM of the unknown from which the fluorescence lidar returns were generated had two components (i.e., $r=2$). For calculational ease, the fluorescence lifetimes of the NO₂ and the fly ash were assumed to be the same.

Our hypothetical lidar is now described. The lidar uses three excitation lines: 457.9 nm, 488.0 nm, and 514.5 nm. The energy of each pulse is 0.1 J and each pulse is much shorter than either the fluorescence lifetime or the detector integration times. Other parameters of the detector are given in Table 1. The receiver field of view was assumed perfectly matched with the laser divergence. The emission spectra were collected from 400 nm to 750 nm in 5 nm increments. Elastic scatter was not included as there are methods of filtering it out of the fluorescence lidar return. The receiver was shot noise limited. The lidar path was horizontal through an atmosphere with a 23 km visibility.

We averaged the signal over 6000 pulses per excitation wavelength for each trial. Adequate lidar returns with sky radiance and photon noise could not be gathered with a much smaller number of pulses. This number is far too large for many applications of fluorescence lidar. However, fluorescence lidar

may be possible for gases whose cross section is much larger than $9 \times 10^{-24} \text{ cm}^2$ or whose concentration is much larger than 100 ppb because fewer pulses would be necessary. The statistical average and standard deviation of the overlap index was calculated from 17 trials. The error bars were defined as plus or minus a standard deviation.

IV. Results and Discussion

A threshold (i.e., rejection level) for the overlap index is required to determine whether a compound is present or absent. We determined one possible criterion as follows. We assumed that the fly ash background we used was either very typical or worse than the actual background. For example, aerosols can be monitored by independent techniques. The RAFA analysis would then be discarded if the aerosol concentration was too high. A reasonable threshold under these conditions would be between the two curves.

The following numerical definition of threshold was tested. The overlap indices with no sky radiance are clearly separable out to 10 km for the mixture of NO_2 and fly ash (p_m) and the fly ash background alone (p_b). A slight dependence on distance was observed for both p_m and p_b , so a threshold, p_t , that was also dependent on distance was defined. The threshold, p_t , was defined as the average of p_m and p_b , i.e.,

$$p_t = \frac{p_m + p_b}{2} \quad (2)$$

Any p above p_t indicates the presence of NO_2 and any p below p_t indicates the absence of NO_2 . This criterion presumes that the user has anticipated the worse fluorescence background interferent possible in a given situation.

The simulation was done with photon counting (i.e., shot) noise and night time sky radiance. The mean sky radiance was subtracted from the signal because methods of subtracting a constant background are available to experimenters. The shot noise associated with sky radiance was not subtracted from the signal because shot noise is random. Actual sky radiance will vary greatly under field conditions. The values of sky radiance used here are crude approximations of a typical moonlit night.

The noise from the sky radiance severely limited the ability of the fluorescence lidar to distinguish between the presence and absence of NO_2 . The functional dependence of the

average overlap index on distance is shown in Figure 2 for night time sky radiance. The overlap indices with and without NO_2 are indistinguishable for distances greater than 400 m.

There are conditions under which the sky radiance would be insignificant. The functional dependence of the average overlap index with the NO_2 calibrant are shown in Figure 3 for the no sky radiance and a shot noise limited signal. The overlap indices with and without NO_2 do not intersect for distances less than 3 km. This is a vast improvement over the night time sky radiance situation.

Simulations done under day light conditions showed that shot noise from day time sky radiance reduced the overlap index to zero with and without NO_2 for all reasonable distances.

V. Conclusions

Photon counting noise with sky radiance severely limits the ability to detect NO_2 . Sky radiance with noise limits the range of the fluorescence lidar, and limits fluorescence lidar to night time applications. The photon noise from the sky radiance is a larger problem than photon noise from the fluorescence alone because the sky radiance is stronger than the fluorescence signal. These limitations are fundamental to lidar and not a limitation of the factor analysis-rank annihilation technique alone.

The noise from sky radiance problem may make the detection of NO_2 impractical. The large number, 6000, of pulses per excitation wavelength required for signal averaging would occupy a large amount of the observers time. The experimenter would have to wait 60 s per excitation wavelength at a very high repetition rate of 100 Hz. This would not be a real time measurement for many applications. Fluorescence lidar may be practical for atmospheric constituents with much higher fluorescence cross sections or concentrations than was used in our simulation.

These calculations are show that RAFA would be limited at large distances by shot noise and sky radiance. The sky radiance used in this study was a crude crude approximation. Better evaluations of the fluorescence lidar technique will require precise sky radiance data under the conditions of the application.

The fluorescence lidar apparatus that we simulated is feasible but would be very marginal. Our fluorescence lidar

model is being used to investigate the effectiveness of possible improvements. Narrowing the receiver field of view could reduce the sky radiance noise. However, the 2 mrad used in our simulation is already too narrow to easily achieve. Using an excitation source with a greater the number of lines would enable the lidar to discriminate NO_2 from even more complex fluorescence backgrounds than the simulated fly ash. In future studies, we will evaluate applications for fluorescence lidar using better data on fluorescence spectra, cross sections, and sky radiance.

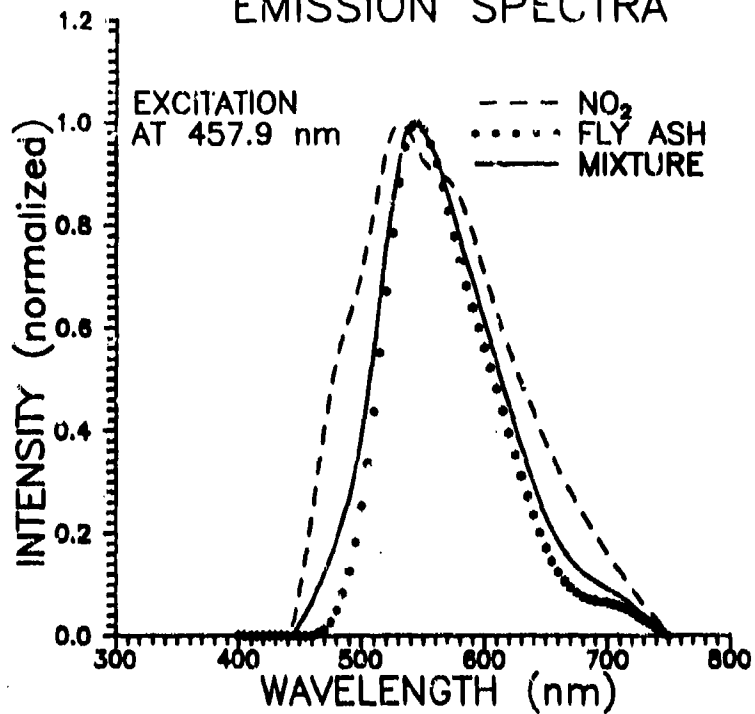
Table 1: Lidar parameters

1.	Laser pulse energy	--	0.1 J
2.	Number pulses	--	6000
3.	Receiver Mirror Diameter	--	0.6 m
4.	Receiver field of view	--	2 mrad
5.	Spectral Bandwidth of System	--	2.5 nm
6.	Transmitter Efficiency	---	0.55
7.	Receiver Efficiency	--	0.54

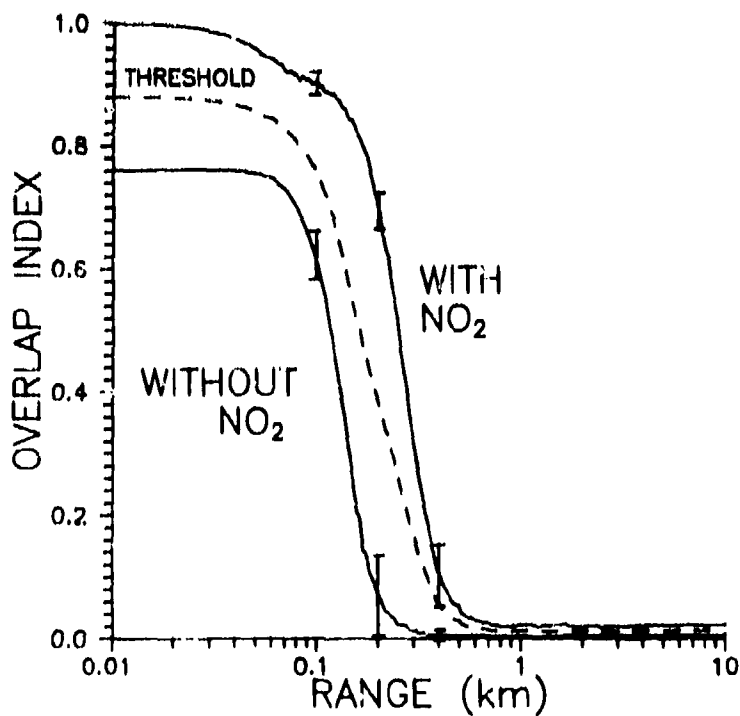
References

1. Raymond Measures, Laser Remote Sensing (Wiley, NY, 1984).
2. David L. Rosen and James B. Gillespie, "Atmospheric extinction effect on analysis of UV fluorescence signatures," Appl. Opt. 28, 4260 (1989).
3. C. N. Ho, G. D. Christian, and E. R. Davidson, "Application of the Method of Rank Annihilation to Quantitative Analyses of Multicomponent Fluorescence Data from the Video Fluorimeter," Anal. Chem. 50, 1108 (1978).
4. E. R. Malinowski and D. G. Howerly, Factor Analysis in Chemistry (Wiley, NY, 1980).
5. Thomas M. Rossi and Isiah M. Warner, "Rank Estimation of Excitation-Emission Matrices Using Frequency Analysis of Eigenvectors," Anal. Chem. 58, 810 (1986).
6. Edward M. Patterson and James B. Gillespie, "Simplified ultraviolet and visible wavelength atmospheric propagation model," Appl. Opt. 28, 425 (1989).
7. Katsumi Sakurai and H. P. Broida, "Spectral Study of NO₂ Fluorescence Excited by 11 Lines of Argon and Krypton Ion Lasers" J. Chem. Phys. 50, 2404 (1969).
8. L. F. Keyser, S. Z. Levine, and F. Kaufman, "Kinetics and Mechanism of NO₂ Fluorescence," J. Chem. Phys. 54, 355 (1971).
9. Armin W. Tucker, Milton Birnbaum, and Curtis L. Fincher, "Fluorescence of Fly Ash Samples: Implications for In Situ and Remote Detection," J. Luminescence 9, 1 (1974).
10. J. A. Gelbwachs, M. Birnbaum, A. W. Tucker, and C. L. Fincher, "Fluorescence determination of atmospheric NO₂," Opto-electronics 4, 155 (1972).

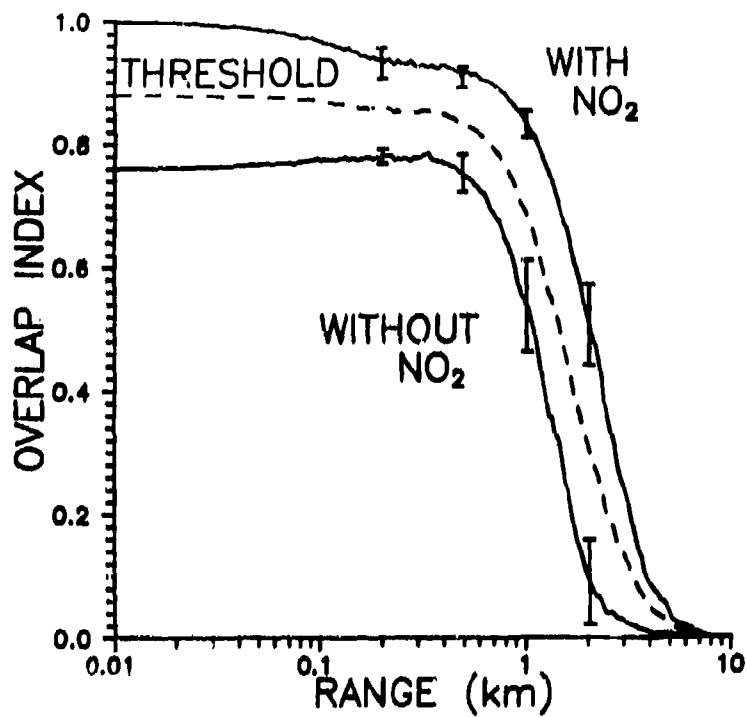
EMISSION SPECTRA



1. Normalized emission spectra of NO₂ (---), fly ash alone (****), and a mixture of fly ash and NO₂ at 457.9 nm excitation (—).



2. Functional dependence of the overlap index on range with photon noise and sky radiance for night time conditions.



3. Functional dependence of the overlap index on range with photon counting noise but no sky radiance.

A Room Temperature Microparticle Based Persistent Spectral Hole Burning Memory

S. Arnold and C.T. Liu*
Microparticle Photophysics Laboratory(MP³L)
Department of Physics
Polytechnic University
333 Jay St., Brooklyn, N.Y. 11201

and

W.B. Whitten and J.M. Ramsey
Oak Ridge National Laboratory
Analytical Chemistry Division
Oak Ridge, TN 37831

RECENT PUBLICATIONS, SUBMITTALS FOR PUBLICATION AND PRESENTATIONS

- A) S. Arnold, C.T. Liu, W.B. Whitten and J.M. Ramsey, "Room Temperature Microparticle based Persistent Spectral Hole Burning Memory", Opt. Lett. 16, 420(1991).**
- B) S. Arnold, C.T. Liu, W.B. Whitten and J.M. Ramsey, "Room Temperature Microparticle based Persistent Spectral Hole Burning Memory", Quantum Electronics Laser Science Conference(QELS, 91)**
- C) S. Arnold, "Room Temperature Persistent Spectral Hole Burning using Dielectric Particles as Photonic Atoms"(invited)
Digest of OSA Meeting on Persistent Spectral Hole Burning
(Optical Society of America, Washington, D.C., 1991), paper FA1**

ABSTRACT

We show both theoretically and experimentally that a random distribution of spherical microparticles may be used as a spectral hole burning memory. This Microparticle Hole Burning Memory, which can be both written and read at room temperature, is a direct consequence of the properties of morphology dependent resonances of microparticles.

*** present address, Dept. of Applied Physics, Columbia University**

The narrow electromagnetic morphologically dependent resonances(MDR's) which are so distinctly present in single particle experiments are virtually washed out in experiments on polydispersed distributions of particles. This is even the case for the narrowly distributed particles produced in space, "space beads".¹ In this letter we present a means for encoding information into such a distribution of particles which takes direct advantage of the narrow MDR's. This procedure known as microparticle hole burning, to our knowledge, is the first example of the use of a collection of microparticles as a medium for persistent spectral hole burning. Unlike all other condensed matter hole burning media the microparticle hole burning medium does not have to be either written or read at cryogenic temperature²; it operates at room temperature.

The principle of the Microparticle Hole Burning Memory(MHB) is based on the fact that a given MDR occurs at a wavelength in proportion to the particle's size(with the refractive index held constant). Thus a collection of particles having a distribution of sizes gives rise to a photophysical response which is heterogeneous. A good example of this effect, as we will see, occurs for the case of the fluorescence excitation spectrum taken on an ensemble of dyed microspheres. Such a spectrum is composed of the sum of spectra from individual particles,³ each with resonances occurring at different wavelengths. Thus the normal homogeneously broadened excitation spectrum of a typical dye at room temperature is found to become inhomogeneous for measurements on an ensemble of dyed particles. Memory may be imprinted by a laser, for example, by preferentially photolyzing molecules within particles having an MDR at resonance with the laser wavelength. The memory may be read out by taking the fluorescence excitation spectrum; photolysis causes fluorescence to be reduced thus putting holes into the excitation spectrum. In what follows we review important aspects of MDR's, construct a simple model for understanding microparticle hole burning, and present results of experiments which confirm our basic idea.

A spherical particle of radius a irradiated by a plane wave of wavelength λ exhibits an enhanced internal field when its optical size X (circumference to incident wavelength ratio, $X=2\pi a/\lambda$) corresponds to a resonant condition. These resonances are distinguished by their polarization P (i.e., TE or TM), angular momentum ℓ , and radial order number s (i.e. the number of nodes of the wavefunction inside the particle). A general mode is labelled $P_{\ell,s}$. The "free spectral range" in X between $P_{\ell,s}$ and $P_{\ell+1,s}$ is dependent chiefly on the refractive index, and consequently the wavelength difference between $P_{\ell,s}$ and $P_{\ell+1,s}$, $\Delta\lambda$, is inversely proportional to X and proportional to λ (i.e. the larger the particle size the closer the spacing in wavelength near a given wavelength).⁴

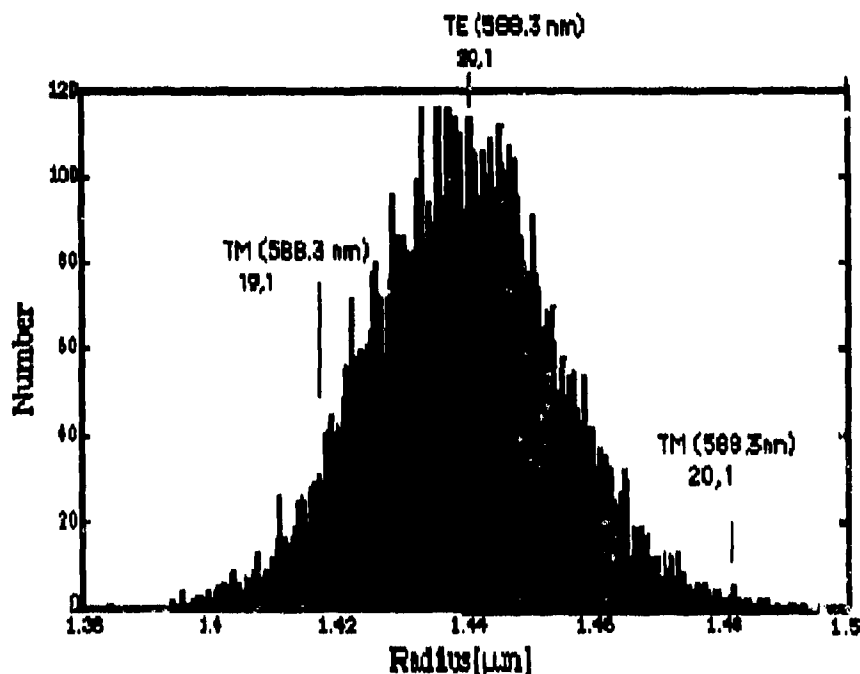


Fig.1. Simulated normal random distribution of 10^4 polystyrene particles having a mean radius of $1.44 \mu\text{m}$ and a standard deviation of 1% of this size. The arrows indicate the parts of the distribution in resonance with a laser at 588.3nm.

In Fig.1 we show a simulated normal random distribution δ of 10^4 polystyrene particles having a mean radius $\langle a \rangle$ of $1.44 \mu\text{m}$ and a standard deviation to average size ratio $\sigma_a/\langle a \rangle$ of 0.01. The arrows indicate the sizes of particles within the distribution which have MDR's in resonance at 588.3nm. Our goal is to model the fluorescence excitation spectrum of this ensemble. Since fluorescence is incoherent, an excitation spectrum for the distribution in Fig. 1 may be constructed by adding the Mie absorption of each of the particles. The curve in Fig.2a is the Mie absorption of a single particle at the center of the distribution ($a=\langle a \rangle=1.44\mu\text{m}$) using a refractive index of $1.59 + 10^{-6}i$.

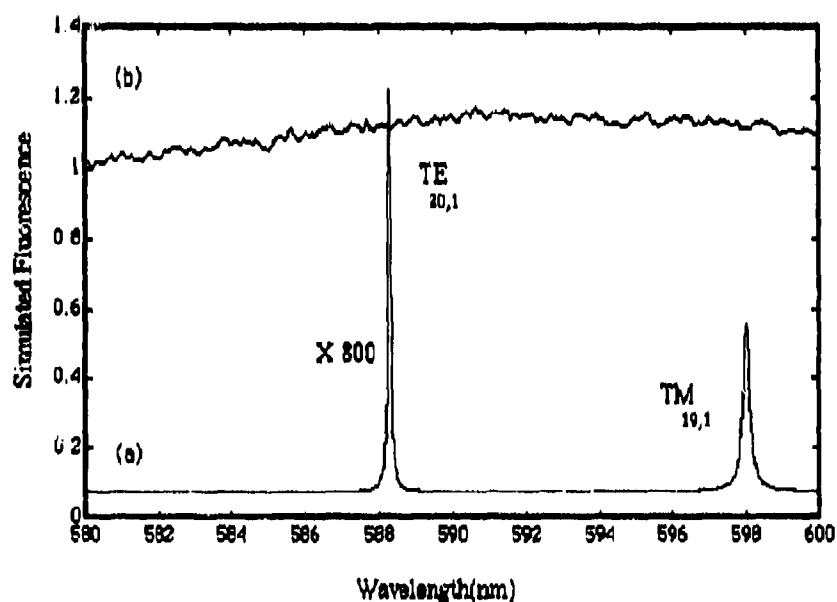


Fig. 2. (a) Simulated fluorescence excitation spectrum for a particle at the center of the distribution, $a=1.44\mu\text{m}$; (b) Simulated fluorescence excitation spectrum for the particle distribution in Fig.1.

The resonant features are clear. As the size of the particle changes the resonances shift in accordance with our previous discussion. The sum of the absorption from all 10^4 particles in Fig.1 is shown in Fig.2b . We see that the

collective fluorescence(Fig.2b) has lost virtually all of the detail present in the single particle spectrum. Now we suppose that an intense laser is projected onto the distribution at a wavelength λ_w of 588.3nm. Although the rate of photolysis is expected to vary spatially due to nonuniform absorption, for simplicity we assume that this rate is proportional to the power absorbed by the entire particle. As a consequence the fluorescence will fall exponentially with exposure time. Using this recipe the initial fluorescence from each particle of size a is multiplied by $F(a) = \exp[-\beta G(a)]$, with $G(a) = a^2 Q_a(2\pi a/\lambda_w) / \langle a \rangle^2 Q_a(2\pi \langle a \rangle / \lambda_w)$, where $Q(X)$ is the Mie absorption efficiency at optical size X , and β is a parameter which is proportional the incident intensity of the photolyzing light, the quantum efficiency for photolysis and time. Fig.3 shows the fluorescence excitation spectra before ($\beta=0$) and after ($\beta=1$ or 20) the simulated photolysis. As one can plainly see, narrow holes are predicted which are clearly distinct from the noise due to number fluctuations. It should be noted that these holes become broadened beyond the width of the TE_{20,1} resonance as β increases.

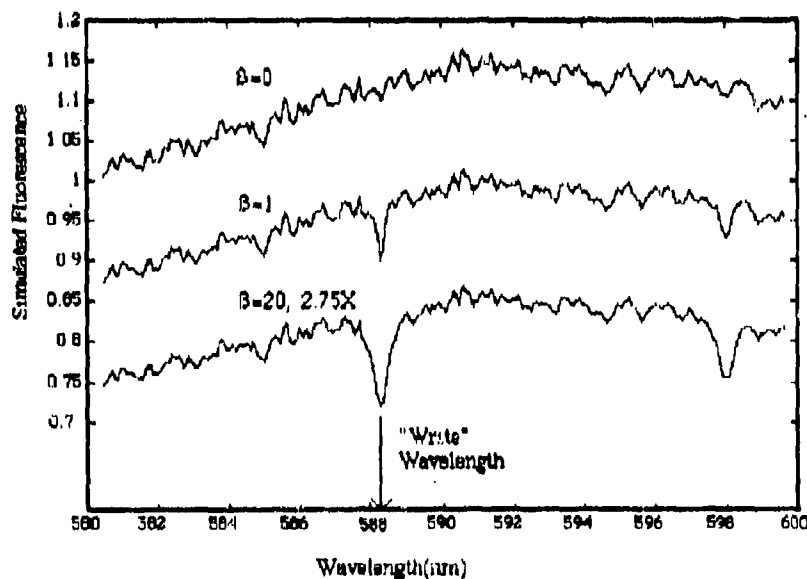


Fig.3. Fluorescence excitation spectra before($\beta=0$) and after two simulated burns ($\beta=1$ and 20) on the particle distribution in Fig.1.

Although all three sizes indicated in Fig.1 contribute to the hole at the "write" wavelength λ_w (i.e.588.3nm), the feature at 598nm in Fig.3 is principally contributed to by particles near the center of the distribution, $a \approx 1.44 \mu\text{m}$. The fluorescence of these particles are bleached by stimulating their $\text{TE}_{20,1}$ resonance. Once bleached the particles will not fluoresce when probed at any of their other resonances. The feature at 598nm in Fig.3 is due in fact to the $\text{TM}_{10,1}$ resonance of particles near $1.44 \mu\text{m}$. Such a feature will be termed subsidiary since it owes its existence to only one of the three groups of particles. In this respect it is interesting to note that the model predicts that such subsidiaries become less distinct as the distribution becomes broader and contains more resonances which can be stimulated by the "write" wavelength (e.g. a distribution such that $\sigma_g / \langle a \rangle \gg \Delta\lambda / \lambda$). All particles in resonance at λ_w contribute to the hole at this wavelength, however, other resonances (i.e. the subsidiary resonances) of these particles are separated from λ_w by an amount which depends distinctly on their individual sizes. Consequently the subsidiary resonances from different particles in the ensemble will not be in register; these subsidiaries become muted in comparison to the hole at λ_w . In the experiments to follow we have chosen just such a distribution.

Our experiments were performed on dyed latex particles ($\langle a \rangle = 12.1 \mu\text{m}$, $\sigma_a = 2.2 \mu\text{m}$) on a cover glass slide. Latex particles dried from a hydrosol were dyed with Nile red by stirring and sonicating the particles in a 10^{-4}M xylene solution. Following centrifugation and decanting, a 1% Triton-X solution was added to the test tube containing the particles. After further stirring centrifugation and decanting, water was added. The contents of the test tube were then agitated by stirring and sonicating. This resulted in a resuspension of the now dyed hydrosol particles. A drop of this hydrosol was placed on a cover glass slide. After air drying, this slide was placed on the stage of a fluorescence microscope and irradiated from above by a CW dye laser beam at 80° from the vertical. Fluorescence was isolated by a filters (Corning CS 2-59 and CS 2-60)

and detected by a cooled photomultiplier. The fluorescence from approximately 2000 particles in an area of 1mm^2 were viewed by this detector.

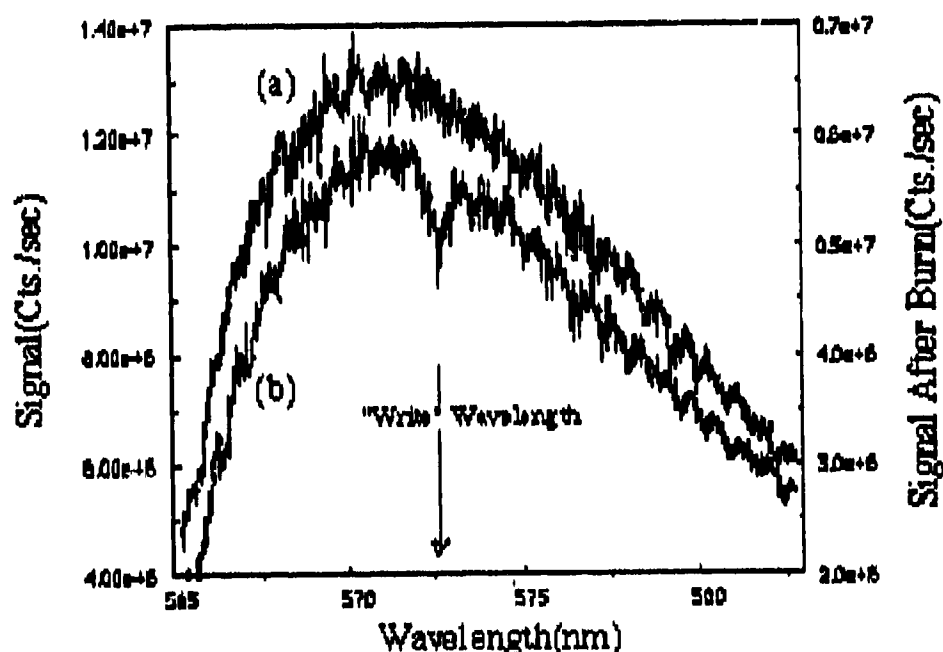


Fig.4. Fluorescence excitation spectra taken before (a) and after (b) projecting a relatively intense laser on the sample at 572.3nm.

Fig.4a shows the fluorescence excitation spectrum recorded on the sample at an incident intensity of 0.4 mW/cm^2 over a period of 10 minutes. Following this scan the sample was irradiated for 5 minutes at 40W/cm^2 with the wavelength fixed at 572.3nm. Fig.4b shows the resulting excitation spectrum taken under the same conditions as in Fig.4a. The overall reduction in luminescence of the scan in Fig.4b in comparison with Fig.4a is due to photolysis of the Nile red dye. The "hole" in the spectrum in Fig.4b at 572.3nm is apparent. The lack of an apparent subsidiary hole is consistent with our model. The breadth of the hole is considerably wider than the width of a narrow resonance for particles of this size. However, this effect is similar to the effect which occurs in the model distribution for large β .

Although our model discloses the basic idea behind MHB, there are many theoretical questions to be answered in connection with this new memory system:

(1) How does one include the effects of the substrate? (2) What is the effect of the proximity of one particle to another? (i.e., many particles touch in our experiments) (3) What is the consequence of a radial dependence in the distribution of dye within the particles? With respect to the first question, our own measurements, and the measurements of others⁶ indicate that resonances remain intact on a glass surface. The second question is much harder to answer, however recent calculation on light scattering from bispheres suggest an alteration in spectra for two identical particles in contact. However, even in this extreme case resonances are still predicted.⁷

MHB may have interesting applications not only as a memory device but also in the diagnostics of particle size distributions. As we have already pointed out the degree to which subsidiary features are present is controlled by the ratio of $\sigma_{\alpha}/\langle a \rangle$ to $\Delta\lambda/\lambda$.

Both theoretical questions and the possible use of MHB as a tool for evaluating size distributions are currently under study in our laboratories.

We would like to acknowledge the assistance of John H. Blalock for making the optical measurement. Research at Oak Ridge was supported by the U.S. Department of Energy, Office of Energy Research, under contract DE-AC05-84OR21400 with Martin Marietta Energy Systems, Inc. S. Arnold and C.T. Liu were cooperatively supported by the NSF and the U.S. Army Chemical Research Development and Engineering Center (under ATM-89-175871) and by a contract from the Joint Services Electronics Program.

References

1. T.R. Lettieri and E. Marx, Appl. Opt. **25**, 4325(1986).
2. W.E. Moerner, ed., *Persistent Spectral Hole Burning: Science and Applications*(Springer-Verlag, Berlin, 1988)
3. L.M. Fojan and S. Arnold, Opt. Lett. **13**, 1 (1988).
4. S.C. Hill and R.E. Benner, in *Optical Effects Associated with Small Particles*, P.W. Barber and R.K. Chang, eds.(World Scientific, Teaneck, N. J., 1988), Chap.1.
5. M. Kalos and Whitlock, *Monte Carlo Methods, Vol.1* , (John Wiley and Sons, New York, 1986), P.47
6. S.C. Hill, R.E. Benner, C.K. Rushforth, and P.R. Conwell, Appl. Opt. **23**, 1680(1984).
7. K.A. Fuller, Appl. Opt. **28**, 3788(1989).

BLANK

**B. PHYSICAL CHARACTERIZATION - LIGHT SCATTERING & INVERSION
CONSTRAINED LINEAR INVERSION OF LIGHT SCATTERED FROM NON-
ABSORBING, NEARLY IDENTICAL SPHERICAL PARTICLES FOR SIZE AND
REAL REFRACTIVE INDEX**

Matthew R. Jones
Bill P. Curry*
M. Quinn Brewster****

***Argonne National Laboratory
9700 South Cass Avenue
Argonne, Il. 60439**

****University of Illinois at Urbana-Champaign
Department of Mechanical and Industrial Engineering
140 Mechanical Engineering Building
1206 West Green Street
Urbana, Il. 61801**

The Fredholm equation of the first kind representing the light scattering by a narrow log normal distribution of non-absorbing aerosol particles is inverted to obtain the particle size distribution function and real refractive index. The deconvolution technique is a generalization of the process previously developed to obtain particle size distribution functions when the optical properties of the particles are known. The solution is obtained by expanding the scattering kernels and the particle size distribution function as linear combinations of Schmidt-Hilbert eigenfunctions. The orthogonality properties of the Schmidt-Hilbert eigenfunctions and of the eigenvectors of the kernel covariance matrix are employed to obtain a solution which minimizes the residual errors subject to a trial function constraint. Application of the trial function constraint requires prior knowledge of the type of distribution. The inversion process is described briefly, and the results from the inversion of several synthetic data sets are presented. It is anticipated that future improvements in the technique will result in a quantitative analysis of the error in the size distribution and in the value obtained for the real refractive index. Optimization of the inputs should lead to a reduction in the number of measurements required for a successful inversion. Also, it is anticipated that further generalization will allow for the retrieval of the imaginary part of the refractive index.

RECENT PUBLICATIONS

A) B. P. Curry, "Inversion of Single Size Particle Scattering Data by Use of a Constrained Eigenfunction Expansion", Proceedings of the 1990 CRDEC Scientific Conference on Obscuration and Aerosol Research, In Preparation.

INTRODUCTION

Measurements of the light scattered by a particle provide an indirect way of determining the particle's properties. Techniques for solving inverse scattering problems are of great interest due to the wide range of potential applications in areas as diverse as combustion, meteorology, geology, and bioengineering. This paper describes a generalization of the constrained eigenfunction method developed by Curry¹ to solve the inverse scattering problem when the optical properties of the scatterers are known. The method described here retrieves the particle size distribution function and the real part of the

refractive index by deconvolving the synthetic measurements of light scattered from a narrow log normal distribution of non-absorbing aerosol particles. A brief description of the technique is followed by the presentation of results from several inversions of synthetic data sets. A full mathematical development of the technique was presented at the 1990 Symposium.

THE SCATTERING EQUATION

In the development of this inversion process, attention was focused on simulating a possible experiment in which measurements were made of the light scattered from nearly identical, non-absorbing spherical particles. It was anticipated that the differential scattering cross sections would be measured. The differential scattering cross sections are equal to the convolution of the particle size and refractive index distribution function (PSRIDF) with the scattering kernels. Thus, the following Fredholm equation of the first kind relates the measured differential scattering cross section to the desired particle size distribution function.

$$\mathbf{G} = \mathbf{G}^{\circ} + \delta\mathbf{G} = \int_0^{\infty} \int_1^{\infty} f(x,n) \mathbf{K}(x,n) dx dn \quad (1)$$

The vector \mathbf{G} represents the set of measured differential scattering cross sections. The vector \mathbf{G}° is the set of error free differential scattering cross sections and the vector $\delta\mathbf{G}$ represents the error associated with each of the measurements. The desired PSRIDF is represented by f . The scattering kernels, \mathbf{K} , are also differential scattering cross sections, and they depend on the polarization of the incident light and Ω , the direction in which the light is scattered, as well as the size parameter and the refractive index of the particle. When the incident light is polarized parallel or perpendicular to the scattering plane, the scattering kernels are simply the ratio shown in Equation 2 where i represents the Mie intensity functions².

$$K(\text{polarization}, \Omega, x, n) = \frac{i(\text{polarization}, \Omega, x, n)}{2k^2} \quad (2)$$

DECONVOLUTION METHOD

The deconvolution method outlined in this section is simply an extension of the derivation given by Curry to include an unknown real refractive index¹. References 3 and 4 are good sources for information on Schmidt-Hilbert theory.

Define a function of size parameter and real refractive index such that

$$M(x,n,x',n') = \sum_j K_j(x,n)K_j(x',n') \quad (3)$$

where j runs from 1 to the number of measurements made. The kernel covariance matrix is defined as

$$N_{jk} = \int_0^\infty \int_0^\infty K_j(x,n)K_k(x,n)dx dn \quad (4)$$

The scattering kernels can be expressed as an expansion of the Schmidt-Hilbert eigenfunctions of M , and the eigenvalues and eigenvectors of the kernel covariance matrix.

$$K_k(x,n) = \sum_j \sqrt{\lambda_j} u_k^j \Phi_j(x,n) \quad (5)$$

Since $f(x,n)$ is sourcewise representable, the PSRIDF can be written as an expansion of the eigenfunctions³.

$$f(x,n) = \sum_j a_j \Phi_j(x,n) \quad (6)$$

Substituting Equations 5 and 6 into Equation 1 gives the following expression for the unconstrained expansion coefficients a_j

$$a_j = \frac{1}{\sqrt{\lambda_j}} \sum_k G_k u_k^j \quad (7)$$

The use of these expansion coefficients produces highly oscillatory, unsatisfactory PSRIDFs. This difficulty is overcome by the introduction of a trial function constraint.

A performance function is defined as

$$Q = \sum_j \delta G_j^2 + \gamma \int_0^\infty \int_0^\infty (f(x,n) - f^t(x,n))^2 dx dn \quad (8)$$

where $f^t(x,n)$ is a trial function of the assumed form and γ is a Lagrange multiplier.

The performance function can be expressed in terms of the expansion coefficients, the eigenvalues, the eigenvectors, and the set of measurements. The constrained expansion coefficients are then determined by finding a minimum in Q with respect to $\{a_j\}$.

$$a_j^c = \frac{a_j \lambda_j + \gamma a_j^t}{\lambda_j + \gamma} \quad (9)$$

The optimal value of the Lagrange multiplier must now be determined. It can be shown that the square norm of the error introduced by applying the constraint is bounded by the parameter referred to by Curry as the residual relative variance or RRV¹. The optimal value of the Lagrange multiplier is found by minimizing the RRV with respect to γ . The constrained PSRIDF is calculated from Equation 6 with $\{a_j^c\}$ replacing the $\{a_j\}$.

Once the constrained PSRIDF has been obtained, the real part of the refractive index is retrieved from

$$W(n_s) = \frac{\int_0^\infty \int_0^\infty W(n) f^c(x, n) dx dn}{\int_0^\infty \int_0^\infty f^c(x, n) dx dn}$$

$$n_s = W^{-1}(W(n_s)) \quad (10)$$

where $W(n)$ is a weighting function. The results presented in this paper were obtained using the phase shift squared, $x^2[n-1]^2$, as the weighting function. Physically, this weighting function corresponds to the small argument form of the Anomalous Diffraction approximation to the extinction efficiency⁵.

To summarize, the deconvolution proceeds according to the following steps:

1. Equation 7 is used to calculate the unconstrained expansion coefficients. Information obtained from the unconstrained solution is used to determine the nature of the trial function.
2. The optimal value of the Lagrange multiplier is determined by increasing γ from zero until a minimum in the RRV is reached. This value of γ is used in Equation 9 to calculate the set of constrained expansion coefficients.
3. If the rms value of the residual errors is less than or equal to the expected error, the PSRIDF is calculated using Equation 6 and the real part of the refractive index is calculated from Equation 10. Otherwise, the trial

function expansion coefficients are set equal to the constrained expansion coefficients, and the procedure is repeated beginning at step 2.

4. If the peak value of the PSRIDF and the retrieved real part of the refractive index are within a specified tolerance of the trial size and refractive index, convergence is obtained. Otherwise, the trial function expansion coefficients are set equal to the constrained expansion coefficients, and the procedure is repeated beginning at step 2.

Three more matters need to be discussed before presenting the results of the deconvolution of several synthetic data sets. First, each of the synthetic measurements are normalized by the average of the measurements. Because of the difficulties associated with making absolute scattering measurements, it is anticipated that such relative measurements will be made in an actual experiment. Secondly, experience has shown that it is helpful to weight the scattering kernels by the imprecision estimates^{1,6}. Finally, the use of a numeric filter is useful in smoothing the PSRIDFs. The filter simply averages the values of the PSRIDF at three neighboring sizes, and sets the value of the PSRIDF at the maximum and minimum sizes to zero.

DECONVOLUTION OF TEN SYNTHETIC DATA SETS

The intention here is to simulate an experiment in which measurements are made of the light scattered from nearly identical, non-absorbing spherical particles. Therefore, it was assumed that $f(x,n)$ is the product of a narrow log normal distribution in x and a Dirac delta function in n .

$$f(x,n) = \frac{1}{\sqrt{2\pi} x \ln(\sigma)} \exp\left\{\frac{-\ln^2(x/x_s)}{2\ln^2(\sigma)}\right\} \delta(n-n_s) \quad (11)$$

In all ten cases presented in this paper, σ , the geometric mean standard deviation, is 1.01. Thus, the distribution is extremely narrow, and the median value x_s corresponds to the peak value. Normally distributed random error with a standard deviation of 5% of the original value has been added to each synthetic data set. Sizes between 5 and 10 μm with a step size of 0.05 μm are considered. The possible values of the real part of the refractive index vary from 1.4 to 1.7 with a step size of 0.01. The incident light is linearly polarized with a wavelength of 0.5145 μm . Synthetic measurements for incident light polarized parallel and perpendicular to the scattering plane are calculated at 50 polar angles ranging from 5° to 175° in steps of 3.47°. The Mie intensity functions used to calculate the

scattering kernels are generated using BHMIE written by Bohren and Huffman. All ten synthetic data sets were generated by a third party, so the authors are unaware of the peak size and refractive index of the PSRIDF prior to inverting the data.

In each case a preliminary solution is obtained in which the entire range of real refractive indices are considered. Once a value for the refractive index is obtained the, range of refractive indices is narrowed to include only the 2 or 4 refractive indices closest to the preliminary result. The inversion process is then repeated and the results are taken to be the retrieved size and refractive index. Table 1 compares the retrieved values with the original values used to generate the synthetic measurements.

Table 1. Comparison of Original and Retrieved Values

Original Size (μm)	Retrieved Size (μm)	Original Ref.Index	Retrieved Ref.Index
5.50	5.40	1.69	1.70
6.00	6.00	1.50	1.50
7.50	7.50	1.41	1.41
9.50	9.45	1.58	1.58
10.0	10.0	1.70	1.69
5.00	5.00	1.40	1.41
9.00	9.05	1.63	1.43
6.00	5.95	1.56	1.56
7.50	7.45	1.46	1.46
8.50	8.45	1.68	1.68

Several of the retrieved particle size distribution functions are compared with the actual distributions in Figures 1-4. These comparisons show that the distributions obtained when the size and refractive index are near the center of the x-n space are better than when these values are near the boundaries of the space. Improved results would be easily obtained in the cases where the retrieved values are near the boundaries of the x-n space by shifting the size and refractive index ranges, and repeating the inversion process.

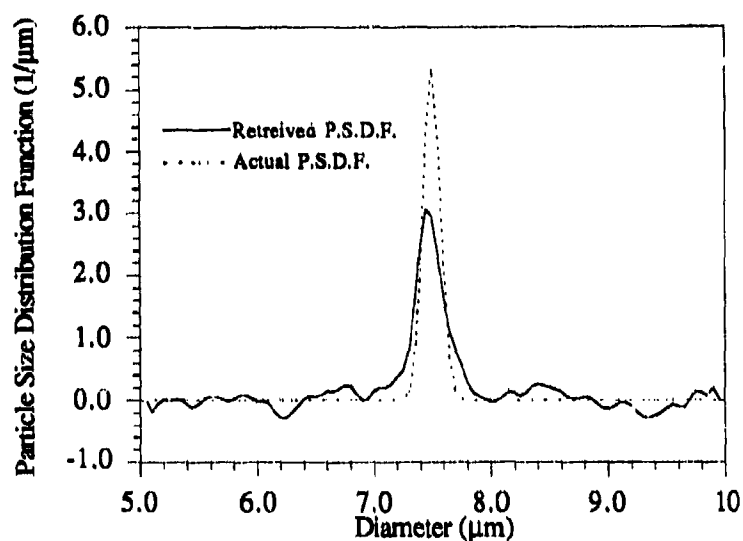


Figure 1. PSDF when both Size and Refractive Index are near the Center of the κ - n Space

Actual Refractive Index = 1.46

Range of Indices Considered in the Final Inversion 1.44-1.48

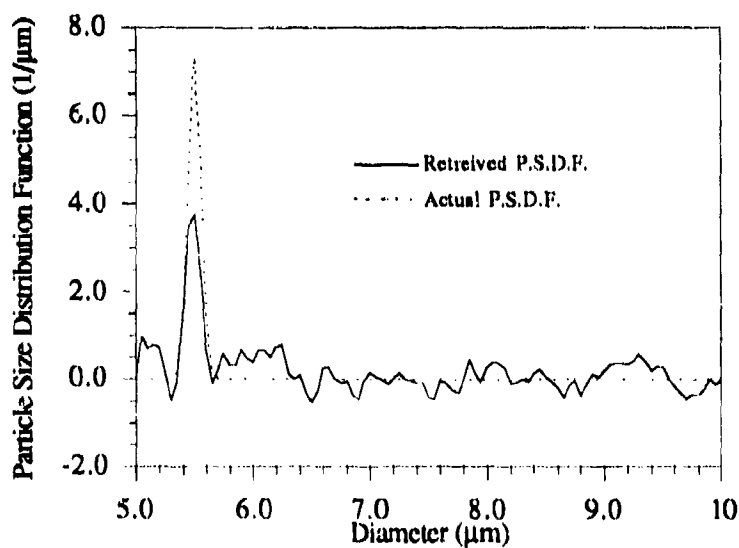


Figure 2. PSDF when the Ref. Index is near the Boundary of the n Space

Actual Refractive Index = 1.69

Range of Indices Considered in the Final Inversion 1.68-1.70

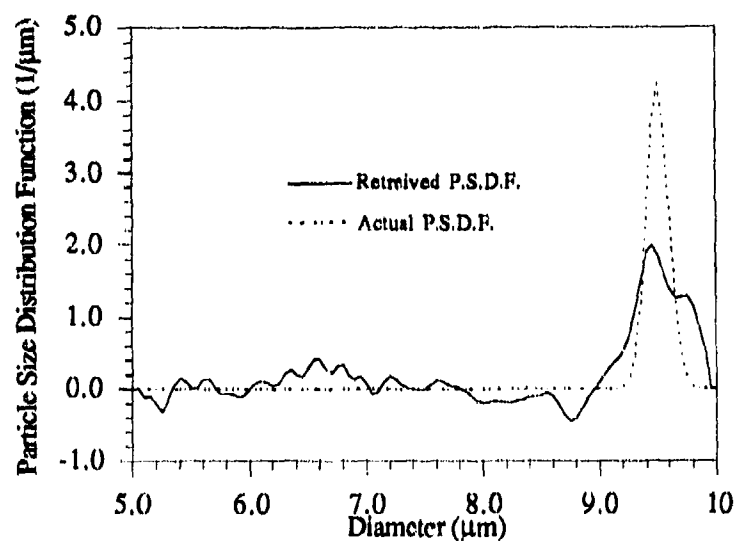


Figure 3. PSDF when the Size is near the Boundary of the x Space
 Actual Refractive Index = 1.46
 Range of Indices Considered in the Final Inversion 1.44-1.48

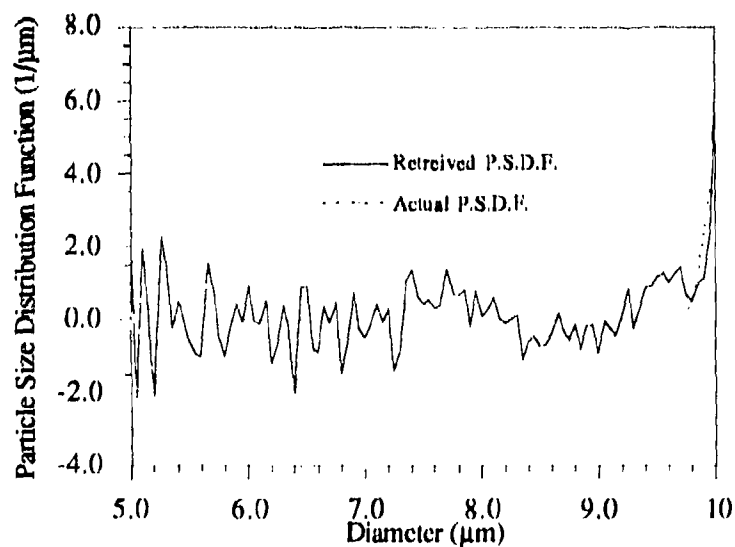


Figure 4. PSDF when both Size and Ref.Index are near the Boundary of the x-n Space
 Actual Refractive Index = 1.70
 Range of Indices Considered in the Final Inversion 1.68-1.70

CONCLUSIONS

The constrained eigenfunction method has been generalized to include retrieval of the real refractive index as well as the particle size distribution function.

ACKNOWLEDGEMENTS

This work was sponsored by the Army Chemical Research, Development, and Engineering Center, Aberdeen Proving Ground, MD under the supervision of J. R. Bottiger. The allocation of time on the Cray-Y/MP for this project by the National Center for Supercomputing Applications at the University of Illinois at Urbana-Champaign under grant number TRA900467N is gratefully acknowledged.

REFERENCES

1. B.P. Curry , "Constrained Eigenfunction Method for the Inversion of Remote Sensing Data: Application to Particle Size Determination from Light Scattering Measurements," Appl. Opt. 28, 1345 (1989).
2. C.F. Bohren and D.R. Huffman, *Absorption and Scattering of Light by Small Particles* (John Wiley & Sons, New York, 1983), pp. 383.
3. J. Mathews and R.L. Walker, *Mathematical Methods of Physics* (Benjamin, New York, 1964), pp. 292-297.
4. G. Arfken, *Mathematical Methods for Physicists* (Academic, New York, 1970), pp.743-747.
5. H.C. van de Hulst, *Light Scattering by Small Particles*, (Dover, New York, 1981), pp.131-134.
6. M.D. King, D.M. Byrne, B.M. Herman, and J.A. Reagan, "Aerosol Size Distributions Obtained by Inversion of Spectral Optical Measurements," J. Atmos. Sci. 35, 2153 (1978).

BLANK

MULTIPHASE ELECTRODYNAMIC TRAPPING AND MANIPULATION OF MICROPARTICLES

B. R. F. Kendall, D. S. Weyandt and M. F. Vollero
Department of Physics
The Pennsylvania State University
University Park, PA 16802

RECENT PUBLICATIONS, SUBMITTALS FOR PUBLICATION, AND PRESENTATIONS:

A) B. R. F. Kendall and E. T. Chesworth, "Measuring the Temperature of Diamagnetically Levitated Microparticles," in Proceedings of the 1990 CRDEC Scientific Conference on Obscuration and Aerosol Research.

1. INTRODUCTION

Three-phase electrodynamic particle traps were originally developed by Wuerker, et al.¹ and others^{2,3} in connection with fusion research. The typical configuration involved six planar electrodes arranged in a cubic pattern. Apertures in the electrodes provided for laser illumination and observation.

Advantages of this type of trap for aerosol studies include relatively wide-angle optical access (especially if modern conducting glass or fine photoetched mesh is used for the electrodes) and a geometry naturally suited to the use of three-axis DC cross-fields for particle manipulation.

2. THREE-PHASE ELECTRODYNAMIC LEVITATION

We have constructed and tested a Wuerker-type three-phase particle trap at frequencies in the range 40 to 1200 Hz and amplitudes of 500-2100V rms. The cube edge dimension was 3.2 cm. A simplified diagram of this trap is shown in Fig. 1. Glass, metal and liquid particles up to at least 80 μ m in diameter were levitated successfully.

3. TWO-PHASE LEVITATION

It can be inconvenient to interface a 3-phase trap, with very high AC potentials on all electrodes, with adjacent electrical devices such as particle injectors operating at low voltages. As well as the obvious problems of electrical arcs and corona discharges, there are more subtle problems of electrical noise generation affecting adjacent image intensifiers, television monitors and similar sensitive equipment. A variant of the basic three-phase trap with zero or very low voltages on one pair of plates was therefore sought.

The solution to this problem is shown in Figure 2. Let the phasors X, Y and Z represent the instantaneous phases and the magnitudes of the AC signals applied to the pairs of electrodes perpendicular to the x, y and z axes, respectively. To the neutral point N of the three-phase system shown in 2(a)

is added an additional AC voltage exactly equal and opposite to that represented by phasor Z. This additional phasor is shown in 2(b). The resultant, shown in 2(c), is a signal of zero amplitude to the z plates, and signals X' and Y' (which are 60 degrees apart and 1.73 times the amplitudes of X and Y) applied to the x and y plates. Internal fields remain exactly the same as in the three-phase case because the same additional AC voltage is added to every electrode, yet only two AC generators are now required, as shown in Fig. 3.

This system is conveniently used with the AC signal applied to the two pairs of plates with their planes vertical, while only low-voltage DC is applied to the top and bottom (z) electrodes to balance the force of gravity. These electrodes carry the injectors and any other sensitive components.

As expected, the new system traps particles just as well as the original but is much more convenient to use.

4. AMPLITUDE OF PARTICLE MOVEMENTS

Although it might appear that a particle in a dynamic trap would be in a constant state of oscillation in three dimensions, it is found in practice that the amplitudes are negligible if a vertical DC field is used to bring the charged particle exactly to the center of the levitation cell and if the mass-to-charge ratio is in the stable range. The positions of particles of 20 μm diameter and optimum mass-to-charge ratio can easily be kept steady within 45 μm at 60Hz. These excursions are further reduced as the frequency is increased.

5. EXTENSION TO DOUBLE CELL

Having low-potential electrodes on two of the faces makes it relatively easy to interface two cells. This double cell was used successfully to exchange particles in either direction between cells. The entire assembly can be mounted inside a transparent dome for controlled-humidity experiments.

6. ADDITIONAL EXPERIMENTS

In addition to the development of the three-phase and two-phase trapping systems with transparent planar electrodes, as discussed above, a number of additional experiments have been carried out. They include:

a) Operation of particle injectors for both solids and liquids in conjunction with both types of multiphase traps.

b) Selection and manipulation of specific particles has been demonstrated by moving the desired particle to the exact center of the cell and progressively rejecting other particles by quickly removing and restoring the correct AC driving voltage. Additional studies of stability parameters will be necessary to put this technique on a more scientific basis. At present it depends greatly on the skill of the operator.

c) After launching positively charged particles (20 micron glass spheres), negative particles were injected into the same cell and the resulting collisions observed by eye. Up to four or five charge exchanges were counted

in some cases before a particle was lost. This work involved highly-charged positive particles and lightly-charged negative particles to reduce the chance of complete neutralization (and hence loss) of the original particle after the first collision.

d) A 5 watt argon laser has been installed and has been used to illuminate levitated solids and liquid droplets. Some interesting effects involving asymmetrical evaporation and large resultant forces on droplets have been observed. These merit further study.

e) A variable-frequency chopped-beam helium-neon laser has been used to study the motions of particles in a multi-phase trap. All particles in a given segment of the trap orbit in the same direction relative to well-defined planes of symmetry. The major orbiting frequency is at the drive frequency although interesting perturbations occur when adjacent particles interact.

f) A double-liquid injector is in the final stages of construction so that oppositely-charged liquid droplets can be injected and manipulated in and between the two sections of a double cell.

7. PROPOSED FUTURE WORK

Future work will include the study of controlled addition of one aerosol droplet to another. Theoretical studies of the multiphase stability criteria, with gravitational effects included, are planned. Additional work is desirable on methods of particle selection and manipulation.

8. REFERENCES

1. R. F. Wuerker, H. M. Goldenberg and R. V. Langmuir, J. Appl. Phys. 30, 441 (1959).
2. A. F. Haught and D. H. Polk, Phys. Fluids 9, 2047 (1966).
3. A. A. Zaritskii, S. Zakharov, and P. G. Kryukov, Soc. Tech. Phys. 16, 174 (1971).

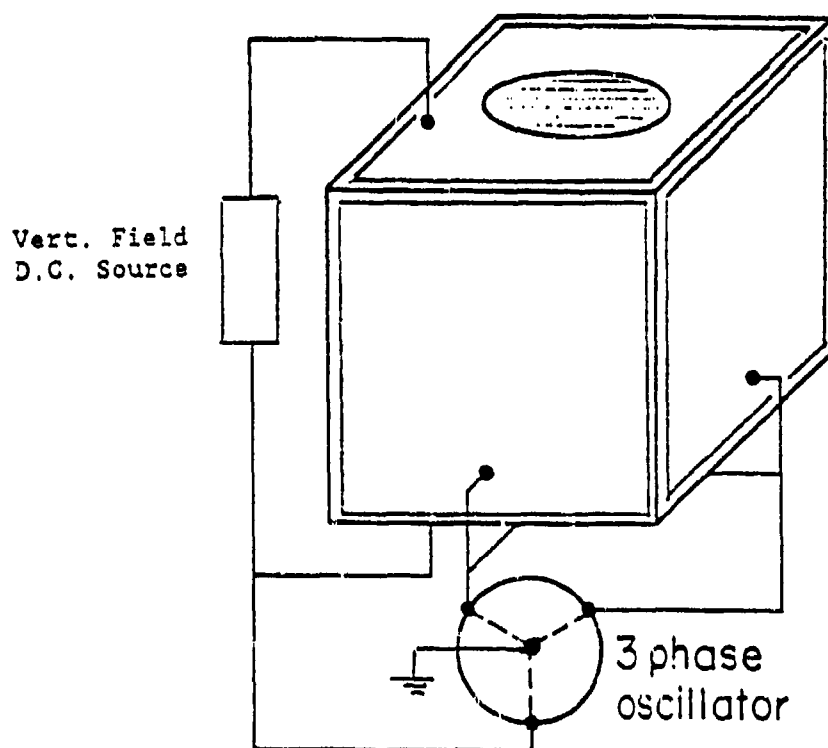


Fig. 1. Three-phase electrodynamic trap. For microparticles, frequencies are typically in the low audio range and amplitudes ~ 500 V rms

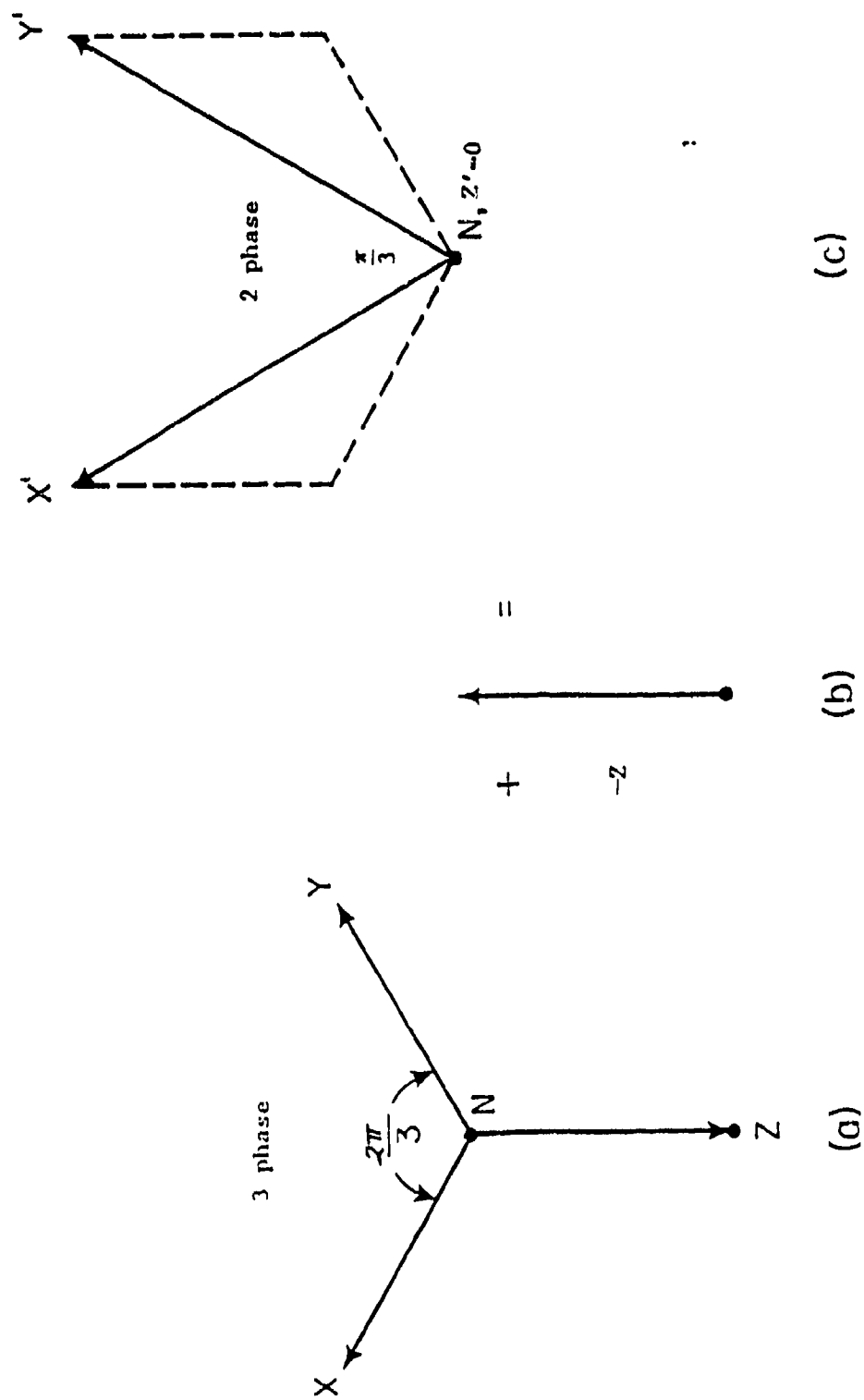


Fig. 2. Derivation of 2 phase, 60° phase difference drive from conventional 3 phase drive

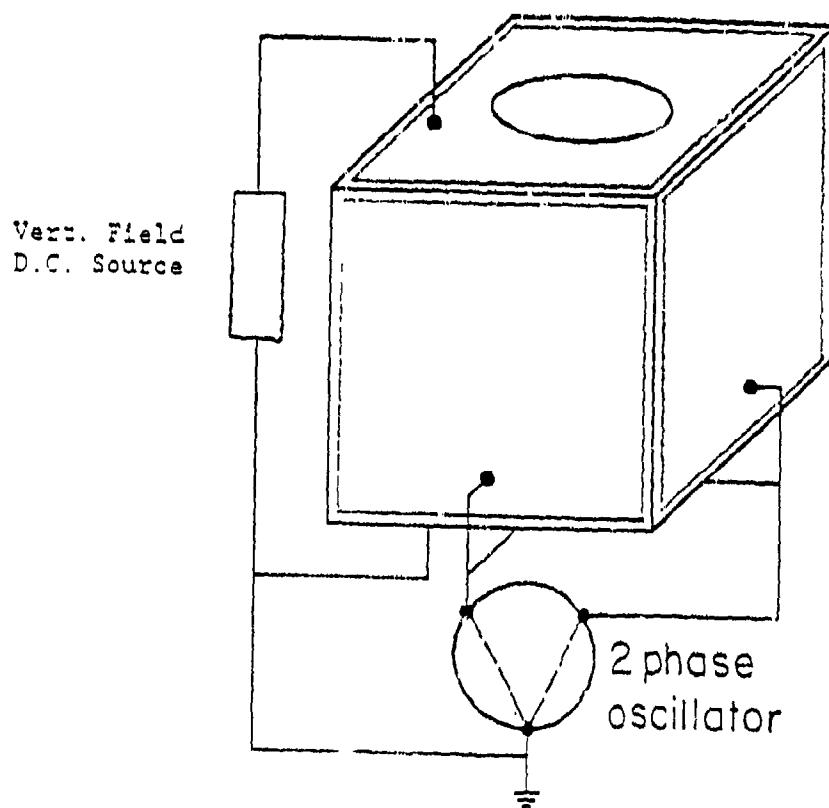


Fig. 3. Two-phase electrodynamic trap. AC amplitudes $\sqrt{3}$ times those of three-phase trap.

SCATTERING AT AND NEAR 0° BY SPHERES AND GLASS FIBERS

Edward S. Fry, G. G. Padmabandu, and Choonghoon Oh
Physics Department
Texas A&M University
College Station, TX 77843-4242

RECENT PUBLICATIONS, SUBMITTALS FOR PUBLICATION, AND PRESENTATIONS:

A) Edward S. Fry and G. G. Padmabandu, "Light Scattering at Zero Degrees by Particulate Suspensions," Proceedings of the 1990 CRDEC Scientific Conference on Obscuration and Aerosol Research.

B) Edward S. Fry, G. G. Padmabandu, and Choonghoon Oh, "Measurements of Scattering At and Near 0° by Glass Fibers," Presented at the 1991 CRDEC Scientific Conference on Obscuration and Aerosol Research, Aberdeen, MD, June, 1991.

C) G. G. Padmabandu, Choonghoon Oh, and Edward S. Fry, "Application of Beam Fanning in a Photorefractive BaTiO₃ Crystal; Measurement of Light Scattering at Zero Degrees by a Single Glass Fiber," in Technical Digest on Photorefractive Materials, Effects, and Devices, (Optical Society of America, Washington, D. C.), Vol. 14, pp. 314-316 (1991).

D) G. G. Padmabandu, Choonghoon Oh, and Edward S. Fry, "Measurement of Light Scattering at 0° by Micron Size Glass Fibers," Submitted to Optics Letters, September, 1991.

ABSTRACT

Studies of light scattering at an angle of zero degrees by single particles have been undertaken. Calculations for single spheres, and both calculations and measurements for glass fibers are presented. The measurements on glass fibers were made using the 0.5145 μm line from an Ar⁺ laser. Data have been obtained as a function of fiber radius from 1 μm to 35 μm and are in excellent agreement with theory. The measurement technique is similar to the two beam coupling technique we used in previous

measurements. However, the present approach is simpler and more robust. It is based on the fanning of a coherent light beam in a photorefractive BaTiO_3 crystal.

Future work will be directed towards increasing the sensitivity so that zero degree scattering by single spheres and other microscopic particles can be measured. Attention will be given to measurements of the scattering angular distribution in the vicinity of zero degrees with millidegree angular resolution.

Introduction

Light scattering near, as well as precisely at, an angle of 0° is of special importance for a variety of reasons. These include: (1) The scattering amplitude and phase at 0° gives the extinction via the optical theorem; the latter is an important fundamental relation underlying a wide body of physics but has previously not been directly verified in the optical region.^[1] (2) Scattering near 0° is so large it significantly affects light propagation through dust, smoke, haze, etc.; consequently, it plays a critical role in imaging and light propagation. (3) Forward scattering can produce erroneous results in experimentally measured optical extinction coefficients and several algorithms have been used to overcome these difficulties.^[2, 3] (4) For identical scattering particulates, there is a coherent scattering effect at zero degrees that, although not yet observed, should increase the scattered intensity by a large factor.^[4] (5) Mueller matrix elements at a 0° scattering angle have been shown to permit classification of the shapes of scattering particles into six symmetry classes, including the class of particles with no symmetries.^[5] (6) Finally, scattering at 0° provides an accurate measure of particle projected areas; in particular, it yields an accurate measure of the radii of scattering spheres that is relatively independent of their index of refraction.

Theoretical Results for Scattering by Spheres at 0°:

Item (6) is of special importance and some theoretical results are provided to illustrate it. Consider the Mueller matrix element S_{11} that gives the scattered intensity I_s for an unpolarized incident intensity I_i (i.e. $I_s = S_{11}I_i$). For a sphere scattering at 0°, $S_{11}(0^\circ) = |S(0^\circ)|^2$, where $S(0^\circ)$ is the complex scattering amplitude.^[4] Fig. 1 shows $S_{11}(0^\circ) \times 10^{-6}$ as a function of the index of refraction for three spheres whose radii differ by 5%. The wavelength is $\lambda = 514.5$ nm. Clearly, for all indices of refraction greater than approximately 1.1, a determination of $S_{11}(0^\circ)$ to an accuracy of ~10% is sufficient to determine the radius to an accuracy of ~3%.

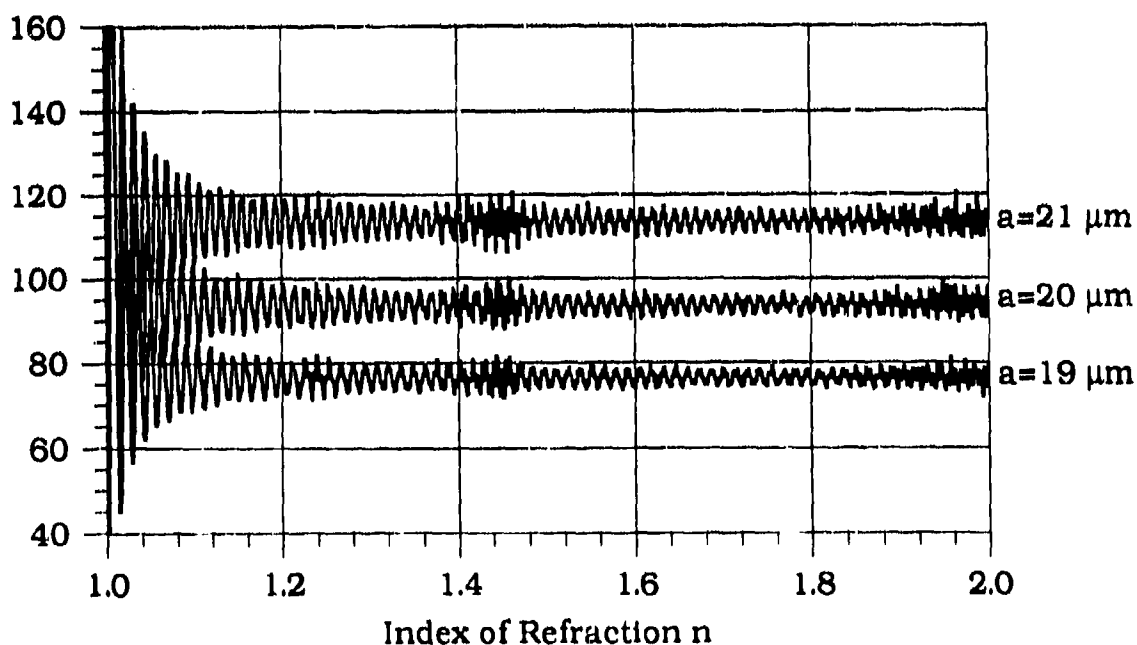


Figure 1. $S_{11}(0^\circ) \times 10^{-6}$ as a function of the index of refraction for three spheres of radii 19 μm , 20 μm , and 21 μm .

For a fixed index of refraction $n = 1.55$, $S_{11}(0^\circ)$ is shown in Fig. 2 as a function of radius. Also shown is the diffraction term which gives the dominant contribution, and which is independent of index of refraction.^[6] It is given by,

$$S_{11(\text{diffraction})}(0^\circ) = 4(\pi a / \lambda)^4. \quad (1)$$

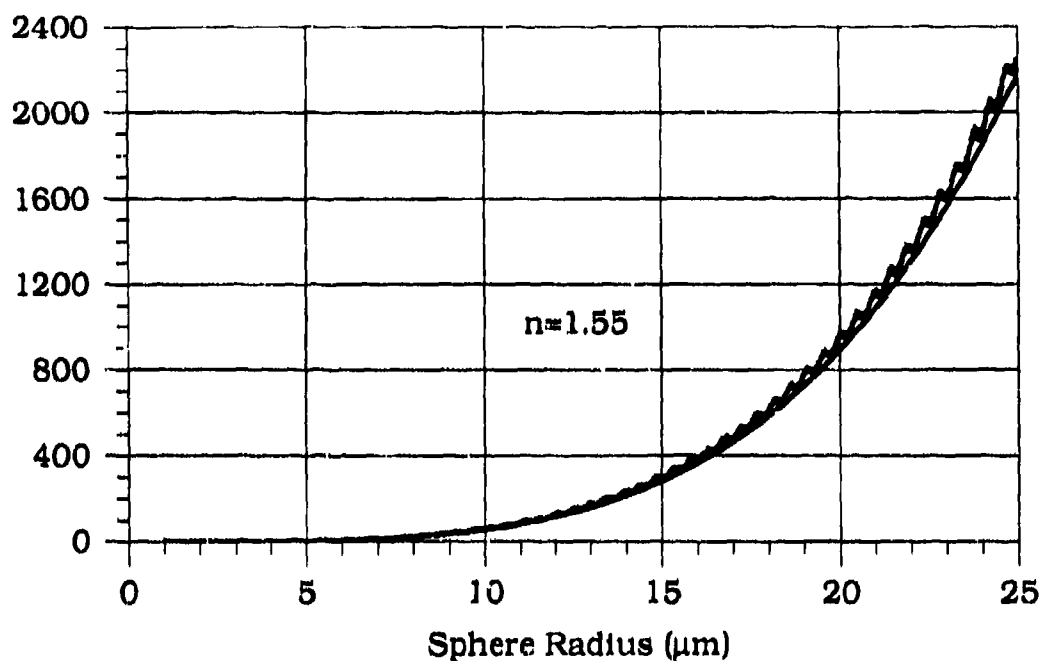


Figure 2. $S_{11}(0^\circ) \times 10^{-6}$ as a function of sphere radius for an index of refraction $n=1.55$. The smooth monotonic increasing curve is the diffraction contribution.

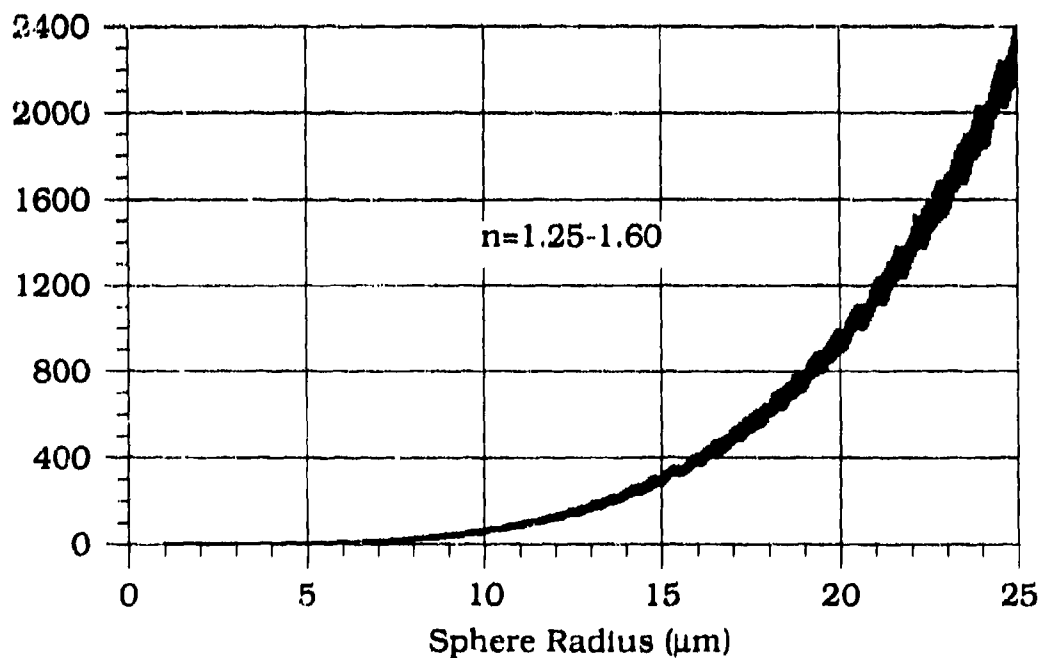


Figure 3. Superimposed plots of $S_{11}(0^\circ) \times 10^{-6}$ as a function of sphere radius from 1 μm to 25 μm for indices of refraction from 1.25 to 1.60 in steps of 0.05.

Fig. 3 shows a superposition of the calculated $S_{11}(0^\circ)$ as a function of radius for indices of refraction $n=1.25$ to 1.60 in steps of 0.05 . Once again, it is clear that a measurement of $S_{11}(0^\circ)$ to an accuracy of $\approx 10\%$ is sufficient to determine the radius to an accuracy of a few percent, independent of the index of refraction in this range. This effect on the relative errors is also apparent by using only the dominant diffraction term to calculate the relation between errors in $S_{11}(0^\circ)$ and the radius a .

$$\frac{\Delta a}{a} = \frac{1}{4} \frac{\Delta[S_{11}(\text{diffraction})(0^\circ)]}{S_{11}(\text{diffraction})(0^\circ)}. \quad (2)$$

Thus, the fractional error in the determination of the radius a is accurately given by $1/4$ the fractional error in the measurement of S_{11} . Finally, Fig. 4 shows details of the calculations in Fig. 3 for radii from $1 \mu\text{m}$ to $6 \mu\text{m}$.

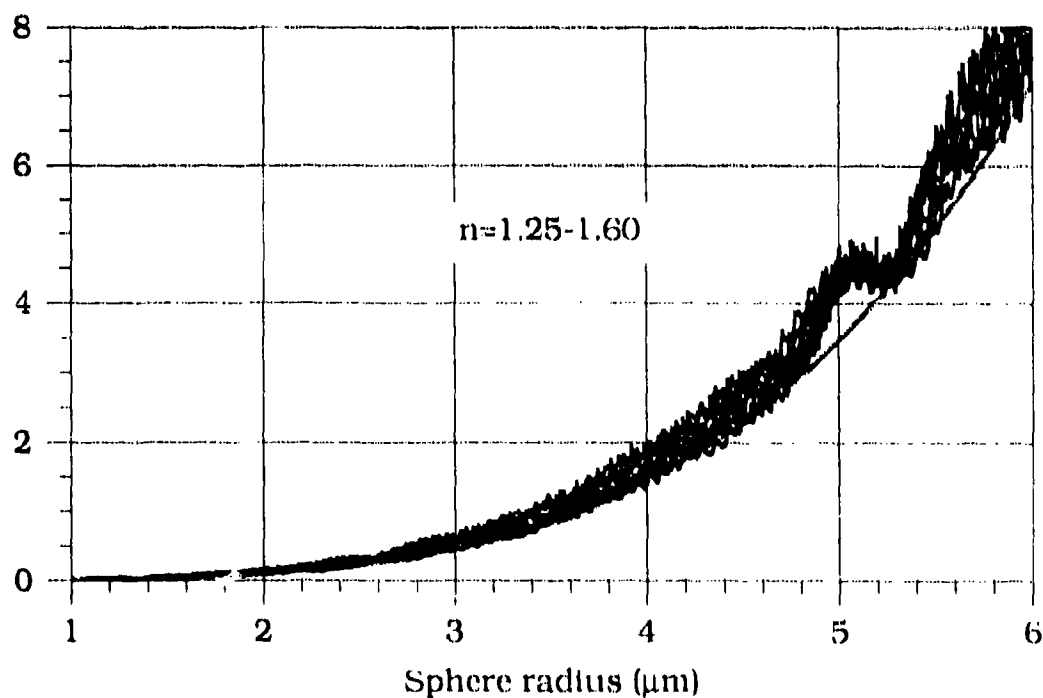


Figure 4. Superimposed plots of $S_{11}(0^\circ) \times 10^{-6}$ as a function of sphere radius from $1 \mu\text{m}$ to $6 \mu\text{m}$ for indices of refraction from 1.25 to 1.60 in steps of 0.05 . The smooth curve is the diffraction term.

Experimental Background:

Experimental studies on light scattering by small particles are generally limited to angles from the near forward direction to the backscattering direction. The limiting experimental factor in the forward direction, $\theta = 0^\circ$, is the unscattered plane wave which is superposed with the scattered spherical wave.^[7] Separation of the two waves is not "impossible" but is difficult.

The identifying characteristic of the light scattered at zero degrees is its phase shift. This phase shift has a spatial time dependence when light is scattered from a moving particle. Our new technique, which takes advantage of the time varying phase shift, will measure light scattering at zero degrees from isolated scatterers that are oscillating on undergoing translation. The approach is based on transient energy coupling with coherent light beams in BaTiO_3 .^[8, 9] Its application to the measurement of scattering at 0° has been previously described.^[10] The present results were obtained using a simplified version based on beam fanning.^[11]

Experimental Results for Glass Fibers:

Fig. 5 shows a schematic of the experimental setup. The cw Ar^+ laser (514.5 nm) is polarized in the plane of the figure, as is the C- axis of each BaTiO_3 crystal. The first crystal is 45° cut and the second is 0° cut. Each crystal was a cube of approximately $5 \times 5 \times 5 \text{ mm}^3$. For all measurements the laser power was kept below 10 mW to maintain a relatively long response time (τ - a few sec). Adjustable apertures A1, A2, and A3 shield the two crystals and the detector from stray light. The lens collects the light that is transmitted through the two crystals and focuses it onto the detector.

The scattering sample is a micron size glass fiber whose axis is normal to the plane of Fig. 5 (and thus to the incident laser beam). The fiber is mounted on a 12 rpm synchronous motor that rotates it in a circle of radius

3 cm. In each rotation, the fiber crosses the laser beam twice, producing two pulses of scattered light. The forward scattered portion of these pulses together with the strong unscattered beam then passes through the two successive BaTiO_3 crystals.

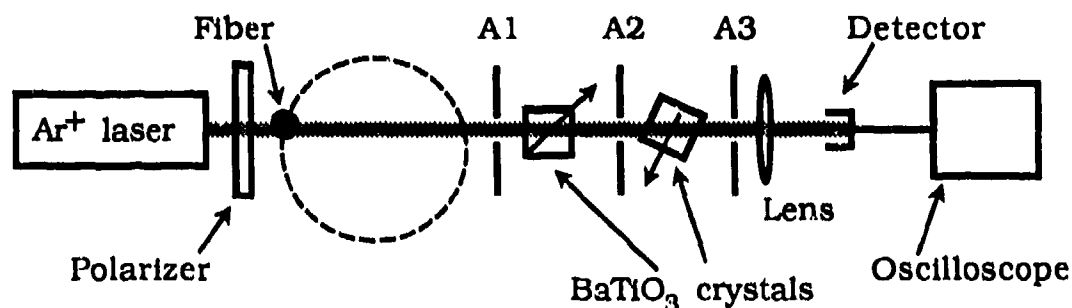


Figure 5. The experimental set-up to measure light scattering at zero degrees by a single glass fiber.

Initially, the crystals were exposed to the direct laser beam for several minutes. The 45° cut crystal produced a very strong beam fanning at normal incidence. However, due to the asymmetry of beam fanning, there was some intensity left on one side of the laser beam. The second crystal further reduced this background. More than 99% of the incident radiation was deviated out of the direct beam path, creating a relatively dark background in the forward direction. Each time the fiber crossed the laser beam, a pulse of light appeared in this dark background. This pulse was detected with a photodiode and the intensity was measured with a sampling oscilloscope. The oscilloscope was triggered by the synchronous motor which rotated the fiber.

Scattering by glass fibers with radii from $1\ \mu\text{m}$ to $27\ \mu\text{m}$ was observed. The observation solid angle for these measurements was a cone with full angle of 0.08° centered at 0° . It was determined by the aperture A3, the collecting lens, and the position of the fiber. The fiber radii were estimated from the angular intensity distributions of their diffraction patterns.

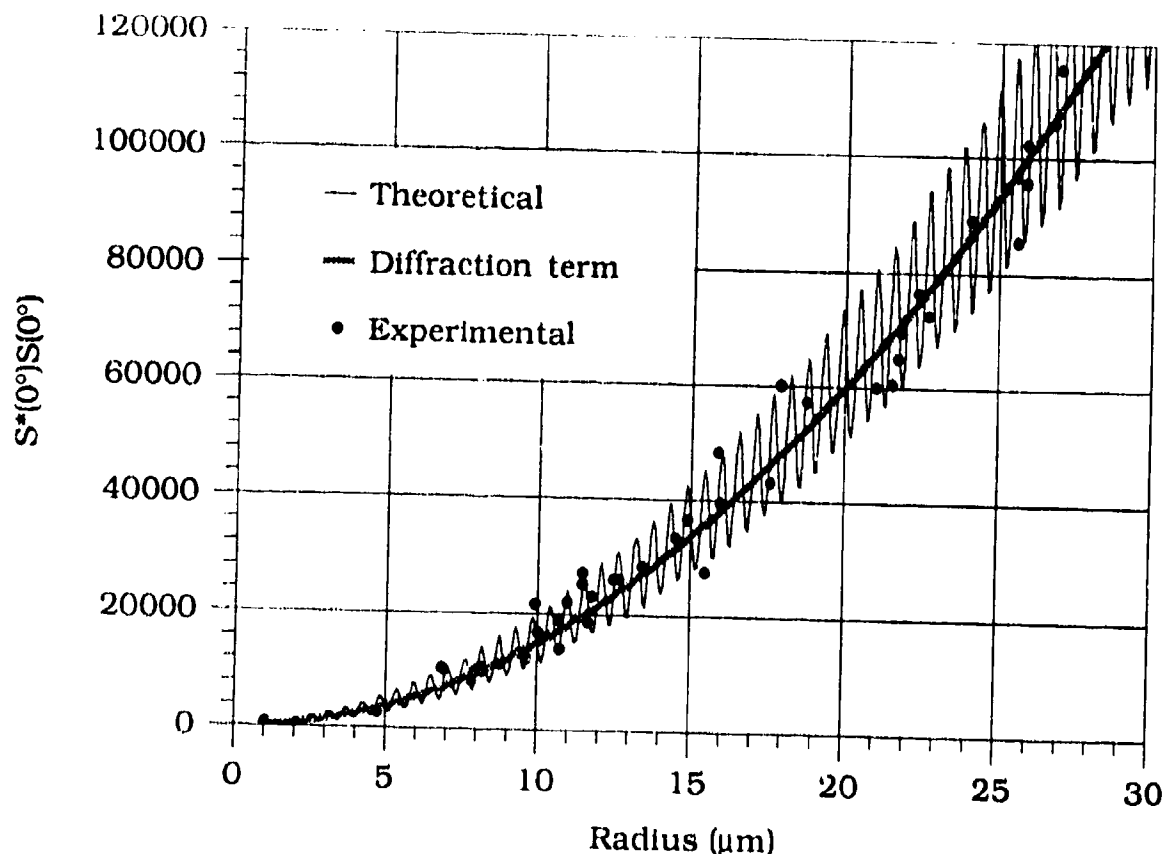


Figure 6. The absolute square of the scattering amplitude at zero degrees, $S^*(0^\circ)S(0^\circ)$, vs. fiber radius.

Black dots in Fig. 6 show the measured intensity vs. the fiber radius. The rapidly oscillating solid line is the theoretical prediction for the scattered intensity at zero degrees.^[4] For reference, the monotonically increasing curve is the diffraction term which is proportional to the square of the radius.^[12] One fitting parameter, the normalization for the ordinate, was used. The data shows very good agreement with theory. Slight variations in the measured intensity are believed to be due to minor imperfections in the fibers. Specifically, a small nonuniformity in the fiber cross section produces a significant change in the forward scattered signal. This is precisely one of the reasons that scattered intensity measurements at 0° are useful for size determinations. (The other principle reason is the relatively negligible dependence on index of refraction for 0° scattering.) At

times, small noise signals were seen due to dust particles crossing the laser beam. These were removed by averaging over several measurements.

Finally, Fig. 7 shows the variation of the forward scattered intensity as a function of the incident laser power for five different fiber radii. The forward scattered intensity measurements are linearly proportional to the incident intensity as expected.

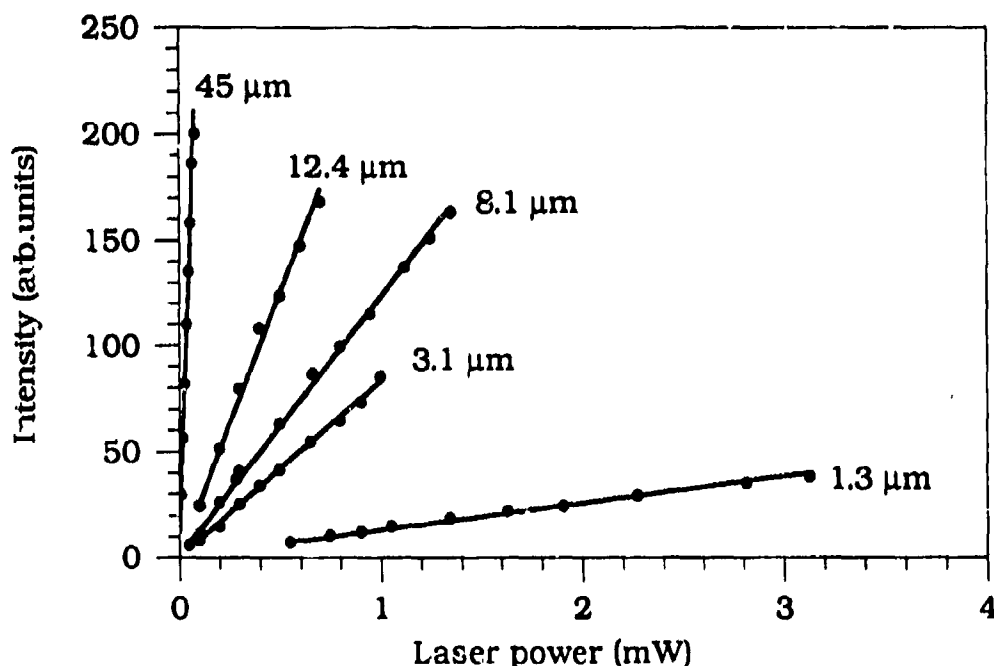


Figure 7. Forward scattered signal as a function of input laser power. Each graph is for a fiber of a different radius ranging from 1.3μ - 45μ .

Summary

A new technique for measuring light scattering at 0° has been successfully demonstrated by measuring the forward scattering from a single micron size glass fiber. Future work will be directed towards measurements and analyses of the forward scattering by single spheres and other particles. This novel technique should also be applicable to measurements of forward scattering from aerosols as well as particle suspensions.

References

1. R. G. Newton, "Optical Theorem and Beyond," Am. J. Phys. **44**, 639-642 (1976).
2. A. Deepak and M. A. Box, "Forward Scattering Corrections for Optical Extinction Measurements in Aerosol Media 1: Monodispersions," Appl. Opt. **17**, 2900-2908 (1978).
3. A. Deepak and M. A. Box, "Forward Scattering Corrections for Optical Extinction Measurements in Aerosol Media 2: Polydispersions," Appl. Opt. **17**, 3169-3176 (1978).
4. C. F. Bohren and D. R. Huffman, "Absorption and Scattering of Light by Small Particles," (Wiley Interscience, New York, 1981).
5. C.-R. Hu, G. W. Kattawar, M. E. Parkin, and P. Herb, "Symmetry Theorems on the Forward and Backward Scattering Mueller Matrices for Light Scattering from a Nonspherical Dielectric Scatterer," Appl. Opt. **26**, 4159-4173 (1987).
6. H. C. Van de Hulst, "Light Scattering by Small Particles," (Dover, New York, 1981) p. 224.
7. H. C. Van de Hulst, "Light Scattering by Small Particles," (Dover, New York, 1981) p. 30.
8. R. S. Cudney, R. M. Pierce, and J. Feinberg, "Transient Detection Microscope," Nature **332**, 424 (1988).
9. N. S. Kwong, Y. Tamita, and A. Yariv, "Optical Tracking Filter Using Transient Energy Coupling," J. Opt. Soc. Am. B **5**, 1788 (1988).
10. G. G. Padmabandu and E. S. Fry, "Measurement of Light Scattering at 0° by Small Particle Suspensions," in Ocean Optics X, R.W. Spinrad, ed., Society Photo-optical Instrumentation Engineers **1302**, (Orlando, FL, 1990), pp. 191-200.
11. G. G. Padmabandu, C. Oh, and E. S. Fry, "Measurement of Light Scattering at 0° by Micron Sized Glass Fibers," Opt. Letters, submitted September, 1991.
12. H. C. Van de Hulst, "Light Scattering by Small Particles," (Dover, New York, 1981) pp. 302-304.

QUASI-BINARY DECISION MAKING USING LIGHT SCATTERING

Po Hu and M. Lax
Physics Department, City College of New York
New York, New York 10031

RECENT PUBLICATIONS, SUBMITTAL FOR PUBLICATION AND PRESENTATIONS:

¹P. Hu, M. Lax, "Single Scattering Inversion Problem", in Proceedings of the 1990 CRDEC Scientific Conference on Obscuration and Aerosol Research.

²B. Yudanin, M. Lax, "POST Adaptation for a Numerical Solution of the Spherically-Symmetric Riemann Problem," J. Mod. Phys. 285-298 (1990).

³B. Yudanin, P. Hu, M. Lax, "Numerical Solution of the Riemann Problem in the Presence of an External Energy Source", in Proceedings of the 1988 CRDEC Scientific Conference on Obscuration and Aerosol Research.

⁴M. Lax, B. Yudanin, "Early-Time Hydrodynamic Response to Pulsed Laser Radiation," Digest - Intl. Conf. on Optical and Millimeter Wave Propagation and Scattering in the Atmosphere, Florence, Italy, 1986.

⁵B. Yudanin, M. Lax, "Hydrodynamical Response to Uniform Laser Absorption in a Droplet," in Proceedings of the CRDC 1985 Scientific Conference on Obscuration and Aerosol Research, edited by R. H. Kohl and D. Stroud (1985).

Abstract

Inversion of light scattering by a single spherical scatterer with or without a layered structure is studied. By numerical simulation of the statistical properties of experiments, we can select those angles that will maximize the ability of the experiment to resolve a sphere from a layered scatterer. Applying statistical decision theory, we obtain a criterion for decision making that minimizes the probability of incorrect guesses.

Introduction

Inversion problems have existed in various branches of engineering and physics for a long time, but in the past twenty years they have received far more attention than ever before because of the available of high speed computers. In the present paper, we are going to invert light scattering information to recognize an inner structure of a spherical object. Because intensities of scattering light are highly nonlinear functions of the size and index of the scatterer, and noise is present, arbitrary pattern recognition is difficult. We will restrict ourselves to distinguishing two kinds of refraction index patterns (uniform or a layered sphere) with a range of parameters. We assume that the scatterer may be one of two kinds of objects: a sphere with a uniform refractive index or a layered sphere with different refraction indices for the core and shell, respectively. Our problems are: (1) For given experimental conditions, is there enough information to make a decision? What is the best choice of angles to yield the most significant statistics. (2) For given experimental data, how should one make a decision that minimizes wrong guesses.

We assume that we already know the following facts: The wave length λ of the light in vacuum is .4416 microns. For the u = uniform sphere (hypotheses 1), the varying parameters are the radius R^u and refraction index n^u , in the ranges $4 \leq R^u/\lambda \leq 8$ and $1.33 \leq n^u \leq 1.8$. For the l = layered sphere (hypotheses 2), the varying parameters are the inner radius R_{in}^l , core and shell refraction indices n_{in}^l and n_{out}^l . They are in the ranges $4 \leq R_{in}^l/\lambda \leq 7$, $1.33 \leq n_{in}^l \leq 1.5$ and $1.55 \leq n_{out}^l \leq 1.8$. The outer radius R_{out}^l of the layered sphere is fixed at $R_{out}^l/\lambda = 8$. Moreover, we assume there is a Gaussian noise added to the scattered intensity with $\sigma/I=0.1$, where σ is the width of the intensity distribution of the Gaussian noise and I is the mean intensity of the light scattered at a given angle.

The method of examining general experimental data to decide between two hypotheses is a classic problem in decision theory. A procedure in the absence of a priori information was proposed by Neyman and Pearson¹ in 1933. Their results are expressed in terms of "maximum likelihood ratios". An excellent overview is given by Kendall and Stuart². A readable description of the Bayes theorem approach to the same problem is given by van Trees³. The close connection between these two approaches is touched on by Middleton⁴ in his section on binary detection systems.

Our problem is more general, in that we must estimate some continuous parameters first, in order to make the best binary decision. In the present application, these parameters are radii and indices of refraction. Thus our problem mixes continuous parameter estimation with discrete parameter detection.

Distinguishability

We propose to study the statistical properties so that we may obtain a criterion for

measuring the distinguishability.

Suppose the experimental light scattering data have been taken at (spherical) scattering angles θ_i and $\phi=0$; the intensity of the scattering light per unit solid angle is denoted as $I(\theta_i)$. We want to relate the observation information to the structure of the scatterer. Because noise is always involved and can not be separated from the experimental data, it will mix the two hypotheses such that they can not be distinguished when the noise level is relatively high. The noise level depends on the experimental apparatus, the environment and the kind of data taken. For a given apparatus and environment, we should measure such data to minimize the relative noise level.

For a single scattering process, the data measured at different angles are not independent; they are correlated through complex formulas (Mie scattering for a sphere and shell). Because of the complex relationships of the scattering formulas, we can not analytically solve and will use numerical simulations to our problem.

Let's say the object is a uniform sphere with the parameter element $\eta^{(1)} \in \{R^u, n^u\}$ in the allowed range and the experimental observation is taken at M angles $\theta_1, \dots, \theta_M$. Here M is a moderate number of order 10. We can regard the scattering as a mapping from the parameter space $\eta^{(1)}$ to an M dimensional observation space $L^M = \{I(\theta_1), \dots, I(\theta_M)\}$. Because noise is present, one point in η space maps to an M dimensional "box" in L^M space. A similar mapping also applies for a layered object. If, at each angle θ_i , separate measurements with P different polarization intensities are made, corresponding to different polarization of the incident and scattered beam, then PM will be the dimension for the observation space. For simplicity of notation, however, we do not always introduce an explicit polarization index.

In the following, we will define a resolution criterion. First, we generate a set $\{\eta^{(j)}\}$ which includes N elements of random parameters $\eta_m^{(j)}$ in the allowed ranges for hypothesis j ($j=1$ for uniform sphere and $j=2$ for layered object), where $m=1, \dots, N$. Here N is a large number of order 1000. The m th element $\eta_m^{(1)}$ of the uniform sphere set $\{\eta^{(1)}\}$ has two parameters R^u and n_m^u , and the m th element $\eta_m^{(2)}$ of the layered object set $\{\eta^{(2)}\}$ contains three parameters $R_{m,\text{in}}^l$, $n_{m,\text{in}}^l$ and $n_{m,\text{out}}^l$. With the added noise, one image for each of the two sets $\{\eta^{(1)}\}$ and $\{\eta^{(2)}\}$ are obtained in the observation space L^M . Within the overlap region of the two images in the observation space L^M the two kinds of objects are indistinguishable from the given M intensity measurements. We will give the definition of overlap later. An event producing an image in the overlap region of the observation space is regarded as an indistinguishable event for the two hypotheses. Counting the number of the events which overlap in the observation space, we may get a measure of indistinguishability between the two cases. The ratio of the number of overlapped events to the total number events represents a measure of the indistinguishability.

We study the probability properties of the two hypotheses. In the observation space,

an image point from one hypothesis can always have a probability of overlap with the an image of the other kind of hypothesis. Therefore we need to precisely define overlap of images in the observation space. We use $N(I(\theta))$ for the number of events such the intensity is in the range of $I(\theta)$ to $I(\theta)+dI(\theta)$ and N for the total number of events. We then define an overlap function:

$$F_p(\theta, I_p; \{\eta^{(1)}\}, \{\eta^{(2)}\}) = \left[\frac{\tilde{N}(I_p^{(1)}(\theta, \{\eta^{(1)}\}))}{N} \frac{\tilde{N}(I_p^{(2)}(\theta, \{\eta^{(2)}\}))}{N} \right]^{1/2} \quad (1)$$

where the subscript p denotes the polarization and the superscript (1) and (2) are for different hypotheses. The set of N (~ 1000) points in $\{\eta^{(j)}\}$ possesses a subset $[\eta^{(j)}(\theta_i)]$ which overlap in the sense that it may no longer be possible to distinguish whether case $j=1$ or $j=2$ is the correct with respect to a single measurement. We can choose a threshold $\alpha_{i,p}$ of indistinguishability for θ_i and measured intensity I_p by using the criteria

$$F(\theta_i, I_p; \{\eta^{(1)}\}, \{\eta^{(2)}\}) \geq \alpha_{i,p} \quad \text{for all } \eta_m^{(j)} \in \{\eta^{(j)}\} \quad (2)$$

to determine the elements of subset $[\eta^{(j)}(\theta_i)]$. For observations at many angles, the joint set of subsets for all measured angles

$$|\eta^{(1)}(\theta_1, \dots, \theta_n)| = \bigcap_{i=1}^n |\eta^{(1)}(\theta_i)| \quad (3)$$

measures the overall fuzziness of the experiment. As an application, we assume the measurement is taken at given angles $\theta=25, 40, 90, 105, 125, 140$ for two polarizations (12 measurements). For simplicity we set all $\alpha_{i,p}$ to be the same $\alpha_{i,p}=\alpha$. In Fig. 1 we show the original set (dots) of parameters for the uniform sphere chosen by Monte Carlo techniques, and its joint subset for 12 measurements (triangles). The ratio of the numbers of the elements of the joint subset and the original set is about 10%. Therefore, about 90% of uniform sphere events (the dots not covered by the triangle in Fig. 1) are distinguishable from the layered events in the L^{12} space. The superscript 12 is the number of dimensions of the observation space, that is the number of measurements. The remaining 10% of the events for the uniform sphere (the triangles in Fig. 1) are indistinguishable from the layered scatterer for the given set of 12 measurements.

To produce a better resolution between these two hypotheses, a trivial approach is to increase the number of the detectors so that the events in the new space L^M ($M>12$) will not overlap as much as in the original space L^{12} . In most experiments, distinguishability is limited by the number of detectors. To make the most of the equipment for a better resolution, one can rearrange the detectors for some optimized angles so that the number of the elements in the joint subset is minimized. This can be done by the following iteration procedure: First we randomly generate two parameter sets $\{\eta^{(1)}\}$ and $\{\eta^{(2)}\}$ as initial sampling sets. Use Eq. (4) below to find the best angle θ_1 by taking a minimum of the overlap function F for two polarizations over θ_1 . Substitute θ_1 and the original sampling sets into Eq. (5), below, to obtain the subsets $[\eta^{(1)}(\theta_1)]$ and $[\eta^{(2)}(\theta_1)]$ by Eq. (5). Iterating this procedure by using the new sets $[\eta^{(j)}(\theta_1)]$ in Eqs. (4)

and (5), we will obtain the second best angle θ_2 and the subset $[\eta^{(j)}(\theta_1, \theta_2)]$. Repeat the iteration procedure (4) and (5) for angles $\theta_1, \theta_2, \theta_3, \dots$ until the number of elements of the joint subset $[\eta^{(j)}(\theta_1, \dots, \theta_n)]$ is less than a desired value. With the optimization completed for $i-1$ angles, we can optimize over θ_i using:

$$\min_{\theta_i} \prod_{p=1}^2 \int_0^\infty dI F_p(\theta_i, I_p; [\eta^{(1)}(\theta_1, \dots, \theta_{i-1})], [\eta^{(2)}(\theta_1, \dots, \theta_{i-1})]) \quad (4)$$

$$\eta_m^{(j)} \in [\eta^{(j)}(\theta_1, \dots, \theta_{i-1}, \theta_i)] \text{ if } F_p(\theta_i, I_p; [\eta^{(1)}(\theta_1, \dots, \theta_{i-1})], [\eta^{(2)}(\theta_1, \dots, \theta_{i-1})]) \geq \alpha_{i,p} \\ \text{for all } \eta_m^{(j)} \in [\eta^{(j)}(\theta_1, \dots, \theta_{i-1})] \quad (5)$$

Here we assumed that intensities of two polarizations (the subscript p) for each angle have been measured.

Decision

In this section, we apply statistical decision theory to the inversion problem. Let H_1 and H_2 denote the two hypotheses; 1 for the uniform sphere and 2 for the layered sphere. Suppose we have obtained a set of experimental data for the intensities at several angles $I_{\text{exp}}(\theta_i)$. We want to decide which class (uniform sphere or layered object) the scatterer belongs to. We can use the least square fit to find the best fit for the hypothesis h :

$$\nu_h = \min_{\eta^{(h)}} \sum_i \left[I_{\text{exp}}(\theta_i) - I(\theta_i, \eta^{(h)}) \right]^2 \quad (6)$$

within the permitted parameter space. A simple statistic to decide between these cases can be chosen as $\nu_1 - \nu_2$. Suppose the experimental data are from a uniform sphere, $k=1$. Then ν_1 is dominated by the experimental noise, usually a small value, while ν_2 is a large value because it is not dominated by noise but by the shift because of an incorrectly chosen hypothesis. For some experimental data the fitting with wrong hypothesis may be small if the number of the detectors is not large enough. The wrong fitting value of ν covers a large range of a uniform scale space. Therefore we use a log scale for the statistic

$$R = \log_{10}(\nu_1 / \nu_2)$$

to decide between the two hypotheses. The decision rule can be obtained as follows. Let's assume we know the conditional probability $P(R | H_h)$ of getting R under hypothesis h . According to Neyman-Pearson¹⁻⁴, when a priori probability and the cost of the decision are unknown, we may use a constraint condition on the probability P_F , of a "false alarm" is:

$$P_F = \alpha = \int_\lambda^\infty P(R | H_1) dR \quad (7)$$

to find the threshold λ , where α is the value permitted for a false alarm (we say H_2 while H_1 is true). After finding the threshold, we shall make decision by the criterion:

$$\text{if } \Lambda(R) > \lambda \quad \text{choose } H_2 \quad (8)$$

$$\text{if } \Lambda(R) < \lambda \quad \text{choose } H_1 \quad (9)$$

where

$$\Lambda(R) = P(R | H_1) / P(R | H_2) \quad (10)$$

is the maximum likelihood ratio.

The conditional probabilities, $P(R | H_h)$, can be obtained (ahead of time) by numerical simulation. As an application, we generate a set consisting of 1000 elements of random parameters for each hypothesis. We then calculate the intensities of the light scattering for these parameters at the angles $\theta = 90, 105, 120, 135, 150, 165$ for both parallel and perpendicular polarizations. Finally we add 10% noise to the calculated intensities and regard the result as pseudo experimental data. To get the distribution profiles for both cases, we also use the least square method

$$v_h^s = \min_{\eta^{(h)}} \sum_i \left[I_{\text{exp}}^s(\theta_i) - I(\theta_i, \eta^{(h)}) \right]^2 \quad (11)$$

to fit the pseudo experimental data with the best parameter $\eta^{(h)}$. Here I_{exp}^s was computed for source s (pseudo experimental data). v_h^s is the best least square fit for a set of experimental data of source s by the hypothesis h within the permitted parameters. Because we used wide ranges for the parameters, the intensities have hundreds of oscillations over the varying parameters. It is difficult to locate a global minimum for v_h^s , because it has hundreds of oscillations over the varying parameters. To make the programs more efficient, we made lookup tables for the Bessel and Legendre functions. Defining $R^s = \log_{10}(v_1^s / v_2^s)$ and counting the number of the events in which R^s falls into the interval $(R, R+dR)$, denoted as $N(R^s)$, we obtain the distribution profile for the source s . In Fig. 2, $N(R^s)$ vs R^s is plotted for both sources. The left profile of this figure is for the source $s=1$ the uniform sphere, while the right one is for the source $s=2$ the layered object. The small overlap between the two curves in Fig. 2. shows that the resolution of these two cases is quite good.

¹J. Neyman and E. S. Pearson, "On the Problem of the Most Efficient Tests of Statistical Hypotheses," *Philosophical Trans. A*, 231, 289 (1933)

²M. G. Kendall and A. Stuart, *The Advanced Theory of Statistics, Volume 2* Hafner Publishing Co, New York (1967)

³H. L. Van Trees, *Detection, Estimation, and Modulation Theory, Part I*, John Wiley and Sons, (1968)

⁴David Middleton, *Introduction to Statistical Communication Theory*, McGraw-Hill (1960)

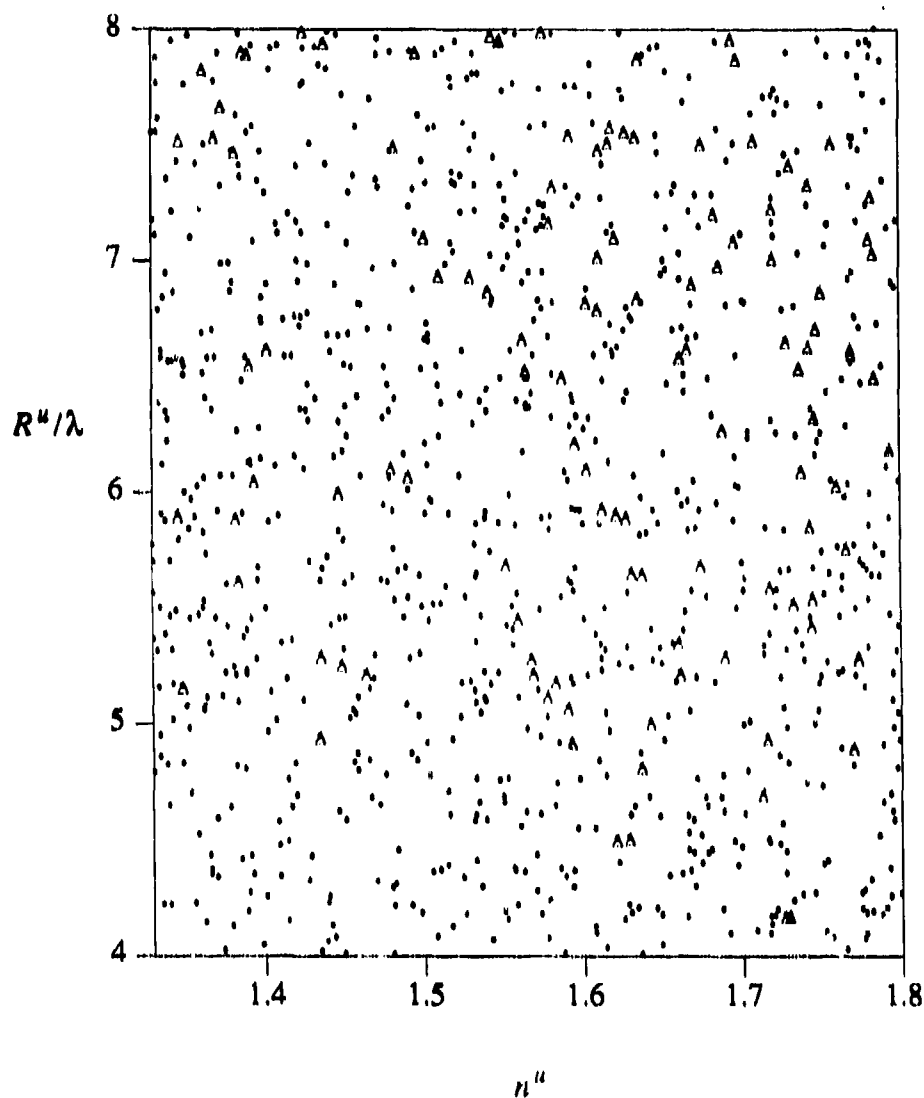


Fig. 1. Joint subset and original parameter set for the uniform sphere. The vertical scale is for R^u/λ . The 1000 dots (and triangles) are randomly selected from the available parameter set $\{\eta^{(1)}\}$ for the uniform sphere. The triangles are for the elements of the joint subset of uniform sphere for the 6 given angles and two polarizations; they are the points indistinguishable from the layered objects. The ratio of the numbers of the triangles and dots is about 10%, or about 90% of the uniform sphere events are distinguishable from layered objects. The original parameter set consists 1000 elements, each one has two components of random numbers for the parameters of the uniform sphere. The two parameters are the radius and refraction index in the ranges of $4 \leq R^u/\lambda \leq 8$ and $1.33 \leq n^u \leq 1.8$. The measurements are taken for the intensities of two polarizations (parallel and perpendicular) at 6 angles $\theta=25, 40, 90, 105, 125, 140$.

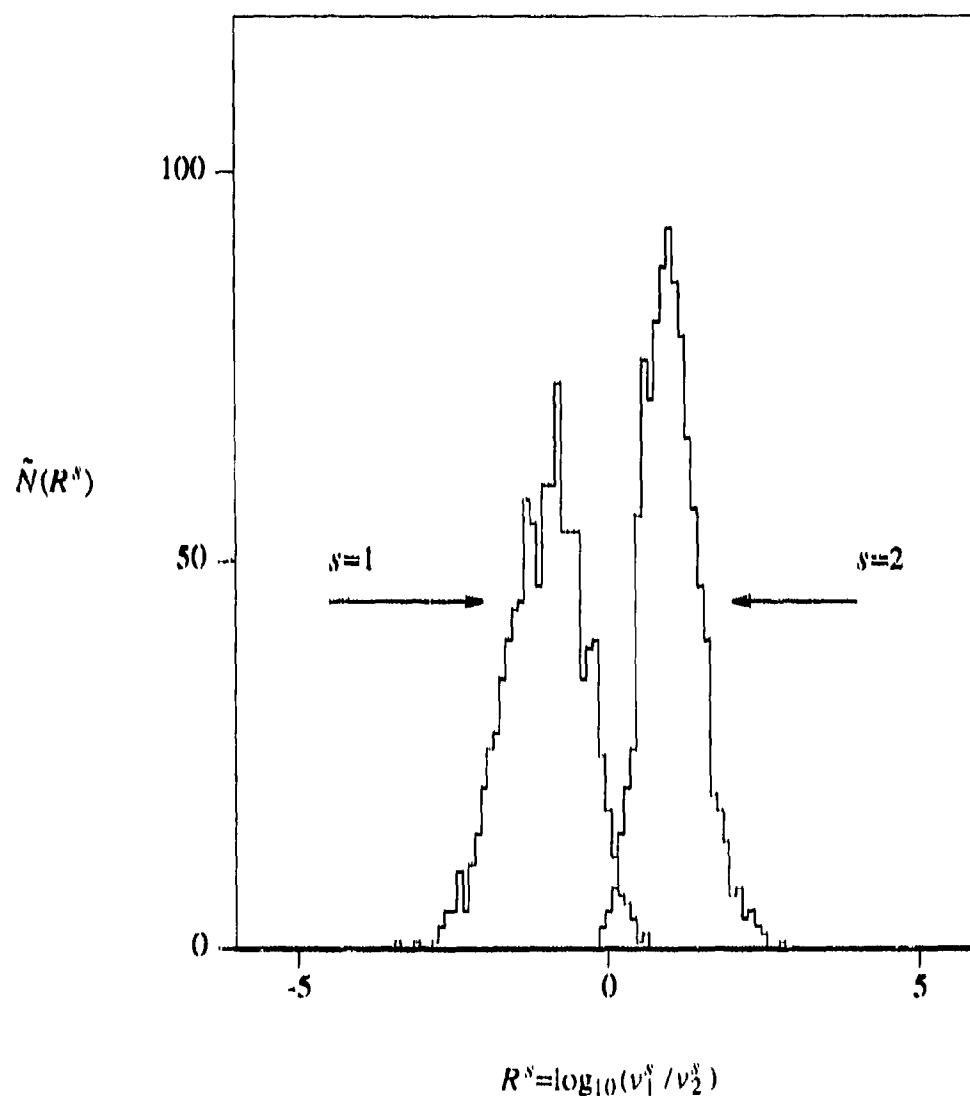


Fig. 2. Distribution profiles. The vertical axis is $\tilde{N}(R^s)$ the number of events per unit R , $dR=0.1$ is used. The left profile is the distribution profile for the appropriate for uniform spherical source, while the right one is for the layered scatterer. The measurements are taken for the intensities of two polarizations (parallel and perpendicular) at 6 angles $\theta=90, 105, 120, 135, 150, 165$ with 10% noise. The uncertainty of the parameter ranges are follows: For the sphere, the two parameters are the radius and refraction index in the ranges of $4 \leq R^u / \lambda \leq 8$ and $1.33 \leq n^u \leq 1.8$. For the layered object, the three parameters are the inner radius and refraction indices in the ranges of $4 \leq R_{in}^l / \lambda \leq 7$, $1.33 \leq n_{in}^l \leq 1.5$ and $1.55 \leq n_{in}^l \leq 1.8$.

A FINITE ELEMENT SOLUTION OF THE MAXWELL EQUATIONS FOR ABSORPTION AND SCATTERING OF ELECTROMAGNETIC RADIATION BY A SPHERICAL PARTICLE

L. Liebman and J. Brock
Chemical Engineering Department
University of Texas, Austin, Texas 78712

RECENT PUBLICATIONS, SUBMITTALS FOR PUBLICATION AND PRESENTATIONS

- "Time resolved Raman spectroscopy from reacting, optically levitated microdroplets," J. C. Carls, G. Moncivais, and J. R. Brock, *Applied Optics*, **29**, 2913-18, 1990.
- "Formation of carbon fibers in corona discharges," J. R. Brock and P. Lim, *Applied Physics Letters*, **58**, 1259-1261, 1991.
- "Time-resolved Raman spectroscopy from reacting optically levitated microdroplets," J. R. Brock and J. C. Carls, *SPIE Proceedings, Nonlinear Optics and Materials*, 1497, 1991.
- "Laser-induced breakout and detonation waves in droplets: II. Model," J. C. Carls, Y. Seo and J. R. Brock, *J. Optical Soc. America B*, **8**, 329-336, 1991.
- "Anisotropic etching of SiO₂ with a 38.2 weight percent hydrofluoric acid aerosol," B. J. Jurcik and J. R. Brock, *J. Electrochem. Soc.*, **138**, 2141, 1991.
- "Laser-assisted wet etching of silicon," P. Lim and J. R. Brock, *Applied Physics Letters*, In Press, 1991.
- "Aerosol jet etching of Hg_{1-x}Cd_xTe," *Applied Physics Letters*, **56**, 1682-1685, 1990 (with B. J. Jurcik and I. Trachtenberg).
- "Explosive vaporization of single droplets," J. C. Carls and J. R. Brock, *J. Appl. Phys.*, In Press.
- "Numerical simulation of particle formation and growth in rapidly expanding axisymmetric flows," B. J. Jurcik and J. R. Brock, *Physics of Fluids A*, In Press, 1991.
- "Laser induced etching of silicon in hydrofluoric acid," *J. Electrochem. Soc.*, **138**, 2141-2145, 1991 (with P. Lim, H. Gerlscher and I. Trachtenberg).
- "Finite element approach to solution of the Maxwell equations for scattering and absorption by dielectric spheres," L. Liebman and J. R. Brock, *Proceedings of the 1990 CRDEC Scientific Conference on Obscuration and Aerosol Research*, CRDEC, U. S. Army, 1991.
- "A new measure for plume obscurant effectiveness," J. R. Brock, *Proceedings of the 1990 CRDEC Scientific Conference on Obscuration and Aerosol Research*, CRDEC, U. S. Army, 1991.
- "Particle formation by homogeneous nucleation in rapidly expanding flows," B. J. Jurcik and J. R. Brock, *Proceedings of the 1990 CRDEC Scientific Conference on Obscuration and Aerosol Research*, CRDEC, U. S. Army, 1991.
- "Research on aerosol plume mechanics and particle growth," J. R. Brock, Final Report, Contract DAAA15-86-K0015, Department of the Army, U. S. Army Armament Munitions Chemical Command, Chemical Research Development & Engineering Center, Aberdeen Proving Ground, MD 21010, July 1991.

ABSTRACT

The problem of scattering and absorption of electromagnetic radiation by particles can be solved analytically for only the simplest cases, but numerical methods allow a straightforward extension to particles with arbitrary inhomogeneities, arbitrary shapes, and nonlinear response. In this paper a recently developed frequency domain method involving CFD techniques is reviewed and applied to the problem of a dielectric sphere of arbitrary size parameter. Numerical results indicating the promise of finite element methods are given and recommendations for further investigations are presented.

INTRODUCTION

Mie theory exactly describes the absorption and scattering of a plane electromagnetic wave by an isotropic, dielectric sphere of arbitrary size and refractive index (van de Hulst, 1957; Kerker, 1969). This conceptually simple analytical solution is well known, but it involves cumbersome computations. Since the advent of high-speed computers,

which utilize parallel and vector processing, much effort has been made to improve the analytical scattering algorithms (Wiscombe, 1979 and 1980). However, while it is relatively simple to generate data for the spherical problem, the analytical calculations can not be extended to arbitrary nonspherical particles. If a numerical rather than an analytical approach is taken, the extension to particles with arbitrary inhomogeneities, arbitrary shapes, and nonlinear response is more apparent since the general governing equations and the solution technique remain unchanged.

Previously a finite difference method was applied to the problem of a linearly polarized plane electromagnetic wave scattered by a perfectly conducting sphere (Ling, 1988). The results demonstrated the applicability of computational fluid dynamics (CFD) methods to the basic scattering problem. In this presentation, the investigation is broadened by using a finite element method to model scattering by a dielectric sphere; results confirm that CFD methods are a promising technique. The objectives of further studies are discussed in the final section.

THEORY

The problem to be solved consists of a plane polarized wave incident on a dielectric particle; only linear scattering is considered. Assuming $\exp(-i\omega t)$ dependence for all fields, the electric and magnetic fields must satisfy the vector wave equation both inside and outside the particle:

$$\nabla^2 \mathbf{E} + k^2 \mathbf{E} = 0 \qquad \nabla^2 \mathbf{H} + k^2 \mathbf{H} = 0 \qquad (1,2)$$

where $k^2 = \omega^2 \epsilon \mu$. Additionally, the boundary conditions

$$\hat{n} \times (\mathbf{E}_I - \mathbf{E}_{II}) = 0 \qquad \hat{n} \times (\mathbf{H}_I - \mathbf{H}_{II}) = 0 \qquad (3,4)$$

require that the tangential components of \mathbf{E} and \mathbf{H} must be continuous across the surface of the particle (Bohren and Huffman, 1983) and the Sommerfeld radiation condition (Stratton, 1941) requires that the scattered fields represent divergent traveling waves as $r \rightarrow \infty$. In equations (3) and (4), "I" denotes the exterior region and "II" denotes the internal region.

By introducing two auxiliary scalar functions, the electric and magnetic Debye potentials, u and v (Kerker, 1969; Born and Wolf, 1959; Borghese, et al., 1979), it is possible to reduce the vector equations (1) and (2) to a set of uncoupled scalar wave equations:

$$\nabla^2 u + k^2 u = 0 \qquad \nabla^2 v + k^2 v = 0. \qquad (5,6)$$

The field quantities can be deduced from the potentials as follows:

$$\mathbf{E} = \nabla \times [\nabla(ru) \times \hat{\mathbf{r}}] + i\omega\mu \nabla \times (rv\hat{\mathbf{r}}) \qquad (7)$$

$$\mathbf{H} = \nabla \times [\nabla(rv) \times \hat{\mathbf{r}}] + i\omega\epsilon \nabla \times (ru\hat{\mathbf{r}}). \qquad (8)$$

Since the field variables are oscillatory in nature over the infinite domain it is advantageous to reformulate the problem once again, this time in terms of a generalized amplitude function which eliminates the oscillations due to the incident field (Ling, 1987). By making use of the superposition property of the fields, the Debye potentials outside the particle can be decomposed into incident and scattered components. The scattered components then are written as

$$u^s = \frac{\cos\phi \sin\theta}{(k^I)^2} f_1^s(r, \theta) \frac{e^{ik^I r}}{r} \quad (9)$$

$$v^s = \left(\frac{\epsilon^I}{\mu^I}\right)^{1/2} \frac{\sin\phi \sin\theta}{(k^I)^2} f_2^s(r, \theta) \frac{e^{ik^I r}}{r} \quad (10)$$

where $f(r, \theta)$ is a Debye amplitude function. Similar expressions can be written for the potentials inside the particle. It should be noted that the formulation of equations (9) and (10) inherently restricts one to the consideration of only axisymmetric problems. For asymmetric cases the ϕ dependence of the Debye potentials can not be factored out explicitly and one must solve for $f(r, \theta, \phi)$.

By substituting equation (9) into (5) and equation (10) into (6) it can be shown that the problem to be solved is

$$-\nabla^2(f_1 e^{ik^I r}) - \frac{2\cot\theta}{r^2} e^{ik^I r} \frac{\partial f_1}{\partial \theta} + \frac{2}{r} e^{ik^I r} \left(\frac{\partial f_1}{\partial r} + ik^I f_1 \right) - e^{ik^I r} f_1 \left(k^2 - \frac{2}{r^2} \right) = 0 \quad (11)$$

$$\left(\frac{\epsilon}{\mu}\right)^{1/2} \left(-\nabla^2(f_2 e^{ik^I r}) - \frac{2\cot\theta}{r^2} e^{ik^I r} \frac{\partial f_2}{\partial \theta} + \frac{2}{r} e^{ik^I r} \left(\frac{\partial f_2}{\partial r} + ik^I f_2 \right) - e^{ik^I r} f_2 \left(k^2 - \frac{2}{r^2} \right) \right) = 0. \quad (12)$$

The boundary conditions (3) and (4) are, in terms of f_1 and f_2 :

$$e^{ik^I r} \epsilon^{II} f_1^{II} - e^{ik^I r} \epsilon^I f_1^s = \frac{\epsilon^I W}{\sin\theta} \quad (13)$$

$$e^{ik^I r} \sqrt{\epsilon^{II}} f_2^{II} - e^{ik^I r} \sqrt{\epsilon^I} f_2^s = \frac{\sqrt{\epsilon^I} W}{\sin\theta} \quad (14)$$

$$e^{ik^I r} \left[\left(\frac{\partial f_1^{II}}{\partial r} + ik^I f_1^{II} \right) - \left(\frac{\partial f_1^s}{\partial r} + ik^I f_1^s \right) \right] = \frac{1}{\sin\theta} \frac{\partial W}{\partial r} \quad (15)$$

$$e^{ik^I r} \left[\left(\frac{\epsilon^{II}}{\mu^{II}} \right)^{1/2} \left(\frac{\partial f_2^{II}}{\partial r} + ik^I f_2^{II} \right) - \left(\frac{\epsilon^I}{\mu^I} \right)^{1/2} \left(\frac{\partial f_2^s}{\partial r} + ik^I f_2^s \right) \right] = \left(\frac{\epsilon^I}{\mu^I} \right)^{1/2} \frac{1}{\sin\theta} \frac{\partial W}{\partial r} \quad (16)$$

where

$$W(r, \theta) = \frac{e^{ikr \cos\theta}}{\sin\theta} - \cot\left(\frac{\theta}{2}\right) \frac{e^{ikr}}{2} - \tan\left(\frac{\theta}{2}\right) \frac{e^{-ikr}}{2} \quad (17)$$

and the radiation condition can be expressed as

$$\lim_{r \rightarrow \infty} \frac{\partial f_1}{\partial r} = 0 \quad \lim_{r \rightarrow \infty} \frac{\partial f_2}{\partial r} = 0. \quad (18)$$

Equations (13) through (16) are formulated for a spherical particle, where "a" is the radius of the sphere. For the general asymmetric problem, equations (13) through (16) must be satisfied at all (x,y) on the particle surface and the partial derivatives are given by $\nabla f \cdot \mathbf{n}$.

FINITE ELEMENT METHOD AND RESULTS

The system of equations is solved numerically on a Cray Y-MP8/864 by a finite element method with 9-node Lagrange quadrilaterals (Becker, et al., 1981) using the subroutine HCGBLE, part of the Boeing Computer Services mathematical library (BCSLIB, 1989). A multiplier method (Carey and Oden, 1984) is used to enforce the jump in solution across the particle boundary, which must coincide with element boundaries. The radiation boundary condition is imposed at a finite artificial surface ($r \ll \infty$) with good accuracy by using a second-order approximation to the Sommerfeld condition (Bayliss, et al., 1982). Both the radiation boundary condition and the jump in flux condition are incorporated into the weak formulation of the differential equation.

Initial investigations have been performed for a CO_2 laser, that has a wavelength *in vacuo* of 10.591 μm , incident on a spherical water particle that has a refractive index of $1.179 + 0.071i$. The particle was isolated and was surrounded by air that was assumed to have a refractive index of 1.0. Size parameters that were studied include 2.97, 5.93, and 11.87, which correspond to water droplets having diameters of 10.0 μm , 20.0 μm , and 40.0 μm .

Results are presented for the 40.0 μm case in Figs. 1 through 3. These results were obtained using a 26×45 uniform mesh having a maximum grid radius of twice the particle radius and required 13.8 seconds of CPU time (with a code that has not been fully vectorized) to determine both f_1 and f_2 over the entire domain. Fig. 1 depicts three-dimensional views of the numerical and analytical solutions of the real part of f_2 . In these graphs the incident wave propagates in the positive z-direction, from the left foreground to the right rear. The particle is centered at the origin which is at the center of the plot, and the x- and z-axes show distances in micrometers. By comparing the top and bottom pictures, the excellent agreement between the two solutions can be seen. Plots of the imaginary part of f_2 and the real and imaginary parts of f_1 show similar agreement.

Figures 2 and 3 show two-dimensional views of the Debye amplitude functions f_1 and f_2 on the centerline of the sphere along the z-axis. The incident wave propagates from left ($\theta = 180^\circ$) to right ($\theta = 0^\circ$), so the forward direction corresponds to the right side of the figures. The numerical solutions are given at the nodal locations while the analytical solutions are represented by continuous curves. Several observations can be made from these figures, the main one again being the good agreement between the numerical and analytical solutions. f_1 and f_2 are also qualitatively similar, which is expected because of the similarity of the governing equations given in (11) and (12) and the boundary conditions given in (13) through (17).

One quantitative measurement of the error of the numerical solution over its domain is given by the mean-square, or L^2 , norm (Becker et al., 1981), which is defined for complex functions as

$$L^2 = \left[\int_{\text{area}} (e e^*) dA \right]^{1/2} \quad (19)$$

where e is the difference between the analytical and the numerical solution and e^* is the complex conjugate of e . The better the numerical approximation, the closer the L^2 norm is to zero. For the 40.0 μm water droplet, the L^2 norms for f_1 and f_2 are both 3.7×10^{-4} .

Figure 4 shows both the computation time and the L^2 norms as a function of size parameter of water droplet. Note that the computation times are not prohibitive and that the relationship between CPU and x is approximately linear. Additionally, the norms do not increase with increasing x , demonstrating, for examples studied so far, that the accuracy of the solutions does not degrade with increasing size parameter. These items support the idea that much larger spherical particles as well as more complicated scatterers can be studied without modifying the underlying solution technique presented here.

RECOMMENDATIONS FOR CONTINUED INVESTIGATIONS

Following is a list of recommendations for further investigations; a short description of necessary requirements accompanies each suggestion.

- (1) Improve current algorithm. Decrease computation times through full vectorization of the finite element code and the use of nonuniform and adaptive grid techniques. These modifications will become important as more difficult scattering problems, including problems in three dimensions, are modelled.
- (2) Add postprocessor. If results are desired in terms of fields, scattering amplitudes, the Mueller matrix, or another quantity, these values can be calculated from the Debye amplitude functions.
- (3) Consider multilayer spheres. This generalization will require minor modifications to the code to allow the handling of more than one material interface. The solution technique will remain unchanged.
- (4) Consider arbitrarily-shaped axisymmetric particles for which the axis of symmetry is aligned with the direction of propagation of the incident field. A grid generating routine that allows the user to define an arbitrary surface of revolution must be added to the code for this case.
- (5) Extend the calculations to asymmetric cases. For asymmetric problems the Debye amplitude functions are functions of r , θ , and ϕ and the problem must be solved in three dimensions.
- (6) Consider nonlinearities. If the optical parameters are dependent on the electromagnetic field, the differential equations that govern the scattering problem are nonlinear.

ACKNOWLEDGMENTS

This work was supported by CRDEC, U.S. Army. We wish to thank Drs. R. Ling, M. Lax, I. Sindoni and E. Stuebing for helpful discussions on this problem.

REFERENCES

- Bayliss, A., M. Gunzburger, and E. Turkel, 1982. *SIAM J. Appl. Math.*, **42**, 430.
- BCSLIB, 1989. *BCSLIB Mathematical/Statistical Library: Advanced Subprograms in Release 12*, Boeing Computer Services, Pub. No. 20462-0516.
- Becker, E. B., G. F. Carey, and J. T. Oden, 1981. *Finite Elements: An Introduction (Vol. I)*, Prentice-Hall, Englewood Cliffs, New Jersey.
- Bohren, C. F., and D. R. Huffman, 1983. *Absorption and Scattering of Light by Small Particles*, Wiley New York.
- Borghese, F., P. Denti, G. Toscano, and O. I. Sindoni, 1979. *Appl. Opt.*, **18**, 116.
- Born, M., and E. Wolf, 1959. *Principles of Optics*, Pergamon, London.
- Carey, G. F., and J. T. Oden, 1984. *Finite Elements: Computational Aspects (Vol. II)*, Prentice-Hall, Englewood Cliffs, New Jersey.
- Kerker, M., 1969. *The Scattering of Light and Other Electromagnetic Radiation*, Academic, New York.
- Ling, R. T., 1987. *AIAA J.*, **25**, 560.
- Ling, R. T., 1988. *J. Appl. Phys.*, **64**, 3785.
- Stratton, J. A., 1941. *Electromagnetic Theory*, McGraw-Hill, New York.
- van de Hulst, H. C., 1957. *Light Scattering by Small Particles*, Wiley, New York.
- Wiscombe, W. J., 1979. National Center for Atmospheric Research Tech. Note, NCAR T-140+STR.
- Wiscombe, W. J., 1980. *Appl. Opt.*, **19**, 1505.

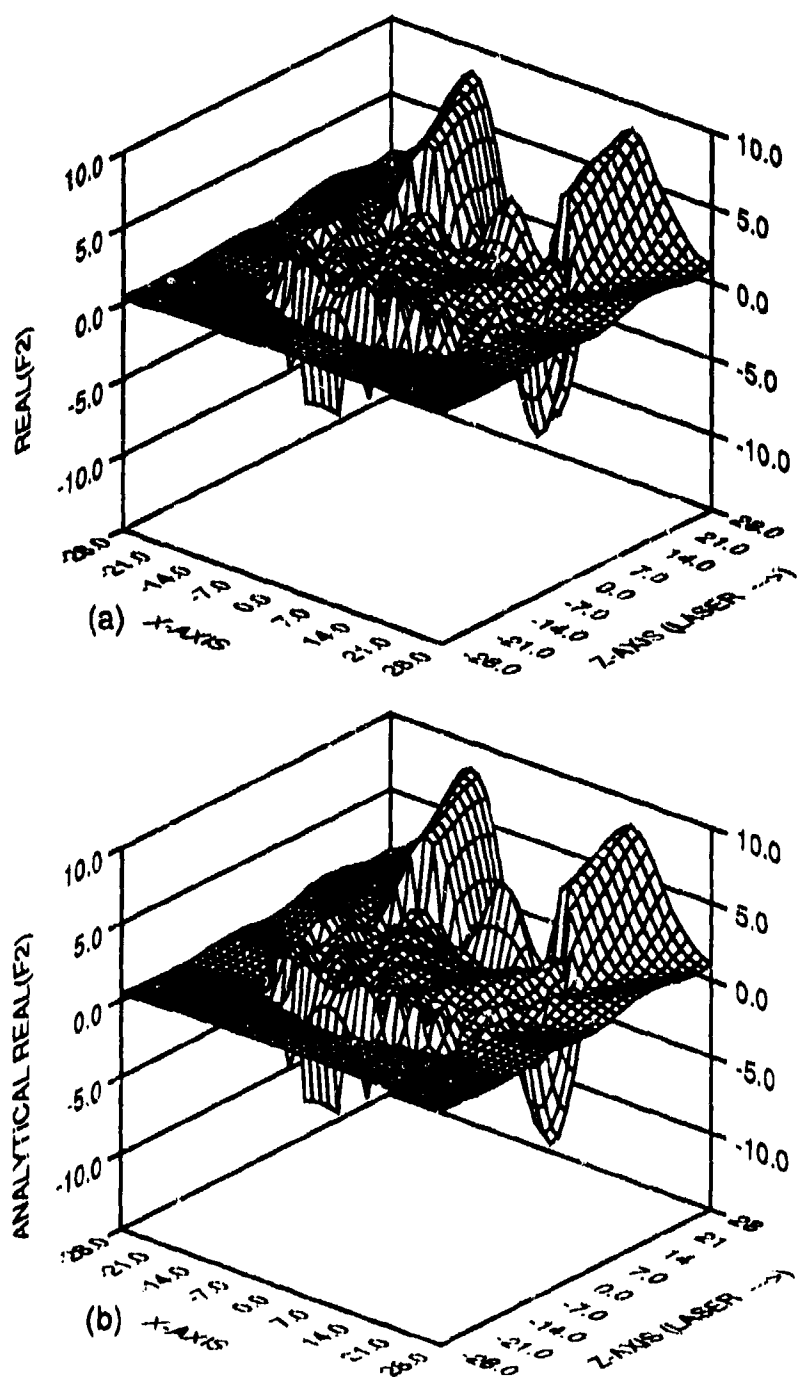


Figure 1. Real part of internal and near-scattered Debye amplitude function f_2 for a spherical water droplet with $x=11.87$ and $m=1.179+0.071i$. (a) Numerical solution. (b) Analytical Solution.

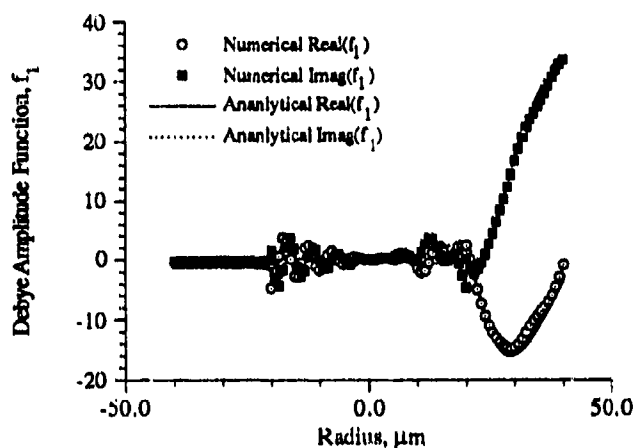


Figure 2. Comparison of numerical and analytical solutions of internal and scattered Debye amplitude function f_1 along the centerline of a sphere having $x=11.87$ and $m=1.179+0.071i$.

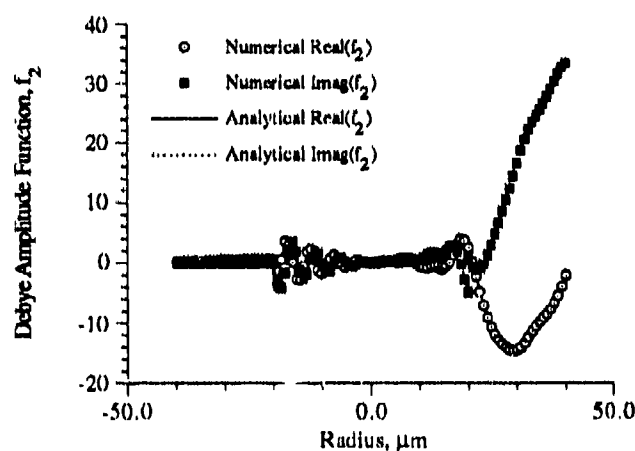


Figure 3. Comparison of numerical and analytical solutions of internal and scattered Debye amplitude function f_2 along the centerline of a sphere having $x=11.87$ and $m=1.179+0.071i$.

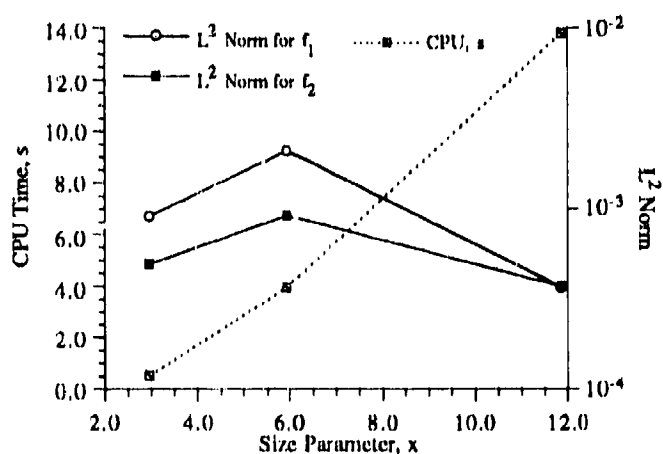


Figure 4. Trends of CPU time and L^2 norms for water droplets of increasing size parameter ($m=1.179+0.071i$). The CPU time is the total time for calculating both Debye amplitude functions, f_1 and f_2 (including output of the results).

BLANK

SIZING SPHERES WITH THE SUBMICRON PARTICLE ANALYZER

Jerold R. Bottiger

Chemical Research, Development, and Engineering Center
Aberdeen Proving Ground, MD 21010-5423

RECENT PUBLICATIONS, SUBMITTALS FOR PUBLICATION, AND PRESENTATIONS

J. Bottiger, "Characterization of Spheres with the Submicron Particle Analyzer: Feasibility", CRDEC Technical Report in preparation.

ABSTRACT

A procedure for systematically comparing experimental and theoretical light scattering properties of dielectric spheres — essentially an inversion technique — was developed and applied to synthetic data of a kind obtainable with the Submicron Particle Analyzer light scattering instrument. We found that with about 12 or more measurements at various scattering angles and polarizations, each with an uncertainty of $\pm 10\%$, we could locate a sphere's parameters on the x-n plane to within a reasonably small connected area. The next step in this work will be to perform inversions on actual experimental measurements from well-characterized spheres.

1. INTRODUCTION

The Submicron Particle Analyzer (SPA) is an instrument built by Wyatt Technology Corp. for the U.S. Army Chemical Research, Development, and Engineering Center (CRDEC) and is used to study light scattering by aerosol particles.^{1,2} It comprises a spherical chamber in the center of which a dilute stream of sampled aerosol particles traverses an intense laser beam, one particle at a time. Light scattered from each particle optionally passes through linear polarizers and is intercepted and measured via 22 optical fibers which are distributed on the surface of the sphere and lead to 22 photomultiplier tubes and associated electronics in a separate instrument rack. The optical fibers, which are terminated on the chamber end with SELFOC gradient index lenses, can be deployed among any of 72 ports on the sphere; the same nine port scattering angles are repeated along eight semi-great circles 45° apart.

The object of the SPA is to gather a set of light scattering data from each aerosol particle, from which physical characteristics of the particles, such as size and shape, may be inferred. The aim of our current research with this instrument is to work out the appropriate types of data to include in the measured sets and to

discover the manner in which those data sets may be manipulated to reveal the desired particle characteristics.

2. OUTLINE OF THE INVERSION METHOD

An inversion method, in the context of the present problem, may be said to have succeeded when it produces numbers for the size and refractive index of a sphere such that the calculated light scattering properties of that sphere agree with the corresponding measured properties. We shall discover acceptable values for x and n (the size parameter and real refractive index) by considering, one pair at a time, "all" possible values of x and n , and repeatedly asking whether the spheres so specified scatter light in agreement with the measurements, and noting the ones that do.

As a starting point, we consider spheres represented by their coordinates on the $x - n$ plane in the limited region $0 < x \leq 10$ (diameters up to about 1.6 micrometers in blue light) and $1.3 \leq n \leq 1.8$ (which covers most dielectric materials). The region is divided into a number of much smaller rectangular areas (pixels) of dimensions Δx and Δn , with the intention of letting the sphere defined by the central coordinates of each pixel stand for all the spheres represented within that pixel. This scheme succeeds if the relevant scattering properties of central spheres in adjacent pixels differ by less than the expected experimental uncertainty. Clearly the pixel resolution must be at least as small as the accuracy with which we wish to recover x and n , but the finer the resolution the lengthier the inversion computation. We choose, rather arbitrarily, $\Delta x = .05$ and $\Delta n = .005$. This results in an array of 20200 pixels, stacked in 200 columns centered at $x = 0.05, 0.10, \dots, 10.00$, and along 101 rows centered at $n = 1.300, 1.305, \dots, 1.800$.

To distinguish spherical from nonspherical particles, eight detectors, without polarizers, are located in a ring at scattering angle $\theta = 55^\circ$, and the incident beam is prepared in a right circularly polarized state. For spherical particles illuminated in this way there can be no variation of light scattering with azimuth angle, ϕ ; uniformity of the eight detector signals confirms particle sphericity. Since the exact path of particles through the Gaussian laser beam is uncontrollable, the incident beam intensity for any particle is not known and so only ratios of intensities provide useful scattering properties. The average intensity measurement of the eight ring detectors will be the denominator for every intensity ratio.

We have chosen to distribute the remaining 14 detectors at scattering angles $40^\circ, 75^\circ, 90^\circ, 105^\circ, 125^\circ$, and 140° with no polarizers and with horizontally oriented polarizers, and at 40° and 90° with diagonally oriented polarizers.

3. CALCULATION OF SCATTERING RATIOS

All the possible intensity ratios (or, equivalently, flux ratios) were calculated with a program based on SMIE, the well-known Mie scattering subroutine written by J. V. Dave³ and which we obtained from Peter Barber.

The SELFOC lenses which collect light in the SPA have a small but finite acceptance angle. An analysis showed that if the magnitude of scattered flux F is known (only) at points 1° apart, and assumed to vary linearly in between, then the flux through the SELFOC circular aperture of 1.1° centered at θ should be written as

$$\bar{F}(\theta) = .1175 F(\theta - 1^\circ) + .7650 F(\theta) + .1175 F(\theta + 1^\circ)$$

The difference between $\bar{F}(\theta)$ and $F(\theta)$ is very small for the size parameters we are considering; nevertheless, this correction for the detector acceptance angle was included.

A typical result is shown in figure 1, where the flux ratio D040 (Diagonal polarizer, $\theta = 40^\circ$) is plotted in two representations over the x-n plane. We see a landscape of sloping valleys and ridges, approximately parallel to lines of $nx = \text{constant}$. For larger values of n or x the ridges become very steep near their crests, a consequence of morphology-dependent resonances; the apparent spikes along some rims are plotting artifacts, which result because the sampling mesh is too coarse to represent the knife-edge ridges.

A smaller pixel size is needed in the vicinity of resonances, but a resolution everywhere which is adequate to this worst case would require far too many pixels to be practical. Instead, we kept the current pixel size and wrote a program to find the minimum and maximum values of each flux ratio over the surface of every pixel. A pixel will be said to be in agreement with an experimental measurement of a flux ratio if the range between the calculated minimum and maximum values of that flux ratio overlaps at all with the experimentally determined range: [measured value \pm uncertainty].

4. TESTING THE INVERSION METHOD

A Fortran program named INVERT was written to explore and test the inversion procedure. It first reads in a number of files, including the computed min/max values for the 14 selected flux ratios, a row of experimental detector calibration coefficients (used in this study to apply controlled errors to the synthetic input data), and an N by 24 array of numbers generated in a separate program and simulating SPA measurements on a run of N particles. When inverting real data, the experimental uncertainty to be associated with each flux ratio measurement for each

particle will be individually determined, based on the measured absolute intensity, but for this feasibility study we have just assigned various uncertainties to flux ratios to observe their effect.

Taking one particle at a time, the program computes the average ring intensity and flux ratios, and then for each pixel checks for agreement between the "measured" range of ratio values and the calculated range of ratio values for each of the flux ratios. In the end, each pixel is assigned a number between 0 and 14 according to the number of measurements with which it agreed. (The program does not literally ask $20,200 \times 14$ times whether an overlap occurs; the calculated min and max input data files have been sorted in ascending order, and are accompanied by integer arrays which relate the sort order to the pixel order. With this information one can write an algorithm to establish pixel hits and misses that runs about a thousand times faster than direct inquiry). The output file written by INVERT is actually a set of statements that instruct a page formatting program (PageGarden, Bloc Publishing Corp.) in drawing a map of the x-n plane. Simple changes to INVERT can alter the information related by the pixel print density.

Because actual measurements of flux ratios may occasionally be in error by more than our best estimate of the experimental uncertainty, it may be desirable to admit solutions that do not necessarily satisfy all 14 of the available measurements. We wanted to see how the number of false returns grew as we pared the number of ratios with which agreement was required, and how the domain of solutions varied with different levels of experimental uncertainty. A few of the many tests done are shown in the following three representative figures.

Four pairs of x,n coordinates (indicated by crosses in the figure) were selected and used to calculate the four rows of scattering measurements that would be produced by the (perfectly operating) SPA instrument sampling the corresponding spheres. These data then were input to INVERT, and INVERT was told they were accurate to within $\pm 3\%$. In the figure, the solidly shaded pixels are those on which flux ratios formed from the input data agree with previously calculated min/max flux ratios for all 14 cases. Partially shaded pixels agreed with 12 or 13 of the flux ratio "measurements", and open pixels with 10 or 11 of them. We believe 3% is an upper limit for the SPA accuracy; under the most favorable conditions that accuracy might be approached by one or two of the detectors. In the upper right of the figure note that some returns for 10-11 agreements have already separated out from the main cluster. Notice also that for very small particles it will be almost impossible to get refractive index information from ratio data.

An accuracy of $\pm 10\%$ is more typical of the expected SPA performance. This is the uncertainty level assumed in figure 3, which show results for the same four spheres. We still see returns that are tightly clustered, except when as few as ten agreements are accepted.

At $\pm 30\%$ uncertainty, figure 4, the number of returns with 10-11 agreements is overwhelming. Even worse than the high number of these returns is the way they are distributed in disconnected patches all over the x-n plane; there is no hint of where the right answer might lie. The pattern looks much better for 12-13 agreements and is quite good for 14 agreements. We expect 30% to be near the lower limit of SPA measurement accuracy.

We have looked at many plots such as those in figures 2-4, including plots in which the input data was corrupted with random errors — though always within the limits set by the assumed experimental uncertainty. There is surprisingly little difference whether the data is actually distorted or not; the nature of the returns is pretty much completely established by the level of experimental uncertainty allowed. Taking 10% as an average uncertainty value for the SPA, we concluded that requiring 13 or more agreements of a pixel to return it as a (possible) inversion solution should produce useful results.

Figure 5 shows the inversion result for 12 spheres, with a 10% uncertainty level assumed in the measurements, and requiring that a pixel agree with at least 13 of the 14 measurements. The outcome is encouraging. We see mostly compact connected patches of returns whose size parameter spread is about 0.3, roughly 0.05 micrometers for blue light. The refractive index spread is not so useful, about 0.1, but the product nx is very accurately determined.

We conclude that it is feasible to characterize small dielectric spheres with data measured by the Submicron Particle Analyzer. We will next undertake the experiments to do so, and if successful, will attempt to extend the method to spheres of larger size and/or made of absorbing materials.

REFERENCES

1. P. J. Wyatt and C. Jackson, "Submicron Particle Analyzer", CRDEC Contractor Report 067, April 1990.
2. P. J. Wyatt et al, "Aerosol Particle Analyzer", *Applied Optics* **27**, 217-221 (1988).
3. J. V. Dave, "Subroutines for Computing the Parameters of the Electromagnetic Radiation Scattered by a Sphere," Report 320-3237 (IBM Scientific Center, Palo Alto, CA, 1968)

OBSERVABLE D040

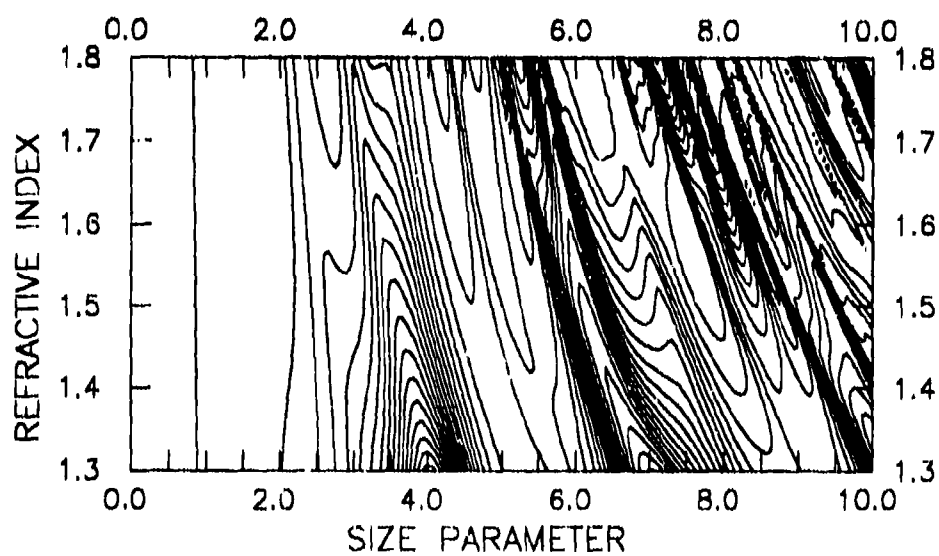
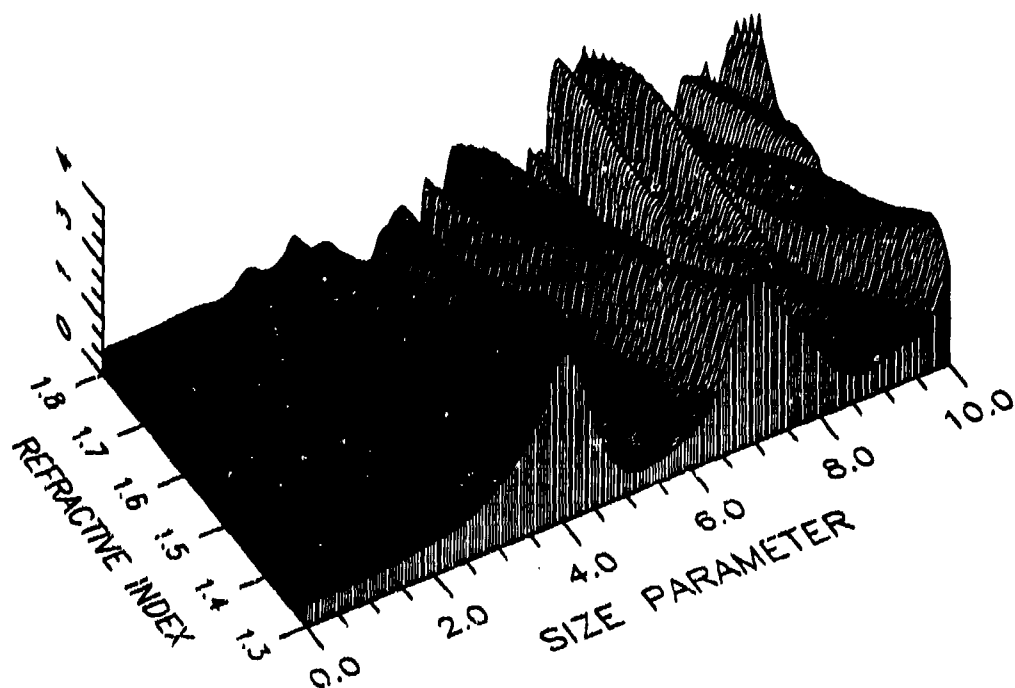
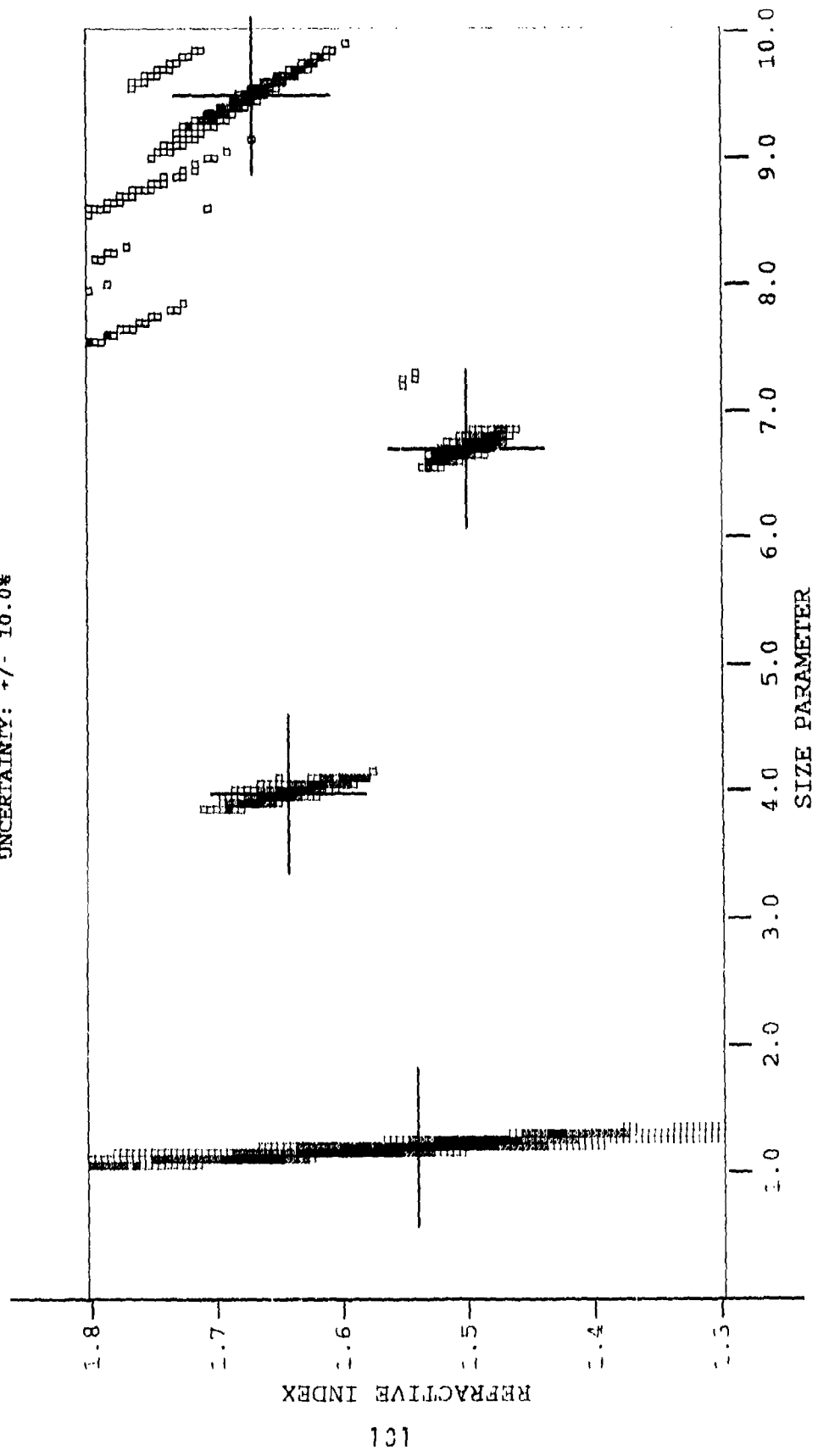


FIGURE 1. TYPICAL MAP OF A SCATTERING RATIO

TEST CASE: expdat22.tst
 UNCERTAINTY: +/- 10.0%



original: +

agreements: 10-11 □, 12-13 ■, 14 ■

FIGURE 3. INVERSIONS OF FOUR SPHERES, ±10% UNCERTAINTY

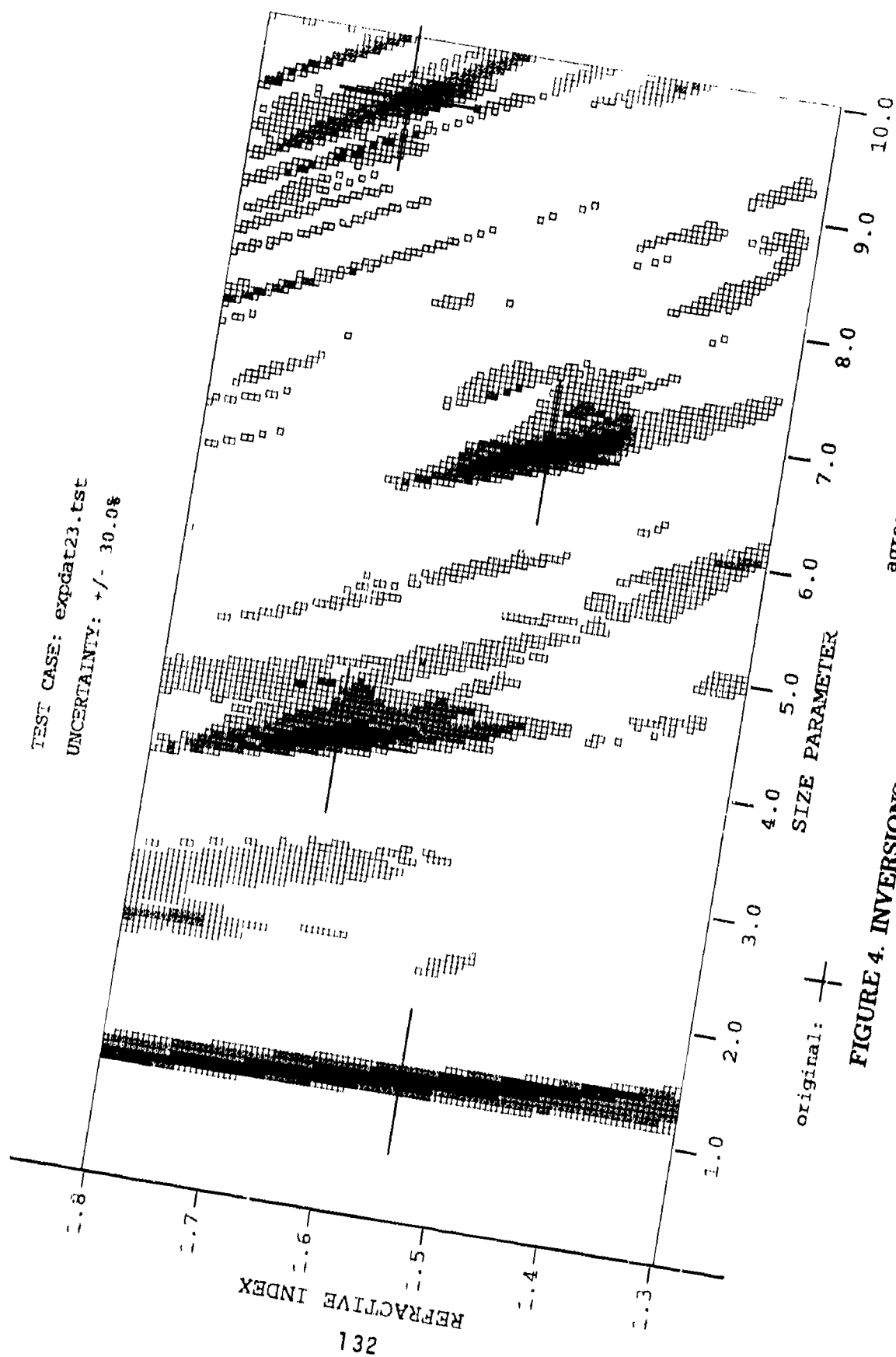
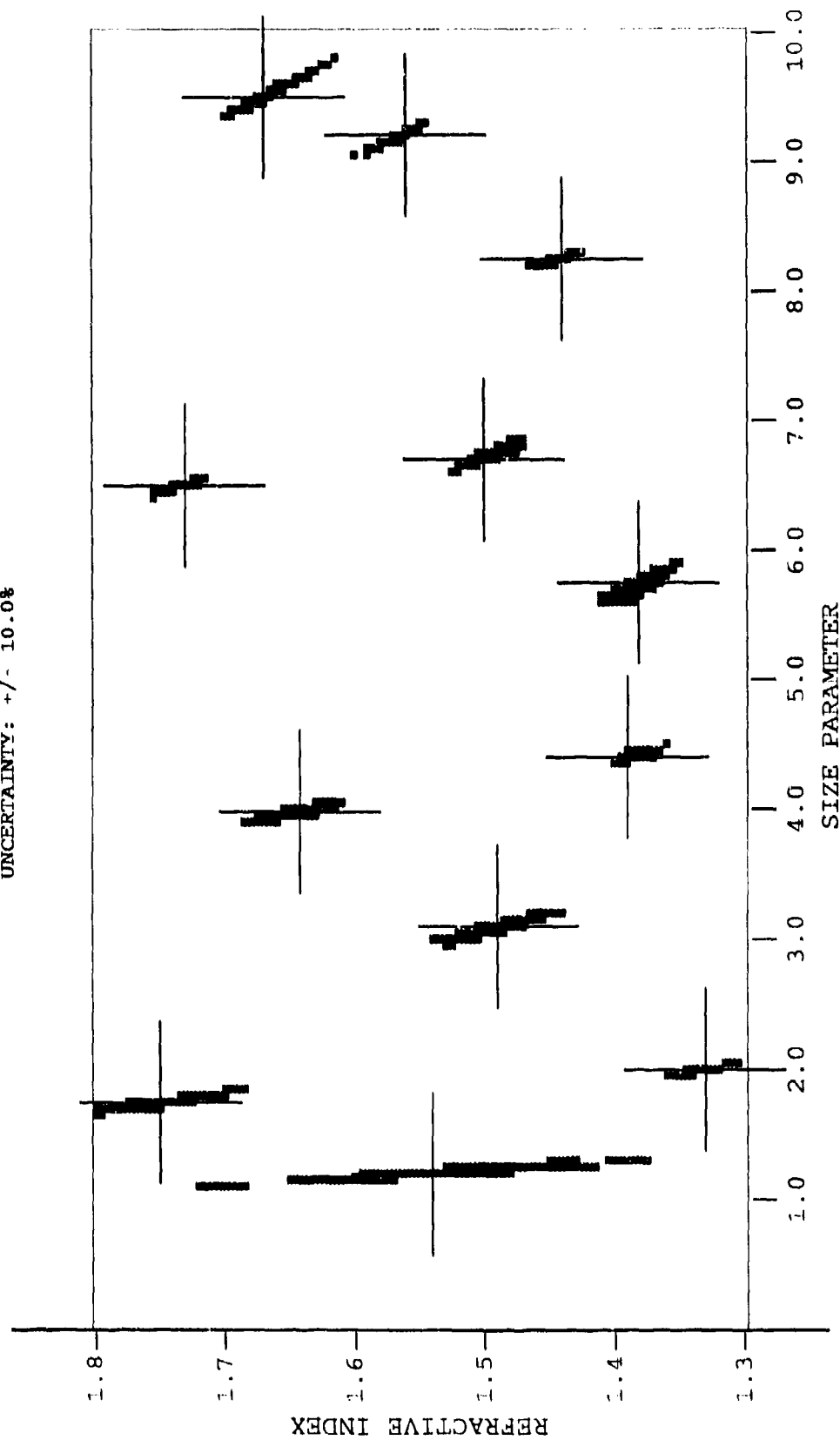


FIGURE 4. INVERSIONS OF FOUR SPHERES, $\pm 30\%$ UNCERTAINTY

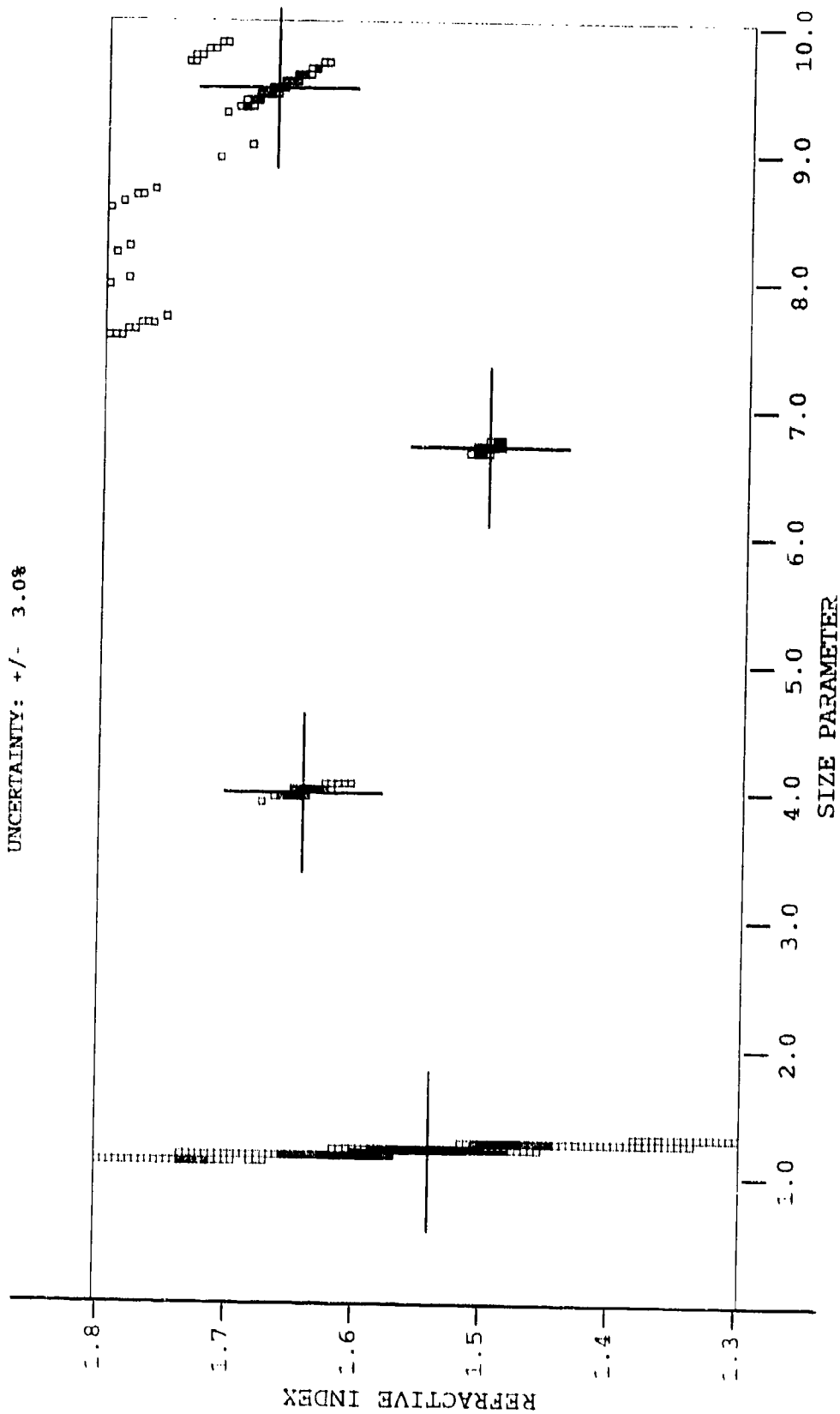
TEST CASE: expdat52.tst
 UNCERTAINTY: +/- 10.0%



original: \pm agreements: 13-14 ■

FIGURE 5. INVERSIONS OF 12 SPHERES, $\pm 10\%$ UNCERTAINTY

TEST CASE: expdat21.tst
 UNCERTAINTY: +/- 3.0%



original: +

agreements: 10-11 □, 12-13 ■, 14 ■

FIGURE 2. INVERSIONS OF FOUR SPHERES, $\pm 3\%$ UNCERTAINTY

OPTICAL RECOGNITION CHARACTERISTICS OF BIOLOGICAL MICROPARTICLES

FLUORESCENCE AND LIGHT SCATTERING AS COMPLIMENTARY TECHNIQUES

B. V. BRONK

RESEARCH DIRECTORATE, CRDEC, APG 21010-5423

W. P. VAN DE MERWE AND L. REINISCH

**UNIFORMED SERVICES UNIVERSITY OF THE HEALTH SCIENCES
BETHESDA, MD**

RECENT PUBLICATIONS, SUBMITTALS AND PRESENTATIONS

1. W. Van de Merwe, D. Huffman, and B. Bronk, "Establishing a standard for polarized light scattering from microbial systems", Proceedings of the International Conference on Lasers, 88, R. C. Sze and F. J. Duarte, Editors, STS Press, McLean Va. (1989).
2. W. Van de Merwe, D. Huffman and B. Bronk, "Reproducibility and sensitivity of polarized light scattering for distinguishing bacterial suspensions", Appl. Opt. 17, 2700-2705 (1989).
3. Burt V. Bronk, Willem P. Van De Merwe, and Donald Huffman, "Polarized light scattering as a means for detecting subtle changes in microbial populations", Chapter 6 In Modern Techniques for Rapid Microbiological Analysis, W. Nelson, ed., VCH International, N.Y. (in press '91).
4. L. Reinisch and B.V. Bronk, "Fluorescence signatures from bacteria: variations and forgeries-can they be distinguished?", U. S. Army Research Office, Workshop on Spectrometry & Spectroscopy for Biologicals, Cashiers, N.C., April 28 -May 1, 1991 pp 11 15.
5. W. Van de Merwe, B. Bronk and D. Huffman, "Reproducibility and sensitivity of measurements of scattered light from a bacterial suspension", Proceedings of the 1988 Scientific Conference on Obscuration and Aerosol Research..
6. B. Bronk, W. Van de Merwe, D. Huffman, and M. Stanley "Relationship of growth conditions and consequent bacterial size to the S34/S11 angular scattering pattern for bacteria", Proceedings of the 1989 Scientific Conference on Obscuration and Aerosol Research CRDEC-SP-026.
7. B. Bronk, W. Van de Merwe, and M. Stanley, "Comparative studies of bacterial shape and its effect on the S34/S11 angular scattering pattern", Proceedings of the 1990 Scientific Conference on Obscuration and Aerosol Research. CRDEC-SP-036.

ABSTRACT

The technique of measuring angular variation of a combination of Mueller matrix elements for a suspension of a single species of microorganisms is considered in combination with the measurement of fluorescence of the same suspension. The case of germination of bacterial spores is considered as a dynamic example. The use of the combined methods is shown to give a characteristic combination which in this case identifies a population as bacterial spores. This is an example showing how two optical methods can be combined to give improved identification of a population of micron sized particles collected from an aerosol.

INTRODUCTION:

During the last several years in various collaborations, we have been considering how biological particles which might be found in aerosols could be distinguished from background and then identified by optical means. The advantage of optical methods is that these are rapid and should be readily automatable.

We started by studying angular polarized light scattering profiles of various pure strains of bacteria and spores in liquid suspensions. We found that a particular combination of Mueller matrix elements, namely $(S_{34} + S_{14})/(S_{11} + S_{31})$, shows interesting changes from one species to another and is extremely sensitive to size and perhaps shape changes within a single species. Unfortunately this extreme sensitivity precludes using this technique alone as a unique "fingerprint" for a bacterial species since bacteria are highly variable in size and shape depending on growth conditions.

On another front, this year we studied the use of steady-state fluorescence of bacteria and spores in liquid suspension as a possible means to rapidly identify populations of microorganisms. We found that these measurements are relatively less sensitive to size and shape changes and show some distinguishing features from one microorganism to another. The fluorescent spectra however do show some changes depending on the method of preparation, and these changes are apt to be as large as the differences between the fluorescent spectra of different species.

In this presentation we take the example of germination of bacterial spores and examine the dynamics of the changes occurring during this

process using both polarized light scattering and fluorescence as an example of the use of combined methods for identification of aerosol particles.

BIOLOGICAL BACKGROUND:

Sporulation is a means that certain species of bacteria have chosen, in the course of evolution, for survival of lean times. Among those bacteria are the Bacilli which are found in great numbers in most areas in the soil. When a given population of bacilli runs out of one or more essential nutrients a type of differentiation takes place in a portion of the bacteria present. A spheroidal or ellipsoidal body forms inside the individual bacterium which is affected. This object becomes the spore, a hardened body with reduced water content which is characterized an index of refraction elevated above that of the bacterium from which it came (which was mostly water), a different chemical composition, and greatly increased survivability in the face of hazards such as UV radiation, ionizing radiation, heat, and antibiotics. The relative impunity of spores to conditions hostile to bacteria is why the U.S. Army must be prepared to detect and defend against them in the unfortunate event of the use of biological weapons by an enemy.

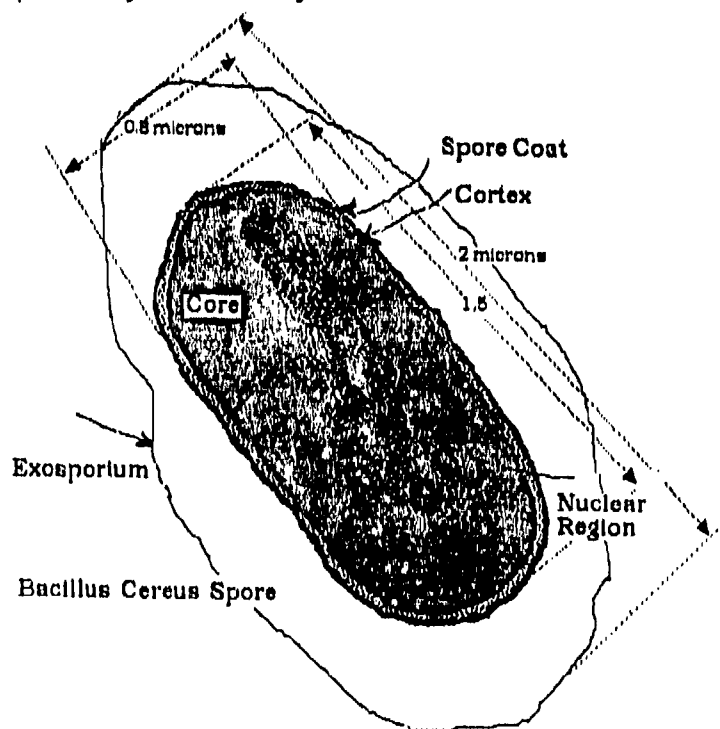


Figure 1. A drawing from electronmicrographs of typical Bacillus cereus spores.

There are other more philosophically satisfying reasons to be interested in bacterial spores. All the genetic information to produce unceasing generations of progeny is contained in a single bacterial spore, however the spore remains dormant until it receives a signal from its environment indicating that conditions are again favorable for the reproductive cycle of its bacterial offspring. Because of the great resistance of spores to environmental hazards, it has been speculated that the first interstellar travelers came here as spores.

The physical and chemical changes which occur after a spore receives a signal from the environment to revert to bacterial form are what is called germination. Numerous such changes take place in a period lasting from several minutes to an hour or more after the germination signal. Examples of these changes follow.

Biological:

- * Spore becomes less heat, radiation and UV resistant to damage.
- * Spore is ready to start reverting to bacterial form.

Chemical:

- * Various chemicals are released into the spores environment.

Physical:

- * Optical density decreases substantially, i.e. much less light is scattered by the germinated spore.

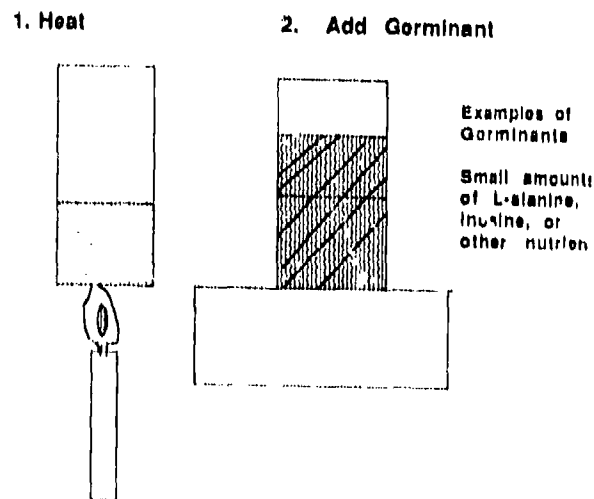


Figure 2. Approximate conditions for germination in the laboratory are illustrated

Results:

In our experiments we found good germinating conditions for spores of two species of bacilli, *B. megaterium* and *B. cereus*. The results of preliminary optical measurements appear similar for both these cases, but at this time we are only prepared to show the results for *B. megaterium*.

To check that germination was occurring we utilized both optical density measurements at 600nm. These register a substantial drop within about twenty minutes when germination occurs. We also examined ~ 100 spores under a phase contrast microscope. When > 80% of these change from a bright white appearance to a dark grey appearance. This is taken to indicate germination.

At various times during the germination process, samples were taken, chilled on ice, centrifuged and resuspended in a buffer at an optical density of about 0.1 at 600 nm for examining the emission fluorescence spectrum for an excitation at a wavelength of ~280 nm. As is seen in Figure 3, the main change in the emission fluorescence spectrum occurs after the heating of the spores (~ 20 minutes at 70 degrees) with relatively little change after adding the germinant.

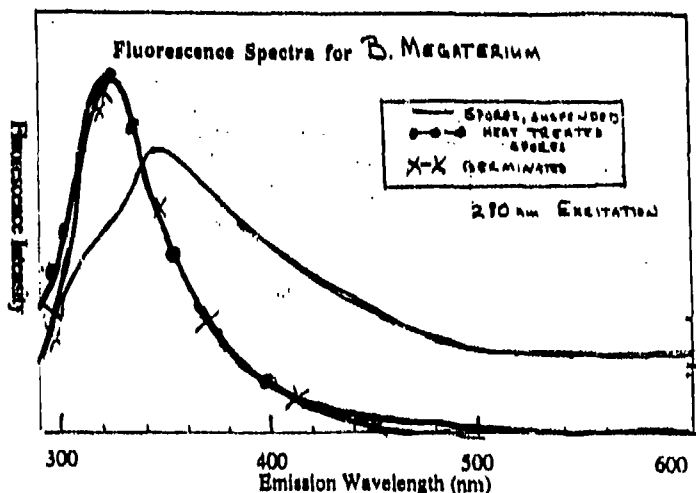


Figure 3. Fluorescence emission for *B. megaterium* spores during germination

Since it was found that substantial changes occur fairly rapidly in the angular pattern for the Mueller matrix combination

$$(S_{34} + S_{14})/(S_{11} + S_{13}) \equiv (S_{34}/S_{11})^\dagger$$

after the addition of the germinant, these measurements were made in the germinating solution. This solution was found to have very little absorbance at 633 nm which was the wavelength for these scattering measurements. As is seen in Figure 4, a small change occurs after the heating step, but a major shift in the pattern occurs after the spores are immersed in the germinating solution. The graph labeled 3 in Figure 4 was generated about 40 minutes after adding the germinating solution during which time most of the rapid changes in the pattern have already occurred. The germinated spores were allowed to grow overnight in a nutrient medium and the scattering pattern for the resulting bacteria washed and resuspended in buffer is seen to have undergone still further changes as is seen in the more oscillatory nature of graph 4 in Figure 4.

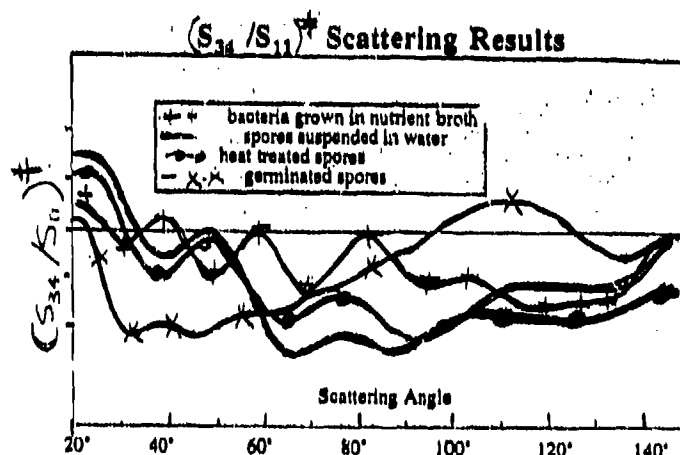


Figure 4. Changes in angular scattering pattern for germinating *B. megaterium* spores.

Conclusions:

For the particular bacterial spores we are presently discussing, the fluorescence emission spectrum changes substantially after heating, but has very little change in form after germination. The spectra all appear typical of what we have observed for a number of bacterial spores. The other approach, the angular (S34/S11)[†] pattern shows very little change after heating, but a very substantial and progressive change occurs during germination. These results, while preliminary, show that, a combination of optical methods is useful in studying the dynamics of spore germination and provides substantial evidence for identifying a given suspension of particles as made up of bacterial spores.

BLANK

S. Mark Haugland

Ezekiel Bahar

Electrical Engineering Department, University of Nebraska-Lincoln

209N WSEC, Lincoln, Nebraska 68588-0511

Arthur H. Carrieri

U. S. Army Chemical Research, Development and Engineering Center

Aberdeen Proving Ground, Maryland 21010-5423

RECENT PUBLICATIONS

- A) E. Bahar, "Full Wave Analysis for Rough Surface Diffuse, Incoherent Radar Cross Sections with Height-Slope Correlations Included," *IEEE Trans. on Antennas and Propagation*, in press, September 1991.
- B) "Acoustic Scattering by Two-Dimensionally Rough Interfaces Between Dissipative Acoustic Media - Full Wave, Physical Acoustics and Perturbation Solutions," *Journal of the Acoustic Society of America*, Vol. 89, No. 1, pp. 19-26, January 1991.
- C) E. Bahar, "Acoustic Backscatter Cross Sections for Rough Sea Surface Excited from Above and Below the Air-Water Interface," *Journal of the Acoustic Society of America*, Vol. 90, No. 1, pp. 433-440, July 1991.
- D) E. Bahar and Y. F. Li, "Scattering Cross Sections of Non-Gaussian Rough Surfaces: Unified Full Wave Approach," *IEEE Transactions on Antennas and Propagation*, in press, 1991.
- E) E. Bahar, S. M. Haugland, and A. H. Carrieri, "Identification of Contaminant Coatings Over Rough Surfaces Using Polarized IR Scattering," *Applied Optics*, in press.
- F) E. Bahar and M. El-Shenawee, "Full Wave Multiple Scattering from Rough Surfaces," *Proceeding of the IEEE AP-S International Symposium and URSI Radio Science Meeting*, Dallas, TX, Vol. IV, pp. 1548-1551, May 1990.
- G) E. Bahar and Y. F. Li, "Statistical Characterization of Random Rough Surfaces Using the Tilt Modulation of the Backscattered Radar Cross Section - Full Wave Approach," *Proceedings of the International Geoscience and Remote Sensing Symposium*, Vol. II, pp. 1401-1403, May 1990.
- H) E. Bahar, "Examination of Full Wave Solutions and 'Exact Numerical Results' for One-Dimensional Slightly Rough Surfaces," *Journal of Geophysical Research*, Vol. 96, No. C9, pp. 17,123-17,131, Sept. 15, 1991.
- I) E. Bahar and M. El-Shenawee, "Use of Supercomputers to Evaluate Singly and Multiply Scattered Electromagnetic Fields from Rough Surfaces," *IEEE Trans. on Magnetics*, in press, September 1991.

ABSTRACT

An optical technique to identify the presence of chemical coatings over rough surfaces is described. It is based on selective use of elements of the 4×4 Mueller matrix. The full wave theory of electromagnetic scattering is used to predict six independent Mueller elements from randomly rough uncoated (dry) and coated (wet) surface materials as functions of the media complex dielectric coefficients, backscattering angle and mid-infrared wavelengths of laser beam excitations that are polarization-modulated. The set of independent elements at beam wavelengths and backscattering angles $\{M_{mn}(\lambda_i, \theta_i)\}$ most sensitive to optically thick contaminant coatings are statistically obtained from the full wave data base, and detection parameters sets $\{\theta_i, \lambda_i\}$ are inputs to another algorithm designed to identify the contaminant coating (when present and interacted by the irradiating beams).

FUTURE WORK

These algorithms facilitate the operation of a multi-CO₂ laser ellipsometer facility now under development at CRDEC for the remote detection of chemical/biological surface contaminants.

1. INTRODUCTION

The objective of this work is to develop algorithms that operate on a Mueller matrix infrared data base for the identification of interstitial liquid chemical coatings (contaminant layers) over a rough surface that separates two semi-infinite media. Statistical techniques widely used in similar remote sensing problems are usually based on spectral reflectance, emissivity, or pulse shape measurements. However, such measurements do not uniquely represent topography and physical properties of the surface and subsurface constituents. We have developed multivariate statistical algorithms for detecting the coatings based on amplitude and phase information in the 16-element Mueller matrix, a measured data field that completely characterizes the surface at beam energies of vibrational resonance in the contaminant and backscattering angles where this contaminant signal is strongest.

An analytical study based on the full wave approach¹ directed us first to develop a method for selecting beam backscattering angles (θ_i) and wavelengths (λ_i) producing independent Mueller elements sensitive to the contamination and uncommon with the background scatterer (terrain). The contaminants of interest are classes of IR-excitable liquids that have a rheology similar to chemical warfare agents. (The contaminant is sometimes referred to as the chemical analyte, and is characterized by its complex dielectric coefficients ϵ_λ .) The algorithms that determine these detection parameters and process the Mueller elements around these input data were specially designed for the CRDEC experimental ellipsometer sensor. Typically, outputs of the first algorithm will specify tuning three of the ellipsometer's four infrared laser transmitters to energies that vibrationally excite the analyte (i.e., at absorption resonance where the analyte's imaginary part of ϵ maximizes), and off-tune a fourth laser to non-resonance beam energy (for measuring a Mueller matrix reference). In the full wave model predictions, it is assumed that the randomly rough coating layer is optically thick. Moreover, the coated and bare surfaces may or may not have the same topography. Initial outputs from the first algorithm train the ellipsometer sensor to recognize candidate Mueller scattering elements containing features of the analyte most useful for making a detection decision. The sensor can be trained for simultaneous analyte detections by its initialization to (θ_i, λ_i) pairs specific to several analyte compounds.

After detection parameter sets $\{\theta_i, \lambda_i\}$ are obtained from the processing of matrix elements calculated by full wave theory, a second algorithm positively identifies a particular coating material. If an alarm condition exists (indicating probable identification of a contaminant), then a third algorithm proceeds to determine confidence of detection. The detection algorithm is based on Hotelling's T-squared method.² It involves a principal axis transformation of a vector whose components are the independent, susceptible (most sensitive to the presence of the coating material), Mueller matrix elements yielding a most probable analyte detection. The transformed vector contains specific information on the analyte coating that is most reliable for making a statistically based decision to discriminate among various coatings, and between coatings and background material (terrain).

An overview of the full wave expressions used to develop a theoretical data base of independent Mueller matrix elements has been published recently.³ The algorithm that first 'targets' all analytes by determining parameters sets $\{\theta_i, \lambda_i\}$ is described in Section 2, and its accompanying identification algorithm (if the analyte is present in the irradiation zone) is described in Section 3. Numerical examples from parameter selection and analyte detection algorithms are presented in Section 4.

2. SELECTION OF INCIDENT ANGLE AND WAVELENGTH FOR OPTIMAL IDENTIFICATION OF THE COATING MATERIAL

For isotropic rough surfaces, the *backscatter* Mueller matrix (per unit area) reduces to the following special form

$$M = \begin{bmatrix} M_{11} & M_{12} & 0 & 0 \\ M_{12} & M_{22} & 0 & 0 \\ 0 & 0 & M_{33} & M_{34} \\ 0 & 0 & -M_{34} & M_{44} \end{bmatrix} \quad (1)$$

A selection of beam incident angle - wavelength pairs, one per chemical coating, that produce the most susceptible Mueller elements (to the coatings and between coatings and substrate) is performed by the first algorithm in two stages. The initial (θ_i, λ_i) selection is based on Mueller element calculations³ by the full wave model for a surface structure including two randomly rough interfaces (Figure 1). The final selection of these parameters is based on experimental data mappings of the six independent Mueller elements (1) in a region $\theta_i \pm \delta\theta_i$ and $\lambda_i \pm \delta\lambda_i$ about initial values θ_i and λ_i . For simplicity, the coating is assumed to be optically thick. Therefore, scattering at the lower rough interface of the coating material is neglected. (Chemical coatings that do not totally attenuate the refracted beam can also be treated by full wave analysis.)⁴

The six independent elements are evaluated at θ_i and λ_i and form a 6-dimensional vector we call p . (The full wave model computations are made over the ellipsometer systems's full angle and spectral ranges.)

$$p = [p_1, p_2, p_3, p_4, p_5, p_6]^t \equiv [M_{11}, M_{12}, M_{22}, M_{33}, M_{34}, M_{44}]^t \quad (2)$$

Let p^c and p^b denote vectors associated with coated (superscript c) and bare (superscript b) rough surfaces, respectively. For each coating of spectral permittivity ϵ_λ , realizations of p are computed as functions of θ and λ with random variations $\Delta\theta$, $\Delta\lambda$, $\Delta\epsilon$, $\Delta < h^2 >$, $\Delta < \sigma^2 >$, and $\Delta\epsilon_c$ that represent equipment tolerances, deviations in the scatterer's physical properties, and variations in rough surface statistical parameters. For these realizations, mean values $< p_k >$ and standard deviations ω_k ($k = 1, 2, 3, 4, 5, 6$) are computed for each element of the vectors p^b and p^c . To

prevent this algorithm from selecting θ_i and λ_i for sufficiently low reflective coating layers, Mueller matrix elements that satisfy the condition $| < p_k^c > | < p_k^b > |$ are ignored. Components of the vector \underline{r} are defined by:

$$r_k \equiv p_k u(| < p_k^c > | - | < p_k^b > |), \quad k = 1, 2, 3, 4, 5, 6 \quad (3)$$

and

$$s_k = \text{components of } \underline{s} \text{ that are non-zero for } k = 1, \dots, L. \quad (4)$$

In the above expression, $u(\cdot)$ is a unit step function, and dimension $L \leq 6$. The standard deviation associated with the corresponding components s_k of the vector \underline{s} is defined as b_k . Finally, the components x_k of the normalized difference vector \underline{x} are defined as follows:

$$x_k = \frac{< s_k^c > - < s_k^b >}{b_k} \quad (5)$$

The magnitude of \underline{x} is the distance between vectors $< \underline{s}^b >$ and $< \underline{s}^c >$ normalized to unit variance. An initial selection of beam parameters (θ_i, λ_i) that make a certain matrix detection event most probable is determined when $x = \sqrt{\underline{x}^T \underline{x}}$ is largest for a specific analyte coating ($\epsilon_{\lambda, \text{aborb}}$), and can be repeated for many physically dissimilar coatings.

3. IDENTIFICATION OF THE COATING MATERIAL

The identification algorithm is based on Hotelling's T-squared method², and involves inverting the specific covariance matrix for $< \underline{s} >$ of Equation (4), i.e., $C \equiv < \underline{s}^b > < \underline{s}^b >^t$. For some natural and manufactured surfaces of interest in remote sensing, $\det(C)$ is vanishingly small. Therefore, to avoid singularities in the inversion operation, the following principal axis transformation⁵ (apply a principal component analysis pre-operation) is performed on the vector $< \underline{s}^b >$:

$$\underline{z} = Z < \underline{s}^b > \quad (6)$$

where Z is the principal axis operator. The covariance matrix of Equation (6) is a diagonal matrix denoted Γ . It is related to the original covariance matrix C as follows:

$$\Gamma = Z C Z^t \quad (7)$$

The operator Z is unitary ($Z^{-1} = Z^t$) since C is real, symmetric, and non-negative definite. The elements of diagonal matrix Γ are, therefore, real eigenvalues ($\gamma_i \geq 0$) solving the following characteristic equation.

$$\det(C - I\gamma_i) = 0 \quad (8)$$

Elements of the i^{th} column of the matrix Z^t are given by the components of the characteristic vector Z_i^t which satisfy the following operator expression.

$$C Z_i^t = \gamma_i Z_i^t \quad (9)$$

Those elements of \underline{z} associated with negligibly small eigenvalues (that cause inversion problems) are not included in constructing $\underline{\zeta}$, a quantity we call the reduced discriminant vector. Its covariance matrix is the $N \times N$ diagonal matrix Γ_0 where $N \leq L$. Denote $\underline{\zeta}_j(\theta_j, \lambda_j)$ the analyte reduced

discriminant vector (ζ associated with the coating material with the subscript $i = 1, 2, \dots, M-1$ evaluated at $\theta = \theta_j$ and $\lambda = \lambda_j$, $j = 1, 2, \dots, M=1$), and ζ_M the background reduced vector discriminant corresponding to ζ for a bare surface. When applying Hotelling's T-squared method to ζ , a new scalar quantity d_{ij}^2 is defined.

$$\begin{aligned} d_{ij}^2 &= [\zeta_i(\theta_j, \lambda_j) - \zeta_M(\theta_j, \lambda_j)]^t \Gamma_0^{-1}(\theta_j, \lambda_j) [\zeta_i(\theta_j, \lambda_j) - \zeta_M(\theta_j, \lambda_j)] \\ &= \sum_{\ell=1}^N \frac{[\zeta_i(\theta_j, \lambda_j)_\ell - \zeta_M(\theta_j, \lambda_j)_\ell]^2}{\gamma_\ell(\theta_j, \lambda_j)} \end{aligned} \quad (10)$$

The values $d_{ij} = \sqrt{d_{ij}^2}$ are stored in a computer data bank and accessed when compared to measured scattering data from bare and coated surfaces. That data base is structured in the following array format.

$$D = \begin{bmatrix} d_{11} & \cdot & \cdot & d_{1M-1} \\ d_{21} & \cdot & \cdot & \cdot \\ \cdot & \cdot & \cdot & \cdot \\ d_{M1} & \cdot & \cdot & d_{MM-1} \end{bmatrix} = \begin{bmatrix} d_1^t \\ d_2^t \\ \cdot \\ d_M^t \end{bmatrix} \quad (11)$$

To identify an unknown surface coated with one of the $M-1$ materials, or to determine whether the surface is bare, it is necessary to build the *identifier vector*:

$$\underline{u}^t = [u_1, u_2, \dots, u_{M-1}], \quad (12)$$

in the following manner. Let $\zeta_u(\lambda_j, \theta_j)$ be the measured reduced discriminant vector ζ for the unknown material at (θ_j, λ_j) . We define u_j the same as d_{ij}^2 in Equation (10) except ζ_i is replaced by ζ_u for the unknown material. The identifier vector \underline{u} now has $M-1$ components. Positive identification of the $M-1$ coating materials is done by evaluating the lengths of c_i of the difference vectors $\underline{u} - \underline{d}_i$:

$$c_i = |\underline{u} - \underline{d}_i|. \quad (13)$$

The identifier vector \underline{u} is classified as representing material n if $c_n < c_\ell$ ($\ell = 1, \dots, M$, $\ell \neq n$), or \underline{u} represents the bare surface if $c_M < c_i$ ($i = 1, \dots, M-1$). The assurance that an identification is true depends on the value of c_n . The smaller c_n is relative to c_i ($i \neq n$) the more assured one is of detecting analyte n . Additional data may lead to a more definite identification. Faster acquisition rates of data will also improve the performance of this algorithm when the chemical coating is highly volatile or diffuses rapidly into the bare surface (e.g., soil).

4. ILLUSTRATIVE EXAMPLES

The coating materials considered are DMMP (Dimethyl methyl phosphonate - $\text{CH}_3\text{PO}(\text{OCH}_3)_2$), DIMP (Diisopropyl methyl phosphonate - $\text{CH}_3\text{PO}(\text{OCH}(\text{CH}_3)_2)_2$), and SF96 (General Electric nomenclature, Polydimethyl siloxane - $[-\text{Si}(\text{CH}_3)_2\text{O}-]_n$). An optimum infrared probe beam wavelength generally corresponds to a strong IR center absorption band ($\text{Im}(-\epsilon)$ is maximum) representing stretching, rocking, or bending normal vibrational modes in primary atom groups of the analyte molecules (viz, laser stimulation of an oscillating molecular dipole moment). DMMP and DIMP have strong P-O-C, C-O, and P=O vibrational modes within the ellipsometer's bandwidth,

while SF96 can be excited into fundamental Si-O-Si and Si-CH₃ vibrations. The background material in these data runs is a composite clay (soil) whose ϵ values were derived from an admixture of three minerals: montmorillonite, kaolin, and illite.

It is assumed that variations $\delta\epsilon$, $\delta < h^2 >$, and $\delta < \sigma_s^2 >$ are uniformly distributed and can cause up to $\pm 5\%$ deviation in the scatterer's physical properties, mean square height and slope, respectively. Therefore,

$$< h^2 > = < h^2 >_0 (1 \pm 0.05r) \quad (14)$$

$$< \sigma_s^2 > = < \sigma_s^2 >_0 (1 \pm (0.05s)) \quad (15)$$

$$\epsilon_i = \epsilon_{iR}(1 \pm 0.05r) - i\epsilon_{iI}(1 \pm 0.05s), \quad i = 1, 2, 3, 4 \quad (16)$$

where r and s are uniformly distributed random variables bounded by $0 \leq (r, s) \leq 1$. The values for the mean square height and slope, $< h^2 >_0$ and $< \sigma_s^2 >_0$ used in this example are $20 \mu\text{m}^2$ and 0.5 , respectively. In Equation (16) ϵ_{iR} and ϵ_{iI} are the real and imaginary parts of permittivity $\epsilon_i(\lambda)$, respectively. The value of ϵ_{iI} ($i = 1$ for DIMP, $i = 2$ for SF96, $i = 3$ for DMMP, and $i = 4 = M$ for composite clay) will peak at vibrational resonance of the material. The CO₂ laser beam excitations that drive these resonances are tuned between the sensor's $9.0 \mu\text{m} \leq \lambda_i \leq 12.5 \mu\text{m}$ bandwidth.

On implementing the algorithm that selects sets of $\{\theta_i, \lambda_i\}$ pairs to identify i coating materials, 50 realizations of the vector p are used to obtain averages $< p >$ and standard deviations ω_k . For these three analyte coatings:

$$\theta_1 = 48^\circ, \lambda_1 = 10.17 \mu\text{m} \text{ for detecting } \epsilon_1 \text{ (DIMP)}$$

$$\theta_2 = 48^\circ, \lambda_2 = 12.35 \mu\text{m} \text{ for detecting } \epsilon_2 \text{ (SF96)}$$

$$\theta_3 = 48^\circ, \lambda_3 = 12.21 \mu\text{m} \text{ for detecting } \epsilon_3 \text{ (DMMP)}.$$

The value of L in Equations (4) and (6) is the minimum number of independent Mueller elements needed to detect the coating material (or bare surface) for each incident angle/wavelength pair. For DIMP, $L = 1$: the Mueller matrix element used to detect it is M_{34} . For each SF96 and DMMP coating, $L = 6$: all six independent Mueller elements are required for singular detections of SF96 and DMMP.

Figure (2a) shows a scatter plot of the reduced discriminant vector component $\zeta_i(\theta_1, \lambda_1)_1$ of Equation (10) trained for coating DIMP. In Figure (2b), the discriminant vector component $\zeta_i(\theta_2, \lambda_2)_2$ is plotted against component $\zeta_i(\theta_2, \lambda_2)_1$, trained for coating SF96. Finally in Figure (2c), the discriminant vector component $\zeta_i(\theta_3, \lambda_3)_2$ is plotted against component $\zeta_i(\theta_3, \lambda_3)_1$, trained for coating DIMP. Note that in all Figures (2a-c) the analyte and background data are clustered and disjointed, so that a partition function can be defined. Mueller element data passed from the ellipsometer sensor can be categorized as within (alarm) or outside (no alarm) the cluster domains of specific materials, separated by the partition function. These data show that the incident angle/wavelength selection algorithm worked reliably in this trial.

The detection algorithm presented in Section 3, was programmed and executed with Mueller element inputs used to build the vector discriminants ζ of Figures (2). Run time was short, and the operation was completed without flaw. In these data, simulated experimental trials produced values of $\zeta_u(\theta_j, \lambda_j)$ ($j = 1, 2, \dots, M-1$) for each of the different analyte coatings and for the background composite clay surface. Results of c_i computations via Equation (13) are shown in Table 1, where

rows 1 through 3 consist of values of ϵ_i ($i = 1, 2, \dots, M$) for rough surface analyte coatings with permittivities: ϵ_1 (DIMP, row 1); ϵ_2 (SF96, row 2); and ϵ_3 (DMMP, row 3). In row 4, ϵ_i is given for the bare composite clay rough surface of permittivity ϵ_4 . A high confidence of analyte discrimination in this trial is clear from inspection of the table data, i.e., diagonal numbers are far less than off-diagonal numbers.

5. CONCLUSIONS

An algorithm based on phase-sensitive light scattering and detection of randomly rough surface interfaces was applied to the remote detection problem. Independent elements of the Mueller matrix are selectively measured at infrared beam energies that coincide with molecular vibrational excitations in the contaminant layers, and angles of incidence determined in part by the scatterer's surface topography. Algorithms process information in these susceptible Mueller elements on the IR-absorbing coatings (analytes) and discern it from information on scattering by the substrate (background). These algorithms can be applied to a full wave theory data bank and the real-time operation of a multi-CO₂ laser, photelastic modulation, ellipsometer instrument now being developed at CRDEC. Initial determinations of beam backscatter angle and wavelength pairs that train the sensor for specific detections is based on full wave computations of groups of six independent Mueller matrix elements, given inputs of topographical detail and complex refractive analyte and substrate. Once detection parameters (θ_i, λ_i) are determined, an algorithm based on Hotelling's T-squared method is applied to identify the coating material (or to verify a non presence). The degree of assurance that a particular identification is correct is also determined by the algorithm.

ACKNOWLEDGEMENTS

This work was sponsored by the U. S. Army Chemical Research, Development and Engineering Center as part of the Laser Standoff Detection Project, Project Number 1C162622A553C, Reconnaissance, Detection and Identification. We are especially grateful to Merrill Milham (CRDEC), Ronald Piffath CRDEC, and Marvin Querry (University of Missouri) for providing the 'optical constants' and absorption spectra for clay and analyte materials.

REFERENCES

- [1] E. Bahar and M. A. Fitzwater, "Scattering and Depolarization of Linearly Polarized Waves by Finitely Conducting Particles," J. Appl. Phys., Vol. 60, pp. 2123-2132, September 1986.
- [2] D. Morrison, *Multivariate Statistical Methods*, 2nd ed. (McGraw-Hill, New York) Chap. 3, p. 116, 1967.
- [3] E. Bahar, S. M. Haugland, and A. H. Carrieri, "Full Wave Solutions for Mueller Matrix Elements Used to Remotely Sense Stratified Structures," Proceedings of IGARSS'91 Remote Sensing: Global Monitoring for Earth Management, Vol. III, pp. 1479-1482, IEEE Catalog No. 91, CH2971-0, Library of Congress No. 90-86187, June 1991.
- [4] E. Bahar and M. A. Fitzwater, "Physical Interpretation of the Full Wave Solutions for the Electromagnetic Fields Scattered from Irregular Stratified Media," Radio Science, Vol. 23, No. 5, pp. 749-759, 1988.

[5] M. Kendall, *Multivariate Analysis*, 2nd ed. (Macmillan Publishing Company, Inc., New York), Chap. 2, pp. 13-29, 1980.

TABLE 1

The Unknown Surface is Compared to:

		DIMP	SF96	DMMP	Composite
Unknown Scattering Surface	DIMP (ϵ_1)	1.9	51.3	19.4	24.4
	SF96 (ϵ_2)	49.4	2.1	34.6	53.1
	DMMP (ϵ_3)	16.9	36.9	1.8	20.5
	Composite (ϵ_4)	24.8	53.7	22.2	0.4

Table 1. A trial run of the identification algorithm computing c_i values from Equation (13) and the *discriminant vectors* of Figures 2a-c. In row 1 of the table, the unknown surface is positively identified as that of DIMP since c_1 is much less than c_2 , c_3 , and c_4 . Similarly, SF96 is detected in row 2, DMMP in row 3, and the bare composite clay surface in row 4.

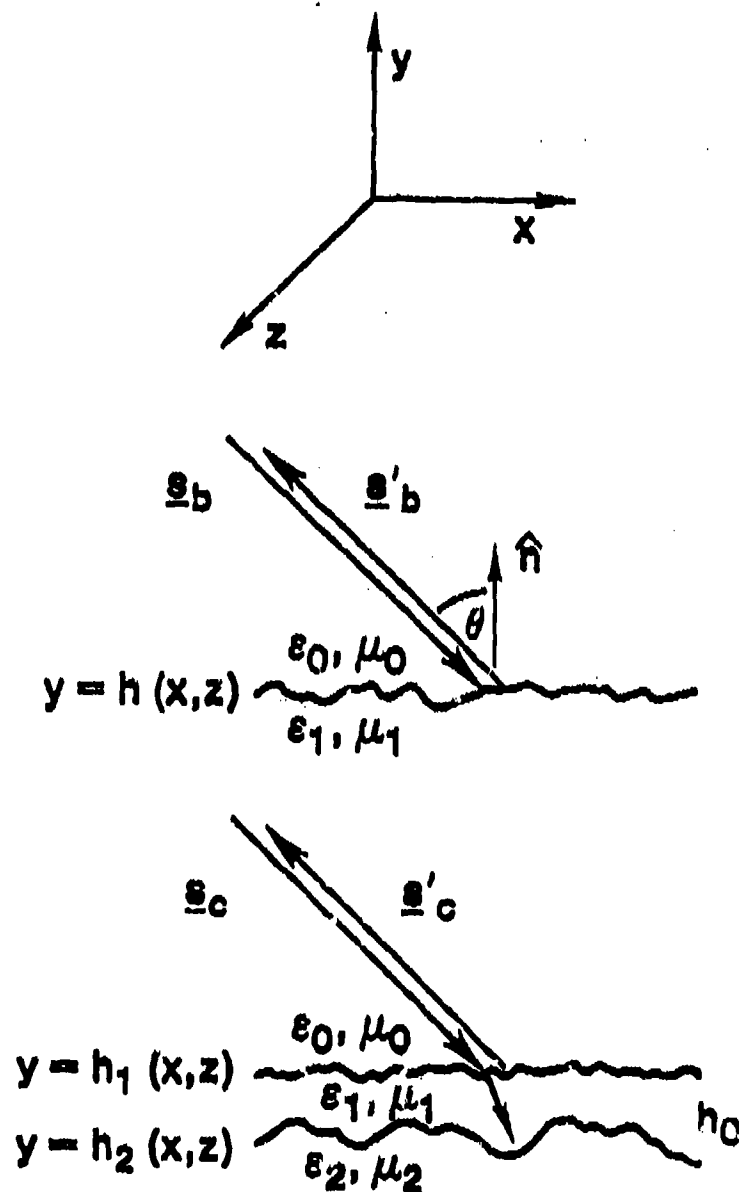


Figure 1. Definition of surfaces and some scattering parameters used in the full wave model code for computation of the Mueller matrix elements. Incident beam and backscattered ray Stokes vectors are \underline{s} and \underline{s}' (b is bare, c is contaminated surface), respectively, media permittivity and permeability are ϵ and μ , respectively, and mean height of coating material (ϵ_1, μ_1) is h_0 .

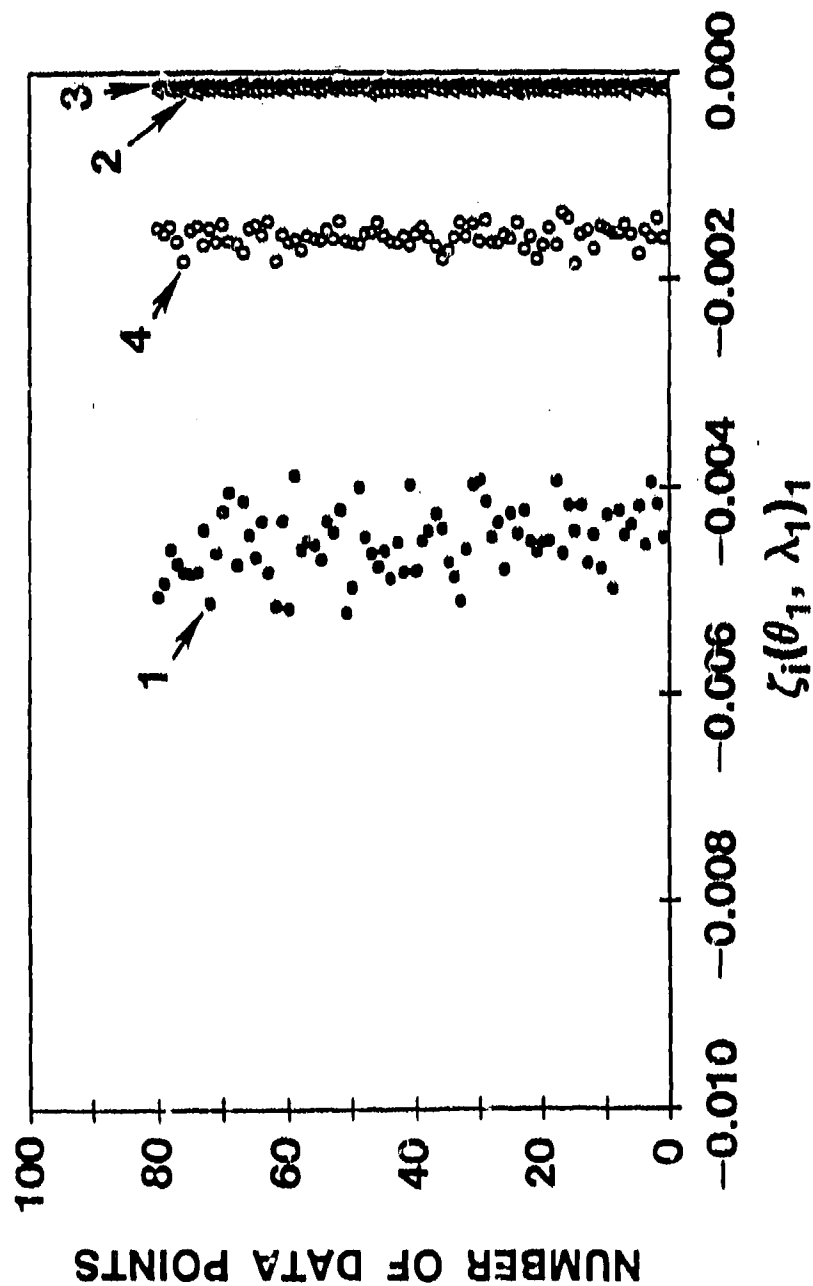


Figure 2a. Scatter plot of values of the reduced discriminant vector component $\zeta_i(\theta_1, \lambda_1)_1$, Equation (10), for four surfaces: $i = 1$, DIMP (cluster 1, closed circles); $i = 2$, SF96 (cluster 2, open triangles); $i = 3$, DMMP (cluster 3, closed triangles); and $i = 4$, composite clay (cluster 4, open circles). The incident beam angle is $\theta_1 = 48^\circ$ and beam wavelength is $\lambda_1 = 10.17 \mu\text{m}$, trained specifically for DIMP.

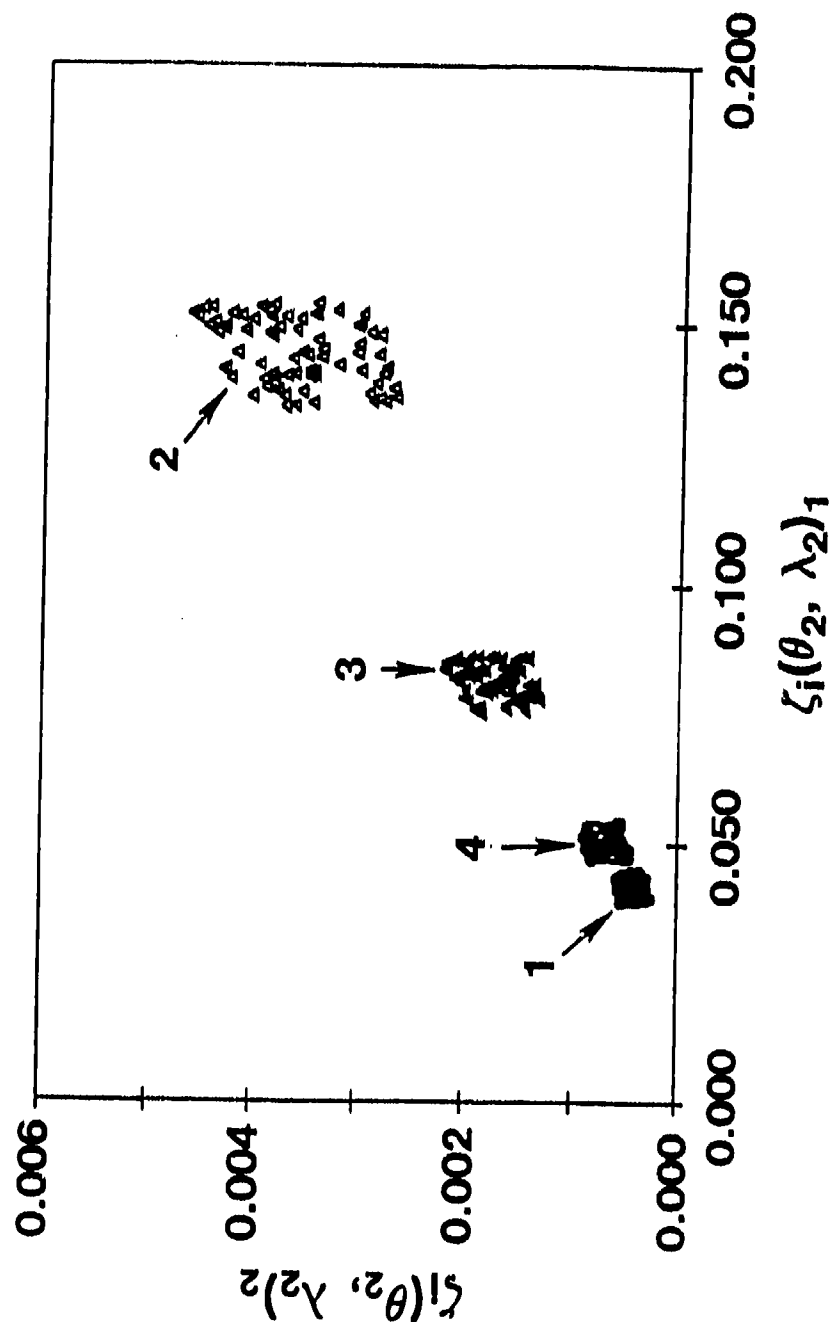


Figure 2b. Values of the discriminant vector component $\zeta_i(\theta_2, \lambda_2)_2$ plotted against component $\zeta_i(\theta_2, \lambda_2)_1$, Equation (10), for four surfaces: $i = 1$, DIMP (cluster 1, closed circles); $i = 2$, SF96 (cluster 2, open triangles); $i = 3$, DMMP (cluster 3, closed triangles); and $i = 4$, composite clay (cluster 4, open circles). The incident beam angle is $\theta_2 = 48^\circ$ and beam wavelength is $\lambda_2 = 12.35 \mu\text{m}$, trained specifically for SF96.

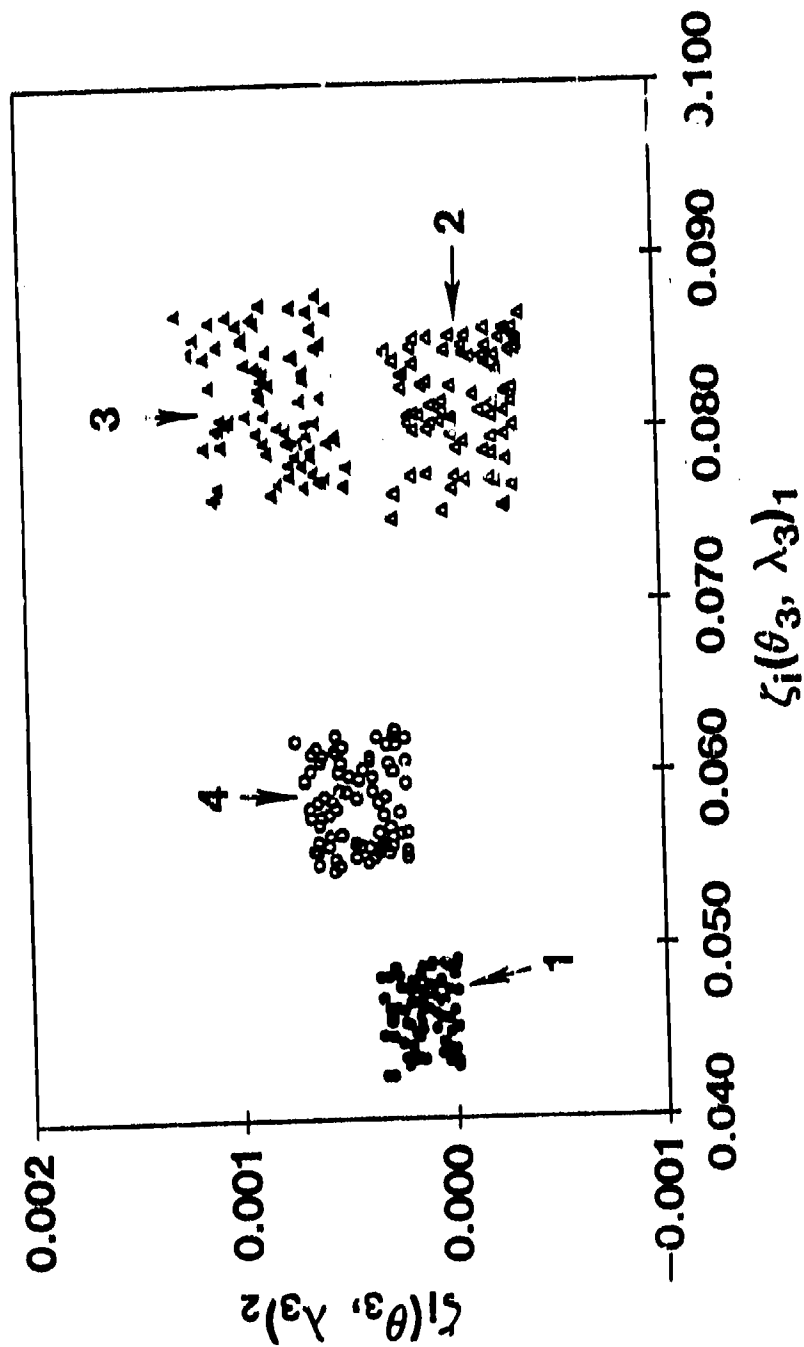


Figure 2c. Values of the discriminant vector component $\zeta_1(\theta_3, \lambda_3)_2$ plotted against component $\zeta_1(\theta_3, \lambda_3)_1$, Equation (10), for four surfaces: $i = 1$, DMP (cluster 1, closed circles); $i = 2$, SF96 (cluster 2, open triangles); $i = 3$, DMMP (cluster 3, closed triangles); and $i = 4$, composite clay (cluster 4, open circles). The incident angle is $\theta_3 = 48^\circ$ and beam wavelength is $\lambda_3 = 12.21 \mu\text{m}$, trained specifically for DMMP.

BLANK

A Side Looking Lidar for measuring cloud droplet size distribution by multiple scattering.

by

Yair Benayahu^{+#}, Shlomo Fastig⁺, Ariel Cohen^{##}, Richard D. Haracz^{*}, Leonard D. Cohen^{*}

**⁺ Department of Atmospheric Optics
Soreq Nuclear Research Center
Yavne, 70600 Israel**

**[#] Department of Atmospheric Sciences
Hebrew University of Jerusalem
Jerusalem, 91904 Israel**

**^{*} Department of Physics and Atmospheric Science
Drexel University
Philadelphia, Pa**

Abstract

A method for measuring multiple scattering by a Side Looking Lidar SLL, in which one of the detectors' field of view is off the laser beam, is presented.

The range-resolved multiple scattering signal, approximated by double scattering, is used to determine the cloud particle size distribution by means of the double scattering phase function.

The results are compared with in situ cloud droplet measurements using an airborne measuring system. The good agreement between the two measurements is presented and discussed.

I Introduction

It is accepted that the contribution of multiple scattering in Lidar measurements from optically dense media causes difficulties in the interpretation of the Lidar signal usually based on a single-scattering approximation. This is due the fact that most methods used in the past for inferring particle sizes from measurements obtained by a Lidar, are based on spectral or angular single scattering measurements⁽¹⁾.

On the other hand, the multiple scattering itself provides an additional piece of information when it can be separated from the single-scattering contribution. This additional information is used here to deduce the cloud droplet size distribution function. The scattering medium in the case discussed below is optically dense and the multiple scattering plays a major role in providing the necessary independent pieces of information for the inversion of the SLL measurements into the size distribution function.

A preliminary approach for measurement of the multiple scattering contribution to the backscattered signal of a pulsed Lidar previously reported (2,3). In the reported measurements, a set of spatial filters in the focal plane of the receiver were used to block the receiver Field Of View (F.O.V.) corresponding to the diverging transmitted beam. Consequently, the measured signal was a result of multiple-scattering effects, the scattering of which originate only from the volumes outside the blocked F.O.V.

In this paper, we present a method for measuring range resolved single and multiple scattering in one wavelength with two detectors. Actual measurements from clouds are used to deduce the double scattering phase function of the cloud particles from which the size distribution function is inferred. The results are compared with in situ cloud droplet measurements using airborne measuring systems.

II Multiple Scattering Measurements by SLL Method

In the SLL measuring technique the total (single and multiple) scattering on the one hand and multiple scattering alone on the other hand are measured simultaneously. The measuring system is schematically described in Fig.1. The laser transmits a pulse in the direction of f_1 (shown in Fig.2). In the focal plane of the telescope (i.e. the receiver), there are two holes s_1 and s_2 . The F.O.V. of the hole s_1 detects a signal consisting mainly of single-scattering contributions containing the laser beam divergence denoted as g_1 . The F.O.V. of the second hole s_2 is directed away from the laser beam so that it consists of only multiple scattered photons that were redirected from direction f_1 to direction f_2 , which is at an angular distance α away from f_1 . The SLL geometry is such that there is no overlap between the laser beam and the F.O.V. of s_2 and thus there must be at least two scattering events to redirect photons from direction f_1 to f_2 . See Fig. 2. The signal received through s_2 is denoted as g_2 .

We note that s_1 chosen for the single scattering F.O.V., is kept very small to reduce the multiple scattered contribution to the measured signal g_1 to a negligible value so that g_1 can be regarded as consisting merely of single scattering contributions. Since the F.O.V.s of s_1 and s_2 are small, the geometry of the SLL system can be simplified at a large distance R_0 from the laser, as shown in Fig.3. The spatial volumes seen through holes s_1 and s_2 can be described as two narrow cylinders separated by a distance $D = \alpha \cdot R_0$.

At any given time, the laser pulse propagates along the left-hand cylinder, one detector measures the return signal along the same cylinder and the second detector measures the return signal along the right-hand cylinder. In this Figure, the detector at s_2 measures scattering events of order 2 (double scattering) and higher. In the case of double scattering, the first scattering event, takes place at a height $(R_0 + z_1)$, along the left-hand cylinder at a scattering angle q . The second scattering event, takes place at a height $(R_0 + z_2)$ along the right-hand cylinder at scattering angle $(p - q)$ back to the detector.

Let us define the height $(R_0 + z_{ss})$ as the height corresponding to the distance from which a single scattering event takes place when the laser position is at f_1 and a measurement g_1 takes place. The time corresponding to this scattering event is equal to $t = 2(R_0 + z_{ss})/c$ where c is the speed of light. The contribution to the signal $g_2(t)$ is from all parts of first scattering events at locations $(R_0 + z_1)$ and the corresponding second scattering locations $(R_0 + z_2)$ Fig.3.

The scattering angles q as a function of z_{ss} , z_1 and D are given by:

$$\theta = 2 \tan^{-1} \left[\frac{D}{2(z_{ss} - z_1)} \right] \quad (1)$$

As the laser pulse penetrates the scattering medium (as z_{ss} increases), the range of z_1 that can contribute to the double scattering measured at the receiver position f_2 will increase as will the range of scattering angles q that will contribute to the double scattering. The range of q [q_{min} , q_{max}] as a function of the single scattering location z_{ss} within the scattering medium for a separation distance D of 10m is shown in Fig. 4. It is shown to increase monotonically as a function of z_{ss} .

An example of multiple scattering measurements of atmospheric clouds is given in Fig. 5 for the separation angle of $d = 7$ mrad. The F.O.V.s of the holes s_1 and s_2 are both 0.5 mrad, and $R_0 = 2.2$ km. The laser wavelength is 0.532 μ m, the Lidar pulse width is 10 ns, and the electronic integration time is 20 ns (corresponding to a 3m spatial resolution). The pulse repetition rate is 20 Hz and we averaged over 8 pulses in each direction. The first curve is the measured signal g_1 and the second curve is the multiple-scattering signal g_2 detected at s_2 . The curve of g_2 is as expected at first much weaker than g_1 but as the pulse penetrates into the cloud g_2 increases sharply relative to g_1 .

III. Retrieval of the double scattering phase function $p_2(q)$ from

double scattering measurements $g_2(z_{ss})$ of a real cloud.

As mentioned above, real clouds cannot be characterized as homogeneous media. This is in particular the case near the cloud surface.

We first assume that the laser signal is scattered by different volumes within a cloud layer all characterized with the same size distribution function except for the number density. This is found to be the case when the layer is horizontal and thus represents the same stage in the growth process of the cloud droplets (4).

Let $s(z)$ be the single scattering volume extinction coefficient for a given cloud depth z . Therefore:

$$P(\theta, z) = \sigma(z)p(\theta) \quad (2)$$

where $p(q)$ is the normalized single scattering phase function.

The use of Eq. 2 leads to the double scattering equation of an inhomogeneous cloud:

$$g_2(z_{ss}) = A \int_0^{z_{max}} \left[p(\theta)p(\pi-\theta)\sigma(z_1)\sigma(z_2) \frac{1}{(R_0+z_2)^2} \frac{\sin^2\theta}{D^2} \exp\left(-\int_L \sigma(t)dt\right) \right] dz_1 \quad (3)$$

where:

$z_{max} = D/\tan(q_{max})$ is the highest first scattering location satisfying the constraint of a common z_{ss} for all double scattering events. See Fig. 3

$|z_2 - z_1| = D/\sin(q)$, $z_2 = z_1 + D/\tan(q)$, L is the total optical path in the cloud and A is the system constant. In the case of double scattering the scattering process is limited to scattering occurring within one plane formed by f_1 and f_2 .

It should be emphasized that $p(q)$ (Eq. 3) dependent on the laser beam polarization. In our case the laser is linearly polarized in the scattering plane and therefore $p(q)=p_1(q)$. We also note that

this equation represents water cloud droplets for which absorption is negligible.

Knowing the value of $S(z)$ (see below) makes it possible to use Eq.3 for the derivation of the double scattering phase function: $p_2(q) = p(q)p(p-q)$.

This is achieved by using a recurrence approach as follows:

The range of angle q contributing to $g_2(z_{ss})$ increases monotonically with z_{ss} . Since the Lidar spatial resolution is constant the value of z_{ss} is varied in steps of $\Delta z_{ss} = \Delta z$, the integrals in Eq. 3 are replaced by the averaging sums:

$$g_2(\Delta z * n) = A \sum_{i=1}^n p_2(\theta_i) \sigma(z_{1i}) \sigma(z_{2i}) \frac{1}{(R_0 + z_{2i})^2} \frac{\sin^2 \theta_i}{D^2} \exp\left(-\int_{L_i} \sigma(t) dt\right) \Delta z \quad (5)$$

where:

$$z_{2i} = \Delta z * i$$

and:

$$z_{1i} = z_{11} + \frac{D}{\tan(\theta_i)}$$

In this case L_i is also varying and is determined by the optical path in the cloud

The initial value of $p_2(q)$ can be chosen as a normalization constant. It follows that $p_2(q)$ is given by:

$$p_2(\theta_n) = \frac{g_2^{(m)}(\Delta z * n) - g_2(\Delta z * (n-1))}{\Delta g_2(\Delta z * n)} \quad (6)$$

where $g_2^{(m)}(\Delta z * n)$ is the measured signal, $g_2(\Delta z * (n-1))$ is given by Eq.5 and:

$$\Delta g_2(\Delta z * n) = A * \sigma(z_{1n}) \sigma(z_{2n}) \frac{1}{(R_0 + z_{2n})^2} \frac{\sin^2 \theta_n}{D^2} \exp\left(\int_{L_n} \sigma(t) dt\right) \Delta z \quad (6a)$$

for any given value of n .

We note that the value of the scattering angle q_i is defined by:

$q_i = [q(Dz^*(i-1)) + q(Dz^*i)]/2$ where $q(Dz^*i)$ is determined by Eq. 1 with $Dz = (z_{ss} - z_1)$.

$p_2(q_i)$ is therefore the average value of $p_2(q)$ in the range $[q(Dz^*(i-1)), q(Dz^*i)]$. Therefore the average value of q representing the first spatial Lidar step within the cloud is about 80 degree (See Figs. 8,9).

IV. The determination of the volume extinction profile $S(z)$.

For the derivation of $S(z)$ we use the single scattering measurements g_1 as obtained through hole s_1 , by applying the backward Klett method (5) for the inversion process:

$$\sigma(z) = \frac{g_1(z)z^2}{\frac{g_1(z_m)z_m^2}{\sigma_m} + 2 \int_z^{z_m} g_1(t)t^2 dt} \quad (7)$$

where $g_1(z)$ is the backscattered signal from a distance z and S_m is the assumed volume extinction coefficient of $z=z_m$ in the cloud. $S(z)$ is the required extinction coefficient profile within the cloud layer.

In order to use the inversion Eq.7 we use the following assumptions:

a. The ratio of the single backscattering coefficient over the extinction coefficient is constant .

This assumption is a direct consequence of the fact that the distribution function is constant vs. z .

b. Klett's inversion method is based on the single scattering Lidar equation.

This assumption is justified by the use of a very narrow F.O.V. which ensures that multiple scattering contributions to g_1 are negligible.

In Fig.6 Multiple/single scattering g_m/g_1 Lidar return signal are calculated by a Monte Carlo code⁽⁷⁾ for a detector F.O.V. of 0.5 mrad, a range to the cloud $R_0=1\text{Km}$, a C1 cloud , a volume extinction coefficient $S=17\text{km}^{-1}$, and a laser wavelength of 0.532 mm.

It can be seen that the multiple scattering calculations g_m (where $m \geq 2$) for a F.O.V. of 0.5 mrad, gives rise to a multiple scattering contribution of less than 5% compared to the single scattering signal up to a penetration depth of $z=100\text{m}$ (corresponding to an optical depth of $t \approx 4$).

c. The main inaccuracy in using Klett's approach is the necessity of choosing a boundary value S_m at z_m . However it has been shown (5,6) that when the medium is very dense the choice of S_m , has a little influence on the accuracy of the results, since $S(r)$ converges rapidly to the real value for any given value S_m .

In our case, we use this result in the following way :
 We chose S_{in} in the depth of the cloud far away from the layer of interest being within the first 60m from the cloud surface.
 Doing so, the results $S(r)$ at $z < 60$ reaches a high degree of accuracy.

V. The Double Scattering Approximation.

The multiple scattering signal g_2 in Eq.5 represent double scattering contribution and neglect higher orders of multiple scattering. In order to check the validity of the double scattering approximation for g_2 a Monte Carlo code (7) was used to compare the relative magnitudes of the various scattering orders, for the SLL geometry.

The results of the calculations are presented in Fig. 7 . Multiple/single scattering SLL return signal through hole $s_2 g_m/g_2$ (where $m>2$) curves is plotted against the cloud penetration depth. The detectors is F.O.V. of 0.5mrad and volume extinction coefficient $S=10\text{km}^{-1}$. It can be seen that the SLL signal g_m (where $m>2$) is less than 5% compared to the double scattering signal g_2 for a penetration depth of 60m when $\phi=3$ mrad and less than 15% for $\phi=7$ mrad. Therefore the double scattering approximation is valid for optical depth value $t < 1$. This requirement is obeyed in all our experiment.

VI. The Determination of the cloud droplet size distribution $f(a)$ from the double scattering phase function $p_2(q)$.

The double scattering phase function $p_2(q)$ can be used as an input data for an analytical inversion method (8,10) in order to yield the cloud droplet size distribution $f(a)$. However since field measurements from real clouds may introduce large errors, we used an additional approach for the inversion of the measured values. This approach is based on the fact that in most practical cases a-priori information on the cloud is available.

In our particular case in-situ measurements provided the general behavior of the distribution function.

Moreover since our measurements were limited to the cloud base zone the distribution function could be assumed to have one maximum within the size range 1-10 μm (4,9).

We therefore assumed a log-normal distribution function for which the geometrical mean radius m and the expansion parameter a are determined from the measurements.

The Log-normal distribution has the form:

$$f(a) = A \cdot \exp \left[-\frac{1}{2} \left(\frac{\text{Log}(a) - \text{Log}(\mu)}{\text{Log}(\alpha)} \right)^2 \right] \quad (8)$$

We thus limit the practical inversion method into the determination of m and a .

In order to simplify the comparison of $p_2^{(m)}(q)$ derived from the measurements with the theoretical $p_2(q, m, a)$ calculated for a given set of m and a , we developed a library of $p_2(q, m, a)$ for a series of average values of m and a in such a way that:

$$p_2(\theta, \mu, \alpha) = p(\theta, \mu, \alpha) p(\pi - \theta, \mu, \alpha) \quad (9)$$

where:

$$p(\theta, \mu, \alpha) = \int_{a_{\min}}^{a_{\max}} \sigma_s(\theta, a) f_{(\mu, \alpha)}(a) da \quad (9a)$$

where $f(m,a)(a)$ is the Log-normal size distribution function and $s_s(q,a)$ is the differential scattering cross section of a particle of a size parameter $2\pi a/\lambda$ (calculated from Mie theory).

In this way we have formed a matrix of the double scattering functions $p_2(q, m, a)$.

The best matched $p_2(q, m, a)$ from the matrix to the "measured" $p_2^{(m)}(q)$ is found by adopting the following criterion:

$$C(\mu, \alpha) = \frac{1}{n} \sum_{i=1}^n \frac{|p_2(\theta_i, \mu, \alpha) - p_2^{(m)}(\theta_i)|}{p_2^{(m)}(\theta_i)} \quad (10)$$

The "measured" $p_2^{(m)}(q)$ is derived from the measurements using Eq. 6 and the parameters m and a are chosen such that C is minimized.

VII. The Sensitivity of the Method to Measurement Errors.

In order to examine the sensitivity of this approach to the measurement accuracy, we have performed several computer simulations.

The simulations were performed as follows:

A trial profile was chosen for the extinction coefficient profile within the cloud layer for a given cloud size distribution function. We then used Eq.5 to calculate $g_2(z_{ss})$ to which we added an error.

The calculate $g_2(z_{ss})$ with the errors was regared as the measurements to which we then applied the recurrence Eq.6 and then we use the inversion method described above to get $f(a)$.

It can be seen (Fig. 8) that the reconstruction of $p_2(q)$ reached a high degree of accuracy for the angular range $q = 15$ to 80 degrees even for random data error up to 10%.

In Figs. 8a and 8b the effect of the random error is seen. The pronounced minimum in the value of the correlation parameter C is smeared as the errors increase.

In the simulation we chose $a=m=2$ the distinct minimum in C can be found even for a random error of as high as 10% in the simulated measurements.

In order to simulate the effect of errors due to the higher orders of multiple scattering contribution, we introduced a systematic error in the form: $g'_2(z) = g_2(z)(1+bz)$ to take into account the increase contribution of multiple scattering as a function of the penetration depth.

Figs. 9, 9a, 9b present the results achieved with simulated measurements containing systematic errors of up to a value of $b=0.5$ which corresponds to a 50% error in the largest penetration depth. It can be seen that even with such a big error the results agree with the assumed distribution to a good degree of accuracy.

VIII. Field Experiments and Results

During the winter of 1990 various measurements were performed in the Israel coastal area intended to determine the cloud droplet number density and size distribution function.

Simultaneous in-situ measurements were taken by a Knollenberg droplet counting system mounted in a air-plane.

In Fig. 10 the SLL-cloud-plane geometry is presented. The penetration path within the cloud is contained in one height layer for which one can assume that the size distribution function is constant (4).

Several profiles of the SLL echoes $g_1(z)$ and $g_2(z)$ were taken as a function of time, one example of which is presented in Fig. 11.

In this example the distance to the cloud is $R_0 = 1.9$ km. The Lidar spatial resolution is 3m. For the calculation we use 20 data points, corresponding to total penetration depth of 60m.

The two curves (not in the same relative units) represent a typical shift of the maximal signals from the shorter distances in g_1 to the longer distances in g_2 for which only multiple scattering contributions are measured.

We note that the fluctuations in g_1 are mainly due to the cloud structure in addition to the extinction.

In order to calculate the value of extinction profile $S(z)$ in this inhomogeneous cloud we used the Klett method Eq.7. boundary value S_m was chosen at a cloud depth of 175m, and as a consequence the extinction profile of ranges up to 60m can be treated with a high degree of accuracy (See Fig 12, and see discussion in IV).

The numerical results of Fig. 12 were then used for the determination of the double scattering "measured" phase function $p_2^{(m)}(q)$, based on Eq. 6.

The double scattering "measured" phase function $p_2^{(m)}(q)$ is shown in Fig. 13 with the best-fit matrix vector element $p_2(q, m, a)$ found by minimizing the correlation parameter C. The minimum was also shown to be well defined either as a function of m or a , See Fig. 13a.

Finally, the corresponding size distribution function of the cloud droplets given in Fig. 14 is compared against the in-situ measurements. As can be seen there is a good agreement between the two curves. We note that the Knollenberg counter did not measure small particles whose radius is smaller than 1.5 microns.

IX. Discussion

The approach discussed is an example of the added information to the Lidar measurements provided by the multiple scattering effect previously treated as a disturbance.

The double scattering phase function $p_2(q)$ is very sensitive to the size distribution parameters. For example $p_2(10)/p_2(80)$ varies by one order of magnitude when the droplet mean size m varied from 1 to 2 mm.

The inversion of field measurements into the size distribution function was shown to be practically possible by using a priori knowledge of the general behavior of the distribution function. By reducing the number of unknowns to the mean radius and the expansion of a log-normal distribution even highly fluctuating inhomogeneous clouds in respect to the number density can provide measurable information on the sizes.

It is practically impossible to perform the rirborn and SLL measurements at the same position. But several in-situ records from the same horizontal cloud layer a few km wide showed almost no variations in the size distribution

(4) and therefore all records cloud from the same height could be used for the discussed comparisons.

Finally, the same approach can be used for different layers in the cloud by varying the Lidar

elevation angle. This way the cloud size distribution and density profiles can be obtained for the study of the droplet growth process in the cloud.

References

1. B.M. Herman, S.R. Browning, and J.A. Reagan, "Determination of aerosol size distribution from Lidar measurements", J.Atmos.Sci., Vol. 28, pp. 763-771 ,(1971).
2. A.I. Carswell and S.R. Pal, "Polarization anisotropy in Lidar multiple scattering from clouds", Appl. Opt. 19, 4123-4126, (1980).
3. S.R. Pal and A.I. Carswell, "Multiple scattering in atmospheric clouds: Lidar Observation", Appl. Opt. 15, 1990-1995, (1976).
4. I.R. Paluch, "Mixing and the cloud droplet size spectrum: Generalization from CCOPE data". J. Atmos. Sci., Vol. 43, No. 18, pp. 1984-1994, (1986).
5. J.D. Klett, "Stable analytical inversion solution for processing Lidar returns", Appl. Opt., Vol. 20, pp. 211-220, (1981).
6. W. Carnuth and R. Reiter, . "Cloud extinction profile measurements by Lidar using Klett's inversion method".App. Optics. Vol. 25, no.17, pp. 2899-2907 (1986).
7. Y. Benayahu and A. Cohen, "Lidar multiple scattering from clouds". Proc. of MUSCLE4, Florence, (1990).
8. Y. Benayahu, S. Fastig and A. Cohen, " Cloud extinction and size distribution from monostatic Lidar multiple scattering measurements". Proc. of MUSCLE4, Florence, (1990).
9. A. Gagin and J. Neumann, " Rain stimulation and cloud physics in Israel ", in Weather and climate modification , Edited by W.N.N. Hess, J .Wiley, pp. 454-484, (1974).
10. A.Ben-David, Y.Benayahu, S.Fastig and A.Cohen, " Retrieval of a double scattering phase function from multiple scattering measurements of atmospheric clouds. (submitted to Appl. Opt.)

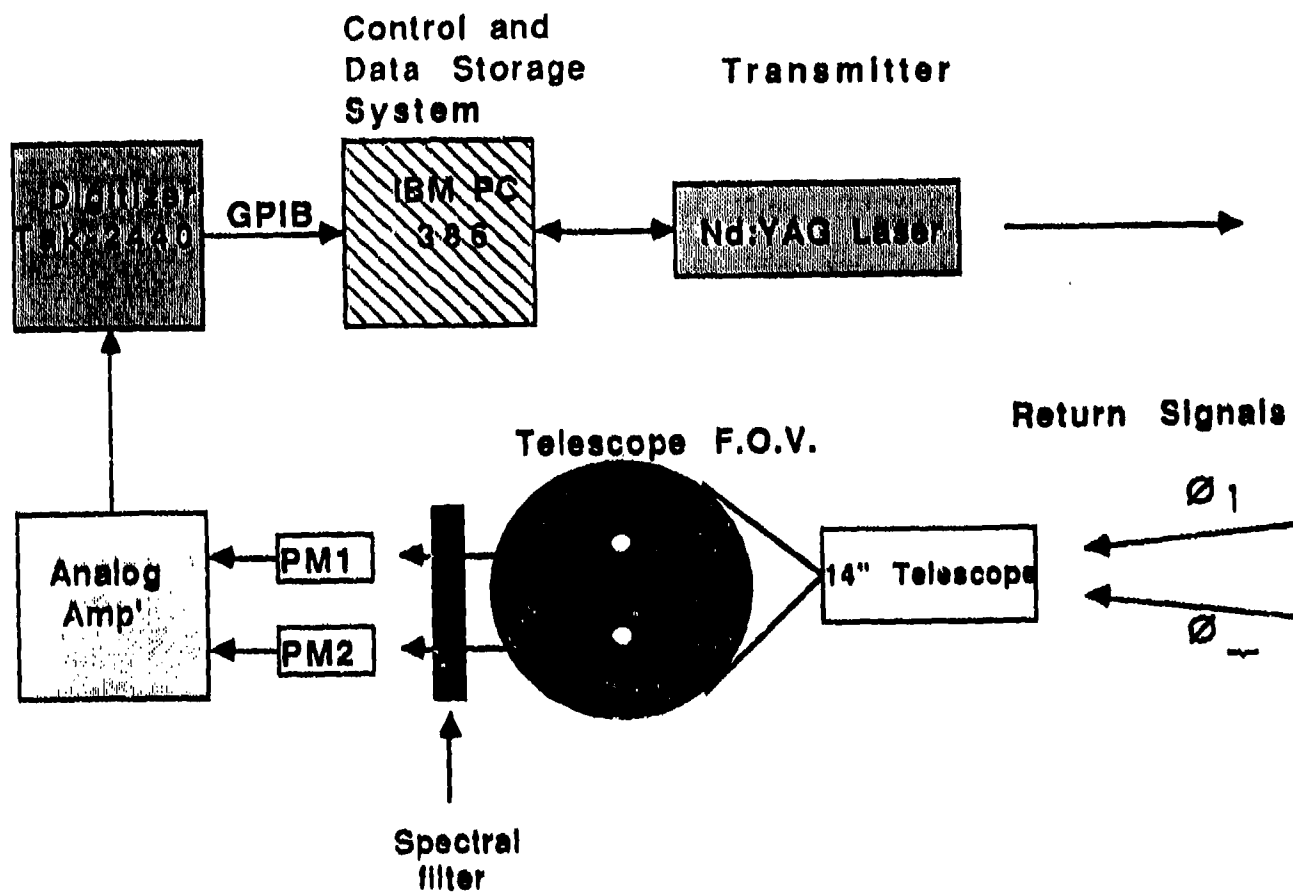


Fig.1 Schematic set of the SLL system.

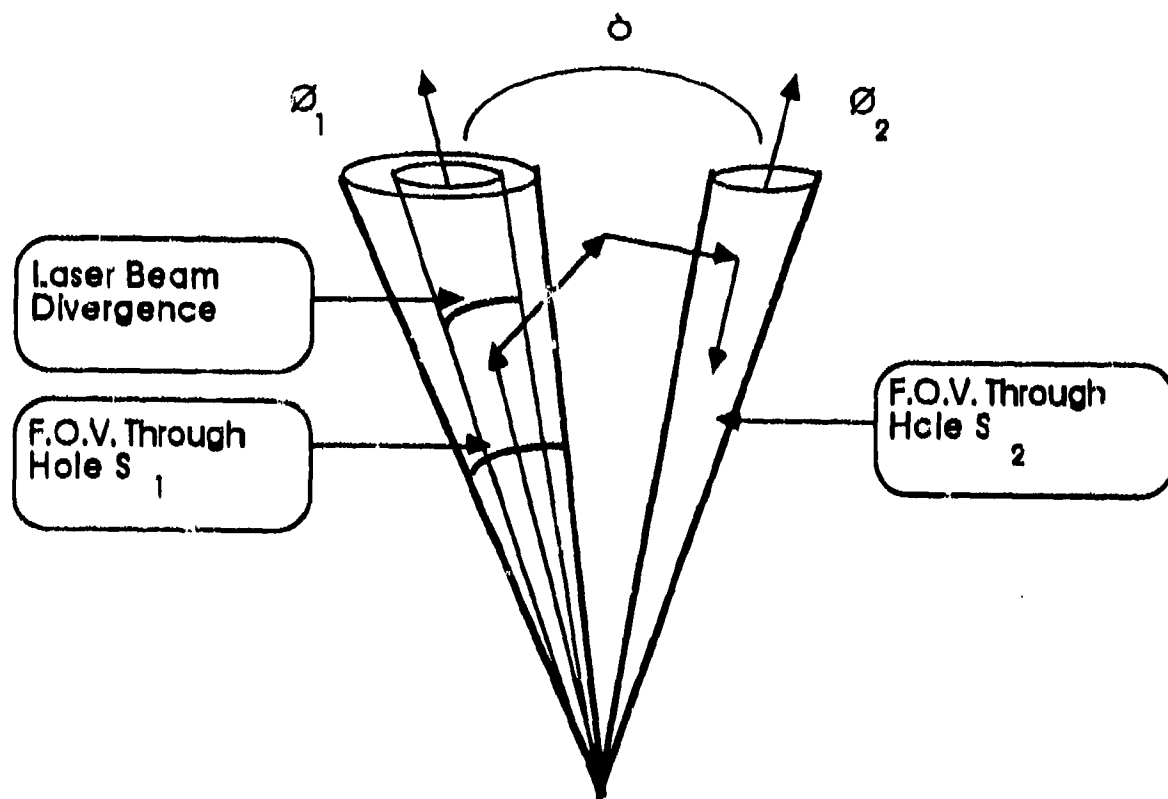


Fig.2 The laser beam divergence and the F.O.V through holes s_1 and s_2 .

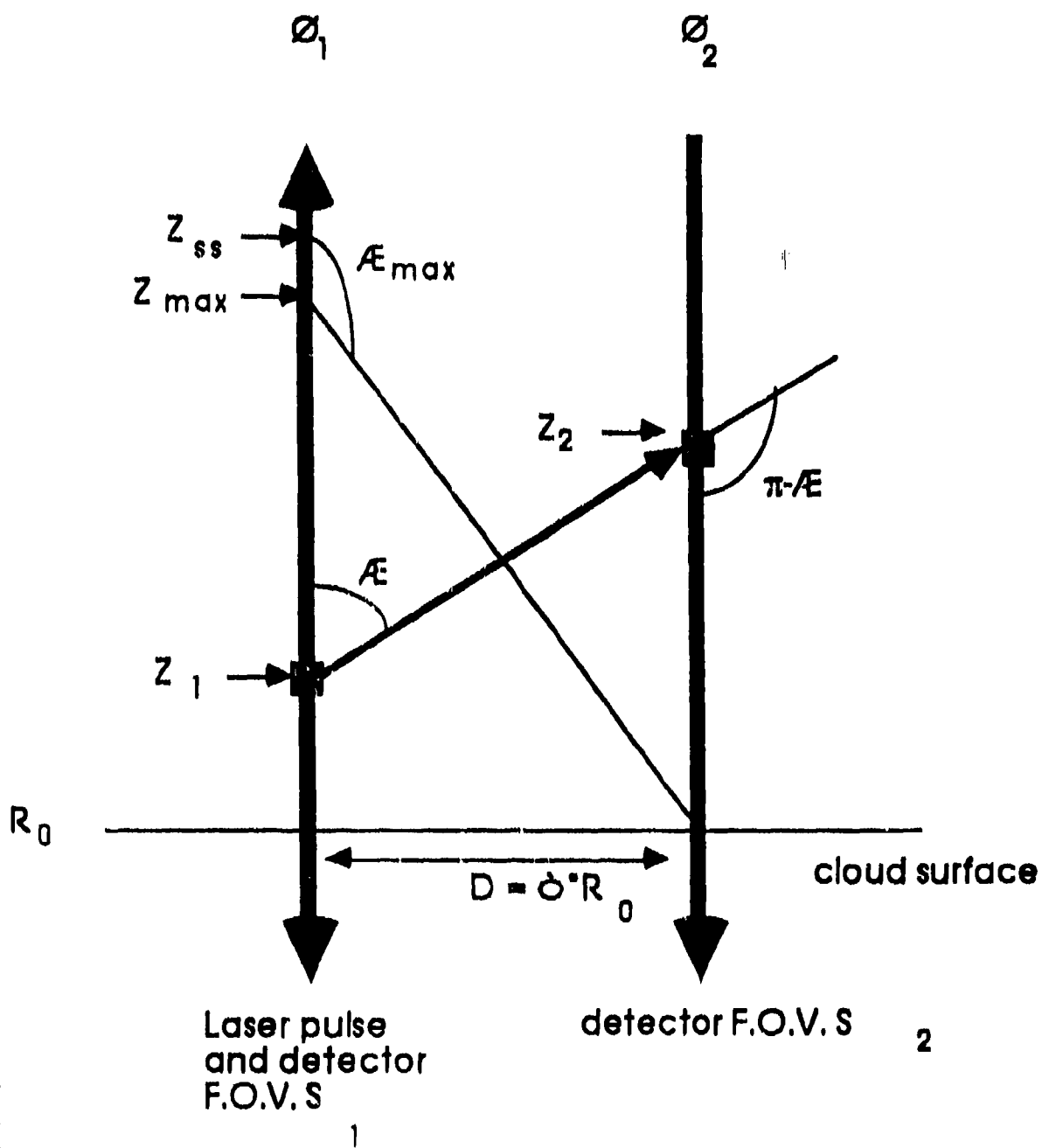


Fig.3 A simplified geometry of the SLL and the double scattering process in the cloud.

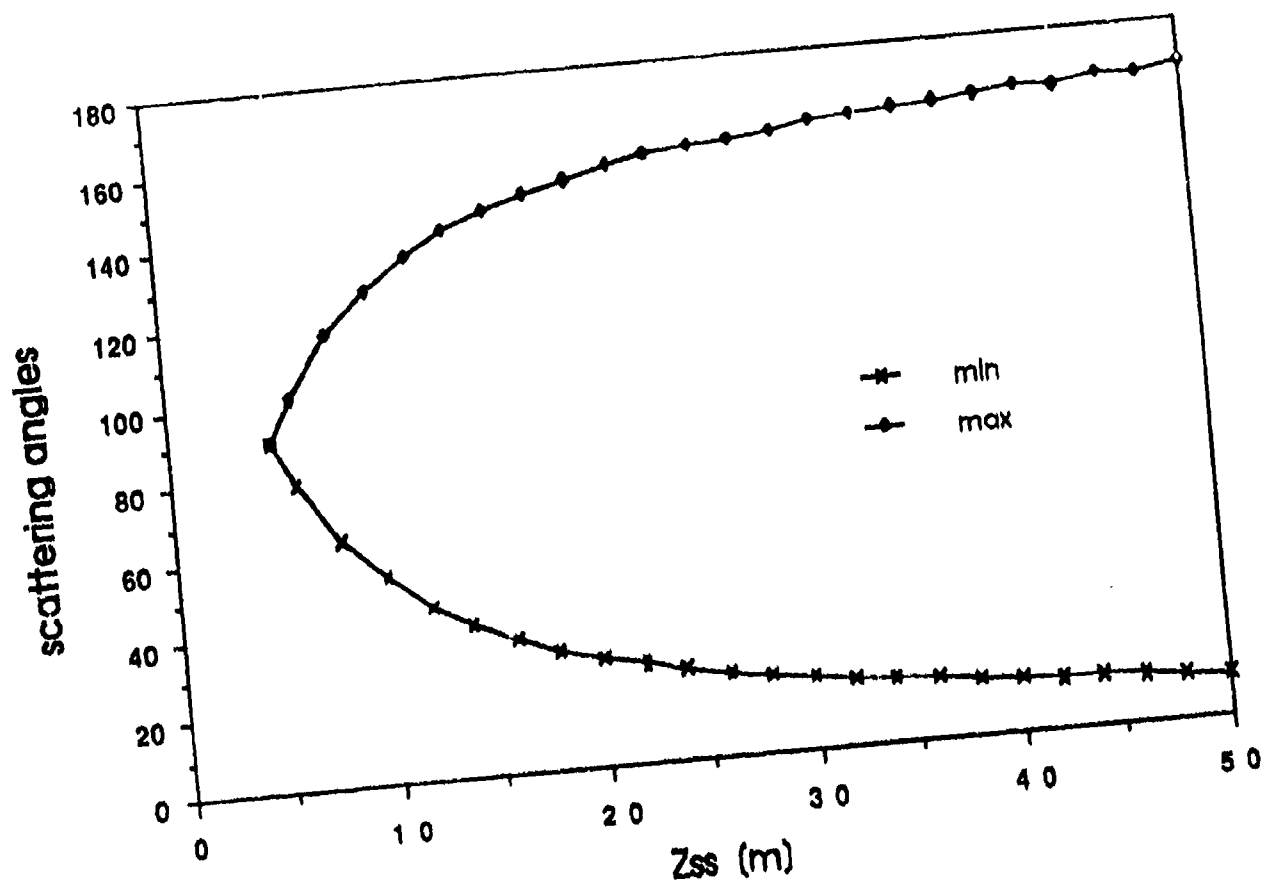


Fig.4 The range of scattering angle $[Q_{min}, Q_{max}]$ that contribute to the double scattering returns as a function of the single scattering location z_{ss} for $D=10m$.

Multiple Scattering Measurements 1/2/90 14:40

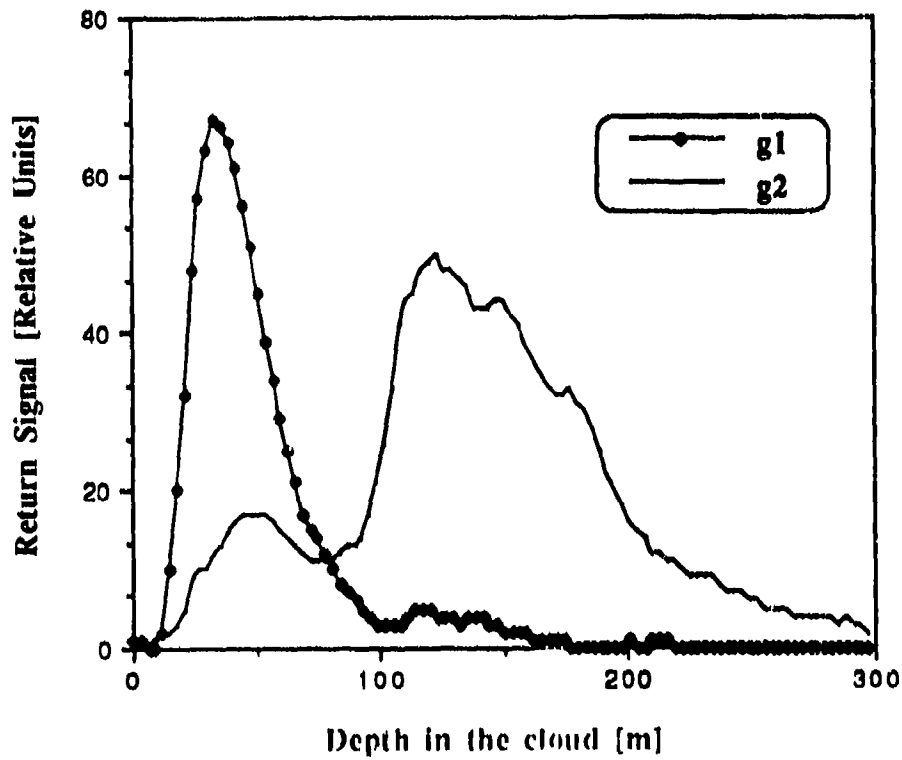


Fig.5 Single and multiple scattering signals g_1 and g_2 . The F.O.V of holes s_1 and s_2 are 0.5 mrad. The angular distance between f_1 and f_2 $\alpha=7\text{mrad}$. The range to the cloud $R_0=2.2\text{Km}$. The laser wavelength is 0.532 m m and the range resolution is 3m.

Lidar Multiple Scattering (On axis calculations)

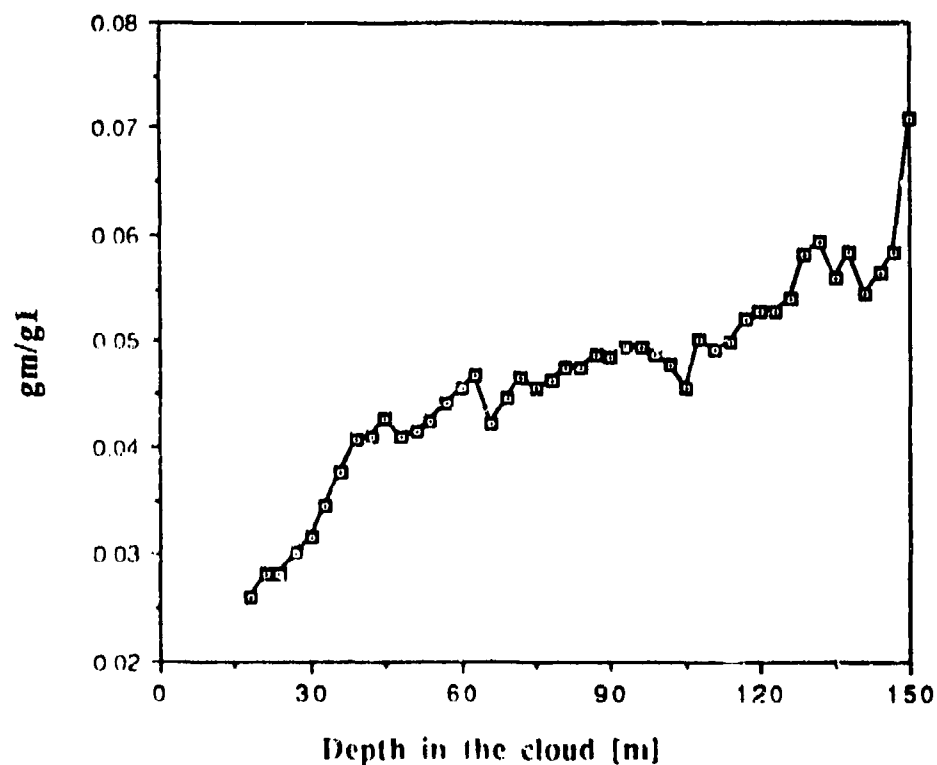


Fig.6 Multiple/single scattering Lidar return signal ratio g_m/g_l , as calculated by M.C code. The detector F.O.V is 0.5 mrad. The range to the cloud $R_0=1$ Km. The cloud is C1 type. The volume extinction coefficient $S=17\text{ km}^{-1}$ and the laser wavelength is 0.532 nm.

SLL Multiple Scattering (Off axis calculations)

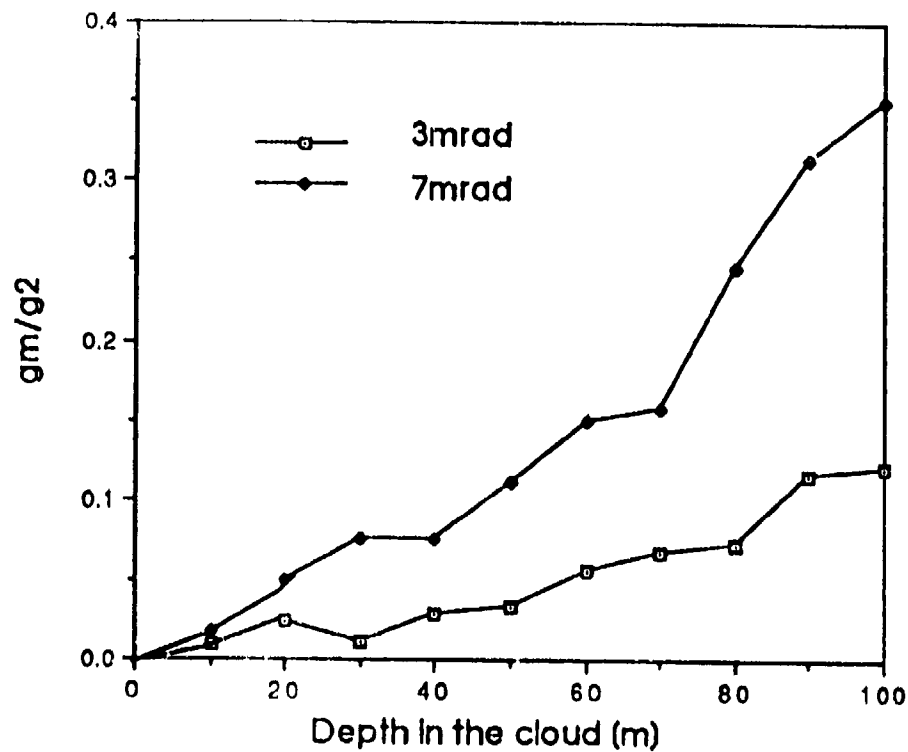


Fig.7 Multiple/single scattering SLL return signal g_m/g_2 ratio through hole s_2 , as calculated by M.C code. The detectors F.O.V are 0.5mrad. The range to the cloud $R_C \approx 1\text{Km}$. The cloud is C1 type. the volume extinction coefficient $S=10\text{km}^{-1}$ and the laser wavelength is 0.532 mm.

Double scattering phase function

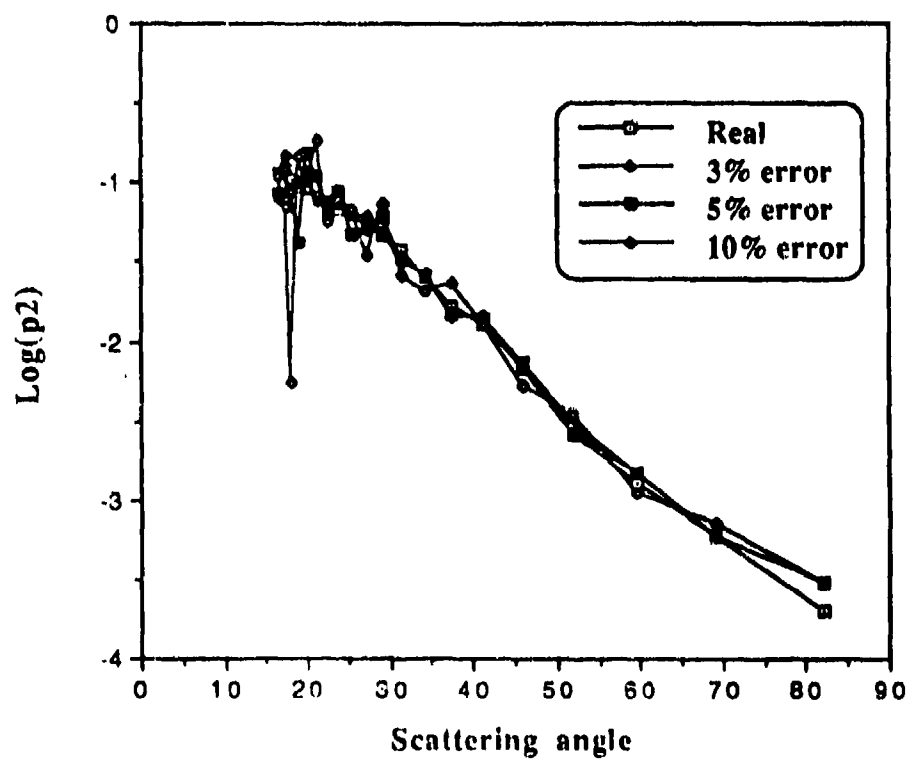


Fig.8 Double scattering phase function $\text{Log}(p_2)$ as computed from g_2 containing various random error. The cloud particle size distribution is log-normal with mean and expansion parameters $m=a=2\text{mm}$.

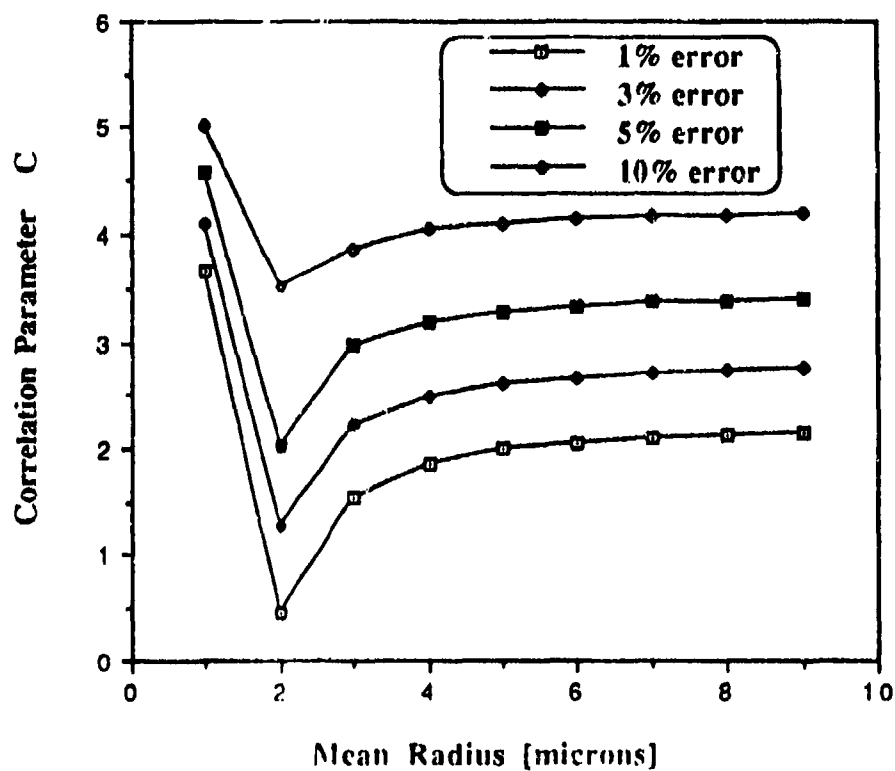


Fig.8a The correlation parameter C as a function of the mean radius parameter m of the Log-normal size distribution function, for various random error.

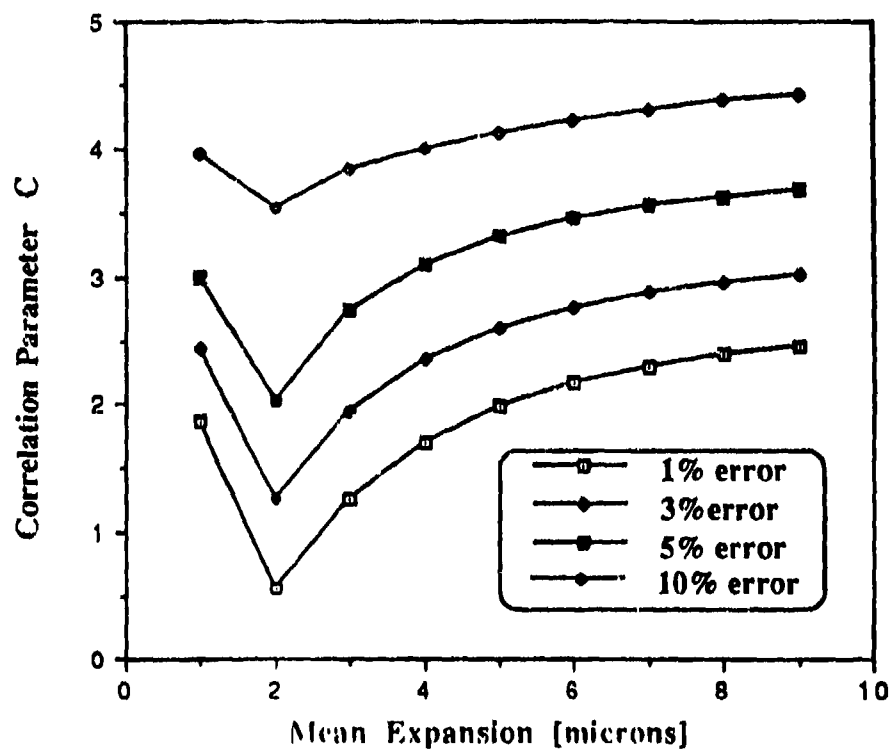


Fig.8b The correlation parameter C as a function of the expansion parameter a of the Log-normal size distribution function, for various random error.

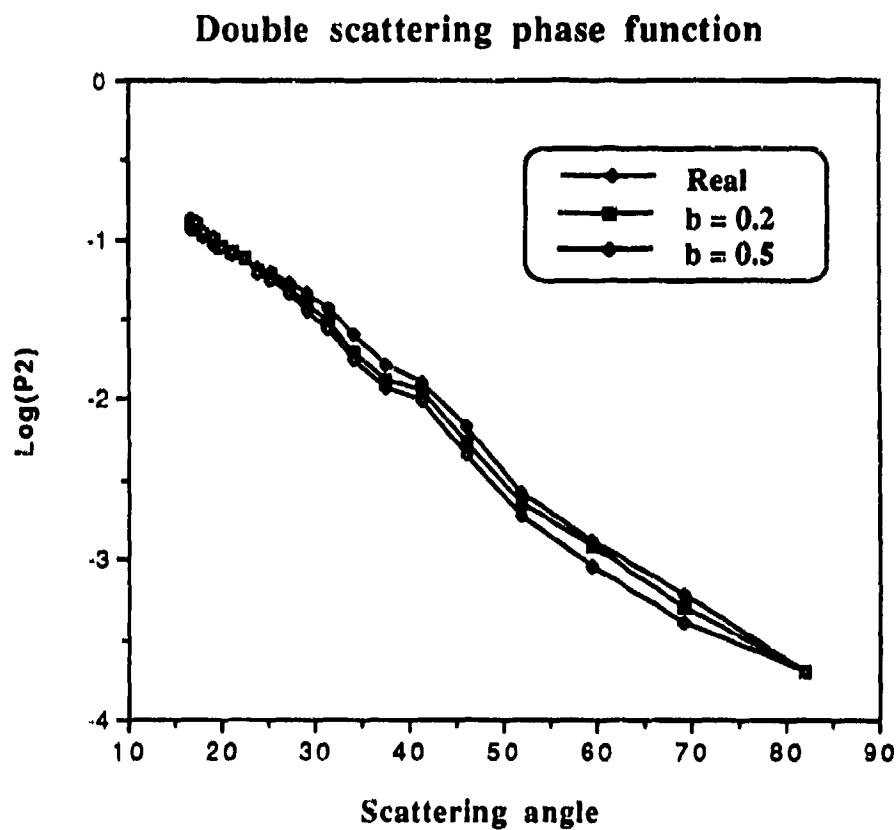


Fig.9 Double scattering phase function $\text{Log}(p_2)$ as computed from g_2 containing various systematic error (see text). The cloud particle size distribution is log-normal with mean and expansion parameters $m = a = 2m$.

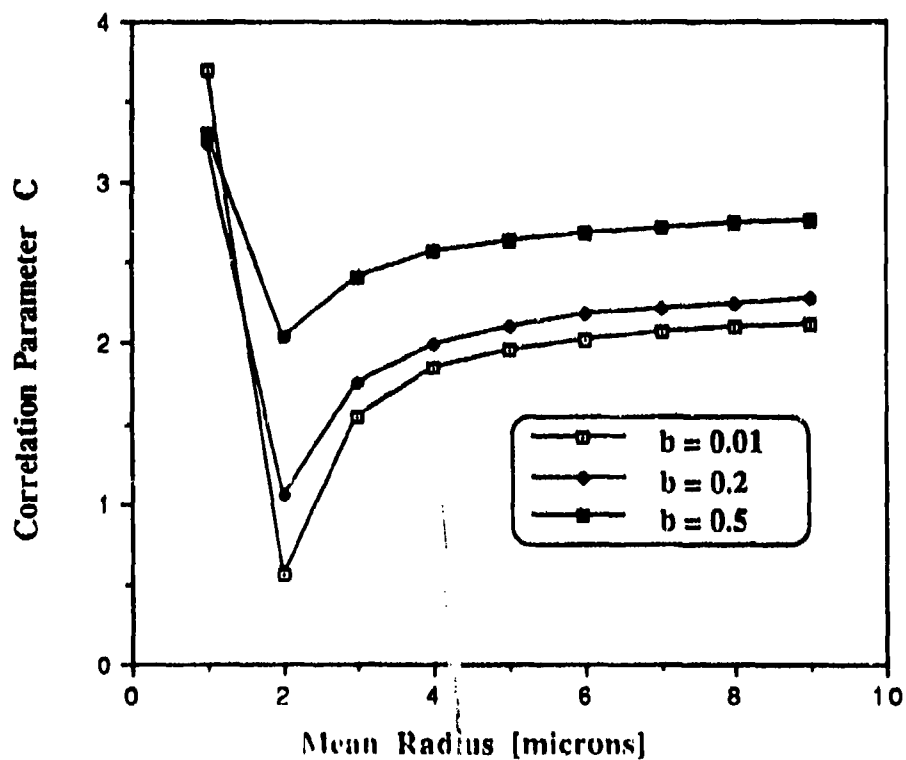


Fig.9a The correlation parameter C as a function of the mean radius parameter m of the Log-normal size distribution function, for various systematic error.

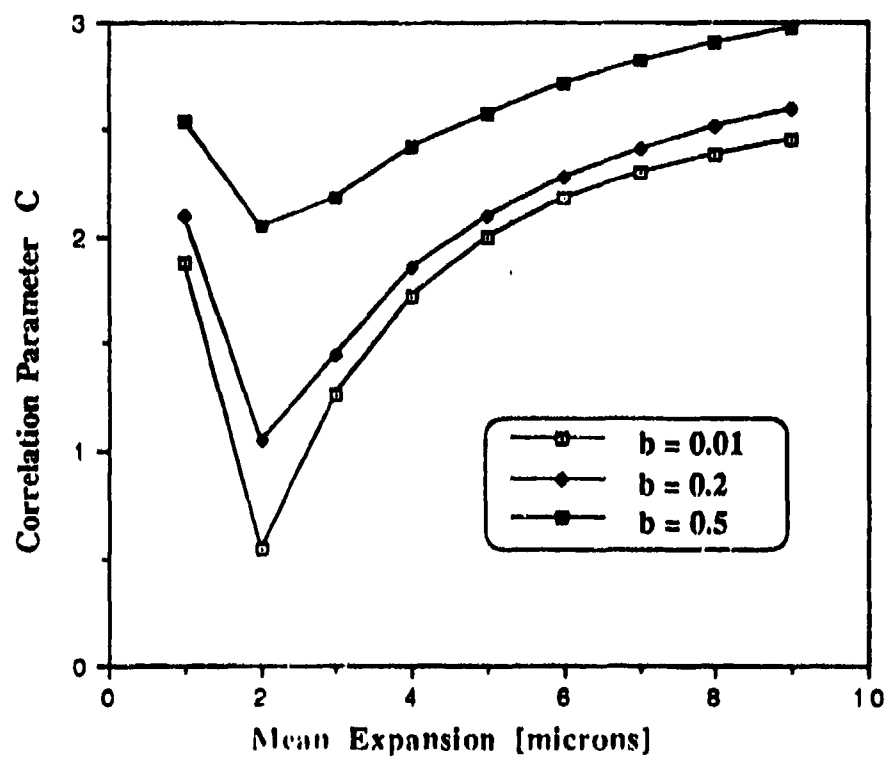


Fig.9b The correlation parameter C as a function of the expansion parameter a of the Log-normal size distribution function, for various systematic error.

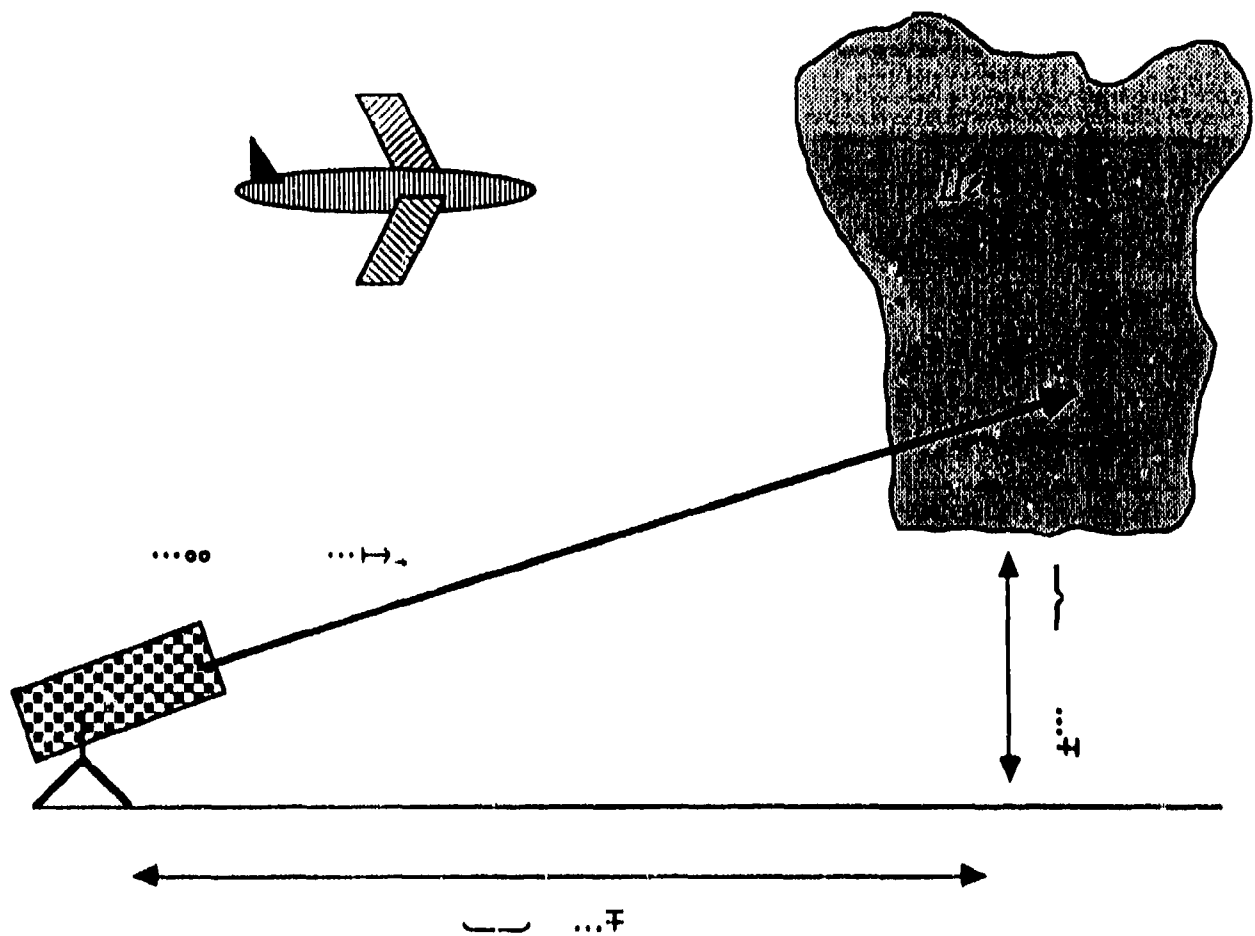


Fig.10 The experiments field set up.

Multiple Scattering Measurement
6/2/90 14:59

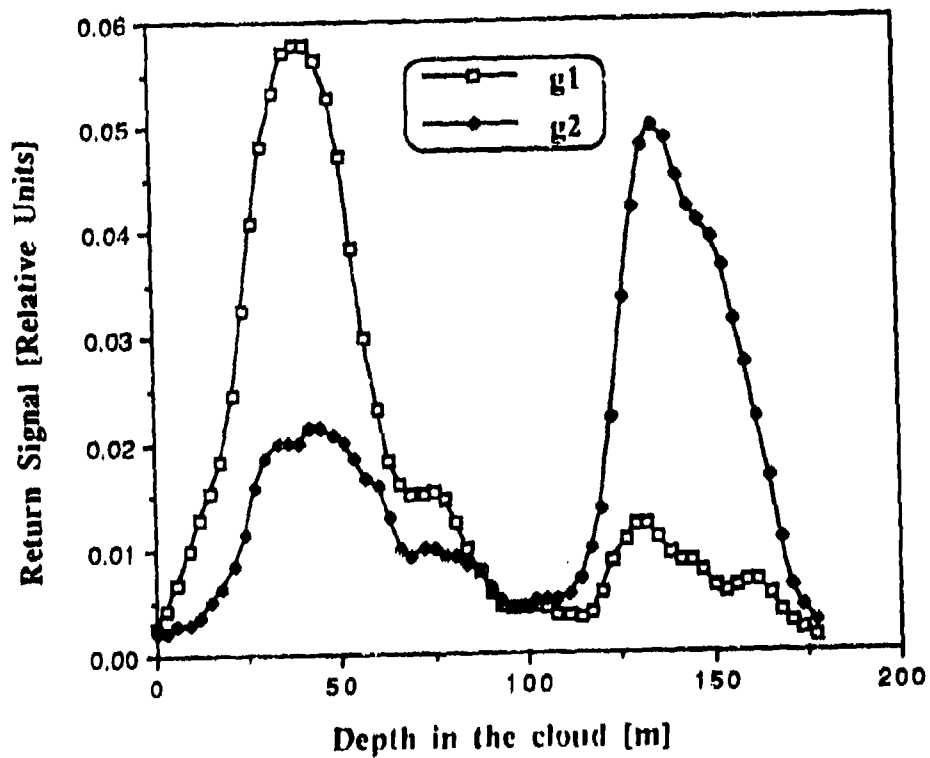


Fig.11 Single and multiple scattering signals g_1 and g_2 . The F.O.V of holes s_1 and s_2 are 0.5 mrad. The angular distance between f_1 and f_2 $d = \text{mrad}$. The range to the cloud $R_0 = 1.9 \text{ Km}$. The laser wavelength is 0.532 μm and the range resolution is 3m.

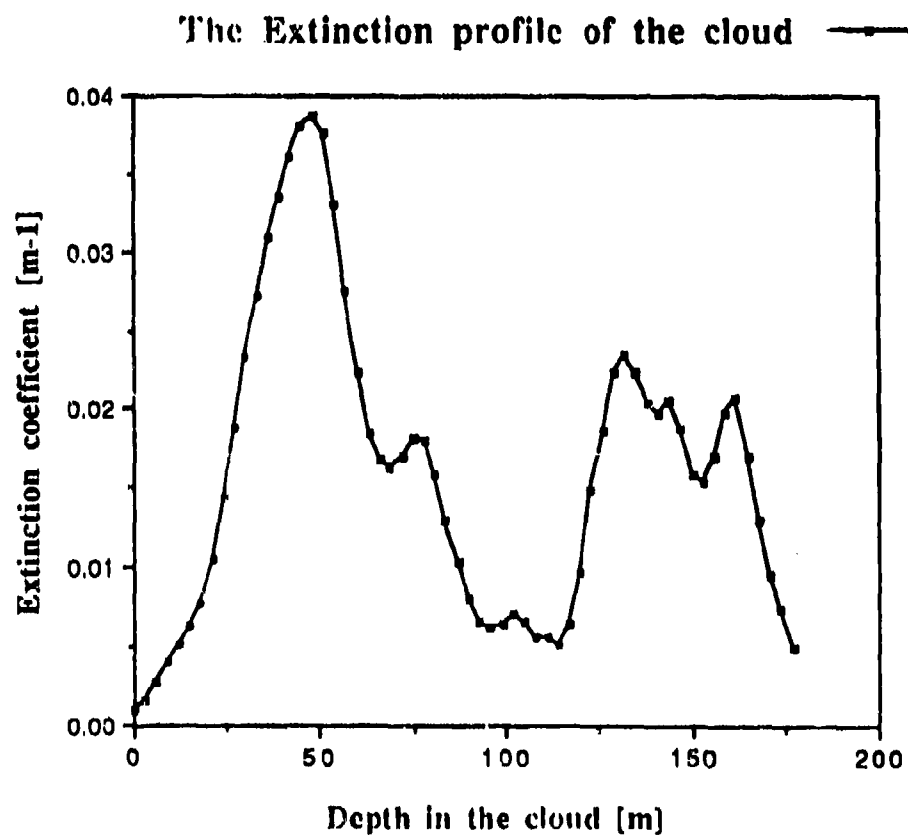


Fig.12 The volume extinction profile in the cloud $S(z)$, as computed from g_1 of fig.11 by Klett method.

Double scattering phase function

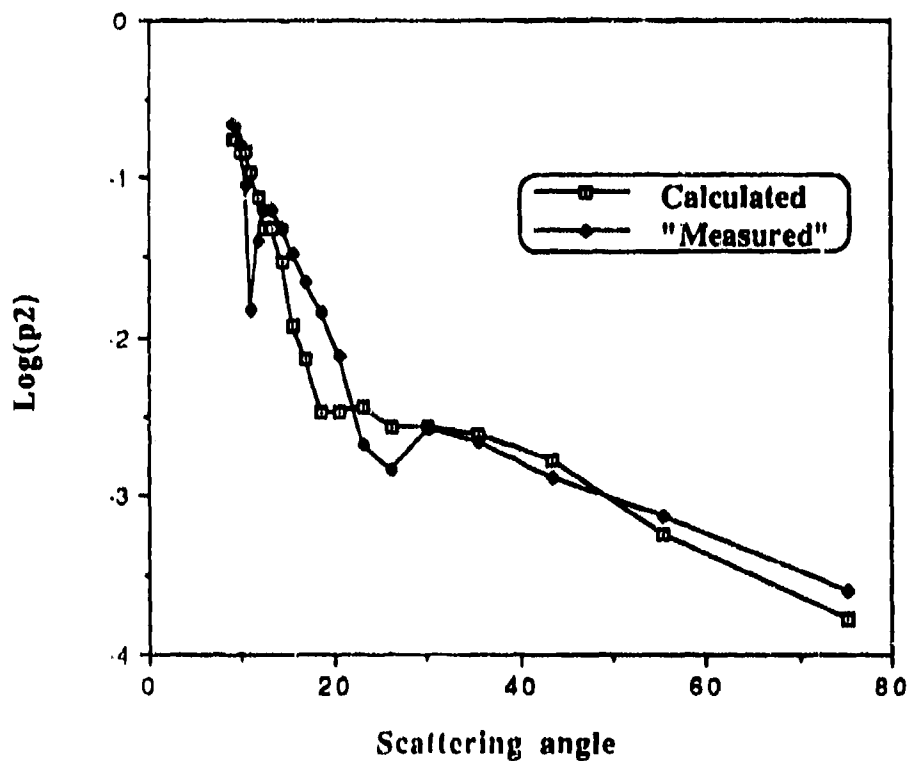


Fig.13 The "measured" Double scattering phase function $\text{Log}(p_2^{(m)}(q))$. Computed by the recursion Eq.5 ,from g_2 of fig.11 and $s(z)$ of fig.12, and the best-fit "calculated" $\text{Log}(p_2(q,m,a))$ (See text).

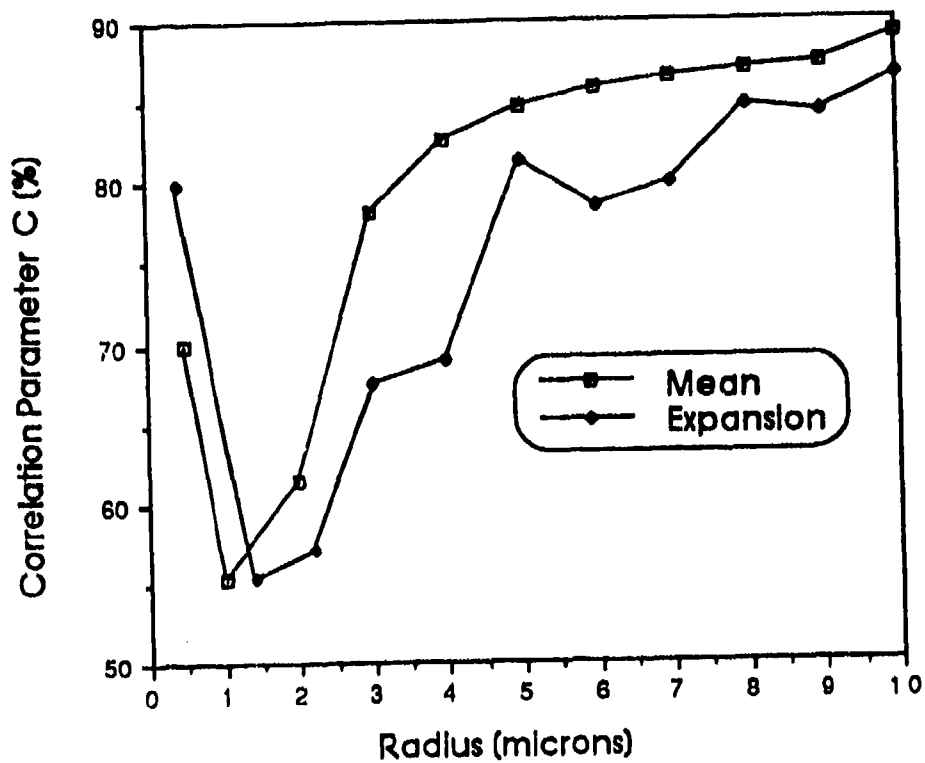


Fig.13a The correlation parameter C as a function of the mean radius m and the expansion parameter a of the Log-normal size distribution function used for $p_2(q, m, a)$ of fig.13.

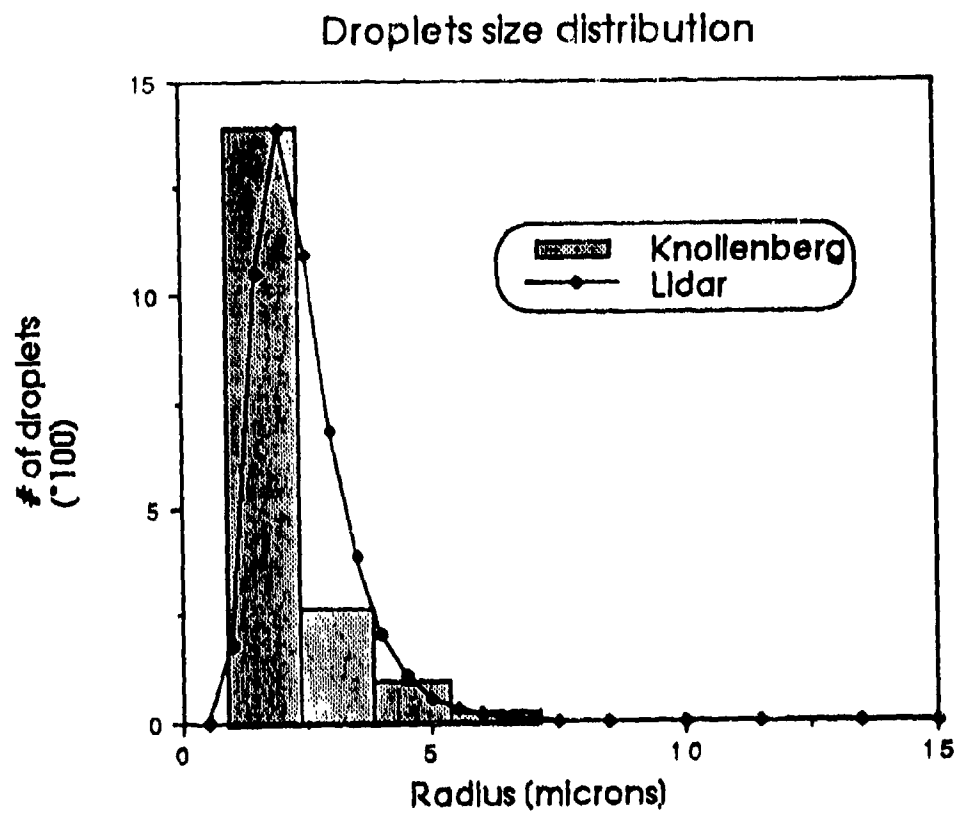


Fig.14 The cloud droplet size distribution measured by Knollenberg droplet counting and SLL measurement (Log-normal with $m=1$ mm and $a=1.1$, see fig.13a) normalize at the peak.

III. NONLINEAR EFFECTS

THE EFFECTS OF PARTICLE NONSPHERICITY ON INTERNAL ELECTROMAGNETIC FIELD DISTRIBUTION

J.P. Barton and D.R. Alexander
Center for Electro-Optics
College of Engineering
University of Nebraska-Lincoln
Lincoln, NE 68588-0656

RECENT PUBLICATIONS, SUBMITTALS FOR PUBLICATION, AND PRESENTATIONS:

- A.) J.P. Barton and D.R. Alexander, "Electromagnetic fields for a beam incident upon a nonspherical particle," Proceedings of the 1990 U.S. Army CRDEC Scientific Conference on Obscuration and Aerosol Research, Aberdeen Proving Ground, Maryland, 1990.
- B.) J.P. Barton and D.R. Alexander, "Electromagnetic fields for an irregularly-shaped, near-spherical particle illuminated by a focused laser beam," Journal of Applied Physics, Vol. 69(12), pp. 7973-7986, 1991.
- C.) J.P. Barton, W. Ma, S.A. Schaub, and D.R. Alexander, "Electromagnetic fields for a beam incident on two adjacent spherical particles," Applied Optics, in press, 1991.
- D.) J.P. Barton and D.R. Alexander, "Electromagnetic field calculations for a tightly focused beam incident upon a microdroplet: Applications to nonlinear optics," SPIE Proceedings, Vol. 1497, in press, 1991.
- E.) J.P. Barton, W. Ma, S.A. Schaub, and D.R. Alexander, "Theoretical determination of the electromagnetic fields for a laser beam incident upon two adjacent spherical particles of arbitrary arrangement," Proceedings of the 2nd International Congress on Optical Particle Sizing, Tempe, Arizona, 1990.
- F.) J.P. Barton, "Theoretical studies of interaction of laser radiation with biological particles," Final Report, Delivery Order 2491, Contract No. DAAL03-86-D-0001, U.S. Army Research Office Scientific Services Program, 1991.
- G.) J.P. Barton and D.R. Alexander, "Recent progress concerning electromagnetic field calculations for a beam incident on an arbitrary particle," presentation at the 1991 U.S. Army CRDEC Scientific Conference on Obscuration and Aerosol Research, June 24-27, 1991, Aberdeen Proving Ground, Maryland.
- H.) J.P. Barton and D.R. Alexander, "Electromagnetic field calculations for a tightly-focused laser beam incident upon a microdroplet: Applications to nonlinear optics," presentation at SPIE's Optical Engineering SouthCentral'91 International Conference on Nonlinear Optics and Materials, May 8-10, 1991, Dallas, Texas.
- I.) S.A. Schaub, D.R. Alexander, and J.P. Barton, "Modeling of the coherent imaging of a spherical aerosol particle illuminated by a plane wave at oblique incidence," submitted to the Journal of the Optical Society of America, 1991.
- J.) G.M. Holtmeier, D.R. Alexander, and J.P. Barton, "High intensity ultraviolet laser interaction with a metallic filament," Journal of Applied Physics, in press, 1991.
- K.) S.A. Schaub, D.R. Alexander, and J.P. Barton, "Theoretical model of the laser imaging of small aerosols: Applications to particle sizing," Applied Optics, in press, 1991.
- L.) D.R. Alexander, J.P. Barton, S.A. Schaub, and G. Holtmeier, "Nonlinear interactions of KrF laser radiation with small water droplets," Applied Optics, in press, 1991.
- M.) D.R. Alexander, S.A. Schaub, and J.P. Barton, "Modeling of a coherent imaging system: application to focus determination in aerosol sizing," Proceedings of the 2nd International Congress on Optical Particle Sizing, Tempe, Arizona, 1990.
- N.) D.R. Alexander, G.M. Holtmeier, K.-D. Song, and J.P. Barton, "Laser interaction with a metallic filament: Ablation dynamics and plasma formation," Proceedings of the 1990 U.S. Army CRDEC Scientific Conference on Obscuration and Aerosol Research, Aberdeen Proving Ground, Maryland, 1990.
- O.) D.R. Alexander, S.A. Schaub, G.M. Holtmeier, and J.P. Barton, "Nonlinear laser interactions with saltwater droplets," SPIE Proceedings, Vol. 1497, in press, 1991.

P.) J. Zhang, D.R. Alexander, and J.P. Barton, "Hybrid inelastic scattering models for particle thermometry: unpolarized emissions," submitted to the Journal of the Optical Society of America, 1991.

Q.) J. Zhang, D.R. Alexander, and J.P. Barton, "Hybrid inelastic scattering models for particle thermometry: polarized emissions," submitted to the Journal of the Optical Society of America, 1991.

R.) D.R. Alexander, J. Zhang, and J.P. Barton, "Hybrid inelastic scattering models for particle thermometry," poster presentation at the 1991 U.S. Army CRDEC Scientific Conference on Obscuration and Aerosol Research, June 24-27, 1991, Aberdeen Proving Ground, Maryland.

S.) D.R. Alexander, S.A. Schaub, G.M. Hoitmeier, and J.P. Barton, "Nonlinear laser interactions with saltwater droplets," presentation at SPIE's Optical Engineering SouthCentral'91 International Conference on Nonlinear Optics and Materials, May 8-10, 1991, Dallas, Texas.

T.) D.E. Poulain, D.R. Alexander, J.P. Barton, S.A. Schaub, and J. Zhang, "Interactions of intense ultraviolet laser radiation with solid aerosols," Journal of Applied Physics, Vol. 67(5), pp. 2283-2288, 1990.

ABSTRACT

Theoretical calculations of the internal particle normalized source function ($S = |\vec{E}|^2$) distribution are presented for plane wave illuminated particles of spherical, prolate spheroidal, and axisymmetric corrugated geometries. For the parameters considered (size parameter = 10.0, complex relative refractive index = $1.33 + 1.0 \times 10^{-8}i$), the calculations indicate that shadow side field enhancement apparently does not require a pure spherical geometry, and can occur in even "nonstandard" geometries, such as the axisymmetric corrugated particle. Future calculations will be performed investigating effects at both higher and lower size parameters, and for additional geometries.

I. INTRODUCTION

In recent years, nonlinear optical effects have been experimentally studied by focusing a laser beam on isolated micron-sized liquid droplets. For weakly absorbing liquids, and for wavelengths of-the-order-of or shorter than the droplet diameter, the curved surfaces of the spherical droplet can result in an internal "focusing" of the incident light so as to create regions of concentrated electromagnetic energy density near the shadow side of the droplet. However, droplets may not always be perfectly spherical because of aerodynamic, elastic, thermal, and/or electromagnetic stresses. In this paper, systematic theoretical calculations are presented investigating the internal electromagnetic field enhancement within **nonspherical** particles.

II. GENERAL THEORY

The electromagnetic field calculations were performed using a recently developed theoretical procedure that permits the determination of the electromagnetic fields for an arbitrary incident field directed upon a homogeneous particle of arbitrarily-defined shape.¹ The theoretical procedure is described in detail in Ref. 1. Only the general assumptions and parameters will be described here.

A particle within an infinite, nonabsorbing, dielectric medium is considered. Both the particle and the surrounding medium are homogeneous, isotropic, and nonmagnetic ($\mu = 1$). A monochromatic field, presumed known, is incident on the particle. The coordinate system origin is located within (and near the center) of the particle. All electromagnetic quantities are nondimensionalized relative to an electric field amplitude characteristic of the incident field (E_0) and all spatial quantities are nondimensionalized relative to a characteristic radius of the particle (a).

Important input parameters for the analysis are as follows: (1) the particle shape function, $\hat{r}(\theta, \phi)$ (A nondimensionalized single-valued function of the spherical coordinate angles that defines the surface of the particle.), (2) the particle size parameter, $\alpha = 2\pi a/\lambda_{ext}$ (λ_{ext} is the wavelength within the surrounding medium.), (3) the complex relative refractive index of the particle, $\bar{n} =$

$\sqrt{\epsilon_{int}/\epsilon_{ext}}$, and (4) the various parameters associated with the character (plane wave, focused beam, propagation direction, etc.) of the incident field.

For the calculations presented here, the incident field is assumed to be a linearly polarized, plane wave. The plane wave propagates parallel to the x-z plane with a propagation direction angle of θ_{bd} relative to the y-z plane. The polarization angle ϕ_{bd} indicates the angle of the direction of the incident electric field polarization relative to the x-z plane. For the calculations presented here, the direction of the incident electric field polarization was kept parallel to the x-z plane ($\phi_{bd} = 0^\circ$) for all cases.

III. SYSTEMATIC CALCULATIONS

In order to investigate the effect of particle geometry on the distribution of the internal electromagnetic field, a set of systematic calculations were performed for a linearly polarized plane wave incident on particles of spherical, prolate spheroidal, and axisymmetric corrugated geometries. A complex relative refractive index of $\bar{n} = 1.33 + 1.0 \times 10^{-8}i$ (approximately that of water in the visible spectrum) and a particle size parameter of $\alpha = 10.0$ were used for all calculations. For the prolate spheroid, a 1.3 to 1.0 axis ratio was chosen,

$$\hat{r}_{ps}(\theta) = 1/\sqrt{(1.3\sin\theta)^2 + (\cos\theta)^2}. \quad (1)$$

The axisymmetric corrugated particle, with corresponding particle shape function,

$$\hat{r}_{ac}(\theta) = 0.92 + 0.08\cos(7\theta), \quad (2)$$

was selected as an example of a "nonstandard" geometry. For the prolate spheroidal and axisymmetric corrugated particles, calculations were performed for incident propagation angles of $\theta_{bd} = 0^\circ, 30^\circ, 45^\circ, 60^\circ$, and 90° .

The results are shown in Figs. 1-11. The plots provide the normalized source function ($S = |\vec{E}|^2$) distribution in the x-z plane. Only the internal particle normalized source function is plotted (the near-field values of S were artificially set to zero) so as to clearly distinguish the particle boundaries. Figure 1 gives the normalized source function distribution for the reference case of a plane wave ($\theta_{bd} = 0^\circ$, incident propagation in the +z axis direction) incident on a spherical particle. The familiar electromagnetic field enhancement near the shadow side of the spherical particle is clearly shown in Fig. 1. From Fig. 1, the peak value of the normalized source function for the spherical particle is approximately 20.

Figures 2-6 show the internal normalized source function distributions for a prolate spheroid with incident propagation angles of $\theta_{bd} = 0^\circ, 30^\circ, 45^\circ, 60^\circ$, and 90° , respectively. Figure 2 is for on-symmetry axis incidence ($\theta_{bd} = 0^\circ$). In comparison with the spherical particle case, the smaller radius of curvature front and back surfaces of the prolate spheroidal particle creates shadow side field enhancement ($S_{max} \approx 30$) greater than that of the spherical particle. As the angle of incidence is increased to $30^\circ, 45^\circ, 60^\circ$, and finally, 90° (Figs. 3-6), the shadow side field enhancement remains, but diminishes with increasing angle. At $\theta_{bd} = 90^\circ$ (Fig. 6) the peak value of the normalized source function is approximately 10.

The results for the axisymmetric corrugated particle are shown in Figs. 7-11. For on-symmetry axis incidence ($\theta_{bd} = 0^\circ$), as shown in Fig. 7, there is again strong field enhancement, greater than that of the spherical particle, and similar to that of the prolate spheroidal particle. As the angle of incidence is increased to $30^\circ, 45^\circ, 60^\circ$, and finally, 90° (Figs. 8-11) the shadow side field enhancement remains but is less diminished and shows an irregular angle of incidence dependence in comparison with the prolate spheroid.

IV. CONCLUSIONS AND FUTURE WORK

For the choice of parameters considered ($\alpha = 10.0$, $\bar{n} = 1.33 + 1.0 \times 10^{-8}i$), shadow side field enhancement within a particle apparently does not require a pure spherical geometry, and can occur in even "nonstandard" geometry particles such as the axisymmetric corrugated particle. Further calculations will be performed investigating effects at both higher and lower size parameters. Other particle geometries will also be considered.

ACKNOWLEDGEMENTS

Certain aspects of this work were performed during the summer of 1991 while Dr. Barton was at CRDEC supported under the auspices of the U.S. Army Research Office Scientific Services Program administrated by Battelle (Delivery Order 2491, Contract No. DAAL03-86-D-0001). Dr. Barton expresses his appreciation to his point-of-contact at CRDEC, Dr. S. Randolph Long, and to Dr. Orazio Sindoni for his assistance in the use of the computing and graphing facilities at CRDEC.

REFERENCES

1. J.P. Barton and D.R. Alexander, "Electromagnetic fields for an irregularly-shaped, near-spherical particle illuminated by a focused laser beam," *Journal of Applied Physics*, Vol. 69(12), pp. 7973-7986, 1991.

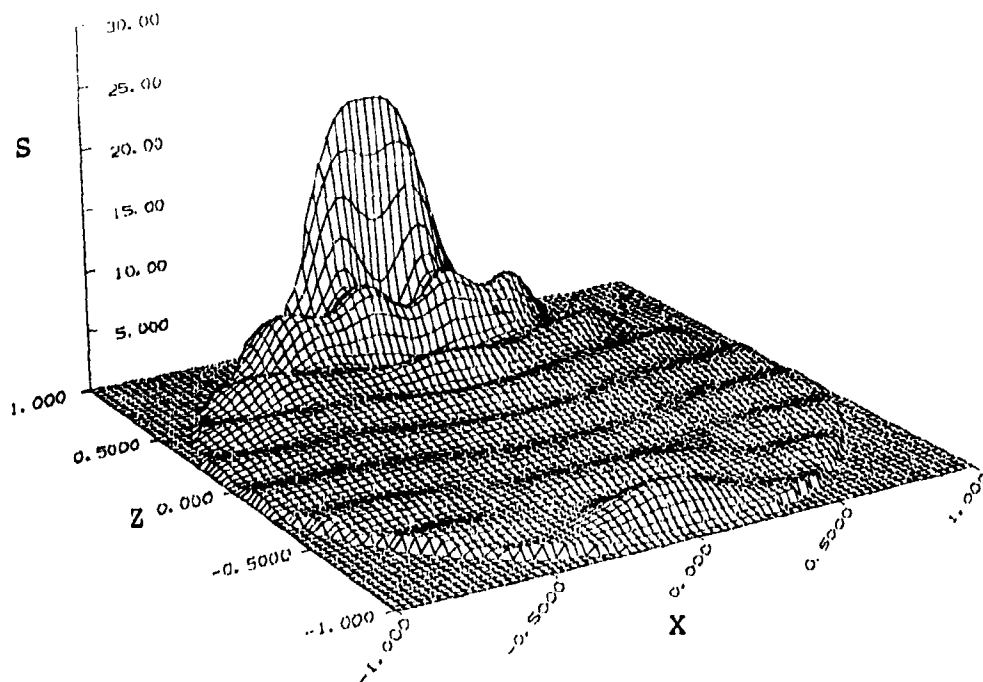


FIG. 1. Internal normalized source function distribution in the x-z plane for a plane wave (0° angle of incidence) incident on a sphere.
 $\bar{n} = 1.33 + 1.0 \times 10^{-8}i$, $\alpha = 10.0$, $\theta_{bd} = 0^\circ$, $\phi_{bd} = 0^\circ$.

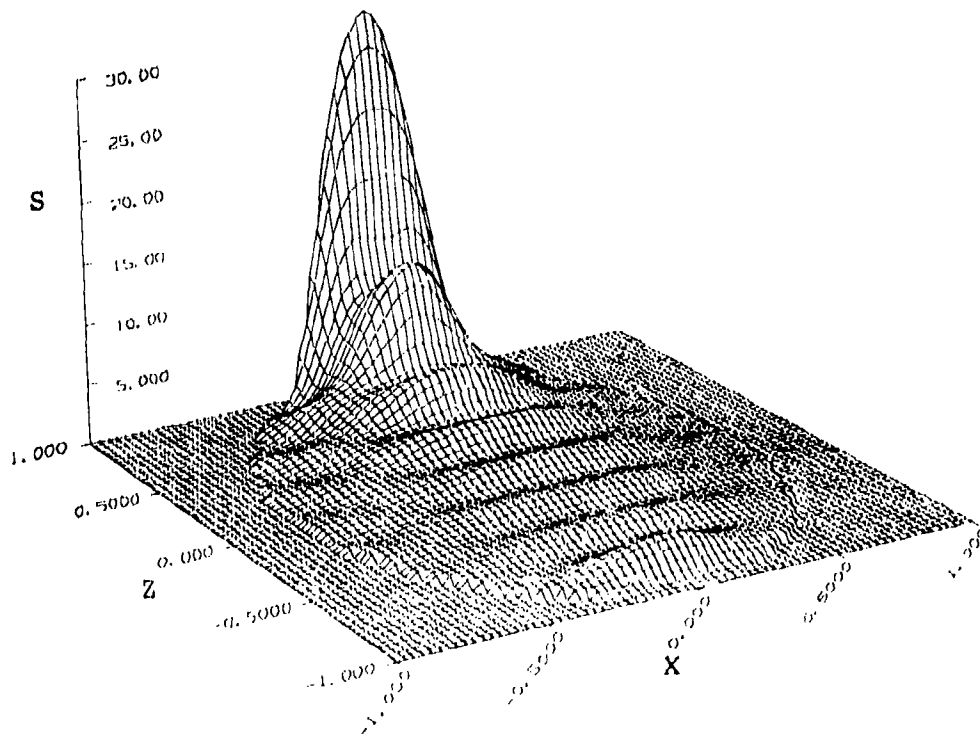


FIG. 2. Internal normalized source function distribution in the x-z plane for a plane wave (0° angle of incidence) incident on a 1.3 to 1.0 axis ratio prolate spheroid.
 $\bar{n} = 1.33 + 1.0 \times 10^{-8}i$, $\alpha = 10.0$, $\theta_{bd} = 0^\circ$, $\phi_{bd} = 0^\circ$.

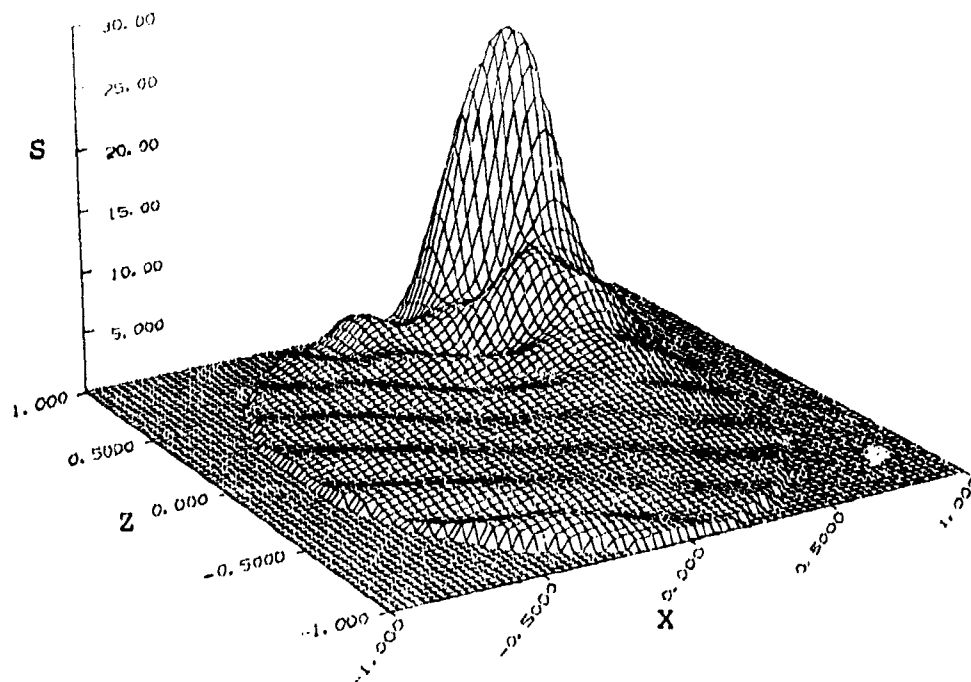


FIG. 3. Internal normalized source function distribution in the x-z plane for a plane wave (30° angle of incidence) incident on a 1.3 to 1.0 axis ratio prolate spheroid. $\bar{n} = 1.33 + 1.0 \times 10^{-8}i$, $\alpha = 10.0$, $\theta_{bd} = 30^\circ$, $\phi_{bd} = 0^\circ$.

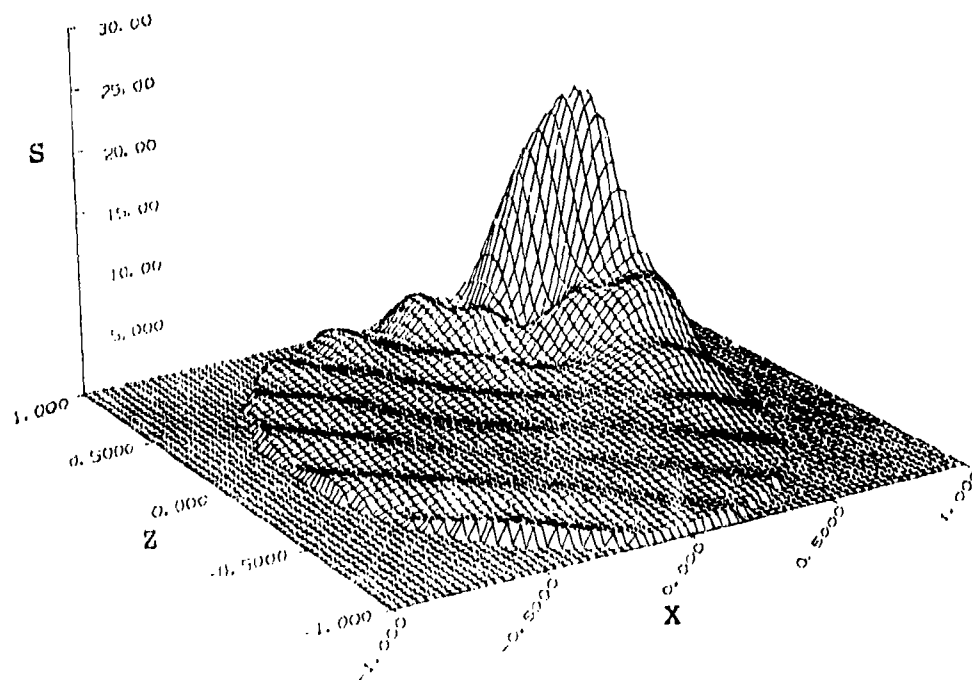


FIG. 4. Internal normalized source function distribution in the x-z plane for a plane wave (45° angle of incidence) incident on a 1.3 to 1.0 axis ratio prolate spheroid. $\bar{n} = 1.33 + 1.0 \times 10^{-8}i$, $\alpha = 10.0$, $\theta_{bd} = 45^\circ$, $\phi_{bd} = 0^\circ$.

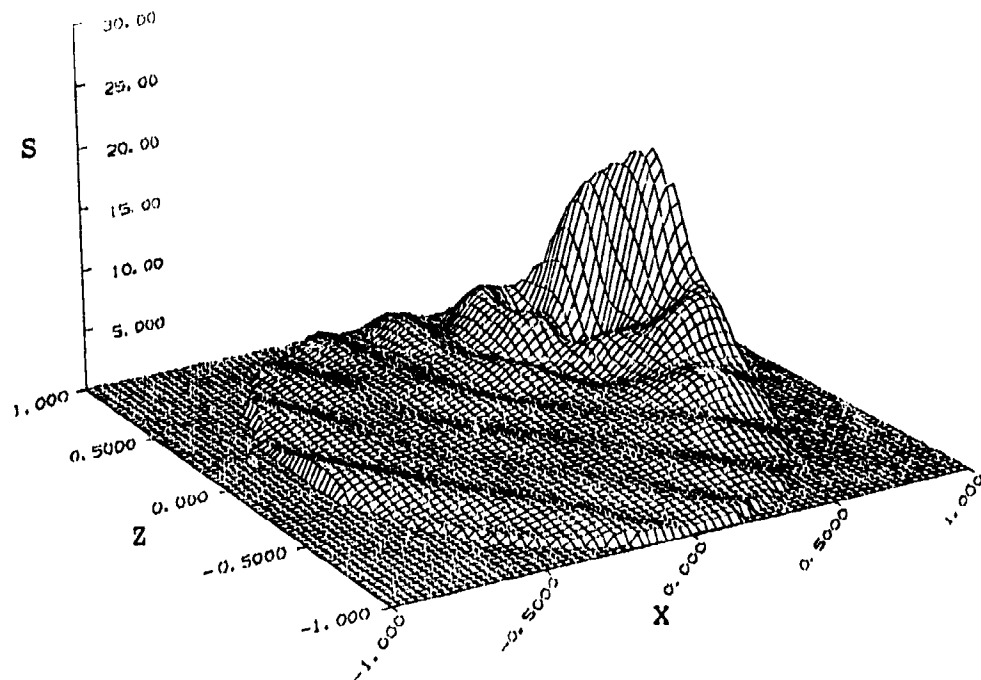


FIG. 5. Internal normalized source function distribution in the x-z plane for a plane wave (60° angle of incidence) incident on a 1.3 to 1.0 axis ratio prolate spheroid. $\bar{n} = 1.33 + 1.0 \times 10^{-8}i$, $\alpha = 10.0$, $\theta_{bd} = 60^\circ$, $\phi_{bd} = 0^\circ$.

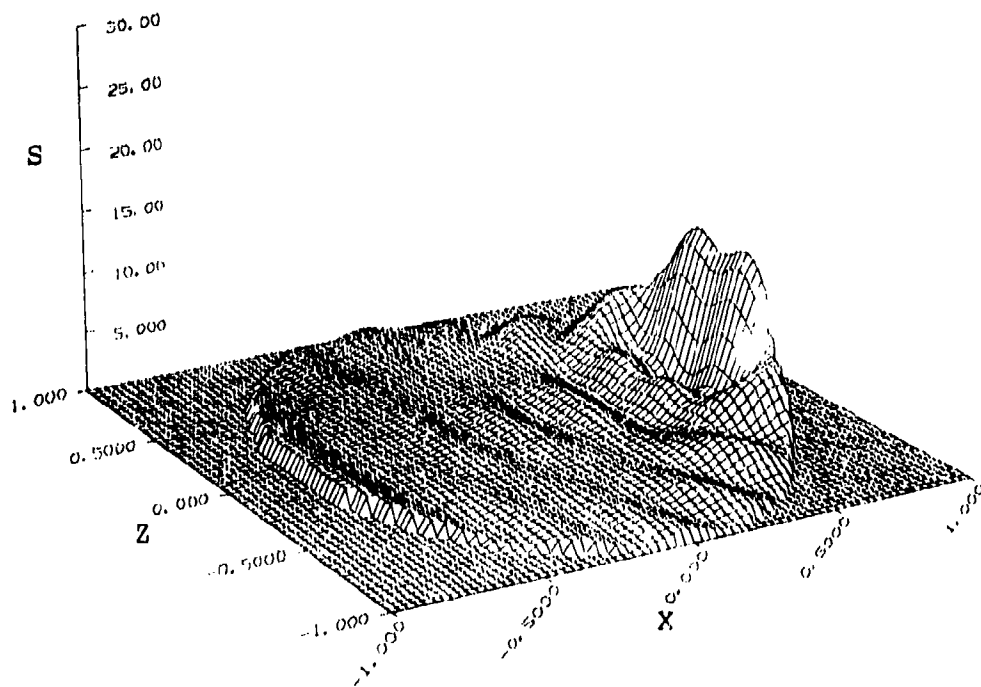


FIG. 6. Internal normalized source function distribution in the x-z plane for a plane wave (90° angle of incidence) incident on a 1.3 to 1.0 axis ratio prolate spheroid. $\bar{n} = 1.33 + 1.0 \times 10^{-8}i$, $\alpha = 10.0$, $\theta_{bd} = 90^\circ$, $\phi_{bd} = 0^\circ$.

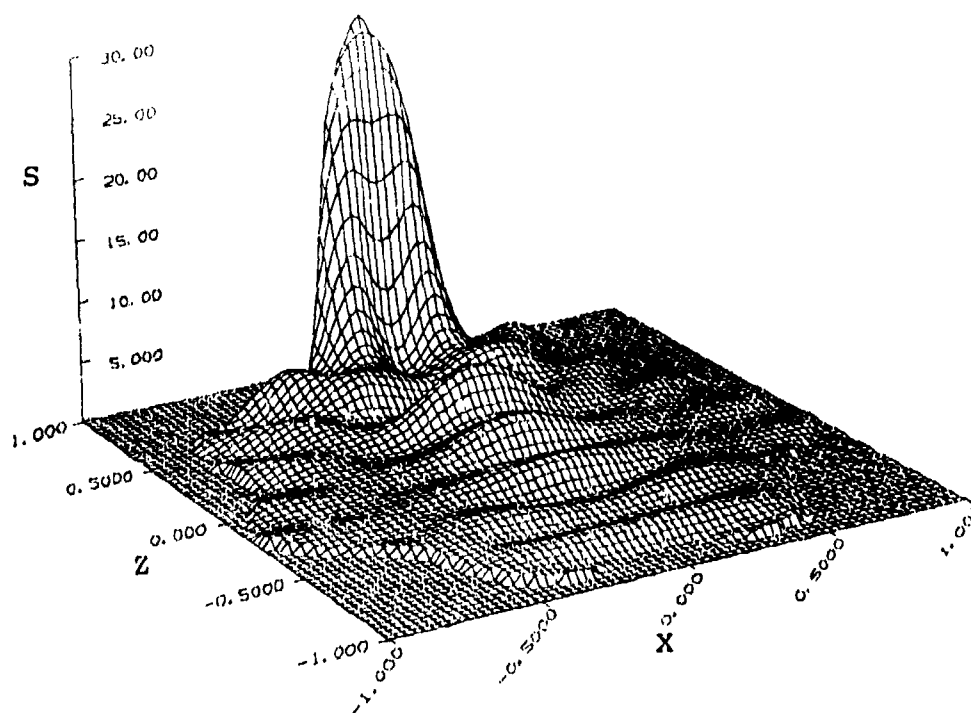


FIG. 7. Internal normalized source function distribution in the x-z plane for a plane wave (0° angle of incidence) incident on an axisymmetric corrugated [$\hat{r}(\theta) = 0.92 + 0.08\cos(7\theta)$] particle. $\bar{n} = 1.33 + 1.0 \times 10^{-8}i$, $\alpha = 10.0$, $\theta_{bd} = 0^\circ$, $\phi_{bd} = 0^\circ$.

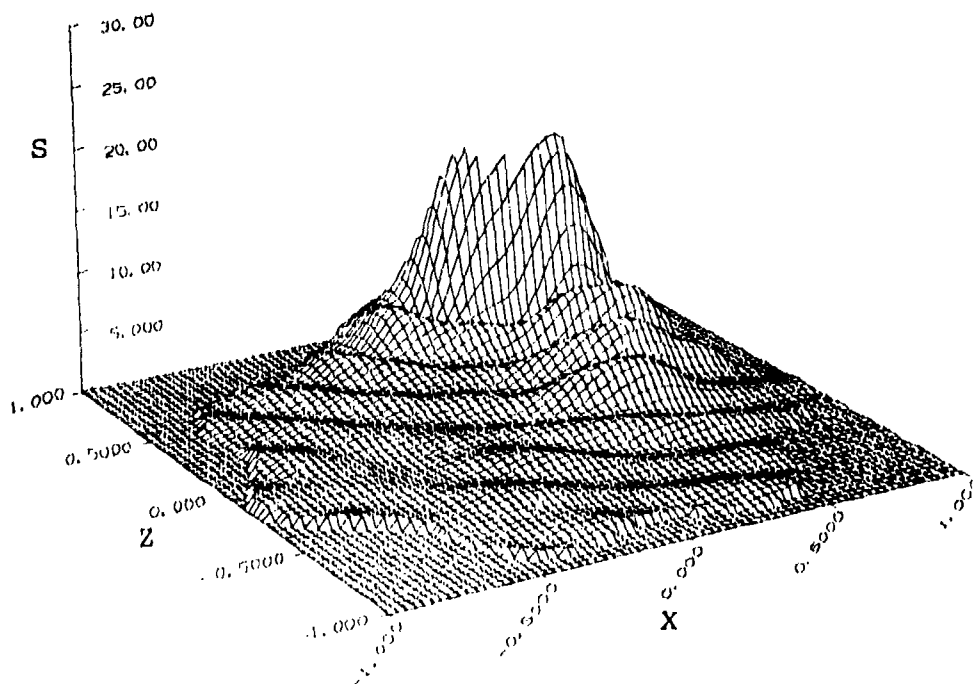


FIG. 8. Internal normalized source function distribution in the x-z plane for a plane wave (30° angle of incidence) incident on an axisymmetric corrugated [$\hat{r}(\theta) = 0.92 + 0.08\cos(7\theta)$] particle. $\bar{n} = 1.33 + 1.0 \times 10^{-8}i$, $\alpha = 10.0$, $\theta_{bd} = 30^\circ$, $\phi_{bd} = 0^\circ$.

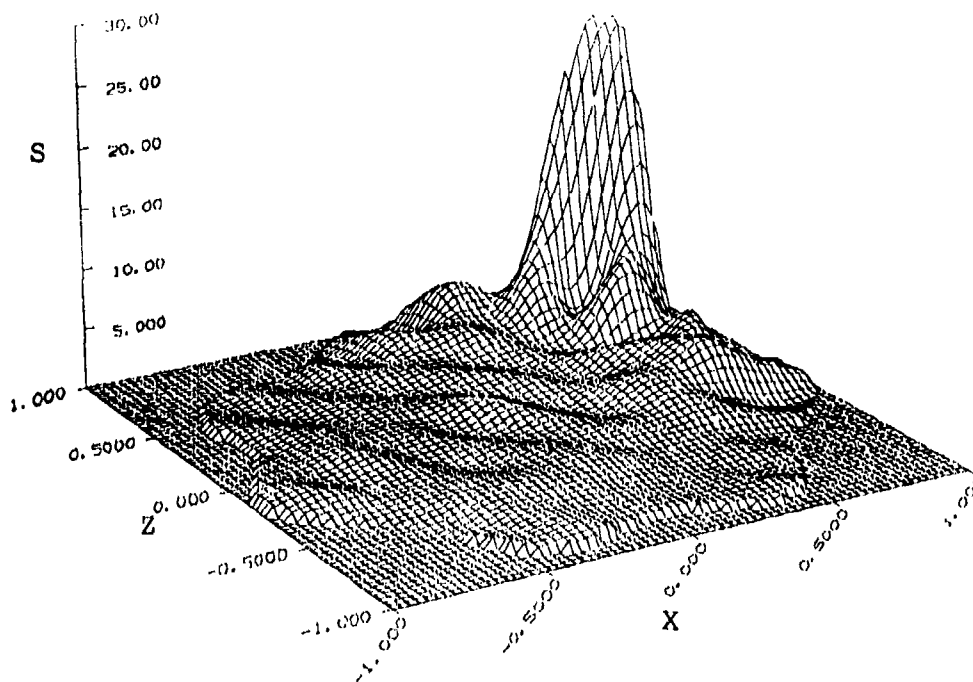


FIG. 9. Internal normalized source function distribution in the x-z plane for a plane wave (45° angle of incidence) incident on an axisymmetric corrugated [$\hat{r}(\theta) = 0.92 + 0.08\cos(7\theta)$] particle. $\bar{n} = 1.33 + 1.0 \times 10^{-8}i$, $\alpha = 10.0$, $\theta_{bd} = 45^\circ$, $\phi_{bd} = 0^\circ$.

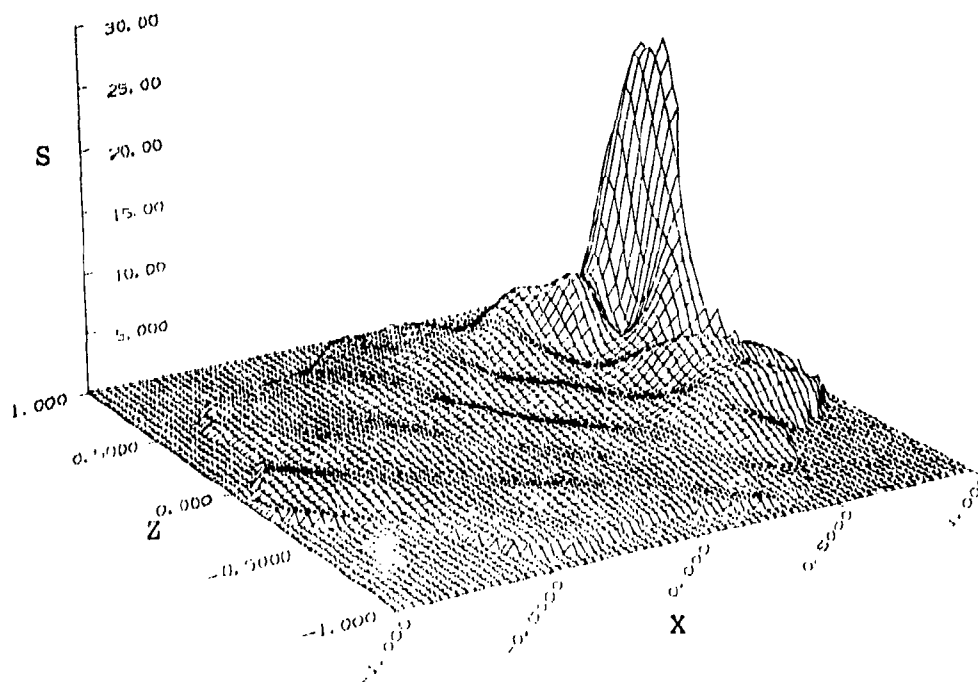


FIG. 10. Internal normalized source function distribution in the x-z plane for a plane wave (60° angle of incidence) incident on an axisymmetric corrugated [$\hat{r}(\theta) = 0.92 + 0.08\cos(7\theta)$] particle. $\bar{n} = 1.33 + 1.0 \times 10^{-8}i$, $\alpha = 10.0$, $\theta_{bd} = 60^\circ$, $\phi_{bd} = 0^\circ$.

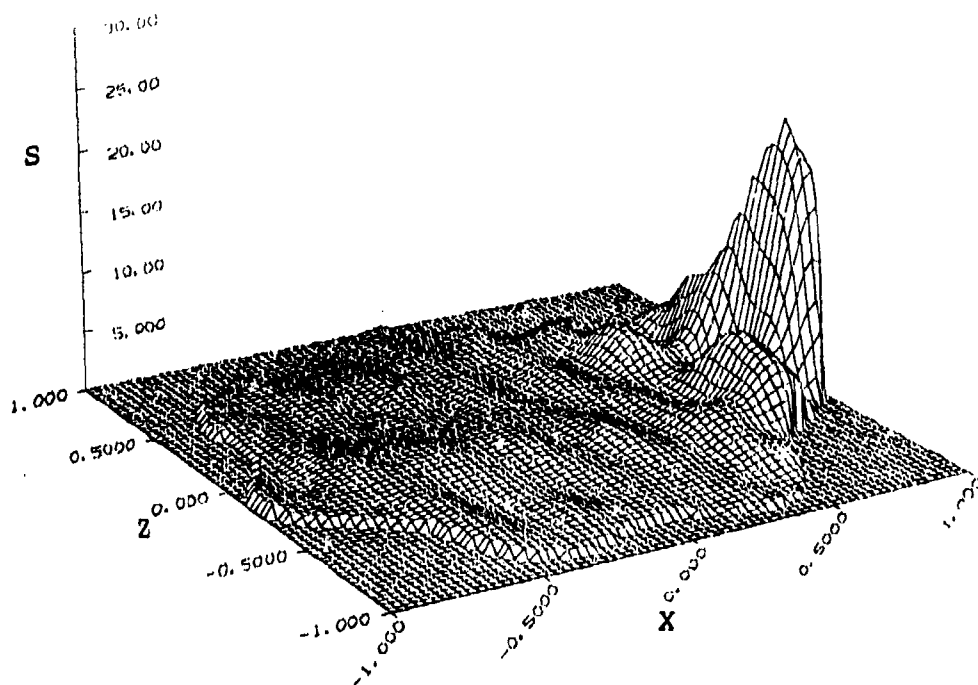


FIG. 11. Internal normalized source function distribution in the x-z plane for a plane wave (90° angle of incidence) incident on an axisymmetric corrugated [$\hat{r}(\theta) = 0.92 + 0.08\cos(7\theta)$] particle. $\bar{n} = 1.33 + 1.0 \times 10^{-8}i$, $\alpha = 10.0$, $\theta_{bd} = 90^\circ$, $\phi_{bd} = 0^\circ$.

BRIDGING THE GAP BETWEEN THE RAYLEIGH AND THOMSON
LIMITS FOR VARIOUS CONVEX BODIES

by

G.R. Fournier and B.T.N. Evans
Defense Research Establishment Valcartier
Courcelette, Quebec G0A 1R0 Canada

RECENT/SUBMITTED PUBLICATIONS

- A) B.T.N. Evans and G.R. Fournier, "Simple Approximation to Extinction Efficiency Valid Over All Size Parameters", *Applied Optics*, 29, 4666-4670 (1990).
- B) G.R. Fournier and B.T.N. Evans, "An Approximation to Extinction Efficiency for Randomly Oriented Spheroids", *Applied Optics*, 30, 2042-2048 (1991)
- C) B.T.N. Evans and G.R. Fournier, "A Procedure for Obtaining An Algebraic Approximation to Certain Integrals", DREV R-4653/91

ABSTRACT

It is well known that the Rayleigh approximation to extinction, scattering and absorption efficiencies for spheres is limited to small size parameters, x , and small values of $|m|x$, where m is the complex index of refraction. It is also known that the Thomson approximation to these same efficiencies is valid for small x and $m = \infty$. We have found a powerful exact transform of the Mie coefficients, for both spheres and infinite cylinders, that removes the m related restrictions of the Rayleigh and Thomson approximations. The resulting approximate series for spheres and infinite cylinders are valid for all m and small x .

If this transform of the Mie coefficients and their series expansion were limited to spheres and infinite cylinders, it would have only limited interest. However, this transform generalizes, in an approximate form, to other convex bodies when a Rayleigh or Thomson-like series can be obtained. These can sometimes be obtained by a method given by Stevenson (1953). Series are available in the latter paper for ellipsoids (which includes spheroids). We will present results of a comparison between the newly obtained series and the exact codes for spheres and spheroids.

1. INTRODUCTION

If a particle is geometrically and optically small enough, then a simple formula can usually be found for the extinction and scattering efficiencies as well as the phase function. Such approximate formulae are usually called the Rayleigh approximation to the scattering¹. If the particle is still geometrically small but optically very large, the Thom-

son approximation results².

Often, however, a small particle may be neither optically small nor very large. This creates a gap that has not been completely filled until now.

In this paper we demonstrate a powerful transform that bridges this gap for spheres and infinite cylinders and, in an approximate way for spheroids.

2. THEORY

2.1 Spheres

We will first derive the general expansion of the Mie coefficients for small size parameters x , and show how the Rayleigh and Thomson expressions result.

Starting with the definition³ of Q_{sca} and Q_{ext} , the scattering and extinction efficiencies respectively, we have

$$Q_{sca} = \frac{2}{x^2} \sum_{n=1}^{\infty} (2n+1) \{|a_n|^2 + |b_n|^2\} \quad [1]$$

and

$$Q_{ext} = \frac{2}{x^2} \sum_{n=1}^{\infty} (2n+1) \{\text{Re}(a_n + b_n)\} \quad [2]$$

where a_n and b_n are the external field Mie coefficients. These Mie coefficients are given by

$$a_n = \frac{\sqrt{\mu} \psi'_n(\sqrt{\epsilon\mu}x) \psi_n(x) - \sqrt{\epsilon} \psi_n(\sqrt{\epsilon\mu}x) \psi'_n(x)}{\sqrt{\mu} \psi'_n(\sqrt{\epsilon\mu}x) \zeta_n(x) - \sqrt{\epsilon} \psi_n(\sqrt{\epsilon\mu}x) \zeta'_n(x)} \quad [3]$$

and

$$b_n = \frac{\sqrt{\epsilon} \psi'_n(\sqrt{\epsilon\mu}x) \psi_n(x) - \sqrt{\mu} \psi_n(\sqrt{\epsilon\mu}x) \psi'_n(x)}{\sqrt{\epsilon} \psi'_n(\sqrt{\epsilon\mu}x) \zeta_n(x) - \sqrt{\mu} \psi_n(\sqrt{\epsilon\mu}x) \zeta'_n(x)} \quad [4]$$

where ϵ and μ are the relative dielectric constant and the relative magnetic permeability, ψ_n is the Riccati-Bessel function of the first kind and ζ_n is the Riccati-Bessel function of the third kind. Note that the b_n coefficients are symmetrical with the a_n coefficients upon substitution of ϵ for μ and vice versa. Hence, we need only discuss a_n in detail.

Expanding a_1 and a_2 in small x we obtain

$$a_1 = \frac{2}{3}i \left(\frac{\epsilon-1}{\epsilon+2} \right) x^3 + \frac{1}{5}i \left(\frac{\epsilon^2 - 6\epsilon + 4 + \epsilon^2\mu}{(\epsilon+2)^2} \right) x^5 + \frac{4}{9} \left(\frac{\epsilon-1}{\epsilon+2} \right)^2 x^6 \\ + \frac{1}{175}i \left(\frac{\epsilon^4\mu^2 + \epsilon^3(9\mu^2 + 35\mu - 25) - \epsilon^2(70\mu + 150) + 200(2\epsilon - 1)}{(\epsilon+2)^3} \right) x^7 + \dots \quad [5]$$

$$a_2 = \frac{1}{15}i \left(\frac{\epsilon-1}{2\epsilon+3} \right) x^5 + \dots \quad [6]$$

$$b_n = a_n, \epsilon \leftrightarrow \mu$$

Expansions for higher order coefficients can also be derived. For classic Rayleigh ($\mu = 1$, $m^2 = \epsilon\mu$),

$$a_1 = \frac{2}{3}i \left(\frac{m^2 - 1}{m^2 + 2} \right) x^3 + \frac{2}{5}i \left(\frac{(m^2 - 1)(m^2 - 2)}{(m^2 + 2)^2} \right) x^5 + \frac{4}{9} \left(\frac{m^2 - 1}{m^2 + 2} \right)^2 x^6 + \frac{1}{175}i \left(\frac{(m^2 - 1)(m^6 + 20m^4 - 200m^2 + 200)}{(m^2 + 2)^3} \right) x^7 + \dots \quad [7]$$

$$b_1 = \frac{1}{45}i(m^2 - 1)x^5 + \dots \quad [8]$$

for Thompson ($\epsilon \rightarrow \infty$, $\mu = 0$),

$$a_1 = \frac{2}{3}ix^3 + \frac{1}{5}ix^5 + \frac{4}{9}x^6 - \frac{1}{7}ix^7 + \dots \quad [9]$$

$$b_1 = -\frac{1}{3}ix^3 + \frac{1}{5}ix^5 + \dots \quad [10]$$

It is immediately apparent that as $m \rightarrow \infty$ the Rayleigh expansion for either a_1 or b_1 does not converge even for small values of x . Hence, the requirement for small optical size $|mx|$. The Thomson expansion having no index dependency applies only to infinite optical size. The problem with the Rayleigh series mathematically arises from the terms in a_n with $\epsilon^2\mu$ and in b_n with $\mu^2\epsilon$. If these terms were set to zero, the divergence problem would disappear. We must, however, recover the lost information without reintroducing the divergence problem.

To do this rewrite a_n to isolate the material properties as

$$a_n = \frac{\psi_n(x) - \left\{ \frac{\sqrt{\epsilon} \psi_n(\sqrt{\epsilon\mu} x)}{\sqrt{\mu} \psi'_n(\sqrt{\epsilon\mu} x)} \right\} \psi'_n(x)}{\zeta_n(x) - \left\{ \frac{\sqrt{\epsilon} \psi_n(\sqrt{\epsilon\mu} x)}{\sqrt{\mu} \psi'_n(\sqrt{\epsilon\mu} x)} \right\} \zeta'_n(x)} \quad [11]$$

Consider the result of letting $\mu \rightarrow 0$ in the expression above (which will make all the $\epsilon^2\mu$ terms zero along with others):

$$\lim_{\mu \rightarrow 0} a_n = \frac{\psi_n(x) - \left\{ \frac{\epsilon x}{n+1} \right\} \psi'_n(x)}{\zeta_n(x) - \left\{ \frac{\epsilon x}{n+1} \right\} \zeta'_n(x)} \quad [12]$$

To recover the full Mie coefficients, transform ϵ in the above limit by

$$\epsilon \rightarrow \frac{\sqrt{\epsilon} (n+1)}{\sqrt{\mu}} \frac{\psi_n(\sqrt{\epsilon\mu} x)}{x \psi'_n(\sqrt{\epsilon\mu} x)} = \mathcal{E}_n \quad [13]$$

and by symmetry

$$\mu \rightarrow \frac{\sqrt{\mu}}{\sqrt{\epsilon}} \frac{(n+1)}{x} \frac{\psi_n(\sqrt{\epsilon\mu}x)}{\psi'_n(\sqrt{\epsilon\mu}x)} = \mathcal{U}_n \quad [14]$$

Both \mathcal{E}_n and \mathcal{U}_n can be considered as transformed material properties. Putting these new variables back into [12] and expanding again in small x we obtain

$$a_1 = \frac{2}{3}i \left(\frac{\mathcal{E}_1 - 1}{\mathcal{E}_1 + 2} \right) x^3 + \frac{1}{5}i \left(\frac{\mathcal{E}_1^2 - 6\mathcal{E}_1 + 4}{(\mathcal{E}_1 + 2)^2} \right) x^5 + \frac{4}{9} \left(\frac{\mathcal{E}_1 - 1}{\mathcal{E}_1 + 2} \right)^2 x^6 \\ - \frac{1}{7}i \left(\frac{\mathcal{E}_1^3 + 6\mathcal{E}_1^2 - 16\mathcal{E}_1 + 8}{(\mathcal{E}_1 + 2)^3} \right) x^7 + \dots \quad [15]$$

$$a_2 = \frac{1}{15}i \left(\frac{\mathcal{E}_2 - 1}{2\mathcal{E}_2 + 3} \right) x^5 + \dots \quad [16]$$

and again by symmetry

$$b_n = a_n, \mathcal{E}_n \leftrightarrow \mathcal{U}_n$$

Note singularities occur if and only if

$$\mathcal{E}_n = -(n+1)/n \quad [17]$$

and

$$\mathcal{U}_n = -(n+1)/n. \quad [18]$$

which requires a real ϵ (or real μ). For all other values of \mathcal{E} and \mathcal{U} the coefficients of series [15] and [16] are finite to all orders of x . Thus [15] and [16] are valid for all non-real values of the refractive index. However, when the conditions [17] and [18] are nearly satisfied many terms in [15] and [16] will be required before the series converges to a given accuracy. For convenience in computations we can rewrite \mathcal{E}_n as

$$\mathcal{E}_1(z) = -\frac{2\epsilon F}{(1+F)}, \mathcal{E}_2(z) = -\frac{3\epsilon(1+3F)}{2+6F-Fz^2}, \dots \quad [19]$$

with

$$F(z) = \frac{z \cot(z) - 1}{z^2}, \text{ and } z = \sqrt{\epsilon\mu}x = (n - ik)x \quad [20]$$

and

$$\mathcal{U}_n = \mathcal{E}_n, \epsilon \leftrightarrow \mu$$

Since the 'Mie' coefficients for the normal incidence infinite cylinder³ are identical to the sphere Mie coefficients apart from the order of the Bessel functions involved, the same procedure can be used to obtain a series for small particles independent of material properties. Oblique incidence can also be done but generates much more complicated expressions.

2.2 Spheroids

The above series [15] etc. by itself is interesting only from the classic nature of the Rayleigh and Thomson series. However, the idea of transforming a Rayleigh like series, (with the optical size constraint) into a series that is independent of the material properties for many types of regular particle shapes would be of practical use. We show here that this can be achieved, in some approximation, with oriented and randomly oriented prolate spheroids.

The Rayleigh approximation (with arbitrary μ) for oriented spheroids^{4,5}, Q_{ray} , is given by

$$Q_{ray} = Q_{sca} + Q_{abs} \quad [21]$$

where

$$Q_{sca} = \frac{8}{3} \frac{b^4 r^2}{p} \left\{ \frac{\sin^2 \theta}{2} (|\eta_1|^2 + |\eta'_1|^2) + \frac{(1 + \cos^2 \theta)}{2} (|\eta_2|^2 + |\eta'_2|^2) \right\} \quad [22]$$

$$Q_{abs} = 4 \frac{br}{p} \operatorname{Re} \left\{ i \left[\frac{\sin^2 \theta}{2} (\eta_1 + \eta'_1) + \frac{(1 + \cos^2 \theta)}{2} (\eta_2 + \eta'_2) \right] \right\} \quad [23]$$

and where

$$p = \sqrt{\cos^2 \theta + r^2 \sin^2 \theta}, \quad a = 2\pi\alpha/\lambda, \quad b = 2\pi\beta/\lambda. \quad [24]$$

Here $r = a/b$ is the aspect ratio (for prolates $r > 1$ and for oblates $r < 1$), α is the length of the semi-axis of rotation, β is the other axis of the spheroid, θ is the angle between the incident radiation and the α or a axis, λ is the wavelength of the scattered radiation. Furthermore

$$\eta_1 = \frac{1}{3(L_1 + \frac{1}{\epsilon-1})} \quad \text{and} \quad \eta'_1 = \frac{1}{3(L_1 + \frac{1}{\mu-1})} \quad [25]$$

$$\eta_2 = \frac{1}{3(L_2 + \frac{1}{\epsilon-1})} \quad \text{and} \quad \eta'_2 = \frac{1}{3(L_2 + \frac{1}{\mu-1})} \quad [26]$$

and the form factors are defined for prolates (i.e. $r > 1$) as

$$L_1 = \frac{(1 - g^2)}{g^2} \left\{ -1 + \frac{1}{2g} \ln \left(\frac{1+g}{1-g} \right) \right\} \quad [27]$$

$$L_2 = \frac{1 - L_1}{2} \quad [28]$$

$$g^2 = 1 - \frac{1}{r^2}. \quad [29]$$

For oblates (i.e. $r < 1$) we have

$$L_1 = \frac{1 + f^2}{f^2} \left\{ 1 - \frac{\tan^{-1} f}{f} \right\} \quad [30]$$

$$L_2 = \frac{1 - L_1}{2} \quad [31]$$

$$f^2 = \frac{1}{r^2} - 1. \quad [32]$$

Normally, $\mu = 1$ in the above and hence η'_1 and η'_2 are both zero. The procedure, as demonstrated for spheres, requires the full expression for the efficiencies, therefore we retain the μ terms.

Since the scattered wave at large distances from finite convex bodies can be approximated by a series of Riccati-Bessel functions, we will use the same material transforms, [13] and [14], but with the arguments modified. The modification is simply an approximation to the effective optical size of an equivalent sphere. For a given orientation this equivalent optical radius, z , is

$$z = \sqrt{\epsilon\mu} \frac{rb}{p} \quad [33]$$

which is the same expression used in the eikonal approximation⁵.

For randomly oriented spheroids the cross sections C_{sca} and C_{abs} must be integrated over all angles. C_{sca} is just [22] multiplied by πb^2 and similarly for C_{abs} from [23]. The efficiencies are then obtained, in the usual way, by normalizing the cross sections by the average projected area. Before applying the material transform, the integration is simple since η_1 , η'_1 , η_2 and η'_2 are independent of the orientation angle. However, after the transform they become dependent which greatly complicates the integrals. Hence to maintain a simple expression we will assume, at first, they are independent of angle and correct, in an approximate fashion, later. This correction will be in terms of the spherical average of the effective optical size, z . Integrating C_{sca} and C_{abs} over $\sin(\theta) d\theta$ from 0 to $\pi/2$ and then normalizing we get

$$\overline{Q}_{sca} = \frac{16}{9} \frac{b^4 r^2}{\overline{A}} \{ |\tilde{\eta}_1|^2 + |\tilde{\eta}'_1|^2 + 2(|\tilde{\eta}_2|^2 + |\tilde{\eta}'_2|^2) \} \quad [34]$$

and

$$\overline{Q}_{abs} = \frac{8}{3} \frac{br}{\overline{A}} \text{Re} \{ i[\tilde{\eta}_1 + \tilde{\eta}'_1 + 2(\tilde{\eta}_2 + \tilde{\eta}'_2)] \} \quad [35]$$

where the normalization factor is, for prolates,

$$\overline{A} = 1 + \frac{r^2}{\sqrt{r^2 - 1}} \sin^{-1} \left(\frac{\sqrt{r^2 - 1}}{r} \right) \quad [36]$$

and for oblates,

$$\overline{A} = 1 + \frac{r^2}{\sqrt{1 - r^2}} \ln \left(\frac{1 + \sqrt{1 - r^2}}{r} \right) \quad [37]$$

and

$$\tilde{\eta}_1 = \frac{1}{3(L_1 + \frac{1}{\epsilon_1 - 1})}, \quad \tilde{\eta}'_1 = \frac{1}{3(L_1 + \frac{1}{\mu_1 - 1})} \quad [38]$$

$$\tilde{\eta}_2 = \frac{1}{3(L_2 + \frac{1}{\epsilon_1 - 1})}, \quad \tilde{\eta}'_2 = \frac{1}{3(L_2 + \frac{1}{\mu_1 - 1})}. \quad [39]$$

Note that in the expressions for \mathcal{E}_1 and \mathcal{U}_1 , [13] and [14], $\sqrt{\epsilon\mu}x$ must be replaced by \bar{z} which follows.

The spherical average of z is

$$\begin{aligned}\bar{z} &= \sqrt{\epsilon\mu} r b \int_0^{\pi/2} \frac{\sin(\theta)}{p} d\theta \\ &= \sqrt{\epsilon\mu} b \frac{\sin^{-1}(g)}{g} \quad \text{for prolates, and} \\ &= \sqrt{\epsilon\mu} b \frac{\ln(f + \sqrt{1+f^2})}{f} \quad \text{for oblates.}\end{aligned}\tag{40}$$

It is found, empirically, that the two latter expressions are good only for very small b and that as $b \rightarrow 1$, $\bar{z} \rightarrow \sqrt{\epsilon\mu}b$. This is to be expected since the equivalent optical radius varies with orientation angle and size in a non-linear way. Again, empirically (for prolates only), a simple solution to this problem is to impose a power, as a function of b on the expression in [40]. The situation for oblates is still under study. From this we finally obtain (for $b < 1$),

$$\bar{z} = \sqrt{\epsilon\mu} b \left[\frac{\sin^{-1}(g)}{g} \right]^{1-b^2} \quad \text{for prolates}\tag{41}$$

3. RESULTS OF COMPARISON

In this section we will demonstrate the accuracy and utility of the expressions and ideas in the last section. First, we will discuss the comparison of the Rayleigh [7], Thomson [9] and our new series [15] with the exact Mie solution.

Figure 1 shows the Mie calculation normalized by the three series as a function of size parameter. The series for Q_{sca} are calculated to fourth order in x and for a refractive index of $500 - 500i$ which corresponds to metals in the millimeter wave region. When $|mx|$ is small both the Rayleigh and the new series are excellent approximations. As expected the Thomson series overestimates Q_{sca} by 25%. The situation reverses when $|mx|$ is very large. Now the Rayleigh series underestimates Q_{sca} by 25%. Note, however, that in the intermediate range of $|mx|$, [15] is still excellent.

To show that [15] adequately models resonances we now choose an index with large real part and small imaginary or absorptive component. Figure 2 is a diagram of Q_{ext} as calculated by Mie theory and the new series [15] for an index of $100 - 10^{-6}i$. Although this index is extreme and not physical, it is used here to demonstrate that it is valid for such unusual cases. This emphasizes that [15] applies to arbitrary indices for small x . Notice that not all resonances are modelled. This is because the higher order Mie coefficients have not been used.

The effect of using the sixth order expansion instead of the fourth order can be seen in Figs. 3 and 4. The cases are Q_{ext} for water at 33 GHz and 95 GHz respectively. It can be seen that the sixth order corrects for both amplitude and skewness around the resonances. Evidently, higher order expansion would improve the accuracy further. It is interesting that the fourth order captures most of the detail, even around the resonances.

Figures 5 and 6 are the same cases as for the previous two diagrams except that prolate spheroids, with an aspect ratio 2, are considered instead of spheres. The exact calculations are performed using the T-Matrix method⁶. Also the size parameter x has been replaced by the semi-minor axis b . As expected the features are similar but many significant changes can be observed. Relative amplitudes and locations of the resonances have changed as well as the underlying trend in the curves. The agreement, while not excellent is still remarkable because of the simplicity of the series compared with the exact calculation for such a large optical size. This large optical size almost makes the T-matrix ill-conditioned. No such problem will occur for the series.

The accuracy of the series for the spheroid would likely improve if numerical integration of the series was performed instead of using the empirical formula [41]. This and small particle scattering from oblates is currently under study.

It is evident from the above calculations that it is possible to obtain series for the efficiencies with out consideration of optical size, for spheres, prolate spheroids and infinite cylinders. It is therefore clear that small particle phase functions can also be computed for arbitrary indices by using the same, material transformed series.

3. CONCLUSIONS AND REMARKS

We have derived a series that lifts the optical size constraint that is inherent in both the Rayleigh and Thomson approximations. This series has been applied to spheres and in an approximate way to prolate spheroids. Comparison of the new series with the exact Mie formalism show excellent agreement. A similar comparison between the T-Matrix method and the randomly oriented prolate spheroid series shows that the agreement is not as good as in the case for spheres. However, a substantial portion of the underlying structure or physics is being modelled correctly. Additional work will be needed to improve the approximation for randomly oriented prolate and oblate spheroids. A study of the numerically integrated series, to randomize the orientation of the spheroids, will likely aid in this direction.

Combining this approach with our previously described techniques^{5,7}, for approximating extinction, scattering and absorption efficiencies, we are obtaining simple formulae for arbitrary materials, particle sizes and aspect ratios.

4. REFERENCES

1. Van de Hulst, H.C., "Light Scattering by Small Particles," Wiley, New York, 1957.
2. Kerker, M., Scheiner, P. and Cooke, D.D., "The Range of Validity of the Rayleigh and Thomson Limits for Lorenz-Mie Scattering," J. Opt. Soc. Am., **68** 135-137, 1978.
3. Kerker, M., "The Scattering of Light and Other Electromagnetic Radiation," Academic Press, New York, 1969.
4. Stevenson, A.F., "Electromagnetic Scattering by an Ellipsoid in the Third Approximation," J. Appl. Phys. **24** 9 1143-1151, 1953.
5. G.R. Fournier and B.T.N. Evans, "An Approximation to Extinction Efficiency for Randomly Oriented Spheroids", *Applied Optics*, **30**, 2042-2048 (1991).
6. Barber, P.W., Hill, S.C. and Hill, A.C., "Light Scattering by Size/Shape Distributions of Soil Particles and Spheroids", *Applied Optics*, **23**, 1025, 1984.
7. B.T.N. Evans and G.R. Fournier, "Simple Approximation to Extinction Efficiency Valid Over All Size Parameters", *Applied Optics*, **29**, 4666-4670 (1990).

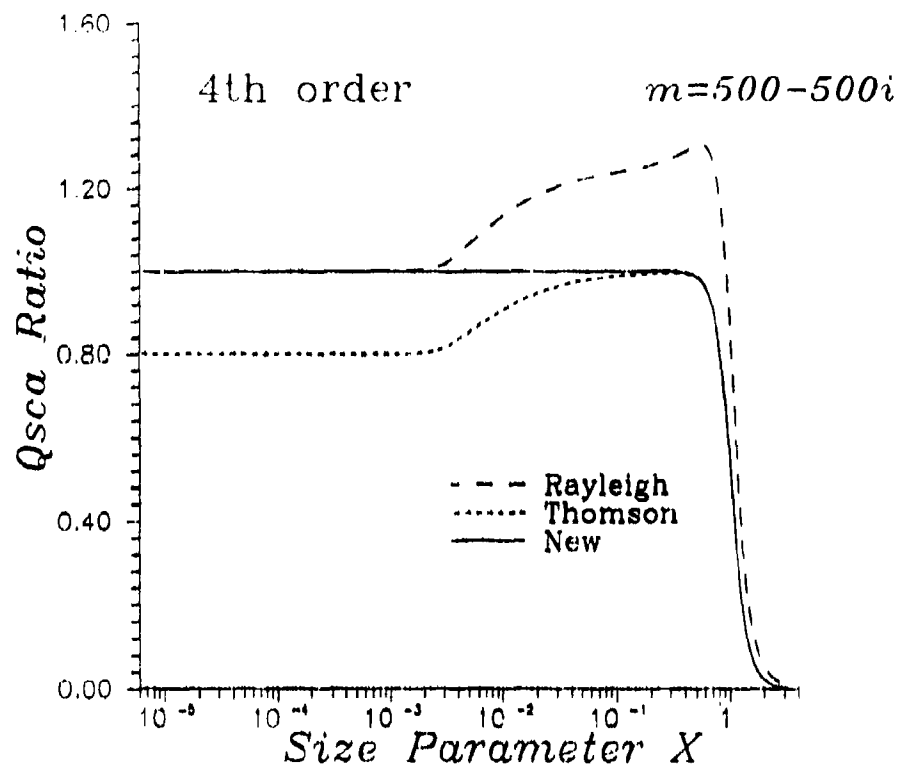


Fig.1 Mie calculation normalized by the three series as a function of size parameter.

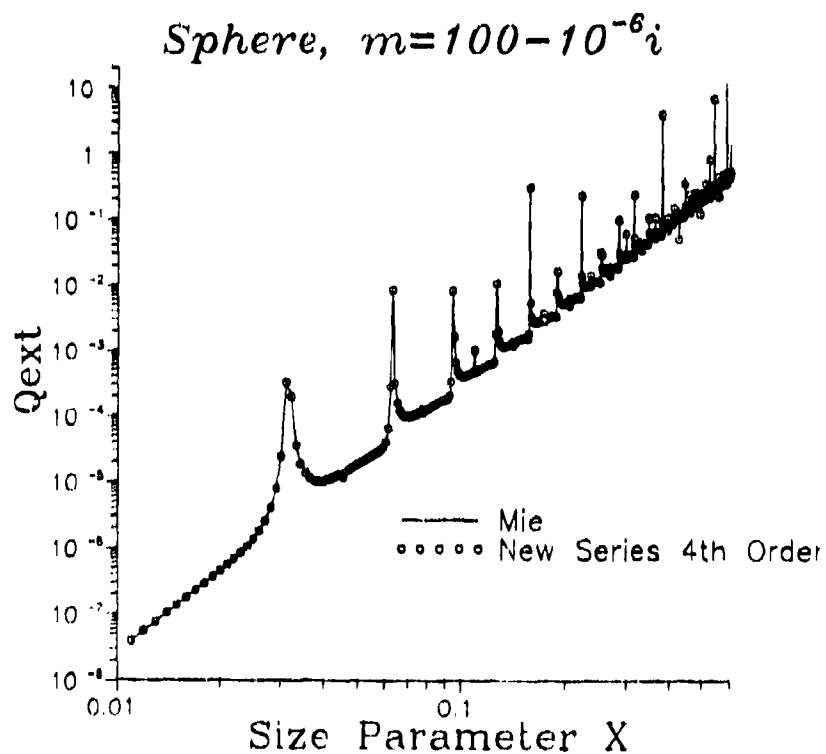


Fig.2 Q_{ext} as calculated by Mie theory and the new series [15] for an index of $100 - 10^{-6}i$.

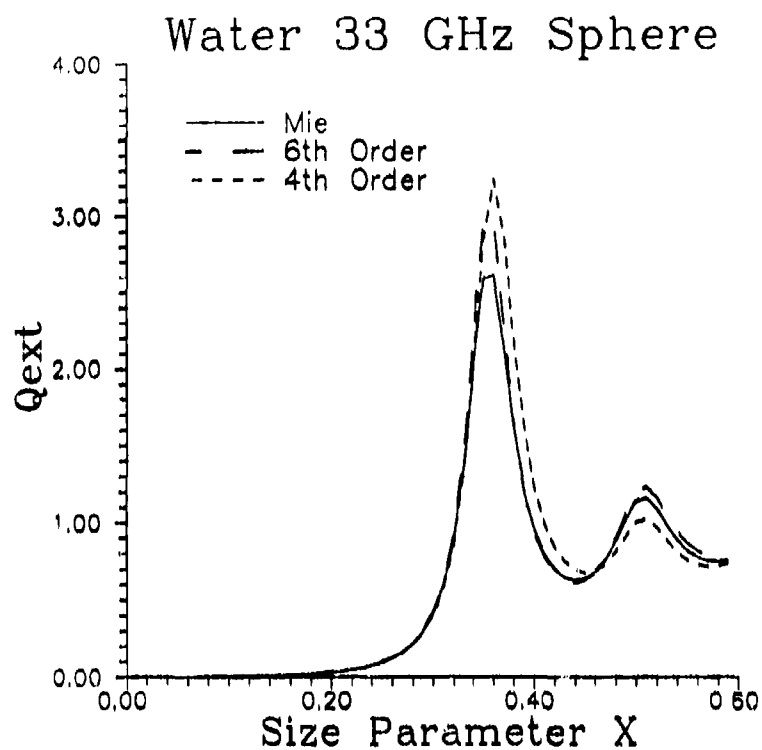


Fig.3 Q_{ext} for water spheres at 33 GHz. Refractive index $m = 8.743 - 0.6400i$.

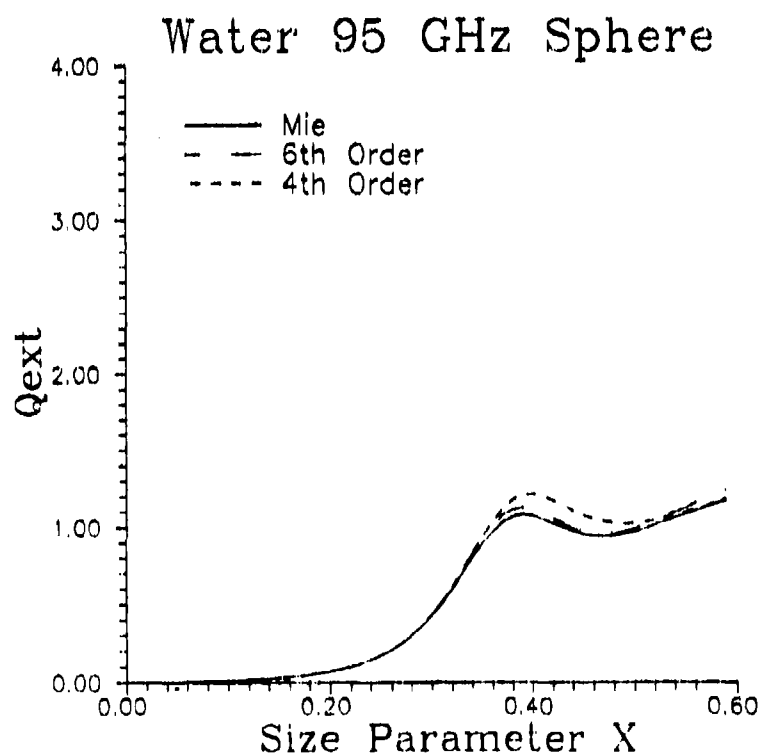


Fig.4 Q_{ext} for water spheres at 95 GHz. Refractive index $m = 8.075 - 1.824i$.

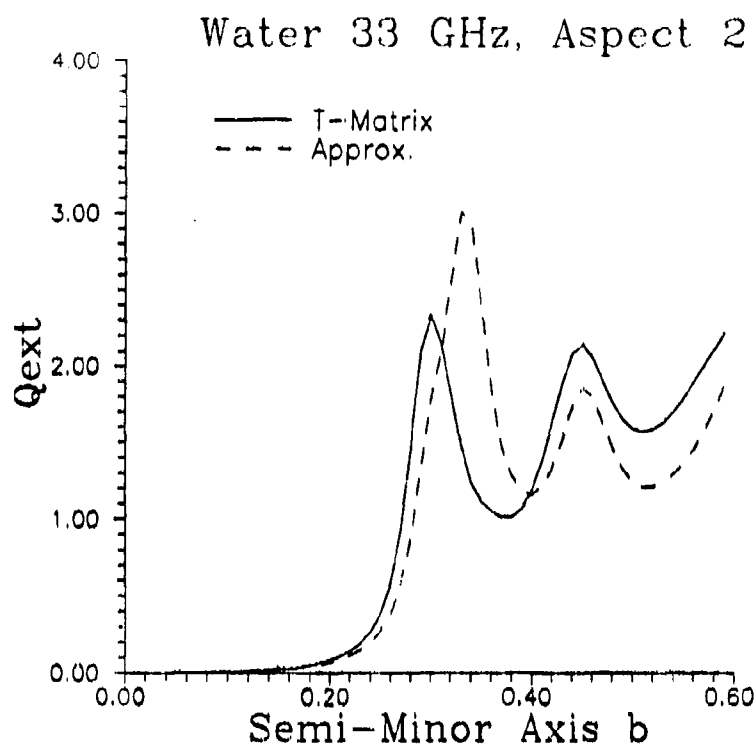


Fig.5 Q_{ext} for water spheroids, $r = 2$, at 33 GHz. Refractive index $m = 8.743 - 0.6409i$.

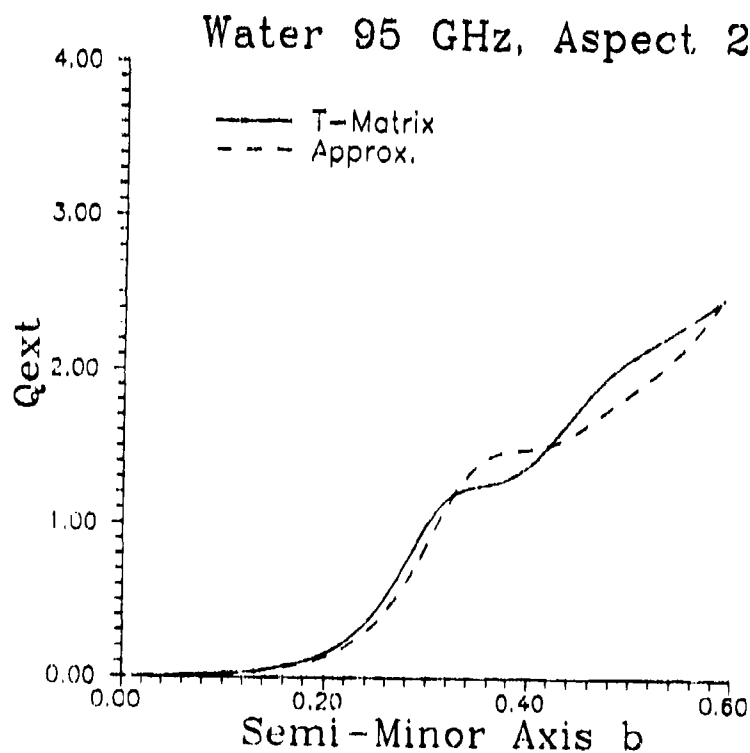


Fig.6 Q_{ext} for water spheroids, $r = 2$, at 95 GHz. Refractive index $m = 8.075 - 1.824i$.

**EXACT FORMULAS FOR REACTIVE
INTEGRALS
ARISING IN THE ELECTROMAGNETIC
SCATTERING PROBLEM
FOR NONHOMOGENEOUS, ANISOTROPIC
BODIES OF REVOLUTION**

**- - Evaluation of Integrals
of Functions Defined by
Riemann Surfaces and zero finding with
applications to Electromagnetism
and aerosol science**

**D. K. Cohoon
Department of Mathematics
West Chester University
West Chester, PA 19383**

February 18, 1992

Contents

- 1 Exact Evaluation of Integrals**
- 2 Reactive Integrals**
- 3 Surface Integral Equation Methods**
 - 3.1 Combined Field Integral Equations**
- 4 Zeros of Functions of a Complex Variable**
- 5 Applications**

Bodies of revolution are structures, including aerosol particles which are fibers and flakes, which have an axis of symmetry with the property that if one examines the scattering body before and after any partial rotation about this axis, an impinging electromagnetic wave can see no difference. The electromagnetic interaction problem is complicated by the fact that every portion of this body of revolution as it is stimulated by the impinging radiation communicates with every other portion of the body of revolution. Because of the rotational symmetry, it seems prudent to represent the components of the induced electric and magnetic fields as a Fourier series and solve an integral equation formulation of the scattering problem by solving for Fourier components of piecewise polynomial approximations of the field components within each cell of the body. This Fourier analysis involves trigonometric integrals which when transformed to the complex plane would involve analysis of functions defined on a Riemann surface. We provide in this paper a new way of evaluating these integrals using only information around an essential singularity.

Bodies of revolution also include bodies that have spheres, cylinders, oblate or prolate spheroids, or a torus as boundaries of a material that responds to the radiation. Analyzing the latter may have some benefit in the controlled thermonuclear fusion problem ([1]) as a design for a material with ultra high absorption efficiency could be obtained inexpensively by computer analysis ([2]). The low cost of computer experimentation may also permit one to design an ultraviolet light absorbing aerosol that will protect man and animals from the coming ozone depletion problem. The material body may have tensor properties, but the body, together with its properties is still unchanged by any partial rotation about the axis of symmetry. This could include, for example, a tensor material which has one property in the direction of the axis of rotation and another property in all directions going radially outward from this axis of symmetry. Here, one might think of cutting a sphere out of a cylinder comprised of closely packed dielectric needles; externally to visible light this sphere might look to our eye like any other round aerosol, but to electromagnetic waves polarized in the direction of the axis (and consequently parallel to these soft dielectric needles) and to those electromagnetic waves polarized in a direction perpendicular to the axis of revolution, the response would be completely different. These materials are used in liquid crystal concepts which may in the future be used as a healthy replacement for video displays. The details of the connection between the integrals discussed in this paper and electromagnetic interaction problems are found in many sources ([21]) but is lucidly explained in Glisson and Wilton ([13]). We explain here a method of evaluating integrals of exponential polynomials of algebraic functions of trigonometric functions from 0 to 2π .

1 Exact Evaluation of Integrals

We introduce a function ξ which represents the distance between two points, represented in cylindrical coordinates as (ρ, θ, z) and $(\tilde{\rho}, \tilde{\theta}, \tilde{z})$ so that

$$\xi = \sqrt{\rho^2 + \tilde{\rho}^2 + z^2 + \tilde{z}^2 - 2 \cdot \rho \cdot \tilde{\rho} \cdot \cos(\psi)} \quad (1.1)$$

where ψ is the difference between θ and θ . The integral under consideration is

$$I_{(t,m)}^{(c)} = \int_0^{2\pi} \frac{\exp(i\xi)}{\xi^t} \cdot \cos(m\psi) d\psi \quad (1.2)$$

where

$$\xi^2 = (A - 2B\cos(\psi)) \quad (1.3)$$

where

$$A^2 > 4B^2 \quad (1.4)$$

where A is positive and m is a nonnegative integer. The function ξ defined by equation (1.3) is an algebraic function defined by a Riemann surface if you make the normal extension to the complex plane by rewriting equation (1.3) in the form,

$$\xi^2 = (A - B \cdot (\zeta + 1/\zeta)) \quad (1.5)$$

where if ζ is equal to $\exp(i\psi)$, then

$$2 \cdot \cos(\psi) = (\zeta + 1/\zeta) \quad (1.6)$$

The rational function ξ^2 has a simple pole at the origin and one zero inside the unit circle and another zero outside the unit circle. The algebraic function ξ is defined by a Riemann surface with a Branch cut from the origin to a zero,

$$\zeta_1 = \frac{A - \sqrt{A^2 - 4B^2}}{2 \cdot B} = \frac{2B}{A + \sqrt{A^2 - 4B^2}} \quad (1.7)$$

of the function ξ^2 that is inside the unit circle

$$|\zeta| = 1 \quad (1.8)$$

and a branch cut from ∞ to the zero,

$$\zeta_2 = \frac{A + \sqrt{A^2 - 4B^2}}{2 \cdot B} \quad (1.9)$$

that is outside the unit circle. If we use the argument function defined by

$$\text{Arg}(x + iy) = \theta \quad (1.10)$$

where if

$$r = \sqrt{x^2 + y^2} \quad (1.11)$$

then, θ , the value of the argument function defined by equation (1.10) is such that

$$r\cos(\theta) + ir\sin(\theta) = x + iy \quad 0 \leq \theta < 2\pi \quad (1.12)$$

We can use a Riemann surface to define the square root of the meromorphic function ξ^2 defined by equation (1.9) to define the algebraic function ξ or use the argument function Arg defined by equations (1.10) and (1.12)

$$\xi =$$

$$i \left[\frac{B |\zeta - \zeta_1| |\zeta - \zeta_2|}{|\zeta|} \right]^{1/2} \exp(i(1/2)(\text{Arg}(\zeta - \zeta_1) + \text{Arg}(\zeta - \zeta_2) - \text{Arg}(\zeta))) \quad (1.13)$$

Thus, an integral of a holomorphic function of ξ around the unit circle will be equal to the integral of the same function around a rectangle inside the unit circle which contains the slit from the origin to ζ_1 . We show how information around the essential singularity will give us an exact formula; our formula will be checked by direct Fourier analysis observing that

$$\frac{1}{(A - 2 \cdot B \cdot \cos(\psi))^{1/2}} = \left(\frac{1}{\sqrt{A}} \right) \sum_{k=0}^{\infty} P_k^{(1)} \cdot 2^k \cdot \cos^k(\psi) \quad (1.14)$$

where

$$P_k^{(1)} = \left(\frac{B}{A} \right)^k \left[\prod_{j=1}^k \left(\frac{2 \cdot j - 1}{2 \cdot j} \right) \right] \quad (1.15)$$

which means that we can think in terms of representing powers of $\cos(\psi)$ as a Fourier series.

2 Reactive Integrals

An exact formula for the values of the reactive integrals has been obtained, and furthermore, the cost of finding the value of the reactive integrals, which were in all other works (e.g. [21] and [13]) carried out by a numerical integration scheme whose computation time increases directly with the m appearing in equation (1.2), is with this exact formula independent of m . Furthermore, this exact formula depends only on values at the essential singularity expansion at ζ equals 0. These formulas have been validated by Fourier expansion and by numerical comparison to 12 or more decimal places with the straightforward numerical integration scheme described in the previous section. The first essential singularity expansion has the form,

$$\frac{1}{\xi^r} = \frac{1}{A^{r/2}} \left[\sum_{q=0}^{\infty} P_q^{(r)} \left(\zeta + \frac{1}{\zeta} \right)^q \right] \quad (2.1)$$

We can expand the function $\cos(\xi)$ by the series

$$\cos(\xi) = \sum_{k=0}^{\infty} \left[\frac{(-1)^k \xi^{2k}}{(2k)!} \right] = \sum_{s=0}^{\infty} C_s \left(\zeta + \frac{1}{\zeta} \right)^s \quad (2.2)$$

We now use the Cauchy product and equations (2.1) and (2.2) to write

$$\left\{ \frac{\cos(\xi)}{\xi^r} \right\} = \frac{1}{A^{r/2}} \left[\sum_{j=0}^{\infty} \left(\sum_{k=0}^j C_{k-j} P_k^{(r)} \right) \left(\zeta + \frac{1}{\zeta} \right)^j \right] \quad (2.3)$$

If we define

$$D_j^{(r)} = \sum_{k=0}^j C_{k-j} P_k^{(r)} \quad (2.4)$$

then equation (2.3) implies that

$$\left\{ \frac{\cos(\xi)}{\xi^\ell} \right\} = \frac{1}{A^{\ell/2}} \left[\sum_{j=0}^{\infty} D_j^{(\ell)} \left(\zeta + \frac{1}{\zeta} \right)^j \right] \quad (2.5)$$

There are two expansions of even and odd powers of $\cos(\psi)$ which enable us to evaluate these contour integrals. The even powers of \cos are given ([17], p 24-26) by

$$\cos^{2\ell}(\psi) = \frac{1}{2^{2\ell}} \left[\sum_{k=0}^{\ell-1} \left\{ 2 \binom{2\ell}{k} \cdot \cos(2(\ell-k)\psi) \right\} + \binom{2\ell}{\ell} \right] \quad (2.6)$$

and the Fourier expansion of an odd power of the cosine ([17], pp 24-26) is

$$\cos^{2q-1}(\psi) = \frac{1}{2^{2q-1}} \left[\sum_{k=0}^{q-1} \left\{ 2 \binom{2q-1}{k} \cdot \cos((2q-2k-1)\psi) \right\} \right] \quad (2.7)$$

If we assume that ζ is equal to $\exp(i\psi)$, then we can use equations (2.6) and (2.7) and the relationship

$$\int_{-\pi}^{\pi} \left(\zeta + \frac{1}{\zeta} \right)^j \cos(m\psi) d\psi = \int_{-\pi}^{\pi} (2^j \cdot \cos^j(\psi) \cos(m\psi)) d\psi \quad (2.8)$$

to evaluate the reactive integrals. We consider first the case where j is equal to 2ℓ and use equation (2.8) and equation (2.6) to obtain for positive even integers m not exceeding 2ℓ the relationship,

$$\int_{-\pi}^{\pi} \left(\zeta + \frac{1}{\zeta} \right)^{2\ell} \left(\frac{1}{2} \right) \left(\zeta^m + \frac{1}{\zeta^m} \right) \frac{d\zeta}{i\zeta} = 2\pi \binom{2\ell}{\ell - m/2} \quad (2.9)$$

to evaluate the reactive integrals. In the case where j is equal to 2ℓ and

$$2\ell - 2k \quad (2.10)$$

we observe that

$$k = \frac{j-m}{2} \quad (2.11)$$

In considering the case where j is equal to $2q-1$ we use the fact that in the case where m is an odd integer and j is equal to $2q-1$ that

$$\int_{-\pi}^{\pi} \left(\zeta + \frac{1}{\zeta} \right)^{2q-1} \left(\frac{1}{2} \right) \left(\zeta^m + \frac{1}{\zeta^m} \right) \frac{d\zeta}{i\zeta} = 2\pi \binom{2q-1}{(2q-1-m)/2} \quad (2.12)$$

We conclude that equation (2.5) implies that

$$\int_{-\pi}^{\pi} \left\{ \frac{\cos(\xi)}{\xi^\ell} \right\} \cdot \cos(m\psi) d\psi =$$

$$\frac{1}{A^{\ell/2}} \left[\sum_{j=0}^{\infty} D_{m+2 \cdot j}^{(\ell)} \cdot 2\pi \cdot \binom{m+2 \cdot j}{j} \right] \quad (2.13)$$

We next develop an expression for integrals involving $\sin(\xi)/\xi$ by first observing that

$$\frac{\sin(\xi)}{\xi} = \sum_{s=0}^{\infty} S_s \left(\zeta + \frac{1}{\zeta} \right)^s \quad (2.14)$$

We then make use of the fact that

$$\begin{aligned} \frac{\sin(\xi)}{\xi^{\ell}} &= \left(\frac{1}{\xi^{\ell-1}} \right) \left(\frac{\sin(\xi)}{\xi} \right) = \\ &= \frac{1}{A^{(\ell-1)/2}} \left[\sum_{q=0}^{\infty} P_q^{(\ell-1)} \left(\zeta + \frac{1}{\zeta} \right)^q \frac{\sin(\xi)}{\xi} \right] \end{aligned} \quad (2.15)$$

Multiplying the series given by equations (2.14) and (2.15) we see that

$$\frac{\sin(\xi)}{\xi^{\ell}} = \frac{1}{A^{(\ell-1)/2}} \left[\sum_{j=0}^{\infty} E_j^{(\ell)} \left(\zeta + \frac{1}{\zeta} \right)^j \right] \quad (2.16)$$

where

$$E_j^{(\ell)} = \sum_{k=0}^j (S_{k-j} \cdot P_k^{(\ell-1)}) \quad (2.17)$$

Thus, we conclude that

$$\begin{aligned} \int_{-\pi}^{\pi} \left(\frac{\sin(\xi)}{\xi^{\ell}} \right) \cos(m\psi) d\psi = \\ \frac{1}{A^{(\ell-1)/2}} \left[\sum_{q=0}^{\infty} \{ E_{m+2 \cdot q}^{(\ell)} 2\pi \} \binom{m+2 \cdot q}{q} \right] \end{aligned} \quad (2.18)$$

By making use of the identity

$$\binom{j}{(j-m)/2} = \binom{j}{(j+m)/2} \quad (2.19)$$

the formula (2.18) and the formula (2.13) can be given a different look, but several different numerical checks all agreed to machine precision. These formulas were checked by numerical computation using Gaussian quadrature. In the case where the observation point is close to the variable of integration or said differently when $2B$ is very nearly as large as A , then the series can converge slowly, but they can still be evaluated accurately if one uses Euler's method of accelerating convergence of sums ([14], pp 201 - 207). The following table shows a weakness in the method without the use of accelerated convergence. When ρ and $\bar{\rho}$ are both equal to 1 and when z and \bar{z} are both equal to 1.1 as in equation (1.1) and we just use 139 terms for the geometric series and we make use of the fact that $\cos(\xi)$ divided by ξ^2 is meromorphic and use the contribution to the reactive integral from the

simple pole at the zero ζa_1 inside the unit circle given by equation (1.7) versus using the Riemann surface concept with just a small number of terms

<i>Essential Singularity Contribution</i>	<i>Gaussian Quadrature Integration</i>	<i>Pole and $\zeta = 0$ Contribution</i>	<i>Mode Index</i>
139 terms			
3.724	3.726	3.726	1
2.842	2.844	2.844	2
2.110	2.112	2.112	3
.472	.4739	.4739	8

For the difficult cases described in the above table over 6000 thousand terms were used along with accelerated convergence and 15 decimal place agreement between the three methods was achieved. The following table shows the capabilities of the formulae when augmented by Euler's method for accelerated convergence for the case where ρ is equal to 1, $\tilde{\rho}$ is equal to $1 + 0.2$, z is equal to 1, and \tilde{z} is equal to $1 + 0.2$. Using the Riemann surface concept and carrying out an expansion about the essential singularity we have

$\frac{\exp(i\xi)}{\xi^n}$ <i>SINGULARITY EXPANSION METHOD</i>	$\cos(m\psi)$ <i>ENHANCED GAUSSIAN QUADRATURE</i>	$d\psi$ $\exp(im\psi)$ <i>MODE INDEX</i>
3.75346548 - (1.5112968)i	3.75346548 - (1.5112968)i	1
.382950948 - (.0520636761)i	.382950948 - (.0520636761)i	10
.0291669710 - (.00285093482)i	.0291669710 - (.00285093483)i	20

Also, the terms of the expansions of $\sin(\xi)$ and $\cos(\xi)$ can be determined by exact formulas by making use of the Jensen Voller's formula, a variant of the Faa Di Bruno formula ([9]). For example the term C_0 appearing in equation (2.2) is given by

$$C_0 = \cos(\sqrt{A}) \quad (2.20)$$

An alternative representation of these integrals in terms of known special functions is found in a much more general setting in Chapter 7 of (Carlson, [5]), where the integral

$$I(r, m) = \int_0^{2\pi} (A - 2 \cdot B \cos(\psi))^{r/2} \cdot \cos(m\psi) d\psi \quad (2.21)$$

arises as a special case, and Carlson's condition for rapid ordinary convergence of the series which states that the ratio

$$\mathcal{R} = \frac{A - 2 \cdot B}{A + 2 \cdot B} \quad (2.22)$$

stay away from zero is equivalent to ours.

3 Surface Integral Equation Methods

In this section we shall show how in the case where the irradiated structure consists of homogeneous regions which are delimited by diffeomorphisms of the interior of a sphere or a torus in three dimensional space (in the body of revolution case) to represent the solution of the scattering problem as the solution of two combined field integral equations with integral operators formed from the Green's functions defined on opposite sides of the separating surfaces. The surface integral equation methods reduce the computational complexity in the sense that they require discretization electric and magnetic fields defined on a surface rather than on a region of three dimensional space. In a general nonrotationally symmetric setting the development which follows is valid for regions which are the interior of diffeomorphisms of N handled spheres.

3.1 Combined Field Integral Equations

Consider a set Ω in \mathbb{R}^3 with boundary surface $\partial\Omega$ on which are induced electric and magnetic surface currents \vec{J}_j and \vec{M}_j . If we have a simple $N + 1$ region problem, where we have N inside and a region outside all N bounded homogeneous aerosol particles corresponds to the region index j being equal to 1 and the region inside corresponds to j values ranging from 2 to $N + 1$, then if the propagation constant k_j in region j is defined also by a function k_j , naturally defined on a Riemann surface as the square root of,

$$k_j^2 = \omega^2 \mu \epsilon - i \omega \mu \sigma \quad (3.1)$$

For a Debye medium (Daniel, [11]) the branch cuts are along the imaginary ω axis. For a Lorentz medium particle (Brillouin, [4], [29]) the branch cuts are in the upper half of the complex ω plane parallel to the real axis. where μ , ϵ , and σ are functions of frequency that assure causality and that the radiation does not travel faster than the speed of light in vacuum. There are two Helmholtz equations, one for the interior of the particle and the other for the exterior, defined by

$$(\Delta + k_j^2)G_r = 4\pi\delta \quad (3.2)$$

where G_j is the temperate, rotationally invariant, fundamental solution ([16]) of the Helmholtz operator. We let

$$J_1 = J = -J_2 \quad (3.3)$$

and

$$M_1 = M = -M_2 \quad (3.4)$$

where we assume that the surface $S_{(1,2)}$ separates region 1 and region 2. We generalize equations (3.3) and (3.4) inductively by saying that for any surface $S_{(j,\tilde{j})}$ separating region j from region \tilde{j} where

$$j < \tilde{j} \quad (3.5)$$

we have

$$J_j = J = -J_{\bar{j}} \quad (3.6)$$

and

$$M_j = M = -M_{\bar{j}} \quad (3.7)$$

We define

$$\mathcal{I} = \{(j, \bar{j}) : S_{(j, \bar{j})} \text{ is a separating surface}\} \quad (3.8)$$

where j is less than \bar{j} . We get a single coupled, combined field integral equation which describes the interaction of radiation with the conglomerate aerosol particle or cluster given by

$$\begin{aligned} \vec{n} \times \vec{E}^{inc} = & \vec{n} \times \sum_{(j, \bar{j}) \in \mathcal{I}} \left\{ \left(\frac{i\omega}{4\pi} \right) \int_{S_{(j, \bar{j})}} \int \vec{J}(\vec{r}) (\mu_j \cdot G_j(r, \vec{r}) + \mu_{\bar{j}} \cdot G_{\bar{j}}(r, \vec{r})) da(\vec{r}) \right. \\ & + \frac{i}{4\pi\omega} \text{grad} \left\{ \int_{S_{(j, \bar{j})}} \int (\text{div}_s \cdot \vec{J}) \left[\frac{G_j(r, \vec{r})}{\epsilon_j} + \frac{G_{\bar{j}}(r, \vec{r})}{\epsilon_{\bar{j}}} \right] da(\vec{r}) \right\} + \\ & \left. \left(\frac{1}{4\pi} \right) \text{curl} \left(\int_{S_{(j, \bar{j})}} \int \vec{M}(\vec{r}) \cdot (G_j(r, \vec{r}) + G_{\bar{j}}(r, \vec{r})) da(\vec{r}) \right) \right\} \end{aligned} \quad (3.9)$$

In addition to equation (3.9) we need equation involving the magnetic vector H^{inc} of the stimulating electromagnetic field which is given by

$$\begin{aligned} \vec{n} \times \vec{H}^{inc} = & \vec{n} \times \sum_{(j, \bar{j}) \in \mathcal{I}} \left\{ \left(\frac{i\omega}{4\pi} \right) \int_{S_{(j, \bar{j})}} \int \vec{M}(\vec{r}) (\epsilon_1 \cdot G_j(r, \vec{r}) + \epsilon_2 \cdot G_{\bar{j}}(r, \vec{r})) da(\vec{r}) \right. \\ & + \left(\frac{i}{4\pi\omega} \right) \text{grad} \left\{ \int_{S_{(j, \bar{j})}} \int (\text{div}_s \cdot \vec{M}) \left[\frac{G_j(r, \vec{r})}{\mu_j} + \frac{G_{\bar{j}}(r, \vec{r})}{\mu_{\bar{j}}} \right] da(\vec{r}) \right\} + \\ & \left. \frac{1}{4\pi} \text{curl} \left(\int_{S_{(j, \bar{j})}} \int \vec{J}(\vec{r}) (G_j(r, \vec{r}) + G_{\bar{j}}(r, \vec{r})) da(\vec{r}) \right) \right\} \end{aligned} \quad (3.10)$$

Once the coupled combined field system (3.9) and (3.10) is solved for \vec{J} and \vec{M} , the surface electric and magnetic currents respectively and we define the surface electric charge density by ([13], p 7)

$$\rho^e(\vec{r}) = \frac{i}{\omega} [\text{div}_s \cdot \vec{J}(\vec{r})] \quad (3.11)$$

and the surface magnetic charge density

$$\rho^m(\vec{r}) = \frac{i}{\omega} [\text{div}_s \cdot \vec{M}(\vec{r})] \quad (3.12)$$

where div_s is the surface divergence. Now for each region index j we define

$$\mathcal{J}(j) = \{\bar{j} : (j, \bar{j}) \in \mathcal{I}\} \quad (3.13)$$

where \mathcal{I} is the set of all indices of separating surfaces defined by (3.8). We now need to be able to express the electric and magnetic fields inside and outside the scattering body. We first define the vector potentials \vec{A}_j and \vec{F}_j by the rules, ([13] [21])

$$\vec{A}_j = \sum_{j \in \mathcal{J}(j)} \left[\frac{\mu_j}{4\pi} \int_{S_{(j,j)}} \int \vec{J}_j(\vec{r}) \cdot \vec{G}_j(r, \vec{r}) d\vec{a}(\vec{r}) \right] \quad (3.14)$$

$$\vec{F}_j = \sum_{j \in \mathcal{J}(j)} \left[\left(\frac{\epsilon_j}{4\pi} \right) \int_{S_{(j,j)}} \int \vec{M}_j(\vec{r}) \cdot \vec{G}_j(r, \vec{r}) d\vec{a}(\vec{r}) \right] \quad (3.15)$$

The scalar potentials are defined in terms of the electric charge density (3.11) and magnetic charge density (3.12) by the rules,

$$\Phi_j(\vec{r}) = \sum_{j \in \mathcal{J}(j)} \left[\left(\frac{1}{4\pi\epsilon_j} \right) \int_{S_{(j,j)}} \int \rho_j^e(\vec{r}) G_j(r, \vec{r}) d\vec{a}(\vec{r}) \right] \quad (3.16)$$

and

$$\Psi_j(\vec{r}) = \sum_{j \in \mathcal{J}(j)} \left[\left(\frac{1}{4\pi\mu_j} \right) \int_{S_{(j,j)}} \int \rho_j^m(\vec{r}) G_j(r, \vec{r}) d\vec{a}(\vec{r}) \right] \quad (3.17)$$

We now can define the electric and magnetic vectors inside the region j in terms of these potentials (3.14), (3.15), (3.16), and (3.17) by the rules,

$$\vec{E}_j = -i\omega\vec{A}_j(r) - \text{grad}(\Phi_j(r) + \frac{1}{\epsilon_j} \text{curl}(\vec{F}_j)(r)) \quad (3.18)$$

and

$$\vec{H}_j = -i\omega\vec{F}_j(r) - \text{grad}(\Psi_j(r) + \frac{1}{\mu_j} \text{curl}(\vec{A}_j)(r)) \quad (3.19)$$

Similar equations apply outside the body, by there the fields represented are the differences \vec{E}_1^s and \vec{H}_1^s between the total electric and magnetic vectors and the electric vector \vec{E}^{inc} and the magnetic vector \vec{H}^{inc} of the incoming wave that is providing the stimulation. Thus ([13]) we see that outside the body,

$$\vec{E}_1^s = -i\omega\vec{A}_1(r) - \text{grad}(\Phi_1(r) + \frac{1}{\epsilon_1} \text{curl}(\vec{F}_1)(r)) \quad (3.20)$$

and

$$\vec{H}_1^s = -i\omega\vec{F}_1(r) - \text{grad}(\Psi_1(r) + \frac{1}{\mu_1} \text{curl}(\vec{A}_1)(r)) \quad (3.21)$$

These equations generalize the formulation of Glisson ([13]) to a three dimensional structure whose regions of homogeneity are diffeomorphisms of the interior of the sphere or a torus in \mathbb{R}^3 . If the scattering structure is not a body of revolution, then the region may be a diffeomorph of an N handled sphere.

4 Zeros of Functions of a Complex Variable

Important design problems can be solved with good algorithms for finding zeros of entire or meromorphic functions of a complex variable. One of the most important problems attached to Riemann's name was the Riemann hypothesis. In this section we discuss some novel homotopy methods ([6]) for finding zeros of analytic functions. The problem of finding modes of propagation in an anisotropic, magnetically lossy coating on a perfect conductor ([10]) is related to the problem of finding complex numbers z such that

$$\cosh(\sqrt{z}) - \frac{A \cdot z + B}{C \cdot z + B} = 0 \quad (4.1)$$

by moving this problem up to a higher algebra where the solution becomes transparent and then following a homotopy path down to the solutions in the space of interest; this permitted the authors to track propagation constants as magnetic properties went through regions of anomalous dispersion and the material thickness changed.

We consider here the problem of finding complex numbers z such that $\sin(z)$ is equal to z . Since there are no polynomial functions $P(z)$ and entire functions $h(z)$ such that

$$-\frac{i}{2}\exp(iz) + \frac{i}{2}\exp(-iz) - z = P(z)\exp(h(z)) \quad (4.2)$$

it is clear from the theorem of Picard that there are an infinite number of solutions of the equation

$$\sin(z) - z = 0 \quad (4.3)$$

We transform the equation,

$$\sin(z) = z \quad (4.4)$$

to an equation in another space by using auxiliary functions so that the transformed equation has the form,

$$\sin(A(s)z(s)) = (z(s) + B(s)) \quad (4.5)$$

where

$$B(s) = (n \cdot \pi i)(1 - s) \quad (4.6)$$

and

$$z(0) = -n\pi i \quad (4.7)$$

and

$$A(s) = i(1 - s) + s \quad (4.8)$$

so that when s is equal to zero, equation (4.5) has the form,

$$\sin(i(-n\pi i)) = \sin(n\pi) = (-n\pi i + n\pi i) \quad (4.9)$$

which is true, and when s is equal to 1, then as the trivial equation (4.9) holds at one end of the homotopy path and if equation (4.5) is preserved all the way along the path, and as this equation has the form

$$\sin(A(1) \cdot z) = z + B(1) \quad (4.10)$$

at s equal to one, since

$$A(1) = 1 \quad (4.11)$$

and

$$B(1) = 0 \quad (4.12)$$

we see that we obtain a solution of equation (4.4) at the other end of the path.

Thus, the problem is finding a scheme for assuring that the equation (4.5) is preserved all the way along the path. Differentiating both sides of equation (4.5) we see that

$$\begin{aligned} z'(s) + B'(s) = \\ \cos(A(s)z(s)) \{A'(s) \cdot z(s) + A(s) \cdot z'(s)\} \end{aligned} \quad (4.13)$$

Collecting terms involving $z'(s)$ we find that

$$\begin{aligned} \{A(s)\cos(A(s)z(s)) - 1\} z'(s) = \\ B'(s) - z(s)A'(s)\cos(A(s)z(s)) \end{aligned} \quad (4.14)$$

which leads, after solving equation (4.14), to a coupled system of differential equations in $x(s)$ and $y(s)$ with known values at $s = 0$. Thus,

$$x'(s) = \text{Real} \left\{ \frac{B'(s) - z(s)A'(s)\cos(A(s)z(s))}{A(s)\cos(A(s)z(s)) - 1} \right\} \quad (4.15)$$

and

$$y'(s) = \text{Imag} \left\{ \frac{B'(s) - z(s)A'(s)\cos(A(s)z(s))}{A(s)\cos(A(s)z(s)) - 1} \right\} \quad (4.16)$$

where

$$\begin{pmatrix} x(0) \\ y(0) \end{pmatrix} = \begin{pmatrix} 0 \\ -n\pi \end{pmatrix} \quad (4.17)$$

These equations have been computer tested and orbits starting at $x(0) + iy(0)$ equal to

$$x(0) + iy(0) = 0 + 2\pi i, \quad (4.18)$$

for example, end up at

$$z = 7.4976 \dots - i2.7686 \dots \quad (4.19)$$

5 Applications

The homotopy method described in the last section provides us with a powerful design tool. By designing parameters in an irradiated toroidal plasma that will increase its efficiency of energy absorption by a factor of 1,000,000 one could in the light of the already successful Fusion reaction in England design practical, commercial fusion reactors which would replace all other means of generating power, abate the global warming, and give us a means of having safe drinking water 10 years from now. Perhaps a large aerosol which specifically absorbs dangerous UV light could be placed in orbit between the the sun and

the earth or one would have enough power to carry out the generation of large quantities of the ozone free radical in any prescribed portion of the Earth's atmosphere. Since half of the effort in solving integral equations of electromagnetic scattering involves finding entries in a matrix operator representing the discretization of the integral equations (3.9) and (3.10), the exact formulas (2.13) and (2.18) for integrals of functions defined on Riemann surfaces have made it easier to accurately determine the interaction of electromagnetic radiation with penetrable bodies having rotational symmetry.

References

- [1] Anderson, Dale A. *Computational Fluid Mechanics and Heat Transfer* New York: McGraw Hill (1984).
- [2] Barton, J. P., D. R. Alexander, and S. A. Schaub. "Internal fields of a spherical particle illuminated by a tightly focused laser beam: focal point positioning effects at resonance." *Journal of Applied Physics*. Volume 65 No. 8 (April 15, 1989) pp 2900-2906
- [3] Barton, J. P., D. R. Alexander, and S. A. Schaub. "Internal and near surface electromagnetic fields for a spherical particle irradiated by a focused laser beam" *Journal of Applied Physics*. Volume 64, no 4 (1988) pp 1632-1639.
- [4] Brillouin, Leon. *Wave Propagation and Group Velocity*. New York: Academic Press (1960).
- [5] Carlson, B. C. *Special Functions of Applied Mathematics* New York: Academic Press (1977)
- [6] Chow, S. N., J. Mallet-Paret, and J. A. Yorke. Finding zeros of maps: homotopy methods that are constructive with probability one. *Math. Comp.* Volume 32 (1978) pp 887-889.
- [7] Chevaillier, Jean Phillippe, Jean Fabre, and Patrice Hamelin. "Forward scattered light intensities by a sphere located anywhere in a Gaussian beam" *Applied Optics*, Vol. 25, No. 7 (April 1, 1986) pp 1222-1225.
- [8] Chevaillier, Jean Phillippe, Jean Fabre, Gerard Grehan, and Gerard Goubet. "Comparison of diffraction theory and generalized Lorenz-Mie theory for a sphere located on the axis of a laser beam." *Applied Optics*, Vol 29, No. 9 (March 20, 1990) pp 1293-1298.
- [9] Cohoon, D. K. "On the nonpropagation of zero sets of solutions of certain homogeneous linear partial differential equations across noncharacteristic hyperplanes", *SAM - TR - 81 - 40* San Antonio, Texas: USAF School of Aerospace Medicine, Brooks AFB, Tx 78235 (December, 1981)
- [10] Cohoon, D. K. and R. M. Purcell. "Homotopy as an electromagnetic design method." *Journal of Wave Material Interaction*, Volume 4, No. 1 (January/April/July) 1989 pp 123 - 147
- [11] Daniel, Vera V. *Dielectric Relaxation* New York: Academic Press (1967).
- [12] Garcia, C. B. and W. I. Zangwill. *Pathways to Solutions, Fixed Points, and Equilibria*. Englewood Cliffs, NJ: Prentice Hall(1981)
- [13] Glisson, A. K. and D. R. Wilton. "Simple and Efficient Numerical Techniques for Treating Bodies of Revolution" University of Mississippi: University, Mississippi USA 38677 *RADC-TR-79-22*
- [14] Hamming, R. W. *Numerical Methods for Scientists and Engineers* New York: McGraw Hill (1962)
- [15] Hochstadt, Harry. *The Functions of Mathematical Physics*. New York: Dover(1986).

- [16] Hörmander, Lars. *Linear Partial Differential Operators* New York: Academic Press (1963)
- [17] Jeffrey, Alan. *Table of Integrals, Series, and Products* New York: Academic Press (1965)
- [18] Kozaki, Shogo. "Scattering of a Gaussian Beam by a Homogeneous Dielectric Cylinder" *Journal of Applied Physics* Volume 53, No. 11 (November, 1982) pp 7195-7200
- [19] Liou, K. N., S. C. Ou, Takano, A., Heymsfield, and W. Kreiss. "Infrared transmission through cirrus clouds: a radiative model for target detection" *Applied Optics* Volume 29, Number 13 (May 1, 1990) pp 1886-1896
- [20] Mackowski, D. W., R. A. Altenkirch, and M. P. Mengue. "Internal absorption cross sections in a stratified sphere" *Applied Optics*, Volume 29, Number 10 (April 1, 1990) pp 1551-1559
- [21] Maatz, J. R. and R. F. Harrington. "Radiation and Scattering from bodies of revolution" *Applied Science Research*, Volume 20 (June, 1969) pp 405-435.
- [22] Monson, B., Vyns Reeta, and R. Gupta. "Pulsed and CW Photothermal Phase Shift Spectroscopy in a Fluid Medium: Theory" *Applied Optics*, Volume 28, No. 13 (July, 1989) pp 2554-2561
- [23] Mugnai, Alberto and Warren J. Wiscombe. "Scattering from nonspherical Chebyshev Particles. I. Cross Sections, Single Scattering Albedo, Asymmetry factor, and backscattered fraction" *Applied Optics*, Volume 25, Number 7 (April 1, 1986) pp 1235-1244.
- [24] Park, Bae-Sig, A. Biswas, and R. L. Armstrong. "Delay of explosive vaporization in pulsed laser heated droplets" *Optics Letters*, Volume 15, No. 4 (February 15, 1990) pp 206-208
- [25] Pinnick, R. G., Abhijit Biswas, Robert L. Armstrong, S. Gerard Jennings, J. David Pendleton, and Gilbert Fernandez. "Micron size droplets irradiated with a pulsed CO₂ laser. Measurement of Explosion and Breakdown Thresholds" *Applied Optics*, Volume 29, No. 7 (March 1, 1990) pp 918-925
- [26] Rosseland, S. *Theoretical Astrophysics: Atomic Theory and the Analysis of Stellar Atmospheres and Envelopes* Oxford, England: Clarendon Press (1936)
- [27] Schaub, S. A., D. R. Alexander, J. P. Barton, and M. A. Emanuel. "Focused laser beam interactions with methanol droplets: effects of relative beam diameter" *Applied Optics* Volume 28, No. 9 (May 1, 1989) pp 1606-1609
- [28] Schiffer, Ralf. "Perturbation approach for light scattering by an ensemble of irregular particles of arbitrary material" *Applied Optics*, Volume 29, Number 10 (April 1, 1990) pp 1536-1550
- [29] Sherman, George C. and Kurt Edmund Oughston. "Description of pulse dynamics in Lorentz media in terms of energy velocity and attenuation of time harmonic waves." *Physical Review Letters*, Volume 47, Number 20 (November, 1981) pp 1451-1454
- [30] Tsai, Wen Chung and Ronald J. Pogorzelski. "Eigenfunction solution of the scattering of beam radiation fields by spherical objects" *Journal of the Optical Society of America* Volume 65, Number 12 (December, 1975) pp 1457-1463
- [31] Tzeng, H. M., K. F. Wall, M. B. Long, and R. K. Chang. "Laser emission from individual droplets at wavelengths corresponding to morphology dependent resonances" *Optics Letters* Volume 9, Number 11 (1984) pp 499-501
- [32] Volkovitsky, O. A. "Peculiarities of light scattering by droplet aerosol in a divergent CO₂ laser beam" *Applied Optics* Volume 26, Number 24 (December 15, 1987) pp 5307-5310
- [33] Wasow, Wolfgang. *Asymptotic Expansions for Ordinary Differential Equations* New York: John Wiley (1965)
- [34] Whittaker, E. T. and G. N. Watson. *A Course of Modern Analysis* London: Cambridge University Press (1986)

SCATTERING BY SPHERES OF NARROW SIZE DISTRIBUTION

R.T. WANG

Space Astronomy Laboratory, Institute for Space Science & Technology, Inc.
Gainesville, FL 32609

RECENT PUBLICATIONS, SUBMITTALS FOR PUBLICATION AND PRESENTATIONS:

A) R.T. Wang and H.C. van de Hulst, "Rainbows: Mie computations and the Airy approximation," *Applied Optics*, 30, 106-117 (1991).

B) J.I. Hage, J.M. Greenberg and R.T. Wang, "Scattering from Arbitrarily Shaped Particles: Theory and Experiment," *Applied Optics*, 30, 1142-1152 (1991).

C) R.T. Wang, "Rainbows and Particle Characterization," submitted to Proc. of the '1990 CRDEC Scientific Conference on Obscuration and Aerosol Research, Battelle Edgewood Operation (Sept. 1990).

D) R.T. Wang, presented at the 1991 CRDEC Scientific Conference under the same title as this article.

ABSTRACT

This article is to summarize an extensive theoretical computation on Mie scattering by spheres whose size is distributed according to the Hansen-Travis' standard size distribution ([Ref. 3]; often abbreviated as the gamma distribution) within narrow limit. The results are presented in graphical forms to show some interesting findings on rainbow and glory phenomena. Comparison of the microwave experiment on scattering by randomly oriented, rough particles [Ref. 7] and the Mie scattering calculation for narrow size distribution of spheres, is also made. This article is an integral part of work planned for submission to public journals.

1. Introduction

Aerosols in the atmosphere are usually found in a wide spread of sizes, shapes and optical properties. Many circumstances exist, however, that we may find fascinating optical phenomena (such as the glory) resulting from the scattering by remarkably uniform particulates. We restrict the discussion here to spherical particles and assume they have the same refractive index $m = m' - im''$. In the following Sec. 2 we briefly explain the mathematics involved in evaluating the scattering by spheres whose sizes are distributed according to the Hansen-Travis' standard size distribution (or simply the gamma distribution [Refs. 2, 3]). The stable, efficient Mie codes [Ref. 8] are employed in all numerical calculations. Sec. 3 illustrates the rainbow intensity profiles for a narrow size distribution of water drops around the effective diameter $2a_0 = 400 \mu\text{m}$ while Sec. 4 depicts the intensity and polarization profiles of the glory scattering by four types of narrow-size-distributed H_2O drops with $2a_0 = 12.5 \mu\text{m}$. Comparison of the microwave angular scattering functions for randomly oriented rough particles [Ref. 7] with three types of the gamma distribution is made in Sec. 5. Summary is made in Sec. 6.

2. Mie Theory Evaluation of the Scattering by Size-distributed Spheres.

* For the distribution function we take the Hansen-Travis' standard size distribution (often abbreviated as the gamma distribution [Ref. 3]), so that the particle number density $n(x)$ at the particle size parameter $x = 2\pi a/\lambda$ is :

$$n(x) = \text{const. } x^{(1-3b)/b} \exp \left[-\frac{x}{x_0 b} \right] \quad (2.1)$$

where b denotes the effective variance of the distribution, which is a measure of the spread of $n(x)$ around the effective size parameter $x_0 = 2\pi a_0/\lambda$. a_0 is the effective particle radius, corresponding to a certain mean radius of the spheres.

* The perpendicular and parallel components of Mie scattering intensity for single sphere are respectively [Refs. 1, 2, 5, 6]:

$$i_1(x, m, \theta) = \left| \sum_{n=1}^{n_{\max}} \frac{2n+1}{n(n+1)} (a_n \tau_n(\mu) + b_n \tau_n(\mu)) \right|^2$$
$$i_2(x, m, \theta) = \left| \sum_{n=1}^{n_{\max}} \frac{2n+1}{n(n+1)} (a_n \tau_n(\mu)) + b_n \tau_n(\mu) \right|^2 \quad (2.2)$$

$\mu = \cos\theta$, $\pi_n(\mu) = dP_n(\mu) / d\mu$, $\tau_n(\mu) = \mu\pi_n(\mu) - (1-\mu^2)d\pi_n(\mu) / d\mu$, and $P_n(\mu)$ is the n-th order Legendre Polynomial of μ .

* The corresponding scattering intensity components for the size distribution are evaluated by integrating (2.2) over x according to the weighting function $n(x)$ of (2.1):

$$I_1 = \frac{\int_{x_1}^{x_2} i_1(x, m, \theta) n(x) dx}{\int_{x_1}^{x_2} n(x) dx} \quad (2.3)$$

$$I_2 = \frac{\int_{x_1}^{x_2} i_2(x, m, \theta) n(x) dx}{\int_{x_1}^{x_2} n(x) dx}$$

* Expressions for the total scattering intensity for unpolarized incident light and the degree of polarization of the scattered light from the distribution are then:

$$S_{11} = (I_1 + I_2) / 2 \quad (2.4)$$

$$P = (I_1 - I_2) / (I_1 + I_2)$$

By virtue of the exponential dependence in (2.1), the integration limits x_1 and x_2 in (2.3) are chosen in such a way that both $n(x_1)$ and $n(x_2)$ fall off from $n(x_c)$ by four orders of magnitude, thereby contributing little to the integrals, i.e., to the scattering. The smaller the value of b , the more rapidly $n(x)$ falls off from $n(x_c)$, and thus x_1 and x_2 get closer to each other and the distribution becomes narrower. Also, in (2.3) a smaller number of divisions, n_{div} , is needed for the interval (x_1, x_2) . For example, $b=0.005$ gives a rather narrow distribution so that $x_1 = 0.71x_c$ and $x_2 = 1.32x_c$, and $n_{div} = 40$ was found to give fairly good convergence of (2.3). We also noticed then the further increase of n_{div} beyond $n_{div} \geq 160$ did not improve substantially the accuracy of evaluating (2.3).

The efficient Mie codes described in [Ref. 8] were employed to carry out the integration (2.3) for the size distribution. Due to the numerical stability, only the 8-digits, single-precision arithmetics (on VAX 11/730 or VAX 11/750 computers) Mie code was found adequate to cover up to $x_c \approx 7000$ in particle size. The CPU time T required for a typical calculation on VAX 11/750 was also clocked:

$$T \approx 0.63 \text{ millisecond} \cdot x_c \cdot n_{div} \cdot (\# \text{ of scattering angles}) \quad (2.5)$$

3. Rainbows by Water Droplets of Narrow Size Distribution

With a small effective variance, $b = 0.005$, we depict in Fig. 1 the rainbow intensity profiles at three visible wavelengths for narrow-size-distributed water droplets with an effective diameter $2a_e = 400 \mu\text{m}$. The Mie results of S_{11} for the size distribution are shown by continuous curves, while the Airy theory S_{11} [Ref. 8] for single size x_e are plotted by dotted curves. The primary rainbow for which $p = 2$, is on the right-hand-side, and the secondary rainbow ($p = 3$) is on the left. Fig. 1 is selected out of many similar plots for various sizes, and we summarize only a few outstanding features:

- (1) Compared to the Mie rainbow profile for single-sized droplets, the Mie S_{11} profile is considerably smoothed out even with such a narrow size distribution. This smoothing is accompanied by the smearing out of the supernumeraries of both $p = 2$ and $p = 3$ rainbows, especially at the 2nd and higher order supernumeraries.
- (2) The Airy and Mie theory results agree strikingly well, both on the magnitude and the position of the main peaks of the primary ($p = 2$) and the secondary ($p = 3$) rainbows. In contrast to the long hours of Mie computation by VAX 11/750, the Airy calculation requires less than two minutes by a 100 times slower PDP11/23 computer. We reiterate therefore that Airy theory is a powerful tool in laboratory study of rainbows.

4. Glories by Water Drops of Narrow Size Distribution

More elusive, but no less important than rainbows, are the glory phenomena, the enhanced backscatterings near $\theta = 180^\circ$, excellent expositions of which based on single-sized droplets can be found in [Ref. 4, 6]. Briefly stated, a glory phenomenon can be seen by an observer as rings, which are often colored, around his own head's shadow on a water droplets cloud. We know this happens only when the droplets are remarkably uniform in size and optical property. Using the similar Mie scattering programs as in the previous sections, an extensive study has been made for a number of effective variances b as well as effective sizes x_e . We present, however, only one set of glory intensity/polarization profiles for water drops of $2a_e = 12.5 \mu\text{m}$, at three visible wavelengths (Fig. 2). In addition to curves corresponding to the effective variances $b = 0.001$, $b = 0.005$ and $b = 0.025$, the glory profiles due to the single size with $2a_e = 12.5 \mu\text{m}$ are also shown for direct comparison.

A few interesting features noted:

- (1) As in the case of rainbows, the effect of the droplet size being distributed is to smooth out the glory intensity/polarization profiles, and the smoothing is more extensive as the effective variance b increases.

- (2) The number of glory intensity peaks/troughs in a given backscatter angular interval increases with the droplet size x_c . Unlike rainbows, the glory can only be clearly seen for relatively small size x_c . This is because the angular spacings between successive glory rings become so small for large x_c (≥ 1000) that only a small spread in droplet size would smear out the profile.
- (3) The intensity profiles for the size-distributed droplets are noticeably different from those for the single size, both in magnitude and in the angular positions of peaks/troughs.
- (4) A distinct glory is observable for $b \leq 0.025$, especially near the first ring closest to $\theta = 180^\circ$. With $b = 0.025$, the second higher rings are considerably smeared out.
- (5) The glory light is positively polarized ($\text{Pol} \sim +50\%$) near $\theta \sim 179^\circ$. This angle depends slightly on x_c (i.e., get closer to $\theta = 180^\circ$ as x_c increases), but is rather insensitive to the value of b .
- (6) Except by the straight Mie computation or via the complex angular momentum theory of Nussenzveig-Kahre [Ref. 4], no systematic explanations are as yet available for the glory phenomena.

5. Comparison of Microwave Scattering by Randomly Oriented Rough Particles with Mie Scattering by Spheres of Narrow Size Distribution

Extending the similar Mie calculations as in the preceding sections, we now turn into a closer look at the microwave scattering by randomly oriented rough particles [Re. 7], where we had also reported the comparisons with both single-sphere and $b = 0.005$ gamma-size-distribution Mie calculations.

Each large data symbol in Figs. 3 & 4 represents the averaged microwave data at each θ and polarization setting (11, 22, or 12) over 272 random orientations of each target, whose particle shape is shown at the figure's upper right corner. x_v denotes the volume-equivalent size parameter, and the two particles shown are both efficient scatterers for having the volume-equivalent phase shift parameter $\rho_v = 2 \cdot x_v \cdot (m^2 - 1)$ near 4, i.e., near the first major resonance. Both particles look like spheres of roughened surface; hence the name, "rough particle."

I_{11} is the intensity of scattering when both the transmitter and receiver polarizations are vertical, I_{22} is for both polarizations being horizontal, and I_{12} ($= I_{21}$) is where one of them is vertical but the other is horizontal. In general, $I_{12} \neq 0$ for nonspherical particles. Even though its

magnitude is rather small compared to I_{11} or I_{22} , the correct expressions for the total intensity S_{11} for unpolarized incident light and the degree of polarization, P , have to take I_{12} into account:

$$S_{11} = \frac{1}{2} (I_{11} + I_{22} + 2I_{12}) \quad (5.1)$$

$$P = (I_{11} - I_{22}) / (I_{11} + I_{22} + 2I_{12})$$

Continuous curves in Figs. 5-6 are calculated by Mie theory for the gamma-size-distributed spheres with $x_e = x_v$ and with $b = 0.001$, $b = 0.005$ and $b = 0.025$, respectively. For readability, the $b = 0.005$ curves are accented by \longleftrightarrow , which seem to give the closest match to the observed microwave data.

Brief summary on the comparison:

- (1) For both rough particle shapes, the intensity component I_{11} is rather well predicted by the narrow size distribution of spheres having $x_e = x_v$. The match between the experiment and theory is perhaps at its best with $b = 0.005$.
- (2) Similar match also exists for the intensity components I_{22} , except in the larger scattering angles: $\theta \gtrsim 80^\circ$, where the theory tends to overestimate the I_{22} magnitude.
- (3) If the rough particles in [Ref. 7] for other sizes are included, the gamma-size-distribution Mie theory gives, in general, a larger backscatter intensity than the experiment.
- (4) For the particle size in Figs. 3 & 4 (or smaller), the polarization by rough particles can be well approximated by the gamma-size-distribution of spheres, but the best effective variance b to be employed is not well defined.
- (5) Since the best match between the experiment and the theory is in $\theta \lesssim 80^\circ$, wherein most of the scattered energy is directed, it is now clear that the asymmetry factor of scattering by rough particles is well approximated by the gamma-distribution Mie theory.

6. Summary

The present Mie calculation work for the narrow-size-distribution of spheres led to the following conclusions:

- * Rainbow intensity profiles can be well predicted by the classical Airy theory for particles as small as $x_e \sim 200$. Its match with Mie theory is particularly excellent at the first peak and a few supernumeraries, both in magnitude and in positions of the peaks. Since Airy theory is much simpler to evaluate than Mie's, it is obviously a powerful tool in characterizing a particle.
- * A realistic explanation of the backscatter glory phenomena may have to take the size distribution of droplets into account. We demonstrated that the Hansen-Travis' standard size distribution function (the gamma distribution) was a very useful model to represent such a distribution.
- * Mie computation of scattering by gamma-size-distributed spheres was shown to match very well the observed angular scattering by a rough particle with $x_v = x_e$, especially at forward angles $\theta \lesssim 80^\circ$ where the scattered radiation is concentrated. Thus the Mie theory would provide precise information on the asymmetry factor of scattering, which is also a crucial information on a radiative transfer problem.

ACKNOWLEDGMENTS

This work was motivated during the tenure of U.S. Army Research Office's contract DAAL03-86-K0021 to the University of Florida. The author thanks Prof. H.C. van de Hulst for many stimulating discussions. He is also indebted to Prof. J.L. Weinberg for providing the computing facility.

References

1. Bohren, C.F. and Huffman, D.R., Absorption and Scattering of Light by Small Particles (Wiley, New York, 1983).
2. Deirmendjian, D., Electromagnetic Scattering on Spherical Polydispersions (Elsevier, New York, 1969)
3. Hansen, J.E. and Travis, L.D., "Light Scattering in Planetary Atmospheres," Space Science Reviews **16**, 527-610 (1974).
4. Kahre, V. and Nussenzweig, H.M., "The Theory of the Glory," in Statistical Mechanics and Statistical Methods in Theory and Application, U. Landman, Ed. (Plenum, New York, 1977), pp. 723-764.
5. Kerker, M., The Scattering of Light and Other Electromagnetic Radiation, (Academic, New York, 1969).
6. Van de Hulst, H.C., Light Scattering by Small Particles (Wiley, New York, 1957).
7. Wang, R.T. "Angular Scattering by Rough Particles," in Proc. of the 1984 Scientific Conference on Obscuration and Aerosol Research, R. Kohl and D. Stroud, Eds., U.S. Army CRDC-SP-85007, pp. 327-363 (June 1985).
8. Wang, R.T. and van de Hulst, H.C., "Rainbows: Mie Computations and the Airy Approximation," Appl. Opt. **30**, 106-117 (1991).

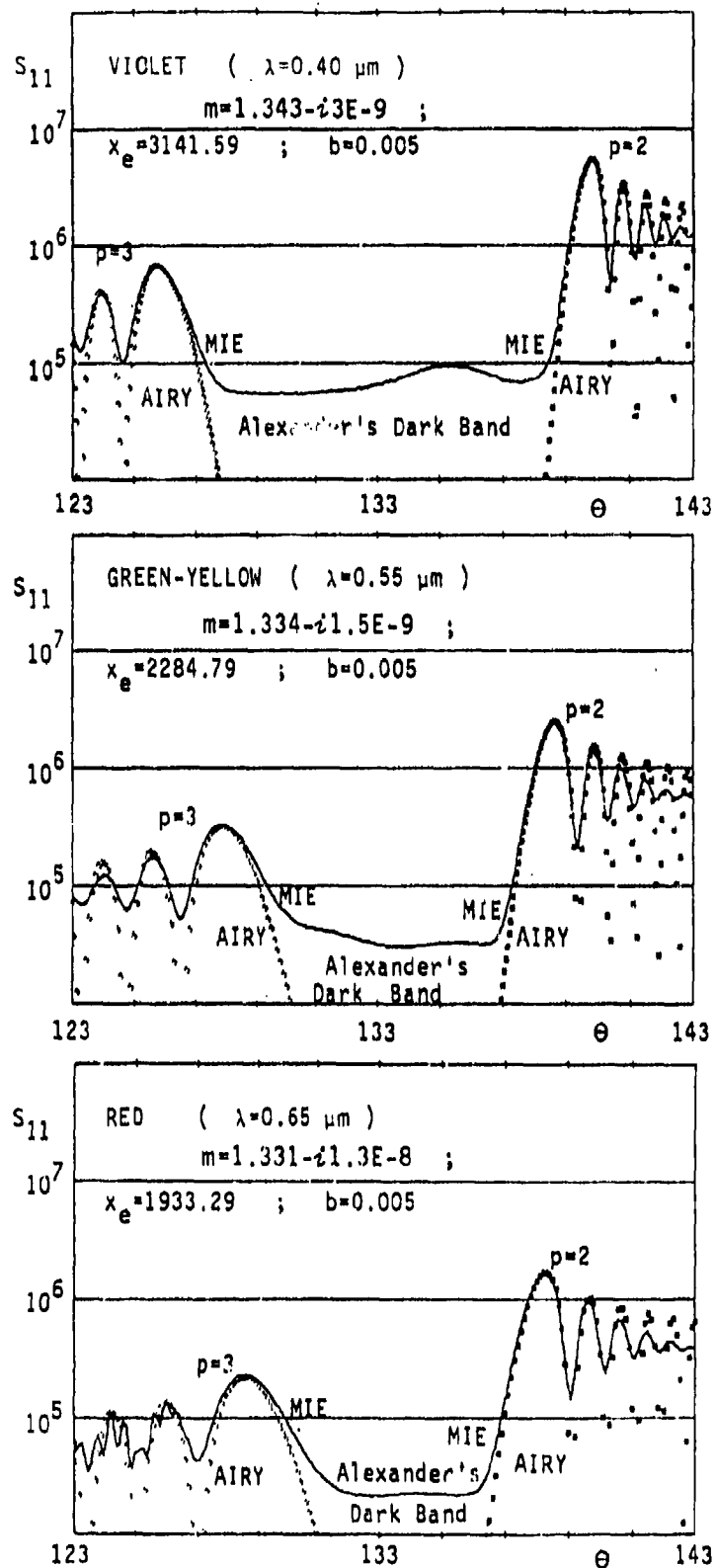


Fig. 1 Mie rainbow intensity profiles for narrow, gamma-size-distributed water drops around $2a_e=0.4 \text{ mm}$. Airy profiles are for the single size: $x_e=2\pi a_e/\lambda$.

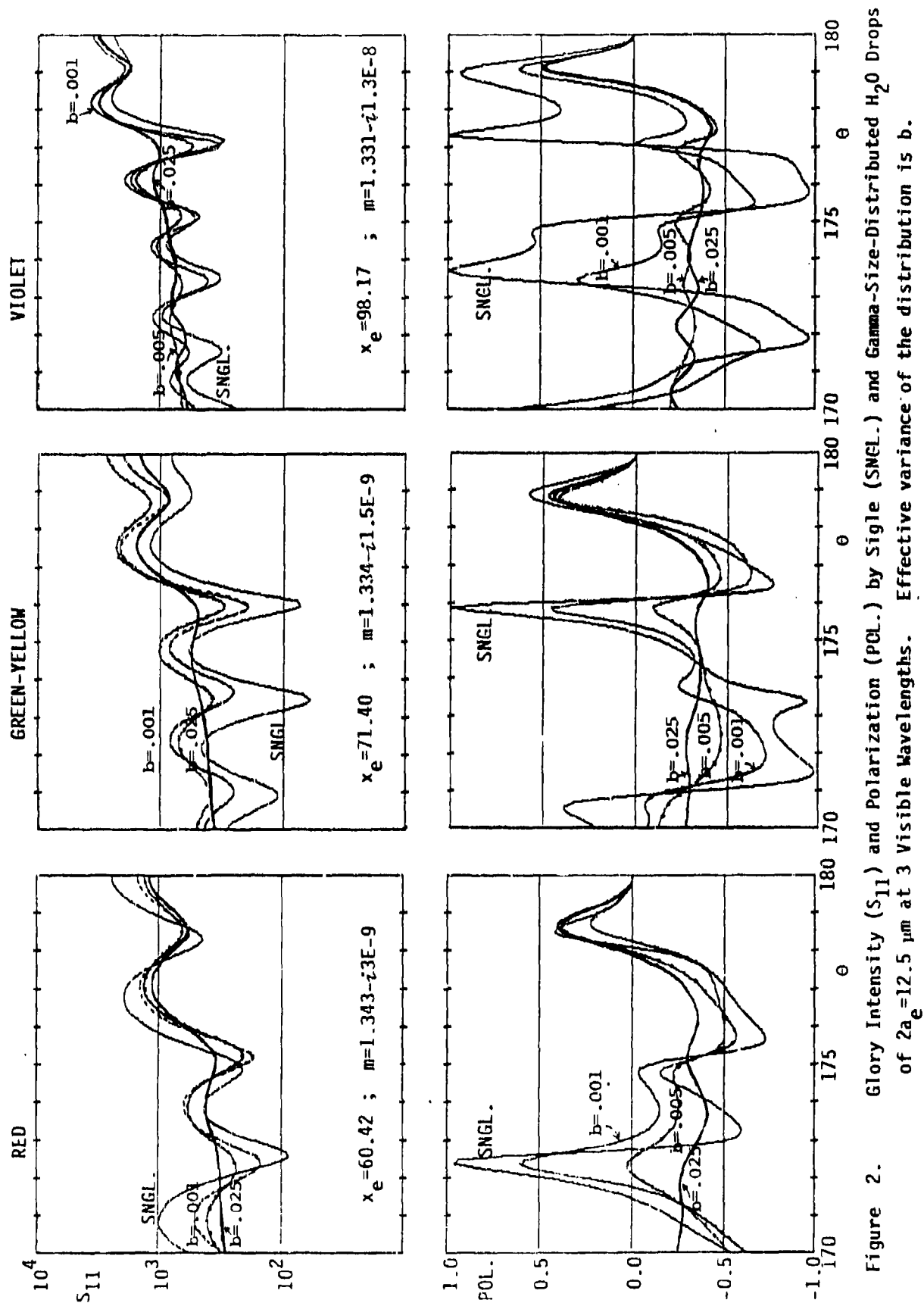


Figure 2. Glory Intensity (S_{11}) and Polarization (POL.) by Sigle (SNGL.) and Gamma-Size-Distributed H_2O Drops of $2a_e = 12.5 \mu m$ at 3 Visible Wavelengths. Effective variance of the distribution is b .

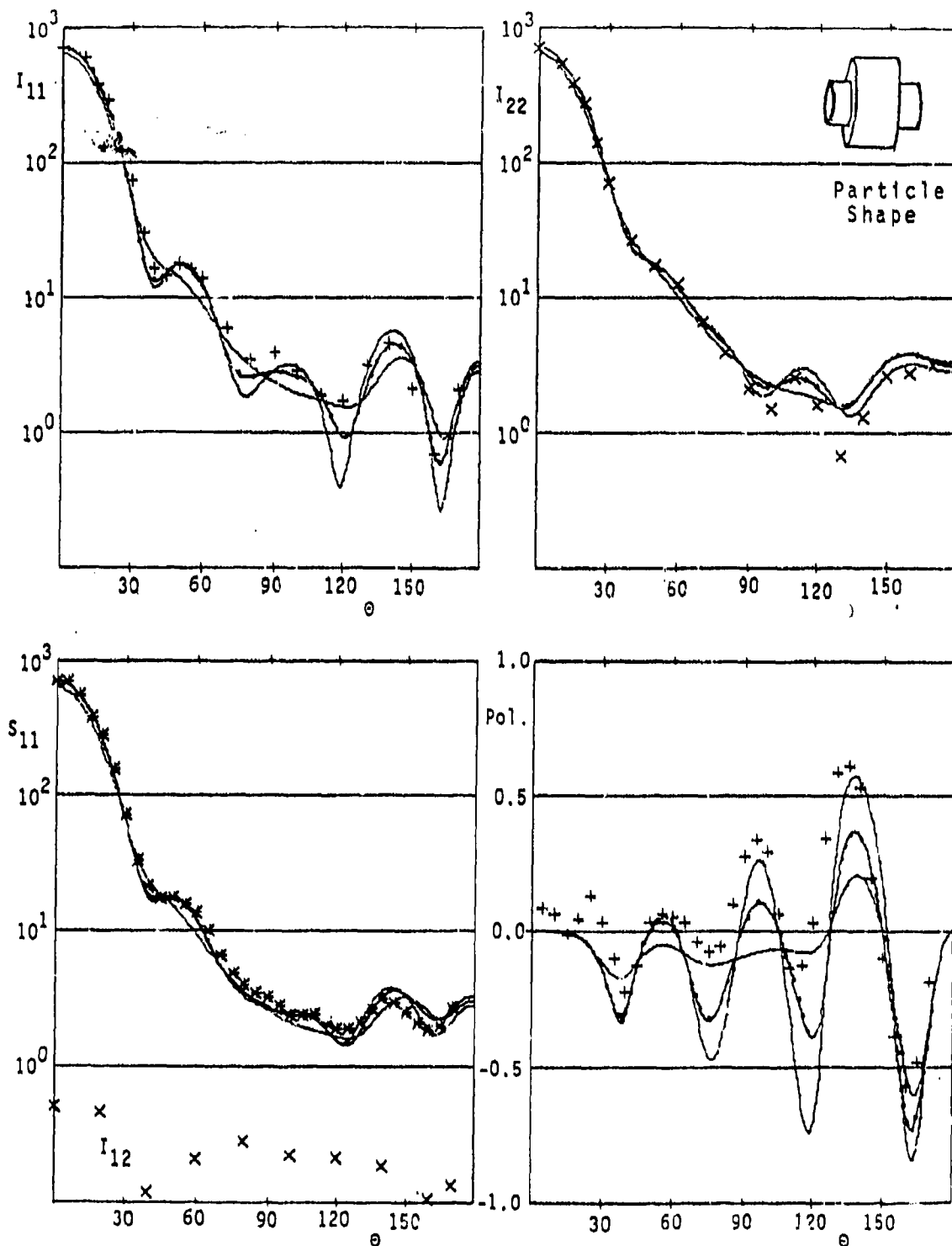


Figure 3. Microwave Scattering Data (symbols) for a Randomly Oriented Rough Particle with $x_v = 5.184$ and $m = 1.388 - i0.005$. Curves are by Mie theory for Hansen-Travis' standard-size-distributed spheres with effective variances $b = 0.001$, $b = 0.005$ and $b = 0.025$, respectively.

(\rightarrow \rightarrow \rightarrow)

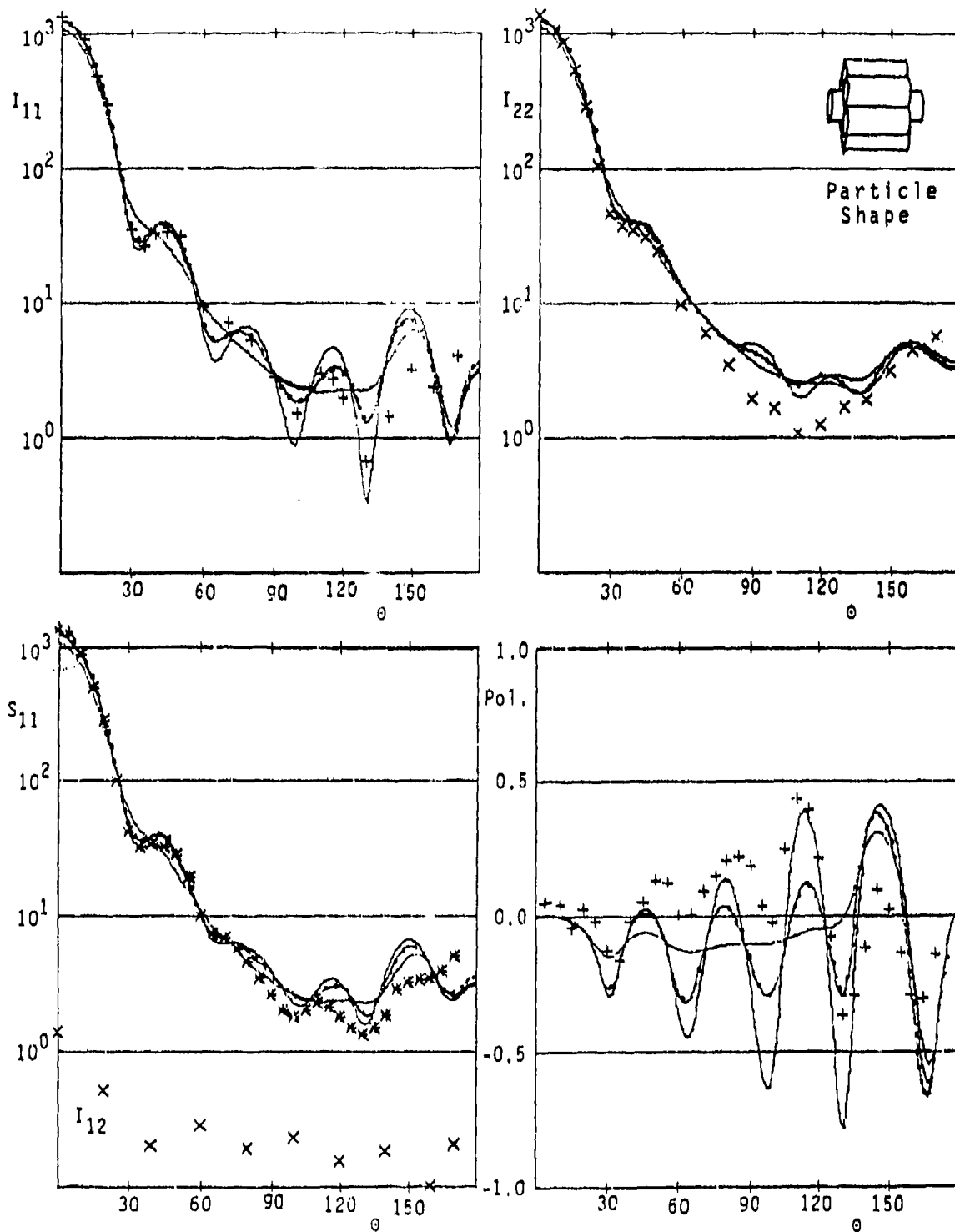


Figure 4. Microwave Scattering Data (symbols) for a Randomly Oriented Rough Particle with $x_v=6.069$ and $m=1.367-i0.005$. Curves are by Mie theory for Hansen-Travis' size-distributed spheres with effective variances $b=0.001$, $b=0.005$ and $b=0.025$, respectively.
(\rightarrow \rightarrow \rightarrow)

VARIATIONAL SCATTERING CALCULATIONS WITH IMPEDANCE BOUNDARY CONDITIONS

B. J. Stoyanov and R. A. Farrell
The Milton S. Eisenhower Research Center
The Johns Hopkins University Applied Physics Laboratory
Laurel, MD 20723

RECENT PUBLICATIONS, SUBMITTALS FOR PUBLICATION AND PRESENTATIONS:

- A) D. E. Freund and R. A. Farrell, "A Variational Principle for the Scattered Wave," *J. Acoust. Soc. Am.* 87, 1847-1860 (1990).
- B) B. J. Stoyanov, R. A. Farrell, and J. F. Bird, "Asymptotic Expansions of Integrals of Two Bessel Functions," in *Asymptotic and Computational Analysis*, edited by R. Wong (Marcel Dekker, Inc., New York, 1990), pp. 723-740.
- C) D. E. Freund and R. A. Farrell, "Variational Scattering Calculations for a Prolate Spheroid," in *Program of the 121st ASA Meeting* (Baltimore, 29 April-3 May 1991), *J. Acoust. Soc. Am.* 89 (No. 4, Pt. 2), 1994 (1991).
- D) B. J. Stoyanov and R. A. Farrell, "Variational Scattering Calculations with Impedance Boundary Conditions," presentation at the 1991 CRDEC Scientific Conference on Obscuration and Aerosol Research (U.S. Army Chemical Research, Development, and Engineering Center, Aberdeen Proving Ground, MD, 24-27 June 1991).

Abstract

Simple and efficient trial fields are developed for the transverse-magnetic plane-wave scattering from penetrable cylinders with impedance boundary conditions. The trial fields are capable of satisfying the boundary conditions, and incorporate a suitable shadow-imitating factor with an adjustable parameter. As is explicitly demonstrated for this test problem, when such trial fields are employed in an appropriately formulated Schwinger-type variational principle, accurate scattering amplitudes and cross sections are obtained for all size parameters and arbitrary scattering directions. Further investigations are underway for the more difficult case of transverse-electric polarization.

Introduction

This work is an extension of the previous variational calculations involving idealized, impenetrable scatterers [1-11] to more realistic penetrable scatterers

with impedance boundary conditions (IBCs). It was shown earlier [1,2,5] that the so-called boundary-Born trial functions with the built-in capability of satisfying the homogeneous Dirichlet and Neumann boundary conditions (BCs) yield reasonable broadband accuracy for a scalar plane-wave scattering from a perfectly-conducting cylinder or a hemicylindrically-embossed plane. However, the large size parameter limits ($ka \gg 1$, where a is the cylinder radius, and $k \equiv 2\pi/\lambda$ is the wavenumber, with λ being the wavelength of incident radiation) of the variational scattering amplitudes in the forward and specular direction were incorrect. In addition, the variational results were contaminated with spurious wiggles or spikes at moderate and large size parameters. Later, upon realization of the crucial role of the shadow-forming wave in forward scattering [12], it was found [7] that, for scatterers with Dirichlet boundary condition, premultiplying the boundary-Born trial function by a simple shadow-imitating factor not only corrected the large size parameter limits but also effectively removed the spurious spikes and wiggles. This was explicitly demonstrated for simple test problems such as plane-wave scattering from perfectly-conducting cylinders [7] and hemicylindrically-embossed planes [8], as well as soft spheres [9,10] and prolate spheroids [11]. Very accurate variational results were obtained for all size parameters and arbitrary scattering angles. For scatterers with Neumann's boundary condition, the boundary-Born trial functions with simple shadowing are not as accurate, and further investigations are underway.

In this paper, after a brief discussion of BCs suitable for penetrable scatterers, the Schwinger-type variational principle and boundary-Born trial fields with simple shadowing are introduced and discussed for a special problem of plane-wave scattering from an infinitely-long impedance cylinder. The cross-sectional view of the problem is depicted in Fig. 1, where the axis of a cylinder having radius a is along the z direction, \vec{k}_i , \vec{k}_s are the incident and scattered

propagation vectors, respectively, and ϕ_s is the scattering angle. The usual polar coordinates ρ, ϕ are used to specify an arbitrary point in a plane normal to the cylinder axis. Only normal plane-wave incidence is considered. [It is unfortunate but, unlike the idealized case of perfect conductor, a general three-dimensional (3-D) problem of oblique incidence cannot be reduced to two scalar (i.e., transverse-magnetic (TM) and transverse-electric (TE)) 2-D scattering problems even for a homogeneous impedance cylinder.] Without loss of generality, the incident plane wave propagating in the x direction is assumed to be of unit amplitude.

It is worthwhile to notice at this point that our approach to developing mathematically simple and physically plausible trial fields [13] by incorporating the essential physics inherent in scattering processes [1,2,5,7,8,14] is a generic one and is not limited to special cases of scattering problems. We are interested in scattering from canonical separable shapes [15,16] because manageable exact solutions are available for these scattering problems, so that the variational calculations can be tested analytically and/or numerically for all size parameters, scattering directions, and polarizations.

The scattering problem can be defined as the solution of the Helmholtz equation for a plane wave normally incident on a cylindrical object where certain BCs are satisfied. At this level, the present investigation examines whether the use of "boundary-Born trial fields with shadowing" can produce all-frequency accuracy in variational solutions with the standard Leontovich BC and with the curvature-dependent IBC. In other words, our goal is to test the efficacy of our trial field design procedure, which is based on physical insight. At a different level, however, one can be confronted with the need to calculate the scattering of an electromagnetic field from a penetrable scatterer. In that event, one is interested in whether IBCs are a reasonable approximation to the rigorous BCs.

These latter issues are explored in the next section and the variational procedures are tested in the final section.

Boundary Conditions for Penetrable Scatterers

Penetrable scatterers are represented by dielectric and/or magnetic objects in electromagnetics and by elastic bodies in acoustics. The rigorous boundary conditions for such scatterers are well known [12,17,18]; e.g., in electromagnetics these consist of the continuity of tangential components of the electric (\vec{E}) and magnetic (\vec{H}) fields at the scatterer boundary. Generally, this requires knowledge of the fields both outside and inside the scatterer, and thus complicates the problem. For the problem of plane-wave scattering by an infinitely-long circular cylinder at normal incidence (see Fig. 1), the rigorous boundary conditions can be written down for both TM($\vec{E} \uparrow \uparrow \hat{z}$) and TE($\vec{H} \uparrow \uparrow \hat{z}$) polarizations as

$$\left. \begin{aligned} \psi_{out}|_s &= \psi_{in}|_s \\ \zeta \frac{\partial \psi_{out}}{\partial n}|_s &= \frac{\partial \psi_{in}}{\partial n}|_s \end{aligned} \right\} \text{ with } \zeta = \begin{cases} \mu / \mu_0, & \text{TM } (\psi = E_z) \\ \epsilon / \epsilon_0, & \text{TE } (\psi = H_z) \end{cases} \quad (1)$$

where ψ represents the electric or magnetic field component along the cylinder axis, ϵ_0, ϵ and μ_0, μ denote electric permittivities and magnetic permeabilities outside and inside the cylinder, respectively, and the normal derivatives are evaluated at the cylinder's surface, $\rho = a$.

On the other hand, significant simplifications usually arise if approximate boundary conditions, such as IBCs, can be employed, since these involve fields only outside a scatterer characterized by relevant surface impedance. The (conventional or standard) Leontovich IBC in its simplest form is [19,20]

$$\vec{E} - \hat{n}(\vec{E} \cdot \hat{n}) = Z_s(\hat{n} \times \vec{H}) \quad (2)$$

where $Z_s = \sqrt{\mu / \epsilon}$ is the surface impedance of the scatterer, and \hat{n} is the unit vector in the outward normal direction.

In many practical situations, the concept of surface impedance as a boundary condition is a suitable approximation to the true physics of the scattering problem, being generally applicable to the so-called locally-reacting surfaces, examples of which are well-known in acoustics as well as electromagnetics [18]. In particular, it has been used to model scatterers with high but finite conductivity, to model surface roughness, to account for coating layers that produce microwave absorption, and to model scattering from overdense plasma [15,21].

For the cylinder scattering, the Leontovich IBC reduces to

$$\left. \frac{\partial \psi}{\partial n} \right|_s + ik\eta \psi|_s = 0 \quad \text{with} \quad \eta = \begin{cases} 1/Z, \text{ TM } (\psi \equiv E_z) \\ Z, \text{ TE } (\psi \equiv H_z) \end{cases} \quad (3)$$

where $Z = Z_r \equiv Z_s / Z_0$ is the relative surface impedance, and $Z_0 = \sqrt{\mu_0 / \epsilon_0} = 120\pi$ (ohms) is the intrinsic impedance of free space. A time variation $e^{-i\omega t}$ has been assumed, with ω being the frequency of the incident wave. In this paper, we shall consider the case of a nonferrous ($\mu \approx \mu_0$) metallic conductor or a lossy dielectric for which $|Z_s| < Z_0$. Then the relative surface impedance can be conveniently expressed [22] in terms of the dimensionless skin-depth parameter $k\delta$ as

$$Z_r = (1 - i)k\delta / 2 \quad (4)$$

where $\delta \equiv \sqrt{2 / \omega\mu\sigma}$ is the skin depth, and σ the conductivity of the scatterer. Note also that in this case, the complex refractive index of the material relative to free space is simply the reciprocal of the relative surface impedance, i.e.,

$$N = \sqrt{\epsilon\mu / \epsilon_0\mu_0} = 1 / Z_r = (1 + i) / k\delta. \quad (5)$$

The Leontovich IBCs are a valid approximation to the rigorous boundary conditions in scattering problems when the following three conditions [20,22] are satisfied, viz.,

$$|N| \gg 1, \quad (6a)$$

$$|\operatorname{Im} N|ka_{\min} \gg 1, \quad (6b)$$

where a_{\min} is the smallest radius of curvature, and

$$(\ell/\delta)^2 \gg 1 \quad (6c)$$

where ℓ is the distance to the nearest significant source. For the problem under consideration, the last requirement is automatically fulfilled, and the first two can be stated as

$$(k\delta)^2 \ll 1 \text{ and } \delta/a \ll 1. \quad (7)$$

More specifically, extensive numerical calculations [23] indicate that when $k\delta \leq 0.141$ and $\delta/a \leq 0.435$ the Leontovich IBCs are expected to provide accuracy with ~1% error at all scattering angles and $0.5 \leq ka \leq 500$.

Generally, for scatterers of larger values of curvature and surface impedance, more sophisticated curvature-dependent IBCs provide a better overall approximation [22]. For the cylinder case, these are given by the same expression (3), except that now

$$Z = \begin{cases} Z_r(1 + iZ_r/2ka) & , \text{ TM} \\ Z_r(1 + iZ_r/2ka)^{-1} & , \text{ TE} . \end{cases} \quad (8)$$

Note the explicit dependence of Z on the radius of curvature. For small surface curvatures (large size parameters) this Z tends to the usual Leontovich form, which therefore can be considered as the zero-order term in the expansion of the surface impedance in terms of the curvature [24].

There are different forms of curvature-dependent IBCs available in the literature [22,24,25], some of which were originally developed by Leontovich [19]. Our numerical and analytical asymptotic analyses show that the choice made in Eq. (8) yields the correct ka -dependence (albeit with an incorrect factor) of the lead term in the small size parameter expansion of the scattering amplitude T defined as in Ref. 16.

Figure 2(a) illustrates the effects of BCs on the TM forward scattering cross-section by comparing results using the (conventional) Leontovich BC, Eq. (3), the curvature dependent IBC, Eq. (8), and the rigorous BC, Eq. (1). These cross sections were calculated with the exact Mie-type solutions derived by standard separation-of-variables techniques in terms of Rayleigh series [16,22]. Three markedly different values of the skin depth are presented to demonstrate the importance of this parameter. Note that for the smallest skin-depth considered, $\lambda\delta = 0.005$, the field barely penetrates the scatterer and all three BCs yield results that are indistinguishable from one another on the scale of plotting (top curve). For larger skin-depth parameters and small size parameters the curvature-dependent IBC provides a more accurate approximation to the exact BC than the Leontovich BC does. All the results coincide at large values of the size parameter, ka , approaching the same limit value of unity, as they should because the field scattered at and very near the forward direction is the same in the high-frequency limit for all cylinders of width $2a$, regardless of the cylinder material, incident polarization, or cylinder geometric cross section [12,16]. For other scattering directions, even though the three BCs yield almost identical results for $ka \gg 1$, these results depend on the skin-depth parameter and polarization, as well as scattering angle.

Tests of Variational Procedures

Our primary interest is not to investigate the relative virtues of various IBCs for approximating the rigorous BCs, but rather to develop and test simple broadband variational solutions for a variety of BCs useful in practical applications. As noted above, our previous experience suggests BCs and shadowing can provide physical insights that prove rewarding in the design of trial fields. The fundamental question addressed in the rest of this paper is whether these considerations continue to hold in the case of penetrable scatterers. Thus we will concentrate on comparisons between exact and variational results for a given BC, and not on the appropriateness of that BC for a given physical problem.

In deriving efficient variational principles and trial fields for impedance scatterers, we follow the approach developed earlier [1,2,7,8] for impenetrable scatterers. Impenetrable scatterers are, of course, appropriately characterized by the well-known [12] Dirichlet (or soft) BC

$$\psi|_s = 0, \text{ TM } (\psi \equiv E_z) \quad (9)$$

and Neumann (or hard) BC

$$\frac{\partial \psi}{\partial n}|_s = 0, \text{ TE } (\psi \equiv H_z) . \quad (10)$$

These idealized BCs represent a special case ($Z_s = 0$) of the IBCs in Eq. (3). The formal structure of the IBCs as a combination of the field and its normal derivative evaluated at the scatterer surface allows one to anticipate the performance of the boundary-Born trial fields with simple shadowing (see below) from the results for impenetrable scatterers [7-11]. In particular, whenever the contribution from the field normal derivative to the IBC is dominant, as is the

case for TE polarization, one can expect inaccuracies similar to those encountered in the variational calculations with the Neumann BC. Our numerical and analytical analyses corroborate this foresight, but will not be discussed here. Physically, as for impenetrable scatterers, this discrepancy is due to the well-established fact [26] that the creeping wave effects are significant for TE polarization, and should be incorporated into the trial fields to render them more accurate in the resonance region. Further investigations of this problem are underway.

The Schwinger-type variational principle [12] for the scattering amplitude for the impedance cylinder problem under consideration can be derived in a straightforward manner and written down in the standard form

$$T^V = N\tilde{N} / D \quad (11a)$$

in terms of line integrals along the cylinder circumference

$$N \propto \int_0^{2\pi} d\phi \left[h(\phi; \phi_s, \eta) K(\vec{\rho}; \phi_i) e^{-i\vec{k}_s \cdot \vec{\rho}} \right]_{\rho=a} \quad (11b)$$

$$\tilde{N} \propto \int_0^{2\pi} d\phi' \left[\tilde{h}(\phi'; \phi_i, \eta) \tilde{K}(\vec{\rho}'; \phi_s) e^{i\vec{k}_i \cdot \vec{\rho}'} \right]_{\rho'=a} \quad (11c)$$

$$D \propto \int_0^{2\pi} d\phi \int_0^{2\pi} d\phi' \left[K(\vec{\rho}; \phi_i) G(k|\vec{\rho} - \vec{\rho}'|; \eta) \tilde{K}(\vec{\rho}'; \phi_s) \right]_{\substack{\rho=a \\ \rho'=a}} \quad (11d)$$

Here

$$K \propto \begin{cases} \partial\psi / \partial\rho|_{\rho=a}, & \text{TM } (\psi \equiv E_z) \\ \psi|_{\rho=a}, & \text{TE } (\psi \equiv H_z) \end{cases} \quad (12a)$$

$$(12b)$$

is the surface current density for each polarization, G is the effective Green function given by a combination of the usual 2-D free-space Green function and its first- and second-order normal derivatives, and h is a simple function of the scattering angle, the impedance parameter, and the integration variable. The quantities with tilde, \tilde{N} , \tilde{K} , and \tilde{h} , represent the adjoint solution, i.e., the solution of the reciprocal problem in which the source and observer are interchanged, so that the reciprocity relation [12,13] is satisfied due to the form of Eq. (11a). Thus, the adjoint field $\tilde{\psi} = \psi(-\tilde{k}_s)$ follows directly from the original field $\psi = \psi(\tilde{k}_i)$ by substitution $\phi_i \rightarrow \phi_s + \pi$. Using Graf's addition theorem [27], the double integral in Eq. (11d) can be reduced to a product of single integrals.

With the correct fields $\psi, \tilde{\psi}$ (and, hence, currents K, \tilde{K}), each of the integrals N, \tilde{N} , and D , as well as their ratio (11a), will yield the correct scattering amplitude T . Then, the differential cross section

$$\sigma = \begin{cases} |T|^2 / (ka)^2 & , \text{ forward } (\phi_s = 0), \\ |T|^2 (4 / \pi ka) & , \text{ otherwise } (\phi_s \neq 0), \end{cases} \quad (13)$$

normalized as for perfectly-conducting cylinders [7], immediately follows. On the other hand, when a trial field containing some error is used for ψ (and $\tilde{\psi}$), the variational-approximate T^V with errors of the second and higher orders is obtained by Eqs. (11) and (12). The first order errors in T^V cancel out due to its inherent stationary property [12], and this is potentially advantageous when compared to other, non-variational approximate techniques.

In developing trial fields for the impedance cylinder problem we followed the Ansatz previously devised for perfect conductors [1,2,7,8]. Namely, starting with the simple Born approximation, i.e., just the incident plane wave, we augment it by the same expression, but evaluated on the scatterer surface and premultiplied by a simple factor, so that the resulting boundary-Born trial

function is capable of satisfying the pertinent BCs. To provide for shadowing, which is important for moderate and large size parameters, this trial function is premultiplied by a simple, shadow-imitating function. The following boundary-Born trial field with shadowing

$$\psi(\vec{\rho}) = [1 - \beta(ka) \cos \phi] \left[e^{i\vec{k}_i \cdot \vec{\rho}} - f(\vec{\rho}) \left(e^{i\vec{k}_i \cdot \vec{\rho}} \Big|_{\rho=a} \right) \right] \quad (14)$$

is capable of satisfying the IBCs by virtue of flexibility provided by $f(\vec{\rho})$. When this trial field is substituted into Eqs. (11),(12), a variational parameter $A(ka, \eta)$ derived from $f(\vec{\rho})$ is obtained, with its "optimal" value found from the stationary condition $\partial T^V / \partial A = 0$.

The shadow-regulating parameter β in Eq. (14) can be adjusted so that the correct large ka -limit of $T^V(\phi_s = 0)$ is obtained [7,8,10], i.e.,

$$T^V(\phi_s = 0) \xrightarrow{ka \rightarrow \infty} T(\phi_s = 0), \quad (15)$$

with the limiting value of T^V derived by employing the asymptotic techniques considered in Ref. 28. According to the physics of wave scattering [12], shadowing is not present for small size parameters because diffraction causes the entire scatterer to be illuminated. Thus, we set $\beta = 0$ for, say, $ka < 1$ by introducing a simple ramp function, $\beta(ka)$. With such a ramp function the shadowed trial field in Eq. (14) goes over to the original boundary-Born field for small ka 's, which yields exceptionally good results in this ka -region for both TM and TE polarizations. It may be noted here that choosing β in this way does not limit the applicability of this procedure to problems where the exact solution is known. All that is actually needed to fix $\beta(ka)$ at large ka is the generic, readily obtainable, physical-optics result for forward scattering. In fact, the variational results

displayed in Figs. 2 and 3 were obtained with a simple, physically reasonable choice of

$$\beta(ka) = \begin{cases} 0, & ka \leq 0.7, \\ (ka - 0.7) / (4.0 - 0.7), & 0.7 < ka < 4.0, \\ 1, & ka \geq 4.0. \end{cases} \quad (16)$$

Numerical results for TM polarization show only minor changes with plausible changes in the choice [10] of the cutoff ka values in the ramp function.

As for perfect conductors [7-11], incorporating the simple shadowing into the boundary-Born trial fields not only corrected the large ka -limit of the TM variational results for forward direction, but also effectively suppressed spurious spikes and/or wiggles for all scattering directions. Thus, while the variational results without shadowing appear to coincide with the exact solutions for the impedance cylinders as plotted in Fig. 2(b), plots on a magnified scale (cf. Fig. 2(c)) reveal significant, ever-increasing errors of the variational results for large size parameters, as well as the presence of spurious wiggles. The simple ramp-function shadowing remarkably removes these discrepancies, as is illustrated in Fig. 2(c). The unshadowed boundary-Born variational results for backscatter are very accurate for small ka 's, but are heavily contaminated with spurious spikes for moderate and large size parameters, as shown in Fig. 3(a). Again, the simple shadowing eliminates the spurious spikes (see Fig. 3(b)), so that the maximum error of less than 4% occurs at $ka \approx 2.1$ for the most demanding case considered of $k\delta = 0.3$ (see Fig. 3(c)).

Summary

For TM scattering from an impedance cylinder, the shadowed-boundary-Born trial fields that incorporate either the Leontovich or curvature-dependent

IBC and simple ramp-function shadowing, yield variational results that are in excellent agreement with the exact solutions for all size parameters and arbitrary scattering angles. Similar results are expected for penetrable scatterers of other shapes and compositions with applicable IBCs to be considered in future research. For TE polarization, the agreement is reasonable but not as accurate, with further investigations underway.

Acknowledgments

We thank S. Favin for his help with the numerical computations. This research was supported by the Navy under contract N00039-89-C-0001.

References

1. J. A. Krill, J. F. Bird, and R. A. Farrell, "Trial Functions in Variational Calculations," in *Proceedings of the 1982 CSL Scientific Conference on Obscuration and Aerosol Research*, edited by R. H. Kohl and Assoc. (Tullahoma, TN, 1983) pp. 201-209.
2. J. A. Krill and R. A. Farrell, "The Development and Testing of a Stochastic Variational Principle for Electromagnetic Scattering," in *Wave Propagation and Remote Sensing, Proceedings of URSI Commission F 1983 Symposium* (European Space Agency, Noordwijk, The Netherlands, 1983), pp. 299-307.
3. J. F. Bird, "Analysis of All-Frequency Variational Behavior of the Kirchhoff Approximation for a Classic Surface-Scattering Model," *J. Opt. Soc. Am. A* **2**, 945-953 (1985).
4. J. F. Bird and R. A. Farrell, "Electromagnetic Scattering Theory," *Johns Hopkins APL Tech. Dig.* **7**, 58-72 (1986).
5. B. J. Stoyanov, J. A. Krill, J. F. Bird, and R. A. Farrell, "Broadband Trial Functions for Surface Scattering with Detailed Analysis for a Simple Model," in *Proceedings of the 1986 CRDEC Scientific Conference on Obscuration and Aerosol Research*, edited by R. H. Kohl and Assoc. (Tullahoma, TN, 1987), to appear.
6. J. F. Bird, R. A. Farrell, E. P. Gray, and B. J. Stoyanov, "Trial Functions for Scattering from Surfaces of Arbitrary Roughness and Variational Test Calculations," in *Proceedings of the 1986 CRDEC Scientific Conference on Obscuration and Aerosol Research*, edited by Kohl and Assoc. (Tullahoma, TN, 1987), to appear.

7. B. J. Stoyanov and R. A. Farrell, "Effects of Simple Shadowing on Variational Calculations," in *Proceedings of the 1987 CRDEC Scientific Conference on Obscuration and Aerosol Research*, edited by E. H. Engquist and K. A. Sisteck (U.S. Army Chemical Research, Development and Engineering Center, Aberdeen Proving Ground, MD, 1988), pp. 347-356.
8. B. J. Stoyanov and R. A. Farrell, "A Physical Approach to Developing All-Frequency Trial Fields in Variational Wave-Scattering Calculations," in revision.
9. D. E. Freund and R. A. Farrell, "Near Field Variational Principle: Scattering from Spheres," in *Proceedings of the 1988 CRDEC Scientific Conference on Obscuration and Aerosol Research*, edited by E. H. Engquist and K. A. Sisteck (U.S. Army Chemical Research, Development and Engineering Center, Aberdeen Proving Ground, MD, 1989), pp. 217-234.
10. D. E. Freund and R. A. Farrell, "A Variational Principle for the Scattered Wave," *J. Acoust. Soc. Am.* **87**, 1847-1860 (1990).
11. D. E. Freund and R. A. Farrell, "Variational Scattering Calculations for a Prolate Spheroid," in *Program of the 121st ASA Meeting* (Baltimore, 27 April-3 May, 1991), *J. Acoust. Soc. Am.* **89** (No. 4, Pt. 2), 1994 (1991).
12. P. M. Morse and H. Feshbach, *Methods of Theoretical Physics*, Part II, McGraw-Hill, New York (1953).
13. D. S. Jones, "A Critique of the Variational Method in Scattering Problems," *IRE Trans. Antennas Propagat.* **AP-4**, 297-301 (1956).
14. M. R. Feinstein and R. A. Farrell, "Trial Functions in Variational Approximations to Long-Wavelength Scattering," *J. Opt. Soc. Am.* **72**, 223-231 (1982).
15. J. J. Bowman, T. B. A. Senior, and P. L. E. Uslenghi, Eds., *Electromagnetic and Acoustic Scattering by Simple Shapes* (North-Holland, Amsterdam, 1969).
16. G. T. Ruck, D. E. Barrick, W. D. Stuart, and C. K. Krichbaum, *Radar Cross Section Handbook* (Plenum, New York, 1970), Vols. 1 and 2.
17. J. A. Stratton, *Electromagnetic Theory* (McGraw-Hill, New York, 1941).
18. L. M. Brekhovskikh, *Waves in Layered Media* (Academic Press, New York, 2nd ed., 1980).
19. M. A. Leontovich, "On the Approximate Boundary Conditions for Electromagnetic Fields on the Surface of Well Conducting Bodies," in *Investigations of Propagation of Radio Waves*, edited by B. A. Vvedensky (Academy of Sciences USSR, Moscow, 1948), Part II, pp. 5-20.

20. T. B. A. Senior, "Impedance Boundary Conditions for Imperfectly Conducting Surfaces," *Appl. Sci. Res., Sec. B*, **8**, 418-436 (1960).
21. R. D. Graglia and P. L. E. Uslenghi, "Surface Currents on Impedance Bodies of Revolution," *IEEE Trans. Ant. and Prop.* **36**, 1313-1317 (1988).
22. K. M. Mitzner, "An Integral Equation Approach to Scattering from a Body of Finite Conductivity," *Radio Sci.* **2**, 1459-1470 (1967).
23. D.-S. Wang, "Limits and Validity of the Impedance Boundary Conditions on Penetrable Surfaces," *IEEE Trans. Antennas Propag.* **AP-35**, 453-457 (1987).
24. R. A. Depine, "Scattering of a Wave at a Periodic Boundary: Analytical Expression for the Surface Impedance," *J. Opt. Soc. Am. A* **5**, 507-510 (1988).
25. J. R. Wait, "Exact Surface Impedance for a Cylindrical Conductor," *Electron. Lett.* **15**, 659-660 (1979).
26. H. C. van de Hulst, *Light Scattering by Small Particles* (Dover, New York, 1981).
27. M. Abramowitz and I. A. Stegun, *Handbook of Mathematical Functions with Formulas, Graphs and Mathematical Tables*, Appl. Math. Ser. No. 55 (National Bureau of Standards, Washington, DC, 1964).
28. B. J. Stoyanov, R. A. Farrell, and J. F. Bird, "Asymptotic Expansions of Integrals of Two Bessel Functions," in *Asymptotic and Computational Analysis*, edited by R. Wong (Marcel Dekker, Inc., New York, 1990), pp. 723-740.

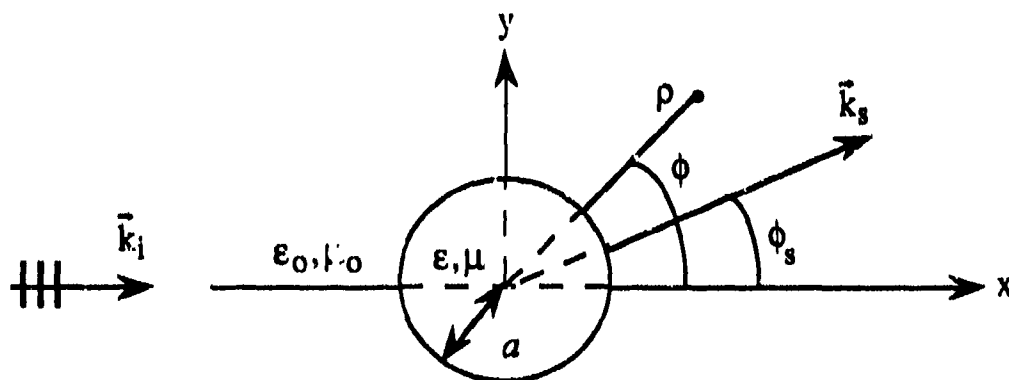


FIGURE 1. SCATTERING CONFIGURATION. Plane-wave scattering by an infinite penetrable circular cylinder at normal incidence.

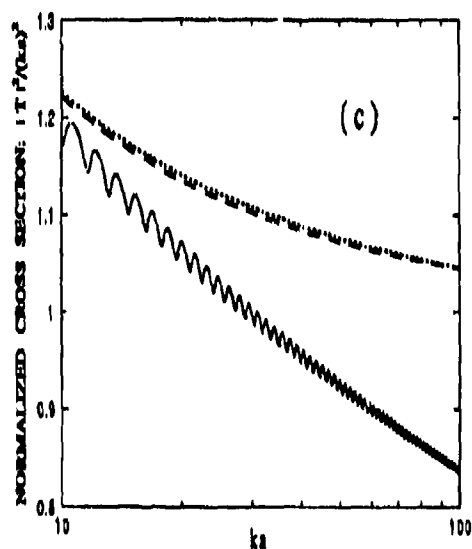
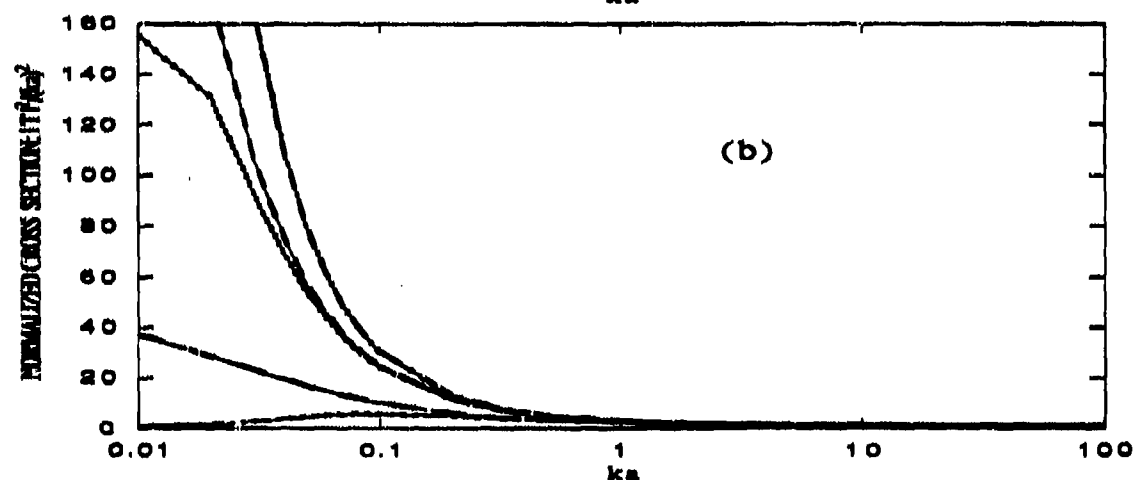
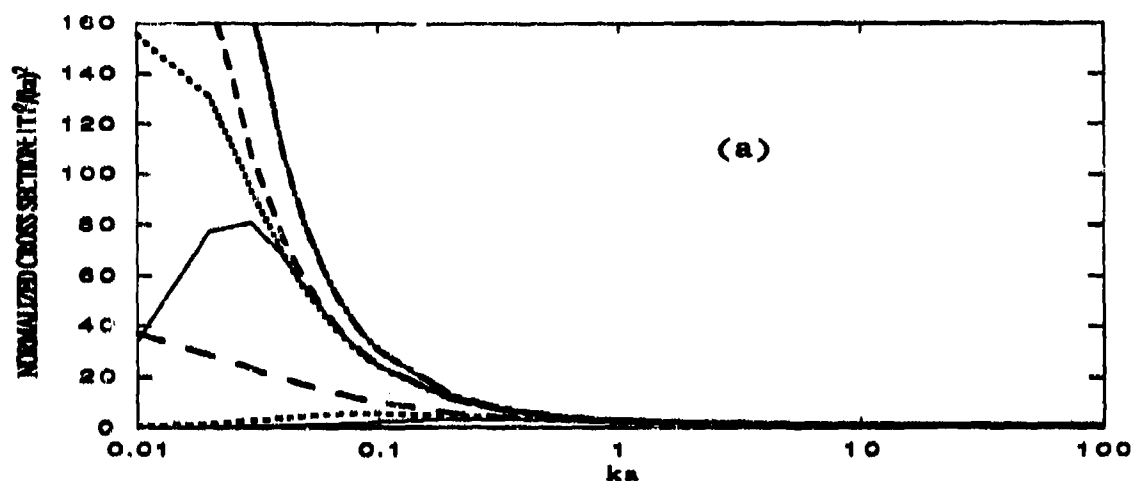


FIGURE 2. TM FORWARD SCATTERING. (a) Plots of the exact normalized cross sections for a penetrable cylinder with the rigorous dielectric (—), Leontovich (---), and impedance curvature-dependent (---) BCs. For $k\delta = 0.005$ the three results are indistinguishable and are given by the top curve, the middle three curves are for $k\delta = 0.05$, and the results for $k\delta = 0.3$ are given in the lower three curves. (b) The exact results for the Leontovich (---) and curvature-dependent (---) IBCs are compared with the corresponding variational results (—) obtained with the boundary-Born trial fields without shadowing for the three values of $k\delta$ as in (a). The variational and exact results appear to coincide on this scale of plotting. (c) Variational boundary-Born results without shadowing (—) and with shadowing (---) are compared with the exact result (---) for the Leontovich BC and $k\delta = 0.3$. The need to incorporate shadowing into the boundary-Born trial field is obvious from the improvements that are evident at this magnified scale.

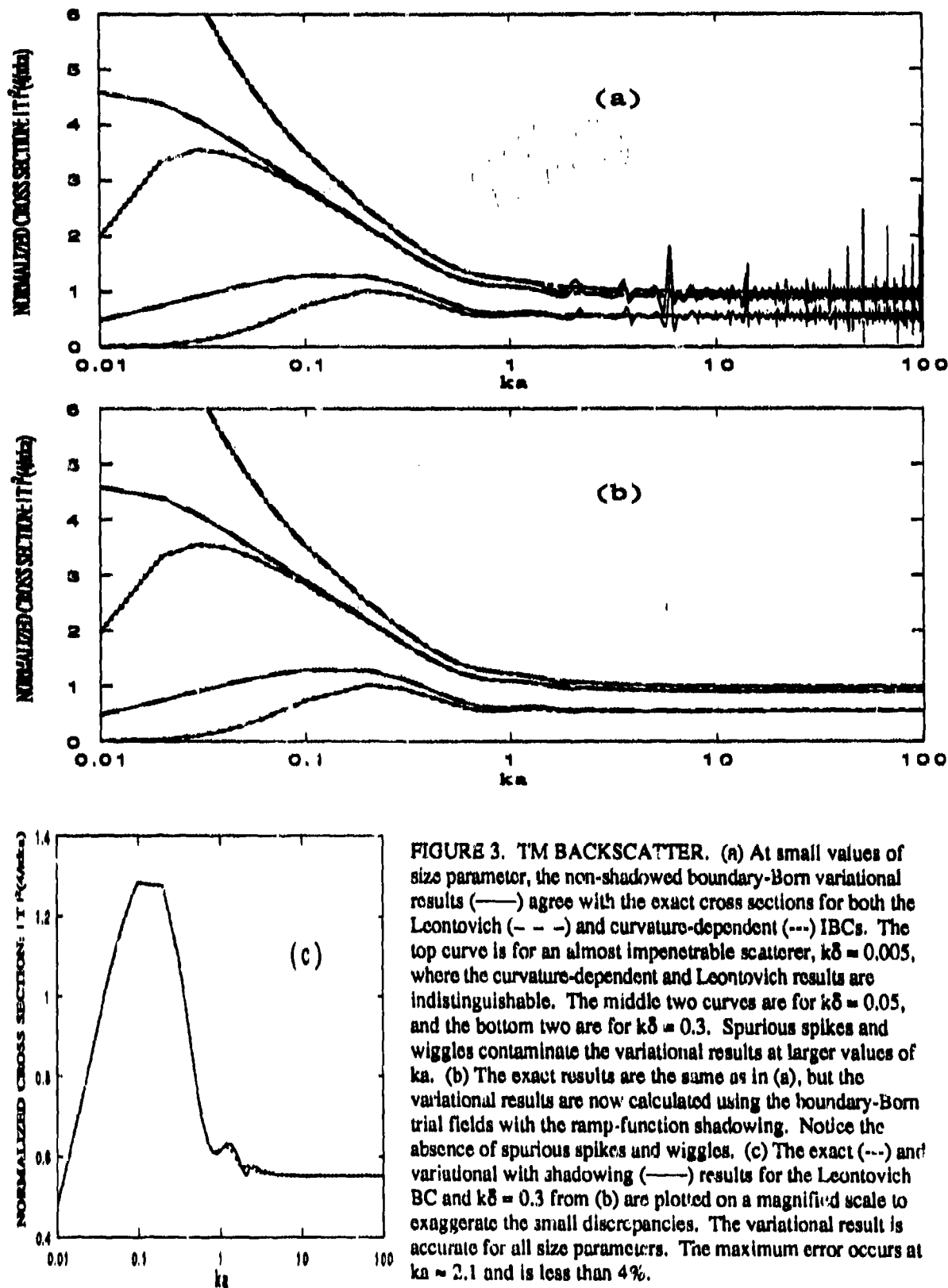


FIGURE 3. TM BACKSCATTER. (a) At small values of size parameter, the non-shadowed boundary-Born variational results (—) agree with the exact cross sections for both the Leontovich (---) and curvature-dependent (---) IBCs. The top curve is for an almost impenetrable scatterer, $k\delta = 0.005$, where the curvature-dependent and Leontovich results are indistinguishable. The middle two curves are for $k\delta = 0.05$, and the bottom two are for $k\delta = 0.3$. Spurious spikes and wiggles contaminate the variational results at larger values of ka . (b) The exact results are the same as in (a), but the variational results are now calculated using the boundary-Born trial fields with the ramp-function shadowing. Notice the absence of spurious spikes and wiggles. (c) The exact (---) and variational with shadowing (—) results for the Leontovich BC and $k\delta = 0.3$ from (b) are plotted on a magnified scale to exaggerate the small discrepancies. The variational result is accurate for all size parameters. The maximum error occurs at $ka \approx 2.1$ and is less than 4%.

BLANK

ON USING DIFFERENTIAL EQUATIONS TO INVERT INTEGRAL EQUATIONS DESCRIBING ELECTROMAGNETIC SCATTERING BY HETEROGENEOUS BODIES

D. K. Cohoon
West Chester University

November 2, 1991

We are interested in predicting the scattering of electromagnetic radiation by heterogeneous aerosol particles. We can represent the electromagnetic fields induced within such a body as the solution of a coupled system of integral equation relating the electric and magnetic vectors of these fields to the electric and magnetic vectors of the stimulating electromagnetic field. The ideas developed here can be applied to bianisotropic structures, but for simplicity we restrict our attention to the case of a nonmagnetic body. By solving a differential equation, we develop a new inverse integral equation where only known functions appear under the integrals.

1 INTRODUCTION

When a scattering body has a general shape, there is no exact solution to the boundary value problem associated with Maxwell's equations. The problem is usually formulated in terms of integral equations where the field quantities \vec{E} and \vec{H} being sought appear both under the integral and outside the integral. The electric field integral equation has the form,

$$\begin{aligned} \vec{E} - \vec{E}^i = & \\ & -grad \left(\int_{\Omega} \frac{div(i\omega\epsilon\vec{E} + \alpha\vec{H} - i\omega\epsilon_0\vec{E})}{\omega\epsilon_0} G(r, s) dv(s) \right) \\ & + \frac{i}{\omega\epsilon_0} grad \left(\int_{\partial\Omega} (i\omega\epsilon\vec{E} + \alpha\vec{H} - i\omega\epsilon_0\vec{E}) \cdot \vec{n} G(r, s) da(s) \right) \\ & + \left(\frac{-i}{\omega\epsilon_0} \right) \left(\int_{\partial\Omega} \left\{ k_0^2 (\sigma_s(\vec{E} - (\vec{n} \cdot \vec{E})\vec{n})) G(r, s) + \right. \right. \\ & \quad \left. \left. div(\sigma_s(\vec{E} - (\vec{n} \cdot \vec{E})\vec{n})) grad(G(r, s)) \right\} da(s) \right) \\ & - i\omega\mu_0 \int_{\Omega} (i\omega\epsilon\vec{E} + \alpha\vec{H} - i\omega\epsilon_0\vec{E}) G(r, s) dv(s) + \\ & - curl \left(\int_{\Omega} (i\omega\mu\vec{H} + \beta\vec{E} - i\omega\mu_0\vec{H}) G(r, s) dv(s) \right) \end{aligned} \quad (1.1)$$

and the magnetic field integral equation for a bianisotropic material is given by

$$\begin{aligned} \vec{H} - \vec{H}^i = & \\ & -grad \left(\int_{\Omega} \frac{div(i\omega\mu\vec{H} + \beta\vec{E} - i\omega\mu_0\vec{H})}{\omega\mu_0} G(r, s) dv(s) \right) \\ & - \frac{i}{\omega\mu_0} grad \int_{\partial\Omega} ((i\omega\mu\vec{H} + \beta\vec{E} - i\omega\mu_0\vec{H}) \cdot \vec{n}) G(r, s) da(s) \\ & - \left(\int_{\partial\Omega} (\sigma_s(\vec{E} - (\vec{n} \cdot \vec{E})\vec{n})) \times (grad(G(r, s))) da(s) \right) \\ & - i\omega\epsilon_0 \int_{\Omega} (i\omega\mu\vec{H} + \beta\vec{E} - i\omega\mu_0\vec{H}) G(r, s) dv(s) + \\ & + curl \left(\int_{\Omega} (i\omega\epsilon\vec{E} + \alpha\vec{H} - i\omega\epsilon_0\vec{E}) G(r, s) dv(s) \right) \end{aligned} \quad (1.2)$$

where ϵ , σ , μ , α , and β are tensors and the Maxwell equations for time harmonic radiation with an $\exp(i\omega t)$ time dependence are given by

$$\text{curl}(\vec{E}) = i\omega\mu_0\vec{H} - \vec{J}_m \quad (1.3)$$

and

$$\text{curl}(\vec{H}) = i\omega\epsilon_0\vec{E} + \vec{J}_e \quad (1.4)$$

where

$$\vec{J}_e = i\omega\epsilon\vec{E} + \alpha\vec{H} - i\omega\epsilon_0\vec{E} \quad (1.5)$$

and

$$\vec{J}_m = i\omega\mu\vec{H} + \beta\vec{E} - i\omega\mu_0\vec{H} \quad (1.6)$$

To simplify the development we assume that the integral equation that we are solving has the form,

$$\vec{E} - \vec{E}^i = \lambda L\vec{E} \quad (1.7)$$

By working with this equation we have developed a resolvent operator \mathcal{R}_λ such that

$$\vec{E}^i - \vec{E} = -\lambda R_\lambda \vec{E}^i \quad (1.8)$$

This resolvent operator R_λ is given by

$$R_\lambda \vec{E}^i(p) = \int_\Omega \mathcal{R}_\lambda(p, q) \vec{E}^i(q) d\nu(q) \quad (1.9)$$

and \mathcal{R}_λ is the solution of the ordinary differential equation, in the independent variable λ , given by

$$\frac{d\mathcal{R}_\lambda}{d\lambda}(p, q) = \int_\Omega \mathcal{R}_\lambda(p, w) \mathcal{R}_\lambda(w, q) d\nu(w) \quad (1.10)$$

with

$$\mathcal{R}_0(p, q) = \mathcal{G}(p, q) \quad (1.11)$$

where

$$L\vec{E}(p) = \int_\Omega \mathcal{G}(p, q) \vec{E}(q) d\nu(q) \quad (1.12)$$

We note that once \mathcal{R}_λ is known, we can predict the interaction of radiation with different orientations of the scattering body simply by applying transformations to \vec{E}^i and calculating \vec{E} for each of the transformed values of \vec{E}^i . This method gives us a kind of homotopy between the scattering problem for a vacuum scatterer to the more complex scattering problem.

2 OPERATOR ITERATES

The main theorem of Calderon and Zygmund ([2]) shows that if we define an operator L on the space $L^2(\Omega, \mathbb{C}^3)$ using the free space Green's function \mathcal{G} by the rule,

$$L\vec{F}(p) = \int_{\Omega} \vec{F}(q) \mathcal{G}(p, q) d\nu(q), \quad (2.1)$$

then the operator norm of L is finite. The theorem of Calderon and Zygmund ([2]) tells us that the integral operators of electromagnetic scattering transform fields producing a finite total power into other fields producing a finite total power. Since all ℓ_p norms on \mathbb{R}^n are equivalent, we may define the norm of L to be

$$\|L\|_{\Omega} = \sup \{ \|Lf\|_{\Omega} : f \in L_2(\Omega, \mathbb{C}^3), \text{ and } \|f\|_{\Omega} = 1 \} \quad (2.2)$$

where

$$f(p) = (f_1(p), f_2(p), f_3(p)) \quad (2.3)$$

implies that

$$\|f\|_{\Omega}^2 = \sum_{i=1}^3 \int_{\Omega} |f_i(y)|^2 d\nu(y) \quad (2.4)$$

It is clear, therefore, that if λ is sufficiently small that the operator norm of λL is smaller than 1. Thus, in everything that follows in this section we shall assume that

$$\|\lambda L\|_{\Omega} < 1 \quad (2.5)$$

It is now easy to derive an expression for $\vec{E}^i - \vec{E}_{\lambda}$ under this assumption. Just using concepts associated with the summation of a geometric series we find that

$$\vec{E}^i - \vec{E}_{\lambda} = -\lambda \left(\sum_{k=1}^{\infty} \lambda^{k-1} L^k \vec{E}^i \right) \quad (2.6)$$

We express the right side of equation (2.6) as an integral operator by introducing the sought after solution finder or resolvent kernel $\mathcal{R}_{\lambda}(p, q)$ via the relationship

$$-\lambda \int_{\Omega} \mathcal{R}_{\lambda}(p, q) \cdot \vec{E}^i(q) d\nu(q) = -\lambda \sum_{k=1}^{\infty} \left(\lambda^{k-1} L^k \vec{E}^i \right) \quad (2.7)$$

Combining (2.6) and (2.7) and the basic definition (2.1) of L in terms of $\mathcal{G}(p, q)$ imply that if we introduce the functions $\mathcal{G}^{(k)}(p, q)$ by the relations,

$$\mathcal{R}_\lambda(p, q) = \mathcal{G}(p, q) + \sum_{k=1}^{\infty} (\lambda^k \mathcal{G}^{(k+1)}(p, q)) \quad (2.8)$$

so that it would then follow that

$$L^k \vec{E}^i = \int_{\Omega} \mathcal{G}^{(k)}(p, q) \vec{E}^i(q) d\nu(q) \quad (2.9)$$

and since

$$L^{k+1} \vec{E}^i = \int_{\Omega} \mathcal{G}(p, w) \left(\int_{\Omega} \mathcal{G}^{(k)}(w, q) \vec{E}^i(q) d\nu(q) \right) d\nu(w) \quad (2.10)$$

and since an interchange of the order of integration in (2.10) implies that in view of (2.9) and the relationship,

$$L^{k+1} \vec{E}^i = L(L^k \vec{E}^i) = L^k(L \vec{E}^i) \quad (2.11)$$

that

$$\begin{aligned} \mathcal{G}^{(k+1)}(p, q) &= \int_{\Omega} \mathcal{G}(p, w) \mathcal{G}^{(k)}(w, q) d\nu(w) \\ &= \int_{\Omega} \mathcal{G}^{(k)}(p, w) \mathcal{G}(w, q) d\nu(w) \end{aligned} \quad (2.12)$$

it will follow upon substitution of (2.12) into (2.8) that

$$\mathcal{R}_\lambda(p, q) = \mathcal{G}(p, q) + \sum_{k=1}^{\infty} \lambda^k \left(\int_{\Omega} \mathcal{G}(p, w) \mathcal{G}^{(k)}(w, q) d\nu(w) \right) \quad (2.13)$$

We now resubstitute the original representation of \mathcal{R}_λ given by (2.8) into (2.12) making use of the fact that

$$\mathcal{G}^{(1)}(p, q) = \mathcal{G}(p, q)$$

to deduce that since (2.8) says that

$$\begin{aligned}\lambda \mathcal{R}_\lambda(p, q) &= \sum_{k=1}^{\infty} \lambda^k \mathcal{G}^{(k)}(p, q) = \\ &= \lambda \left(\mathcal{G}(p, q) + \sum_{k=1}^{\infty} \lambda^k \mathcal{G}^{(k+1)}(p, q) \right),\end{aligned}\quad (2.14)$$

and since

$$\begin{aligned}\sum_{k=1}^{\infty} \lambda^k \mathcal{G}^{(k+1)}(p, q) &= \sum_{k=1}^{\infty} \left(\int_{\Omega} \mathcal{G}(p, w) \mathcal{G}^{(k)}(w, q) d\nu(w) \right) = \\ &= \int_{\Omega} \mathcal{G}(p, w) \left(\sum_{k=1}^{\infty} \lambda^k \mathcal{G}^{(k)}(w, q) \right) d\nu(w) = \int_{\Omega} \mathcal{G}(p, w) \lambda \mathcal{R}_\lambda(w, q) d\nu(w)\end{aligned}\quad (2.15)$$

the relation,

$$\mathcal{R}_\lambda(p, q) = \mathcal{G}(p, q) + \lambda \left(\int_{\Omega} \mathcal{G}(p, w) \mathcal{R}_\lambda(w, q) d\nu(w) \right) \quad (2.16)$$

is valid for λ with a sufficiently small absolute value. Our next objective is to obtain an expression for

$$\mathcal{Q}(\lambda, \tilde{\lambda}) = \left(\frac{\mathcal{R}_{\tilde{\lambda}} - \mathcal{R}_\lambda}{\tilde{\lambda} - \lambda} \right) \quad (2.17)$$

and take the limit as $\tilde{\lambda}$ approaches λ .

We begin by noticing that in view of equations (2.12) (2.14), and (2.16), we obtain the relation,

$$\begin{aligned}\lambda \int_{\Omega} \mathcal{R}_\lambda(p, w) \mathcal{G}(w, q) d\nu(w) - \tilde{\lambda} \int_{\Omega} \mathcal{G}(p, w) \mathcal{R}_{\tilde{\lambda}}(w, q) d\nu(w) = \\ \int_{\Omega} \left\{ \sum_{j=0}^{\infty} \left(\lambda^{j+1} \mathcal{G}^{(j+1)}(p, w) \mathcal{G}(w, q) \right) - \right. \\ \left. \sum_{j=0}^{\infty} \left(\tilde{\lambda}^{j+1} \mathcal{G}^{(j+1)}(w, q) \mathcal{G}(p, w) \right) \right\} d\nu(w)\end{aligned}\quad (2.18)$$

In working with equation (2.18) we will make use of the standard identity

$$\lambda^{j+1} - \tilde{\lambda}^{j+1} = (\lambda - \tilde{\lambda}) \left(\sum_{k=0}^j \lambda^k \tilde{\lambda}^{j-k} \right) \quad (2.19)$$

and the fact that (2.12) implies that

$$\sum_{j=0}^{\infty} \left(\sum_{k=0}^j (\lambda^k \tilde{\lambda}^{j-k} \mathcal{G}^{(j+2)}(p, q)) \right) = \sum_{j=0}^{\infty} \left(\sum_{k=0}^j (\lambda^k \tilde{\lambda}^{(j-k)}) \left(\int_{\Omega} \mathcal{G}(p, w) \mathcal{G}^{(j+1)}(w, q) d\nu(w) \right) \right) \quad (2.20)$$

However, in order to proceed we need the following Lemma.

Lemma 2.1 *If \mathcal{G} is a dyadic Calderon-Zygmund kernel (Calderon and Zygmund [2]) on the open set Ω of \mathbb{R}^n and if $\mathcal{G}^{(k)}$ is defined by equation (2.12), then if j is a nonnegative integer,*

$$\int_{\Omega} \mathcal{G}(p, w) \mathcal{G}^{(j+1)}(w, q) d\nu(q) = \int_{\Omega} \mathcal{G}^{(k+1)}(p, w) \mathcal{G}^{(j-k+1)}(w, q) d\nu(q) \quad (2.21)$$

for all integers k between 0 and j .

Proof of Lemma 2.1. The proof of the Lemma will proceed by induction on j . If $j = 0$, then $k = 0$ and equation (2.21) is a tautology. Thus, we let $\mathcal{P}(j + 1)$ be the sentence that says that equation (2.21) is valid for the nonnegative integer j . We have just observed that $\mathcal{P}(1)$ is true, and we proceed to prove that $\mathcal{P}(n)$ implies that $\mathcal{P}(n + 1)$ is true. We note that $\mathcal{P}(n)$ is always true if $k = 0$ or if $k = j$, and we consequently assume that $0 < k < j$ and proceed by induction on j . The definition of $\mathcal{G}^{(j+1)}(w, q)$ and the inductive hypothesis imply that

$$\begin{aligned} \int_{\Omega} \mathcal{G}(p, w) \mathcal{G}^{(j+1)}(w, q) d\nu(w) &= \int_{\Omega} \mathcal{G}(p, w) \int_{\Omega} (\mathcal{G}(w, u) \mathcal{G}^{(j)}(u, q)) d\nu(u) d\nu(w) = \\ \int_{\Omega} \mathcal{G}(p, w) \int_{\Omega} \mathcal{G}^{(k-1)+1}(w, u) \mathcal{G}^{(j-1)-(k-1)+1}(u, q) d\nu(q) d\nu(w) \end{aligned} \quad (2.22)$$

Interchanging the order of integration in equation (2.22) implies that

$$\begin{aligned}
& \int_{\Omega} \mathcal{G}(p, w) \mathcal{G}^{(j+1)}(w, q) d\nu(w) = \\
& \int_{\Omega} \left(\int_{\Omega} \mathcal{G}^{(k-1)+1}(w, u) \right) \mathcal{G}^{(j-k+1)}(u, q) d\nu(u) \\
& = \int_{\Omega} \mathcal{G}^{(k+1)}(p, u) \mathcal{G}^{(j-k+1)}(u, q) d\nu(u)
\end{aligned} \tag{2.23}$$

and this completes the proof of Lemma 2.1.

We will now use Lemma 2.1, equation (2.21), to rewrite equation (2.20) in the form

$$\begin{aligned}
& \sum_{j=0}^{\infty} \left(\sum_{k=0}^j \lambda^k \tilde{\lambda}^{j-k} \mathcal{G}^{(j+2)}(p, q) \right) = \\
& \sum_{j=0}^{\infty} \left(\sum_{k=0}^j \left(\lambda^k \tilde{\lambda}^{j-k} \int_{\Omega} \mathcal{G}^{(k+1)}(p, w) \mathcal{G}^{(j-k+1)}(w, q) d\nu(w) \right) \right)
\end{aligned} \tag{2.24}$$

We will now prove the validity of another Lemma. This Lemma will be more abstract and will treat properties of sequences of, possibly, noncommuting linear transformations $\{A_1, A_2, A_3, \dots\}$ and $\{B_1, B_2, B_3, \dots\}$ where the A_k map a Banach space Y onto a Banach space Z , and the B_j map a Banach space X onto the Banach space Y , and the conditions under which one may define the product of a series of the form,

$$A = \sum_{k=0}^{\infty} (\alpha_k A_{k+1})$$

and a series of the form

$$B = \sum_{j=0}^{\infty} (\beta_j B_{j+1})$$

While the Lemma which follows may appear to be formally obvious, a proof is needed because of the interchange of infinite processes.

The Lemma is the following.

Lemma 2.2 *Let $\{A_1, A_2, A_3, \dots\}$ be a sequence of bounded linear transformations of the Banach space Y with norm, $\| \cdot \|_Y$ into the Banach space Z with norm, $\| \cdot \|_Z$. Let $\{B_1, B_2, B_3, \dots\}$ be a sequence of bounded linear*

transformations of the Banach space X with norm, $\| \cdot \|_X$, into the Banach space Y such that if

$$\| A_j \|_{(Y,Z)} = \sup \{ \| A_j f \|_Z : f \in Y \text{ and } \| f \|_Y = 1 \}$$

and

$$\| B_k \|_{(X,Y)} = \sup \{ \| B_k f \|_Y : f \in X \text{ and } \| f \|_X = 1 \}$$

then there are positive real constants C_A , C_B , R_A , and R_B with the property that

$$\| A_{k+1} \|_{(Y,Z)} \leq C_A R_A^k$$

and

$$\| B_{j+1} \|_{(X,Y)} \leq C_B R_B^j$$

for

$$\{j, k\} \subset \{1, 2, 3, \dots\}.$$

If λ and $\tilde{\lambda}$ are such that $\lambda R_A < 1$ and $\tilde{\lambda} R_B < 1$, then

$$\left(\sum_{k=0}^{\infty} (\lambda^k A_{k+1}) \right) \left(\sum_{j=0}^{\infty} (\tilde{\lambda}^j B_{j+1}) \right) = \sum_{j=0}^{\infty} \left(\sum_{k=0}^j (\lambda^k \tilde{\lambda}^{j-k} A_{k+1} B_{j+1-k}) \right) \quad (2.25)$$

and either side of this equation represents a bounded linear transformation of the Banach space X into the Banach space Z .

Proof of Lemma 2.2. Since B_{j+1-k} maps X into Y and A_{k+1} maps Y into Z , it is clear that $A_{k+1} B_{j+1-k}$ transforms elements of X linearly and continuously into Z . Also, the hypothesis of Lemma 2.2 guarantee that both sides of equation (2.25) define uniformly series of bounded linear operators acting on the Banach space X and that, consequently, any rearrangement of terms leaves the sum unchanged. Since

$$\lambda^k \tilde{\lambda}^\ell = \lambda^k \tilde{\lambda}^{j-k}$$

if $k + \ell = j$, the Lemma follows by induction on the products of the number of terms in finite partial sums approximating the left side of (2.25).

We now apply Lemma 2.2 to prove the following.

Lemma 2.3 *If \mathcal{R}_λ is defined for complex numbers λ by equation (2.8) or (2.14), then the relationship (2.12) represents $\mathcal{G}^{(j+2)}$ and*

$$\int_{\Omega} \mathcal{R}_\lambda(p, w) \mathcal{R}_{\tilde{\lambda}}(w, q) d\nu(w) = \sum_{j=0}^{\infty} \left(\sum_{k=0}^j (\lambda^k \tilde{\lambda}^{j-k} \mathcal{G}^{(j+2)}(p, q)) \right) \quad (2.26)$$

Proof of Lemma 2.3. By equation (2.8) we see that

$$\mathcal{R}_\lambda(p, w) = \sum_{k=0}^{\infty} (\lambda^k \mathcal{G}^{(k+1)}(p, w)) \quad (2.27)$$

Thus, by Lemma 2.2 it follows that

$$\begin{aligned} & \int_{\Omega} \mathcal{R}_\lambda(p, w) \mathcal{R}_{\tilde{\lambda}}(w, q) d\nu(w) \\ &= \int_{\Omega} \left(\sum_{k=0}^{\infty} (\lambda^k \mathcal{G}^{(k+1)}(p, w)) \right) \left(\sum_{j=0}^{\infty} (\tilde{\lambda}^j \mathcal{G}^{(j+1)}(w, q)) \right) d\nu(w) = \\ &= \int_{\Omega} \left(\sum_{j=0}^{\infty} \left(\sum_{k=0}^j (\lambda^k \tilde{\lambda}^{j-k} \mathcal{G}^{(k+1)}(p, w) \mathcal{G}^{(j-k+1)}(w, q)) \right) \right) d\nu(w) \end{aligned} \quad (2.28)$$

Now using the relation (2.22) and the definition, equation (2.12), of $\mathcal{G}^{(j+1)}(p, q)$ we see that

$$\mathcal{G}^{(j+2)}(p, q) = \int_{\Omega} \mathcal{G}^{(k+1)}(p, w) \mathcal{G}^{(j-k+1)}(w, q) d\nu(w) \quad (2.29)$$

Thus, Lemma 2.3 and equation (2.26) then follows as a result of substituting equation (2.29) into equation (2.28). This completes the proof of Lemma 2.3.

We now complete the proof of the final Lemma which will give us an expression for $\mathcal{R}_\lambda(p, q) - \mathcal{R}_{\tilde{\lambda}}(p, q)$. Equation (2.16) then tells us that

$$\begin{aligned} & \mathcal{R}_\lambda(p, q) - \mathcal{R}_{\tilde{\lambda}}(p, q) = \\ &= \lambda \int_{\Omega} \mathcal{G}(p, w) \mathcal{R}_\lambda(w, q) d\nu(w) - \tilde{\lambda} \int_{\Omega} \mathcal{G}(p, w) \mathcal{R}_{\tilde{\lambda}}(w, q) d\nu(w) \end{aligned} \quad (2.30)$$

Substitution of the power series representation, equation (2.8), of $\mathcal{R}_\lambda(w, q)$ into (2.30), we can obtain the relationship,

$$\begin{aligned} \mathcal{R}_\lambda(p, q) - \mathcal{R}_{\tilde{\lambda}}(p, q) = & \sum_{j=0}^{\infty} \left(\lambda^{j+1} \mathcal{G}^{(j+2)}(p, q) - \tilde{\lambda}^{j+1} \mathcal{G}^{(j+2)}(p, q) \right) = \\ & \lambda \int_{\Omega} \mathcal{G}(p, w) \left(\sum_{j=0}^{\infty} \left(\lambda^j \mathcal{G}^{(j+1)}(w, q) \right) \right) d\nu(w) - \\ & \tilde{\lambda} \int_{\Omega} \mathcal{G}(p, w) \left(\sum_{j=0}^{\infty} \left(\tilde{\lambda}^j \mathcal{G}^{(j+1)}(w, q) \right) \right) d\nu(w) \end{aligned} \quad (2.31)$$

Substituting (2.19) into equation (2.31) gives us the following lemma

Lemma 2.4 . If $\mathcal{R}_\lambda(p, q)$ is given by equation (2.8), where $\mathcal{G}^{(k)}(p, q)$ is defined by (2.12), then

$$\begin{aligned} \mathcal{R}_\lambda(p, q) - \mathcal{R}_{\tilde{\lambda}}(p, q) = & (\lambda - \tilde{\lambda}) \left(\sum_{j=0}^{\infty} \left(\sum_{k=0}^j \left(\lambda^k \tilde{\lambda}^{j-k} \mathcal{G}^{(j+2)}(p, q) \right) \right) \right) \end{aligned} \quad (2.32)$$

These Lemmas enable one to prove the following theorem.

Theorem 2.1 If $\mathcal{R}_\lambda(p, q)$ is defined by (2.7) and (2.8), and $\mathcal{G}(p, q)$ is a Calderon Zygmund Kernel (Calderon and Zygmund [2]), then

$$\begin{aligned} \mathcal{R}_\lambda(p, q) - \mathcal{R}_{\tilde{\lambda}}(p, q) = & (\lambda - \tilde{\lambda}) \int_{\Omega} \mathcal{R}_\lambda(p, w) \mathcal{R}_{\tilde{\lambda}}(w, q) d\nu(w) \end{aligned} \quad (2.33)$$

and

$$\frac{d\mathcal{R}_\lambda}{d\lambda}(p, q) = \int_{\Omega} \mathcal{R}_\lambda(p, w) \mathcal{R}_\lambda(w, q) d\nu(w) \quad (2.34)$$

where

$$\mathcal{R}_0(p, q) = \mathcal{G}(p, q) \quad (2.35)$$

Proof of Theorem 2.1. Equation (2.33) follows by substituting equation (2.26) into (2.31). Equation (2.34) follows by dividing both sides of (2.33) by $\lambda - \tilde{\lambda}$ and taking the limit as $\tilde{\lambda}$ approaches λ . Equation (2.35) follows from equation (2.16).

In solving the initial value problem suggested by this theorem we note that the Cauchy integral theorem tells us that an integral of \mathcal{R}_λ over a curve or a path of λ values in the complex plane is independent of path if one path can be deformed into another without crossing a pole of \mathcal{R}_λ .

References

- [1] Burr, John G., David K. Cohoon, Earl L. Bell, and John W. Penn. Thermal response model of a Simulated Cranial Structure Exposed to Radiofrequency Radiation. *IEEE Transactions on Biomedical Engineering*. Volume BME-27, No. 8 (August, 1980) pp 452-460.
- [2] Calderon, A. P. and A. Zygmund. On the existence of certain singular integrals. *Acta Mathematica*. Volume 88 (1952) pp 85-139
- [3] Cohoon, D. K., J. W. Penn, E. L. Bell, D. R. Lyons, and A. G. Cryer. *A Computer Model Predicting the Thermal Response to Microwave Radiation SAM-TR-82-22* Brooks AFB, Tx 78235: USAF School of Aerospace Medicine. (RZ) Aerospace Medical Division (AFSC) (December, 1982).
- [4] Hochstadt, Harry. *The Functions of Mathematical Physics*. New York: Dover(1986).
- [5] Whittaker, E. T. and G. N. Watson. *A Course of Modern Analysis* London: Cambridge University Press (1986).

An Algorithm for the Eigenvalues of the Angular Spheroidal Harmonics and An Exact Solution to the Problem of Describing Electromagnetic Interaction with Anisotropic Structures Delimited by N Confocal Spheroids

D. K. Cohoon

March 9, 1992

Contents

Introduction

Spheroidal Coordinates

Vector Calculus for Oblate Spheroids

Prolate Spheroid Scattering – an Exact Solution

References

1 Introduction

Prolate spheroids are cigars and footballs and oblate spheroids are falling raindrops and doorknobs. A spheroid is an ellipse rotated about an axis. If it is rotated about a major axis it is a prolate spheroid. If it is rotated about a minor axis, it is an oblate spheroid. In the halls of Congress a certain young representative had his desk in a most undesirable location; for some reason, however, he was able to rise instantly and give brilliant rebuttals of the arguments of his opposition. It turned out that the roof was a spheroid and his desk was at one of the focal points and the desk of the opposition was at the other focal point. He could hear the whispered planning of the opposition long before they got up to speak. Unlike the wedding guest described 2000 years ago, he refused to move up to a place of greater honor, and, his secret remaining with himself, others were content to allow him to remain in his more humble post.

Spheroid scattering is important because it provides challenges for general purpose codes, and because one is interested in the propagation of electromagnetic information through clouds of spheroids, such as falling raindrops. The computer codes developed may also have a bearing on the design of liquid crystal devices, such as liquid crystal television sets and computer monitors which would, as they use natural room light, be far safer for the users, often young girls, than cathode ray tube (CRT) devices currently in use. Young children, in poor urban settings, often spend hours huddled close to television sets. If they are going to do this anyway, let us, for the sake of the children, make television screens safer with a liquid crystal design. The ability to remember sight together with sound, may provide a way to teach and make literate a larger segment of human society all over the world; we have many serious problems to solve, and no one knows from where the genius to create a solution may come.

The Helmholtz equation can be solved in spheroidal coordinates, and using this solution, we can obtain solutions of the Faraday and Ampere Maxwell equations. Note that if Ψ is a solution of the Helmholtz equation, then if \vec{r} is the radial vector, then

$$\vec{M} = \text{curl}(\vec{r} \cdot \Psi) \quad (1.1)$$

and

$$\vec{N} = (1/k)\text{curl}(\vec{M}) \quad (1.2)$$

can be used to obtain a solution of Maxwell's equations. We proceed to define these computations in spheroidal coordinates.

2 Spheroidal Coordinates

Consider an ellipse with foci at $(0, -d/2)$ and $(0, d/2)$ on the z axis and if

$$r^2 = x^2 + y^2 \quad (2.1)$$

and (r, z) is a point on the generating curve for the spheroid, then if we define for r_1 being the distance between (r, z) and $(0, -d/2)$ and if r_2 is the distance between $(0, d/2)$ and (r, z) , and if we then define ξ by the rule,

$$\xi = (r_1 + r_2)/(2 \cdot c) \quad (2.2)$$

and define η by the relation,

$$\eta = (r_1 - r_2)/(2 \cdot c) \quad (2.3)$$

where c is a constant, we have a set of coordinates for describing points within a spheroid. We shall actually use a slightly different set of coordinates that are qualitatively the same. We can define points on the surface of the spheroid as all those points (ξ, η, ϕ) for which ξ is a constant, which since an ellipse is the locus of points such that the sum of the distances from fixed foci is a constant is embodied in the definition of ξ given by equation, (2.2). The other coordinate surface defined by setting η equal to a constant is a hyperbola, as this says simply that the difference of the distances between two foci is a constant. The third coordinate surface defined by setting ϕ equal to a constant is simply a plane passing

through the axis of rotation. We give an alternative definition of the spheroidal coordinates and show that this definition is compatible with the more intuitive definitions of equations (2.2) and (2.3). The relations between spheroidal and Cartesian coordinates are given by

$$x = \frac{d}{2} [(1 - \eta^2)(\xi^2 + 1)]^{1/2} \cos(\phi) \quad (2.4)$$

and

$$y = \frac{d}{2} [(1 - \eta^2)(\xi^2 + 1)]^{1/2} \sin(\phi) \quad (2.5)$$

and

$$z = \frac{d}{2} \eta \xi \quad (2.6)$$

Going back to the equation for an oblate spheroid we have that

$$\begin{aligned} (x^2 + y^2)/A^2 + z^2/B^2 &= \\ \frac{(d^2/4)(1 - \eta^2)(\xi^2 + 1)}{A^2} + \frac{(d^2/4)\eta^2\xi^2}{B^2} &= \\ \frac{d^2}{4} \left[\frac{1 - \eta^2}{(d/2)^2} + \frac{\eta^2}{(d/2)^2} \right] &= 1 \end{aligned} \quad (2.7)$$

if we simply let A and B be defined by

$$A = \frac{d}{2} \sqrt{\xi^2 + 1} \quad (2.8)$$

and

$$B = \frac{d}{2} |\xi| \quad (2.9)$$

For the oblate spheroid, we have

$$A > B \quad (2.10)$$

and the foci of the ellipse may be thought to be on the x axis located at

$$x = C = \sqrt{A^2 - B^2} = d/2 \quad (2.11)$$

and the sum of the distances from a fixed point on the surface to the two foci is $2A$ which happens to be

$$2A = d\sqrt{\xi^2 + 1} = r_1 + r_2 \quad (2.12)$$

If we compare equation (2.12) with the earlier equation (2.2) we can see easily the connection between ξ and ξ and that setting either one of these equal to a constant defines a surface of a spheroid.

We now try to develop the unit vectors in the direction of the normals to the coordinate surfaces $\xi = \text{constant}$ or $\eta = \text{constant}$. Note that if we had a general coordinate transformation relationship

$$\begin{pmatrix} x \\ y \\ z \end{pmatrix} = \begin{pmatrix} x(u, v, w) \\ y(u, v, w) \\ z(u, v, w) \end{pmatrix} \quad (2.13)$$

and the unit vector in the direction of the normal to the coordinate surface

$$u = \text{constant} \quad (2.14)$$

is given by

$$\vec{e}_u = \frac{d\vec{R}}{du} / \left(\left\| \frac{d\vec{R}}{du} \right\| \right) \quad (2.15)$$

where

$$\vec{R} = x\vec{e}_x + y\vec{e}_y + z\vec{e}_z \quad (2.16)$$

If we imagine an arc in three dimensional space and try to describe it in Cartesian and spheroidal coordinate. Assume that the arc $\vec{R}(t)$ is defined as an orbit defined by a continuous parameter t . Let $s(t_2)$ minus $s(t_1)$ denote the arc length between $\vec{R}(t_2)$ and $\vec{R}(t_1)$ on this curve so that

$$\left(\frac{ds}{dt} \right)^2 = \left(\frac{dx}{dt} \right)^2 + \left(\frac{dy}{dt} \right)^2 + \left(\frac{dz}{dt} \right)^2 \quad (2.17)$$

In order to get values of parameters h_ξ , h_η , and h_ϕ so that we may express the Laplacian and curl operations in spheroidal coordinates we observe that equation (2.4) implies that

$$\frac{\partial x}{\partial \xi} = \frac{d}{2} [(1 - \eta^2)]^{1/2} \xi [(\xi^2 + 1)]^{-1/2} \cos(\phi) \quad (2.18)$$

From equation (2.5) we see that

$$\frac{\partial y}{\partial \xi} = \frac{d}{2} [(1 - \eta^2)]^{1/2} \xi [(\xi^2 + 1)]^{-1/2} \sin(\phi) \quad (2.19)$$

From equation (2.6) we see that

$$\frac{\partial z}{\partial \xi} = \frac{d}{2} \eta \quad (2.20)$$

Thus, using the unit vector equation (2.15) and equations (2.18) and (2.19) and (2.20) we see that the unit vector \vec{e}_ξ is given by

$$\begin{aligned} \vec{e}_\xi = & \sqrt{\frac{\xi^2 + 1}{\xi^2 + \eta^2}} \left[\xi \sqrt{\frac{1 - \eta^2}{\xi^2 + 1}} \cos(\phi) \vec{e}_x + \right. \\ & \left. \xi \sqrt{\frac{1 - \eta^2}{\xi^2 + 1}} \sin(\phi) \vec{e}_y + \eta \vec{e}_z \right] \end{aligned} \quad (2.21)$$

Thus, we see that the length factors In an analogous manner we write down the unit vector \vec{e}_η by the rule

$$\begin{aligned} \vec{e}_\eta = & \sqrt{\frac{1 - \eta^2}{\xi^2 + \eta^2}} \left[-\eta \sqrt{\frac{\xi^2 + 1}{1 - \eta^2}} \cos(\phi) \vec{e}_x + \right. \\ & \left. -\eta \sqrt{\frac{\xi^2 + 1}{1 - \eta^2}} \sin(\phi) \vec{e}_y + \xi \vec{e}_z \right] \end{aligned} \quad (2.22)$$

We observe from equations (2.4), (2.5), and (2.6) that

$$\frac{\partial x}{\partial \phi} = -\frac{d}{2} [(1 - \eta^2)(\xi^2 + 1)]^{1/2} \sin(\phi), \quad (2.23)$$

$$\frac{\partial y}{\partial \phi} = \frac{d}{2} [(1 - \eta^2)(\xi^2 + 1)]^{1/2} \cos(\phi) \quad (2.24)$$

and

$$\frac{\partial z}{\partial \phi} = 0 \quad (2.25)$$

Finally, again making use of the equation (2.15) and equations (2.23) and (2.24) and (2.25) we see that the unit vector \vec{e}_ϕ is given by

$$\vec{e}_\phi = -\sin(\phi)\vec{e}_x + \cos(\phi)\vec{e}_y \quad (2.26)$$

It is clear from the definition, equation (2.15) used in creating equations (2.21), (2.22), and (2.23) that there are scalar functions h_ξ , h_η , and h_ϕ of ξ and η that satisfy

$$h_\xi \vec{e}_\xi = \frac{\partial x}{\partial \xi} \vec{e}_x + \frac{\partial y}{\partial \xi} \vec{e}_y + \frac{\partial z}{\partial \xi} \vec{e}_z, \quad (2.27)$$

$$h_\eta \vec{e}_\eta = \frac{\partial x}{\partial \eta} \vec{e}_x + \frac{\partial y}{\partial \eta} \vec{e}_y + \frac{\partial z}{\partial \eta} \vec{e}_z \quad (2.28)$$

and

$$h_\phi \vec{e}_\phi = \frac{\partial x}{\partial \phi} \vec{e}_x + \frac{\partial y}{\partial \phi} \vec{e}_y + \frac{\partial z}{\partial \phi} \vec{e}_z \quad (2.29)$$

We notice that these vectors \vec{e}_ξ , \vec{e}_η , \vec{e}_ϕ are pairwise orthogonal in the sense that

$$\vec{e}_\eta \cdot \vec{e}_\xi = \vec{e}_\eta \cdot \vec{e}_\phi = \vec{e}_\xi \cdot \vec{e}_\phi = 0 \quad (2.30)$$

We can use these relationships to represent the vector \vec{R} defined by equation (2.16) in terms of \vec{e}_ξ , \vec{e}_η , and \vec{e}_ϕ . We see that

$$\vec{R} = (\vec{R} \cdot \vec{e}_\xi) \vec{e}_\xi + (\vec{R} \cdot \vec{e}_\eta) \vec{e}_\eta + (\vec{R} \cdot \vec{e}_\phi) \vec{e}_\phi \quad (2.31)$$

where

$$(\vec{R} \cdot \vec{e}_\xi) = \frac{x}{h_\xi} \cdot \frac{\partial x}{\partial \xi} + \frac{y}{h_\xi} \cdot \frac{\partial y}{\partial \xi} + \frac{z}{h_\xi} \cdot \frac{\partial z}{\partial \xi}, \quad (2.32)$$

$$(\vec{R} \cdot \vec{e}_\eta) = \frac{x}{h_\eta} \cdot \frac{\partial x}{\partial \eta} + \frac{y}{h_\eta} \cdot \frac{\partial y}{\partial \eta} + \frac{z}{h_\eta} \cdot \frac{\partial z}{\partial \eta}, \quad (2.33)$$

and

$$(\vec{R} \cdot \vec{e}_\phi) = \frac{x}{h_\phi} \cdot \frac{\partial x}{\partial \phi} + \frac{y}{h_\phi} \cdot \frac{\partial y}{\partial \phi} + \frac{z}{h_\phi} \cdot \frac{\partial z}{\partial \phi}, \quad (2.34)$$

First, substituting equations (2.18), (2.19), (2.20), (2.4), (2.5), and (2.6) into equation (2.32) we obtain

$$(\vec{R} \cdot \vec{e}_\xi) = \frac{d}{2} \cdot \xi \cdot \sqrt{\frac{\xi^2 + 1}{\xi^2 + \eta^2}} \quad (2.35)$$

Next, determining that

$$\frac{\partial x}{\partial \eta} = \frac{d}{2} [(\xi^2 + 1)]^{1/2} (-\eta) [(1 - \eta^2)]^{-1/2} \cos(\phi) \quad (2.36)$$

and that

$$\frac{\partial y}{\partial \eta} = \frac{d}{2} \left[\sqrt{\frac{\xi^2 + 1}{1 - \eta^2}} \right] (-\eta) \sin(\phi) \quad (2.37)$$

Equations (2.36), (2.37), and (2.4), (2.5), and (2.6) tell us that

$$(\vec{R} \cdot \vec{e}_\eta) = -\eta \frac{d}{2} \sqrt{\frac{1 - \eta^2}{\xi^2 + \eta^2}} \quad (2.38)$$

For a general coordinate transformation from an (x, y, z) frame to a (u, v, w) frame we have the relationship,

$$\begin{aligned} \left(\frac{dx}{dt} \right)^2 + \left(\frac{dy}{dt} \right)^2 + \left(\frac{dz}{dt} \right)^2 &= \left\{ \left[\left(\frac{\partial x}{\partial u} \right)^2 + \left(\frac{\partial y}{\partial u} \right)^2 + \left(\frac{\partial z}{\partial u} \right)^2 \right] \left(\frac{du}{dt} \right)^2 + \right. \\ &\left[\left(\frac{\partial x}{\partial v} \right)^2 + \left(\frac{\partial y}{\partial v} \right)^2 + \left(\frac{\partial z}{\partial v} \right)^2 \right] \left(\frac{dv}{dt} \right)^2 + \left[\left(\frac{\partial x}{\partial w} \right)^2 + \left(\frac{\partial y}{\partial w} \right)^2 + \left(\frac{\partial z}{\partial w} \right)^2 \right] \left(\frac{dw}{dt} \right)^2 \\ &+ 2 \left[\frac{\partial x}{\partial u} \cdot \frac{\partial x}{\partial v} + \frac{\partial y}{\partial u} \cdot \frac{\partial y}{\partial v} + \frac{\partial z}{\partial u} \cdot \frac{\partial z}{\partial v} \right] \frac{du}{dt} \cdot \frac{dv}{dt} + \\ &+ 2 \left[\frac{\partial x}{\partial u} \cdot \frac{\partial x}{\partial w} + \frac{\partial y}{\partial u} \cdot \frac{\partial y}{\partial w} + \frac{\partial z}{\partial u} \cdot \frac{\partial z}{\partial w} \right] \frac{du}{dt} \cdot \frac{dw}{dt} + \\ &\left. + 2 \left[\frac{\partial x}{\partial v} \cdot \frac{\partial x}{\partial w} + \frac{\partial y}{\partial v} \cdot \frac{\partial y}{\partial w} + \frac{\partial z}{\partial v} \cdot \frac{\partial z}{\partial w} \right] \frac{dv}{dt} \cdot \frac{dw}{dt} \right\} \quad (2.39) \end{aligned}$$

Making use of the orthogonality of the ξ , η , and ϕ coordinate system we see that with

$$(u, v, w) = (\xi, \eta, \phi) \quad (2.40)$$

that all of the terms in equation (2.39) with a factor of 2 vanish, and that

$$\left(\frac{dx}{dt} \right)^2 + \left(\frac{dy}{dt} \right)^2 + \left(\frac{dz}{dt} \right)^2 = h_\xi^2 \left(\frac{d\xi}{dt} \right)^2 + h_\eta^2 \left(\frac{d\eta}{dt} \right)^2 + h_\phi^2 \left(\frac{d\phi}{dt} \right)^2 \quad (2.41)$$

Thus, for oblate spheroidal coordinates we obtain upon making use of equation (2.41) the following expressions for h_ξ , h_η , and h_ϕ . From this equation and equations (2.18), (2.19), and (2.20) we see that

$$h_\xi = \frac{d}{2} \sqrt{\frac{\xi^2 + \eta^2}{\xi^2 + 1}} \quad (2.42)$$

Next observe that

$$h_\eta = \frac{d}{2} \sqrt{\frac{\xi^2 + \eta^2}{1 - \eta^2}} \quad (2.43)$$

Finally equations (2.23), (2.24), and (2.25) imply that

$$h_\phi = \frac{d}{2} \sqrt{(1 - \eta^2)(\xi^2 + 1)} \quad (2.44)$$

In order to carry out vector calculus in oblate spheroidal coordinates we need the following relations. Equations (2.42), (2.43), and (2.44) imply that

$$h_\xi h_\eta h_\phi = \frac{d^3}{8} (\xi^2 + \eta^2) \quad (2.45)$$

Also, equations (2.42), (2.43), and (2.44) imply that

$$\frac{h_\eta h_\phi}{h_\xi} = \frac{d}{2} (\xi^2 + 1) \quad (2.46)$$

The other two similar relations are

$$\frac{h_\xi \cdot h_\eta}{h_\phi} = \frac{d}{2} \left(\frac{\xi^2 + \eta^2}{(\xi^2 + 1)(1 - \eta^2)} \right) \quad (2.47)$$

and

$$\frac{h_\xi \cdot h_\phi}{h_\eta} = \frac{d}{2} (1 - \eta^2) \quad (2.48)$$

The above relations are needed to define the Helmholtz equation in oblate spheroidal coordinates. In order to define the curl operation in oblate spheroidal coordinates we need the product pairs as well Equations (2.42) and (2.43) imply that

$$h_\xi \cdot h_\eta = \frac{d^2}{4} \frac{\xi^2 + \eta^2}{\sqrt{(\xi^2 + 1)(1 - \eta^2)}} \quad (2.49)$$

Equations (2.42) and (2.44) imply that

$$h_\xi \cdot h_\phi = \frac{d^2}{4} \sqrt{(\xi^2 + \eta^2)(1 - \eta^2)} \quad (2.50)$$

Finally, equations (2.43) and (2.44) imply that

$$h_\eta \cdot h_\phi = \frac{d^2}{4} \sqrt{(\xi^2 + \eta^2)(\xi^2 + 1)} \quad (2.51)$$

The curl operator in a general orthogonal coordinate system of orthogonal u , v , and w coordinates is given by

$$\begin{aligned} \text{curl}(\vec{E}) = & \\ & \frac{1}{h_v h_w} \left[\frac{\partial}{\partial v} (h_w E_w) - \frac{\partial}{\partial w} (h_v E_v) \right] \vec{e}_u + \\ & \frac{1}{h_u h_w} \left[\frac{\partial}{\partial w} (h_u E_u) - \frac{\partial}{\partial u} (h_w E_w) \right] \vec{e}_v + \end{aligned}$$

$$\frac{1}{h_u h_v} \left[\frac{\partial}{\partial u} (h_v E_v) - \frac{\partial}{\partial v} (h_u E_u) \right] \vec{e}_w \quad (2.52)$$

Equation (2.52) may be derived from combining the representation of Cartesian frame unit vectors in terms of \vec{e}_u , \vec{e}_v , and \vec{e}_w and using the *gradient* equation,

$$\text{grad}(\Psi) = \frac{1}{h_u} \frac{\partial \Psi}{\partial u} \vec{e}_u + \frac{1}{h_v} \frac{\partial \Psi}{\partial v} \vec{e}_v + \frac{1}{h_w} \frac{\partial \Psi}{\partial w} \vec{e}_w \quad (2.53)$$

since (2.53) can be used to express the curl of a vector field as the gradient cross this vector field. The divergence is given by

$$\begin{aligned} \text{div}(\vec{E}) &= \left(\frac{1}{h_u h_v h_w} \right) \left\{ \left(\frac{\partial}{\partial u} \right) (h_v h_w \cdot E_u) \right. \\ &\quad \left. \left(\frac{\partial}{\partial v} \right) (h_u h_w \cdot E_v) + \left(\frac{\partial}{\partial w} \right) (h_u h_v \cdot E_w) \right\} \end{aligned} \quad (2.54)$$

It is easy to show that

$$\text{curl}(\text{curl}(\vec{E})) = \text{grad}(\text{div}(\vec{E})) - \Delta \vec{E} \quad (2.55)$$

where

$$\begin{aligned} \Delta \Psi &= \frac{1}{h_u h_v h_w} \left\{ \frac{\partial}{\partial u} \left(\frac{h_v h_w}{h_u} \frac{\partial \Psi}{\partial u} \right) + \right. \\ &\quad \left. \frac{\partial}{\partial v} \left(\frac{h_u h_w}{h_v} \frac{\partial \Psi}{\partial v} \right) + \frac{\partial}{\partial w} \left(\frac{h_u h_v}{h_w} \frac{\partial \Psi}{\partial w} \right) \right\} \end{aligned} \quad (2.56)$$

The relationship (2.55) implies that

$$\Delta(\text{curl}(\vec{E})) = -\text{curl}(\text{curl}(\text{curl}(\vec{E}))) = \text{curl}(\Delta(\vec{E})) \quad (2.57)$$

since

$$\text{curl}(\text{grad}(\Psi)) = \vec{0} \quad (2.58)$$

The Mie solution is based on applying the curl three times in succession to the vector $\vec{R}\Psi$ where

$$\vec{R} = \text{grad} \left(\frac{x^2 + y^2 + z^2}{2} \right) = x\vec{e}_x + y\vec{e}_y + z\vec{e}_z \quad (2.59)$$

which means that since for any vector field \vec{F} and any scalar function Ψ it is true that

$$\text{curl}(\vec{F}\Psi) = \Psi \text{curl}(\vec{F}) + \text{grad}(\Psi) \times \vec{F} \quad (2.60)$$

that if \vec{R} is defined by (2.59) that

$$\text{curl}(\Psi \vec{R}) = \text{grad}(\Psi) \times \vec{R} \quad (2.61)$$

and since we also have the relationship,

$$\Delta(\Psi \vec{R}) = \{\Delta(\Psi)\} \vec{R} + 2 \cdot \text{grad}(\Psi) \quad (2.62)$$

Substituting equation (2.62) into equation (2.57) we see that in case Ψ satisfies

$$\Delta\Psi + k^2\Psi = 0 \quad (2.63)$$

that, since both the curl of a gradient and the divergence of a curl vanish,

$$\text{curl}(\text{curl}(\text{curl}(\Psi\vec{R}))) = \text{curl}(-\Delta\Psi) = +k^2\text{curl}(\Psi\vec{R}) \quad (2.64)$$

Equation (2.64) is the basis of the Asano and Yamamoto solution ([1]) as well as the classical Mie solution for isotropic materials. For example, for an isotropic material we could let the electric vector be given by

$$\vec{E} = a \cdot \vec{M} + b \cdot \vec{N}, \quad (2.65)$$

where

$$\vec{M} = \frac{1}{k} \cdot \text{curl}(\vec{R}\Psi) \quad (2.66)$$

and where

$$\vec{N} = \frac{1}{k^2} \cdot \text{curl}(\text{curl}(\vec{R}\Psi)) \quad (2.67)$$

with Ψ being a solution of the scalar Helmholtz equation (2.63). Then if the magnetic vector \vec{H} is defined by

$$\vec{H} = \frac{1}{-i\omega\mu}(k \cdot a \cdot \vec{N} + k \cdot b \cdot \vec{M}) \quad (2.68)$$

then the pair of vector valued functions (2.65) and (2.68) are solutions of both the Faraday and Ampere Maxwell equations for isotropic spheroids.

3 Vector Calculus for Oblate Spheroids

The Helmholtz operator in a general orthogonal ξ , η , and ϕ coordinate system may be expressed in the form is

$$\begin{aligned} \Delta\Psi + k^2\Psi = & \frac{1}{h_\xi h_\eta h_\phi} \left\{ \frac{\partial}{\partial\xi} \left(\frac{h_\eta h_\phi}{h_\xi} \frac{\partial\Psi}{\partial\xi} \right) + \right. \\ & \frac{\partial}{\partial\eta} \left(\frac{h_\xi h_\phi}{h_\eta} \frac{\partial\Psi}{\partial\eta} \right) + \\ & \left. \frac{\partial}{\partial\phi} \left(\frac{h_\xi h_\eta}{h_\phi} \frac{\partial\Psi}{\partial\phi} \right) \right\} + k^2\Psi \end{aligned} \quad (3.1)$$

and using the values of h_ξ , h_η , and h_ϕ for an oblate spheroidal coordinate system we have upon making the substitutions of equations (2.46), (2.48), (2.47), and (2.51) into equation (3.1) we deduce that

$$\begin{aligned} \Delta\Psi + k^2\Psi = & \left\{ \frac{\partial}{\partial\xi} \left((\xi^2 + 1) \frac{\partial\Psi}{\partial\xi} \right) + \frac{\partial}{\partial\eta} \left((1 - \eta^2) \frac{\partial\Psi}{\partial\eta} \right) \right. \\ & \left. + \frac{\partial^2\Psi}{\partial\phi^2} \right\} \end{aligned}$$

$$\begin{aligned}
& + \frac{\xi^2 + \eta^2}{(\xi^2 + 1)(1 - \eta^2)} \frac{\partial^2 \Psi}{\partial \phi^2} \Big\} \\
& + k^2 \frac{d^2}{4} (\xi^2 + \eta^2) \Psi = 0
\end{aligned} \tag{3.2}$$

We now seek solutions of equation (3.2) of the form

$$\Psi = R(\xi)S(\eta)\exp(im\phi) \tag{3.3}$$

and substitute equation (3.3) into equation (3.2) and then divide all terms of this equation by the function Ψ defined by equation (3.3) after making use of the relationship

$$\begin{aligned}
& \frac{\xi^2 + \eta^2}{(\xi^2 + 1)(1 - \eta^2)} = \\
& \frac{1}{1 - \eta^2} - \frac{1}{\xi^2 + 1}
\end{aligned} \tag{3.4}$$

and making the substitution

$$c^2 = k^2 d^2 / 4 \tag{3.5}$$

we obtain the relation,

$$\begin{aligned}
& \left\{ \frac{\partial}{\partial \eta} \left((1 - \eta^2) \frac{\partial}{\partial \eta} S(c, \eta) \right) \right\} / S(c, \eta) \\
& - \frac{m^2}{1 - \eta^2} + c^2 \eta^2 = \\
& - \left\{ \frac{\partial}{\partial \xi} \left((\xi^2 + 1) \frac{\partial}{\partial \xi} R(c, \xi) \right) \right\} / R(c, \xi) + \\
& \frac{m^2}{\xi^2 + 1} + c^2 \xi^2 = -\lambda_{(m,n)}
\end{aligned} \tag{3.6}$$

From equation (3.6) we obtain a kind of Rayleigh Ritz functional for the value of $\lambda_{(m,n)}$. Equation (3.6) tells us that

$$\begin{aligned}
& \lambda_{(m,n)} = \\
& \left\{ \int_{-1}^1 \left[(1 - \eta^2) \left(\frac{dS}{d\eta} \right)^2 + S^2 \left\{ (-c^2 \eta^2) + \frac{m^2}{1 - \eta^2} \right\} \right] d\eta \right\} / \left\{ \int_{-1}^1 S^2 d\eta \right\}
\end{aligned} \tag{3.7}$$

We note that when c is equal to zero, we are dealing with a sphere and that the angular functions are the associated Legendre functions $P_n^m(\eta)$ so it makes sense that we want S to behave like the function $P_n^m(\eta)$ when c is zero. We note that either $n - m$ is even or odd, and we know the initial conditions exactly in each case. We use partial derivative notation for functions $G(c, \eta)$ and note that

$$D_2 G(c, 0) = \lim_{\eta \rightarrow 0} \frac{\partial G}{\partial \eta} \tag{3.8}$$

and define the initial conditions for the second order ordinary differential equation satisfied by the functions $S(c, \eta)$. We find that if $n - m$ is an even integer

$$S_{(m,n)}(c, 0) = \{(-1)^{(n-m)/2}(n+m)!\} / \left\{2^n \left(\frac{n-m}{2}\right)! \left(\frac{n+m}{2}\right)!\right\} \quad (3.9)$$

and

$$D_2 S_{(m,n)}(c, 0) = 0 \quad (3.10)$$

and when $n - m$ is an odd number that

$$S_{(m,n)}(c, 0) = 0 \quad (3.11)$$

and that

$$D_2 S_{(m,n)}(c, 0) = \{(-1)^{(n-m-1)/2}(n+m+1)!\} / \left\{2^n \left(\frac{n-m-1}{2}\right)! \left(\frac{n+m+1}{2}\right)!\right\} \quad (3.12)$$

With these initial conditions we have completely specified S and its partial derivative and mixed partial derivative as a function of η , c , and λ and we also know that

$$\lambda(0) = n(n+1) \quad (3.13)$$

This gives us an initial value problem and an ordinary differential equation

$$\lambda'(c) = F(c, \lambda) \quad (3.14)$$

where the function F is determined by differentiating both sides of equation (3.7) with respect to c and collecting terms involving $\lambda'(c)$, and then dividing all terms by the coefficient of $\lambda'(c)$ to get the first order ordinary differential equation (3.14). By the uniqueness of the Cauchy problem, different initial values cannot lead to the same eigenvalue at

$$c = k \cdot \frac{d}{2} \quad (3.15)$$

This is effective if c is real, but if k is complex, then we think of c as being a function of a parameter s defined by

$$c(s) = s \cdot k \cdot \frac{d}{2} \quad (3.16)$$

and with the same initial condition develop an ordinary differential equation of the form,

$$\lambda'(s) = G(s, \lambda) \quad (3.17)$$

Once these eigenfunctions are known, the steps for getting an exact solution for N layer isotropic spheroids is clear. The vector valued functions \vec{M} described in the previous section are proportional to the curl of $\vec{R}\Psi$, where

$$\begin{aligned} \vec{R}\Psi &= R_n(\xi) S_{(m,n)}(\eta) \exp(im\phi) \left\{ \frac{d}{2} \right. \\ &\quad \left. \left(\xi \sqrt{\frac{\xi^2+1}{\xi^2+\eta^2}} \vec{e}_\xi - \eta \sqrt{\frac{1-\eta^2}{\xi^2+\eta^2}} \vec{e}_\eta \right) \right\} \end{aligned} \quad (3.18)$$

All three components appear in the \vec{M} vector represented in spheroidal coordinates and this is given by

$$\begin{aligned} \text{curl}(\vec{R}\Psi) = & \vec{e}_\xi \left\{ -im\eta \sqrt{\frac{1}{(\xi^2+1)(\xi^2+\eta^2)}} \Psi \right\} + \\ & \vec{e}_\eta \left\{ im\xi \sqrt{\frac{1}{(1-\eta^2)(\xi^2+\eta^2)}} \Psi \right\} + \\ & \vec{e}_\phi \left\{ \frac{\sqrt{(\xi^2+1)(1-\eta^2)}}{\xi^2+\eta^2} \left(\eta \frac{\partial}{\partial \xi} - \xi \frac{\partial}{\partial \eta} \right) \Psi \right\} \end{aligned} \quad (3.19)$$

This is $k \cdot \vec{M}$ and by expressing \vec{N} in terms of the curl of \vec{M} , we obtain the vector fields, a combination of which, can be used to represent the electric and magnetic vectors inside and outside the spheroid. The scattering problem is then solved by matching the η and the ϕ components of the electric and magnetic vectors across the boundaries of the spheroidal scatterer.

4 Prolate Spheroid Scattering – an Exact Solution

Here we consider a tensor material whose regions of continuity of tensorial electric permittivity and magnetic permeability are delimited by confocal spheroids. We assume that the foci are on the z-axis at $(0, 0, d/2)$ and $(0, 0, -d/2)$. We assume that the N confocal spheroids are defined by equations of the form,

$$\xi = \xi_i \quad (4.1)$$

where the relationship between Cartesian and Prolate spheroidal coordinates are given by equations

$$x = \frac{d}{2} [(1-\eta^2)(\xi^2-1)]^{1/2} \cos(\phi) \quad (4.2)$$

and

$$y = \frac{d}{2} [(1-\eta^2)(\xi^2-1)]^{1/2} \sin(\phi) \quad (4.3)$$

and by equation (2.6) which is the same in oblate and prolate coordinates, which means that the equation of the i th spheroid (4.1) is, in Cartesian coordinates given by

$$\frac{x^2 + y^2}{(d^2/4)(\xi^2-1)} + \frac{z^2}{(d \cdot \xi)^2/4} = 1 \quad (4.4)$$

We use the curl operator in a coordinate system with the same angle coordinate ϕ of spherical coordinates that runs from 0 to 360 degrees so that in spherical, spheroidal, cylindrical, or toroidal coordinates the Faraday Maxwell equation is defined by

$$\text{curl}(\vec{E}) = \frac{1}{h_\eta h_\phi} \left[\frac{\partial}{\partial \eta} (h_\phi E_\phi) - im h_\eta E_\eta \right] \vec{e}_\xi +$$

$$\begin{aligned} & \frac{1}{h_\xi h_\phi} \left[imh_\xi E_\xi - \frac{\partial}{\partial \xi} (h_\phi E_\phi) \right] \vec{e}_\eta + \\ & \frac{1}{h_\xi h_\eta} \left[\frac{\partial}{\partial \xi} (h_\eta E_\eta) - \frac{\partial}{\partial \eta} (h_\xi E_\xi) \right] \vec{e}_\phi = \\ & - i\omega\mu_\xi H_\xi \vec{e}_\xi - i\omega\mu_\eta H_\eta \vec{e}_\eta - i\omega\mu_\phi H_\phi \vec{e}_\phi \end{aligned} \quad (4.5)$$

We can solve equation (4.5) for components of the magnetic vector; this is simply a statement of Faraday's law which says that if one integrates the tangential component of the electric vector around the boundary of a surface, the value is equal to the negative time derivative of the normal component of the magnetic flux $\vec{B} \cdot \vec{n}$ integrated over the surface.

Ampere's law states that if we integrate the tangential component of the magnetic vector around the boundary of a surface that this is equal to the normal component of the current, which includes displacement current or the time derivative of the vector \vec{D} as well as conduction current \vec{J} , integrated over the surface. The Ampere Maxwell equation is, therefore, in this coordinate system, given by

$$\begin{aligned} \text{curl}(\vec{H}) &= \frac{1}{h_\eta h_\phi} \left[\frac{\partial}{\partial \eta} (h_\phi H_\phi) - imh_\eta H_\eta \right] \vec{e}_\xi + \\ & \frac{1}{h_\xi h_\phi} \left[imh_\xi H_\xi - \frac{\partial}{\partial \xi} (h_\phi H_\phi) \right] \vec{e}_\eta + \\ & \frac{1}{h_\xi h_\eta} \left[\frac{\partial}{\partial \xi} (h_\eta H_\eta) - \frac{\partial}{\partial \eta} (h_\xi H_\xi) \right] \vec{e}_\phi = \\ & (i\omega\epsilon_\xi + \sigma_\xi) E_\xi \vec{e}_\xi + (i\omega\epsilon_\eta + \sigma_\eta) E_\eta \vec{e}_\eta + (i\omega\epsilon_\phi + \sigma_\phi) E_\phi \vec{e}_\phi \end{aligned} \quad (4.6)$$

Solving equation (4.5) for \vec{H}_ξ we see that

$$\vec{H}_\xi = \frac{i}{\omega\mu_\xi} \left(\frac{1}{h_\eta h_\phi} \right) \left[\frac{\partial}{\partial \eta} (h_\phi E_\phi) - imh_\eta E_\eta \right] \quad (4.7)$$

Equating the η components of both sides of the Ampere Maxwell equation (4.6) and substituting equation (4.7) into this equation we deduce that

$$\begin{aligned} & \left[(i\omega\epsilon_\eta + \sigma_\eta) + \frac{1}{h_\xi h_\phi} \left[imh_\xi \left\{ \frac{i}{\omega\mu_\xi} \left(\frac{1}{h_\eta h_\phi} \right) imh_\eta \right\} \right] \right] E_\eta = \\ & \frac{1}{h_\xi h_\phi} \left[imh_\xi \left\{ \frac{i}{\omega\mu_\xi} \left(\frac{1}{h_\eta h_\phi} \right) \frac{\partial}{\partial \eta} (h_\phi E_\phi) \right\} - \frac{\partial}{\partial \xi} (h_\phi H_\phi) \right] \end{aligned} \quad (4.8)$$

We can introduce functions A_η and B_η such that equation (4.8) may be rewritten as

$$E_\eta = A_\eta \frac{\partial}{\partial \eta} (h_\phi E_\phi) - B_\eta \frac{\partial}{\partial \xi} (h_\phi H_\phi) \quad (4.9)$$

Similarly, it is clear that by equating the η components of both sides of (4.5) and solving the Ampere Maxwell equation (4.6) for E_ξ we see that we can find functions F_η and G_η such that

$$H_\eta = F_\eta \frac{\partial}{\partial \eta} (h_\phi H_\phi) - G_\eta \frac{\partial}{\partial \xi} (h_\phi E_\phi) \quad (4.10)$$

where if we define $k(\mu_\eta, \epsilon_\xi)$ by the rule,

$$k(\mu_\eta, \epsilon_\xi)^2 = (\omega^2 \mu_\eta \epsilon_\xi - i\omega \mu_\eta \sigma_\xi) \quad (4.11)$$

then

$$F_\eta = \frac{im/h_\eta}{m^2 + k(\mu_\eta, \epsilon_\xi)^2 \cdot h_\phi^2} \quad (4.12)$$

We now solve equation (4.6) for E_ξ obtaining the relationship

$$E_\xi = \frac{1}{i\omega \epsilon_\xi + \sigma_\xi} \left[\frac{1}{h_\eta h_\phi} \right] \left[\frac{\partial}{\partial \eta} (h_\phi H_\phi) - im h_\eta H_\eta \right]$$

We can, thus, express E_ξ in terms of E_ϕ and H_ϕ and can similarly express H_ξ . If we make all of these substitutions into the \vec{e}_ϕ components of both sides of the Faraday and Ampere Maxwell equations we get two coupled partial differential equations in the E_ϕ and H_ϕ variables.

Thus, we have a coupled system of elliptic equations of second order in the angular components of the electric and magnetic vectors, with all other components of the electric and magnetic vectors being simply expressed in terms of these components.

References

- [1] Asano, Shoji and Gliichi Yamamoto. "Light Scattering by a Spheroidal Particle" *Applied Optics. Volumes 14, Number 1* (1975) pages 29 - 49.
- [2] Bouwkamp, C. J. "On Spheroidal Wave Functions of Order Zero" *Journal of Math. Phys.* Volume 26 (1947) pp 79-92
- [3] Cohoon, David K. "Free commutative semigroups of right invertible operators with decomposable kernels" *Journal of Mathematical Analysis and Applications. Volume 19, Number 2* (August, 1970) pp 274-281.
- [4] Elliott, Douglas F. and K. Ramamohan Rao. *Fast Transforms Algorithms, Analysis, and Applications* New York: Academic Press (1982).
- [5] Everitt, Brian. *Cluster Analysis* New York: Halsted Press (1980)
- [6] Fisher, M. A., J. A. Friedman, and J. W. Tukey "PRIM-9 An Interactive Multidimensional Data Display System. Stanford Linear Accelerator Publication 1408" (1974)
- [7] Flammer, Carson. *Spheroidal Wave Functions* Stanford, California: Stanford University Press (1957)
- [8] Friedman, Avner. *Stochastic Differential Equations and Applications.* New York: Academic Press (1975)
- [9] Garcia, C. B. and W. I. Zangwill. *Pathways to Solutions, Fixed Points, and Equilibria.* Englewood Cliffs, NJ: Prentice Hall(1981)
- [10] Grenander, Ulf. "Regular structures. Lectures in Pattern Theory. Volume III" New York: Springer (1980)
- [11] Jones, M. N. *Spherical Harmonics and Tensors for Classical Field Theory* Chichester, England: Research Studies Press Ltd (1985)
- [12] Hochstadt, Harry. *The Functions of Mathematical Physics.* New York: Dover(1986).

- [13] Hörmander, Lars. *Linear Partial Differential Operators* New York: Academic Press (1963)
- [14] Huber, Peter J. "Projection pursuit" *Annals of Statistics*. Vol. 13, No. 2 (June, 1985) pp 435-525.
- [15] Jenkins, Gwilym M. and Donald G. Watts. *Spectral Analysis and its applications*. San Francisco: Holden Day (1969)
- [16] King, Ronald W. P. and Charles W. Harrison. *Antennas and Waves: A Modern Approach* Cambridge, Massachusetts: The M.I.T. Press (1969)
- [17] Koopmans, L. H. *The spectral analysis of time series* New York: Wiley (1974)
- [18] Liu, S. C., and D. K. Cohoon. "Limiting Behaviors of Randomly Excited Hyperbolic Tangent Systems" *The Bell System Technical Journal*, Volume 49, Number 4 (April, 1970) pp 543-560.
- [19] Lee, Kai Fong. *Principles of Antenna Theory* New York: John Wiley (1984)
- [20] Meixner, J. "Asymptotische Entwicklung der Eigenwerte und Eigenfunktionen der Differentialgleichungen der Sphäroid Funktionen und der Mathieuschen Funktionen" *J. angew Math. Mech.* Volume 28 (1948) pp 304-310
- [21] Monzingo, Robert A. and Thomas W. Miller. *Introduction to Adaptive Arrays* New York: John Wiley and Sons (1980).
- [22] Milligan, Thomas A. *Modern Antenna Design* New York: McGraw Hill (1985)
- [23] Patrick, Edward A., M.D., Ph.D. and James M. Fattu, M.D., Ph.D. *Artificial Intelligence with Statistical Pattern Recognition* Englewood Cliffs, N.J.: Prentice Hall (1986).
- [24] Srinivasan, S. K. and R. Rasudevan. *Introduction to random differential equations and their applications* New York: American Elsevier (1971)
- [25] Stutzman, Warren L. and Gary A. Thiele. *Antenna Theory and Design* New York: Wiley (1981)
- [26] Uhlenbeck, G. E. and L. S. Ornstein. "On the theory of Brownian Motion" *Phys. Rev.* 36 (1930) pp 823-841
- [27] Wait, James R. *Introduction to Antennas and Propagation* London: Peter Peregrinus (1986)
- [28] Wang, Wan Xian and Ru T. Wang. Corrections and Developments on the Theory of Scattering by Spheroids - Comparison with Experiments *Journal of Wave Material Interaction* Volume 2 (1987) pages 227-241
- [29] Wang, W. X. "Higher Order Terms in the Expressions of Spheroidal Eigenvalues" *Journal of Wave Material Interactions*. Volume 2 (1987) pp 217-226
- [30] Wang, W. X. "The Spheroidal Radial Functions of the Second Kind at High Aspect Ratio" *Journal of Wave Material Interaction*. Volume 2 (1987) pp 207-216
- [31] Whittaker, E. T. and G. N. Watson. *A Course of Modern Analysis* London: Cambridge University Press (1986).

BLANK

OPTICAL AND ABSORPTION EFFICIENCIES OF, AND POWER DENSITY DISTRIBUTIONS WITHIN N LAYER BIANISOTROPIC SPHERES SUBJECTED TO ELECTROMAGNETIC WAVES

R. H. Fricke1

D. K. Cohoon

March 5, 1992

We consider the problem of determining the optical and absorption efficiency of a class of N layer full tensor electromagnetically bianisotropic spheres to a plane polarized electromagnetic radiation. Considerable flexibility ([47]) has been demonstrated with two layer structures in relating their properties in such a way that these particles have an extremely high optical and absorption efficiency. Groundwork has been laid for the design of materials with differing electromagnetic properties in different directions which have extremely high efficiencies of absorption.

By careful analysis it would be possible to do the same for a heterogeneous radiation source(Barton [8], Chevaillier [19] [18], Chylek [20] Schaub [42], Tsui [46], Yeh [57]) when these spheres are placed in an ambient medium with material properties such that if Ω is an open set in the ambient medium and

$$\int_{\Omega} \operatorname{div}(\vec{E} \times \vec{H}^*) dv = 0,$$

then \vec{E} and \vec{H} are both zero in Ω

In this paper we describe the exact solution to the problem of describing the interaction of electromagnetic radiation with an N layer structure whose regions of continuity of tensorial electromagnetic properties are separated by concentric spheres. We assume that each of the layers are bianisotropic. For the most general case, the radial functions are solutions of a system of equations, and we get a four parameter family for each index in each layer. However, we also get an interesting, but easily computerizable example.

Bianisotropic materials have been used (Ferencz [25], Gamo [26], Hebenstreit [29], Shiozawa, [44] and Yeh [56]) in modeling a medium moving through an electromagnetic field. We consider also the possibility of an electromagnetic field whose spatial distribution would suggest a complex source that would include an off center laser beam interaction with a droplet or a radar beam sweeping across a stationary structure. By considering a layered spherically symmetric structure whose core may be metallic and with outer layers having complex material properties or containing sources of radiation, we may be able to predict the level of the hazard experienced by an individual with a metallic bone replacement or clamp who is placed in such a field.

The source of internal power density distribution for a bianisotropic structure exposed to external sources is distinct from anisotropic materials, since terms involving the product of the electric vector \vec{E} and the magnetic vector \vec{H} appear in the internal power density distribution. Using the concepts contained in this paper, a solution of an energy equation with a tensor conductivity can be obtained by an exact formula when the electromagnetic properties do not change during the exposure process. Using the derived energy density distribution as a source term, a more general nonlinear heat equation, taking into account radiative conductivity concepts can be derived. Several authors (Barton [8], Chylek [22], Schaub [42]) simply assume that the power density depends on the square of the length of the electric vector times the conductivity. In a bianisotropic material, however, there is a power density contribution from the coupling of the electric and magnetic vectors (see equation (5.2.6)).

Contents

1	A Mie Like Solution for Bianisotropic Sphere Scattering	4
1.1	Introduction	4
1.2	Problem Definition	4
1.3	Spherical Harmonics and Orthogonality Relations	5
1.4	Plane Wave Spectral Decomposition	7
1.5	The Full Tensor Solution	12
1.6	A Specific Class of Examples	16
2	Expansion Coefficient Relations	28
2.1	Representations of E and H	28
2.2	Transition Matrices	35
2.3	Determination of Expansion Coefficients	41
3	Optical and Absorption Efficiency	42
3.1	Definition of Terms	42
3.2	Computer Calculations	44
3.3	Highly Efficient Two Layer Spheres	53
4	Spatially Complex Sources	55
4.1	Expansion Coefficient Determination	55
4.2	An Exterior Complex Source	57
4.3	Interior Sources	58
5	Energy Balance	63
5.1	General Considerations	63
5.2	Bianisotropy and E H Coupling	63
5.3	Computer Output	65
5.4	Thermal Response to Radiation	69
	References	69

1 A Mie Like Solution for Bianisotropic Sphere Scattering

1.1 Introduction

Although it is possible to develop an integral equation formulation of the problem of describing the scattering of electromagnetic radiation by a bounded three dimensional body (Jones [33], pp 528-529), the only bounded body for which a truly exact solution has been obtained to the problem for describing its response to electromagnetic radiation have been those with spherical symmetry. It is possible to give a representation (Jones [33], pp 490 to 495) of the fundamental Green's tensor $\bar{\bar{\Gamma}}$ satisfying

$$\text{curl}(\text{curl}(\bar{\bar{\Gamma}})) - k^2 \bar{\bar{\Gamma}} = \bar{\bar{I}}\delta \quad (1.1.1)$$

in terms of vector spherical harmonics and to use these to develop a concise derivation of the solution of the problem of describing scattering by a sphere (Jones [33] pp 496-526). Some earlier work on anisotropic sphere scattering ([28] [32]), [49], [53]) have extended the classical result of Mie ([34] 1908) which is believed to have been first obtained by Clebsch ([23] 1863). We describe, here, an exact Mie like solution that is applicable to a class of bianisotropic spheres.

1.2 Problem Definition

We assume that $\bar{\bar{\epsilon}}$ and $\bar{\bar{\mu}}$ are tensors defining the permeability and permittivity that are functions of the spatial variables and the frequency ω of the radiation. Here Maxwell's equations have the form

$$\text{curl}(\vec{E}) = -i\omega\bar{\bar{\mu}}\vec{H} - \bar{\bar{\alpha}}\vec{E} \quad (1.2.1)$$

and

$$\text{curl}(\vec{H}) = i\omega\bar{\epsilon}\vec{E} + \bar{\sigma}\vec{E} + \bar{\beta}\vec{H} \quad (1.2.2)$$

In the ambient medium we assume that the tensors $\bar{\alpha}$ and $\bar{\beta}$ are the zero tensor $\bar{0}$. In this paper the energy balance is described which enables us to validate a computer code for describing the interaction of radiation with an N layer bianisotropic sphere where the layers may be separated by impedance sheets. The inner core may be penetrable or perfectly conducting.

1.3 Spherical Harmonics and Orthogonality Relations

The basic idea of the code is that the induced and scattered electric and magnetic vectors can be expressed in terms of

$$\vec{A}_{(m,n)} = \left[im \frac{P_n^m(\cos(\theta))}{\sin(\theta)} \vec{e}_\theta - \frac{d}{d\theta} P_n^m(\cos(\theta)) \vec{e}_\phi \right] \exp(im\phi), \quad (1.3.1)$$

$$\vec{B}_{(m,n)} = \left[\frac{d}{d\theta} P_n^m(\cos(\theta)) \vec{e}_\theta + im \frac{P_n^m(\cos(\theta))}{\sin(\theta)} \vec{e}_\phi \right] \exp(im\phi), \quad (1.3.2)$$

and

$$\vec{C}_{(m,n)} = P_n^m(\cos(\theta)) \exp(im\phi) \vec{e}_r, \quad (1.3.3)$$

where \vec{e}_r , \vec{e}_θ , and \vec{e}_ϕ are the unit vectors perpendicular, respectively, to the $r = 0$, $\theta = 0$, and $\phi = 0$, coordinate planes, and where $P_n(\cos(\theta))$ is the ordinary Legendre function defined by Rodrigues's formula

$$P_n(z) = \frac{1}{2^n n!} \left(\frac{d}{dz} \right)^n (z^2 - 1)^n \quad (1.3.4)$$

The associated Legendre functions P_n^m are given by

$$P_n^m(z) = (1 - z^2)^{m/2} \left(\frac{d}{dz} \right)^m P_n(z) \quad (1.3.5)$$

It is obvious that even without integrating over a sphere that the dot product of either of $\vec{A}_{(m,n)}$ or $\vec{B}_{(m,n)}$ with $\vec{C}_{(m,n)}$ is zero. The orthogonality of the functions $\exp(im\phi)$ and

$\exp(im\phi)$ on the unit circle for $m \neq \hat{m}$ show that if as in ([11]) we define the inner product of two vector valued functions $\vec{U}(\theta, \phi)$ and $\vec{V}(\theta, \phi)$ defined on the unit sphere by,

$$\langle \vec{U}, \vec{V} \rangle = \int_0^{2\pi} \int_0^\pi \vec{U}(\theta, \phi) \cdot \vec{V}(\theta, \phi)^* \sin(\theta) d\theta d\phi \quad (1.3.6)$$

with two different values of m are orthogonal. If we take the dot product of two distinct members of the collection

$$S = \{ \vec{A}_{(m,n)}, \vec{B}_{(m,n)}, \vec{C}_{(m,n)} : m \in \mathbb{Z}, \text{ and } n \in \{|m|, |m|+1, \dots\} \}, \quad (1.3.7)$$

with the same values of m and make use of ([2], p 333) the negative index relationship

$$P_\nu^{-\mu}(z) = \frac{\Gamma(\nu - \mu + 1)}{\Gamma(\nu + \mu + 1)} \left[P_\nu^\mu(z) - \frac{2}{\pi} \exp(-i\mu\pi) \sin(\mu\pi) Q_\nu^\mu(z) \right] \quad (1.3.8)$$

we find that any two members with different values of n are orthogonal with respect to the inner product defined by equation (1.3.6). For example, to see that

$$\langle \vec{A}_{(m,n)}, \vec{B}_{(m,r)} \rangle = 0 \quad (1.3.9)$$

for all n and r we note that this dot product reduces to

$$im(2\pi) \int_0^\pi \frac{d}{d\theta} [P_n^m(\cos(\theta)) P_r^m(\cos(\theta))] d\theta = im(2\pi) \int_{-1}^1 \frac{d}{dx} \{P_n^m(x) P_r^m(x)\} dx \quad (1.3.10)$$

The details of the remaining orthogonality relations are found in ([11]) or can be derived from properties of the Legendre functions described in Jones ([33]).

Plane waves in free space can be represented using the functions described above by carrying out the expansion (Bell, [10] page 51 and Jones [33], page 490, equation 94)

$$\exp(-ik_0 r \cos(\theta)) = \sum_{n=0}^{\infty} a_n P_n(\cos(\theta)) j_n(k_0 r) \quad (1.3.11)$$

where the expansion coefficients a_n are given by (see Jones [33], page 490)

$$a_n = (-i)^n (2n+1). \quad (1.3.12)$$

These coefficients are determined by letting $z = k_0 r$, carrying out a Taylor series expansion in z , and making use of the orthogonality relationships

$$\int_0^\pi P_n(\cos(\theta)) P_m(\cos(\theta)) \sin(\theta) d\theta = \begin{cases} 2/(2n+1) & \text{if } n = m \\ 0 & \text{if } n \neq m \end{cases} \quad (1.3.13)$$

This equation is based on the relation (Bell [10], page 61)

$$\int_{-1}^1 (z^2 - 1)^n dz = \int_{-1}^1 (z - 1)^n (z + 1)^n dz = \frac{2^{2n+1} (n!)^2}{(2n + 1)!} \cdot (-1)^n \quad (1.3.14)$$

which follows from integration by parts in the left side of equation (1.3.13). This relationship can be proven using the Rodrigues definition (equation 1.3.4). By using the notion that the algebraic structure formed by linearly combining these vector fields in a ring of radial functions is invariant under the curl operation also enables one to get an exact solution to the scattering problem for bianisotropic spheres.

1.4 Plane Wave Spectral Decomposition

An alternative to the consideration of a full wave solution is the utilization of a plane wave spectral decomposition, where specially selected plane waves with carefully chosen (i) amplitudes, (ii) polarizations, and (iii) frequencies are used to represent a complex impinging wave. Two calculations are shown here. They represent the response of a sphere of brain tissue to a complex radiation field. For the purpose of illustration we give plots of the real part of the radial component of the electric vector on the intersection of this sphere of brain tissue with a plane whose normal coincides with the laboratory z-axis. The two following plots show the real part of the radial component of the electric vector on this slice at two different times.

Figure 1.4.1. This figure shows the real part of the radial component of the electric vector in a slice of a sphere subjected to plane waves coming from two different directions. The time of observation is .3 times the common period of the two waves after a reference time.

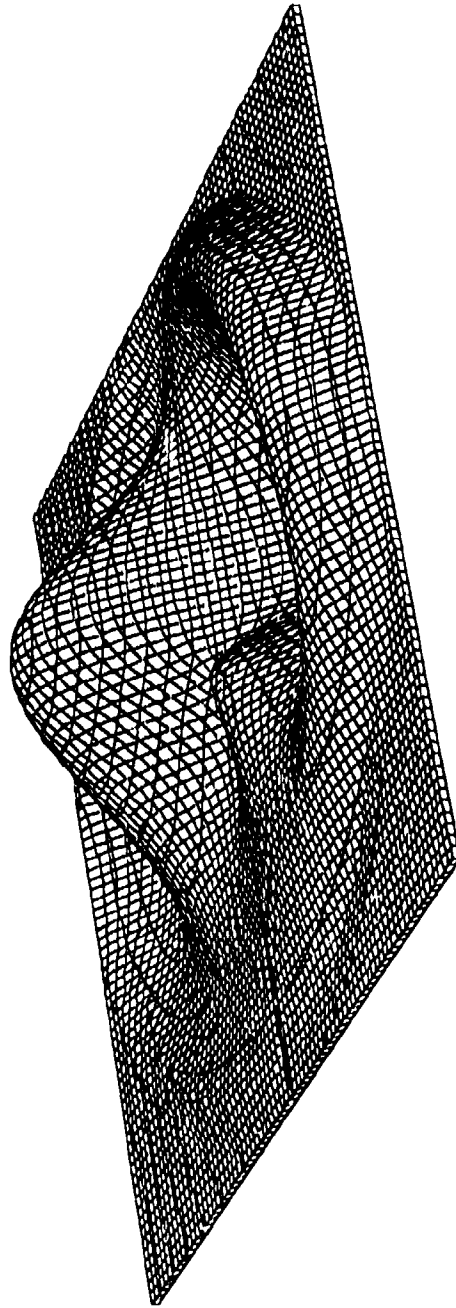


Figure 1.4.2. This figure shows the real part of the radial component of the electric vector in a slice of a sphere subjected to two plane waves coming from different directions. The time of observation is .5 times the period of the waves.

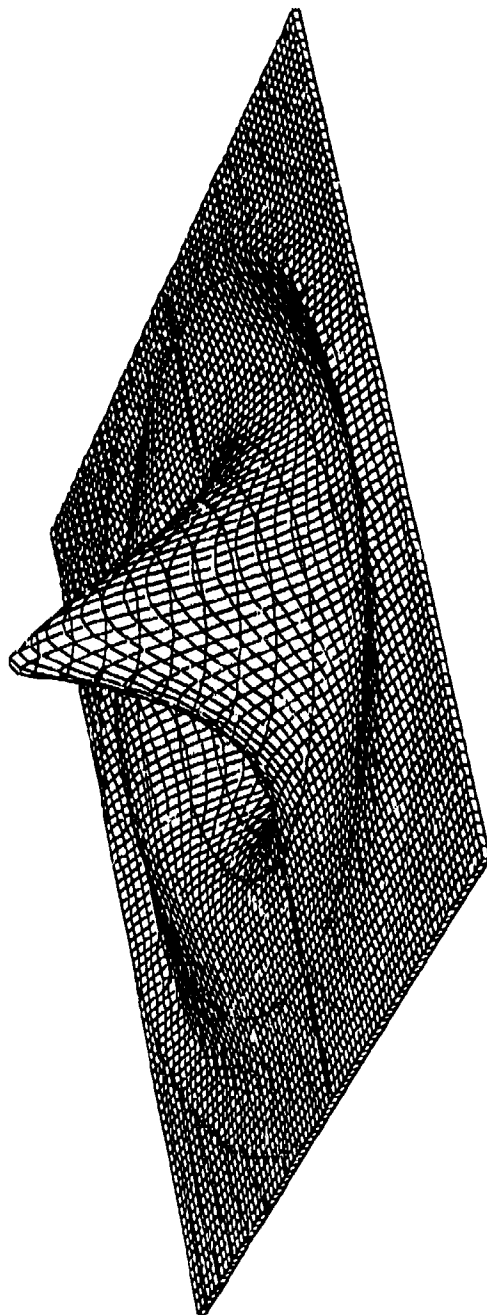
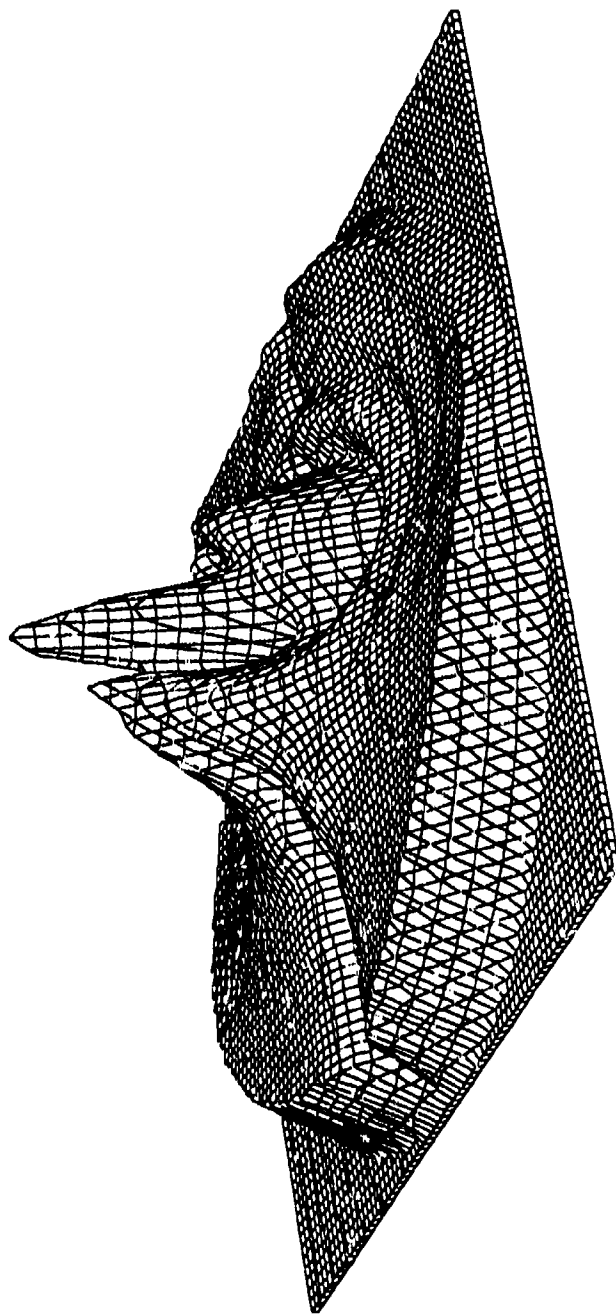


Figure 1.4.3. The figure below shows the length of the Poynting vector in a slice of the sphere subjected to plane waves of the same frequency coming from two different directions. All observation times give the same plot.



The program is capable of producing on any intersection of the sphere with any plane passing through its center the

- the real part of any component of the electric or magnetic vector (6 different 3D plots)
- the imaginary part of any component of the electric or magnetic vector (6 different 3D plots)
- the absolute value of the Poynting vector
- the absolute value of the radial component of the Poynting vector
- the square of the length of the electric vector
- the square of the length of the magnetic vector

It was found that there are considerable possibilities for cooperative interactions of phase related sources with this brain tissue sphere described in Bell ([10]).

Let us assume that the incoming radiation is a plane wave traveling in the direction

$$\vec{e}_{z_b} = \sin(\theta_b)\cos(\phi_b)\vec{e}_x + \sin(\theta_b)\sin(\phi_b)\vec{e}_y + \cos(\theta_b)\vec{e}_z \quad (1.4.1)$$

Assume further that we look at field distributions in the intersection of the structure with a plane passing through the origin and that the normal vector to this plane is

$$\vec{e}_{z_o} = \sin(\theta_o)\cos(\phi_o)\vec{e}_x + \sin(\theta_o)\sin(\phi_o)\vec{e}_y + \cos(\theta_o)\vec{e}_z \quad (1.4.2)$$

The unit vector in the direction of the y_b axis is defined as a constant c times the cross product of \vec{e}_z and the unit vector in the beam direction or

$$\vec{e}_{y_b} = c(\vec{e}_z \times \vec{e}_{z_b}) \quad (1.4.3)$$

which implies that

$$\vec{e}_{y_b} = -\sin(\phi_b)\vec{e}_x + \cos(\phi_b)\vec{e}_y \quad (1.4.4)$$

Then there is only one choice for the unit vector in the direction of the positive x_b axis, namely

$$\vec{e}_{x_b} = \vec{e}_{y_b} \times \vec{e}_b =$$

$$\cos(\theta_b)\cos(\phi_b)\vec{e}_x + \cos(\theta_b)\sin(\phi_b)\vec{e}_y + (-\sin(\theta_b))\vec{e}_z \quad (1.4.5)$$

We assume that the electric vector of the incoming wave is polarized along the x_b axis and that we would like to use the answer to a different plane wave interaction problem associated with the direction of propagation being the laboratory z axis and the direction of polarization being the laboratory x axis. In case,

$$\theta_b = \theta_o = 0 \quad (1.4.6)$$

we see that $\theta = 0$ and

$$\phi = \phi_b - \phi_o \quad (1.4.7)$$

This fact is a specialization of the general relation,

$$\begin{aligned} \vec{e}_{x_b} \cdot \vec{e}_{x_o} = \\ \cos(\theta_b)\cos(\theta_o)\cos(\phi_b - \phi_o) + \sin(\theta_b)\sin(\theta_o) \end{aligned} \quad (1.4.8)$$

The rest of the story is obtained by simply computing the angle between the x_b axis and the z_o axis. By computing another dot product we find that

$$\begin{aligned} \cos(\theta) = \sin(\theta_b)\sin(\theta_o)\cos(\phi_b)\cos(\phi_o) + \\ \sin(\theta_b)\sin(\theta_o)\sin(\phi_b)\sin(\phi_o) + \cos(\theta_b)\cos(\theta_o) \end{aligned} \quad (1.4.9)$$

By requiring that θ be the inverse cosine of the right side of equation (1.4.9) we can use the standard Mie solution for plane wave incidence to determine the field distributions in the plane whose normal is \vec{e}_o . We note that in case

$$\phi_o = \phi_b = 0$$

that equation (1.4.9) implies that

$$\cos(\theta) = \cos(\theta_b - \theta_o)$$

which is exactly the solution that one would expect.

1.5 The Full Tensor Solution

We assume that if \vec{V} is a vector, then

$$\begin{aligned} \text{curl}(\vec{V}) = & \frac{1}{r \sin(\theta)} \left[\frac{\partial}{\partial \theta} (\sin(\theta) V_\phi) - \frac{\partial V_\theta}{\partial \phi} \right] \vec{e}_r + \\ & \frac{1}{r} \left[\frac{1}{\sin(\theta)} \left(\frac{\partial V_r}{\partial \phi} \right) - \frac{\partial}{\partial r} (r V_\phi) \right] \vec{e}_\theta + \\ & \frac{1}{r} \left[\frac{\partial}{\partial r} (r V_\theta) - \frac{\partial}{\partial \theta} V_r \right] \vec{e}_\phi \end{aligned} \quad (1.5.1)$$

We then find that if we define vector fields \vec{A} , \vec{B} , \vec{C} by the rules

$$\vec{A} = F(r) \vec{A}_{(m,n)} \quad (1.5.2)$$

$$\vec{B} = F(r) \vec{B}_{(m,n)} \quad (1.5.3)$$

$$\vec{C} = F(r) \vec{C}_{(m,n)} \quad (1.5.4)$$

that then

$$\begin{aligned} \text{curl}(\vec{A}) = & n(n+1) \frac{F(r)}{r} \vec{C}_{(m,n)} + \\ & \frac{1}{r} \frac{\partial}{\partial r} (r F(r)) \vec{B}_{(m,n)}(\theta, \phi) \end{aligned} \quad (1.5.5)$$

$$\text{curl}(\vec{C}) = \frac{F(r)}{r} \vec{A}_{(m,n)} \quad (1.5.6)$$

and

$$\text{curl}(\vec{B}) = -\frac{1}{r} \frac{\partial}{\partial r} (r F(r)) \vec{A}_{(m,n)} \quad (1.5.7)$$

For each pair (m, n) of indices we seek a special solution of Maxwell's equations in the full tensor bianisotropic material of the form,

$$\vec{E} = \mathcal{A}(r) \vec{A}_{(m,n)} + \mathcal{B}(r) \vec{B}_{(m,n)} + \mathcal{C}(r) \vec{C}_{(m,n)} \quad (1.5.8)$$

We now attempt to find combinations of the functions $\mathcal{A}(r)$, $\mathcal{B}(r)$, and $\mathcal{C}(r)$ which satisfy Maxwell's equations. The first Maxwell equation obtained by taking the curl of both sides of equation (1.5.8) is, making use of equations (1.5.5), (1.5.7), and (1.5.6), we see that

$$\text{curl}(\vec{E}) = n(n+1) \frac{\mathcal{A}(r)}{r} \vec{C}_{(m,n)} +$$

$$\begin{aligned}
& \frac{1}{r} \left(\frac{\partial}{\partial r} \right) (r \mathcal{A}(r)) \vec{B}_{(m,n)} + \\
& \frac{1}{r} \left(\frac{\partial}{\partial r} \right) (r \mathcal{B}(r)) \vec{A}_{(m,n)} + \frac{\mathcal{C}(r)}{r} \vec{A}_{(m,n)} \\
& = -i\omega \bar{\mu} \vec{H} - \bar{\alpha} \vec{E}
\end{aligned} \tag{1.5.9}$$

Thus, in general we see from equation (1.5.9) that there are linear functions, \mathcal{F} , \mathcal{G} , and \mathcal{H} , of several variables such that

$$\mathcal{F} = \mathcal{F}(\mathcal{A}(r), \frac{\mathcal{A}(r)}{r}, \mathcal{A}'(r), \mathcal{B}(r), \frac{\mathcal{B}(r)}{r}, \mathcal{B}'(r), \mathcal{C}(r)), \tag{1.5.10}$$

by which we mean that there are constants f_j with

$$j \in \{1, 2, 3, 4, 5, 6, 7\} \tag{1.5.11}$$

such that

$$\begin{aligned}
\mathcal{F} = & f_1 \mathcal{A}(r) + f_2 \frac{\mathcal{A}(r)}{r} + f_3 \mathcal{A}'(r) + \\
& f_4 \mathcal{B}(r) + f_5 \frac{\mathcal{B}(r)}{r} + f_6 \mathcal{B}'(r) + f_7 \mathcal{C}(r),
\end{aligned} \tag{1.5.12}$$

$$\mathcal{G} = \mathcal{G}(\mathcal{A}(r), \frac{\mathcal{A}(r)}{r}, \mathcal{A}'(r), \mathcal{B}(r), \frac{\mathcal{B}(r)}{r}, \mathcal{B}'(r), \mathcal{C}(r)), \tag{1.5.13}$$

and similarly

$$\mathcal{H} = \mathcal{H}(\mathcal{A}(r), \frac{\mathcal{A}(r)}{r}, \mathcal{A}'(r), \mathcal{B}(r), \frac{\mathcal{B}(r)}{r}, \mathcal{B}'(r), \mathcal{C}(r)), \tag{1.5.14}$$

so that the magnetic field is given by

$$\vec{H} = \mathcal{F}(r) \vec{A}_{(m,n)} + \mathcal{G}(r) \vec{B}_{(m,n)} + \mathcal{H}(r) \vec{C}_{(m,n)} \tag{1.5.15}$$

We now obtain the final Maxwell equation by taking the curl of both sides of equation (1.5.15), and from it equations for a four parameter family of vector valued radial functions needed to represent the general field as a linear combination of solutions of the form (1.5.8) in a full tensor bianisotropic material. In the traditional Mie solution (Mie [34]) the radial functions are spherical Bessel functions.

$$\begin{aligned}
\text{curl}(\vec{H}) = & n(n+1) \frac{\mathcal{F}(r)}{r} \vec{C}_{(m,n)} + \\
& \frac{1}{r} \left(\frac{\partial}{\partial r} \right) (r \mathcal{F}(r)) \vec{B}_{(m,n)} +
\end{aligned}$$

$$\begin{aligned} \frac{1}{r} \left(\frac{\partial}{\partial r} \right) (r \mathcal{G}(r)) \vec{A}_{(m,n)} + \frac{\mathcal{H}(r)}{r} \vec{A}_{(m,n)} \\ = - (i\omega \vec{\epsilon} + \vec{\sigma}) \vec{E} + \vec{\beta} \vec{H} \end{aligned} \quad (1.5.16)$$

In order to see the general form of the last Maxwell equation (1.5.16) note, for example, that

$$\begin{aligned} \frac{1}{r} \left(\frac{\partial}{\partial r} \right) (r \mathcal{F}) = \frac{1}{r} \left(\frac{\partial}{\partial r} \right) [f_1 r \mathcal{A} + f_2 \mathcal{A} + f_3 r \mathcal{A}'(r) + \\ f_4 \mathcal{B}(r) + f_5 \frac{\mathcal{B}(r)}{r} + f_6 \mathcal{B}'(r) + f_7 \mathcal{C}(r)] \end{aligned} \quad (1.5.17)$$

Expanding the right side of equation (1.5.17) we find that

$$\begin{aligned} \frac{1}{r} \left(\frac{\partial}{\partial r} \right) (r \mathcal{F}) = f_1 \frac{\mathcal{A}(r)}{r} + f_1 \mathcal{A}'(r) + f_2 \frac{\mathcal{A}'(r)}{r} \\ + f_3 \frac{\mathcal{A}'(r)}{r} + f_3 \mathcal{A}''(r) + f_4 \frac{\mathcal{B}(r)}{r} + f_4 \mathcal{B}'(r) + f_5 \frac{\mathcal{B}'(r)}{r} + \\ f_6 \frac{\mathcal{B}'(r)}{r} + f_6 \mathcal{B}''(r) + f_7 \frac{\mathcal{C}(r)}{r} + f_7 \mathcal{C}'(r) \end{aligned} \quad (1.5.18)$$

We can then see that the final form of the resulting system of equations in the radial functions is given by,

$$\mathcal{K} \vec{A}_{(m,n)} + \mathcal{L} \vec{B}_{(m,n)} + \mathcal{M} \vec{C}_{(m,n)} = \vec{0} \quad (1.5.19)$$

We get three ordinary differential equations in the unknown radial functions $\mathcal{A}(r)$, $\mathcal{B}(r)$, and $\mathcal{C}(r)$ that are used to represent the electric vector. Assuming that the terms in the tensors are such that we can eliminate the undifferentiated function \mathcal{C} from the equation obtained by equating coefficients of $\vec{C}_{(m,n)}$ on both sides of equation (1.5.16) we get a system of two simultaneous second order differential equations in the radial functions \mathcal{A} and \mathcal{B} . A solution is specified by giving values of \mathcal{A} , \mathcal{B} and their first derivatives at a prescribed point R_p , where $r = R_p$ might represent the outer spherical boundary of the layer of interest. Thus, there are four independent solutions in each layer. By emulating the solution of the specific example, which follows, we see that the complete solution is obtained by using continuity of tangential components of \vec{E} and \vec{H} across the spherical boundaries separating regions of continuity of tensorial electromagnetic properties. A solution \vec{E} and \vec{H} of Maxwell's equations is then for each Fourier mode corresponding to

the index m and in the layer corresponding to index p a linear combination of the four solutions corresponding to

$$(\mathcal{A}(R_p), \mathcal{A}'(R_p), \mathcal{B}(R_p), \mathcal{B}'(R_p)) = (1, 0, 0, 0), \quad (1.5.20)$$

$$(\mathcal{A}(R_p), \mathcal{A}'(R_p), \mathcal{B}(R_p), \mathcal{B}'(R_p)) = (0, 1, 0, 0), \quad (1.5.21)$$

$$(\mathcal{A}(R_p), \mathcal{A}'(R_p), \mathcal{B}(R_p), \mathcal{B}'(R_p)) = (0, 0, 1, 0), \quad (1.5.22)$$

and

$$(\mathcal{A}(R_p), \mathcal{A}'(R_p), \mathcal{B}(R_p), \mathcal{B}'(R_p)) = (0, 0, 0, 1), \quad (1.5.23)$$

As it will turn out that these functions depend only on n and p and not on m . Thus, replacing \mathcal{A} by $\mathcal{A}_{(n,p)}^{(j)}$, where j runs over the indices 1 through 4 to denote the four independent solutions, we see that the general representation of the electric vector in the p th layer is given by

$$\begin{aligned} \vec{E} = \sum_{(m,n) \in \mathcal{I}} \left\{ \sum_{j=1}^4 a_{(m,n)}^{(p,j)} \left[\mathcal{A}_{(n,p)}^{(j)}(r) \vec{A}_{(m,n)}(\theta, \phi) + \right. \right. \\ \left. \left. \mathcal{C}_{(n,p)}^{(j)}(r) \vec{C}_{(m,n)}(\theta, \phi) + \mathcal{B}_{(n,p)}^{(j)}(r) \vec{B}_{(m,n)}(\theta, \phi) \right] \right\} \end{aligned} \quad (1.5.24)$$

Note that the three functions $\mathcal{A}_{(n,p)}^{(j)}$ and $\mathcal{B}_{(n,p)}^{(j)}$ and $\mathcal{C}_{(n,p)}^{(j)}$ appearing in equation (1.5.24) are not independent, but the linear combination in the summand of equation (1.5.24) represents a vector valued solution of Maxwell's equations in the full tensor bianisotropic material. Using equation (1.5.15) we see that we can write the the magnetic field in the form

$$\begin{aligned} \vec{H} = \sum_{(m,n) \in \mathcal{I}} \left\{ \sum_{j=1}^4 a_{(m,n)}^{(p,j)} \left[\mathcal{F}_{(n,p)}^{(j)}(r) \vec{A}_{(m,n)}(\theta, \phi) + \right. \right. \\ \left. \left. \mathcal{H}_{(n,p)}^{(j)}(r) \vec{C}_{(m,n)}(\theta, \phi) + \mathcal{G}_{(n,p)}^{(j)}(r) \vec{B}_{(m,n)}(\theta, \phi) \right] \right\} \end{aligned} \quad (1.5.25)$$

Using equations (1.5.24) and (1.5.25) and requiring continuity of tangential components of \vec{E} and \vec{H} across the boundary $r = R_p$ we can relate expansion coefficients in layer p to those in layer $p + 1$ by four equations in four unknowns. Certainly, if we had a perfectly conducting core there would be no trouble in reducing the number of unknowns at the first spherical boundary by requiring that the tangential component of the electric vector vanish on this surface. For a penetrable core the matter is a little more delicate as one

must select a pair of independent solutions with at worst an integrable singularity at the origin.

With what we have developed and will develop we can describe scattering of a general source by a spherical core that is

- hollow,
- perfectly conducting,
- anisotropic with diagonal tensors having the theta and phi components equal, and
- bianisotropic and satisfying the conditions described in the following section,

surrounded by any number of spherically symmetric layers which are bianisotropic with tensors satisfying conditions in the Heritage of Gauss paper ([13]).

In the remainder of this paper we discuss an example with nontrivial values of $\bar{\bar{\alpha}}$ and $\bar{\bar{\beta}}$ where the electric and magnetic fields can be represented using Bessel functions with complex index and argument.

1.6 A Specific Class of Examples

We give a simple exact Mie like solution for a class of bianisotropic N layer magnetic, penetrable spherically symmetric structures. We consider a special class of diagonal $\bar{\bar{\alpha}}$ and $\bar{\bar{\beta}}$ coupling tensors with complex numbers α_r and β_r being their radial parts and with complex numbers α and β being their tangential components and assume some additional special relations between these. We shall use a modified complex propagation constant k which in each layer has a square given by

$$k^2 = \omega^2 \mu \epsilon - i \omega \mu \sigma + \alpha \beta \quad (1.6.1)$$

For the propagation constant defined by equation (1.6.1) we seek a simple Mie like electric vector solution of both the Faraday Maxwell equation (1.2.1) and the Ampere Maxwell equation (1.2.2) which has the form,

$$\vec{E} = \sum_{(m,n) \in I} \left\{ a_{(m,n)} Z_n^{(a)}(kr) \vec{A}_{(m,n)}(\theta, \phi) + \right.$$

$$c_{(m,n)} \frac{Z_n^{(c)}(kr)}{kr} \vec{C}_{(m,n)}(\theta, \phi) + \frac{b_{(m,n)}}{kr} \left(- \left(\frac{\partial}{\partial r} \right) (r Z_n^{(b)}(kr)) \right) \vec{B}_{(m,n)}(\theta, \phi) \} \quad (1.6.2)$$

where the three radial functions $Z_n^{(a)}$, $Z_n^{(b)}$, and $Z_n^{(c)}$ are to be derived and the functions $\vec{A}_{(m,n)}$, $\vec{B}_{(m,n)}$, and $\vec{C}_{(m,n)}$ are defined by equations (1.3.1), (1.3.2), and (1.3.3). We shall derive relationships needed between the radial functions $Z_n^{(a)}$, $Z_n^{(b)}$, and $\vec{C}_{(m,n)}$ and the complex expansion coefficients $a_{(m,n)}$, $b_{(m,n)}$, and $c_{(m,n)}$ needed to get an interesting, but easily computed, exact Mie like solutions for the response of a class of N layer bianisotropic spheres to both plane waves and complex sources.

We now begin to develop the consequences of Maxwell's equations by noting that equation (1.6.2) and the three basic curl relationships, (1.5.5), (1.5.6), and (1.5.7) and the Faraday Maxwell equation (1.2.1) imply that $\text{curl}(\vec{E})$ is given by

$$\begin{aligned} \text{curl}(\vec{E}) = & \sum_{(m,n) \in \mathcal{I}} \left\{ a_{(m,n)} \left[n(n+1) \frac{Z_n^{(a)}(kr)}{r} \vec{C}_{(m,n)} + \frac{1}{r} \frac{\partial}{\partial r} (r Z_n^{(a)}(kr)) \vec{B}_{(m,n)} \right] + \right. \\ & c_{(m,n)} \frac{Z_n^{(c)}(kr)}{kr^2} \vec{A}_{(m,n)} + b_{(m,n)} \frac{1}{kr} \left(\frac{\partial}{\partial r} \right)^2 (r Z_n^{(b)}(kr)) \vec{A}_{(m,n)} \Big\} = \\ & -\bar{\alpha} \left[\sum_{(m,n) \in \mathcal{I}} \left\{ a_{(m,n)} Z_n^{(a)}(kr) \vec{A}_{(m,n)} + c_{(m,n)} \frac{Z_n^{(c)}}{kr} \vec{C}_{(m,n)} + \right. \right. \\ & \left. \left. \frac{b_{(m,n)}}{kr} \left(- \left(\frac{\partial}{\partial r} \right) (r Z_n^{(b)}(kr)) \right) \vec{B}_{(m,n)} \right\} \right] - i\omega \bar{\mu} \vec{H} \end{aligned} \quad (1.6.3)$$

This is the completely general Faraday Maxwell equation for electric vectors given by equation (1.6.2). We want to solve equation (1.6.3) for \vec{H} so that we can substitute this vector valued function into the Ampere Maxwell equation (1.2.2) and determine what types of equations the three radial functions $Z_n^{(a)}$, $Z_n^{(b)}$, and $Z_n^{(c)}$ should satisfy. Solving equation (1.6.3) for $\bar{\mu} \vec{H}$, we see that in general if we simply assume that $\bar{\alpha}$ is a diagonal tensor whose action on a vector represented in spherical coordinates is defined by,

$$\bar{\alpha} \cdot \vec{E} = \begin{pmatrix} \alpha_r & 0 & 0 \\ 0 & \alpha & 0 \\ 0 & 0 & \alpha \end{pmatrix} \begin{pmatrix} E_r \\ E_\theta \\ E_\phi \end{pmatrix} \quad (1.6.4)$$

that then making use of equation (1.6.4)

$$\begin{aligned}
 -i\omega\bar{\mu}\vec{H} = & \sum_{(m,n) \in \mathcal{I}} \left\{ \left[a_{(m,n)} n(n+1) \frac{Z_n^{(a)}(kr)}{r} + \alpha_r c_{(m,n)} \frac{Z_n^{(c)}(kr)}{kr} \right] \vec{C}_{(m,n)} \right. \\
 & + \left[a_{(m,n)} \frac{1}{r} \frac{\partial}{\partial r} (r Z_n^{(a)}(kr)) - \alpha b_{(m,n)} \left(\frac{1}{kr} \right) \left(\frac{\partial}{\partial r} \right) (r Z_n^{(b)}(kr)) \right] \vec{B}_{(m,n)} + \\
 & \left. \left[c_{(m,n)} \frac{Z_n^{(c)}(kr)}{kr^2} + b_{(m,n)} \frac{1}{kr} \left(\frac{\partial}{\partial r} \right)^2 (r Z_n^{(b)}(kr)) + \alpha a_{(m,n)} Z_n^{(a)}(kr) \right] \vec{A}_{(m,n)} \right\} \quad (1.6.5)
 \end{aligned}$$

In the previous section we allowed $\bar{\alpha}$, $\bar{\beta}$, $\bar{\epsilon}$, $\bar{\mu}$, and $\bar{\sigma}$ to be general tensors and solved for the general radial functions $\mathcal{C}(r)$, $\mathcal{B}(r)$, and $\mathcal{A}(r)$ used in the representation (1.5.8) of the electric vector, we now assume that all these tensors have the same form as the complex $\bar{\alpha}$ tensor given by equation (1.6.4).

With these assumptions, we see that for our simplified bianisotropic material, the magnetic vector will then have the form

$$\begin{aligned}
 \vec{H} = & \sum_{(m,n) \in \mathcal{I}} \left[\frac{i}{\omega\mu_r} \left\{ a_{(m,n)} \frac{Z_n^{(a)}(kr) n(n+1)}{r} + \alpha_r c_{(m,n)} \frac{Z_n^{(c)}(kr)}{kr} \right\} \vec{C}_{(m,n)} \right. \\
 & + \frac{i}{\omega\mu} \left\{ a_{(m,n)} \frac{1}{r} \frac{\partial}{\partial r} (r Z_n^{(a)}(kr)) - \alpha b_{(m,n)} \frac{1}{kr} \left(\frac{\partial}{\partial r} \right) (r Z_n^{(b)}(kr)) \right\} \vec{B}_{(m,n)} + \\
 & \left. \frac{i}{\omega\mu} \left\{ c_{(m,n)} \frac{Z_n^{(c)}(kr)}{kr^2} + b_{(m,n)} \left(\frac{1}{kr} \right) \left(\frac{\partial}{\partial r} \right)^2 (r Z_n^{(b)}(kr)) + \alpha a_{(m,n)} Z_n^{(a)}(kr) \right\} \vec{A}_{(m,n)} \right] \quad (1.6.6)
 \end{aligned}$$

Applying the curl operation to both sides of equation 1.6.6 using the three curl equations (1.5.5), (1.5.6) and (1.5.7) we obtain an expanded form of the Ampere Maxwell equation given by,

$$\begin{aligned}
 \text{curl}(\vec{H}) = & \left(\frac{i}{\omega\mu_r} \right) \frac{1}{r} \left\{ a_{(m,n)} \frac{Z_n^{(a)}(kr) n(n+1)}{r} + \alpha_r c_{(m,n)} \frac{Z_n^{(c)}(r)}{kr} \right\} \vec{A}_{(m,n)} + \\
 & \left(\frac{i}{\omega\mu} \right) \left(\frac{-1}{r} \frac{\partial}{\partial r} \right) \left(r \left\{ a_{(m,n)} \frac{1}{r} \frac{\partial}{\partial r} (r Z_n^{(a)}(kr)) \right. \right. \\
 & \left. \left. - \alpha b_{(m,n)} \frac{1}{kr} \frac{\partial}{\partial r} (r Z_n^{(b)}(kr)) \right\} \vec{A}_{(m,n)} + \right.
 \end{aligned}$$

$$\begin{aligned}
& \left(\frac{i}{\omega\mu} \right) \frac{n(n+1)}{r} \left\{ c_{(m,n)} \frac{Z_n^{(c)}(kr)}{kr^2} + \right. \\
& \left. b_{(m,n)} \frac{1}{kr} \left(\frac{\partial}{\partial r} \right)^2 (r Z_n^{(b)}(kr)) + \alpha a_{(m,n)} Z_n^{(a)}(kr) \right\} \vec{C}_{(m,n)} + \\
& \left(\frac{i}{\omega\mu} \right) \frac{1}{r} \frac{\partial}{\partial r} \left(r \left\{ c_{(m,n)} \frac{Z_n^{(c)}(kr)}{kr^2} + \right. \right. \\
& \left. \left. b_{(m,n)} \frac{1}{kr} \left(\frac{\partial}{\partial r} \right)^2 (r Z_n^{(b)}(kr)) + \alpha a_{(m,n)} Z_n^{(a)}(kr) \right\} \right) \vec{B}_{(m,n)} \\
& = (i\omega\bar{\epsilon} + \bar{\sigma}) \vec{E} + \bar{\beta} \vec{H} \tag{1.6.7}
\end{aligned}$$

To make use of the Ampere Maxwell equation (1.6.7), we need to use our original equation (1.6.2) for \vec{E} and equation (1.6.6) for \vec{H} to obtain

$$\begin{aligned}
& (i\omega\bar{\epsilon} + \bar{\sigma}) \vec{E} + \bar{\beta} \vec{H} = \\
& \sum_{(m,n) \in \mathcal{I}} \left\{ \left[(i\omega\epsilon + \sigma) a_{(m,n)} Z_n^{(a)}(r) + \frac{i\beta}{\omega\mu} \left\{ \frac{c_{(m,n)}}{kr^2} Z_n^{(c)}(kr) + \right. \right. \right. \\
& \left. \left. \frac{b_{(m,n)}}{kr} \left(\frac{\partial}{\partial r} \right)^2 (r Z_n^{(b)}(kr)) + \alpha a_{(m,n)} Z_n^{(a)}(kr) \right\} \right] \vec{A}_{(m,n)}(\theta, \phi) + \\
& \left[(i\omega\epsilon + \sigma) \frac{b_{(m,n)}}{kr} \left(-\frac{\partial}{\partial r} \right) (r Z_n^{(b)}(kr)) + \right. \\
& \left. \left[\frac{i\beta}{\omega\mu} \left\{ a_{(m,n)} \frac{1}{r} \frac{\partial}{\partial r} (r Z_n^{(a)}(kr)) + \frac{\alpha b_{(m,n)}}{kr} \left(-\frac{\partial}{\partial r} (r Z_n^{(b)}(kr)) \right) \right\} \right] \vec{B}_{(m,n)}(\theta, \phi) \right. \\
& \left. + \left[(i\omega\epsilon_r + \sigma_r) c_{(m,n)} \frac{Z_n^{(c)}(kr)}{kr} + \right. \right. \\
& \left. \left. \frac{i\beta_r}{\omega\mu_r} \left\{ a_{(m,n)} Z_n^{(a)}(kr) \frac{n(n+1)}{r} + \alpha_r \frac{c_{(m,n)} Z_n^{(c)}(r)}{kr} \right\} \right] \vec{C}_{(m,n)}(\theta, \phi) \right] \tag{1.6.8}
\end{aligned}$$

The solution of the electromagnetic interaction problem is then obtained by relating coefficients on both sides of equation (1.6.7) and making use of orthogonality relations to get differential equations for the, a priori unknown, radial functions, $Z_n^{(a)}$, $Z_n^{(b)}$, and $Z_n^{(c)}$.

Equation (1.6.7) coupled with equation (1.6.8) is the key to the development of a system of ordinary differential equations satisfied by the radial functions. Using orthogonality properties of the vector functions $\vec{A}_{(m,n)}$ and $\vec{B}_{(m,n)}$ and $\vec{C}_{(m,n)}$ defined, respectively, by (1.3.1) and (1.3.2), and (1.3.3) we shall develop three relationships involving only the radial

functions, express one of these radial functions in terms of the others, and get an uncoupled system whose solutions will be Bessel functions with complex index and argument. by equating their coefficients on both sides of equation (1.6.7). Equating coefficients of $\vec{A}_{(m,n)}$ on both sides of equation (1.6.7) we find that

$$\begin{aligned} & \left[\left(\frac{i}{\omega \mu_r} \right) \frac{1}{r} \left\{ a_{(m,n)} \frac{Z_n^{(a)}(kr) n(n+1)}{r} + \alpha_r c_{(m,n)} \frac{Z_n^{(c)}(kr)}{kr} \right\} + \right. \\ & \quad \left(\frac{i}{\omega \mu} \right) \left(\frac{-1}{r} \frac{\partial}{\partial r} \right) \left(r \left\{ a_{(m,n)} \frac{1}{r} \frac{\partial}{\partial r} (r Z_n^{(a)}(kr)) \right. \right. \\ & \quad \left. \left. - \alpha b_{(m,n)} \frac{1}{kr} \frac{\partial}{\partial r} (r Z_n^{(b)}(kr)) \right\} \right) \Big] = \\ & \quad \left[(i\omega \epsilon + \sigma) a_{(m,n)} Z_n^{(a)}(kr) + \frac{i\beta}{\omega \mu} \left\{ \frac{c_{(m,n)}}{kr^2} Z_n^{(c)}(kr) + \right. \right. \\ & \quad \left. \left. \frac{b_{(m,n)}}{kr} \left(\frac{\partial}{\partial r} \right)^2 (r Z_n^{(b)}(kr)) + \alpha a_{(m,n)} Z_n^{(a)}(kr) \right\} \right] \quad (1.6.9) \end{aligned}$$

We can see the consistency of this equation with the equations obtained for the special case of anisotropic spherical structures ([15]). If in equation (1.6.9) we set $\vec{\alpha}$ and $\vec{\beta}$ equal to the zero tensor, we obtain

$$\begin{aligned} & \left[\left(\frac{i}{\omega \mu_r} \right) \frac{1}{r} \left\{ a_{(m,n)} \frac{Z_n^{(a)}(kr) n(n+1)}{r} \right\} + \right. \\ & \quad \left. \left(\frac{i}{\omega \mu} \right) \left(\frac{-1}{r} \frac{\partial}{\partial r} \right) \left(r \left\{ a_{(m,n)} \frac{1}{r} \frac{\partial}{\partial r} (r Z_n^{(a)}(kr)) \right\} \right) \right] = [(i\omega \epsilon + \sigma) a_{(m,n)} Z_n^{(a)}(kr)] \quad (1.6.10) \end{aligned}$$

or upon multiplying both sides of equation (1.6.10) by $-i\omega \mu$ we find that if we define the propagation constant for a class of anisotropic structures ([15]) by the rule,

$$k_a^2 = \omega^2 \mu \epsilon - i\omega \mu \sigma \quad (1.6.11)$$

that then $Z_n^{(a)}$ satisfies,

$$\left(\frac{\mu}{\mu_r} \right) Z_n^{(a)}(k_a r) \frac{n(n+1)}{r^2} - k_a^2 Z_n^{(a)}(k_a r) = \frac{1}{r} \left(\frac{\partial}{\partial r} \right)^2 (r Z_n^{(a)}(k_a r)) \quad (1.6.12)$$

which, with the propagation constant k_a being defined by (1.6.11) rather than by (1.6.1), is exactly the equation satisfied by the radial function $Z_n^{(a)}$ for an anisotropic sphere ([15]).

We can also, in a similar fashion, relate coefficients of $\vec{B}_{(m,n)}$ on both sides of equation (1.6.7) with k^2 defined by (1.6.1) to obtain the relationship.

$$\begin{aligned} & \left(\frac{i}{\omega\mu} \right) \frac{1}{r} \frac{\partial}{\partial r} \left(r \left\{ c_{(m,n)} \frac{Z_n^{(c)}(kr)}{kr^2} + \right. \right. \\ & \left. \left. b_{(m,n)} \frac{1}{kr} \left(\frac{\partial}{\partial r} \right)^2 (r Z_n^{(b)}(kr)) + \alpha a_{(m,n)} Z_n^{(a)}(kr) \right\} \right) = \\ & \left[(i\omega\epsilon + \sigma) \frac{b_{(m,n)}}{kr} \left(-\frac{\partial}{\partial r} \right) (r Z_n^{(b)}(kr)) + \right. \\ & \left. \left[\frac{i\beta}{\omega\mu} \left\{ a_{(m,n)} \frac{1}{r} \frac{\partial}{\partial r} (r Z_n^{(a)}(kr)) + \frac{\alpha b_{(m,n)}}{kr} \left(-\frac{\partial}{\partial r} (r Z_n^{(b)}(kr)) \right) \right\} \right] \right] \end{aligned} \quad (1.6.13)$$

If in equation (1.6.13) we equate the terms operated on by 1 over r times the partial derivative with respect to r , and then divide all terms on both sides by r we deduce that equation (1.6.13) is implied by the simpler relation,

$$\begin{aligned} & \left(\frac{i}{\omega\mu} \right) \left\{ c_{(m,n)} \frac{Z_n^{(c)}(kr)}{kr^2} + \right. \\ & \left. b_{(m,n)} \frac{1}{kr} \left(\frac{\partial}{\partial r} \right)^2 (r Z_n^{(b)}(r)) + \alpha a_{(m,n)} Z_n^{(a)}(r) \right\} = \\ & \left[(i\omega\epsilon + \sigma) \frac{b_{(m,n)}}{k} (-Z_n^{(b)}(r)) + \right. \\ & \left. \left[\frac{i\beta}{\omega\mu} \left\{ a_{(m,n)} (Z_n^{(a)}(r)) - \frac{\alpha b_{(m,n)}}{k} (Z_n^{(b)}(r)) \right\} \right] \right] \end{aligned} \quad (1.6.14)$$

Equating coefficients of $\vec{C}_{(m,n)}$ on both sides of our specialized Ampere Maxwell equation (1.6.7) with k defined by (1.6.1) reveals that

$$\begin{aligned} & \left(\frac{i}{\omega\mu} \right) \frac{n(n+1)}{r} \left\{ c_{(m,n)} \frac{Z_n^{(c)}(kr)}{kr^2} + \right. \\ & \left. b_{(m,n)} \frac{1}{kr} \left(\frac{\partial}{\partial r} \right)^2 (r Z_n^{(b)}(kr)) + \alpha a_{(m,n)} Z_n^{(a)}(kr) \right\} = \\ & + \left[(i\omega\epsilon_r + \sigma_r) c_{(m,n)} \frac{Z_n^{(c)}(kr)}{kr} + \right. \\ & \left. \frac{i\beta_r}{\omega\mu_r} \left\{ a_{(m,n)} Z_n^{(a)}(kr) \frac{n(n+1)}{r} + \alpha_r \frac{c_{(m,n)} Z_n^{(c)}(kr)}{kr} \right\} \right] \end{aligned} \quad (1.6.15)$$

To compare equation (1.6.14) and equation (1.6.15) we multiply both sides of equation (1.6.15) by $r/(n(n+1))$ and we find that

$$\left(\frac{i}{\omega\mu}\right) \left\{ \frac{c_{(m,n)}}{kr^2} Z_n^{(c)}(kr) + b_{(m,n)} \left(\frac{1}{kr}\right) \left(\frac{\partial}{\partial r}\right)^2 (rZ_n^{(b)}(kr)) + \alpha a_{(m,n)} Z_n^{(a)}(kr) \right\} =$$

$$\left(\frac{i\omega\epsilon_r + \sigma_r}{n(n+1)}\right) c_{(m,n)} \frac{Z_n^{(c)}(kr)}{k} +$$

$$\beta_r \frac{i}{\omega\mu_r} a_{(m,n)} Z_n^{(a)}(kr) + \left(\frac{\alpha_r \beta_r}{n(n+1)}\right) \left(\frac{i}{\omega\mu_r} c_{(m,n)}\right) \frac{Z_n^{(c)}(kr)}{k} \quad (1.6.16)$$

Since the left side of equation (1.6.16) is identical to the left side of equation (1.6.14) it is clear that we have consistency between equation (1.6.16) and equation (1.6.14) provided that

$$(i\omega\epsilon + \sigma)(-b_{(m,n)} Z_n^{(b)}(r)) +$$

$$\left(\frac{i\beta}{\omega\mu}\right) k a_{m,n} Z_n^{(a)}(kr) - \left(\frac{i\beta\alpha}{\omega\mu}\right) b_{(m,n)} Z_n^{(b)}(kr) =$$

$$\left(\frac{i\omega\epsilon_r + \sigma_r}{n(n+1)}\right) c_{(m,n)} Z_n^{(c)}(kr) +$$

$$\frac{i\beta_r k}{\omega\mu_r} a_{(m,n)} Z_n^{(a)}(kr) + \frac{\alpha_r \beta_r}{n(n+1)} \left(\frac{i}{\omega\mu_r}\right) c_{(m,n)} Z_n^{(c)}(kr) \quad (1.6.17)$$

where k is defined by (1.6.1).

We note that the consistency relation given by equation (1.6.17) specializes for the case of the ordinary anisotropic sphere, where the coupling tensors $\bar{\alpha}$ and $\bar{\beta}$, are both equal to the zero tensor, to the simple anisotropic sphere relation of ([15]) given by

$$(i\omega\epsilon + \sigma)(-b_{(m,n)} Z_n^{(b)}(k_n r)) = \left(\frac{i\omega\epsilon_r + \sigma_r}{n(n+1)}\right) c_{(m,n)} Z_n^{(c)}(k_n r) \quad (1.6.18)$$

where k_n is given by (1.6.11) We note that equation (1.6.18) is satisfied if

$$Z_n^{(c)}(k_n r) = Z_n^{(b)}(k_n r) \quad (1.6.19)$$

and

$$c_{(m,n)} = -n(n+1) \left(\frac{i\omega\epsilon + \sigma}{i\omega\epsilon_r + \sigma_r}\right) b_{(m,n)} \quad (1.6.20)$$

which are identical to the relations derived in ([15]) for anisotropic spheres.

We, however, now again suppose that k is defined more generally by (1.6.1) and collect the terms multiplying the coefficients $a_{(m,n)}$, $b_{(m,n)}$, and $c_{(m,n)}$ in equation (1.6.9). In doing so we rewrite (1.6.9) in the form,

$$\begin{aligned} & \left[\left(\frac{i}{\omega\mu_r} \right) \left(\frac{1}{r} \right) Z_n^{(a)}(kr) \frac{n(n+1)}{r} - (i\omega\epsilon + \sigma) Z_n^{(a)}(kr) \right. \\ & \quad \left. - \frac{i\beta}{\omega\mu} \alpha Z_n^{(a)}(kr) - \frac{i}{\omega\mu} \frac{1}{r} \left(\frac{\partial}{\partial r} \right)^2 (r Z_n^{(a)}(kr)) \right] a_{(m,n)} + \\ & \quad \left[\left(\frac{-i}{\omega\mu} \right) \frac{\alpha}{k} - \frac{i\beta}{\omega\mu k} \right] \left\{ \frac{1}{r} \left(\frac{\partial}{\partial r} \right)^2 (r Z_n^{(b)}(kr)) \right\} b_{(m,n)} + \\ & \quad \left[\left(\frac{i\alpha_r}{\omega\mu_r} - \frac{i\beta}{\omega\mu} \frac{1}{kr^2} \right) Z_n^{(c)}(kr) \right] c_{(m,n)} = 0 \end{aligned} \quad (1.6.21)$$

By rearranging equations as we have done we are attempting to develop, for our class of bianisotropic spheres, relationships for the radial functions analogous to the relationships, (1.6.12) and (1.6.19), for anisotropic spheres. Thus, collecting the coefficients of $a_{(m,n)}$, $b_{(m,n)}$, and $c_{(m,n)}$ in equation (1.6.14) we have

$$\begin{aligned} & \left[\left(\frac{i}{\omega\mu} \right) \alpha Z_n^{(a)}(kr) - \frac{i\beta}{\omega\mu} Z_n^{(a)}(kr) \right] a_{(m,n)} \\ & + \left[\frac{i}{\omega\mu} \left(\frac{1}{kr} \right) \left(\frac{\partial}{\partial r} \right)^2 (r Z_n^{(b)}(kr)) + \frac{\sigma + i\omega\epsilon}{k} Z_n^{(b)}(kr) \right. \\ & \quad \left. + \frac{i\beta\alpha}{\omega\mu k} Z_n^{(b)}(kr) \right] b_{(m,n)} + \frac{i}{\omega\mu} \left(\frac{1}{kr^2} \right) Z_n^{(c)}(kr) c_{(m,n)} = 0 \end{aligned} \quad (1.6.22)$$

Equation (1.6.22) yields the relationship

$$\begin{aligned} & b_{(m,n)} \frac{i}{\omega\mu} \frac{1}{kr} \left(\frac{\partial}{\partial r} \right)^2 (r Z_n^{(b)}(kr)) = \\ & - \left[\frac{i}{\omega\mu} \alpha Z_n^{(a)}(kr) - \frac{i\beta}{\omega\mu} Z_n^{(a)}(kr) \right] a_{(m,n)} - \\ & \left[\frac{\sigma + i\omega\epsilon}{k} Z_n^{(b)}(kr) + \frac{i\beta\alpha}{\omega\mu k} Z_n^{(b)}(kr) \right] b_{(m,n)} \\ & - \frac{i}{\omega\mu} \frac{1}{kr^2} Z_n^{(c)}(kr) c_{(m,n)} \end{aligned} \quad (1.6.23)$$

with the k being given by (1.6.1).

Equation (1.6.15), after collecting terms multiplying the same coefficients, yields the relationship

$$\begin{aligned}
 & \frac{n(n+1)}{r} \left\{ b_{(m,n)} \frac{i}{\omega\mu} \frac{1}{kr} \left(\frac{\partial}{\partial r} \right)^2 (r Z_n^{(b)}(kr)) \right\} \\
 &= \left\{ \frac{-n(n+1)}{r} \left(\frac{i}{\omega\mu} \frac{1}{kr^2} Z_n^{(c)}(kr) \right) + \beta_r \left(\frac{i}{\omega\mu_r} \right) \frac{\alpha_r}{kr} Z_n^{(c)}(kr) \right. \\
 & \quad \left. + \frac{i\omega\epsilon_r + \sigma_r}{kr} Z_n^{(c)}(kr) \right\} c_{(m,n)} + \\
 & a_{(m,n)} \left\{ \frac{-i}{\omega\mu} \frac{n(n+1)}{r} \alpha Z_n^{(a)}(kr) + \beta_r \left(\frac{i}{\omega\mu_r} \right) Z_n^{(a)}(kr) \frac{n(n+1)}{r} \right\} \quad (1.6.24)
 \end{aligned}$$

Multiplying all terms of equation (1.6.24) by $r/(n(n+1))$ we find that

$$\begin{aligned}
 & \left\{ b_{(m,n)} \frac{i}{\omega\mu} \frac{1}{kr} \left(\frac{\partial}{\partial r} \right)^2 (r Z_n^{(b)}(kr)) \right\} = \\
 & \left\{ - \left[\frac{i}{\omega\mu} \frac{1}{kr^2} Z_n^{(c)}(r) \right] + \left(\frac{i\alpha_r\beta_r}{\omega\mu_r} \right) \frac{1}{kn(n+1)} Z_n^{(c)}(kr) \right. \\
 & \quad \left. + \frac{i\omega\epsilon_r + \sigma_r}{kn(n+1)} Z_n^{(c)}(kr) \right\} c_{(m,n)} + \\
 & \left\{ \frac{-i}{\omega\mu} \alpha Z_n^{(a)}(kr) + \left(\frac{i\beta_r}{\omega\mu_r} \right) Z_n^{(a)}(kr) \right\} a_{(m,n)} \quad (1.6.25)
 \end{aligned}$$

Solving for the term

$$U = \frac{i}{\omega\mu} \frac{1}{kr} \left(\frac{\partial}{\partial r} \right)^2 (r Z_n^{(b)}(kr)) b_{(m,n)} \quad (1.6.26)$$

in equations (1.6.25) and (1.6.23) we find that equating the two expressions for U yields,

$$\begin{aligned}
 & - \left[\alpha \frac{i}{\omega\mu} Z_n^{(a)}(kr) - \frac{i\beta}{\omega\mu} Z_n^{(a)}(kr) \right] a_{(m,n)} \\
 & - \left[\frac{\sigma + i\omega\epsilon}{k} Z_n^{(b)}(kr) + \frac{i\beta}{\omega\mu} \frac{\alpha}{k} Z_n^{(b)}(kr) \right] b_{(m,n)} \\
 & - c_{(m,n)} \left(\frac{i}{kr^2\omega\mu} \right) Z_n^{(c)}(kr) = \\
 & - \left[\frac{i\alpha}{\omega\mu} Z_n^{(a)}(kr) - \frac{i\beta_r}{\omega\mu_r} Z_n^{(a)}(kr) \right] a_{(m,n)} - \\
 & \left[\left(\frac{i}{\omega\mu} \right) \frac{1}{kr^2} Z_n^{(c)}(kr) - \frac{i\omega\epsilon_r + \sigma_r}{kn(n+1)} Z_n^{(c)}(kr) \right]
 \end{aligned}$$

$$- \left(\frac{\alpha_r \beta_r}{k \omega \mu_r n(n+1)} \right) Z_n^{(c)}(kr) \Big] c_{(m,n)} \quad (1.6.27)$$

Equation (1.6.27) implies, after subtracting identical terms from both sides of the equation, that

$$\begin{aligned} & \left[-\frac{i\omega\epsilon_r + \sigma_r}{kn(n+1)} - \frac{\beta_r \alpha_r}{k\omega\mu_r n(n+1)} \right] c_{(m,n)} Z_n^{(c)}(kr) = \\ & - \left(\frac{i\beta}{\omega\mu} - \frac{i\beta_r}{\omega\mu_r} \right) Z_n^{(a)}(kr) a_{(m,n)} + \\ & \left[\frac{\sigma + i\omega\epsilon}{k} + \frac{i\beta\alpha}{\omega\mu k} \right] Z_n^{(b)}(kr) b_{(m,n)} \end{aligned} \quad (1.6.28)$$

Solving equation (1.6.17) for $c_{(m,n)} Z_n^{(c)}(kr)$ we find that

$$\begin{aligned} & \left\{ \frac{i\omega\epsilon_r + \sigma_r}{n(n+1)} + \frac{i\alpha_r \beta_r}{\omega\mu_r n(n+1)} \right\} c_{(m,n)} Z_n^{(c)}(kr) = \\ & \left\{ -(i\omega\epsilon + \sigma) - \frac{i\beta\alpha}{\omega\mu} \right\} b_{(m,n)} Z_n^{(b)}(kr) + \\ & \left(\frac{i\beta k}{\omega\mu} - \frac{i\beta_r k}{\omega\mu_r} \right) a_{(m,n)} Z_n^{(a)}(kr) \end{aligned} \quad (1.6.29)$$

We could use this relationship (1.6.29) to eliminate $Z_n^{(c)}$ but we would end up with a coupled system in the other two radial functions. However, for a simpler chiral sphere where

$$\frac{\beta}{\mu} = \frac{\beta_r}{\mu_r}, \quad (1.6.30)$$

equation (1.6.29) has the form

$$c_{(m,n)} Z_n^{(c)}(kr) = -n(n+1) \left(\frac{i\omega\epsilon + \sigma + i\beta\alpha/(\omega\mu)}{(i\omega\epsilon_r + \sigma_r) + (i\alpha_r \beta_r)/(\omega\mu_r)} \right) b_{(m,n)} Z_n^{(b)}(kr) \quad (1.6.31)$$

If we assume that equation (1.6.29) is satisfied, and equation (1.6.30) is valid so that equation (1.6.31) is valid and, furthermore, that

$$\frac{i\alpha}{\omega\mu} = \frac{i\beta}{\omega\mu}, \quad (1.6.32)$$

then equation (1.6.14) will be of the form

$$\frac{i}{\omega\mu} \left[-n(n+1) \left(\frac{i\omega\epsilon + \sigma + i\beta\alpha/(\omega\mu)}{(i\omega\epsilon_r + \sigma_r) + (i\alpha_r \beta_r)/(\omega\mu_r)} \right) \right] b_{(m,n)} \frac{Z_n^{(b)}(r)}{kr^2} +$$

$$\left(\frac{i}{\omega\mu}\right) b_{(m,n)} \left(\frac{1}{kr} \left(\frac{\partial}{\partial r}\right)^2\right) (r Z_n^{(b)}(r)) =$$

$$\frac{\sigma + i\omega\epsilon}{k} b_{(m,n)} (-Z_n^{(b)}(r)) - \frac{i\beta\alpha}{\omega\mu k} b_{(m,n)} Z_n^{(b)}(r) \quad (1.6.33)$$

If we also impose the condition

$$\frac{i\alpha_r}{\omega\mu_r} = \frac{i\beta}{\omega\mu} \quad (1.6.34)$$

then equation (1.6.9) takes on the form

$$\left(\frac{in(n+1)}{\omega\mu_r r^2}\right) Z_n^{(a)}(r) + \left(\frac{-i}{\omega\mu}\right) \frac{1}{r} \left(\frac{\partial}{\partial r}\right)^2 (r Z_n^{(a)}(r)) =$$

$$(i\omega\mu + \sigma) Z_n^{(a)}(r) + \frac{i\beta\alpha}{\omega\mu} Z_n^{(a)}(r) \quad (1.6.35)$$

Multiplying all terms of equation (1.6.35) by $i\omega\mu$ and observing that

$$k^2 = k_a^2 + \alpha \cdot \beta \quad (1.6.36)$$

where k_a is defined by (1.6.11) and k is defined by (1.6.1) we see that

$$-\frac{\mu n(n+1)}{\mu_r r^2} Z_n^{(a)} + \frac{1}{r} \left(\frac{\partial}{\partial r}\right)^2 (r Z_n^{(a)}(r)) =$$

$$-k_a^2 Z_n^{(a)}(r) - \alpha\beta Z_n^{(a)}(r) \quad (1.6.37)$$

or if we introduce the variable

$$\zeta_a = \frac{\mu}{\mu_r} \quad (1.6.38)$$

the ordinary differential equation (1.6.37) satisfied by $Z_n^{(a)}(kr)$ is

$$\frac{1}{r} \left(\frac{\partial}{\partial r}\right)^2 (r Z_n^{(a)}(kr)) + \left[(k_a^2 + \alpha\beta) - \zeta_a \frac{n(n+1)}{r^2} \right] Z_n^{(a)}(kr) = 0 \quad (1.6.39)$$

where k_a is given by (1.6.11) and k is given by (1.6.1)

The spherical Bessel function is defined as

$$\Psi_\nu(z) = \frac{\sqrt{\pi} J_{\nu+1/2}(z)}{\sqrt{2}\sqrt{z}} \quad (1.6.40)$$

where $\Psi_\nu(z)$ satisfies

$$\frac{1}{z} \left(\frac{\partial}{\partial z}\right)^2 (z \Psi_\nu(z)) + \left[1 + \frac{\nu(\nu+1)}{z^2} \right] \Psi_\nu(z) = 0 \quad (1.6.41)$$

Dividing all terms of equation (1.6.37) by

$$k^2 = k_a^2 + \alpha\beta = \omega^2\mu\epsilon + \beta\alpha - i\omega\mu\sigma \quad (1.6.42)$$

we have with the definition

$$z^2 = (\omega^2\mu\epsilon - i\omega\mu\sigma + \beta\alpha)r^2 = k^2r^2 \quad (1.6.43)$$

the fact that equation (1.6.39) implies

$$\frac{1}{z} \left(\frac{\partial}{\partial z} \right)^2 (z\Psi_\nu(z)) + \left[1 - \frac{\zeta_a n(n+1)}{z^2} \right] \Psi_\nu = 0 \quad (1.6.44)$$

where

$$\nu(\nu+1) = \zeta_a n(n+1) \quad (1.6.45)$$

We can find a simple formula for the index ν of the form

$$\nu = \frac{-1 + \sqrt{1 + 4\zeta_a n(n+1)}}{2} \quad (1.6.46)$$

Equation (1.6.33) gives the second equation which implies that

$$\begin{aligned} \frac{i}{\omega\mu} \left\{ \frac{1}{kr^2} \right\} \left[-n(n+1) \left(\frac{i\omega\epsilon + \sigma + i\beta\alpha/(\omega\mu)}{(i\omega\epsilon_r + \sigma_r) + (i\alpha_r\beta_r)/(\omega\mu_r)} \right) \right] Z_n^{(b)}(kr) \\ + \left(\frac{i}{\omega\mu} \right) \left(\frac{1}{kr} \left(\frac{\partial}{\partial r} \right)^2 \right) (rZ_n^{(b)}(kr)) = \\ \frac{\sigma + i\omega\epsilon}{k} (-Z_n^{(b)}(kr)) - \frac{i\beta\alpha}{\omega\mu k} Z_n^{(b)}(kr) \end{aligned} \quad (1.6.47)$$

Multiplying all terms of equation (1.6.47) by $-i\omega\mu kr^2$ and using equation (1.6.36) we deduce from equation (1.6.47) that

$$\begin{aligned} \left(\frac{1}{r} \left(\frac{\partial}{\partial r} \right)^2 \right) (rZ_n^{(b)}(kr)) + (k_a^2 + \alpha\beta) Z_n^{(b)}(kr) - \\ \frac{1}{r^2} \left[-n(n+1) \left(\frac{i\omega\epsilon + \sigma + i\beta\alpha/(\omega\mu)}{(i\omega\epsilon_r + \sigma_r) + (i\alpha_r\beta_r)/(\omega\mu_r)} \right) \right] Z_n^{(b)}(kr) = 0 \end{aligned} \quad (1.6.48)$$

where k_a is defined by (1.6.11) and k is defined by (1.6.1). Letting ζ_b be defined by

$$\zeta_b = \left(\frac{i\omega\epsilon + \sigma + i\beta\alpha/(\omega\mu)}{(i\omega\epsilon_r + \sigma_r) + (i\alpha_r\beta_r)/(\omega\mu_r)} \right) \quad (1.6.49)$$

Substituting equation (1.6.49) into equation (1.6.31) we deduce that

$$c_{(m,n)} Z_n^{(c)} = -n(n+1) \zeta_b Z_n^{(b)} b_{(m,n)} \quad (1.6.50)$$

The equation (1.6.49) is substituted into equation (1.6.48) to yield the equation,

$$\begin{aligned} & \left(\frac{1}{r} \left(\frac{\partial}{\partial r} \right)^2 \right) (r Z_n^{(b)}(kr)) \\ & + \left[(k_a^2 + \alpha\beta) - \frac{n(n+1)\zeta_b}{r^2} \right] Z_n^{(b)}(kr) = 0 \end{aligned} \quad (1.6.51)$$

where k_a is defined by (1.6.11) and k is defined by (1.6.1)

Combinations of solutions of equations (1.6.39) and (1.6.51) and their derivatives are used to represent the electric and magnetic fields induced inside an N layered sphere where each layer has nontrivial magnetic properties and the electric and magnetic properties are coupled in the sense that the layers are bianisotropic.

2 Expansion Coefficient Relations

2.1 Representations of E and H

Substituting equation (1.6.31) into (1.6.2) and making use of the relation defined by equation (1.6.49) and the modified propagation constant k defined by (1.6.1) we see that we can satisfy the Faraday and Ampere Maxwell equations for the special class of bianisotropic spheres treated in the previous section with an electric vector of the form,

$$\begin{aligned} \vec{E} = \sum_{(m,n) \in \mathcal{I}} & \left\{ a_{(m,n)} Z_n^{(a)}(kr) \vec{A}_{(m,n)}(\theta, \phi) + \right. \\ & [-n(n+1) \{\zeta_b\}] b_{(m,n)} \frac{Z_n^{(b)}(kr)}{kr} \vec{C}_{(m,n)}(\theta, \phi) + \\ & \left. \frac{b_{(m,n)}}{kr} \left(- \left(\frac{\partial}{\partial r} \right) (r Z_n^{(b)}(kr)) \right) \vec{B}_{(m,n)}(\theta, \phi) \right\} \end{aligned} \quad (2.1.1)$$

where the radial functions $Z_n^{(a)}$ and $Z_n^{(b)}$ satisfy equations (1.6.39) and (1.6.51).

Now making use of a form of the relation (1.6.51) given by

$$\left(\frac{1}{r} \left(\frac{\partial}{\partial r} \right)^2 \right) (r Z_n^{(b)}(kr)) =$$

$$+ \left[\frac{n(n+1)\zeta_b}{r^2} - (k_a^2 + \alpha\beta) \right] Z_n^{(b)}(kr), \quad (2.1.2)$$

where k_a is defined by (1.6.11) and k is defined by (1.6.1) and its square is equal to the square of k_a plus $\alpha\beta$, we will be able to simplify the equation,

$$\text{curl}(\vec{E}) = \sum_{(m,n) \in I} \left\{ \right.$$

$$a_{(m,n)} \left[n(n+1) \frac{Z_n^{(a)}(kr)}{r} \vec{C}_{(m,n)} + \frac{1}{r} \frac{\partial}{\partial r} (r Z_n^{(a)}(kr)) \vec{B}_{(m,n)} \right] +$$

$$(-n(n+1)\zeta_b) b_{(m,n)} \frac{Z_n^{(b)}(kr)}{kr^2} \vec{A}_{(m,n)} +$$

$$b_{(m,n)} \frac{1}{kr} \left(\frac{\partial}{\partial r} \right)^2 (r Z_n^{(b)}(kr)) \vec{A}_{(m,n)} \left. \right\} \quad (2.1.3)$$

In fact, substituting equation (2.1.2) into equation (2.1.3) we see that

$$\text{curl}(\vec{E}) =$$

$$\sum_{(m,n) \in I} \left\{ a_{(m,n)} \left[n(n+1) \frac{Z_n^{(a)}(r)}{r} \vec{C}_{(m,n)} + \frac{1}{r} \frac{\partial}{\partial r} (r Z_n^{(a)}(kr)) \vec{B}_{(m,n)} \right] + \right.$$

$$(-n(n+1)\zeta_b) b_{(m,n)} \frac{Z_n^{(b)}(kr)}{kr^2} \vec{A}_{(m,n)} +$$

$$b_{(m,n)} \frac{1}{kr} \left[\frac{n(n+1)\zeta_b}{r^2} - (k_a^2 + \alpha\beta) \right] Z_n^{(b)}(kr) \vec{A}_{(m,n)} \left. \right\} \quad (2.1.4)$$

where k_a is given by (1.6.11) and k by equation (1.6.1).

Some telescoping in the right side of equation (2.1.4) yields the reduced form,

$$\text{curl}(\vec{E}) =$$

$$\sum_{(m,n) \in I} \left\{ a_{(m,n)} \left[n(n+1) \frac{Z_n^{(a)}(kr)}{r} \vec{C}_{(m,n)} + \frac{1}{r} \frac{\partial}{\partial r} (r Z_n^{(a)}(kr)) \vec{B}_{(m,n)} \right] + \right.$$

$$- b_{(m,n)} \frac{1}{r} [(k_a^2 + \alpha\beta)] Z_n^{(b)}(kr) \vec{A}_{(m,n)} \left. \right\}$$

$$= i\omega \bar{\mu} \vec{H} - \bar{\beta} \vec{E} \quad (2.1.5)$$

again with k and k_a defined by (1.6.1) and (1.6.11), respectively.

Defining a new function $W_n^{(a)}$ by the rule

$$W_n^{(a)}(kr) = \frac{1}{kr} \left(\frac{\partial}{\partial r} \right) (r Z_n^{(a)}(kr)) \quad (2.1.6)$$

or equivalently by

$$W_n^{(a)}(kr) = \lim_{z \rightarrow kr} \left(\frac{1}{z} \right) \frac{\partial}{\partial z} (z \Psi_\nu^{(a)}(z)) \quad (2.1.7)$$

where $\Psi_\nu^{(a)}$ is defined by (1.6.44) and where ζ_a is related to the parameter ν in equation (2.1.7) by equation (1.6.38). We define $W_n^{(b)}(r)$ by changing a to b in equation (2.1.7).

Using the new function $W_n^{(a)}$ defined by equation (2.1.7) we define

$$\begin{aligned} \text{curl}(\vec{E}) = \\ \sum_{(m,n) \in \mathcal{I}} \left\{ a_{(m,n)} \left[n(n+1) \frac{Z_n^{(a)}(kr)}{r} \vec{C}_{(m,n)} + a_{(m,n)} k W_n^{(a)}(kr) \vec{B}_{(m,n)} \right] + \right. \\ \left. - b_{(m,n)} \frac{1}{r} \left[(k_a^2 + \alpha\beta) \right] Z_n^{(b)}(kr) \vec{A}_{(m,n)} \right\} \\ = i\omega \bar{\mu} \vec{H} - \bar{\beta} \vec{E} \end{aligned} \quad (2.1.8)$$

where k and k_a are defined by (1.6.1) and (1.6.11), respectively.

In terms of the function $W_n^{(a)}(kr)$ we express the function \vec{H} by the rule,

$$\begin{aligned} i\omega \bar{\mu} \vec{H} = \\ \sum_{(m,n) \in \mathcal{I}} \left\{ a_{(m,n)} \left[n(n+1) \frac{Z_n^{(a)}(kr)}{r} \vec{C}_{(m,n)} + a_{(m,n)} k W_n^{(a)}(kr) \vec{B}_{(m,n)} \right] + \right. \\ \left. - b_{(m,n)} \frac{1}{r} \left[(k_a^2 + \alpha\beta) \right] Z_n^{(b)}(kr) \vec{A}_{(m,n)} \right\} + \\ \sum_{(m,n) \in \mathcal{I}} \left\{ a_{(m,n)} \beta Z_n^{(a)}(kr) \vec{A}_{(m,n)}(\theta, \phi) + \right. \\ \left. \beta_r [-n(n+1) \{\zeta_b\}] b_{(m,n)} \frac{Z_n^{(b)}(kr)}{kr} \vec{C}_{(m,n)}(\theta, \phi) + \right. \\ \left. \beta \frac{b_{(m,n)}}{kr} \left(- \left(\frac{\partial}{\partial r} \right) (r Z_n^{(b)}(kr)) \right) \vec{B}_{(m,n)}(\theta, \phi) \right\} \end{aligned} \quad (2.1.9)$$

with k being given by (1.6.1) and k_a by (1.6.11)

Collecting terms we find that equation (1.6.31) which relates the function $c_{(m,n)}Z_n^{(c)}$ to the function $Z_n^{(b)}$ can be used to derive the relationship,

$$\begin{aligned}
 -i\omega\bar{\mu}\vec{H} = & \sum_{(m,n) \in \mathcal{I}} \left\{ \left[a_{(m,n)}n(n+1) \frac{Z_n^{(a)}(kr)}{r} + \alpha_r c_{(m,n)} \frac{Z_n^{(c)}(kr)}{kr} \right] \vec{C}_{(m,n)} \right. \\
 & + \left[a_{(m,n)} \frac{1}{r} \frac{\partial}{\partial r} (r Z_n^{(a)}(kr)) - \alpha b_{(m,n)} \left(\frac{1}{kr} \right) \left(\frac{\partial}{\partial r} \right) (r Z_n^{(b)}(kr)) \right] \vec{B}_{(m,n)} + \\
 & \left. \left[c_{(m,n)} \frac{Z_n^{(c)}(kr)}{kr^2} + b_{(m,n)} \frac{1}{kr} \left(\frac{\partial}{\partial r} \right)^2 (r Z_n^{(b)}(kr)) + \alpha a_{(m,n)} Z_n^{(a)}(kr) \right] \vec{A}_{(m,n)} \right\} \quad (2.1.10)
 \end{aligned}$$

and we could then use the differential equation (2.1.2) to simplify equation (2.1.10).

So far we have been trying to develop representations of the electric and magnetic vector in a special class of bianisotropic spheres. Let us now consider an N layered sphere and let k_p denote the propagation constant in the p th layer given by

$$k_p^2 = \omega^2 \mu^{(p)} \epsilon^{(p)} - i\omega \mu^{(p)} \sigma^{(p)} + \alpha^{(p)} \beta^{(p)} \quad (2.1.11)$$

where for the layer with index p , where p runs from 1 to N for the actual layers of the sphere and where $N+1$ is the region outside the sphere, and where $\mu^{(p)}$, $\epsilon^{(p)}$, $\sigma^{(p)}$, $\alpha^{(p)}$ and $\beta^{(p)}$ are respectively the tangential components of (i) the magnetic permeability, (ii) the permittivity, (iii) the conductivity, (iv) the Faraday Maxwell equation coupling tensor, and (v) the Maxwell equation coupling tensor, where these five tensors all have the same form as that given in equation (1.6.4).

Let us develop the full theory using the functions,

$$W_{(n,p)}^{(a,j)}(k_p r) = \frac{1}{k_p r} \left(\frac{\partial}{\partial r} \right) (r Z_{(n,p)}^{(a,j)}(k_p r)) \quad (2.1.12)$$

where the propagation constant k_p is given by (2.1.11) and where $Z_{(n,p)}^{(a,j)}(k_p r)$ is the singular solution if $j = 3$ and the solution with the integrable singularity at $r = 0$ corresponds to $j = 1$.

The expansion coefficients in layer p associated with the functions, $Z_{(n,p)}^{(a,1)}(k_p r)$ and with the functions $W_{(n,p)}^{(a,1)}(k_p r)$ which have the integrable singularity at the origin will be

denoted by $a_{(m,n)}^{(p)}$ and $b_{(m,n)}^{(p)}$ and the coefficients $\alpha_{(m,n)}^{(p)}$ and $\beta_{(m,n)}^{(p)}$ will be multipliers of the functions $Z_{(n,p)}^{(a,3)}(k_p r)$ and $W_{(n,p)}^{(a,3)}(k_p r)$ which are singular at $r = 0$. The electric vector with general representation given by equation (1.6.2) is in the p th layer of the multilayer bianisotropic sphere represented by

$$\begin{aligned} \vec{E}_p = & \sum_{(m,n) \in \mathcal{I}} \left\{ [a_{(m,n)}^{(p)} Z_{(n,p)}^{(a,1)}(k_p r) + \alpha_{(m,n)}^{(p)} Z_{(n,p)}^{(a,3)}(k_p r)] \vec{A}_{(m,n)}(\theta, \phi) + \right. \\ & [-n(n+1) \{\zeta_b\}] b_{(m,n)}^{(p)} \frac{Z_{(n,p)}^{(a,1)}(k_p r)}{k_p r} \vec{C}_{(m,n)}(\theta, \phi) + \\ & [-n(n+1) \{\zeta_b\}] \beta_{(m,n)}^{(p)} \frac{Z_{(n,p)}^{(a,3)}(k_p r)}{k_p r} \vec{C}_{(m,n)}(\theta, \phi) + \\ & \left. [-b_{(m,n)}^{(p)} W_{(n,p)}^{(b,1)}(k_p r) - \beta_{(m,n)}^{(p)} W_{(n,p)}^{(b,3)}(k_p r)] \vec{B}_{(m,n)}(\theta, \phi) \right\} \quad (2.1.13) \end{aligned}$$

where k_p is defined by (2.1.11).

Using our previous expression for the magnetic field vector but using the definitions (2.1.12) and the fact that the k_p defined by (2.1.11) is the propagation constant in the p th layer, we see that the Ampere Maxwell equation with a coupling tensor defined by (1.6.4) the magnetic vector in the innermost layer with p equal to 1 has the form,

$$\begin{aligned} \vec{H} = & \sum_{(m,n) \in \mathcal{I}} \left[\frac{i}{\omega \mu_r} \left\{ a_{(m,n)}^{(p)} \frac{Z_{(n,p)}^{(a,1)}(k_p r) n(n+1)}{r} + \alpha_r c_{(m,n)}^{(p)} \frac{Z_{(n,p)}^{(c,1)}(k_p r)}{k_p r} \right\} \vec{C}_{(m,n)} \right. \\ & + \frac{i}{\omega \mu} \left\{ a_{(m,n)}^{(p)} k W_{(n,p)}^{(a,1)}(k_p r) + \alpha b_{(m,n)}^{(p)} \frac{1}{k_p r} \left(-\frac{\partial}{\partial r} \right) (r Z_{(n,p)}^{(b,1)}(k_p r)) \right\} \vec{B}_{(m,n)} + \\ & \left(\frac{i}{\omega \mu} \right) \left\{ c_{(m,n)}^{(p)} \frac{Z_{(n,p)}^{(c,1)}(k_p r)}{k_p r^2} + \right. \\ & \left. b_{(m,n)}^{(p)} \left(\frac{1}{k_p r} \right) \left(\frac{\partial}{\partial r} \right)^2 (r Z_{(n,p)}^{(b,1)}(k_p r)) + \alpha a_{(m,n)}^{(p)} Z_{(n,p)}^{(a,1)}(k_p r) \right\} \vec{A}_{(m,n)} \Big] \quad (2.1.14) \end{aligned}$$

where k_p is given by (2.1.11) Now using equation (1.6.50) and equation (1.6.20) we see that equation (2.1.14) can be simplified by the telescoping of terms and specifically making use of the relation that is derivable from equations (1.6.50) and (1.6.51) given by

$$\begin{aligned} & c_{(m,n)}^{(p)} \frac{Z_{(n,p)}^{(c,1)}(k_p r)}{k_p r^2} + \\ & b_{(m,n)}^{(p)} \left(\frac{1}{k_p r} \right) \left(\frac{\partial}{\partial r} \right)^2 (r Z_{(n,p)}^{(b,1)}(k_p r)) = \\ & b_{(m,n)}^{(p)} \left[- \frac{(\omega^2 \mu^{(p)} \epsilon^{(p)} - i \omega \mu^{(p)} \sigma^{(p)} + \alpha^{(p)} \beta^{(p)})}{k_p} \right] Z_{(n,p)}^{(b,1)}(k_p r) \end{aligned} \quad (2.1.15)$$

In doing this we see that the magnetic vector in the core of the multilayer spherical structure corresponding to $p = 1$ is given by

$$\begin{aligned} \vec{H} = & \sum_{(m,n) \in \mathcal{I}} \left[\frac{i}{\omega \mu_r^{(p)}} \left\{ a_{(m,n)}^{(p)} \frac{Z_{(n,p)}^{(a,1)}(k_p r) n(n+1)}{r} - \alpha_r \zeta_b n(n+1) b_{(m,n)}^{(p)} \frac{Z_{(n,p)}^{(b,1)}(k_p r)}{k_p r} \right\} \vec{C}_{(m,n)} \right. \\ & + \frac{i}{\omega \mu^{(p)}} \left(\left\{ a_{(m,n)}^{(p)} k_p W_{(n,p)}^{(a,1)}(k_p r) + \alpha b_{(m,n)}^{(p)} (-W_{(n,p)}^{(b,1)}(k_p r)) \right\} \vec{B}_{(m,n)} + \right. \\ & \left. \left. \left\{ b_{(m,n)}^{(p)} [-k_p] Z_{(n,p)}^{(b,1)}(k_p r) + \alpha^{(p)} a_{(m,n)}^{(p)} Z_{(n,p)}^{(a,1)}(k_p r) \right\} \vec{A}_{(m,n)} \right) \right] \end{aligned} \quad (2.1.16)$$

where k_p is defined by (2.1.11) and where we have made use of the relation,

$$k_p = \frac{\omega^2 \mu^{(p)} \epsilon^{(p)} - i \omega \mu^{(p)} \sigma^{(p)} + \alpha^{(p)} \beta^{(p)}}{k_p} \quad (2.1.17)$$

We now consider the representation of the magnetic vector in an interior layer of a multilayer sphere that does not contain the center of the sphere. The magnetic vector has the representation in terms of functions $Z_{(n,p)}^{(a,1)}$ and $Z_{(n,p)}^{(b,1)}$ which have integrable singularities at the origin, and the functions $Z_{(n,p)}^{(a,3)}$ and $Z_{(n,p)}^{(b,3)}$ whose representation, in the case considered here involves Hankel functions with complex index. The magnetic vector representation in a penetrable shell is given by

$$\vec{H} = \sum_{(m,n) \in \mathcal{I}} \left[\left(\frac{i}{\omega \mu_r^{(p)}} \right) \left\{ a_{(m,n)}^{(p)} \frac{Z_{(n,p)}^{(a,1)}(k_p r) n(n+1)}{r} + \right.$$

$$\begin{aligned}
& \alpha_{(m,n)}^{(p)} \frac{Z_{(n,p)}^{(a,3)}(k_p r) n(n+1)}{r} + (-1) \left(\alpha_{(m,n)}^{(p)} \zeta_b n(n+1) b_{(m,n)}^{(p)} \frac{Z_{(n,p)}^{(b,1)}(k_p r)}{k_p r} + \right. \\
& \left. \alpha_{(m,n)}^{(p)} \zeta_b n(n+1) \beta_{(m,n)}^{(p)} \frac{Z_{(n,p)}^{(b,3)}(k_p r)}{k_p r} \right) \Big\} \vec{C}_{(m,n)} + \\
& \frac{i}{\omega \mu^{(p)}} \left\{ a_{(m,n)}^{(p)} k_p W_{(n,p)}^{(a,1)}(k_p r) + \alpha_{(m,n)}^{(p)} k_p W_{(n,p)}^{(a,3)}(k_p r) \right\} \vec{B}_{(m,n)} + \\
& \left(\frac{-i}{\omega \mu^{(p)}} \right) \left\{ \alpha_{(m,n)}^{(p)} b_{(m,n)}^{(p)} (W_{(n,p)}^{(b,1)}(k_p r)) + \alpha_{(m,n)}^{(p)} \beta_{(m,n)}^{(p)} (W_{(n,p)}^{(b,3)}(k_p r)) \right\} \vec{B}_{(m,n)} + \\
& \left(\frac{i}{\omega \mu^{(p)}} \right) [-k_p] \left\{ b_{(m,n)}^{(p)} Z_{(n,p)}^{(b,1)}(k_p r) + \beta_{(m,n)}^{(p)} Z_{(n,p)}^{(b,3)}(k_p r) \right\} \vec{A}_{(m,n)} + \\
& \left(\frac{i}{\omega \mu^{(p)}} \right) \left\{ \alpha_{(m,n)}^{(p)} a_{(m,n)}^{(p)} Z_{(n,p)}^{(a,1)}(k_p r) + \alpha_{(m,n)}^{(p)} \alpha_{(m,n)}^{(p)} Z_{(n,p)}^{(a,3)}(k_p r) \right\} \vec{A}_{(m,n)} \Big] \quad (2.1.18)
\end{aligned}$$

where k_p is given by equation (2.1.11) and we have made use of equation (2.1.17).

We now consider the representation of the electric vector in the core region $p = 1$ of the multilayer, spherically symmetric bianisotropic structure. Making use of equation (1.6.51) we deduce from equation (1.6.2) that

$$\begin{aligned}
\vec{E}_p = \sum_{(m,n) \in \mathcal{I}} & \left\{ a_{(m,n)} Z_{(n,p)}^{(a,1)}(k_p r) \vec{A}_{(m,n)}(\theta, \phi) + \right. \\
& [-n(n+1) \{\zeta_b\}] b_{(m,n)} \frac{Z_{(n,p)}^{(b,1)}(k_p r)}{k_p r} \vec{C}_{(m,n)}(\theta, \phi) + \\
& \left. \frac{b_{(m,n)}}{k_p r} \left(- \left(\frac{\partial}{\partial r} \right) (r Z_{(n,p)}^{(b,1)}(k_p r)) \right) \vec{B}_{(m,n)}(\theta, \phi) \right\} \quad (2.1.19)
\end{aligned}$$

where k_p is given by (2.1.11).

Equating tangential components of \vec{E} across the shell $r = R_p$ equation (2.1.13), the representation of the electric vector in a shell region, implies that equating coefficients of $\vec{A}_{(m,n)}(\theta, \phi)$ leads, for r equal to R_p to the relation,

$$\begin{aligned}
& [a_{(m,n)}^{(p)} Z_{(n,p)}^{(a,1)}(k_p r) + \alpha_{(m,n)}^{(p)} Z_{(n,p)}^{(a,3)}(k_p r)] \\
& = [a_{(m,n)}^{(p+1)} Z_{(n,p+1)}^{(a,1)}(k_{p+1} r) + \alpha_{(m,n)}^{(p+1)} Z_{(n,p+1)}^{(a,3)}(k_{p+1} r)] \quad (2.1.20)
\end{aligned}$$

Multiplying both sides of equation (2.1.13) by $\vec{B}_{(m,n)}$ and integrating over the sphere $r = R_p$, we deduce, for r equal to R_p that

$$[b_{(m,n)}^{(p)} Z_{(n,p)}^{(b,1)}(k_p r) + \beta_{(m,n)}^{(p)} Z_{(n,p)}^{(b,3)}(k_p r)]$$

$$= [b_{(m,n)}^{(p+1)} Z_{(n,p+1)}^{(b,1)}(k_{p+1}r) + \beta_{(m,n)}^{(p+1)} Z_{(n,p+1)}^{(b,3)}(k_{p+1}r)] \quad (2.1.21)$$

We now set up the differential equations which state that the tangential components of the magnetic vector are continuous across the boundary of a sphere separating regions of continuity of tensorial electric properties. Equation (2.1.18) implies, upon equating tangential components \vec{H} , on each side of the boundary $r = R_p$, by taking the dot product of both sides of (2.1.18) with respect to $\vec{B}_{(m,n)}$ and integrating over the sphere $r = R_p$ that

$$\begin{aligned} & \frac{i}{\omega\mu^{(p)}} \left\{ a_{(m,n)}^{(p)} k_p W_{(n,p)}^{(a,1)}(k_p r) + \alpha_{(m,n)}^{(p)} k_p W_{(n,p)}^{(a,3)}(k_p r) \right\} + \\ & \left(\frac{-i}{\omega\mu^{(p)}} \right) \left\{ \alpha^{(p)} b_{(m,n)}^{(p)} (W_{(n,p)}^{(b,1)}(k_p r)) + \alpha^{(p)} \beta_{(m,n)}^{(p)} (W_{(n,p)}^{(b,3)}(k_p r)) \right\} = \\ & \frac{i}{\omega\mu^{(p+1)}} \left\{ a_{(m,n)}^{(p+1)} k_{p+1} W_{(n,p+1)}^{(a,1)}(k_{p+1}r) + \alpha_{(m,n)}^{(p+1)} k_{p+1} W_{(n,p+1)}^{(a,3)}(k_{p+1}r) \right\} + \\ & \left(\frac{-i}{\omega\mu^{(p+1)}} \right) \left\{ \alpha^{(p+1)} b_{(m,n)}^{(p+1)} (W_{(n,p+1)}^{(b,1)}(k_{p+1}r)) + \alpha^{(p+1)} \beta_{(m,n)}^{(p+1)} (W_{(n,p+1)}^{(b,3)}(k_{p+1}r)) \right\} \quad (2.1.22) \end{aligned}$$

Using equation (2.1.18) and equating coefficients of the vector \vec{A} on both sides of the spherical shell $r = R_p$ we have

$$\begin{aligned} & \left(\frac{i}{\omega\mu^{(p)}} \right) [-k_p] \left\{ b_{(m,n)}^{(p)} Z_{(n,p)}^{(b,1)}(k_p r) + \beta_{(m,n)}^{(p)} Z_{(n,p)}^{(b,3)}(k_p r) \right\} \\ & \left(\frac{i}{\omega\mu^{(p)}} \right) \left\{ \alpha^{(p)} a_{(m,n)}^{(p)} Z_{(n,p)}^{(a,1)}(k_{p+1}r) + \alpha^{(p)} \alpha_{(m,n)}^{(p)} Z_{(n,p)}^{(a,3)}(k_{p+1}r) \right\} = \\ & \left(\frac{i}{\omega\mu^{(p+1)}} \right) \left\{ b_{(m,n)}^{(p+1)} [-k_{p+1}] Z_{(n,p+1)}^{(b,1)}(k_{p+1}r) \right. \\ & \quad \left. + \beta_{(m,n)}^{(p+1)} [-k_{p+1}] Z_{(n,p+1)}^{(b,3)}(k_{p+1}r) \right\} \\ & \left(\frac{i}{\omega\mu^{(p+1)}} \right) \left\{ \alpha^{(p+1)} a_{(m,n)}^{(p)} Z_{(n,p+1)}^{(a,1)}(k_{p+1}r) + \alpha^{(p+1)} \alpha_{(m,n)}^{(p+1)} Z_{(n,p+1)}^{(a,3)}(k_{p+1}r) \right\} \quad (2.1.23) \end{aligned}$$

2.2 Transition Matrices

We now attempt to develop transition matrices which will relate expansion coefficients in one layer to expansion coefficients in another layer. We start with equation (2.1.22);

we find, after multiplying both sides of this equation by $\mu^{(p)}$ and dividing both sides of equation (2.1.22) by k_p , that

$$\begin{aligned} & \left\{ a_{(m,n)}^{(p)} W_{(n,p)}^{(a,1)}(k_p r) + \alpha_{(m,n)}^{(p)} W_{(n,p)}^{(a,3)}(k_p r) \right\} + \\ & \left\{ \left(-\frac{\alpha^{(p)}}{k_p} \right) b_{(m,n)}^{(p)} (W_{(n,p)}^{(b,1)}(k_p r)) + \left(-\frac{\alpha^{(p)}}{k_p} \right) \beta_{(m,n)}^{(p)} (W_{(n,p)}^{(b,3)}(k_p r)) \right\} = \\ & \left(\frac{\mu^{(p)} k_{p+1}}{\mu^{(p+1)} k_p} \right) \left\{ a_{(m,n)}^{(p+1)} W_{(n,p+1)}^{(a,1)}(k_p r) + \alpha_{(m,n)}^{(p+1)} W_{(n,p+1)}^{(a,3)}(k_p r) \right\} + \\ & \left(\frac{-\mu^{(p)} \alpha^{(p+1)}}{\mu^{(p+1)} k_p} \right) \left\{ b_{(m,n)}^{(p+1)} (W_{(n,p+1)}^{(b,1)}(k_p r)) + \beta_{(m,n)}^{(p+1)} (W_{(n,p+1)}^{(b,3)}(k_p r)) \right\} \end{aligned} \quad (2.2.1)$$

Multiplying both sides of equation (2.1.18) by $\vec{A}_{(m,n)}(\theta, \phi)$ and observing that

$$\begin{aligned} & \lim_{r \rightarrow R_p^-} \int_{S_p(r)} \vec{H} \cdot \vec{A}_{(m,n)}(\theta, \phi) dA = \\ & \lim_{r \rightarrow R_p^+} \int_{S_p(r)} \vec{H} \cdot \vec{A}_{(m,n)}(\theta, \phi) dA \end{aligned} \quad (2.2.2)$$

we derive equation (2.1.23). From this, after multiplying all terms by $-i\omega\mu^{(p)}k_p$ and dividing all terms by k_p^2 , where k_p is defined by (2.1.11), we derive the relation that

$$\begin{aligned} & \left(\frac{\alpha^{(p)}}{k_p} \right) \left\{ a_{(m,n)}^{(p)} Z_{(n,p)}^{(a,1)}(k_p r) + \alpha_{(m,n)}^{(p)} Z_{(n,p)}^{(a,3)}(k_p r) \right\} + \\ & \left\{ b_{(m,n)}^{(p)} Z_{(n,p)}^{(b,1)}(k_p r) + \beta_{(m,n)}^{(p)} Z_{(n,p)}^{(b,3)}(k_p r) \right\} = \\ & \left(\frac{\mu^{(p)} \alpha^{(p+1)}}{\mu^{(p+1)} k_p} \right) \left\{ a_{(m,n)}^{(p+1)} Z_{(n,p+1)}^{(a,1)}(k_{p+1} r) + \alpha_{(m,n)}^{(p+1)} Z_{(n,p+1)}^{(a,3)}(k_{p+1} r) \right\} + \\ & \left[-\frac{\mu^{(p)} k_{p+1}}{\mu^{(p+1)} k_p} \right] \cdot \left\{ b_{(m,n)}^{(p+1)} Z_{(n,p+1)}^{(b,1)}(k_{p+1} r) + \beta_{(m,n)}^{(p+1)} Z_{(n,p+1)}^{(b,3)}(k_{p+1} r) \right\}, \end{aligned} \quad (2.2.3)$$

where k_p and k_{p+1} are defined by (2.1.11).

We now define parameters which appear in the matrix relating expansion coefficients in one layer to those in an adjacent layer. We obtain these by considering terms appearing in equation (2.2.3)

$$\rho_{(b,3)}^{(p+1)} = \left(\frac{\mu^{(p)}}{\mu^{(p+1)}} \right) \left[-\frac{k_{p+1}}{k_p} \right] \quad (2.2.4)$$

Also

$$\rho_{(a,3)}^{(p+1)} = \left(\frac{\mu^{(p)} \alpha^{(p+1)}}{\mu^{(p+1)} k_p} \right) \quad (2.2.5)$$

with k_p and k_{p+1} being defined by (2.1.11). A similar term appearing in the inner shell matrix is

$$\rho_{(a,3)}^{(p)} = \left(\frac{\alpha^{(p)}}{k_p} \right) \quad (2.2.6)$$

A term in the second row of the outer shell matrix is

$$\rho_{(a,2)}^{(p+1)} = \left(\frac{\mu^{(p)} k_{p+1}}{\mu^{(p+1)} k_p} \right) \quad (2.2.7)$$

Another term appearing in second row of the matrix is

$$\rho_{(b,2)}^{(p+1)} = \left(\frac{-\mu^{(p)} \alpha^{(p+1)}}{\mu^{(p+1)} k_p} \right) \quad (2.2.8)$$

The corresponding term in the inner shell matrix is

$$\rho_{(b,2)}^{(p)} = \left(\frac{-\alpha^{(p)}}{k_p} \right) \quad (2.2.9)$$

With the special functions $Z_{(n,p)}^{(a,j)}$, defined by (1.6.39), and $Z_{(n,p)}^{(b,j)}$, defined by (1.6.51), and the derivative terms defined by equation (2.1.12) being evaluated at the separating spherical boundary $r = R_p$, we see that the matrix equation relating expansion coefficients in layer p to those in layer $p+1$ is given by

$$\begin{bmatrix} Z_{(n,p)}^{(a,1)} & Z_{(n,p)}^{(a,3)} & 0 & 0 \\ W_{(n,p)}^{(a,1)} & W_{(n,p)}^{(a,3)} & \rho_{(b,2)}^{(p)} W_{(n,p)}^{(b,1)} & \rho_{(b,2)}^{(p)} W_{(n,p)}^{(b,3)} \\ \rho_{(a,3)}^{(p)} Z_{(n,p)}^{(a,1)} & \rho_{(a,3)}^{(p)} Z_{(n,p)}^{(a,3)} & Z_{(n,p)}^{(b,1)} & Z_{(n,p)}^{(b,3)} \\ 0 & 0 & W_{(n,p)}^{(b,1)} & W_{(n,p)}^{(b,3)} \end{bmatrix} \begin{bmatrix} a_{(m,n)}^{(p)} \\ \alpha_{(m,n)}^{(p)} \\ b_{(m,n)}^{(p)} \\ \beta_{(m,n)}^{(p)} \end{bmatrix} = \begin{bmatrix} Z_{(n,p+1)}^{(a,1)} & Z_{(n,p+1)}^{(a,3)} & 0 & 0 \\ W_{(n,p+1)}^{(a,1)} & W_{(n,p+1)}^{(a,3)} & \rho_{(b,2)}^{(p+1)} W_{(n,p+1)}^{(b,1)} & \rho_{(b,2)}^{(p+1)} W_{(n,p+1)}^{(b,3)} \\ \rho_{(a,3)}^{(p+1)} Z_{(n,p+1)}^{(a,1)} & \rho_{(a,3)}^{(p+1)} Z_{(n,p+1)}^{(a,3)} & \rho_{(b,3)}^{(p+1)} Z_{(n,p+1)}^{(b,1)} & \rho_{(b,3)}^{(p+1)} Z_{(n,p+1)}^{(b,3)} \\ 0 & 0 & W_{(n,p+1)}^{(b,1)} & W_{(n,p+1)}^{(b,3)} \end{bmatrix} \begin{bmatrix} a_{(m,n)}^{(p+1)} \\ \alpha_{(m,n)}^{(p+1)} \\ b_{(m,n)}^{(p+1)} \\ \beta_{(m,n)}^{(p+1)} \end{bmatrix} \quad (2.2.10)$$

This equation can be written more compactly in the form

$$T_n^{(p)}(k_p R_p) \begin{bmatrix} a_{(m,n)}^{(p)} \\ \alpha_{(m,n)}^{(p)} \\ b_{(m,n)}^{(p)} \\ \beta_{(m,n)}^{(p)} \end{bmatrix} = T_n^{(p+1)}(k_{p+1} R_p) \begin{bmatrix} a_{(m,n)}^{(p+1)} \\ \alpha_{(m,n)}^{(p+1)} \\ b_{(m,n)}^{(p+1)} \\ \beta_{(m,n)}^{(p+1)} \end{bmatrix} \quad (2.2.11)$$

To compute the inverse of the matrix $T_n^{(p)}$ we need its transpose which is given by

$$\begin{bmatrix} Z_{(n,p)}^{(a,1)}(k_p R_p) & W_{(n,p)}^{(a,1)}(k_p R_p) & \rho_{(a,3)}^{(p)} Z_{(n,p)}^{(a,1)}(k_p R_p) & 0 \\ Z_{(n,p)}^{(a,3)}(k_p R_p) & W_{(n,p)}^{(a,3)}(k_p R_p) & \rho_{(a,3)}^{(p)} Z_{(n,p)}^{(a,3)}(k_p R_p) & 0 \\ 0 & \rho_{(b,2)}^{(p)} W_{(n,p)}^{(b,1)}(k_p R_p) & Z_{(n,p)}^{(b,1)}(k_p R_p) & W_{(n,p)}^{(b,1)}(k_p R_p) \\ 0 & \rho_{(b,2)}^{(p)} W_{(n,p)}^{(b,3)}(k_p R_p) & Z_{(n,p)}^{(b,3)}(k_p R_p) & W_{(n,p)}^{(b,3)}(k_p R_p) \end{bmatrix} = (T_n^{(p)})^{transpose} \quad (2.2.12)$$

Wronskian relations will show that we can define a new matrix $Q_n^{(p)}$ by the rule

$$Q_n^{(p)} = T_n^{(p)}(k_p R_p)^{-1} T_n^{(p+1)}(k_{p+1} R_p). \quad (2.2.13)$$

Using equations (2.2.11) and (2.2.13) we see that the expansion coefficients in the core are related to the expansion coefficients in the outer shell by the rule,

$$\begin{bmatrix} a_{(m,n)}^{(1)} \\ 0 \\ b_{(m,n)}^{(1)} \\ 0 \end{bmatrix} = Q_n^{(1)} Q_n^{(2)} \dots Q_n^{(N)} \begin{bmatrix} a_{(m,n)}^{(N+1)} \\ \alpha_{(m,n)}^{(N+1)} \\ b_{(m,n)}^{(N+1)} \\ \beta_{(m,n)}^{(N+1)} \end{bmatrix} \quad (2.2.14)$$

This gives us four equations in four unknowns, since we assume that the expansion coefficients $\alpha_{(m,n)}^{(N+1)}$ and $\beta_{(m,n)}^{(N+1)}$ are determined; these expansion coefficients could define a complex source such as a radar or laser beam in the near field (Barton [8] and [9], Pinnick [39] and [37]). Solving equation (2.2.14) we find values of $a_{(m,n)}^{(1)}$ and $b_{(m,n)}^{(1)}$ and assuming that $\alpha_{(m,n)}^{(1)}$ and $\beta_{(m,n)}^{(1)}$ are both zero, we can easily obtain the expansion coefficients in every layer of the structure. If we define the matrix $\mathcal{R}_n^{(p)}$ by the rule,

$$\mathcal{R}_n^{(p)} = T_n^{(p+1)}(k_{p+1} R_p)^{-1} T_n^{(p)}(k_p R_p) \quad (2.2.15)$$

We see that the definition of $\mathcal{R}_n^{(p)}$ by equation (2.2.15) implies the relationship

$$\mathcal{R}_n^{(p)} \begin{bmatrix} a_{(m,n)}^{(p)} \\ \alpha_{(m,n)}^{(p)} \\ b_{(m,n)}^{(p)} \\ \beta_{(m,n)}^{(p)} \end{bmatrix} = \begin{bmatrix} a_{(m,n)}^{(p+1)} \\ \alpha_{(m,n)}^{(p+1)} \\ b_{(m,n)}^{(p+1)} \\ \beta_{(m,n)}^{(p+1)} \end{bmatrix} \quad (2.2.16)$$

between expansion coefficients in adjacent layers of the spherical structure.

These computations using equation (2.2.16) are facilitated by the fact that we have exact formulas for the determinant and inverses of the 4 by 4 matrices $T_n^{(p)}$. Let the determinant of $T_n^{(p)}$ be defined by

$$\begin{aligned} \Delta_p &= Z_{(n,p)}^{(a,1)}(k_p R_p) W_{(n,p)}^{(a,3)}(k_p R_p) \\ &\quad \{ Z_{(n,p)}^{(b,1)}(k_p R_p) W_{(n,p)}^{(b,3)}(k_p R_p) - W_{(n,p)}^{(b,1)}(k_p R_p) Z_{(n,p)}^{(b,3)}(k_p R_p) \} + \\ &\quad (-1) [Z_{(n,p)}^{(a,3)}(k_p R_p) W_{(n,p)}^{(a,1)}(k_p R_p)] \\ &\quad \{ Z_{(n,p)}^{(b,1)}(k_p R_p) W_{(n,p)}^{(b,3)}(k_p R_p) - W_{(n,p)}^{(b,1)}(k_p R_p) Z_{(n,p)}^{(b,3)}(k_p R_p) \} \end{aligned} \quad (2.2.17)$$

which means that the determinant Δ_p is the product of two Wronskians $\mathcal{W}_{(n,p)}^{(a)}$ and $\mathcal{W}_{(n,p)}^{(b)}$ where

$$\mathcal{W}_{(n,p)}^{(b)} = Z_{(n,p)}^{(b,1)}(k_p R_p) W_{(n,p)}^{(b,3)}(k_p R_p) - W_{(n,p)}^{(b,1)}(k_p R_p) Z_{(n,p)}^{(b,3)}(k_p R_p) \quad (2.2.18)$$

We find that equation (2.2.17) and the Wronskian relationship,

$$\mathcal{W}_{(n,p)}^{(a)}(k_p R_p) = \frac{-i}{(k_p R_p)^2} \quad (2.2.19)$$

enables us to compute determinants with no roundoff error. This enables us to get exact formulas for the entries of the inverse of this matrix. If $(T_n^{(p)}(k_p R_p)^{-1})_{(i,j)}$ denotes the entry in the i th row and j th column of the inverse of the matrix $T_n^{(p)}$, then the entry in row 1 and column 1 of the inverse is

$$(T_n^{(p)}(k_p R_p)^{-1})_{(1,1)} = W_{(n,p)}^{(a,3)}(k_p R_p) \mathcal{W}_{(n,p)}^{(b)}(k_p R_p) / \Delta_p, \quad (2.2.20)$$

The (1,2) entry is

$$(T_n^{(p)}(k_p R_p)^{-1})_{(1,2)} = -Z_{(n,p)}^{(a,3)}(k_p R_p) \mathcal{W}_{(n,p)}^{(b)}(k_p R_p) / \Delta_p, \quad (2.2.21)$$

The (1,3) term is

$$(T_n^{(p)}(k_p R_p)^{-1})_{(1,3)} = 0 \quad (2.2.22)$$

The (1,4) term is

$$(T_n^{(p)}(k_p R_p)^{-1})_{(1,4)} = -(Z_{(n,p)}^{(a,3)}(k_p R_p) \left(\frac{-\alpha^{(p)}}{k_p} \right) \mathcal{W}_{(n,p)}^{(b)}(k_p R_p)) / \Delta_p, \quad (2.2.23)$$

Equations (2.2.20), (2.2.21), (2.2.22), and (2.2.23) define the first row of the transition matrix. The entry in row 2 and column 1 of the inverse is

$$(T_n^{(p)}(k_p R_p)^{-1})_{(2,1)} = -W_{(n,p)}^{(a,1)}(k_p R_p) \mathcal{W}_{(n,p)}^{(b)}(k_p R_p) / \Delta_p, \quad (2.2.24)$$

The entry in row 2 and column 2 of the inverse is

$$(T_n^{(p)}(k_p R_p)^{-1})_{(2,2)} = Z_{(n,p)}^{(a,1)}(k_p R_p) \mathcal{W}_{(n,p)}^{(b)}(k_p R_p) / \Delta_p, \quad (2.2.25)$$

The entry in row 2 and column 3 of the inverse is

$$(T_n^{(p)}(k_p R_p)^{-1})_{(2,3)} = 0 \quad (2.2.26)$$

The entry in row 2 and column 4 of the inverse is

$$(T_n^{(p)}(k_p R_p)^{-1})_{(2,4)} = (Z_{(n,p)}^{(a,1)}(k_p R_p) \left(\frac{-\alpha^{(p)}}{k_p} \right) \mathcal{W}_{(n,p)}^{(b)}(k_p R_p)) / \Delta_p, \quad (2.2.27)$$

Equations (2.2.24), (2.2.25), (2.2.26), and (2.2.27) define the second row of the transition matrix. The (3,1) entry is

$$(T_n^{(p)}(k_p R_p)^{-1})_{(3,1)} = W_{(n,p)}^{(b,3)}(k_p R_p) \left(\frac{-\alpha^{(p)}}{k_p} \right) \mathcal{W}_{(n,p)}^{(b)}(k_p R_p) / \Delta_p, \quad (2.2.28)$$

The (3,2) entry is

$$(T_n^{(p)}(k_p R_p)^{-1})_{(3,2)} = 0 \quad (2.2.29)$$

The (3,3) entry is

$$(T_n^{(p)}(k_p R_p)^{-1})_{(3,3)} = W_{(n,p)}^{(b,3)}(k_p R_p) \mathcal{W}_{(n,p)}^{(a)}(k_p R_p) / \Delta_p, \quad (2.2.30)$$

The (3,4) entry is

$$(T_n^{(p)}(k_p R_p)^{-1})_{(3,4)} = -Z_{(n,p)}^{(b,3)}(k_p R_p) \mathcal{W}_{(n,p)}^{(a)}(k_p R_p) / \Delta_p, \quad (2.2.31)$$

Equations (2.2.28), (2.2.29), (2.2.30), and (2.2.31) define the third row of the matrix. The (4,1) entry is given by

$$(T_n^{(p)}(k_p R_p)^{-1})_{(4,1)} = -W_{(n,p)}^{(b,1)}(k_p R_p) \left(\frac{-\alpha^{(p)}}{k_p} \right) \mathcal{W}_{(n,p)}^{(a)}(k_p R_p) / \Delta_p, \quad (2.2.32)$$

The (4,2) entry is

$$(T_n^{(p)}(k_p R_p)^{-1})_{(4,2)} = 0 \quad (2.2.33)$$

The (4,3) entry is

$$(T_n^{(p)}(k_p R_p)^{-1})_{(4,3)} = -W_{(n,p)}^{(b,1)}(k_p R_p) \mathcal{W}_{(n,p)}^{(a)}(k_p R_p) / \Delta_p, \quad (2.2.34)$$

Finally, the (4,4) entry of the inverse of $T_n^{(p)}$ is

$$(T_n^{(p)}(k_p R_p)^{-1})_{(4,4)} = Z_{(n,p)}^{(b,1)}(k_p R_p) \mathcal{W}_{(n,p)}^{(a)}(k_p R_p) / \Delta_p, \quad (2.2.35)$$

We have therefore obtained round-off error free expressions for the entries of the inverse of $T_n^{(p)}(k_p R_p)$. Thus, except for the expression relating the expansion coefficients in equation (2.2.14), all computations are carried out by exact formulas. The matrix inverse computation requires no subtractions or additions and consequently there is no round off error if the Bessel and Hankel functions of complex index and their derivatives can be computed precisely.

2.3 Determination of Expansion Coefficients

Let us suppose that we have an N layer sphere subject to plane wave radiation. By multiplying the inverse of $T_n^{(p)}$ evaluated at $k_p R_p$ by the matrix $T_n^{(p+1)}$ evaluated at $k_{p+1} R_p$ we obtaining the matrix

$$\mathcal{T}_n^{(p)} = T_n^{(p)}(k_p R_p)^{-1} T_n^{(p+1)}(k_{p+1} R_p) \quad (2.3.1)$$

relating the expansion coefficients in layer p to those in layer $p+1$. We then multiply all of these matrices (2.3.1) obtaining a matrix

$$\mathcal{T} = \mathcal{T}_n^{(1)} \cdot \mathcal{T}_n^{(2)} \cdot \dots \cdot \mathcal{T}_n^{(N)} \quad (2.3.2)$$

where N is the number of layers of the sphere which relates the expansion coefficients in the core to the expansion coefficients in the space surrounding the sphere. This gives four equations in four unknowns. But it is really simpler than that. Using the second and fourth rows of this matrix equation, we can relate the expansion coefficients of the

scattered radiation to the known expansion coefficients of the incoming radiation. We then have in the first and third rows of this equation a formula for the expansion coefficients in the inner core.

3 Optical and Absorption Efficiency

3.1 Definition of Terms

The optical efficiency of a general N layer sphere exposed to plane wave radiation is defined to be

$$O_e = \left(\frac{Q_s + Q_a}{\|\vec{S}^i\|} \right) \left(\frac{1}{\pi R_N^2} \right) \quad (3.1.1)$$

where

$$\vec{S}^i = \text{the incoming radiation's Poynting vector} \quad (3.1.2)$$

and where

$$Q_a = \text{the total absorbed power} \quad (3.1.3)$$

and

$$Q_s = \text{the total scattered power} \quad (3.1.4)$$

and

$$R_N = \text{the radius of the outer shell} \quad (3.1.5)$$

The absorption efficiency is

$$A_e = \left(\frac{Q_a}{\|\vec{S}^i\|} \right) \left(\frac{1}{\pi R_N^2} \right) \quad (3.1.6)$$

These efficiencies O_e and A_e are unitless as Q_s and Q_a both have the units of Watts, and the Poynting vector \vec{S}^i has the units of Watts per square meter, and the apparent projected size, π times the square of the radius, has the units of square meters.

These quantities can all be computed systematically just with a knowledge of the expansion coefficients of the scattered radiation and the expansion coefficients of spherical harmonic representation of the plane wave representing the impinging electromagnetic

wave. Suppose that \vec{E}^s and \vec{H}^s are the electric and magnetic vectors of the scattered radiation and suppose that \vec{E}^i and \vec{H}^i are the electric and magnetic vectors of the incoming radiation that stimulates the sphere filled with electromagnetic material. The quantity

$$Q_s + Q_a = \text{the total extinguished power} \quad (3.1.7)$$

is called the *extinction* and is calculated by integrating the Poynting vector,

$$\vec{S} = (1/2)(\vec{E}^s + \vec{E}^i) \times (\vec{H}^s + \vec{H}^i)^* \quad (3.1.8)$$

over the outer surface of the sphere. For a plane wave, the result of integrating

$$\vec{S}^i = (1/2)(\vec{E}^i) \times (\vec{H}^i)^* \quad (3.1.9)$$

over the surface of a sphere is zero, since the average value of the normal vector to this surface is zero. The rate at which energy leaves the surface of the sphere as a result of reradiation of the energy incident on it is similarly determined by integrating

$$\vec{S}^s = (1/2)(\vec{E}^s) \times (\vec{H}^s)^* \quad (3.1.10)$$

over the surface of the sphere.

In this section we shall study how absorption and optical efficiency depend on the wavelength or the frequency of the incoming radiation, but we shall transform this wavelength or frequency, respectively, into a unitless quantity called the size parameter. If

$$\omega = 2 \cdot \pi \cdot f \quad (3.1.11)$$

then the size parameter is defined as

$$s_\lambda = \frac{2 \cdot \pi \cdot R_N}{\lambda} \quad (3.1.12)$$

where

$$2 \cdot \pi \cdot \lambda^{-1} = \omega \cdot \sqrt{(\mu_0 \epsilon_0)} = 2 \cdot \pi \cdot f \sqrt{(\mu_0 \epsilon_0)} \quad (3.1.13)$$

or

$$\lambda = \frac{2\pi}{(\omega \sqrt{\mu_0 \epsilon_0})} \quad (3.1.14)$$

where

$$\mu_0 = 4\pi \times 10^{-7} \quad (3.1.15)$$

and

$$\epsilon_0 = 8.854 \times 10^{-12} \quad (3.1.16)$$

are the free space magnetic permeability and electrical permittivity.

3.2 Computer Calculations

If we look at the representation of expansion coefficients in terms of index of refraction, we find that as this index of refraction gets close to an imaginary part of $\sqrt{2}$ and a real part near zero, that there is very strong scattering and absorption at apparently periodic values of the size parameter. The first graph below shows the absorption efficiency of a spherical particle with an index of refraction m given by

$$m = .0001 + i(1.4140) \quad (3.2.1)$$

and the subsequent graph shows the optical efficiency for the same index of refraction.

Absorption Efficiency vs Size Parameter
 $m: (0.0001, 1.4140)$

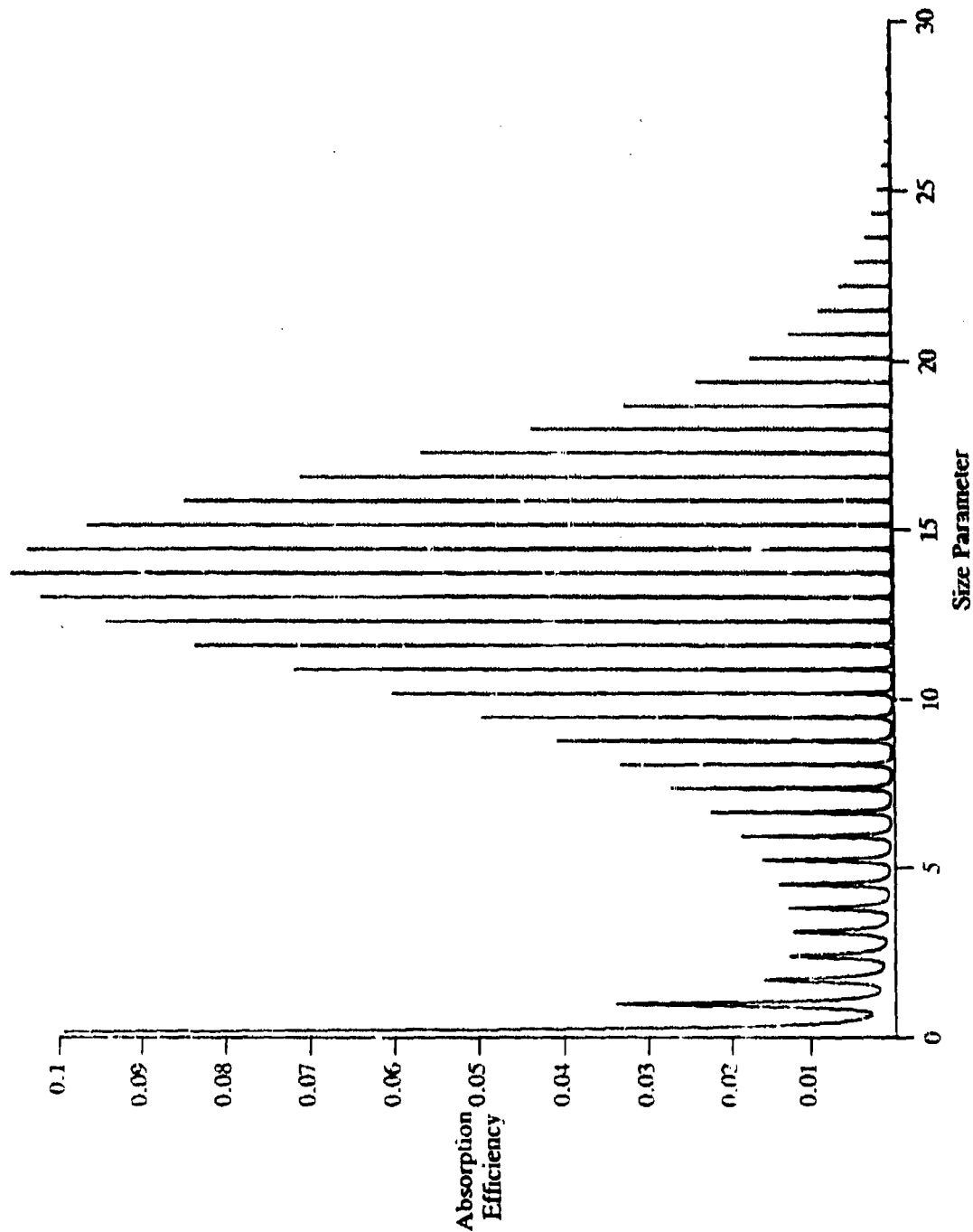


Figure 3.2.1. This graph shows the total absorbed power divided by the product of the length of the Poynting vector of the incident radiation times π times the square of the radius of the sphere.

Optical Efficiency vs Size Parameter
 $m: (0.0001, 1.4140)$

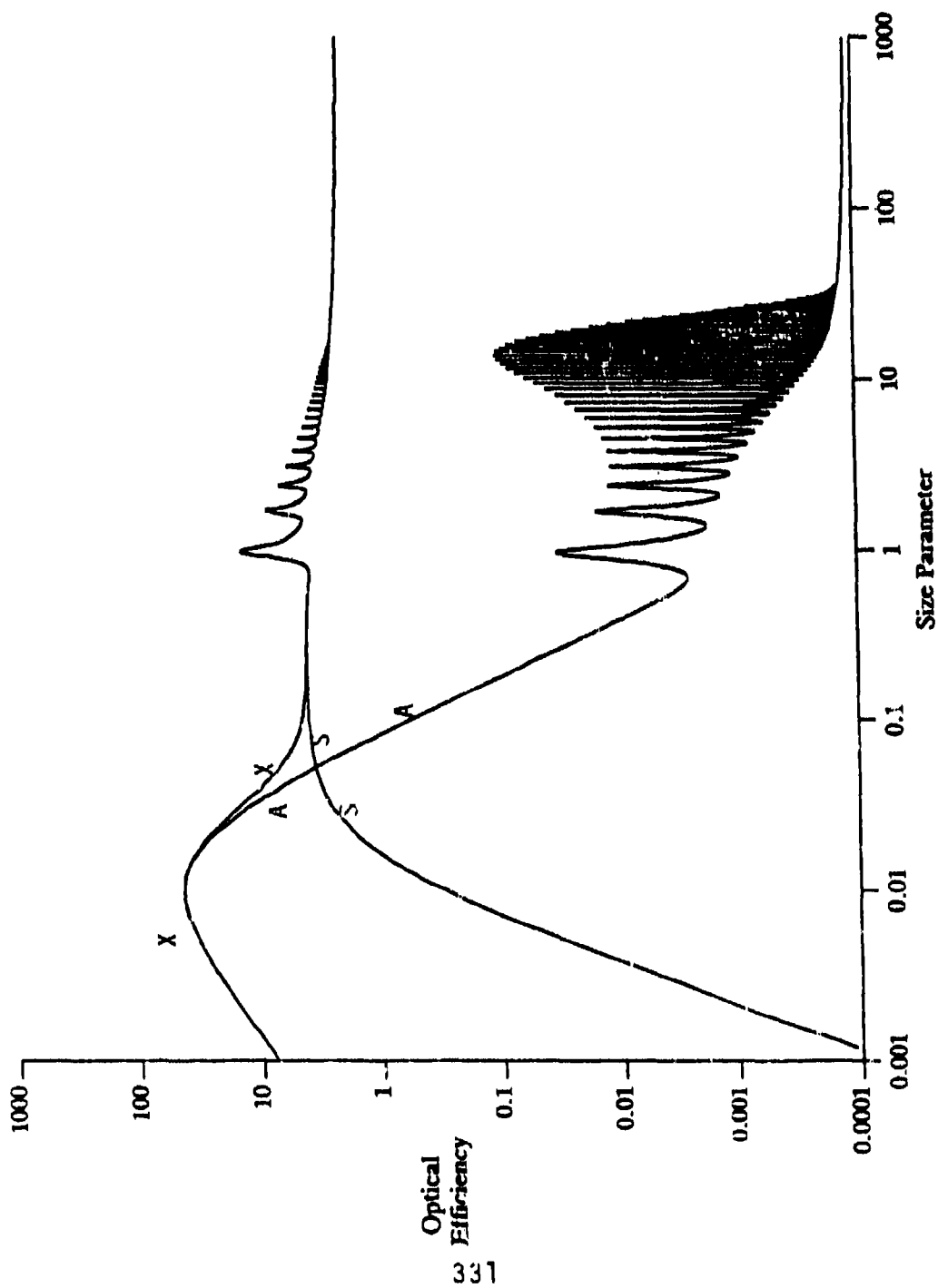


Figure 3.2.2. This graph shows the extinction, X, absorption, denoted by A, and scattering, S, efficiency as a function of the size parameter of a one layer sphere with an index of refraction of $.0001 + 1.414i$.

These graphs suggest that scattering is much more important than absorption, but as we allow the size parameters to become very large there is a cross over in the scattering and absorption efficiency curves for the same index of refraction. This is shown in the next computation represented on a logarithmic scale which considers size parameters as large as 1000. In this graph, there are the same early maximums as before, but they simply cannot be seen on the logarithmic scale. Some of the maximums are shown in the following table

size parameter	absorption efficiency	optical efficiency
.010000E0	.43077010E + 2	.3090E + 6
.973500E0	.13852698E + 2	.2388E + 4
.168930E1	.86167641E + 1	.9345E + 3
.239210E1	.66955849E + 1	.6547E + 3
.309430E1	.56436135E + 1	.6412E + 3
.379800E1	.49728349E + 1	.7194E + 3
.450370E1	.45070065E + 1	.8206E + 3

On the vertical axis of these graphs we are computing the logarithm of the efficiencies. When the imaginary part of the index of refraction is slightly above the square root of two, we see a strong peak in optical efficiency that is due to absorption efficiency. The graphs which follow show, over a small range of size parameteres, results for an index of refraction of

$$m = .0001 + i(1.4144) \quad (3.2.2)$$

Absorption Efficiency vs Size Parameter $m: (0.0001, 1.4144)$

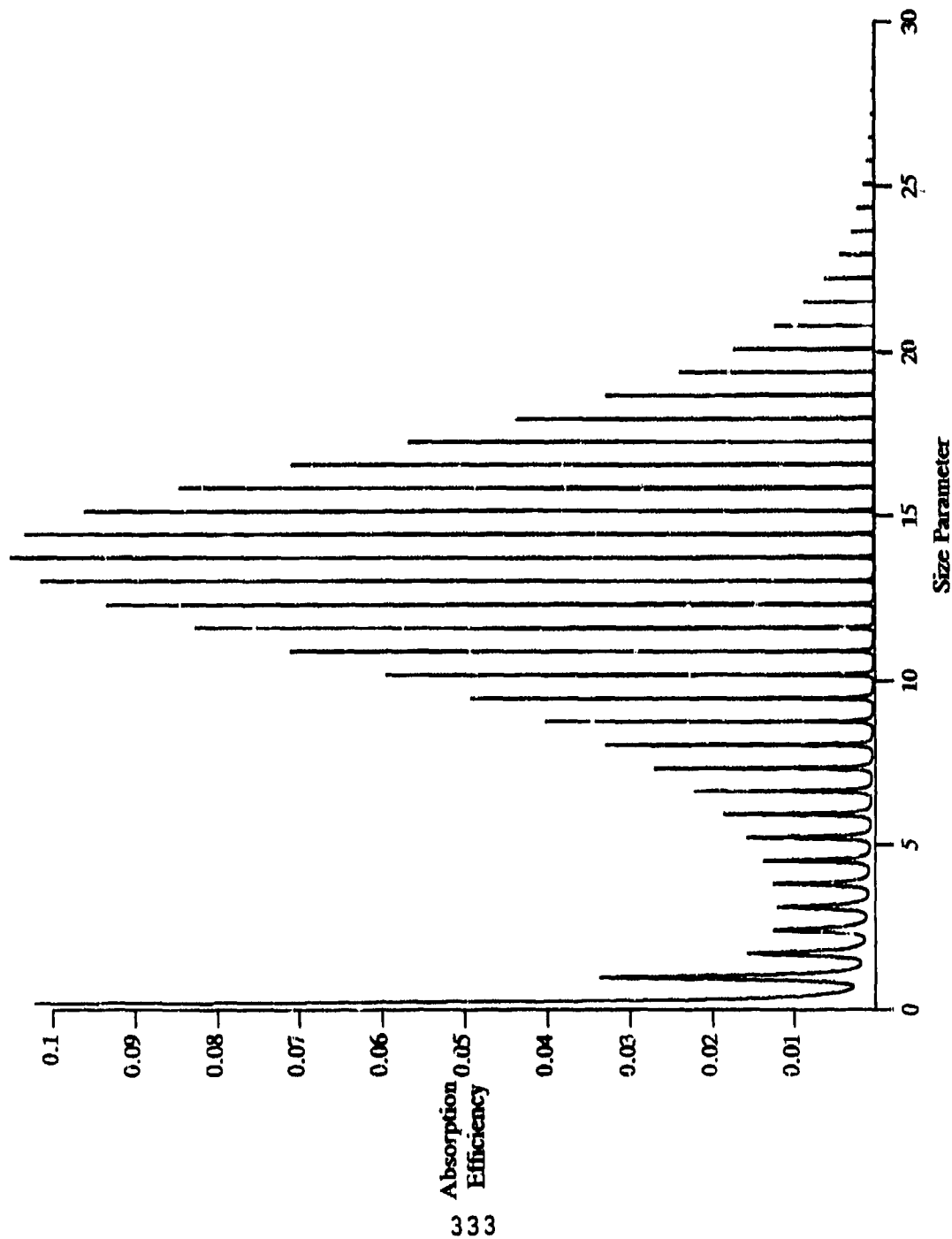


Figure 3.2.3. This graph shows the absorption efficiency, defined in section 3.1, as a function of the size parameter of a one layer sphere with an index of refraction of $.0001 + i(1.4144)$

Optical Efficiency vs Size Parameter
 $m: (0.0001, 1.4144)$

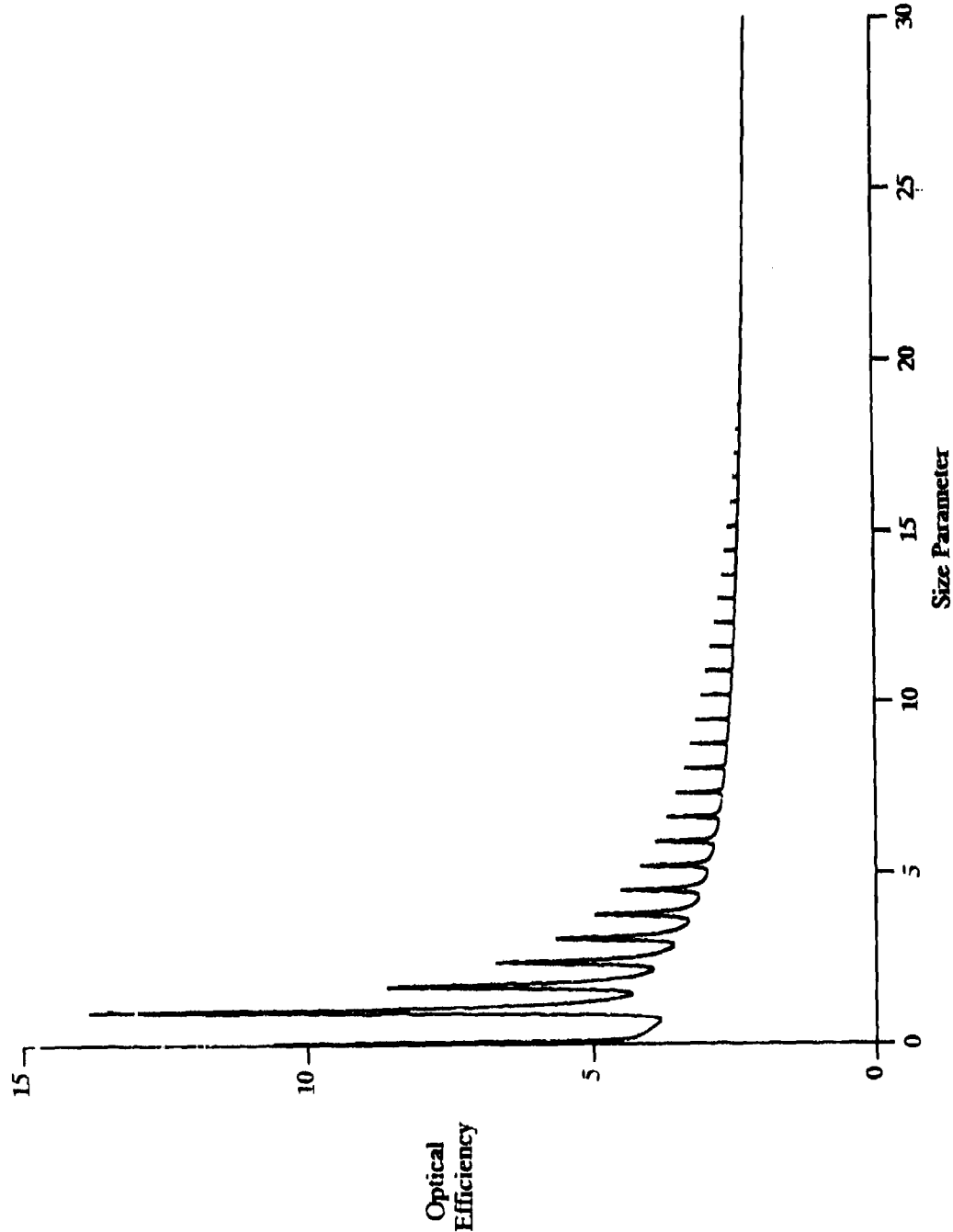
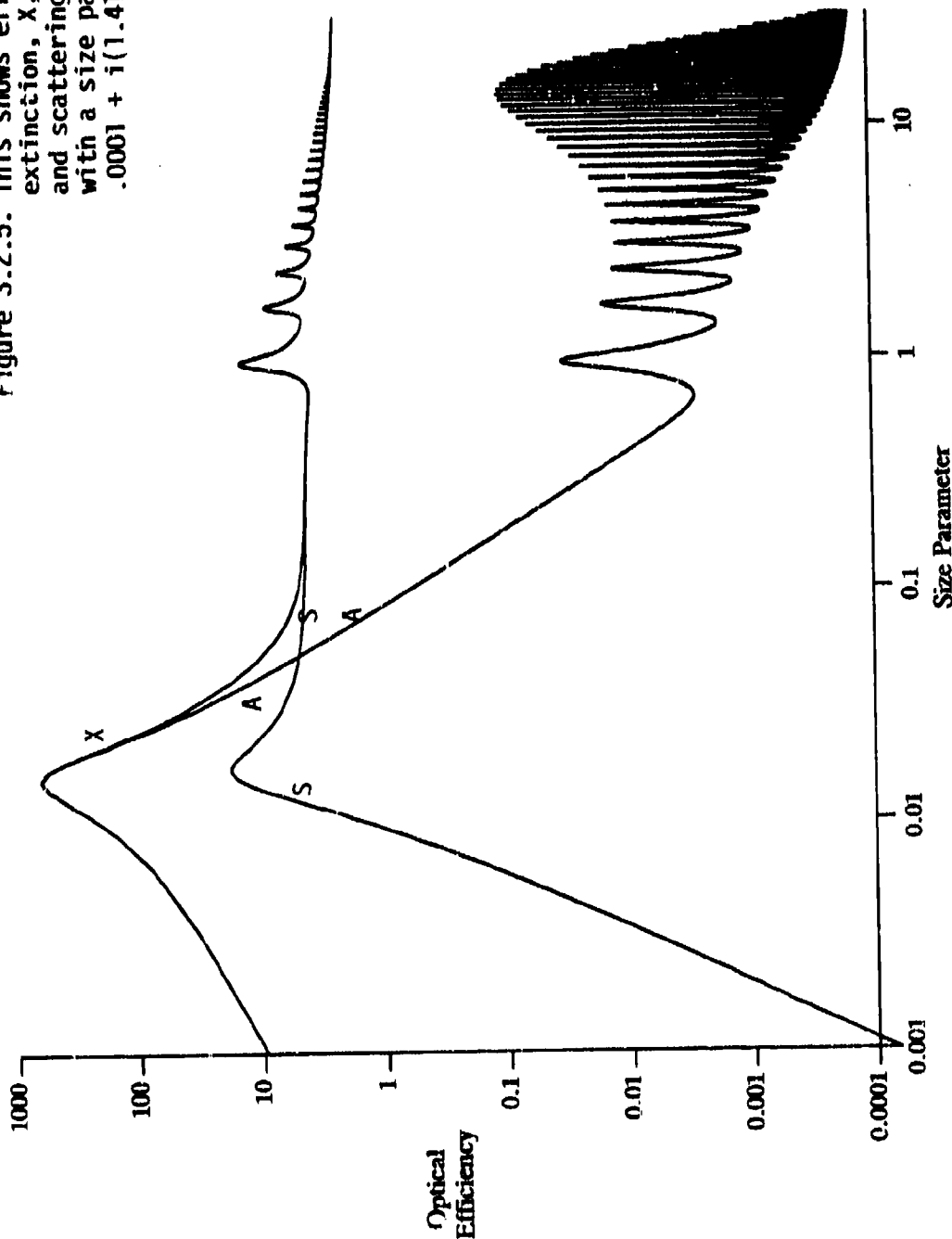


Figure 3.2.4. This graph shows the optical efficiency of a one layer sphere as a function of size parameter when the sphere has an index of refraction of $.0001 + i(1.4144)$.

Optical Efficiency vs Size Parameter
 $m: (0.0001, 1.4144)$

Figure 3.2.5. This shows efficiencies of extinction, X , absorption, A , and scattering, S , for a sphere with a size parameter of $.0001 + i(1.4144)$.



The topmost curve represents extinction, which is scattering plus absorption efficiency. To the left of the size parameter where we see a crossing of curves in the narrow region where we can see three curves, they are from top to bottom, (i) extinction, (ii) absorption, and (iii) scattering efficiency. In the region to the right of the crossover point, where we can see three curves, they are from top to bottom (i) extinction (or optical), (ii) scattering, and (iii) absorption efficiency.

Optical Efficiency vs Size Parameter
 $m: (0.0001, 1.4144)$

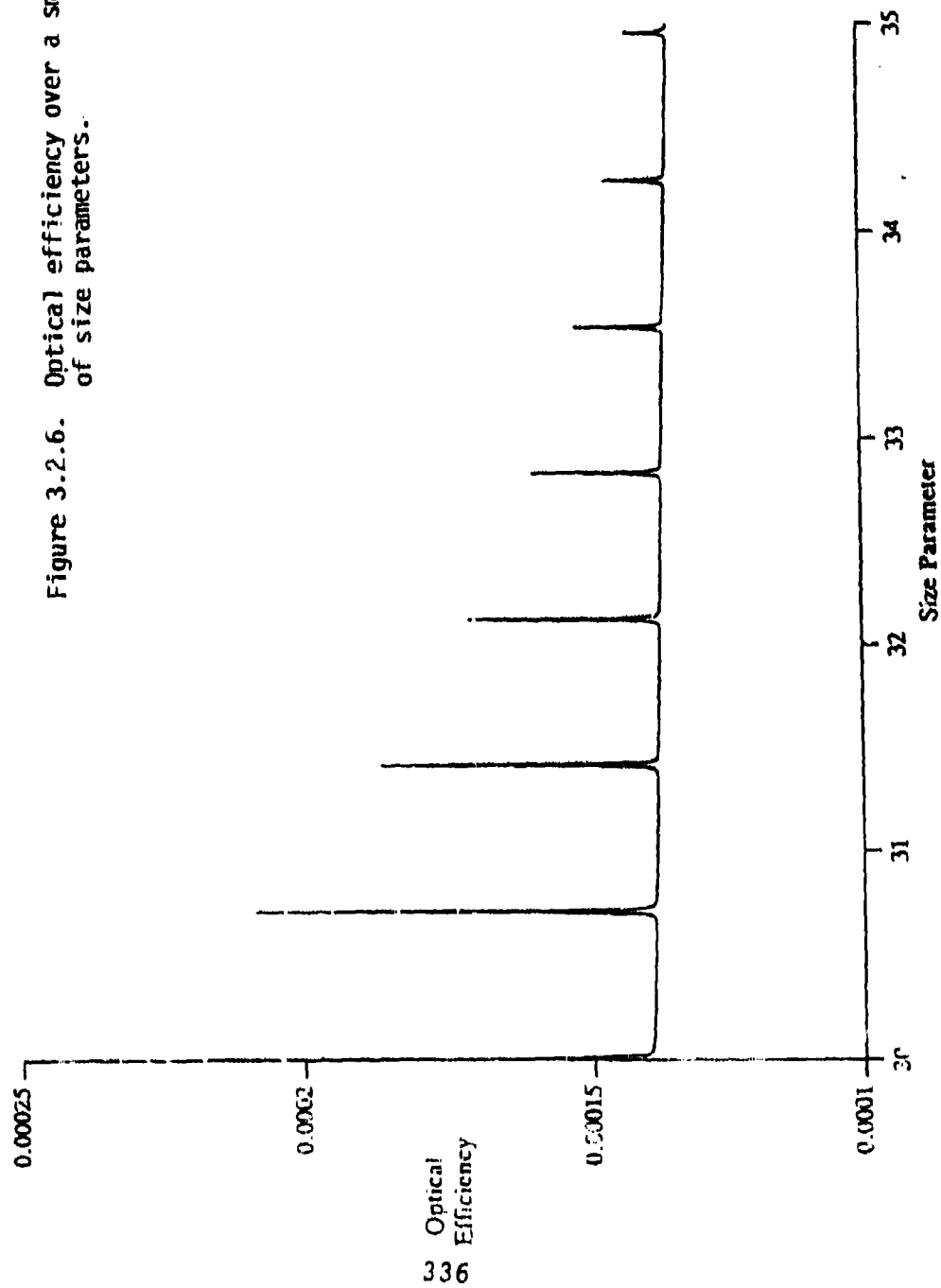


Figure 3.2.6. Optical efficiency over a small range of size parameters.

In these calculations going out to large size parameters, around 8000 size parameters were considered along with a procedure which searched for the maximums and the troughs in the graph. The following table shows a computation of the low points in the graph of absorption efficiency.

size parameter	absorption efficiency
.700	.38222365E + 1
.147	.43105236E + 1
.218	.39434158E + 1
.289	.35937823E + 1
.360	.33305300E + 1
.431	.33305300E + 1
.502	.29903701E + 1

Note that the locations of the troughs in the above table are in between the maximums indicated in the previous table. For this particular calculation great care must be exercised in locating the maximums. When the spherical particle has a greater permittivity, the peaks are broader and can generally be observed graphically by a straightforward computation with evenly spaced size parameters.

Absorption Efficiency as a function of size parameter
 Avg Frequency = 1000 Megahertz, Radius = 5.0 centimeters
 Total absorbed power = 1.80313536E-5 Watts
 $\epsilon = 59.86$
 μ radial = $2+0.1i$, and μ tangential = $4+0.2i$
 $\sigma = 1.00152$ mhos per meter
 Constant index of refraction = (15.59143572, 2.69320705)

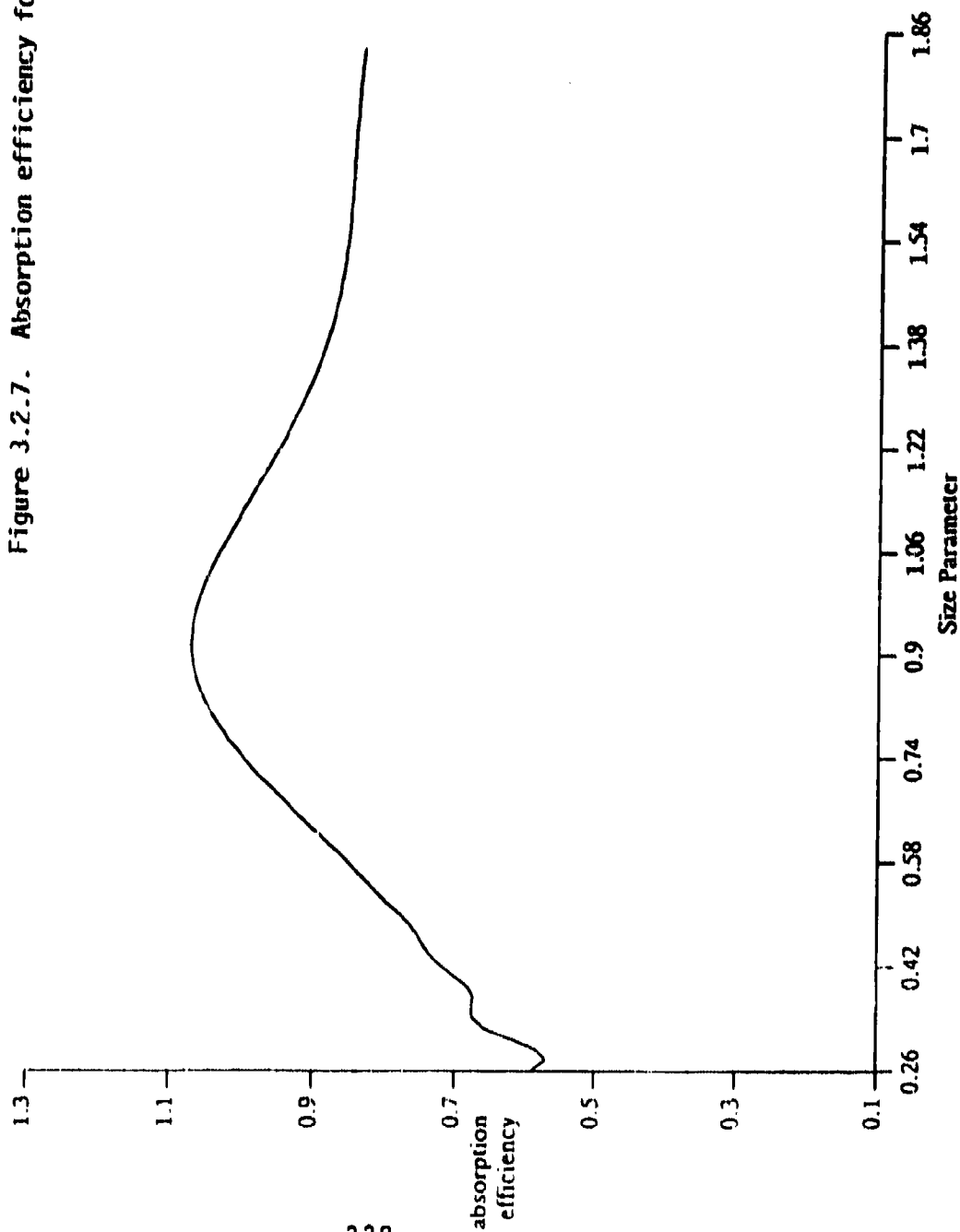


Figure 3.2.7. Absorption efficiency for a lossy sphere.

Optical Efficiency as a function of size parameter
 Frequency = 1000 Megahertz, Avg Radius = 5.0 centimeters
 Total absorbed power = $1.80313536 \times 10^{-5}$ Watts
 $\epsilon = 59.86$
 μ radial = $2 + 0.1i$, and μ tangential = $4 + 0.2i$
 $\sigma = 1.00152$ mhos per meter
 The power density is in Watts per cubic meter

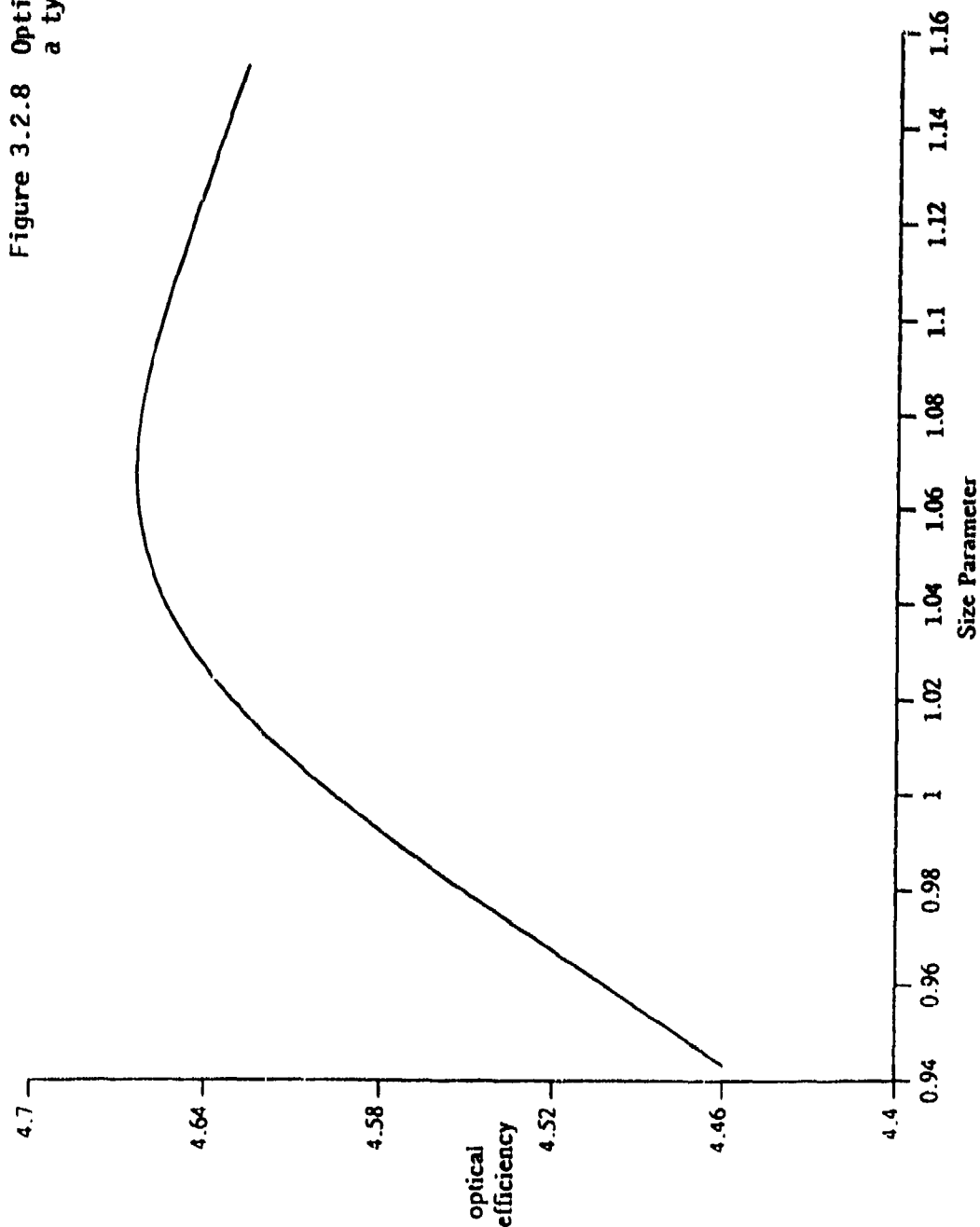


Figure 3.2.8 Optical efficiency for a typical lossy sphere.

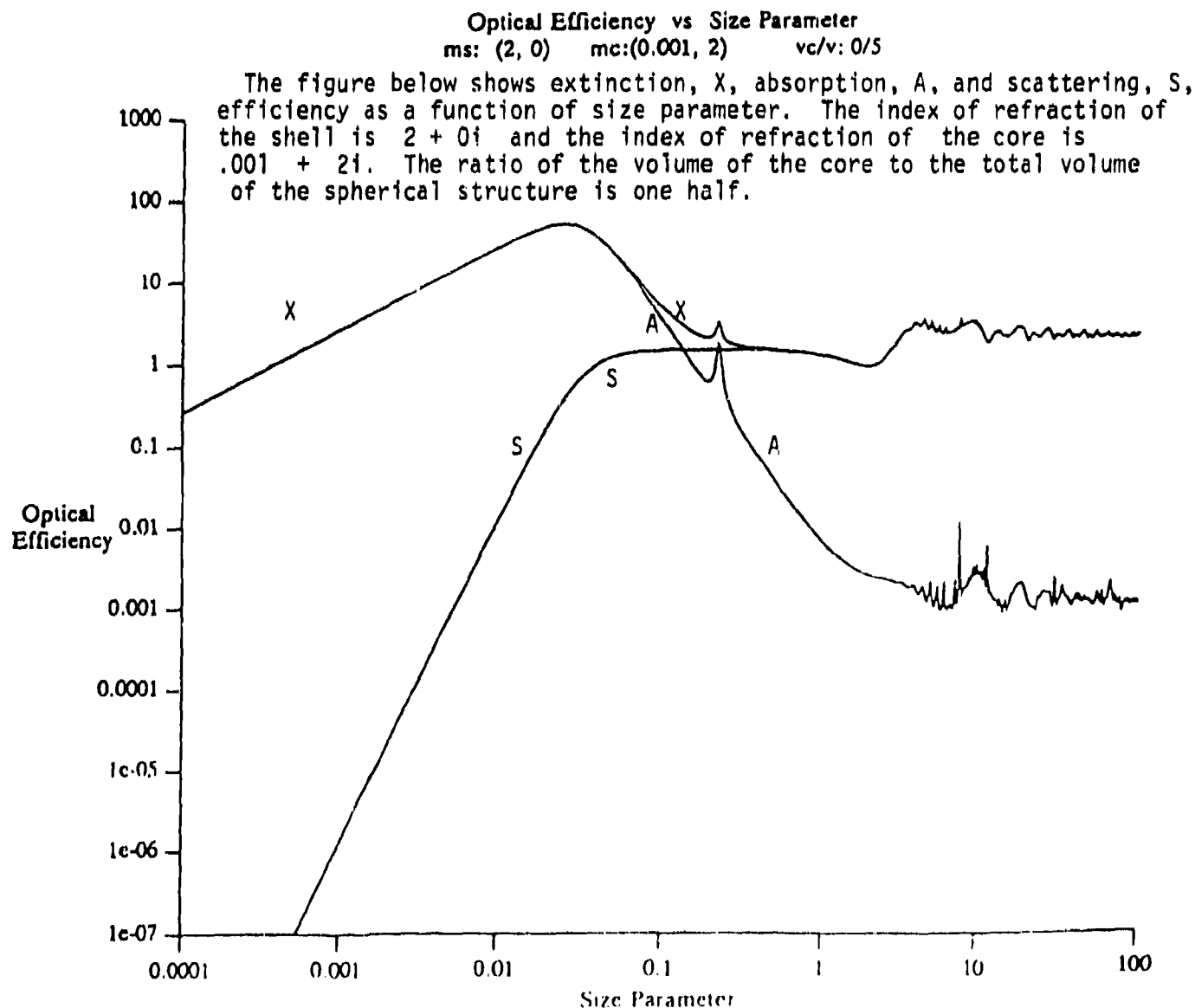
3.3 Highly Efficient Two Layer Spheres

Van de Hulst ([47]) develops the relation between the permittivity ϵ_1 of the core of radius qR , where q is a number between zero and one and the permittivity ϵ_2 of the shell of outer radius R which will produce a very high efficiency. This relationship ([47]) is

$$\epsilon_1 = \left(\frac{(1 - 2q^3)\epsilon_2^2 + \epsilon_2(4 + 2q^3)}{(2 - 2q^3) + \epsilon_2(1 + 2q^3)} \right) \quad (3.3.1)$$

The following shows some computations of efficiency for two layer structures which nearly satisfy this relationship.

Figure 3.3.1



Backscattering vs Size Parameter
 ms: (2, 0) mc: (0, 2), (1.e-6, 2) vc/v: 0.5

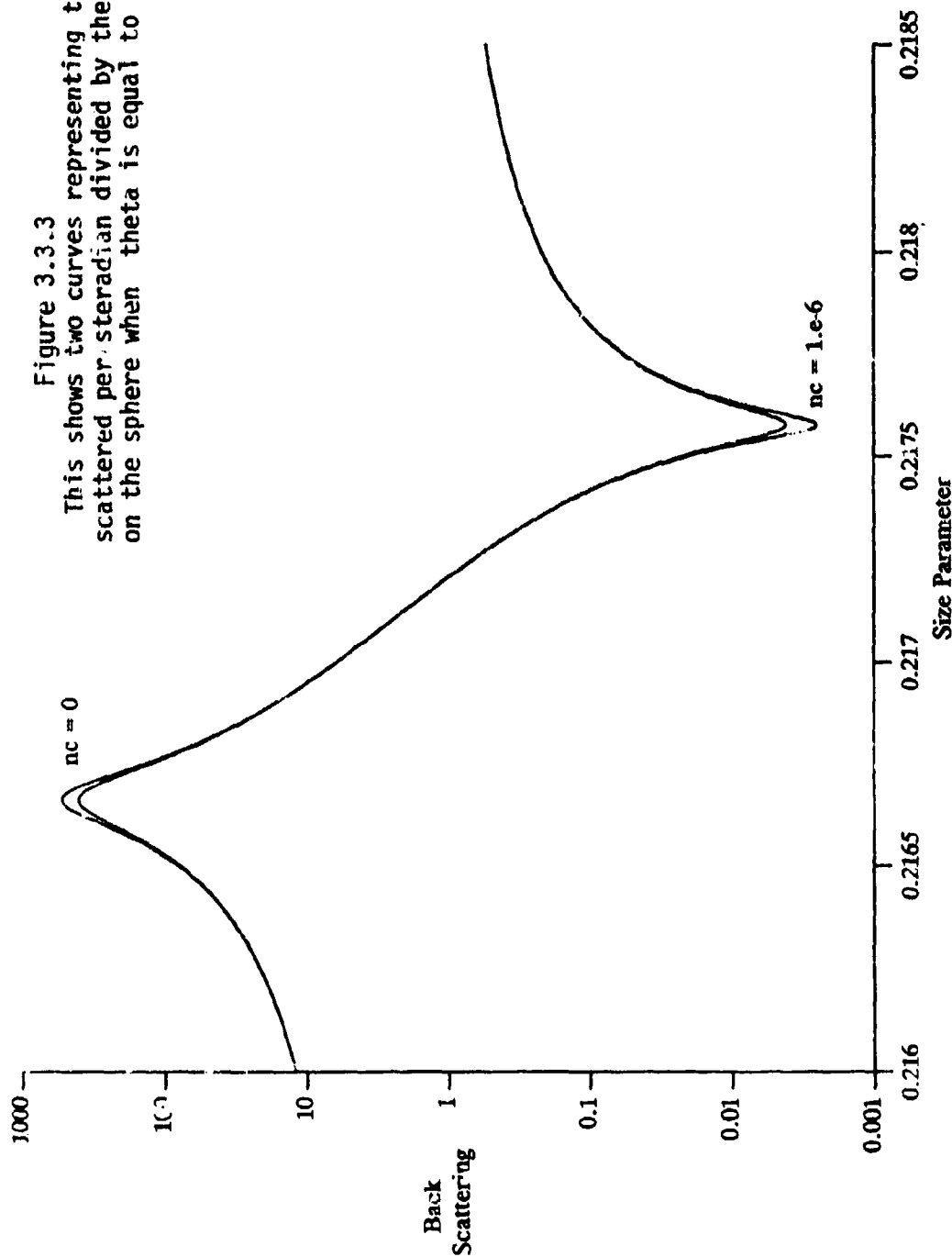


Figure 3.3.3
 This shows two curves representing the total power scattered per steradian divided by the power incident on the sphere when θ is equal to 180 degrees.

This figure shows backscattered power versus size parameter for a pair of two layer spheres. The index of refraction of the shell is $2+0i$, and the index of the inner core is either $2i$ or $.000001 + 2i$, and are marked above as $nc = 0$ or $nc = 1.e-6$.

Optical Efficiency vs Size Parameter
 ms: (2, 0) mc:(1.e-6. 2) vc/v: 0.5

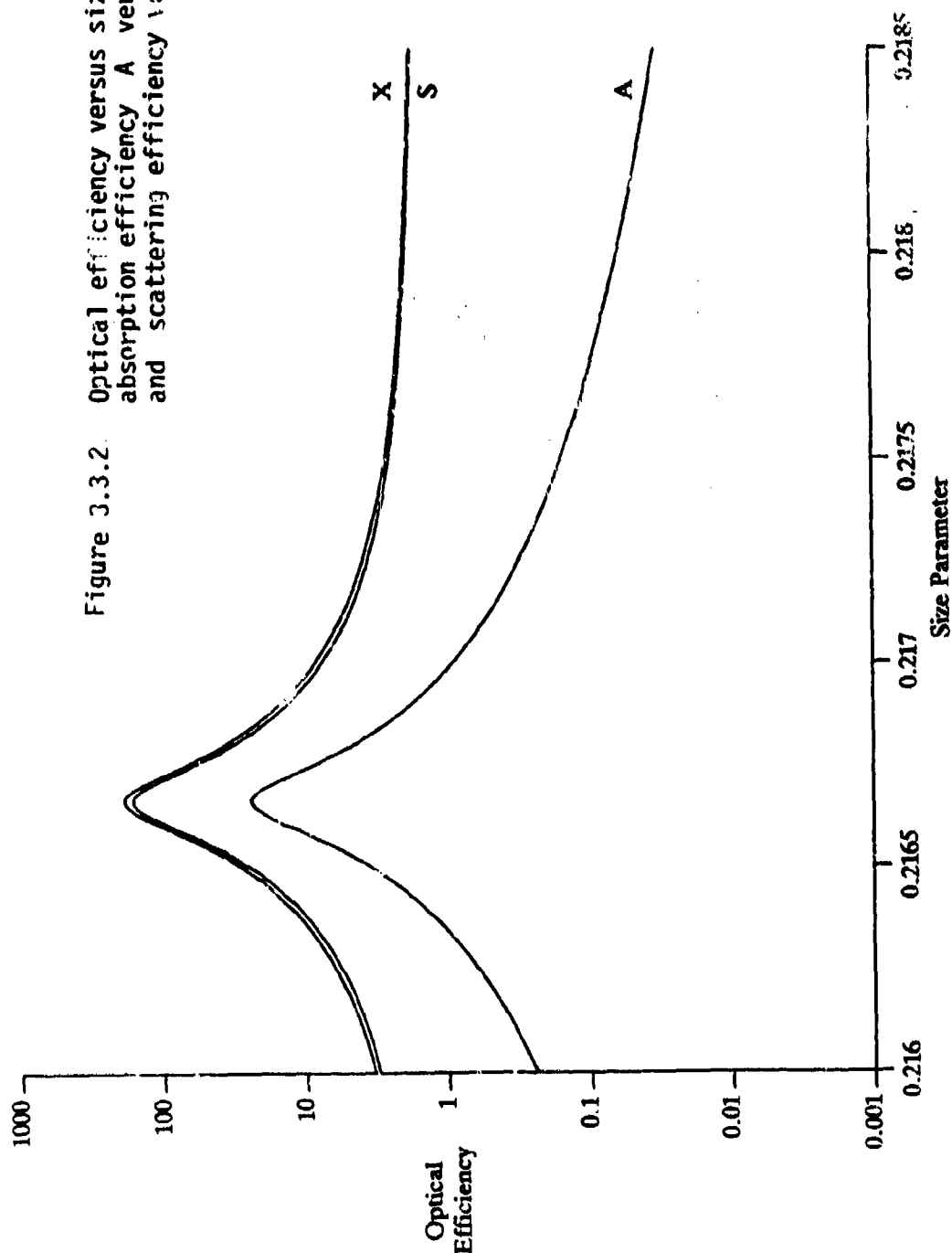
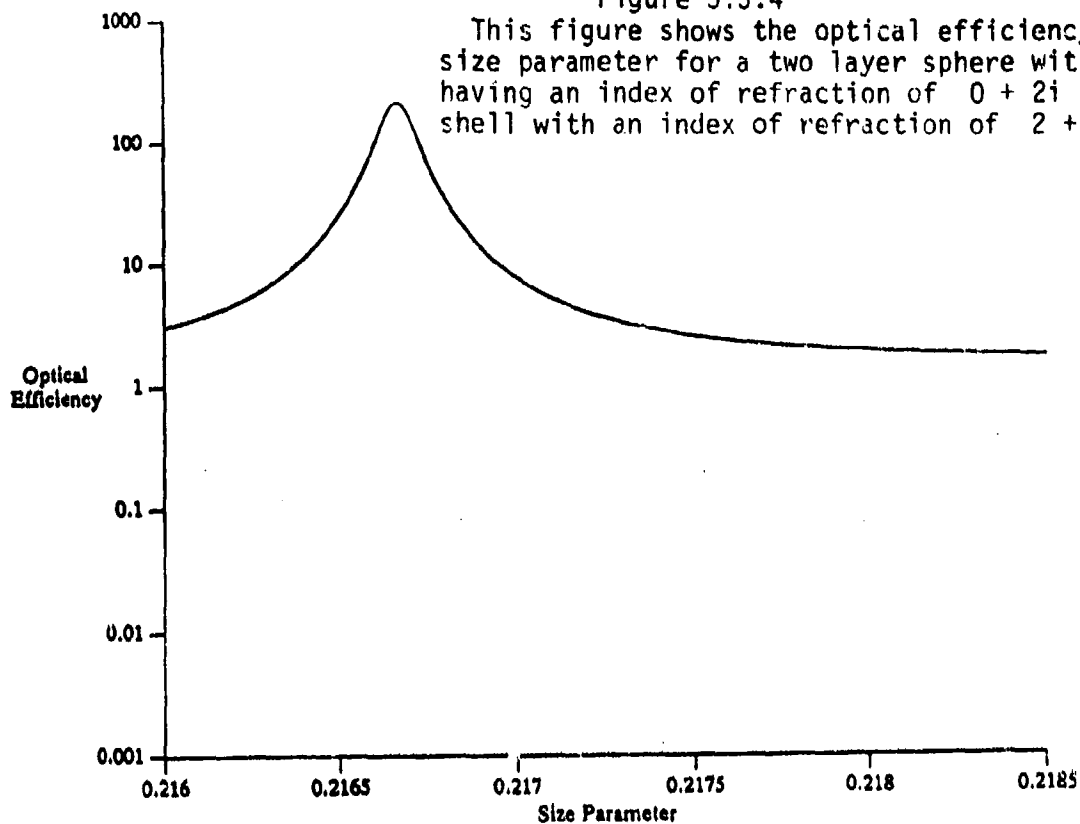


Figure 3.3.2 Optical efficiency versus size parameter, absorption efficiency A versus size parameter, and scattering efficiency versus size parameter.

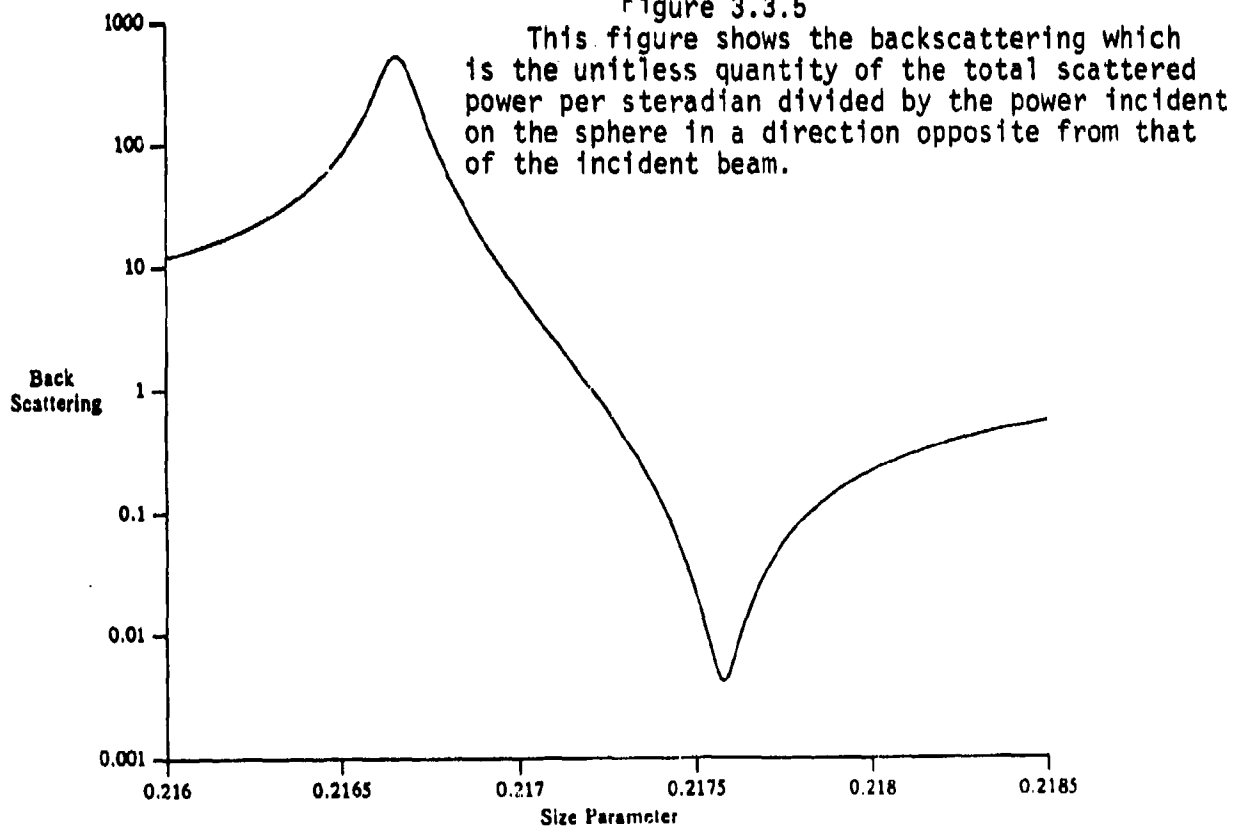
In the above figure X represents extinction, S scattering, and A absorption efficiency. The ratio of the volume of the core to the total volume of the sphere is .5

Figure 3.3.4



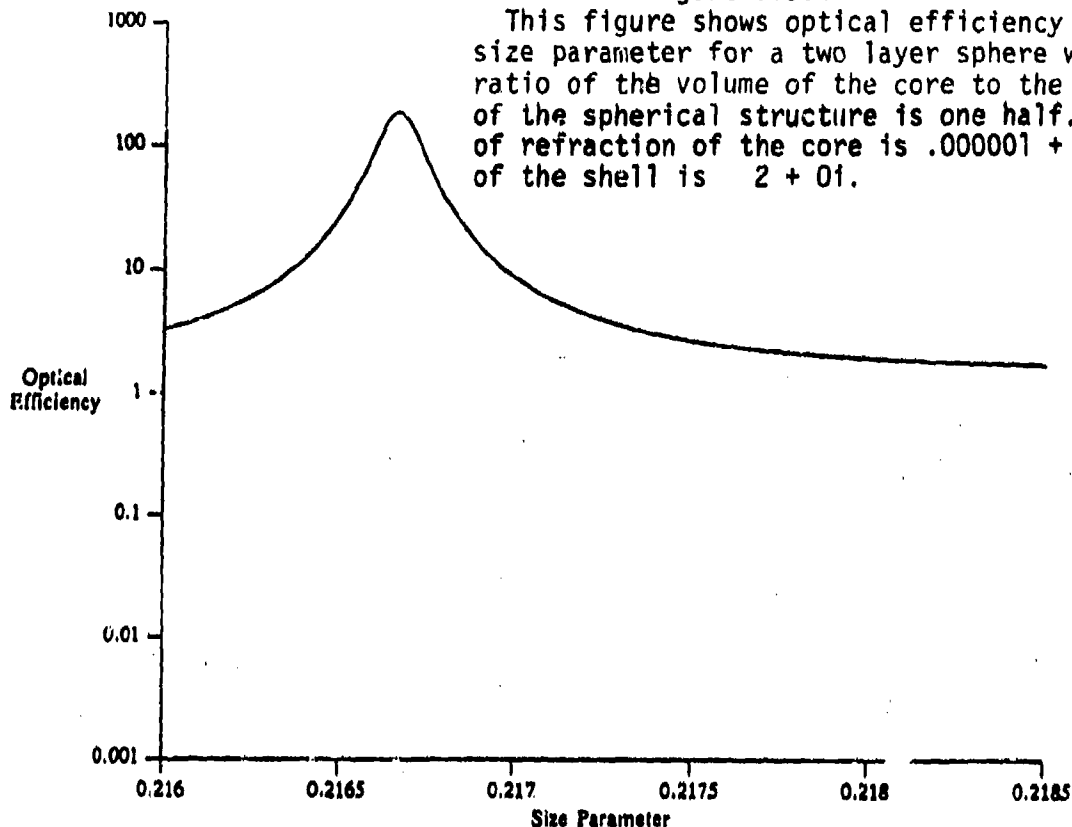
Backscattering vs Size Parameter
 $m_1: (2, 0)$ $m_2: (0, 2)$ $v_0/v_i: 0.5$

Figure 3.3.5



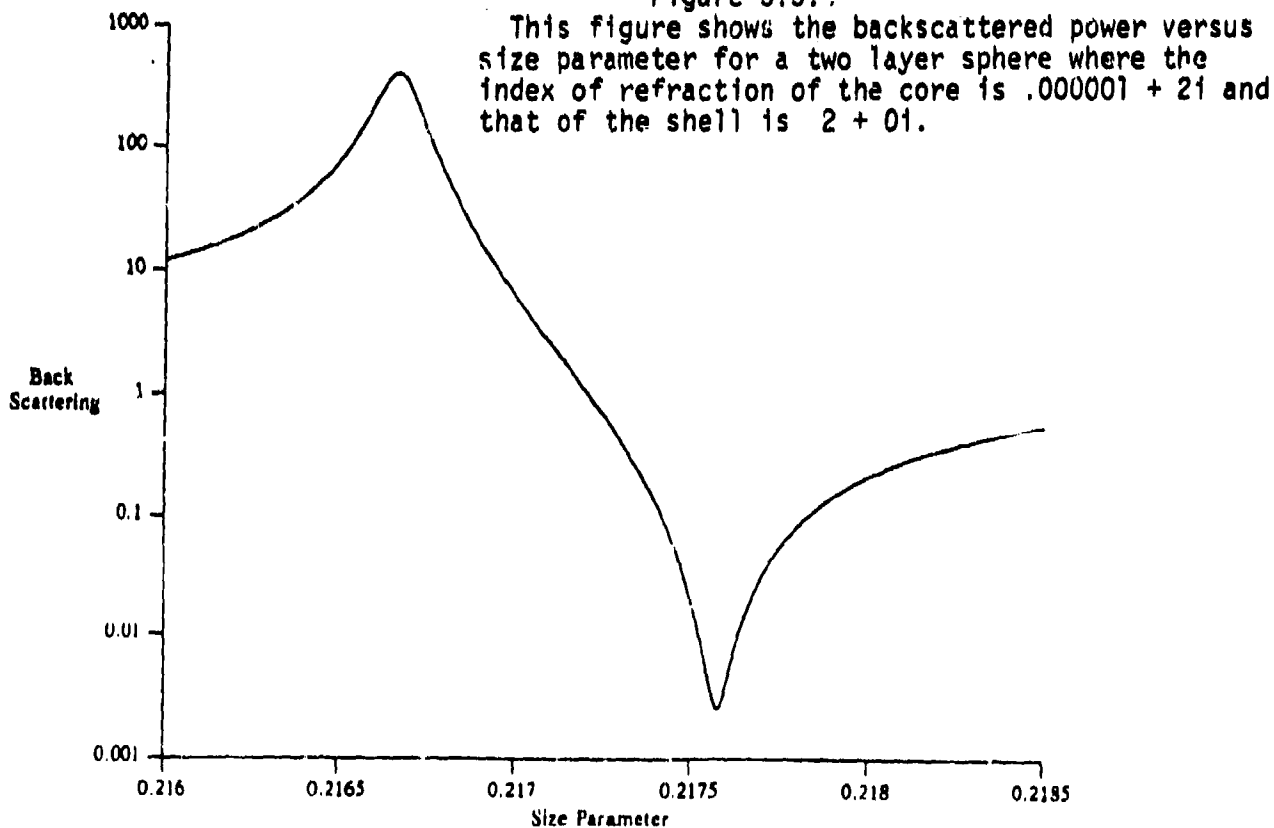
Optical Efficiency vs Size Parameter
 ms: (2, 0) mc: (1.e-6, 2) vc/v: 0.5

Figure 3.3.



Backscattering vs Size Parameter
 ms: (2, 0) mc: (1.e-6, 2) vc/v: 0.5

Figure 3.3.



4 Spatially Complex Sources

4.1 Expansion Coefficient Determination

We provide the user with an analysis of the response of an N layer structure to spatially and temporally complex sources of electromagnetic radiation. Let $\vec{E}(x, y, z, t)$ and $\vec{H}(x, y, z, t)$ be the electric and magnetic fields of a complex source with Fourier transforms $\hat{\vec{E}}(x, y, z, \omega)$ and $\hat{\vec{H}}(x, y, z)$. We suppose that this radiation source exists in layer

$$p \in \{2, 3, \dots, N+1\}.$$

where N is the number of layers in the spherical structure. Let us suppose that this energy source in layer p has an electric vector (see equation 2.1.1) given by

$$\begin{aligned} \vec{E} = \sum_{(m,n) \in \mathcal{I}} \left\{ \tilde{a}_{(m,n)} Z_{(n,p)}^{(a,1)}(r) \vec{A}_{(m,n)}(\theta, \phi) + \right. \\ \left. [-n(n+1) \{ \zeta_b^{(p)} \} \tilde{b}_{(m,n)} \frac{Z_{(n,p)}^{(b,1)}(r)}{k_p r} \vec{C}_{(m,n)}(\theta, \phi) + \right. \\ \left. \frac{\tilde{b}_{(m,n)}}{k_p r} \left(- \left(\frac{\partial}{\partial r} \right) (r Z_{(n,p)}^{(b,1)}(r)) \right) \vec{B}_{(m,n)}(\theta, \phi) \right\} \end{aligned} \quad (4.1.1)$$

Observe that the coefficients $\tilde{a}_{(m,n)}^{(p)}$ are determined for every $p > 1$ by the relation,

$$\begin{aligned} \lim_{r \rightarrow R_{p-1}} \left[\frac{\int \int_{C(r)} \hat{\vec{E}}_p(x, y, z, \omega) \cdot \vec{A}_{(m,n)}(\theta, \phi)^* \sin(\theta) d\theta d\phi}{\int \int_{C(r)} \vec{A}_{(m,n)}(\theta, \phi) \cdot \vec{A}_{(m,n)}(\theta, \phi)^* \sin(\theta) d\theta d\phi} \right] \\ = \tilde{a}_{(m,n)}^{(p)} Z_{(n,p)}^{(a,1)}(R_{p-1}) \end{aligned} \quad (4.1.2)$$

where

$$C(r) = \{(x, y, z) : x^2 + y^2 + z^2 = r^2\} \quad (4.1.3)$$

Thus, equation (4.1.2) gives us the expansion coefficients for the representation of \vec{E} just outside the sphere $C(R_{p-1})$ defined by equation (4.1.3). The coefficients $\tilde{b}_{(m,n)}^{(p)}$ are determined by the equation,

$$\lim_{r \rightarrow R_{p-1}} \left[\frac{\int \int_{C(r)} \hat{\vec{E}}_p(x, y, z, \omega) \cdot \vec{B}_{(m,n)}(\theta, \phi)^* \sin(\theta) d\theta d\phi}{\int \int_{C(r)} \vec{B}_{(m,n)}(\theta, \phi) \cdot \vec{B}_{(m,n)}(\theta, \phi)^* \sin(\theta) d\theta d\phi} \right]$$

$$= \tilde{b}_{(m,n)}^{(p)}(-W_{(n,p)}^{(b,1)}(R_{p-1})) \quad (4.1.4)$$

where, using the definition (see equation 2.1.12),

$$W_{(n,p)}^{(b,j)}(r) = \frac{1}{k_p r} \left(\frac{\partial}{\partial r} \right) (r Z_{(n,p)}^{(b,j)}(r)) \quad (4.1.5)$$

and the functions $\vec{A}_{(m,n)}(\theta, \phi)$ and $\vec{B}_{(m,n)}(\theta, \phi)$ are given by equations (1.3.1) and (1.3.2). We will show that the integrals in the denominators in equations (4.1.2) and (4.1.4) can be determined by an exact formula. To exactly evaluate the integrals appearing in the denominators, we use the equation (see Bell [10], equation 11 and equation 18) which states that

$$\begin{aligned} \int_{-\pi}^{\pi} \int_0^{\pi} \left\{ \left(\frac{d}{d\theta} P_n^m(\cos(\theta)) \right)^2 + m^2 \frac{P_n^m(\cos(\theta))^2}{\sin^2(\theta)} \right\} \sin(\theta) d\theta d\phi = \\ = \left(\frac{2}{2n+1} \right) \cdot \left(\frac{(n+m)!}{(n-m)!} \right) n(n+1) \end{aligned} \quad (4.1.6)$$

where the functions $P_n^m(x)$ are defined by

$$P_n^m(x) = \frac{(1-x^2)^{m/2}}{2^n n!} D^{n+m}(x^2-1)^n \quad (4.1.7)$$

of the associated Legendre function.

We use the basic definition

$$P_n^m(x) = \left(\frac{(1-x^2)^{m/2}}{2^n n!} \right) D^{n+m}(x^2-1)^n \quad (4.1.8)$$

of the associated Legendre function. If

$$x = \cos(\theta) \quad (4.1.9)$$

then

$$d\theta = -\frac{dx}{\sqrt{1-x^2}} \quad (4.1.10)$$

and

$$\begin{aligned} \int_0^{\pi} P_n^m(\cos(\theta))^2 \sin(\theta) d\theta = \\ \frac{1}{2^{2n}(n!)^2} \int_{-1}^{+1} (1-x^2)^m (D^{n+m}(x^2-1)^n)^2 dx = \frac{2(n+m)!}{(2n+1)(n-m)!} \end{aligned} \quad (4.1.11)$$

The orthogonality relationship follows from the fact that

$$\frac{d}{d\theta} = \frac{dx}{d\theta} \frac{d}{dx} = -\sin(\theta) \frac{d}{dx} \quad (4.1.12)$$

implies that

$$\begin{aligned} A_{(n,r)}^m &= \int_0^\pi \left[\frac{d}{d\theta} P_n^m(\cos(\theta)) \right] \left[\frac{d}{d\theta} P_r^m(\cos(\theta)) \right] \sin(\theta) d\theta \\ &= \int_{-1}^1 (1-x^2) \frac{d}{dx} P_n^m(x) \frac{d}{dx} P_r^m(x) dx. \end{aligned} \quad (4.1.13)$$

The derived identity then follows from an integration by parts and a use of the differential equation relationship,

$$\begin{aligned} (1-x^2) \left[\left(\frac{d}{dx} \right)^2 P_n^m(x) \right] + (-2x) \frac{d}{dx} P_n^m(x) = \\ \left[-n(n+1) + \frac{m^2}{1-x^2} \right] P_n^m(x) \end{aligned} \quad (4.1.14)$$

Details of the analysis can be found in ([11]) and the basic properties of P_n^m are found in ([52])

4.2 An Exterior Complex Source

We now define intralayer relationships that give us the induced field when there are no sources in layers indexed by

$$p \in \{2, 3, \dots, N\}$$

where N is the number of layers in the sphere. The intralayer relationship yields, for a penetrable core,

$$\begin{bmatrix} a_{(m,n)}^{(1)} \\ 0 \\ b_{(m,n)}^{(1)} \\ 0 \end{bmatrix} = \mathcal{S}_N \begin{bmatrix} \tilde{a}_{(m,n)}^{(N+1)} \\ \alpha_{(m,n)}^{(N+1)} \\ \tilde{b}_{(m,n)}^{(N+1)} \\ \beta_{(m,n)}^{(N+1)} \end{bmatrix} \quad (4.2.1)$$

We can separate the four, a priori unknown coefficients, from the known expansion coefficients of the known external source by rewriting equation (4.2.1) in the form

$$\begin{bmatrix} a_{(m,n)}^{(1)} \\ 0 \\ b_{(m,n)}^{(1)} \\ 0 \end{bmatrix} - S_N \begin{bmatrix} 0 \\ \alpha_{(m,n)}^{(N+1)} \\ 0 \\ \beta_{(m,n)}^{(N+1)} \end{bmatrix} = S_N \begin{bmatrix} \tilde{a}_{(m,n)}^{(N+1)} \\ 0 \\ \tilde{b}_{(m,n)}^{(N+1)} \\ 0 \end{bmatrix} \quad (4.2.2)$$

Thus, relating the a priori unknown coefficients to the known expansion coefficients $\tilde{a}_{(m,n)}^{(N+1)}$ and $\tilde{b}_{(m,n)}^{(N+1)}$ reduces to the problem of finding the inverse of the matrix

$$\mathcal{T} = \bar{\mathcal{I}} - S_N \quad (4.2.3)$$

4.3 Interior Sources

We now suppose that there are interior sources in the layers. This could be important in assessing the impact of a sweeping radar on a person living near the radar who has one or more metallic implants to replace broken bones or clamps to hold them in place. The potentially serious nature of this can be seen from the fact that ([55] p 40) has used this concept to postulate a design for an electromagnetic missile.

With interior sources, the expansion coefficients in the free space surrounding the N layer sphere and the expansion coefficients in the inner core will be shown to be related by affine transformations rather than linear transformations.

We model complex sources in a layer by allowing an arbitrary representation of a source in terms of an expansion in a Hilbert space of vector valued functions. We assume that if the shell containing the source lies between $r = R_p$ and $r = R_{p+1}$ and represent the expansion coefficients of the electric field due to this source in the inner shell in terms of expansion coefficients $\tilde{a}_{(m,n)}^{(p)}$, $\tilde{b}_{(m,n)}^{(p)}$. We assume that these are given and represent a source located at a point $r = \tilde{R}_p$ that is between $r = R_p$ and $r = R_{p+1}$. These are obtained by assuming that the source is unaffected by the medium and that the currents, say in a dipole source, are used to represent an electric vector $\tilde{\vec{E}}_p$. This electric vector is then

represented on the inner shell by the relations,

$$\begin{aligned} \lim_{r \rightarrow R_p} & \left[\frac{\int \int_{C(r)} \vec{E}_p(x, y, z, \omega) \cdot \vec{A}_{(m,n)}(\theta, \phi)^* \sin(\theta) d\theta d\phi}{\int \int_{C(r)} \vec{A}_{(m,n)}(\theta, \phi) \cdot \vec{A}_{(m,n)}(\theta, \phi)^* \sin(\theta) d\theta d\phi} \right] \\ & = \tilde{a}_{(m,n)}^{(p)} Z_{(n,p)}^{(a,1)}(k_p R_p) \end{aligned} \quad (4.3.1)$$

The values of the expansion coefficients $\tilde{b}_{(m,n)}^{(p)}$ of this source field on the shell $r = R_p$ are given by

$$\begin{aligned} \lim_{r \rightarrow R_p} & \left[\frac{\int \int_{C(r)} \vec{E}_p(x, y, z, \omega) \cdot \vec{B}_{(m,n)}(\theta, \phi)^* \sin(\theta) d\theta d\phi}{\int \int_{C(r)} \vec{B}_{(m,n)}(\theta, \phi) \cdot \vec{B}_{(m,n)}(\theta, \phi)^* \sin(\theta) d\theta d\phi} \right] \\ & = \tilde{b}_{(m,n)}^{(p)} (-W_{(n,p)}^{(b,1)}(k_p R_p)) \end{aligned} \quad (4.3.2)$$

Thus, we know the electric field due to the isolated source at this point on the shell $r = R_p$. However, unlike the source in the space surrounding the N layer spherical structure we cannot assume that the field is represented by these expansion coefficients and the expansion coefficients $\alpha_{(m,n)}^{(p)}$ and $\beta_{(m,n)}^{(r)}$ used to represent the radiation emanating from the inner shell, as there may be additional sources coming from beyond $r = R_p$ that are due to external sources and reflections of these sources from the layer $r = R_p$. Instead we approximate the representation of this source by a finite linear combination of vector spherical wave functions and assume that at some point $r = \tilde{R}_p$ possibly just slightly smaller than the location of the actual source, so that value of the field at the point considered would not be singular, we impose essentially an impedance boundary condition (Wu [55]) at $r = R_p$ which will give us a relationship between the general expansion coefficients $\alpha_{(m,n)}^{(p,-)}$ and $\beta_{(m,n)}^{(p,-)}$ and $a_{(m,n)}^{(p,-)}$ and $b_{(m,n)}^{(p,-)}$ used to represent the fields when $r < \tilde{R}_p$ and the expansion coefficients $\alpha_{(m,n)}^{(p,+)}$ and $\beta_{(m,n)}^{(p,+)}$ and $a_{(m,n)}^{(p,+)}$ and $b_{(m,n)}^{(p,+)}$ that are used to represent the fields when $r > \tilde{R}_p$. We suppose that the magnetic vector just outside $r = \tilde{R}_p$ is denoted by \vec{H}_p^+ and that the magnetic vector just inside $r = \tilde{R}_p$ is given by \vec{H}_p^- and that the boundary conditions used to relate the expansion coefficients $\alpha_{(m,n)}^{(p,-)}$ and $\beta_{(m,n)}^{(p,-)}$ and $a_{(m,n)}^{(p,-)}$ and $b_{(m,n)}^{(p,-)}$ for $R_p < r < \tilde{R}_p$ to the expansion coefficients $\alpha_{(m,n)}^{(p,+)}$ and $\beta_{(m,n)}^{(p,+)}$ and $a_{(m,n)}^{(p,+)}$ and $b_{(m,n)}^{(p,+)}$ for $R_{p+1} > r > \tilde{R}_p$ are continuity of tangential components of \vec{E} and the nonhomogeneous impedance boundary condition

$$\vec{n} \times (\vec{H}_p^+ - \vec{H}_p^-) = (i\omega\epsilon + \sigma) (\vec{E}_p - (\vec{E}_p \cdot \vec{e}_r) \vec{e}_r) \quad (4.3.3)$$

Taking the dot product of both sides of equation (4.3.3) with respect to the vector

$$\vec{V}_B = \vec{B}_{(m,n)}(\theta, \phi)$$

and integrating over the sphere $r = \tilde{R}_p$ we see that

$$\begin{aligned} & \frac{i}{\omega\mu(p)} \left\{ a_{(m,n)}^{(p,+)} k_p W_{(n,p)}^{(a,1)}(k_p \tilde{R}_p) + \alpha_{(m,n)}^{(p,+)} k_p W_{(n,p)}^{(a,3)}(k_p \tilde{R}_p) \right\} + \\ & \left(\frac{-i}{\omega\mu(p)} \right) \left\{ \alpha_{(m,n)}^{(p)} b_{(m,n)}^{(p,+)} (W_{(n,p)}^{(b,1)}(k_p \tilde{R}_p)) + \alpha_{(m,n)}^{(p)} \beta_{(m,n)}^{(p,+)} (W_{(n,p)}^{(b,3)}(k_p \tilde{R}_p)) \right\} = \\ & \frac{i}{\omega\mu(p)} \left\{ a_{(m,n)}^{(p,-)} k_p W_{(n,p)}^{(a,1)}(k_p \tilde{R}_p) + \alpha_{(m,n)}^{(p,-)} k_p W_{(n,p)}^{(a,3)}(k_p \tilde{R}_p) \right\} + \\ & \left(\frac{-i}{\omega\mu(p)} \right) \left\{ \alpha_{(m,n)}^{(p)} b_{(m,n)}^{(p,-)} (W_{(n,p)}^{(b,1)}(k_p \tilde{R}_p)) + \alpha_{(m,n)}^{(p)} \beta_{(m,n)}^{(p,-)} (W_{(n,p)}^{(b,3)}(k_p \tilde{R}_p)) \right\} + \\ & (i\omega\epsilon^{(p)} + \sigma^{(p)}) [-\tilde{b}_{(m,n)}^{(p)} W_{(n,p)}^{(b,1)}(k_p \tilde{R}_p) - \tilde{\beta}_{(m,n)}^{(p)} W_{(n,p)}^{(b,3)}(k_p \tilde{R}_p)] \end{aligned} \quad (4.3.4)$$

Taking the dot product of both sides of equation (4.3.3) with respect to the vector

$$\vec{V}_A = \vec{A}_{(m,n)}(\theta, \phi)$$

and integrating over the sphere $r = \tilde{R}_p$ we see that

$$\begin{aligned} & \left(\frac{i}{\omega\mu(p)} \right) [-k_p] \left\{ b_{(m,n)}^{(p,+)} Z_{(n,p)}^{(b,1)}(k_p \tilde{R}_p) + \beta_{(m,n)}^{(p,+)} Z_{(n,p)}^{(b,3)}(k_p \tilde{R}_p) \right\} = \\ & \left(\frac{i}{\omega\mu(p)} \right) \left\{ \alpha_{(m,n)}^{(p)} a_{(m,n)}^{(p,+)} Z_{(n,p)}^{(a,1)}(k_p \tilde{R}_p) + \alpha_{(m,n)}^{(p)} \alpha_{(m,n)}^{(p,+)} Z_{(n,p)}^{(a,3)}(k_p \tilde{R}_p) \right\} + \\ & (i\omega\epsilon^{(p)} + \sigma^{(p)}) [\tilde{a}_{(m,n)}^{(p)} Z_{(n,p)}^{(a,1)}(k_p \tilde{R}_p) + \tilde{\alpha}_{(m,n)}^{(p)} Z_{(n,p)}^{(a,3)}(k_p \tilde{R}_p)] \end{aligned} \quad (4.3.5)$$

Using the fact that $\tilde{\alpha}_{(m,n)}^{(p)} = 0$ and $\tilde{\beta}_{(m,n)}^{(p)} = 0$ and that the coefficients $\tilde{a}_{(m,n)}^{(p)}$ and $\tilde{b}_{(m,n)}^{(p)}$ are completely known gives us a simple relationship between the expansion coefficients (see equation 2.1.13)

$$\begin{aligned} & [a_{(m,n)}^{(p,+)} Z_{(n,p)}^{(a,1)}(k_p \tilde{R}_p) + \alpha_{(m,n)}^{(p,+)} Z_{(n,p)}^{(a,3)}(k_p \tilde{R}_p)] \\ & = [a_{(m,n)}^{(p,-)} Z_{(n,p)}^{(a,1)}(k_p \tilde{R}_p) + \alpha_{(m,n)}^{(p,-)} Z_{(n,p)}^{(a,3)}(k_p \tilde{R}_p)] \end{aligned} \quad (4.3.6)$$

and multiplying both sides of the relationship

$$\vec{E}_p^+(\tilde{R}_p) \cdot \vec{e}_r = \vec{E}_p^-(\tilde{R}_p) \cdot \vec{e}_r \quad (4.3.7)$$

by $\tilde{B}_{(m,n)}(\theta, \phi)$ and integrating over the sphere $r = \tilde{R}_p$ we see that

$$\begin{aligned} & [-b_{(m,n)}^{(p,+)} W_{(n,p)}^{(b,1)}(k_p \tilde{R}_p) - \beta_{(m,n)}^{(p,+)} W_{(n,p)}^{(b,3)}(k_p \tilde{R}_p)] \\ &= [-b_{(m,n)}^{(p,-)} W_{(n,p)}^{(b,1)}(k_p \tilde{R}_p) - \beta_{(m,n)}^{(p,-)} W_{(n,p)}^{(b,3)}(k_p \tilde{R}_p)] \end{aligned} \quad (4.3.8)$$

We define

$$\xi_{(m,n)}^{(p,2)} = 0 = \xi_{(n,n)}^{(p,2)} \quad (4.3.9)$$

and

$$\xi_{(m,n)}^{(p,1)} = (i\omega e^{(p)} + \sigma^{(p)}) \tilde{a}_{(m,n)}^{(p)} Z_{(n,p)}^{(a,1)}(k_p \tilde{R}_p) \quad (4.3.10)$$

and finally,

$$(i\omega e^{(p)} + \sigma^{(p)}) \xi_{(m,n)}^{(p,3)} = -\tilde{b}_{(m,n)}^{(p)} W_{(n,p)}^{(a,1)}(\tilde{R}_p) \quad (4.3.11)$$

The expansion coefficients on opposite sides of the sphere $r = \tilde{R}_p$ are in view of equations (4.3.5), (4.3.4), (4.3.6) and (4.3.8) and equations (4.3.9), (4.3.10), and (4.3.11) are related by

$$\begin{bmatrix} a_{(m,n)}^{(p,-)} \\ \alpha_{(m,n)}^{(p,-)} \\ b_{(m,n)}^{(p,-)} \\ \beta_{(m,n)}^{(p,-)} \end{bmatrix} = \begin{bmatrix} a_{(m,n)}^{(p,+)} \\ \alpha_{(m,n)}^{(p,+)} \\ b_{(m,n)}^{(p,+)} \\ \beta_{(m,n)}^{(p,+)} \end{bmatrix} - S_{(n,p)}^{-1} \begin{bmatrix} \xi_{(m,n)}^{(p,1)} \\ \xi_{(m,n)}^{(p,2)} \\ \xi_{(m,n)}^{(p,3)} \\ \xi_{(m,n)}^{(p,4)} \end{bmatrix} \quad (4.3.12)$$

To complete the determination of the relationship between expansion coefficients in one layer to those in the next one we use equation (2.2.11) and equation (2.2.13) to write

$$\begin{bmatrix} a_{(m,n)}^{(p,-)} \\ \alpha_{(m,n)}^{(p,-)} \\ b_{(m,n)}^{(p,-)} \\ \beta_{(m,n)}^{(p,-)} \end{bmatrix} = Q_n^{(p)} \begin{bmatrix} a_{(m,n)}^{(p+1,-)} \\ \alpha_{(m,n)}^{(p+1,-)} \\ b_{(m,n)}^{(p+1,-)} \\ \beta_{(m,n)}^{(p+1,-)} \end{bmatrix} - S_{(n,p)}^{-1} \begin{bmatrix} \xi_{(m,n)}^{(p,1)} \\ \xi_{(m,n)}^{(p,2)} \\ \xi_{(m,n)}^{(p,3)} \\ \xi_{(m,n)}^{(p,4)} \end{bmatrix} \quad (4.3.13)$$

Now as there are no sources in the core region we have for the simplest structure with a source in a single shell the relationship

$$\begin{bmatrix} a_{(m,n)}^{(1,+)} \\ 0 \\ b_{(m,n)}^{(1,+)} \\ 0 \end{bmatrix} = Q_n^{(1)} Q_n^{(2)} \begin{bmatrix} a_{(m,n)}^{(3,-)} \\ \alpha_{(m,n)}^{(3,-)} \\ b_{(m,n)}^{(3,-)} \\ \beta_{(m,n)}^{(3,-)} \end{bmatrix} - Q_n^{(1)} S_{(n,2)}^{-1} \begin{bmatrix} \xi_{(m,n)}^{(2,1)} \\ \xi_{(m,n)}^{(2,2)} \\ \xi_{(m,n)}^{(2,3)} \\ \xi_{(m,n)}^{(2,4)} \end{bmatrix} \quad (4.3.14)$$

where the known field representation coefficients $\xi_{(m,n)}^{(p,1)}$, $\xi_{(m,n)}^{(p,2)}$ and $\xi_{(m,n)}^{(p,4)}$ and $\xi_{(m,n)}^{(p,3)}$ are given by equations (4.3.10), (4.3.9), and (4.3.11) respectively. The general relationship is given by

$$\begin{bmatrix} a_{(m,n)}^{(1,+)} \\ 0 \\ b_{(m,n)}^{(1,+)} \\ 0 \end{bmatrix} = Q_n^{(1)} Q_n^{(2)} \dots Q_n^{(N)} \begin{bmatrix} a_{(m,n)}^{(N+1,-)} \\ \alpha_{(m,n)}^{(N+1,-)} \\ b_{(m,n)}^{(N+1,-)} \\ \beta_{(m,n)}^{(N+1,-)} \end{bmatrix} - \sum_{p=1}^{N-1} Q_n^{(1)} Q_n^{(2)} \dots Q_n^{(p)} S_{(n,p+1)}^{-1} \begin{bmatrix} \xi_{(m,n)}^{(p,1)} \\ \xi_{(m,n)}^{(p,2)} \\ \xi_{(m,n)}^{(p,3)} \\ \xi_{(m,n)}^{(p,4)} \end{bmatrix} \quad (4.3.15)$$

As before, if the expansion coefficients $a_{(m,n)}^{(N+1,-)}$ and $b_{(m,n)}^{(N+1,-)}$ of the external source are known, then we have a system of 4 equations in 4 unknowns connecting the expansion coefficients in the source free core and the expansion coefficients $\alpha_{(m,n)}^{(N+1,-)}$ and $\beta_{(m,n)}^{(N+1,-)}$ of the radiation scattered by the N layer bianisotropic structure.

5 Energy Balance

5.1 General Considerations

The total power absorbed by a general structure can be determined by a Poynting vector analysis on the surface of the body. The total energy absorbed is the total energy entering the body minus the total energy scattered away from the body.

5.2 Bianisotropy and E H Coupling

In this section we consider the unusual energy balance relationships associated with the interaction of radiation with a bianisotropic material ([13]). The energy balance analysis for an isotropic sphere is carried out in great detail in (Bell [11]). An interchange of dot product and cross product in the triple scalar product implies that the total absorbed

power P_a is given by

$$\begin{aligned} P_a &= (1/2) \operatorname{Re} \int \int_{C(R_N)} (\vec{E}_{N+1} \times \vec{H}_{N+1})^* \cdot \vec{n} dA \\ &= (1/2) \operatorname{Re} \int \int_{C(R_N)} [(\vec{E}_N \times \vec{H}_{N+1}^*) \cdot \vec{n}] dA \end{aligned} \quad (5.2.1)$$

where we have used the fact that on the spherical boundary $r = R_N$ we have

$$\vec{n} \times \vec{E}_{N+1} = \vec{n} \times \vec{E}_N \quad (5.2.2)$$

because tangential components of \vec{E} are assumed to be continuous across boundaries separating regions of continuity of tensorial electromagnetic properties. We next make use of the fact that for an impedance boundary condition on the surface of the scattering body that

$$(\vec{H}_{N+1}^* - \vec{H}_N^*) \times \vec{n} = \sigma_s (\vec{E}_N^* - (\vec{E}_N^* \cdot \vec{n}) \vec{n}) \quad (5.2.3)$$

where σ_s is the impedance sheet conductivity. From equations (5.2.3) and (5.2.1) we see that

$$\begin{aligned} P_a &= (1/2) \operatorname{Re} \int \int_{C(R_N)} (\vec{E}_N \times \vec{H}_N)^* \cdot \vec{n} dA + \\ &+ (1/2) \operatorname{Re} \int \int_{C(R_N)} [\vec{E}_N \cdot (\sigma_s (\vec{E}_N^* - (\vec{E}_N^* \cdot \vec{n}) \vec{n}))] dA \end{aligned} \quad (5.2.4)$$

Using this and the fact that

$$\operatorname{div}(\vec{E} \times \vec{H}^*) = \vec{H}^* \cdot \operatorname{curl}(\vec{E}) - \vec{E} \cdot \operatorname{curl}(\vec{H}^*) \quad (5.2.5)$$

we derive a formula for the internal energy density. For a sweeping beam or a stationary beam interacting with a bianisotropic body or a stationary beam interacting with a moving body (Hebenstreit [29]) there may be unusual couplings of the electromagnetic energy with the structure. For a general one layer structure covered by an impedance sheet the internal energy density is given in terms of the bilinear form

$$\begin{aligned} b(\vec{E}, \vec{H}) &= \\ &= \int_{V_2} \{ (\vec{E}_2^* \cdot (i\omega \vec{\epsilon} + \vec{\sigma}) \vec{E}_2) + (\vec{E}_2 \cdot (-i\omega \vec{\epsilon}^* + \vec{\sigma}^*) \vec{E}_2^*) \} dv + \\ &+ \int_{V_2} \{ (\vec{E}_2^* \cdot (\vec{\alpha}) \vec{H}_2) + (\vec{E}_2 \cdot (\vec{\alpha}^*) \vec{H}_2^*) \} dv + \end{aligned}$$

$$\begin{aligned}
& - \int_{V_2} \left\{ (\vec{H}_2 \cdot (i\omega \vec{\mu}^* \vec{H}_2^*)) + (\vec{H}_2^* \cdot (-i\omega \vec{\mu} \vec{H}_2)) \right\} dv + \\
& \int_{V_2} \left\{ (\vec{H}_2 \cdot \vec{\beta}^* \vec{E}_2^*) + (\vec{H}_2^* \cdot \vec{\beta} \vec{E}_2) \right\} dv + \\
& \int_{S_2} (\sigma_s^* + \sigma_s) \left\{ (\vec{E}_2 \cdot \vec{E}_2^*) - (\vec{E}_2 \cdot \vec{n})(\vec{E}_2^* \cdot \vec{n}) \right\} da
\end{aligned} \tag{5.2.6}$$

where S_2 is the bounding surface and V_2 is the interior volume. This can be used as a source term for the heat equation and can be used to predict the response of the structure to a sweeping beam or the response of a moving structure to a stationary beam (Ferencz [25], Gamo [26], Hebenstreit [29], and Shiozawa, [44]). Energy balance computations were carried out in (Bell, Cohoon, and Penn [10], [11]) for isotropic structures and in (Cohoon [15]) for anisotropic structures. These energy balance computations involve comparing the total energy entering the structure minus the total energy reflected from the structure to the sum of the integrals of the power density distributions in the impedance sheets and in the layers themselves.

5.3 Computer Output

Electromagnetic Energy Deposition, in a Concentric Layered Sphere.

Frequency = 1.000E+03 MHz.

Field Strength = 1.00 V/M Number of Regions = 2

Core Radius = 1.1 cm Shell Radius = 3.3 cm

Core Properties

Relative Permittivity (Radial): (50.00, 0.00)

Relative Permittivity (Angular): (50.00, 0.00)

Relative Permeability (Radial): (2.00, 1.00)
 Relative Permeability (Angular): (2.00, 1.00)
 Conductivity (Mho/M) (Radial): (.600, .600)
 Conductivity (Mho/M) (Angular): (.600, .600)
 Impedance Sheet Cond. (Mho/M): (0.00E+00, 0.00E+00)
 Surface Boundary (cm) = 1.1

Shell Properties

Relative Permittivity (Radial): (30.00, 0.00)
 Relative Permittivity (Angular): (60.00, 0.00)
 Relative Permeability (Radial): (2.00, 1.00)
 Relative Permeability (Angular): (5.00, 3.00)
 Conductivity (Mho/M) (Radial): (.200, .600)
 Conductivity (Mho/M) (Angular): (.400, .600)
 Impedance Sheet Cond. (Mho/M): (0.00E+00, 0.00E+00)
 Surface Boundary (cm) = 3.3

Total Absorbed Power = 9.10716094E-6 Watts
 (by Poynting vector analysis on the surface
 and by volume integration of the power density
 over the interior)

Average Absorbed Power = 6.04996E-2 Watts/Meter**3

The fact that the total absorbed power obtained by a Poynting vector method and the total absorbed power obtained by volume integration of the power density distribution nearly coincide represents a confirmation of the correctness of the coding implementing the solution for an anisotropic sphere. The determination of the total absorbed power by the Poynting vector method is described in (Jones [33]) and in full detail in (Bell, [11]). For the plane wave problem described in Jones ([33]) we can give exact formulas for the

total absorbed power in terms of the total power entering the sphere minus the total power scattered away from the sphere ([33], page 504, equation 126). We let $\alpha_{(n,N+1)}$ and $\beta_{(n,N+1)}$ denote the expansion coefficients of the scattered radiation and by carrying out an energy balance book keeping on the boundary we observe that the total absorbed power is

$$P_a = \frac{\pi |E_0|^2}{k_0^2} \sqrt{\frac{\epsilon_0}{\mu_0}} \left[\operatorname{Re} \sum_{n=1}^{\infty} (2n+1) (\alpha_{(n,N+1)} + \beta_{(n,N+1)}) \right] - \frac{\pi |E_0|^2}{k_0^2} \sqrt{\frac{\epsilon_0}{\mu_0}} \left[\sum_{n=1}^{\infty} (2n+1) (|\alpha_{(n,N+1)}|^2 + |\beta_{(n,N+1)}|^2) \right] \quad (5.3.1)$$

This is referred to as the Poynting vector method in the computer output; the last number is the result of numerically integrating the power density distribution over the interior of the sphere. The difficulty of this numerical integration is evident from the following plot of the internal power density distribution for an anisotropic structure with a radial permittivity that is higher than the tangential permittivity.

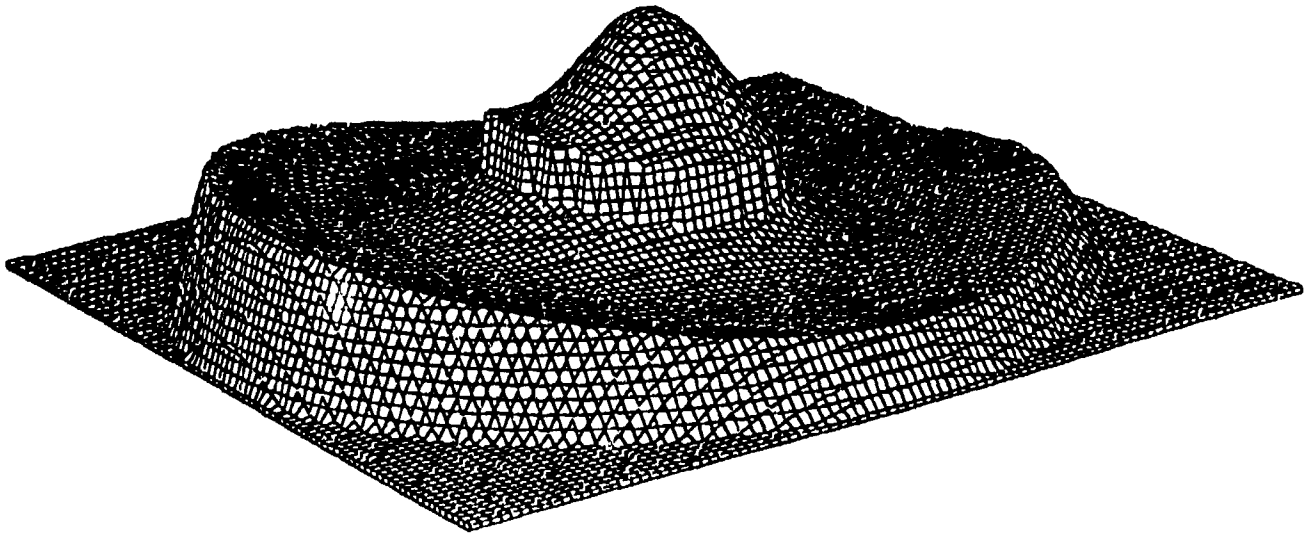


Figure 5.3.1 The electric and magnetic power density distribution on an equatorial slice of a two layer sphere subjected to a single plane wave. The core in this sphere and the one on the following page are identical. The difference is the protective nature of the shell in the following figure.

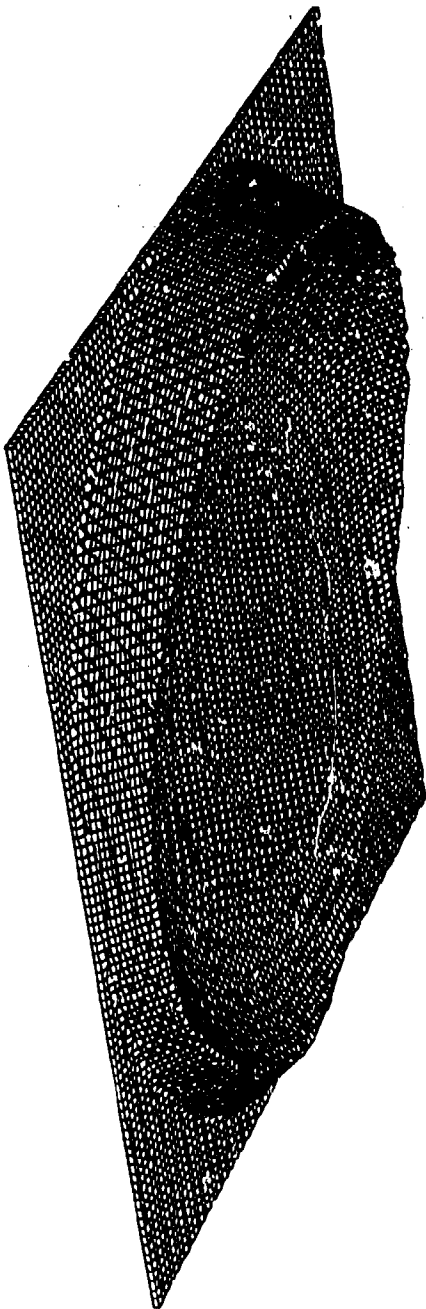


Figure 5.3.2.

The electromagnetic power density distribution on an equatorial slice of a two layer sphere subjected to electromagnetic radiation. Here the nature of the shell is such that the electromagnetic energy tends to be shunted away from the core. The ratio of the radius of the core to the radius of the outer shell is 1.1 to 3.3. The radial relative permittivity is 30 and the tangential relative permittivity is 60. These numbers are reversed in Figure 5.3.1.

5.4 Thermal Response to Radiation

The absorption of radiation results in a temperature increase. An energy equation describing this change of state is given by

$$\rho \frac{De}{Dt} = \left(\frac{\partial}{\partial t} \right) Q_{in} + \left(\frac{\partial}{\partial t} \right) Q_{out} + (-p \text{div}(\vec{v})) + \text{div}(\overline{\overline{K}} \text{grad}(T)) + \Phi, \quad (5.4.1)$$

where e is equal to $c_v T$ with T denoting the temperature, and c_v denoting the specific heat at constant volume, Φ is the viscous dissipation function (Anderson, Tannehill and Pletcher [1], pages 188-189), \vec{v} is the fluid velocity, ρ is the density, p is the pressure, $\overline{\overline{K}}$ is the tensor thermal conductivity, the term representing the transfer by radiation from one part of the fluid to another is given by (Siegel and Howell [43], page 689)

$$\left(\frac{\partial}{\partial t} \right) Q_{out} = \text{div} \left(\frac{16\sigma_e T^3}{3a_R} \cdot \text{grad}(T) \right), \quad (5.4.2)$$

where the internal radiative conductivity is given by

$$k_r = \frac{16\sigma_e T^3}{3a_R}, \quad (5.4.3)$$

where a_R is the Rosseland mean absorption coefficient (Siegel [43], p 504 and Rosseland [41]) and where σ_e (Siegel [43], page 25) is the hemispherical total emissive power of a black surface into vacuum having a value of

$$\sigma_e = 5.6696 \times 10^{-8} \text{ Watts / (meters}^2 \text{ }^\circ\text{K)}, \quad (5.4.4)$$

and where if $\mathcal{B}(\vec{E}, \vec{H})$ represents the absorbed electromagnetic energy per unit volume, whose integral is, (after conversion from cgs units) equal to the $b(\vec{E}, \vec{H})$ given by equation (5.2.6) then

$$\left(\frac{\partial}{\partial t} \right) Q_{in} = \mathcal{B}(\vec{E}, \vec{H}). \quad (5.4.5)$$

In general solving equation (5.4.1) requires the simultaneous solution of the Maxwell, continuity, and momentum equations (see Jones [33], p 775). However, for low levels of radiation the energy equation (5.4.1) reduces to a simple heat equation with a source term which can be solved by dovetailing ([12], [14]) it to the solution of the Maxwell equations. The experimental verification of the latter procedure is described in ([12]) and in ([14]).

References

- [1] Anderson, Dale A., John C. Tannehill, and Richard H. Pletcher *Computational Fluid Mechanics and Heat Transfer* New York: McGraw Hill (1984)
- [2] Abramowitz, Milton, and Irene Stegun. *Handbook of Mathematical Functions with Formulas, Graphs and Mathematical Tables. NBS Applied Math Series 55* Washington, D.C.: U.S. Government Printing Office (1972)
- [3] Altman, C., A. Schatzberg, and K. Suchy. "Symmetries and scattering relations in plane stratified anisotropic, gyrotropic, and bianisotropic media" *Applied Physics B (Germany) Vol B26, No. 2* (1981) pp 147-153
- [4] Altman, C. and A. Schatzberg. "Reciprocity and equivalence in reciprocal and nonreciprocal media through reflection transformations of the current distributions" *Applied Physics B(Germany) Volume B28, No 4* (August, 1982) pp 327-333
- [5] Altman, C., Schatzberg, K. Suchy. "Symmetry transformations and time reversal of currents and fields in bounded bianisotropic media" *IEEE Transactions on Antennas and Propagation. Vol. AP 32, No. 11* (November, 1984) pp 1204-1210
- [6] Altman, C., A. Schatzberg, and K. Suchy. "Symmetries and scattering relations in plane stratified anisotropic, gyrotropic, and bianisotropic media" *Applied Physics B.(Germany) Volume B26, No. 2* (1981) pp 147-153
- [7] Avdeev, V. B., A. V. Demin, Yu A. Kravtsov, M. V. Tinin, A. P. Yarygin. "The interferential integral method" *Radiophys. Quantum Electronics. Vol 31, No. 11* (1988) pp 907-921
- [8] Barton, J. P., D. R. Alexander, and S. A. Schaub. "Internal fields of a spherical particle illuminated by a tightly focused laser beam: focal point positioning effects at resonance." *Journal of Applied Physics. Volume 65 No. 8* (April 15, 1989) pp 2900-2906
- [9] Barton, J. P., D. R. Alexander, and S. A. Schaub. "Internal and near surface electromagnetic fields for a spherical particle irradiated by a focused laser beam" *Journal of Applied Physics. Volume 64, no 4* (1988) pp 1632-1639.
- [10] Bell, Earl L., David K. Cohoon, and John W. Penn. *Mie: A FORTRAN program for computing power deposition in spherical dielectrics through application of Mie theory. SAM-TR-77-11* Brooks AFB, Tx 78235: USAF School of Aerospace Medicine (RZ) Aerospace Medical Division (AFSC) (August, 1977)

- [11] Bell, Earl L., David K. Cohoon, and John W. Penn. *Electromagnetic Energy Deposition in a Concentric Spherical Model of the Human or Animal Head SAM-TR-79-6* Brooks AFB, Tx 78235: USAF School of Aerospace Medicine (RZ) Aerospace Medical Division (AFSC) (December, 1982).
- [12] Burr, John G., David K. Cohoon, Earl L. Bell, and John W. Penn. Thermal response model of a Simulated Cranial Structure Exposed to Radiofrequency Radiation. *IEEE Transactions on Biomedical Engineering. Volume BME-27, No. 8* (August, 1980) pp 452-460.
- [13] Cohoon, D. K. "Uniqueness of electromagnetic interaction problems associated with bianisotropic bodies covered by impedance sheets" Rassius, George (Ed) *Heritage of Gauss* Singapore: World Scientific Publishing (1991)
- [14] Cohoon, D. K., J. W. Penn, E. L. Bell, D. R. Lyons, and A. G. Cryer. *A Computer Model Predicting the Thermal Response to Microwave Radiation SAM-TR-82-22* Brooks AFB, Tx 78235: USAF School of Aerospace Medicine. (RZ) Aerospace Medical Division (AFSC) (December, 1982).
- [15] Cohoon, D. K. "An exact solution of Mie Type for Scattering by a Multilayer Anisotropic Sphere" *Journal of Electromagnetic Waves and Applications, Volume 3, No. 5* (1989) pp 421-448
- [16] Cohoon, D. K. and R. M. Purcell. An exact formula for the interaction of radiation with an N layer anisotropic sphere and its computer implementation. *Notices of the American Mathematical Society* (January, 1989).
- [17] Chen, H. C. "Electromagnetic wave propagation in bianisotropic media--a coordinate free approach." *Proceedings of the 1985 International Symposium on Antennas and Propagation, Japan- A Step to New Radio Frontiers. Kyoto, Japan 1985* Volume 1 Tokyo: Institute of Electronic Commun. Eng. (1985) pp 253-256.
- [18] Chevaillier, Jean Phillippe, Jean Fabre, and Patrice Hamelin. "Forward scattered light intensities by a sphere located anywhere in a Gaussian beam" *Applied Optics, Vol. 25, No. 7* (April 1, 1986) pp 1222-1225.
- [19] Chevaillier, Jean Phillippe, Jean Fabre, Gerard Grehan, and Gerard Gousbet. "Comparison of diffraction theory and generalized Lorenz-Mie theory for a sphere located on the axis of a laser beam." *Applied Optics, Vol 29, No. 9* (March 20, 1990) pp 1293-1298.
- [20] Chylek, Petr, J. D. Pendleton, and R. G. Pinnick. "Internal and near surface scattered field of a spherical particle at resonant conditions" *Applied Optics, Volume 24, No. 23* (December 1, 1985) pp 3940-3943

- [21] Chylek, Petr, Maurice A. Jarzembski, Vandana Srivastava, and Ronald G. Pinnick. "Pressure dependence of the laser induced breakdown thresholds of gases and droplets" *Applied Optics, Volume 29, No. 15* (May 20, 1990) pp 2303-2306
- [22] Chylek, Petr, Maurice A. Jarzembski, Vandana Srivastava, R. G. Pinnick, J. David Pendleton, and John P. Cruncheon. "Effect of spherical particles on laser induced breakdown of gases" *Applied Optics, Volume 26, No. 5* (March 1, 1987) pp 760-762
- [23] Clebsch, R. F. A. "Über die Reflexion an einer Kugelfläche" *Crelle's Journal, Volume 61* (1863) p 195.
- [24] Daniele, V. "Electromagnetic properties of Rotating Bodies" *Alta Freq. Vol 52, No. 3* (May-June, 1983) pp 146-148.
- [25] Ferencz, C. "Geometric questions of electromagnetic wave propagation in moving media" *Acta Tech. Acad. Sci. Hungary. Volume 100, no 3-4* (1987) pp 195-205
- [26] Gamo, H. "A generalized reciprocity theorem for electromagnetic optics in the moving media" Ensenada, Mexico: Conference on optics in four dimensions *AIP Conference Proceedings (USA) No. 65* (1980) pp 106-122
- [27] Garcia, C. B. and W. I. Zangwill. Pathways to Solutions, Fixed Points, and Equilibria. Englewood Cliffs, NJ: Prentice Hall(1981)
- [28] Holoubek, J. "A simple representation of small angle light scattering from an anisotropic sphere," *Journal of Polymer Science, Part A-2, Volume 10* (1972) pp 1094-1099.
- [29] Hebenstreit, H. "Constitutive relations for moving plasmas" *Z. Naturforsch. A. Volume 34A, No. 2* (1979) pp 147-154
- [30] Hochstadt, Harry. *The Functions of Mathematical Physics*. New York: Dover(1986).
- [31] Hormander, Lars. *Linear Partial Differential Operators* New York: Academic Press (1963)
- [32] Hovhannessian, S. S., and V. A. Baregamian. "The diffraction of a plane electromagnetic wave on an anisotropic sphere," *Isdatelsva Akad. Nauk. of Armenia, S. S. R. Physics Volume 16* (1981) pp 37-43
- [33] Jones, D. S. *Theory of Electromagnetism* Oxford: Pergamon Press(1964)
- [34] Mie, G. "Beiträge zur Optik trüber Medien speziell kolloidaler Metallösungen," *Ann. Phys. 25* (1908) p 377.
- [35] Mrozowski, M. and J. Mazur. "Coupled mode analysis of waveguiding structures containing bianisotropic media". *IEEE Trans. Magn. (USA) Vol. 24, No. 2, pt. 2* (1988) pp 1975-1977

- [36] Mrozowski, M. "General solutions to Maxwell's equations in a bianisotropic medium: a computer oriented spectral domain approach" *Arch. Elektron. and Uebertragungstech (Germany)* Vol. 40, No. 3 (May-June, 1986) pp 195-197.
- [37] Pinnick, R. G. and J. D. Pendleton. *Applied Optics*. Vol 29 (1990) page 918
- [38] Mugnai, Alberto and Warren J. Wiscombe. "Scattering from Nonspherical Chelyshev Particles. I: Cross Sections, Single Scattering Albedo, Asymmetry Factor, and Backscattered Radiation" *Applied Optics*, Volume 25, No. 7 pp 1235-1244.
- [39] Pinnick, R. G., P. Chylek, M. Jarzembski, E. Creegan, and V. Srivastava, G. Fernandez, J. D. Pendleton, and A. Biswas. "Aerosol induced laser breakdown thresholds wavelength dependence" *Applied Optics*. Vol 27, No. 5 (March 1, 1988) pp 987-996
- [40] Richardson, C. B., R. L. Hightower, and A. L. Pigg. "Optical measurement of the evaporation of sulfuric acid droplets" *Applied Optics*. Volume 25, No. 7 (April 1986) pp 1226-1229
- [41] Rosseland, S. *Theoretical Astrophysics: Atomic Theory and the Analysis of Stellar Atmospheres and Envelopes*. Oxford, England: Clarendon Press (1936).
- [42] Schaub, Scott A., Dennis R. Alexander, John P. Barton, and Mark A. Emanuel. "Focused Laser Beam Interactions with Methanol Droplets: Effects of Relative Beam Diameter" *Applied Optics*. Volume 28, No. 9 (May 1, 1989) pp 1666-1669
- [43] Siegel, Robert, and John R. Howell. *Thermal Radiation Heat Transfer* New York: Hemisphere Publishing Company (1981)
- [44] Shiozawa, T. "Electrodynamics of rotating relativistic electron beams" *Proceedings of the IEEE*. Volume 66, No. 6 (June, 1978) pp 638-650
- [45] Suchy, K., C. Altman, A. Schatzberg. "Orthogonal mappings of time-harmonic electromagnetic fields in inhomogeneous bianisotropic media" *Radio Science(USA)* Vol. 20, No. 2 (March-April, 1985) pp 149-160.
- [46] Tsai, Wen-Chung, and Ronald J. Pogorzelski. "Eigenfunction solution of the scattering of beam radiation fields by spherical objects." *Journal of the Optical Society of America*. Volume 63, No. 12 (December, 1975) pp 1457-1463
- [47] Van de Hulst, H. C. *Light Scattering by Small Particles* New York: John Wiley (1957)
- [48] Waggoner, Alan P. and Lawrence F. Radke. "Enhanced cloud clearing by pulsed CO₂ lasers." *Applied Optics*. Volume 28, No. 15 (August 1, 1989) pp 3039-3043

- [49] Wang, R. T. and J. M. Greenberg. "Scattering by spheres with nonisotropic refractive indices" *Applied Optics, Volume 15* (1976) p 1212
- [50] Weiglhofer, W. "Isotropic chiral media and scalar Hertz potentials" *Journal of Physics A. Math. Gen. Vol. 21, no. 9* (May 7, 1988) pp 2249-2251
- [51] Weiglhofer, W. "Scalarization of Maxwell's equations in general homogeneous bianisotropic media" *IEE Proc. H (GB) Vol. 134, No. 4* (1987) pp 357-360
- [52] Whittaker, E. T. and G. N. Watson. *A Course of Modern Analysis* London: Cambridge University Press (1986).
- [53] Wolff, I. "A description of the spherical three layer resonator with an anisotropic dielectric material. *IEEE MTT-S Digest* (1987) pp 307-310
- [54] Wu, Tai Tsun, Ronald W. P. King, and Hao-Ming Shin. "Circular cylindrical lens as a line source electromagnetic missile launcher" *IEEE Transactions on Antennas and Propagation Volume 37, Number 1* (January, 1989) pages 39-44
- [55] Wu, Tai Tsun, Ronald W. P. King, and Hao-Ming Shin. "Spherical lens as a launcher of electromagnetic missiles" *Journal of Applied Physics. Volume 62, Number 10* (November 15, 1987) pp 4036-4040
- [56] Yeh, C. "Scattering of Obliquely Incident Microwaves by a Moving Plasma Column" *Journal of Applied Physics, Volume 40, Number 13* (December, 1966) pp 5066-5075.
- [57] Yeh, C. S. Colak, and P. Barber. "Scattering of sharply focused beams by arbitrarily shaped dielectric particles" *Applied Optics. Vol. 21, No. 24* (December 15, 1982) pp 4426-4433.

6 Acknowledgements

The author wishes to thank Dr. J. W. Frazer for reading the manuscript, correcting errors, and making helpful suggestions. I wish to thank Dr. A. J. Barnett of the Department of Physics at the University of Manchester for allowing the use of his Coulomb wave function code.

Discretization of Integral Equation Formulations of Electromagnetic Scattering Problems

D. K. Cohoon

February 18, 1992

Contents

1 INTRODUCTION

1.1 Integral Equations for Bianisotropic Materials

2 Layered Materials

2.1 MAGNETIC SLAB IE

3 DISCRETIZATION

3.1 PIECEWISE LINEAR APPROXIMATION

There are as yet no exact solutions to the problem of describing the interaction of electromagnetic radiation with aerosol particles having a complex shape, e.g. N handed spheres, toroids, fibers, flakes, and complex cross linked particles such as those found in cirrus clouds. Those whose regions of homogeneity are delimited by a surface generated by rotating a curve about an axis, are bodies of revolution if the electromagnetic properties are also invariant with respect to rotation about this axis. The interaction of arbitrary linearly responding materials to electromagnetic radiation can be described by volume integral equations, whose accurate solution may tax even the most advanced computers. However, for bodies of revolution we can by Fourier analyzing the field we can represent the field by solving integral equations in the surface electric and magnetic current Fourier components on the generating curve - - a one dimensional integral equation instead of a three dimension integral equation.

We illustrate the method of discretization of integral equations in an elementary way in this paper by considering an interesting integral equation formulation of the problem of the interaction of electromagnetic radiation with an anisotropic magnetic slab. This problem can be solved exactly, and the accuracy of our discrete representation can be verified by comparison with the exact solution.

1 INTRODUCTION

The most general linearly responding materials are bianisotropic. The Faraday and Ampere Maxwell equations for time harmonic radiation have the usual forms

$$\text{curl}(\mathbf{E}) = -i\omega\mathbf{B}$$

and

$$\text{curl}(\mathbf{H}) = i\omega\mathbf{D} + \boldsymbol{\sigma}\mathbf{E}$$

where the magnetic flux \mathbf{B} and the electric displacement \mathbf{D} depend on both the electric and the magnetic vector.

1.1 Integral Equations for Bianisotropic Materials

We can make Maxwell's equations look like the standard Maxwell equations with complex sources by introducing the generalized electric and magnetic current densities by the relations,

$$\text{curl}(\mathbf{E}) = i\omega\mu_0\mathbf{H} - \mathbf{J}_m \quad (1.1.1)$$

and

$$\text{curl}(\mathbf{H}) = i\omega\epsilon_0\mathbf{E} + \mathbf{J}_e \quad (1.1.2)$$

where

$$\mathbf{J}_e = i\omega\epsilon\mathbf{E} + \boldsymbol{\alpha}\mathbf{H} - i\omega\epsilon_0\mathbf{E} \quad (1.1.3)$$

and

$$\mathbf{J}_m = i\omega\mu\mathbf{H} + \boldsymbol{\beta}\mathbf{E} - i\omega\mu_0\mathbf{H} \quad (1.1.4)$$

The formulation of integral equations for bianisotropic materials, therefore, is carried out by the analysis of the following coupled system of integral equations based on the notion of electric and magnetic charges defined by the two continuity equations

$$\text{div}(\mathbf{J}_e) + \frac{\partial\rho_e}{\partial t} \quad (1.1.5)$$

and

$$\text{div}(\mathbf{J}_m) + \frac{\partial\rho_m}{\partial t} \quad (1.1.6)$$

Having developed this the coupled system of integral equations describing the interaction of electromagnetic radiation with a bounded bianisotropic body Ω is given by the following relations. The electric field integral equation is given by

$$\begin{aligned} \mathbf{E} - \mathbf{E}^i = & -\text{grad} \left(\int_{\Omega} \frac{\text{div}(\mathbf{J}_e)}{\omega\epsilon_0} G(r,s) dv(s) \right) \\ & + \frac{i}{\omega\epsilon_0} \text{grad} \left(\int_{\partial\Omega} (\mathbf{J}_e \cdot \mathbf{n}) G(r,s) da(s) \right) \end{aligned}$$

$$\begin{aligned}
& -i\omega\mu_0 \int_{\Omega} \mathbf{J}_e G(r, s) dv(s) + \\
& - \operatorname{curl} \left(\int_{\Omega} \mathbf{J}_m G(r, s) dv(s) \right)
\end{aligned} \tag{1.1.7}$$

and the magnetic field integral equation may be expressed as

$$\begin{aligned}
\mathbf{H} - \mathbf{H}^i = & -\operatorname{grad} \left(\int_{\Omega} \frac{\operatorname{div}(\mathbf{J}_m)}{\omega\mu_0} G(r, s) dv(s) \right) \\
& - \frac{i}{\omega\mu_0} \operatorname{grad} \left(\int_{\partial\Omega} (\mathbf{J}_m \cdot \mathbf{n}) G(r, s) da(s) \right) \\
& - i\omega\epsilon_0 \int_{\Omega} \mathbf{J}_m G(r, s) dv(s) + \\
& + \operatorname{curl} \left(\int_{\Omega} \mathbf{J}_e G(r, s) dv(s) \right)
\end{aligned} \tag{1.1.8}$$

where $G(r, s)$ is the rotation invariant, temperate fundamental solution of the Helmholtz equation,

$$(\Delta + k_0^2)G = \delta \tag{1.1.9}$$

given by

$$G(r, s) = \frac{\exp(-ik_0 |r - s|)}{4\pi |r - s|} \tag{1.1.10}$$

Substituting (1.1.3) and (1.1.4) into equations (1.1.7) and (1.1.8) we obtain, the coupled integral equations for bianisotropic materials. The electric field integral equation for a bianisotropic material is given by,

$$\begin{aligned}
\mathbf{E} - \mathbf{E}^i = & -\operatorname{grad} \left(\int_{\Omega} \frac{\operatorname{div}(i\omega\epsilon\mathbf{E} + \alpha\mathbf{H} - i\omega\epsilon_0\mathbf{E})}{\omega\epsilon_0} G(r, s) dv(s) \right) \\
& + \frac{i}{\omega\epsilon_0} \operatorname{grad} \left(\int_{\partial\Omega} (i\omega\epsilon\mathbf{E} + \alpha\mathbf{H} - i\omega\epsilon_0\mathbf{E} \cdot \mathbf{n}) G(r, s) da(s) \right) \\
& - i\omega\mu_0 \int_{\Omega} i\omega\epsilon\mathbf{E} + \alpha\mathbf{H} - i\omega\epsilon_0\mathbf{E} G(r, s) dv(s) + \\
& - \operatorname{curl} \left(\int_{\Omega} i\omega\mu\mathbf{H} + \beta\mathbf{E} - i\omega\mu_0\mathbf{H} G(r, s) dv(s) \right)
\end{aligned} \tag{1.1.11}$$

and the magnetic field integral equation for a bianisotropic material is given by

$$\begin{aligned}
\mathbf{H} - \mathbf{H}^i = & -\operatorname{grad} \left(\int_{\Omega} \frac{\operatorname{div}(i\omega\mu\mathbf{H} + \beta\mathbf{E} - i\omega\mu_0\mathbf{H})}{\omega\mu_0} G(r, s) dv(s) \right) \\
& - \frac{i}{\omega\mu_0} \operatorname{grad} \int_{\partial\Omega} (i\omega\mu\mathbf{H} + \beta\mathbf{E} - i\omega\mu_0\mathbf{H} \cdot \mathbf{n}) G(r, s) da(s) \\
& - i\omega\epsilon_0 \int_{\Omega} (i\omega\mu\mathbf{H} + \beta\mathbf{E} - i\omega\mu_0\mathbf{H}) G(r, s) dv(s) + \\
& + \operatorname{curl} \left(\int_{\Omega} i\omega\epsilon\mathbf{E} + \alpha\mathbf{H} - i\omega\epsilon_0\mathbf{E} G(r, s) dv(s) \right)
\end{aligned} \tag{1.1.12}$$

In the subsequent sections we shall explore methods of resolving these integral equations on existing computers using novel, powerful analytical methods of solution.

2 Layered Materials

We have formulated some one dimensional scattering problems associated with magnetic materials, and solutions obtained from the differential equation formulations have been substituted into the integral equations and have been shown to satisfy them exactly. For magnetic materials, a single integral equation was obtained and the significance of surface values of the derivative of the electric vector were shown to be important. For higher order splines all terms arising in a matrix representation of the integral equation formulation of the problem, and all iterates of the integrals could be computed exactly. Using distribution theory concepts, we have combined the electric and magnetic field integral equations for the case of a plane wave that is incident normally on the magnetic slab.

2.1 MAGNETIC SLAB IE

We consider in this section radiation normally incident on a magnetic slab, and assume that the electric vector of the incident radiation has the form

$$\mathbf{E}^i = E_0 \exp(-ik_0 z) \mathbf{e}_x \quad (2.1.1)$$

so that the magnetic vector of the incident radiation defined by the Maxwell equation,

$$\begin{aligned} -i\omega\mu_0 \mathbf{H}^i &= \text{curl}(\mathbf{E}^i) = \\ &= -\mathbf{e}_y \left(-\frac{\partial}{\partial z} \right) E_0 \exp(-ik_0 z) \\ &= -ik_0 E_0 \exp(-ik_0 z) \mathbf{e}_y \end{aligned} \quad (2.1.2)$$

is after dividing both sides of equation (2.1.2) by $-i\omega\mu$ is given by

$$\mathbf{H}^i = \left(\frac{k_0 E_0}{\omega\mu_0} \right) \exp(-ik_0 z) \mathbf{e}_y \quad (2.1.3)$$

Within the magnetic slab, where the permittivity ϵ , the permeability μ , and the conductivity σ are diagonal tensors in Cartesian coordinates, the first Maxwell equation has the form,

$$\begin{aligned} \text{curl}(\mathbf{H}) &= (i\omega\epsilon_x + \sigma_x) E_x \mathbf{e}_x + (i\omega\epsilon_y + \sigma_y) E_y \mathbf{e}_y \\ &\quad + (i\omega\epsilon_z + \sigma_z) E_z \mathbf{e}_z \end{aligned} \quad (2.1.4)$$

However, if the stimulating electric vector has only an x component, then the same is true of the reflected, induced, and transmitted radiation, and, thus, we may assume that within the slab that this is also true. Hence, we assume that within the slab,

$$\mathbf{E} = \rho(z) \exp(-i\omega t) \mathbf{e}_x = E_x \mathbf{e}_x \quad (2.1.5)$$

Since then

$$\text{curl}(\mathbf{E}) = -\mathbf{e}_y \left(-\frac{\partial}{\partial z} \right) E_x = -i\omega\mu_y H_y \mathbf{e}_y \quad (2.1.6)$$

we conclude that

$$H_y = \frac{i}{\omega\mu_y} \frac{\partial E_x}{\partial z} \quad (2.1.7)$$

Using (3.4) we conclude that

$$\text{curl}(\mathbf{H}) = \mathbf{e}_x \left(-\frac{\partial}{\partial z} \right) H_y \quad (2.1.8)$$

which implies that

$$\begin{aligned} \text{curl}(\mathbf{H}) &= \\ \mathbf{e}_x \left[\left(\frac{i}{\omega\mu_y^2} \mu_y^{(1)}(z) \right) \frac{\partial E_x}{\partial z} - \frac{i}{\omega\mu_y} \frac{\partial^2 E_x}{\partial z^2} \right] \\ &= \mathbf{e}_x (i\omega\epsilon_x + \sigma_x) E_x \end{aligned} \quad (2.1.9)$$

Thus, multiplying all terms of this last equation by $i\omega\mu_y$ we see that

$$\begin{aligned} \frac{\partial^2 E_x}{\partial z^2} - \frac{\mu_y^{(1)}(z)}{\mu_y(z)} \frac{\partial E_x}{\partial z} \\ = (-\omega^2\mu_y\epsilon_x + i\omega\mu_y\sigma_x) E_x \end{aligned} \quad (2.1.10)$$

We are, therefore, seeking an impulse response of the equation,

$$\begin{aligned} \frac{\partial^2 E_x}{\partial z^2} + \omega^2\mu_0\epsilon_0 E_x = \\ \frac{\mu_y^{(1)}}{\mu_y} \frac{\partial E_x}{\partial z} + (\omega^2(\mu_0\epsilon_0 - \mu_y\epsilon_x) + i\omega\mu_y\sigma_x) E_x \end{aligned} \quad (2.1.11)$$

We introduce the variable

$$\tau = \omega^2\mu_y\epsilon_x - i\omega\mu_y\sigma_x - \omega^2\mu_0\epsilon_0, \quad (2.1.12)$$

where we agree that ϵ , μ , and σ take their free space values outside the slab, and assume that $E - E^i$ has the form,

$$\begin{aligned} E - E^i &= c \int_{-\infty}^{\infty} \tau \bar{E}_x \exp(-ik_0 |z - \tilde{z}|) d\tilde{z} \\ &+ b \int_{-\infty}^{\infty} \frac{\mu_y^{(1)}(\tilde{z})}{\mu_y(\tilde{z})} \frac{\partial E_x}{\partial \tilde{z}} \exp(-ik_0 |z - \tilde{z}|) d\tilde{z} \end{aligned} \quad (2.1.13)$$

where we write the global magnetic permeability via the relationship

$$\mu_y(z) = (Y(z) - Y(z-L))(\hat{\mu}_y - \mu_0) + \mu_0 \quad (2.1.14)$$

where

$$Y(z) = \begin{cases} 1 & \text{if } z \geq 0 \\ 0 & \text{if } z < 0 \end{cases} \quad (2.1.15)$$

is the Heaviside function and

$$Y^{(1)}(z) = \delta(z) \quad (2.1.16)$$

is the Dirac delta function and where we think of μ as the permeability at any point and think of $\hat{\mu}$ as the value of permeability inside the slab. Thus, with this definition and recognizing the tangential component of the magnetic field as being proportional to the reciprocal of the the magnetic permeability times the derivative of the electric vector with respect to z in view of the relationship

$$H_y = \frac{i}{\omega\mu_y} \frac{\partial E_x}{\partial z}$$

and seek a representation of the form,

$$\begin{aligned} E_x - E^i &= c \int_0^L \tau E_x \exp(-ik_0 |z - \tilde{z}|) d\tilde{z} \\ &+ b \int_0^L \frac{\mu_y^{(1)}(\tilde{z})}{\mu_y(\tilde{z})} \frac{\partial E_x}{\partial \tilde{z}} \exp(-ik_0 |z - \tilde{z}|) d\tilde{z} \\ &+ b \left(1 - \frac{\mu_0}{\mu_y(0)}\right) \frac{\partial E_x}{\partial z}(0) \exp(-ik_0 z) \\ &- b \left(1 - \frac{\mu_0}{\mu_y(L)}\right) \frac{\partial E_x}{\partial z}(L) \exp(ik_0 z) \exp(-ik_0 L) \end{aligned} \quad (2.1.17)$$

Theorem 2.1 If E_x satisfies (2.1.17) and E_x is twice continuously at points inside and outside the slab, then (a) outside the slab $E - E^i$ has the representation

$$E - E^i = \begin{cases} C^r \exp(ik_0 z) & \text{for } z < 0 \\ C^t \exp(-ik_0 z) & \text{for } z > L \end{cases} \quad (2.1.18)$$

where C^r is the reflection coefficient, and C^t is the coefficient defining the transmitted radiation (c) if a function E_x that is differentiable inside and outside the slab satisfies the integral equation, then E_x is continuous on the entire real line, and furthermore, if $H - H^i$ is determined from (2.1.17) via the relationship

$$\begin{aligned} H - H^i &= \frac{-i}{2\omega\mu_0} \int_0^L \tau E_x \exp(-ik_0(z - \tilde{z})) d\tilde{z} \\ &+ \frac{i}{2\omega\mu_0} \int_0^L \tau E_x \exp(-ik_0(\tilde{z} - z)) d\tilde{z} \\ &+ \frac{i}{2\omega\mu_0} \int_0^L \frac{\mu_y^{(1)}(\tilde{z})}{\mu_y} \frac{\partial E_x}{\partial \tilde{z}} \exp(-ik_0(z - \tilde{z})) d\tilde{z} \end{aligned}$$

$$\begin{aligned}
& + \frac{-i}{2\omega\mu_0} \int_z^L \frac{\mu_y^{(1)}(z)}{\mu_y} \frac{\partial E_x}{\partial \tilde{z}} \exp(-ik_0(\tilde{z} - z)) d\tilde{z} \\
& + \frac{i}{2\omega\mu_0} \left(1 - \frac{\mu_0}{\mu_y(0)}\right) \frac{\partial E_x}{\partial z}(0) \exp(-ik_0 z) \\
& + \frac{i}{2\omega\mu_0} \left(1 - \frac{\mu_0}{\mu_y(L)}\right) \frac{\partial E_x}{\partial z}(L) \exp(ik_0 z) \exp(-ik_0 L)
\end{aligned} \tag{2.1.19}$$

and $H - H^i$ is continuous across the boundaries of the magnetic slab. Furthermore, the classical solutions of the integral equation (2.1.17) are solutions of Maxwell's equations provided that

$$b = \frac{i}{2k_0} \tag{2.1.20}$$

and

$$c = -\frac{i}{2k_0} \tag{2.1.21}$$

Proof. Equations (2.1.20) and (2.1.21), which represent the evaluation of the parameters in the integral equation (2.1.17) follows by substituting (2.1.17) into Maxwell's equations. We begin by computing the first and second partial derivatives of E_x with respect to z from the integral equations and we then use these expressions to show that (2.1.20) and (2.1.21) are needed in order that Maxwell's equations be satisfied. We find, upon breaking up the integral from 0 to L into the integral from 0 to z plus the integral from z to L and differentiating, that

$$\begin{aligned}
& \frac{\partial E}{\partial z} - \frac{\partial E^i}{\partial z} = c\tau E_x - c\tau E_x \\
& c(-ik_0) \int_0^z \tau E_x \exp(-ik_0(z - \tilde{z})) d\tilde{z} + \\
& c(ik_0) \int_z^L \tau E_x \exp(-ik_0(\tilde{z} - z)) d\tilde{z} + \\
& b \frac{\mu_y^{(1)}}{\mu_y} \frac{\partial E_x}{\partial \tilde{z}} \Big|_{\tilde{z}=z} - b \frac{\mu_y^{(1)}}{\mu_y} \frac{\partial E_x}{\partial \tilde{z}} \Big|_{\tilde{z}=z} + \\
& (-ik_0)b \int_0^z \frac{\mu_y^{(1)}(\tilde{z})}{\mu_y(\tilde{z})} \frac{\partial E_x}{\partial \tilde{z}} \exp(-ik_0(z - \tilde{z})) d\tilde{z} \\
& + (ik_0)b \int_z^L \frac{\mu_y^{(1)}(\tilde{z})}{\mu_y(\tilde{z})} \frac{\partial E_x}{\partial \tilde{z}} \exp(-ik_0(\tilde{z} - z)) d\tilde{z} \\
& + (-ik_0)b \left(1 - \frac{\mu_0}{\mu_y(0)}\right) \frac{\partial E_x}{\partial z}(0) \exp(-ik_0 z) \\
& - (ik_0)b \left(1 - \frac{\mu_0}{\mu_y(L)}\right) \frac{\partial E_x}{\partial z}(L) \exp(ik_0 z) \exp(-ik_0 L)
\end{aligned} \tag{2.1.22}$$

We now take the derivative of both sides of this last equation with respect to z obtaining

$$\frac{\partial^2 E}{\partial z^2} - \frac{\partial^2 E^i}{\partial z^2} =$$

$$\begin{aligned}
& c(-ik_0)^2 \int_0^z \tau E_x \exp(-ik_0(z - \tilde{z})) d\tilde{z} + (-ik_0)c\tau E_x \\
& - (ik_0)c\tau E_x + c(ik_0)^2 \int_z^L \tau E_x \exp(-ik_0(\tilde{z} - z)) d\tilde{z} + \\
& (-ik_0)b \frac{\mu_y^{(1)}(\tilde{z})}{\mu_y(\tilde{z})} \frac{\partial E_x}{\partial \tilde{z}} \Big|_{\tilde{z}=z} + (-ik_0)^2 b \int_0^z \frac{\mu_y^{(1)}(\tilde{z})}{\mu_y(\tilde{z})} \frac{\partial E_x}{\partial \tilde{z}} \exp(-ik_0(z - \tilde{z})) d\tilde{z} + \\
& - (ik_0)b \frac{\mu_y^{(1)}(\tilde{z})}{\mu_y(\tilde{z})} \frac{\partial E_x}{\partial \tilde{z}} \Big|_{\tilde{z}=z} + (-ik_0)^2 b \int_z^L \frac{\mu_y^{(1)}(\tilde{z})}{\mu_y(\tilde{z})} \frac{\partial E_x}{\partial \tilde{z}} \exp(-ik_0(\tilde{z} - z)) d\tilde{z} \\
& + (-ik_0)^2 b \left(1 - \frac{\mu_0}{\mu_y(0)}\right) \frac{\partial E_x}{\partial z}(0) \exp(-ik_0 z) \\
& - (ik_0)^2 b \left(1 - \frac{\mu_0}{\mu_y(L)}\right) \frac{\partial E_x}{\partial z}(L) \exp(ik_0 z) \exp(-ik_0 L) \quad (2.1.23)
\end{aligned}$$

We now make use of the fact that

$$\begin{aligned}
-k_0^2(E - E^i) = & -k_0^2 \left\{ c \int_0^L \tau E_x \exp(-ik_0 |z - \tilde{z}|) d\tilde{z} \right. \\
& + b \int_0^L \frac{\mu_y^{(1)}(z)}{\mu_y} \frac{\partial E_x}{\partial \tilde{z}} \exp(-ik_0 |z - \tilde{z}|) d\tilde{z} \\
& + b \left(1 - \frac{\mu_0}{\mu_y(0)}\right) \frac{\partial E_x}{\partial z}(0) \exp(-ik_0 z) \\
& \left. - b \left(1 - \frac{\mu_0}{\mu_y(L)}\right) \frac{\partial E_x}{\partial z}(L) \exp(ik_0 z) \exp(-ik_0 L) \right\} \quad (2.1.24)
\end{aligned}$$

and substitute it into our equation for the difference between the second partial derivatives of the stimulated and incident electric field vectors. Rewriting (2.1.23) to make this substitution transparent we see that

$$\begin{aligned}
& \frac{\partial^2 E}{\partial z^2} - \frac{\partial^2 E^i}{\partial z^2} = \\
& - (k_0)^2 \left\{ c \int_0^z \tau E_x \exp(-ik_0(z - \tilde{z})) d\tilde{z} \right. \\
& + c \int_z^L \tau E_x \exp(-ik_0(\tilde{z} - z)) d\tilde{z} \\
& + b \int_0^z \frac{\mu_y^{(1)}(\tilde{z})}{\mu_y(\tilde{z})} \frac{\partial E_x}{\partial \tilde{z}} \exp(-ik_0(z - \tilde{z})) d\tilde{z} \\
& + b \int_z^L \frac{\mu_y^{(1)}(\tilde{z})}{\mu_y(\tilde{z})} \frac{\partial E_x}{\partial \tilde{z}} \exp(-ik_0(\tilde{z} - z)) d\tilde{z} \\
& \left. + b \left(1 - \frac{\mu_0}{\mu_y(0)}\right) \frac{\partial E_x}{\partial z}(0) \exp(-ik_0 z) \right.
\end{aligned}$$

$$\begin{aligned}
& - b \left(1 - \frac{\mu_0}{\mu_y(L)} \right) \frac{\partial E_x}{\partial z} (L) \exp(ik_0 z) \exp(-ik_0 L) \Big\} \\
& - 2(ik_0)c\tau E_x + 2(-ik_0)b \frac{\mu_y^{(1)}(z)}{\mu_y(z)} \frac{\partial E_x}{\partial z}
\end{aligned} \tag{2.1.25}$$

Simplifying the above equation we find that

$$\begin{aligned}
& \frac{\partial^2 E}{\partial z^2} - \frac{\partial^2 E^i}{\partial z^2} = -k_0^2(E_x - E_x^i) \\
& - 2cik_0\tau E_x - 2ik_0b \frac{\mu_y^{(1)}(z)}{\mu_y(z)} \frac{\partial E_x}{\partial z}
\end{aligned} \tag{2.1.26}$$

We next simplify this equation by making use of the fact that the electric vector, E_x^i , of the incident radiation satisfies the free space Helmholtz equation

$$\frac{\partial^2 E^i}{\partial z^2} + k_0^2 E^i = 0 \tag{2.1.27}$$

Substituting this into the previous equation we find that

$$\begin{aligned}
& \frac{\partial^2 E_x}{\partial z^2} + k_0^2 E_x = \\
& - 2cik_0\tau E_x - 2ik_0b \frac{\mu_y^{(1)}(z)}{\mu_y(z)} \frac{\partial E_x}{\partial z}
\end{aligned} \tag{2.1.28}$$

We now need to select c and b in the above equation so that the equation is identical to equation (2.1.11) where τ is given by

$$\begin{aligned}
\tau &= \omega^2 \mu_y \epsilon_x - i\omega \mu_y \sigma_x - \omega^2 \mu_0 \epsilon_0 \\
&= k^2 - k_0^2 = k^2 - \omega^2 \mu_0 \epsilon_0
\end{aligned} \tag{2.1.29}$$

We see that we need

$$- 2ik_0b = 1 \tag{2.1.30}$$

and

$$2ik_0c = 1 \tag{2.1.31}$$

In order to define the operations we note here that, while it is true that we cannot in general multiply distributions, certain orders of distributions can act upon spaces larger than the infinitely differentiable functions. For example, order 0 distributions can act on the continuous functions with compact support, and order one distributions can act on the differentiable functions with compact support, et cetera which will enable us to define the product of an order 0 distribution u and a continuous function f by the rule,

$$(uf, \phi) = (u, f\phi) \tag{2.1.32}$$

where ϕ is a test function. However, the function uf is not a general distribution, but is a continuous linear functional on the space of continuous functions with compact support. The integral equation is then derived by recognizing that in view of equation (2.1.9) that

$$\begin{aligned} \frac{\partial^2 E_x}{\partial z^2} + k_0^2 E_x = \\ - i\omega\mu_y^{(1)}(z)H_y - \tau E_x \end{aligned} \quad (2.1.33)$$

By convolving the fundamental solution of the left side of this equation with the right side we obtain the integral equation. Since, as we have shown ([6], [21]), every solution of the integral equation is a solution of Maxwell's equations and the solutions of the integral equation satisfy automatically the Silver Mueller radiation conditions and tangential components of the electric and magnetic vectors are automatically continuous across the boundaries, the solution of the integral equation is necessarily the solution of Maxwell's equations. Since the solution to this electromagnetic interaction problem is unique, the function space under consideration is the space of functions which are, along with their derivatives, continuous up to the boundaries. When the slab is nonmagnetic, then uniqueness may be proven in the function space ([21], pp 69-130) consisting of all vector valued functions ϕ such that

$$\int_{\Omega} |\phi|^2 dv + \int_{\Omega} |\text{curl}(\phi)|^2 dv < \infty \quad (2.1.34)$$

3 DISCRETIZATION

To approximate the integral equations on a computer with a finite memory, we divide the slab with which the radiation is interacting into thin wafers separated by planes whose normals are perpendicular to the planes defining the boundaries of the slab.

3.1 PIECEWISE LINEAR APPROXIMATION

We consider approximate integral equations of the form

$$\begin{aligned} \vec{E}(z) - \vec{E}^i(z) = \\ \sum_{j=1}^N \int_{z_{j-1}}^{z_j} \{A_j + B_j(y - z_j^*)\} K(z, y) dy + \\ \sum_{j=1}^N \int_{z_{j-1}}^{z_j} B_j L(z, y) dy + \\ F(z)B_1 - G(z)B_N \end{aligned} \quad (3.1.1)$$

where we suppose that the numbers z_j are defined by

$$0 = z_0 < z_1 < \dots < z_{j-1} < z_j < \dots < z_N = L \quad (3.1.2)$$

and that within the subinterval (z_{j-1}, z_j) , the electric vector is approximated by

$$\vec{E} = (A_j + B_j(z - z_j^*))\vec{e}_x, \quad (3.1.3)$$

where the constants A_j and B_j contain the $\exp(i\omega t)$ time dependence. We have a separate equation for each value of z . At this stage there are several methods to obtain a matrix equation from this continuum of approximate equations. One obvious method is point matching by selecting two points ζ_{2j-1} and ζ_{2j} in the subinterval $[z_{j-1}, z_j]$. This gives us a system of $2N$ equations in $2N$ unknowns, which have the form

$$\begin{aligned} E(\zeta_{2\ell-q+1}) - E^i(\zeta_{2\ell-q+1}) = \\ A_\ell + B_\ell(\zeta_{2\ell-q+1} - z_\ell^*) - E^i(\zeta_{2\ell-q+1}) = \\ \sum_{j=1}^N \int_{z_{j-1}}^{z_j} \{A_j + B_j(y - z_j^*)\} K(\zeta_{2\ell-q+1}, y) dy + \\ \sum_{j=1}^N \int_{z_{j-1}}^{z_j} B_j L(\zeta_{2\ell-q+1}, y) dy + \\ F(\zeta_{2\ell-q+1}) B_1 - G(\zeta_{2\ell-q+1}) B_N \end{aligned} \quad (3.1.4)$$

Defining

$$\delta_{(j,\ell)} = \begin{cases} 1 & j = \ell \\ 0 & j \neq \ell \end{cases} \quad (3.1.5)$$

We now use the delta function notation to rewrite the previous equation to make it look like a matrix equation. We find that

$$\begin{aligned} \sum_{j=1}^N \delta_{(j,\ell)} \{A_j + B_j(\zeta_{2\ell-q+1} - z_j^*)\} \\ - \sum_{j=1}^N \left\{ A_j \int_{z_{j-1}}^{z_j} K(\zeta_{2\ell-q+1}, y) dy + \right. \\ \left. B_j \int_{z_{j-1}}^{z_j} (y - z_j^*) K(\zeta_{2\ell-q+1}, y) dy \right\} - \\ \sum_{j=1}^N \delta_{(j,1)} B_j F(\zeta_{2\ell-q+1}) + \\ \sum_{j=1}^N \delta_{(j,N)} B_j G(\zeta_{2\ell-q+1}) = E^i(\zeta_{2\ell-q+1}) \end{aligned} \quad (3.1.6)$$

We now represent this last equation in the matrix form

$$T \begin{pmatrix} A_1 \\ B_1 \\ A_2 \\ B_2 \\ \vdots \\ \vdots \\ A_N \\ B_N \end{pmatrix} = T\bar{\xi} = \begin{pmatrix} E^i(\zeta_1) \\ E^i(\zeta_2) \\ E^i(\zeta_3) \\ E^i(\zeta_4) \\ \vdots \\ \vdots \\ E^i(\zeta_{2N-1}) \\ E^i(\zeta_{2N}) \end{pmatrix} \quad (3.1.7)$$

We now describe the entries of the matrix T . Note that if we define

$$\xi_{2j-1+p} = \begin{cases} A_j & p = 0 \\ B_j & p = 1 \end{cases} \quad (3.1.8)$$

that then the system of equations may be expressed more compactly in the form

$$\sum_{j=1}^N \left(\sum_{p=0}^1 T_{(2\ell-1+q, 2j-1+p)} \xi_{2j-1+p} \right) = E^i(\zeta_{2\ell-q+1}) \quad (3.1.9)$$

where $q \in \{0, 1\}$. If $p = 0$, then for each $q \in \{0, 1\}$ we have

$$T_{(2\ell-1+q, 2j-1+p)} = \delta_{(j,\ell)} - \int_{z_{j-1}}^{z_j} K(\zeta_{2\ell-q+1}, y) dy \quad (3.1.10)$$

On the other hand if $p = 1$, then again for each $q \in \{0, 1\}$ we have

$$\begin{aligned} T_{(2\ell-1+q, 2j-1+p)} = & \\ & \delta_{(j,\ell)} (\zeta_{2\ell-q+1} - z_\ell^*) \\ & - \int_{z_{j-1}}^{z_j} K(\zeta_{2\ell-q+1}, y) dy \\ & - \int_{z_{j-1}}^{z_j} L(\zeta_{2\ell-q+1}, y) dy \\ & - \delta_{(j,1)} F(\zeta_{2\ell-q+1}) \\ & + \delta_{(j,N)} G(\zeta_{2\ell-q+1}) \end{aligned} \quad (3.1.11)$$

Therefore, the solution of the matrix equation (3.1.7)

$$T\bar{\xi} = \bar{E}^i \quad (3.1.12)$$

then gives parameters in an approximate representation of the electric vector of the induced electromagnetic field.

References

- [1] Barber, P. W., Om P. Gandhi, M. J. Hagmann, Indira Chatterjee. "Electromagnetic Absorption in a Multilayer Model of Man" *IEEE Transactions on Biomedical Engineering. Volume BME - 26, Number 7* (1979) pp 400-405
- [2] Brillouin, Leon. *Wave Propagation and Group Velocity*. New York: Academic Press (1960).
- [3] Burr, John G., David K. Cohoon, Earl L. Bell, and John W. Penn. Thermal response model of a Simulated Cranial Structure Exposed to Radiofrequency Radiation. *IEEE Transactions on Biomedical Engineering. Volume BME-27, No. 8* (August, 1980) pp 452-460.
- [4] Calderon, A. P. and A. Zygmund. "On the Existence of Certain Singular Integrals" *Acta Mathematica Volume 88* (1985) pp 85-139
- [5] Cohen, L. D., R. D. Haracz, A. Cohen, and C. Acquista. "Scattering of light from arbitrarily oriented finite cylinders." *Applied Optics. Volume 21* (1983) pp 742 - 748.
- [6] Cohoon, D. K. "Uniqueness of Solutions of Electromagnetic Interaction Problems Associated with Scattering by Bianisotropic Bodies Covered with Impedance Sheets" *IN Rassias, George M. (Editor) The Mathematical Heritage of C. F. Gauss* Singapore: World Scientific (1991) pp 119-132
- [7] Cohoon, D. K., J. W. Penn, E. L. Bell, D. R. Lyons, and A. G. Cryer. *A Computer Model Predicting the Thermal Response to Microwave Radiation SAM-TR-82-22* Brooks AFB, Tx 78235: USAF School of Aerospace Medicine. (RZ) Aerospace Medical Division (AFSC) (December, 1982).
- [8] Colton, David and Rainer Kress. *Integral Equation Methods in Scattering Theory* New York: John Wiley and Sons (1983)
- [9] Daniel, Vera V. *Dielectric Relaxation* New York: Academic Press (1967).
- [10] Glisson, A. K. and D. R. Wilton. "Simple and Efficient Numerical Techniques for Treating Bodies of Revolution" University of Mississippi. University, Mississippi USA 38677 *RADC-TR-79-22*
- [11] Gohberg, I. C. and I. A. Feldman. *Convolution Equations and Projection Methods for their Solution* Providence: American Mathematical Society (1974)
- [12] Guru, Bhag Singh and Kun Mu Chen. "Experimental and theoretical studies on electromagnetic fields induced inside finite biological bodies" *IEEE Transactions on Microwave Theory and Techniques. Volume MTT-24, No. 7* (1976).
- [13] Hagmann, M. J. and O. P. Gandhi. "Numerical calculation of electromagnetic energy deposition in man with grounding and reflector effects" *Radio Science Volume 14, Number 6* (1979) pp 23 -29

- [14] Hagmann, M. J. and O. P. Gandhi. "Numerical calculation of electromagnetic energy deposition for a realistic model of man." *IEEE Transactions on Microwave Theory and Techniques Volume MTT-27, Number 9* (1979) pp 804-809.
- [15] Hagmann, M. J. and R. L. Levin. "Nonlocal energy deposition - - problem in regional hyperthermia" *IEEE Transactions on Biomedical Engineering. Volume 33* (1986) pp 405 - 411.
- [16] Haracz, Richard, D. Leonard D. Cohen, and Ariel Cohen. "Scattering of linearly polarized light from randomly oriented cylinders and spheroids." *Journal of Applied Physics. Volume 58, Number 9* (November, 1958) pp 3322 - 3327.
- [17] Hochstadt, Harry. *The Functions of Mathematical Physics*. New York: Dover(1986).
- [18] Hörmander, Lars. *Linear Partial Differential Operators* New York: Academic Press (1963)
- [19] Jaggard, D. L. and N. Engheta. *ChirosorbTM* as an invisible medium. *Electronic Letters. Volume 25, Number 3* (February 2, 1989) pp 173-174.
- [20] Kleinman, R. E. "Low frequency electromagnetic scattering" In P. L. Uslenghi (Ed) *Electromagnetic Scattering* New York: Academic Press (1978)
- [21] Li, Shu Chen. Interaction of Electromagnetic Fields with Simulated Biological Structures. Ph.D. Thesis(Temple University, Department of Mathematics 038-16, Philadelphia, Pa 19122) (1986). 454 pages
- [22] Livesay, D. E. and Kun-Mu Chen. "Electromagnetic fields induced inside arbitrarily shaped biological bodies" *IEEE Transactions on Microwave Theory and Techniques. Volume MTT-22, Number 12* (1974) pp 1273 - 1280.
- [23] Mautz, J. R. and R. F. Harrington. "Radiation and Scattering from bodies of revolution" *Applied Science Research. Volume 20* (June, 1969) pp 405-435.
- [24] Neittaanmaki, Pekka and Jukka Saranen. "Semi - discrete Galerkin approximation methods applied to initial boundary value problems for Maxwell's equations in anisotropic inhomogeneous media." *Proceedings of the Royal Society of Edinburgh. Volume 89 A* (1981) pp 125 - 133.
- [25] Ramm, A. G. "Numerical solution of integral equations in a space of distributions." *Journal of Mathematical Analysis and Applications. Volume 110* (1980) pp 384-390
- [26] Ramm, A. G. *Theory and applications of some new classes of integral equations* New York: Springer Verlag (1980)
- [27] Saranen, Jukka. "On generalized harmonic fields in domains with anisotropic homogeneous media." *Journal of Mathematical Analysis and Applications. Volume 88, Number 1* (1982) pp 104 - 182.

- [28] Saranen, Jukka. *Some remarks about the convergence of the horizontal line method for Maxwell's equations* Jyvaskyla 10, Finland: University of Jyvaskyla Department of Mathematics. Report 23 (1980)
- [29] Shepherd, J. W. and A. R. Holt. "The scattering of electromagnetic radiation from finite dielectric circular cylinders." *Journal of Physics A. Math. Gen.* 16 (1983) pp 651-652.
- [30] Sherman, George C. and Kurt Edmund Oughston. "Description of pulse dynamics in Lorentz media in terms of energy velocity and attenuation of time harmonic waves." *Physical Review Letters, Volume 47, Number 20* (November, 1981) pp 1451 - 1454.
- [31] Shifrin, K. S. *Scattering of Light in a Turbid Medium*. Moscow - Leningrad: Gosudarstvennoye Izdatel'stvo Tekhiko - Teoreticheskoy Literatury Moscow Leningrad (1951)
- [32] Tsai, Chi-Taou, Habib Massoudi, Carl H. Durney, and Magdy F. Iskander. A Procedure for Calculating Fields Inside Arbitrarily Shaped, Inhomogeneous Dielectric Bodies Using Linear Basis Functions with the Moment Method. *IEEE Transactions on Microwave Theory and Techniques, Volume MTT-34, Number 11* (November, 1986) pp 1131-1139.
- [33] Whittaker, E. T. and G. N. Watson. *A Course of Modern Analysis* London: Cambridge University Press (1986).
- [34] Uzunoglu, N. K. and N. G. Alexopoulos and J. G. Fikioris. "Scattering from thin and finite dielectric cylinders" *Journal of the Optical Society of America. Volume 68, Number 2* (1978) pp 194 - 197.
- [35] Uzunoglu, N. K. and A. R. Holt. "The scattering of electromagnetic radiation from dielectric cylinders" *Journal of Physics A. Math. Gen. Volume 10, Number 8*
- [36] Whittaker, E. T. and G. N. Watson. *A Course of Modern Analysis* London: Cambridge University Press (1986).

BLANK

INDEX A

Index of Authors

Alexander, D.R.	191	Eversole, J.D.	51
Arnold, S.	73	Farrell, R.A.	239
Bahar, E.	143	Fastig, S.	157
Barton, J.P.	191	Fournier, G.R.	201
Benayahu, Y.	157	Frickel, R.H.	279
Bottiger, J.R.	125	Fry, E.S.	99
Brewster, M.Q.	83	Fu, X-D	47
Brock, J.	41,117	Gillespie, J.B.	61
Bronk, B.V.	135	Hadad, A.	33
Campillo, A.J.	51	Haracz, R.D.	157
Carrieri, A.H.	143	Haugland, S.M.	143
Cermak, J.E.	33	Hu, P.	109
Cohen, A.	157	Huckaby, J.L.	15
Cohen, L.D.	157	Jones, M.R.	83
Cohoon, D.K.	213,257,269	Jovanovic, S.	47
	285,365	Kendall, B.R.F.	93
Curry, B.P.	83	Lax, M.	109
Dale, J.M.	57	Liebman, L.	117
Evans, B.T.N.	201	Lim, P.	41

Lin, H.B.	51	Ray, A.K.	15
Littman, H.	47	Reinisch, L.	135
Liu, C.T.	73	Rosen, D.L.	61
Merritt, C.D.	51	Seaver, M.	9
Morgan, M.H. III	47	Stoyanov, B.J.	239
Oh, C.	99	Van De Merwe, W.P.	135
Paccione, J.	47	Vollero, M.F.	93
Padmabandu, G.G.	99	Wang, R.T.	227
Peele, J.R.	9	Weyandt, D.S.	93
Poreh, M.	33	Whitten, W.B.	57, 73
Ramsey, J.M.	57, 73		

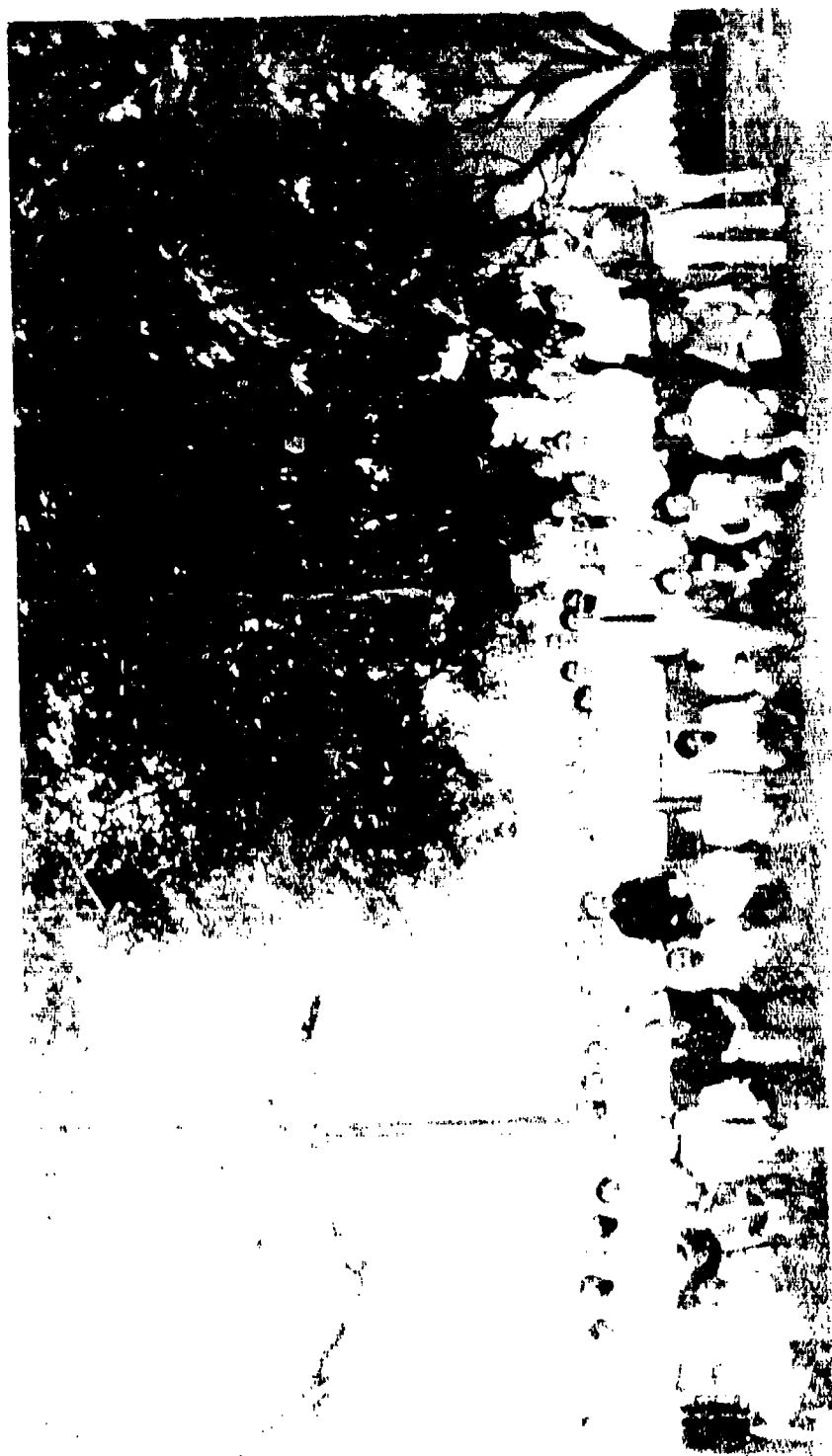
INDEX B

Index of Author's Organizations

● Argonne National Laboratory	83
● City College of New York, Physics Department	109
● Colorado State University	33
● Defense Research Establishment Valcartier	201
● Drexel University, Department of Physics & Atmospheric Sciences	157
● Hebrew University of Jerusalem, Department of Atmospheric Sciences	157
● Naval Research Laboratory	9, 51
● Oak Ridge National Laboratory	57, 73
● Pennsylvania State University, Department of Physics	93
● Polytechnic University, Department of Physics	73
● Potomac Photonics, Inc.	51
● Rensselaer Polytechnic Institute, Department of Chemical Engineering	47
● Soreq Nuclear Research Center, Department of Atmospheric Optics	157
● Space Astronomy Laboratory, Institute for Space & Technology, Inc.	227
● Technion-Israel Institute of Technology	33
● Texas A & M University, Physics Department	99
● The Johns Hopkins University, The Milton S. Eisenhower Rsch Ctr, Applied Physics Laboratory	239

• Uniformed Services University of Health Sciences	135
• U.S. Army Chemical Research, Development & Engineering Center	125, 135, 143
• U.S. Army Atmospheric Sciences Laboratory	61
• University of Illinois at Urbana-Champaign	83
• University of Kentucky, Chemical Engineering Department	15
• University of Texas, Chemical Engineering Department	41, 117
• University of Nebraska-Lincoln, Center for Electro-Optics College of Engineering	191
• University Nebraska-Lincoln, Electrical Engineering Department	143
• West Chester University	213, 257, 269, 285, 365

APPENDIX A
PHOTOGRAPH OF 1991 CONFERENCE ATTENDEES



1991 CRDEC SCIENTIFIC CONFERENCE ON OBSCURATION AND AEROSOL RESEARCH

Pictured from left to right are:

First Row

S. A. Lucas	W. B. Whitten	Bob Keesee
J. C. Swindal	N. M. Witriol	Ron Pinnick
J. P. Barton	R. H. Frickel	Ariel Cohen
P. A. Lawless	D. E. Hagen	Dennis Alexander
H. Littman	S. Arnold	Frank Poleski
Esam Khaled	David Rosen	Walter Bach
Ali Serpengüzel	B. R. Kendall	Burt Bronk
Kim Juvan	Po Hu	James B. Gillespie
Dipakbin Q. Chowdhury	Glenn Rubel	Mark Seaver
M. J. Smith	Orazio I. Sindoni	Mel Lax
Wan-Xian Wang	Jerold Bottiger	Ed Stuebing
Jing-Gang Xie	Matthew Jones	Keng Leong
Gang Chen	Morris H. Morgan, III	David Cohoon
Ru Wang	George Ritchie	David Leach
		Jay Eversole

Third Row

Second Row

Blair Evans
J. R. White
H. B. Lin

Steve Hill

Janon Embury
Lorcan Folan
Kirk Fuller
Robert Armstrong

Fourth Row

Dee W. Pack
Ed S. Fry
Howard Lee
Tony Campillo
Bill Curry

APPENDIX B

1991 CRDEC Scientific Conference on
Obscuration and Aerosol Research

Attendees List

AGNES AKINYEMI
COMMANDER
US ARMY CRDEC
ATTN SMCCR DDT/A AKINYEMI
APG MD 21010

(301) 671-5744

DENNIS ALEXANDER
UNIVERSITY OF NEBRASKA LINCOLN
CENTER FOR ELECTRO OPTICS
248 WSEC
LINCOLN NE 68588 0656

(402) 472-3091

RALPH W ALEXANDER JR
UNIVERSITY OF MISSOURI ROLLA
PHYSICS DEPARTMENT
ROLLA MO 65401

(314) 341-4781

ROBERT L ARMSTRONG
NEW MEXICO STATE UNIVERSITY
DEPARTMENT OF PHYSICS
P O BOX 3D
LAS CRUCES NM 88003

(505) 646-3832

STEPHEN ARNOLD
POLYTECHNIC INSTITUTE OF N Y
DEPT OF PHYSICS
333 JAY ST
BROOKLYN NY 11201

(718) 260-3085 (3381)

WALTER BACH
US ARMY RESEARCH OFFICE
PO BOX 12211
RESEARCH TRIANGLE PK NC 27709

(919) 549-0641

JOHN P BARTON
UNIVERSITY OF NEBRASKA LINCOLN
CENTER FOR ELECTRO OPTICS
248 WSEC
LINCOLN NE 68588 0656

(402) 472-5081

JEFFREY BERGMAN
COMMANDER
US ARMY CRDEC
SMCCR RST E BLDG E3220
APG MD 21010-5423

(301) 671-4622

JEROLD BOTTIGER
COMMANDER
US ARMY CRDEC
ATTN SMCCR RSP B/J BOTTIGER
APG MD 21010 5423

JAMES R BROCK
UNIVERSITY OF TEXAS/AUSTIN
DEPT OF CHEMICAL ENGINEERING
AUSTIN TX 78712

(512) 471-3348

ANTHONY CAMPILLO
NAVAL RESEARCH LAB
ATTN CODE 6546/A CAMPILLO
WASHINGTON DC 20375 5000

(202) 767-2057

JOHN CARPIN
COMMANDER
US ARMY CRDEC
ATTN SMCCR RST E/J CARPIN
APG MD 21010 5423

(301) 671-2764

ARTHUR H CARRIERI
COMMANDER
ATTN SMCCR DDT
APG MD 21010-5423

(301) 671-5943

LAVERNE CASH
COMMANDER
US ARMY CRDEC
ATTN SMCCR RSP B
APG MD 21014

(301) 671-4294

GANG P. CHEN
YALE UNIVERSITY
DEPT OF APPLIED PHYSICS
PO BOX 2157 YALE STATION
NEW HAVEN CT 06520

(203) 432-4235

THOMAS CHESWORTH
SEVEN MTS SCIENTIFIC INC
PO BOX 650
ROALSBURG PA 16827

(814) 466-6559

D Q CHOWDHURY
CLARKSON UNIVERSITY
ECE DEPARTMENT
POTSDAM NY 13699-5720

ARIEL COHEN
HEBREW UNIVERSITY
DEPT OF ATMOSPHERIC SCIENCES
JERUSALEM
ISRAEL

972-2-639003

DAVID COHOON
WEST CHESTER UNIVERSITY
DEPT OF MATHEMATICS
WEST CHESTER PA 19383

(215) 436-2641

WILLIAM CURRY
ARGONNE NATIONAL LAB
9700 S CASS AVENUE
ENG PHYSICS 207
ARGONNE IL 60439 4841

(708) 972-7683

EDWIN DAUBER
W L GORE & ASSOCIATES
PO BOX 1550
ELKTON MD 21922-1550

(301) 392-3300

ROBERT DOHERTY
COMMANDER
US ARMY CRDEC
ATTN SMCCR RSP B/R DOHERTY
APG MD 21010 5423

(301) 671-2326

WILLIAM H DONOVAN
COMMANDER
US ARMY CRDEC
ATTN SMCCR DDW (CPT DONOVAN
APG MD 21010-5423

(301) 671-5536

JAY EMBURY
COMMANDER
US ARMY CRDEC
ATTN SMCCR RSP-B/J EMBRY
APG MD 21010

(301) 671-2326

BLAIR EVANS
DEFENSE RESCH EST VALCARTIER
2459 PIE XI BLVD NORTH
PO BOX 8800
COURCELETTE QUEBEC
GOA 1RO

(418) 844-4299

JAY EVERSOLE
NAVAL RESEARCH LAB
ATTN CODE 6546/J EVERSOLE
WASHINGTON DC 20375 5000

(202) 767-2057

RICHARD FARRELL
JOHNS HOPKINS UNIVERSITY
APPLIED PHYSICS LAB
JOHNS HOPKINS ROAD
LAUREL MD 20707

(301) 953-6229

DENNIS FLANIGAN
COMMANDER
US ARMY CRDEC
ATTN SMCCR RSP B/D FLANNIGAN
APG MD 21010 5423

(301) 671-2760

LORCAN M FOLAN
POLYTECHNIC UNIVERSITY
DEPT OF PHYSICS
333 JAY STREET
BROOKLYN NY 11201

(718) 260-3381

DAVID FREUND
JOHNS HOPKINS UNIVERSITY
APPLIED PHYSICS LAB
JOHNS HOPKINS ROAD
LAUREL MD 20723

(301) 792-6260

ROBERT FRICKEL
COMMANDER
US ARMY CRDEC
ATTN SMCCR RSP B/R FRICKEL
APG MD 21010 5423

EDWARD FRY
TEXAS A&M UNIVERSITY
DEPT OF PHYSICS
COLLEGE STATION TX 77843

(409) 845-1910

KIRK FULLER
ATMOSPHERIC SCIENCE DEPT
COLORADO STATE UNIVERSITY
FT COLLINS CO 80523

(303) 491-8644

JAMES B GILLESPIE
US ARMY ATMOSPHERIC SCIENCES
ATTN SLCAS BW R/J GILLESPIE
WHT SANDS MISSILE RNG NM 88002

(505) 678-6609

JOHN GREEN
COMMANDER
US ARMY CRDEC
ATTN SMCCR MUT
APG MD 21010-5423

(301) 671-3190

ROBERT E GREEN
JOHNS HOPKINS UNIVERSITY
MATERIALS SCIENCE & ENG DEPT
MARYLAND HALL 102
BALTIMORE MD 21218

(301) 338-6115

DONALD HAGEN
UNIVERSITY OF MISSOURI ROLLA
CLOUD PHYSICS RESEARCH
G 7 NORWOOD HALL
ROLLA MO 65401 0249

(314) 341-4351

DICK HARACZ
DREXEL UNIVERSITY
DEPT OF PHYS & ATMOSPHERIC SCI
32ND & CHESTNUT STREETS
PHILADELPHIA PA 19104

ROGER HILASKI
COMMANDER
US ARMY CRDEC
ATTN SMCCR RST E
APG MD 21010-5423

(301) 671-4622

STEVEN HILL
US ARMY ATMOS SCIENCES LAB
WHT SANDS MISSILE RNG NM 88002

(315) 268-2904

PO HU
CITY COLLEGE OF NEW YORK
DEPT OF PHYSICS
CONVENT AVE & 138TH STREET
NEW YORK NY 10031

(212) 690-6864

MATHEW R JONES
ARGONNE NATIONAL LABORATORIES
9700 S CASS AVENUE
ENGINEERING PHYSICS 207
ARGONNE, IL 60439 4841

(310) 333-6918

KIMBERLY JUVAN
YALE UNIVERSITY
DEPT OF APPLIED PHYSICS
PO BOX 2157 YALE STATION
NEW HAVEN CT 06520

(203) 432-4234

ROBERT G KEESEE
STATE UNIVERSITY OF NEW YORK
DEPT OF ATMOSPHERIC SCIENCES
ALBANY NY 12222

(814) 863-3574

BRUCE KENDALL
PENNSYLVANIA STATE UNIVERSITY
DEPT OF PHYSICS
104 DAVEY LABORATORY
UNIVERSITY PARK PA 16802

(814) 863-0080

MILTON KERKER
CLARKSON UNIVERSITY
POTSDAM NY 13676

(315) 268-2390

ESAM KHALED
CLARKSON UNIVERSITY
ECE DEPARTMENT
POTSDAM NY 13678

(315) 263-0032

JAMES D KLETT
PAR ASSOCIATES
4507 MOCKINGBIRD ST
LAS CRUCES NM 88001

(505) 521-9448

THOMAS J KULLE
COMMANDER
US ARMY CRDEC
ATTN SMCCR PPI APSILLAB
APG MD 21010-5423

(301) 671-4204/2519

JOE KURTZ
CODE 691
NASA GODDARD SPACE FLIGHT CNTR
GREENBELT MD 20771

(301) 286-4452

PHIL A LAWLESS
RESEARCH TRIANGLE INSTITUTE
PO BOX 12194
RESEARCH TRIANGLE PK NC 27709

(919) 541-6782

MELVIN LAX
CITY COLLEGE OF NEW YORK
PHYSICS DEPT
NEW YORK NY 10031

(212) 650-6864

DAVID LEACH
YALE UNIVERSITY
DEPT OF APPLIED PHYSICS
PO BOX 2157 YALE STATION
NEW HAVEN CT 06520

(203) 432-4234

M HOWARD LEE
UNIVERSITY OF GEORGIA
DEPT OF PHYSICS
ATHENS GA 30602

(404) 542-3539

KENG H LEONG
ARGONNE NATIONAL LAB
BLDG 207
9700 S CASS AVE
ARGONNE IL 60439 4841

(708) 972-3254

THOMAS R LETTIERI
NATIONAL INSTITUTE OF
STANDARDS AND TECHNOLOGY
MET A117
GAITHERSBURG MD 20899

(301) 975-3496

H B LIN
NAVAL RESEARCH LAB
ATTN CODE 6546/H B LIN
WASHINGTON DC 20375 5000

(202) 767-2057

HOWARD LITTMAN
RENSSELAER POLYTECH INSTITUTE
DEPT OF CHEMICAL ENGINEERING
131 RICKETTS BUILDING
TROY NY 12180 3590

(518) 276-6039

S A LUCES
PHYSICAL SCIENCE LAB
NMSU
LAS CRUCES NM 88003

FOUAD G MAJOR
THE CATHOLIC UNIV OF AMERICA
PHYSICS DEPT
HANNAN HALL
WASHINGTON DC 20064

(202) 319-6193

SEBASTIAN MASTRANGELO
DUPONT COMPANY
15 YORKRIDGE TRAIL
HOCKESSIN DE 19707

(302) 239-7893

MORRIS H MORGAN
RENSSELAER POLYTECH INSTITUTE
DEPT OF CHEMICAL ENGINEERING
131 RICKETTS BLDG
TROY NY 12180 3590

(518) 276-6059

DEE PACK
THE AEROSPACE CORPORATION
SPACE & ENVIRONMENTAL TECH CTR
M2/251, P.O. BOX 92957
LOS ANGELES, CA 90009 2957

ERICA PETERSEN
COMMANDER
US ARMY CRDEC
ATTN SMCCR RSP-B/E PETERSEN
APG MD 21010 5423

(301) 671-4294

RONALD PINNICK
US ARMY ATMOSPHERIC SCIENCES
ATTN SLCAS AR/R PINNICK
WHITE SANDS MISSILE RANGE
NM 88002 5501

(505) 678-5634

FRANKLIN POLESKI
COMMANDER US ARMY FOREIGN
SCIENCE AND TECHNOLOGY CENTER
ATTN AIFRIB/F POLESKI
220 SEVENTH ST NE
CHARLOTTESVILLE VA 22901

(804) 980-7868

MICHAEL POREH
COLORADO STATE UNIVERSITY
ENGINEERING RESEARCH CENTER
FORT COLLINS CO 80523

(303) 491-8204

MARVIN QUERRY
UNIVERSITY OF MISSOURI
342 ADMINISTRATIVE CENTER
KANSAS CITY MO 64110

(816) 276-2504

ASIT RAY
UNIVERSITY OF KENTUCKY
DEPT OF CHEMICAL ENGINEERING
161 ANDERSON HALL
LEXINGTON KY 40502

(606) 257-7990

CHUN-HSUN RIN
COMMANDER
US ARMY CRDEC
ATTN SMCCR DDW/C H RIN
APG MD 21010 5423

(301) 671-2140

GEORGE RITCHIE
RIDER COLLEGE
2083 LAWRENCEVILLE RD
LAWRENCEVILLE NJ 08648

(609) 895-5415

RON C ROBBINS
COMMANDER
US ARMY CRDEC
ATTN SMCCR DDT
APG MD 21010-5423

(301) 671-5558

D ROSEN
U.S. ARMY ATMOSPHERIC SCIENCES
ATTN SLCAS BW 3/D ROSEN
WHT SANDS MISSILE RNG NM 88002

WILLIAM ROUSE
COMMANDER
US ARMY CRDEC
ATTN SMCCR MUD
APG MD 21010-5423

(301) 671-3016

DANIEL ROUSEFF
JHU/APL
JOHNS HOPKINS ROAD
LAUREL MD 20723

(301) 792-5000/8540

HARRY SALEM
COMMANDER IJS ARMY
CRDEC RSCH DIR TOXICOLOGY DIV
ATTN SMCCR RST/H SALEM
APG MD 21010 5423

(301) 671-3034

MARK SEAVER
NAVAL RESEARCH LAB
ATTN CODE 6540/M SEAVER
WASHINGTON DC 20375 5000

(202) 767-9422-

ALI SERPENGUZEL
YALE UNIVERSITY
DEPT OF APPLIED PHYSICS
PO BOX 2157 YALE STATION
NEW HAVEN CT 06520

(203) 432-4235

TROY SHAVER
UNIVERSITY OF TENNESSEE
BH GOETHEST PARKWAY
TULLAHOMA TN 37388

(615) 455-0631 EXT. 357

ORAZIO SINDONI
COMMANDER
US ARMY CRDEC
ATTN SMCCR RSP-B/O SINDONI
APG MD 21010 5423

(301) 671-4404

MICHAEL J SMITH
COMMANDER
US ARMY CRDEC
P O BOX 49
GUNPOWDER BR
APG MD 21014

(301) 671-2326

BASIL STOYANOV
JOHNS HOPKINS UNIVERSITY
JOHNS HOPKINS
APPLIED PHYSICS LABORATORY
LAUREL MD 20707

(301) 953-6261

EDWARD STUEBING
COMMANDER
US ARMY CRDEC
ATTN SMCCR RSP-B/E STUEBING
APG MD 21010

(301) 671-3089

CHRIS SWINDAL
DEPT OF APPLIED PHYSICS
YALE UNIVERSITY
P O BOX 2157 YALE STATION
NEW HAVEN CT 06520-2157

(203) 432-4321

RICARDO TORRES
COMMANDER
US ARMY CRDEC
ATTN SMCCR-DDT
APG MD 21010-5423

(301) 671-5568

TATE H TSANG
UNIVERSITY OF KENTUCKY
DEPT OF CHEMICAL ENGINEERING
LEXINGTON KY 40506 0046

(606) 257-2825

WILLEM VAN DE MERWE
UNIFORMED SERVICES UNIV
OF HEALTH SCIENCES
LASER BIOPHYSICS CENTER
4301 JONES BRIDGE ROAD
BETHESDA MD 20814 4799

(301) 295-5674

RU T WANG
INSTITUTE OF SPACE SCIENCE
& TECHNOLOGY
SPACE ASTRONOMY LAB
1810 N W 6TH STREET
GAINESVILLE FL 32609

(904) 371-4778

WAN-XIAN WANG
INSTITUTE FOR SPACE SCIENCE
& TECHNOLOGY
SPACE ASTRONOMY LAB
1810 N W 6TH STREET
GAINESVILLE FL 32609

(904) 371-4778

JOHN R WHITE
COMMANDER
US ARMY CRDEC
ATTN SMCCR RSP-B/J R WHITE
APG MD 21010 5423

W B WHITTEN
OAK RIDGE NATIONAL LAB
ANALYTICAL CHEM DIV MS 6142
PO BOX 2008
OAK RIDGE TN 37831

(615) 574-4921

NORMAN WITRIOL
COMMANDER
US ARMY CRDEC
ATTN SMCCR RSP B/O
APG MD 21010-5423

(301) 278-7067

J G XIE
MEW MEXICO STATE UNIVERSITY
PHYSICS DEPARTMENT
BOX 3D
LAS CRUCES, NM 88003

(505) 646-5199

CURTIS ZIMMERMAN
COMMANDER
US ARMY CRDEC
ATTN SMCCR RSP B
GEO CENTERS
APG MD 21010-5423

(301) 671-4294

BLANK

TECHNICAL AGENDA

MONDAY, 24 JUNE

- 9:00 Registration
- 9:50 Opening *Edward W. Stuebing*, Coordinator, CRDEC
- Welcome *Michael A. Parker*, Technical Director, CRDEC
- Announcements, *Deborah Clark*, Administrative Host, Battelle

I. AEROSOL DYNAMICS

A. VAPOR - PARTICLE INTERACTIONS

Moderator: Glenn Rubel

- 10:10 *M.E. Seaver* (NRL), Condensation of Organic Vapors onto Evaporating Water drops
- 10:30 *K. Leong* (Argonne), Adsorption of Heavy Alcohols onto Simulated Atmospheric Aerosols
- 10:50 *A.K. Ray* and *J. L. Huckaby* (Univ. of KY), Characterization of Absorbed Layers on Single Particles by Elastic and Raman Scattering
- 11:20 *J.R. Brock*, *C-W Chong*, *B. J. Jurcik* (Univ. of TX/Austin), Formation and Growth of Particles in Rapidly Expanding Flows
- 11:50 LUNCH

B. TRANSPORT AND DISPERSION OF AEROSOLS

- 1:15 *J.R. Brock* (Univ. of TX/Austin), Formation and Growth of Conductive Carbon Fibers in Corona Discharges
- 1:35 *T. Tsang* (Univ. of KY), Second Order Closure Modeling of Dispersion of Smoke in Convective Boundary Layers
- 1:55 *M. Poreh* and *J. E. Cermak* (CO State Univ.), Statistical Analysis of Concentration Fluctuations for Plumes in Simulated ASL
- 2:15 *H. Littman*, *M. H. Morgan III*, and *J. D. Paccione* (RPI), Transport of Particulate Aerosols in Pipes
- 2:35 BREAK

II. AEROSOL CHARACTERIZATION METHODS

B. PHYSICAL CHARACTERIZATION - LIGHT SCATTERING AND INVERSION (Cont.)

- 3:15 *B.P. Curry* and M. R. Jones (Argonne), Single Particle Inversion Study
- 3:35 *J. Bottiger* (CRDEC), Feasibility of Direct Inversion for Small Spheres
- 3:55 *M. Lax* and P. Hu (CUNY), Semi-Binary Decisions from Light Scattering Data
- 4:15 *P.A. Lawless* and S.V.R. Mastrangelo (Research Triangle Institute), Stochastic Reconstruction-A New Data Inversion Technique
- 4:35 Adjourn

WEDNESDAY, 26 JUNE

II. AEROSOL CHARACTERIZATION METHODS

B. PHYSICAL CHARACTERIZATION - LIGHT SCATTERING AND INVERSION (Cont.)

- 8:30 *E. Fry*, G. G. Padmabandee, and C. Oh (TX A & M Univ.), Measurements of Scattering At and Near 0° by Glass Fibers

III. NONLINEAR EFFECTS

Moderator: John White

- 8:50 *R.L. Armstrong*, J-G Xie, T.E. Ruekgauer, and R.G. Pinnick (NMSU), Evaporative Instability in Pulsed Laser-Heated Droplets
- 9:10 *J.P. Barton* and D. R. Alexander (Univ. of NB/Lincoln), Recent Progress Concerning Electromagnetic Field Calculations for a Beam Incident Upon an Arbitrary Particle
- 9:30 *G. Chen* (Yale Univ.), S. Hill, P. Barber (Clarkson Univ.), and R. K. Chang (Yale), Frequency Splitting of Degenerate Spherical Cavity Modes due to Shape Distortion of Flowing Droplets
- 9:50 BREAK
- 10:30 *K. Juvan*, D. Leach and R. Chang (Yale Univ.), Phase-Modulation Broadening of Elastic Scattering due to Intensity-Dependent Index of Refraction Effects

OVERVIEW AND DISCUSSION

- 10:50 *E.W. Stuebing* (CRDEC), Overview of Aerosol Research Program and Discussion of Directions for Future Research in the CRDEC Aerosol Science Program

- 11:50 LUNCH

A. POSTER PREVIEWS (Auditorium) (Cont.)

- IV *D. Cohoon* (West Chester Univ.), Algorithms for the Determination of Electromagnetic Interaction of General Sources of Radiation with Multi-layer Bi-anisotropic Spheres and Cylinders
- IV *D. Cohoon* (West Chester Univ.), Algorithms for the Solution of Integral Equations Describing the Interaction of Radiation with General Structures and Bodies of Revolution, Including Bi-anisotropic Oblate and Prolate Spheroids
- IV *D. Cohoon* (West Chester Univ.), A Connection Between Modes of Propagation in Anisotropic Coatings and the Theory of Analytic Functions of Exponential Type
- IV *J.R. Brock* (Univ. of TX/Austin), Finite Elements Solution to Maxwell Equation

3:30 B. POSTER SESSION (Seminar Area) (3:30-5:30)

THURSDAY, 27 JUNE

IV. OPTICAL PROPERTIES OF AEROSOLS

Moderators: Orazio Sindoni, Robert Fricke

- 8:30 *D. Cohoon* (West Chester Univ.), Mueller Matrix Computations for Multilayer, Magnetically Lossy, Anisotropic Spheres
- 8:50 *R. T. Wang* (ISST), Scattering by Spheres of Narrow Size Distribution
- 9:10 *E. Bahar*, S. M. Haugland, and A. H. Carrieri (Univ. of NB/Lincoln), Mueller Matrix Elements for Optically Thin Chemical Coating Layers Over Rough Surfaces
- 9:30 BREAK
- 9:50 *A. Pluchino* and D. W. Pack (Aerospace Corp), A Close Up Look at the Rainbow
- 10:10 *S. Hill*, P. Barber, D. Q. Chowdhury, M. Mazundir, and E. Khaled (Clarkson Univ.), Resonances in Inhomogeneous Droplets
- 10:30 *M. Kerker* (Clarkson Univ.), Scattering of Evanescent Wave by a Particle on a Surface
- 10:50 BREAK
- 11:10 *B. Evans* and G. R. Fournier (Defence Research Establishment Valcartier), Bridging the Gap Between the Rayleigh and Thomson Limits for Various Convex Bodies
- 11:30 *L.D. Cohen*, A. Cohen, R. D. Haracz (Drexel Univ.), A. Ben-David (Science and Tech. Corp), and Y. Benayahu (Soreq Nuclear Research Center), Cloud Particle Size Distribution Functions from LIDAR Multiple Scattering